

AD-A213 297

WRDC-TR-89-3074
Volume II

STRESS INTENSITY FACTORS FOR CRACKING
METAL STRUCTURES UNDER RAPID THERMAL LOADING

VOL II - Theoretical Background

An-Yu Kuo, Peter C. Riccardella, Shu S. Tang and Curtis S. Carney

Structural Integrity Assoc. Inc.
3150 Almaden Expressway, Suite 226
San Jose, CA 95118-1250

and

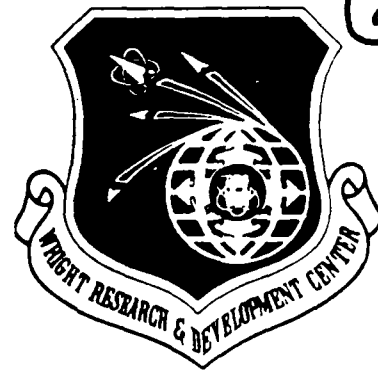
Reji John
G. A. Hartman
Joseph P. Gallagher
J. L. Kroupa

University of Dayton Research Institute
Dayton, OH 45469

August 1989

Final Report For Period October 1987 - April 1989

Approved for public release; distribution is unlimited



DTIC
ELECTE
OCT 10 1989
S B D

FLIGHT DYNAMICS LABORATORY
WRIGHT RESEARCH AND DEVELOPMENT CENTER
AIR FORCE SYSTEMS COMMAND
WRIGHT-PATTERSON AIR FORCE BASE, OHIO 45433-6553

89 10 10100

NOTICE

When Government drawings, specifications, or other data are used for any purpose other than in connection with a definitely Government-related procurement, the United States Government incurs no responsibility or any obligation whatsoever. The fact that the government may have formulated or in any way supplied the said drawings, specifications, or other data, is not to be regarded by implication, or otherwise in any manner construed, as licensing the holder, or any other person or corporation; or as conveying any rights or permission to manufacture, use, or sell any patented invention that may in any way be related thereto.

This report is releasable to the National Technical Information Service (NTIS). At NTIS, it will be available to the general public, including foreign nations.

This technical report has been reviewed and is approved for publication.

Joseph J. Burns, Jr.
CHRISTOPHER J. MAZUR, Capt
Fatigue, Fracture & Reliability Gp
Structural Integrity Branch

George P. Sendeckyj
GEORGE P. SENDECKYJ, Act Tech Mgr
Fatigue, Fracture & Reliability Gp
Structural Integrity Branch

FOR THE COMMANDER

James L. Rudd
JAMES L. RUDD, Chief
Structural Integrity Branch
Structures Division

If your address has changed, if you wish to be removed from our mailing list, or if the addressee is no longer employed by your organization please notify WRDC/FIBEC, WPAFB, OH 45433-6553 to help us maintain a current mailing list.

Copies of this report should not be returned unless return is required by security considerations, contractual obligations, or notice on a specific document.

REPORT DOCUMENTATION PAGE

Form Approved
OMB No. 0704-0188

1- REPORT SECURITY CLASSIFICATION unclassified			1b RESTRICTIVE MARKINGS		
2a. SECURITY CLASSIFICATION AUTHORITY			3. DISTRIBUTION / AVAILABILITY OF REPORT Approved for public release; distribution unlimited		
2b. DECLASSIFICATION / DOWNGRADING SCHEDULE					
4. PERFORMING ORGANIZATION REPORT NUMBER(S) SIR-89-023			5. MONITORING ORGANIZATION REPORT NUMBER(S) WRDC-TR-89-3074, Vol. II		
6a. NAME OF PERFORMING ORGANIZATION Structural Integrity Assoc., Inc.		6b. OFFICE SYMBOL (If applicable)	7a. NAME OF MONITORING ORGANIZATION Flight Dynamics Laboratory (WRDC/FIBEC) Wright Research & Development Center		
6c. ADDRESS (City, State, and ZIP Code) 3150 Almaden Expressway, Suite 226 San Jose, CA 95118-1250			7b. ADDRESS (City, State, and ZIP Code) Wright-Patterson AFB, OH 45433-6553		
8a. NAME OF FUNDING / SPONSORING ORGANIZATION DOD SBIR Program Office		8b. OFFICE SYMBOL (If applicable)	9. PROCUREMENT INSTRUMENT IDENTIFICATION NUMBER F33615-87-C-3250		
8c. ADDRESS (City, State, and ZIP Code) Washington D.C. 20301-0001			10. SOURCE OF FUNDING NUMBERS		
	PROGRAM ELEMENT NO. 65502F	PROJECT NO. 3005	TASK NO. 40	WORK UNIT ACCESSION NO. 07	
11. TITLE (Include Security Classification) Stress Intensity Factors for Cracking Metal Structures Under Rapid Thermal Loading: Volume II Theoretical Background					
12. PERSONAL AUTHOR(S) A. Kuo, P. Riccardella, S. Tang, C. Carney, R. John, G. Hartman, J. Gallagher & J. Kroupa					
13a. TYPE OF REPORT Final		13b. TIME COVERED FROM 10 87 TO 04 89		14. DATE OF REPORT (Year, Month, Day) August 1989	
15. PAGE COUNT 367					
16. SUPPLEMENTARY NOTATION This is a Small Business Innovative Research Program, Phase II Final Report					
17. COSATI CODES			18. SUBJECT TERMS (Continue on reverse if necessary and identify by block number)		
FIELD	GROUP	SUB-GROUP	Stress Intensity Factor, Fracture Mechanics, Rapid Thermal Pulse, Crack Growth, High Temperature, Analysis		
13	13				
20	05				
19. ABSTRACT (Continue on reverse if necessary and identify by block number)					
<p>An SBIR Phase II study has been conducted on a novel method of calculating cracktip stress intensity factors for cracked metal structures under rapid thermal pulse loadings. The work couples a Green's function integration technique for transient thermal stresses with the well-known influence function approach for calculating stress intensity factors. A total of seven most commonly used crack models were investigated in this study. A computer program implementing the methodology designated THERMO-K, was developed and delivered with the Phase II project report. Temperature, stress and stress intensity factor solutions predicted by THERMO-K for all seven crack models have been verified by comparing them with finite element results or experimental measurements. Operable on an IBM-pc or compatible, the program demonstrates the ability to accurately calculate stress intensity factors, with very short turnaround times, and immediate graphics visualization of the results. (Continued)</p>					
20. DISTRIBUTION / AVAILABILITY OF ABSTRACT UNCLASSIFIED/UNLIMITED <input type="checkbox"/> SAME AS RPT <input checked="" type="checkbox"/> DTIC USERS			21. ABSTRACT SECURITY CLASSIFICATION Unclassified		
22a. NAME OF RESPONSIBLE INDIVIDUAL Capt Christopher J. Mazur			22b. TELEPHONE (Include Area Code) (513) 255-6104		22c. OFFICE SYMBOL WRDC/FIBEC

19. Continued

Based on the success of this Phase II study, it is concluded that the computer program THERMO-K resulting from this study is an easy to use, fast, and accurate tool, for predicting stress intensity factors for a wide range of metallic (or other) structures of interest to the Air Force, under rapid thermal pulses. It has also been demonstrated that THERMO-K can be connected with other fracture mechanics computer programs such as MODGRO, in order to use the resulting stress intensity data in crack propagation or critical flaw size predictions.

3 The resulting THERMO-K program would thus be expected to have extensive benefits and commercial applications to the Air Force and other organizations concerned with fracture mechanics and flaw tolerant design of airframe and other structures subjected to thermal transient loading conditions.

67-20-1000

1000-1000

Acknowledgments

The authors wish to acknowledge the support and participation of Captain Chris Mazur and Dr. George Sendekyj of the Flight Dynamics Laboratory, Wright Research and Development Center.

Accession For	
NTIS GRA&I	<input checked="" type="checkbox"/>
DTIC TAB	<input type="checkbox"/>
Unannounced	<input type="checkbox"/>
Justification	
By	
Distribution/	
Availability Codes	
Dist	Avail and/or Special
A-1	



TABLE OF CONTENTS

<u>Section</u>	<u>Page</u>
1.0 INTRODUCTION AND PROGRAM SCOPE	1-1
2.0 THEORETICAL BACKGROUND OF CRACK MODEL 1 - A FINITE CRACK IN AN INFINITE PLATE	2-1
2.1 Assumptions	2-1
2.2 Governing Equations	2-2
2.3 Influence Functions for Stress Intensity Factor	2-3
2.4 Principle of Superposition	2-4
2.5 Green's Function Concept for Time Integration	2-4
2.6 Green's Function for Fully Heat Conductive Cracks Cracks	2-5
2.7 Green's Function for Partially Heat Conductive Cracks	2-9
2.8 Finite Element Verification of Crack Model 1	2-13
2.9 References	2-16
3.0 THEORETICAL BACKGROUND OF CRACK MODEL 2 - A SINGLE-EDGE CRACK IN A SEMI-INFINITE PLATE	3-1
3.1 Assumptions	3-1
3.2 Governing Equations	3-2
3.3 Influence Functions for Stress Intensity Factor	3-3
3.4 Principle of Superposition	3-4
3.5 Green's Function Concept for Time Integration	3-4
3.6 Green's Function for Fully Heat Conductive Cracks	3-5
3.7 Green's Function for Partially Heat Conductive Cracks	3-11
3.8 Finite Element Verification of Crack Model 2	3-16
3.9 References	3-19
4.0 THEORETICAL BACKGROUND OF CRACK MODEL 3 - A RADIAL CRACK EMANATING FROM A CIRCULAR HOLE	4-1
4.1 Assumptions	4-1
4.2 Governing Equations	4-2
4.3 Influence Functions for Stress Intensity Factor	4-3
4.4 Principle of Superposition	4-8
4.5 Green's Function Concept for Time Integration	4-8
4.6 Green's Function for Fully Heat Conductive Cracks	4-9
4.7 Green's Function for Partially Heat Conductive Cracks	4-16
4.8 Finite Element Verification of Crack Model 3	4-21
4.9 References	4-24

TABLE OF CONTENTS
(continued)

<u>Section</u>	<u>Page</u>
5.0 THEORETICAL BACKGROUND OF CRACK MODEL 4 - A SINGLE-EDGE CRACK PLATE	5-1
5.1 Assumptions	5-1
5.2 Governing Equations	5-2
5.3 Influence Functions for Stress Intensity Factor	5-3
5.4 Principle of Superposition	5-5
5.5 Green's Function Concept for Time Integration	5-6
5.6 Green's Function for Fully Heat Conductive Cracks	5-6
5.7 Green's Function for Partially Heat Conductive Cracks	5-14
5.8 Finite Element Verification of Crack Model 4	5-20
5.9 References	5-25
6.0 THEORETICAL BACKGROUND OF CRACK MODEL - A CENTER-CRACK PLATE	6-1
6.1 Assumptions	6-1
6.2 Governing Equations	6-2
6.3 Influence Functions for Stress Intensity Factor	6-3
6.4 Principle of Superposition	6-4
6.5 Green's Function Concept for Time Integration	6-4
6.6 Green's Function for Fully Heat Conductive Cracks	6-5
6.7 Green's Function for Partially Heat Conductive Cracks	6-13
6.8 Finite Element Verification of Crack Model 5	6-19
6.9 References	6-21
7.0 THEORETICAL BACKGROUND OF CRACK MODEL 6 - A SEMICIRCULAR SURFACE CRACK IN A HALF-SPACE	7-1
7.1 Assumptions	7-1
7.2 Governing Equations	7-2
7.3 Influence Function for Stress Intensity Factors	7-2
7.4 Principle of Superposition	7-16
7.5 Green's Function Concept for Time Integration	7-17
7.6 Green's Function for Fully Heat Conductive Cracks	7-18
7.7 Green's Function for Partially Heat Conductive Cracks	7-24
7.8 Finite Element Verification of Crack Model 6	7-30
7.9 References	7-39

TABLE OF CONTENTS
(continued)

<u>Section</u>	<u>Page</u>
8.0 THEORETICAL BACKGROUND OF CRACK MODEL 7 - A QUARTER-CIRCULAR SURFACE CRACK IN A QUARTER-SPACE .	8-1
8.1 Assumptions	8-1
8.2 Governing Equations	8-2
8.3 Influence Functions for Stress Intensity Factor .	8-2
8.4 Principle of Superposition	8-19
8.5 Green's Function Concept for Time Integration .	8-20
8.6 Green's Function for Fully Heat Conductive Cracks	8-20
8.7 Green's Function for Partially Heat Conductive Cracks	8-29
8.8 Finite Element Verification of Crack Model 7 .	8-37
8.9 References	8-44
9.0 LIMITATIONS ON DECOUPLED, LINEARIZED THEORIES	9-1
9.1 Limitation of Uncoupled, Quasi-Static Thermoelasticity Theory	9-1
9.2 Limitation of Linear Elastic Fracture Mechanics (LEFM)	9-5
9.3 Summary	9-7
9.4 References	9-7
10.0 EXPERIMENTAL VERIFICATION OF THERMO-K	10-1
10.1 Selection of Specimen Geometry and Material . .	10-1
10.2 Baseline Fracture Toughness Tests	10-3
10.3 Heat Sources - Infrared Spot Heaters	10-3
10.4 Calibration of Heat Sources	10-4
10.5 Temperature Verification Tests	10-5
10.6 Strain Verification Tests	10-7
10.7 Thermal-Mechanical Fracture Tests	10-8
10.8 Summary	10-13
10.9 References	10-14
11.0 LINKING OF THERMO-K WITH LIFE PREDICTION CODE MODGRO.	11-1
11.1 Analytical Procedure	11-1
11.2 Code Implementation	11-3
11.3 Sample Analysis	11-4
11.4 Summary	11-5
11.5 References	11-5

TABLE OF CONTENTS
(continued)

<u>Section</u>	<u>Page</u>
APPENDICES	
A EFFECTS OF CRACK SURFACE HEAT CONDUCTANCE ON STRESS INTENSITY FACTORS	A-1
B NUMERICAL INTEGRATION SCHEME FOR INTEGRATING INFLUENCE FUNCTIONS FOR 2-D CRACK MODELS	B-1
C EDGE SOLUTION FOR COMPLEMENTARY STRESS FUNCTION Ψ . . .	C-1
D INFLUENCE FUNCTIONS FOR SEMICIRCULAR CRACK IN A SEMI-INFINITE SOLID	D-1
E DETERMINATION OF THE COEFFICIENTS FOR THE APPROXIMATED MAPPING FUNCTION IN EQUATION (4-8b) . . .	E-1

LIST OF TABLES

<u>Section</u>	<u>Page</u>
7-1 Comparison of Results	7-33
10-1 Thermophysical Properties of AISI-SAE 1095 Steel . .	10-15
10-2 Results from Baseline Fracture Toughness Tests . . .	10-16
10-3 Test Program for Temperature and Strain Verification Tests	10-17
10-4 Plane Stress K_1 Values Calculated Using Different Methods	10-18
10-5 Program for Thermal-Mechanical Fracture Tests . . .	10-19
10-6 Test Results for Mode 1 Tests	10-20
10-7 Test Results for Mixed Mode Tests	10-21
11-1 Parameters Used for Fatigue Crack Growth Analysis. .	11-6
11-2 Results of Crack Growth Analyses With and Without Thermal Stresses	11-7

LIST OF FIGURES

<u>Figure</u>	<u>Page</u>
1-1 Schematic of Cracked Plate Subjected to Rapid Thermal Pulses	1-5
1-2 Crack Model 1 - A Finite Crack in an Infinite Plate.	1-6
1-3 Crack Model 2 - A Single-edge-crack in a Semi-infinite Plate	1-7
1-4 Crack Model 3 - A Radial Crack Emanating From a Circular Hole in an Infinite Plate	1-8
1-5 Crack Model 4 - Single-edge-crack in an Infinitely Long, Finite Width Plate Strip	1-9
1-6 Crack model 5 - A Center Crack in an Infinitely Long, Finite Width Plate Strip	1-10
1-7 Crack Model 6 - A Semicircular Surface Crack in a Half-space	1-11
1-8 Crack Model 7 - A Quarter-circular Crack at the Corner of a Quarter-space	1-12
2-1 A Finite Crack in an Infinite Plate Subjected to Heat Sources	2-17
2-2 Concept of Influence Function	2-18
2-3 Concept of Green's Function	2-19
2-4 A Point Heat Source in an Uncracked Plate	2-20
2-5(a) Finite Element Mesh for a Finite Crack in an Infinite Plate	2-21
2-5(b) Finite Element Mesh Near the Crack Region	2-22
2-6 Normal Stresses Due to an Instantaneous Heat Source at (2 inch, 0 inch) (Fully Conductive Crack)	2-23
2-7 Stress Intensity Factors Due to an Instantaneous Heat Source at (2 inch, 0 inch) (Fully Conductive Crack)	2-24

LIST OF FIGURES
(continued)

<u>Figure</u>	<u>Page</u>
2-8 Stress Intensity Factor Due to an Instantaneous Heat Source at (0 inch, 1 inch) (Fully Conductive Crack)	2-25
2-9 Stress Intensity Factors Due to an Instantaneous Heat Source at (1.4 inch, 0.4 inch) (Fully Conductive Crack)	2-26
2-10 Stress Intensity Factors Due to an Instantaneous Heat Source at (0.6 inch, 0.6 inch) (Fully Conductive Crack)	2-27
2-11 Stress Intensity Factors Due to an Instantaneous Heat Source at (0.6 inch, 0.6 inch) (Insulated Crack)	2-28
3-1 A Semi-Infinite Plate with a Single-edge-crack Subjected to Heat Sources	3-21
3-2 Concept of Influence Function	3-22
3-3 Concept of Green's Function	3-23
3-4 A Point Heat Source in an Uncracked Plate	3-24
3-5(a) Finite Element Mesh for Crack Model 2 Verification Problems	3-25
3-5(b) Finite Element Mesh Near Crack Region	3-26
3-6 Normal Stresses Due to an Instantaneous Heat Source at (1.5 inch, 0.5 inch) (Fully Conductive Crack).	3-27
3-7 Stress Intensity Factors Due to an Instantaneous Heat Source at (1.5 inch, 0.5 inch) (Fully Conductive Crack)	3-28
3-8 Stress Intensity Factors Due to an Instantaneous Heat Source at (1.5 inch, 0.5 inch) (Insulated Crack)	3-29
4-1 A Radial Crack Emanating From a Circular Hole in an Infinite Plate Subjected to Point Heat Sources	4-25
4-2 Concept of Influence Function Approach	4-26

LIST OF FIGURES
(continued)

<u>Figure</u>	<u>Page</u>
4-3 Conformal Mapping for Influence Function Solutions .	4-27
4-4 Concept of Green's Function Approach	4-28
4-5 An Uncracked Plate with a Circular Hole Subjected to a Point Heat Source at (r', θ')	4-29
4-6 Verification of Mode I Influence Function	4-30
4-7(a) FEM-2D Mesh for a Radial Crack Emanating From a Hole	4-31
4-7(b) Finite Element Mesh Near the Crack Region	4-32
4-8 Comparison of Temperatures at $\theta=0$ (Fully Conductive Crack)	4-33
4-9 Comparison of Normal Stresses at $\theta=0$ (Fully Conductive Crack)	4-34
4-10 Comparison of Shear Stresses at $\theta=0$ (Fully Conductive Crack)	4-35
4-11(a) Comparison of Temperature at $\theta=0$ (Insulated Crack $t = dt = 86$ sec)	4-36
4-11(b) Comparison of Temperature at $\theta=0$ (Insulated Crack $t = 3dt = 258$ sec)	4-37
4-12 Comparison of Normal Stresses at $\theta=0$ (Insulated Crack)	4-38
4-13 Comparison of Shear Stresses at $\theta=0$ (Insulated Crack)	4-39
5-1 A Single-edge-crack Plate Strip Subjected to Point Heat Sources	5-26
5-2 Concept of Influence Function	5-27
5-3 Concept of Green's Function	5-28
5-4 A Point Heat Source in an Uncracked Plate	5-29

LIST OF FIGURES
(continued)

<u>Figure</u>	<u>Page</u>
5-5 Edge Stress $\sigma_{xx}(0,y;t)$ Due to an Instantaneous Heat Source	5-30
5-6 Edge Stress $\sigma_{xx}(0,y;t)$ Due to an Instantaneous Heat Source	5-31
5-7 A Plate Strip Subjected to Arbitrary Edge Loads	5-32
5-8 A Single-edge-crack Plate Under Uniform Tension	5-33
5-9 A Single-edge-crack Plate Under Remote Bending	5-34
5-10 A Single-edge Plate Under Uniform Shear	5-35
5-11 NASTRAN Mesh for Heat Transfer and Thermal Stress Analyses for a Fully Heat Conductive Single-edge-crack	5-36
5-12 NASTRAN Mesh Near Heat Source	5-37
5-13 Comparison of Temperatures at $y=0$ for Case 5-1	5-38
5-14 Comparison of Normal Stresses at $y=0$ for Case 5-1	5-39
5-15 Comparison of Temperatures at $y=0$ for Case 5-2	5-40
5-16 Comparison of Normal Stresses at $y=0$ for Case 5-2	5-41
5-17 Comparison of Shear Stresses at $y=0$ for Case 5-2	5-42
5-18 Comparison of Temperatures at $y=0$ for Case 5-3	5-43
5-19 Comparison of Normal Stresses at $y=0$ for Case 5-3	5-44
5-20 Comparison of Shear Stresses at $y=0$ for Case 5-3	5-45
5-21 Comparison of Temperatures at $y=0$ for Case 5-4	5-46
5-22 Comparison of Normal Stresses at $y=0$ for Case 5-4	5-47
5-23 Comparison of Temperatures at $y=0$ for Case 5-5	5-48
5-24 Comparison of Normal Stresses at $y=0$ for Case 5-5	5-49
5-25 Comparison of Shear Stresses at $y=0$ for Case 5-5	5-50

LIST OF FIGURES
(continued)

<u>Figure</u>	<u>Page</u>
5-26 Comparison of Temperatures at $y=0$ for Case 5-6 . . .	5-51
5-27 Comparison of Normal Stresses at $y=0$ for Case 5-6 . . .	5-52
5-28 Comparison of Shear Stresses at $y=0$ for Case 5-6 . . .	5-53
5-29 Comparison of Temperatures at $y=0$ for Case 5-7 . . .	5-54
5-30 Comparison of Normal Stresses at $y=0$ for Case 5-7 . . .	5-55
5-31 Variation of K_I Calculated Using the Displacement Method With Distance from the Crack Tip	5-56
5-32 Comparison of Transient K_I Predicted by THERMO-K With the Finite Element Results	5-57
5-33(a) Finite Element Mesh (FEM2D) for Crack Model 4 . . .	5-58
5-33(b) Finite Element Mesh Near the Crack Region	5-59
5-34 Comparison of Temperatures at $y=0$ for an Insulated Single-edge-crack Plate (time = 100 sec.)	5-60
5-35 Comparison of Temperatures of $y=0$ for an Insulated Single-edge-crack Plate (time = 150 sec.)	5-61
5-36 Comparison of Normal Stresses at $y=0$ for an Insulated Single-edge-crack Plate	5-62
5-37 Comparison of Shear Stresses at $y=0$ for an Insulated Single-edge-crack Plate	5-63
6-1 A Center-Crack Plate Subjected to Point Heat Sources	6-22
6-2 Concept of Influence Function	6-23
6-3 Concept of Green's Function	6-24
6-4 A Point Heat Source in an Uncracked Plate	6-25
6-5 A Plate Strip Subjected to Arbitrary Edge Loads	6-26
6-6 A Center-Crack Plate Under Combined Uniform Tension and Shear	6-27

LIST OF FIGURES
(continued)

<u>Figure</u>	<u>Page</u>
6-7(a) Finite Element Mesh (FEM2D) for Crack Model 5 . . .	6-28
6-7(b) Finite Element Mesh Near the Crack Region . . .	6-29
6-8 Comparison of Temperature at $y=0$, $t = 100$ sec. . .	6-30
6-9 Comparison of Temperatures at $y=0$, $t = 150$ sec. . .	6-31
6-10 Comparison of Normal Stresses at $y=0$	6-32
6-11 Comparison of Shear Stresses at $y=0$	6-33
7-1 A Semicircular Surface Crack in a Semi-infinite Space ($y \geq 0$)	7-41
7-2(a) A Pair of Unit Normal Forces Applied at $(\bar{r}, \bar{\theta})$ of the Crack Surface	7-42
7-2(b) A Pair of Unit Radial Forces Applied at $(\bar{r}, \bar{\theta})$ of the Crack Surface	7-43
7-2(c) A Pair of Unit Tangential Forces Applied at $(\bar{r}, \bar{\theta})$ of the Crack Surface	7-44
7-3 Concept of Green's Function	7-45
7-4 An Instantaneous Heat Source in a Half-space . . .	7-46
7-5 Verification of Mode I Stress Intensity Factor of Circular Crack in an Infinite Solid	7-47
7-6 Verification of Mode II Stress Intensity Factor of Circular Crack in an Infinite Solid	7-48
7-7 Verification of Mode III Stress Intensity Factor of Circular Crack in an Infinite Solid	7-49
7-8 Comparison of Crack in a Semi-infinite Solid Results	7-50
7-9 Axisymmetric Finite Element Model for Verification of Temperature and Stress	7-51

LIST OF FIGURES
(continued)

<u>Figure</u>	<u>Page</u>
7-10 Axisymmetric Finite Element Mesh at the Crack Location	7-52
7-11 Comparison of Temperature Transients Due to a Unit Step Heat Source in a Semi-infinite Solid With a Fully Conductive Crack Surface	7-53
7-12 Comparison of Temperature Profiles Due to a Unit Step Heat Source in a Semi-infinite Solid With a Fully Conductive Crack Surface	7-54
7-13 Comparison of σ_{zz} Stress Transient Due to a Unit Step Heat Source in a Semi-infinite Solid With a Fully Conductive Crack Surface	7-55
7-14 Comparison of σ_{zz} Stress Profiles Due to a Unit Step Heat Source in a Semi-infinite Solid With a Fully Conductive Crack Surface	7-56
7-15 Axisymmetric Finite Element Model for Verification of Temperature for a Crack With Insulated Surface .	7-57
7-16 Finite Element Mesh at the Crack Region for Semicircular Crack in a Semi-infinite Solid with Insulated Crack Surface	7-58
7-17 Comparison of Temperatures Predicted by THERMO-K and Finite Element Method (T vs. Time)	7-59
7-18 Comparison of Temperatures Predicted by THERMO-K and Finite Element Method (T vs. r)	7-60
7-19 Comparison of Temperature Profiles Due to a Unit Step Heat Source in a Semi-infinite Solid With a Fully Insulated Crack Surface at t=50 and 100 Seconds	7-61
8-1 A Quarter-Circular Surface Crack in a Quarter-Space.	8-46
8-2(a) A Pair of Unit Normal Forces Applied at $(\bar{r}, \bar{\theta})$ of the Crack Surface	8-47
8-2(b) A Pair of Unit Radial Forces Applied at $(\bar{r}, \bar{\theta})$ of the Crack Surface	8-48

LIST OF FIGURES
(continued)

<u>Figure</u>	<u>Page</u>
8-2(c) A Pair of Unit Tangential Forces Applied at $(\bar{r}, \bar{\theta})$ of the Crack Surface	8-49
8-3 Concept of Green's Function	8-50
8-4 An Instantaneous Heat Source in a Quarter-Space	8-51
8-5 Verification of Mode I Stress Intensity Factor of Circular Crack in an Infinite Solid	8-52
8-6 Verification of Mode II Stress Intensity Factor of Circular Crack in an Infinite Solid	8-53
8-7 Verification of Mode III Stress Intensity Factor of Circular Crack in an Infinite Solid	8-54
8-8 Axisymmetric Finite Element Model for Verification of Temperature and Stress	8-55
8-9 Axisymmetric Finite Element Mesh at the Crack Location	8-56
8-10 Comparison of Temperature Transients Due to a Unit Step Heat Source in a Quarter-infinite Solid With a Fully Conductive Crack Surface	8-57
8-11 Comparison of Temperature Profiles Due to a Unit Step Heat Source in a Quarter-infinite Solid With a Fully Conductive Crack Surface	8-58
8-12 Axisymmetric Finite Element Model for Verification of Temperature for a Crack With Insulated Surface	8-59
8-13 Finite Element Mesh at the Crack Region for Quarter- circular Crack in a Quarter-infinite Solid With Insulated Crack Surface	8-60
8-14 Comparison of Temperatures Predicted by THERMO-K and Finite Element Method (T vs. Time)	8-61
8-15 Comparison of Temperatures Predicted by THERMO-K and Finite Element Method (T vs. r)	8-62

LIST OF FIGURES
(continued)

<u>Figure</u>	<u>Page</u>
8-16 Comparison of Temperature Profiles Due to a Unit Step Heat Source in a Semi-infinite Solid With a Fully Insulated Crack Surface at $t=50$ and 100 Seconds . . .	8-63
10-1 Overview of Specimen Geometries Used During the Experimental Verification of THERMO-K	10-22
10-2 Compact Tension Specimens Used for Baseline Fracture Toughness Test	10-23
10-3 Schematic of Thermal Loading Test Setup	10-24
10-4 Test Setup for Calibration of Heat Sources	10-25
10-5 Calibration Data and Fit Curve for the Spot Heater	10-26
10-6 Test Setup for Temperature Verification Tests	10-27
10-7 Temperature Profile Maintained at Source Location for Temperature and Strain Verification Tests	10-28
10-8 Rate of Heat Input at Source Location Corresponding to Temperature Profile in Figure 10-7	10-29
10-9 Results for Symmetrical Temperature Verification Tests at Locations 0, 1 and 2	10-30
10-10 Results for Symmetrical Temperature Verification Tests at Locations 3, 4 and 5	10-31
10-11 Results for Symmetrical Temperature Verification Tests at Locations 6, 7 and 9	10-32
10-12 Results for Symmetrical Temperature Verification Tests at Locations 10 and A	10-33
10-13 Results of Asymmetrical Temperature Verification Tests at Locations 0, 1 and 2	10-34
10-14 Results of Asymmetrical Temperature Verification Tests at Locations 3, 4 and 5	10-35
10-15 Results of Asymmetrical Temperature Verification Tests at Locations 6, 7 and 9	10-36

LIST OF FIGURES
(continued)

<u>Figure</u>	<u>Page</u>
10-16 Results of Asymmetrical Temperature Verification Tests at Locations 10 and A	10-37
10-17 Test Setup for Strain Verification Tests	10-38
10-18 Results for Symmetrical Strain Verification Tests - Strains	10-39
10-19 Results for Symmetrical Strain Verification Tests - Stress	10-40
10-20 Results for Asymmetrical Strain Verification Tests - Strain	10-41
10-21 Results for Asymmetrical Strain Verification Tests - Stress	10-42
10-22 Test Setup for Thermal-Mechanical Fracture Tests	10-43
10-23 Principle of Superposition Used to Calculate the Stress Intensity Factor Due to Eccentric Pin Load	10-44
10-24 Procedure for Conducting Thermal-Mechanical Fracture Tests	10-45
10-25 $K_{1,ther}$ Predicted Using THERMO-K for Mode 1 Thermal-Mechanical Fracture Tests	10-46
10-26 $K_{1,ther}$ Required to Fracture the Specimens as a Function of Applied $K_{1,mech}$	10-47
10-27 Plot Showing Constant $K_{1,total}$ ($=K_{1,ther} + K_{1,mech}$) for Different Levels of $K_{1,mech}$	10-48
10-28 Plot of Temperatures Achieved at the Crack Tip and the Source for Various Levels of $K_{1,mech}$	10-49
10-29 Time to Fracture the Specimen by Thermal Loading as a Function of Applied $K_{1,mech}$	10-50

LIST OF FIGURES
(continued)

<u>Figure</u>	<u>Page</u>
10-30 $K_{1,ther}$ and $K_{2,ther}$ Predicted Using THERMO-K for Mixed Mode Thermal-Mechanical Fracture Tests . . .	10-51
10-31 Comparison of Mixed Mode Thermal-Mechanical Fracture Data With Some K_1 - K_2 Fracture Envelope Curves . . .	10-52
11-1 Flowchart for Linking THERMO-K and MODGRO	11-8
11-2 Mechanical and Thermal Loading Configurations Used Crack Growth Analysis	11-9
11-3 Stress Distribution in the Uncracked Plate at Steady State	11-10
11-4 Steady State Thermal K_1 Versus Crack Length Relationship for Two Different Locations of Heat Source	11-11
A-1 A Crack in a Linear Elastic Solid	A-18
A-2 Local Coordinate at Crack Border	A-19
A-3 A Finite Crack in an Infinite Plate	A-20
A-4 Effects of Crack Surface Thermal Conductivity on K_{II}	A-21
A-5 Temperature Jumps at the Crack Surface	A-22
A-6 Size Effects	A-23
B-1 Local Coordinates for Influence Function Integration for Crack Models 2, 3, and 4	B-4
B-2 Local Coordinates for Influence Function Integration for Crack Models 1 and 5	B-5

LIST OF FIGURES
(concluded)

<u>Figure</u>	<u>Page</u>
C-1 A Plate Strip Subjected to Arbitrary Edge Loads . .	C-10
C-2 Two Basic Loading Cases	C-11
C-3 thru	
C-16 Edge Effect Functions	C-12-C-25
D-1 Grid on Surface of Half-Space	D-8
D-2 Auxiliary Coordinate for Singular Solutions . . .	D-9

1.0 INTRODUCTION AND PROGRAM SCOPE

Analytical techniques are needed by the Air Force for predicting stress intensity factors of cracked metallic structures subjected to rapid thermal pulses. A schematic of such a problem is illustrated in Figure 1-1. General purpose numerical techniques such as finite element methods are currently available for the solution of such problems. However, they require time-consuming finite element modeling of the structural configuration, including the crack, and detailed thermal/stress analysis must be performed for each thermal transient to be addressed.

The modeling is further complicated by the extremely steep stress gradients which exist in the vicinity of the cracktip. The stress singularities at the cracktip dictate the use of an extremely fine finite element mesh in this region, or a special element which has the appropriate crack tip singularity built into the element interpolation functions. Furthermore, multiple finite element models and analyses are required for a single structure if we desire the stress intensity factors as a function of crack size, which is usually the case.

Thus, the objective of this study is to provide a convenient and accurate way to calculate the stress intensity factors caused by rapid thermal pulses, for use in conjunction with existing crack growth prediction software (MODGRO) used by the Air Force to predict crack growth and fracture in flaw tolerant design applications.

As a result of the Phase II effort reported here, an IBM-PC based computer program, THERMO-K, has been developed based on the concepts of Green's function and influence function. THERMO-K calculates stresses and stress intensity factors by integrating the closed-form Green's function solutions to the general thermoelasticity problem of a point heat source in a cracked structure. A total of seven crack models were investigated in

this study, namely, as shown in Figures 1-2 to 1-8, (1) a finite crack in an infinite plate, (2) a single-edge crack in a semi-infinite plate, (3) a radial crack emanating from a circular hole in an infinite plate, (4) a single-edge crack in an infinitely long, finite width plate strip, (5) a center crack in an infinitely long, finite width plate strip, (6) a semicircular surface crack in a half-space, and (7) a quarter-circular surface crack at the corner of a quarter-space. For a given crack geometry, the stress distribution and stress intensity factors due to any number of randomly located heat sources (or sinks) can be calculated by THERMO-K in a few minutes. An experimental study was also conducted to obtain reference solutions for crack Model 4. Results of THERMO-K have been verified by comparing them with finite element solutions or the experimental measurements. Good agreement between THERMO-K solutions and finite element results and/or experimental data was observed.

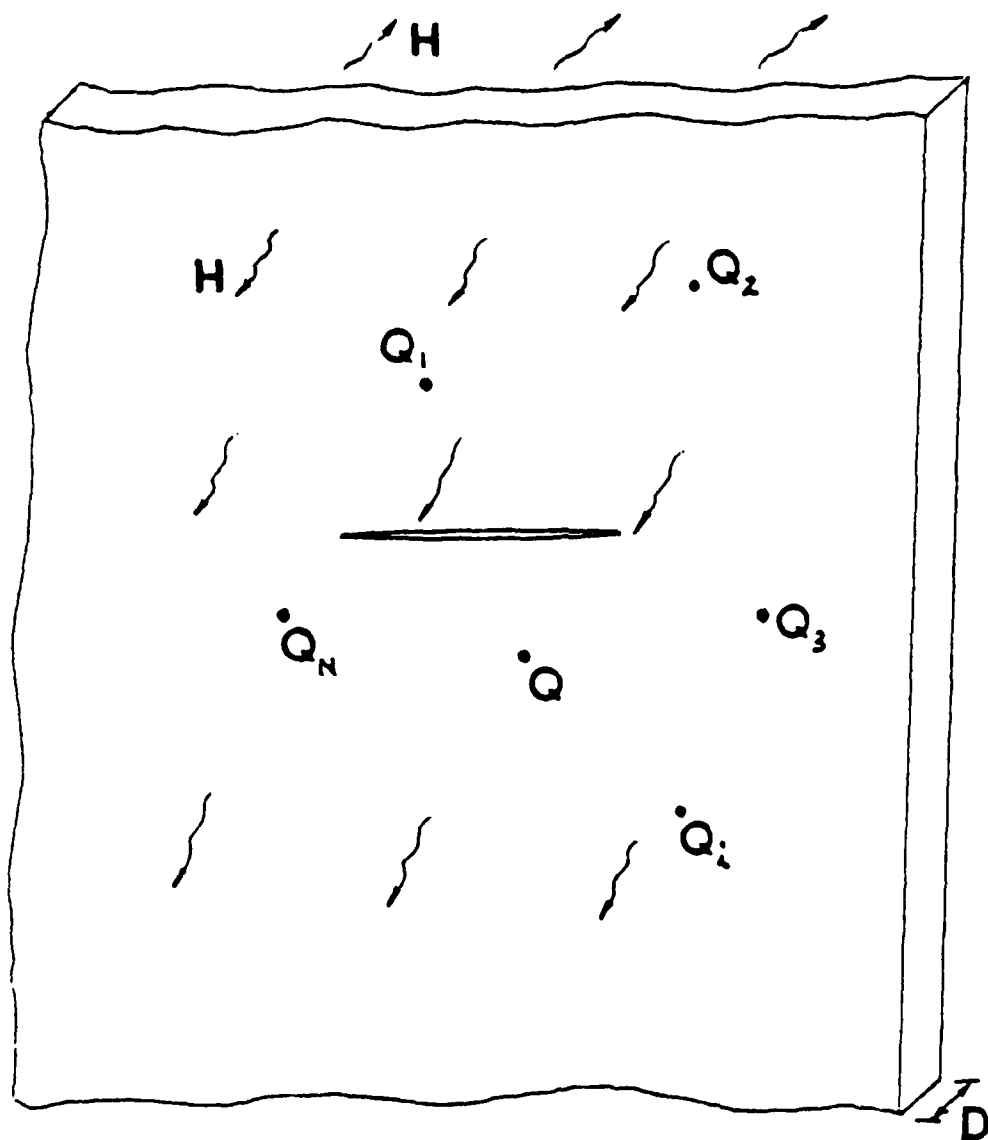
THERMO-K combines and links several independent program modules using a unique "software bus" concept, and is a menu driven, user-friendly software package with extensive graphics capabilities.

The stress intensity factor results generated by THERMO-K are useful as input to any of a number of fatigue crack growth and fracture prediction programs used by the Air Force. An example of such a computer program, MODGRO has been included on the THERMO-K software bus. It has been shown in this study that a direct data link between THERMO-K and MODGRO is possible.

This volume of the report, Volume II, contains eleven sections and five appendices. This report is divided into two volumes. Volume I of this report gives the general program structure and user instruction of THERMO-K. A few sample problems are also included in Volume I to guide first time users into the program. Section 2 through Section 8 provide the theoretical background for each of the seven crack models, respectively. Inside these

sections, governing equations, temperature and stress solutions, and Green's function for a fully heat conductive as well as partially heat conductive crack is discussed and derived in detail. At the end of Sections 2 and 8, the THERMO-K solutions were compared with an independent finite element solutions. Since the user may not want to go through all the sections between Section 2 and Section 8 at once, each of those sections has been written in such way that it is self-contained and the user can read them separately. Section 9 describes the limitations on the decoupled, quasi-static thermoelasticity and linear elastic fracture mechanics (LEFM) theories used in this study. From this section, it is found that the decoupled, quasi-static thermoelasticity and LEFM theories are very accurate for most of the practical problems of interest to the Air Force. However, it is recommended that users of the computer program read Section 9 when analyzing a problem with a relatively high heating rate or a long crack to make sure that the underline theories used to develop THERMO-K is still applicable. Section 10 provides the equipment setup, specimen design, test procedure as well as measured data for an experimental verification task of THERMO-K performed by the University of Dayton at Dayton, Ohio. Good agreement between experimental results and analytical solutions obtained by THERMO-K is observed. Section 11 discusses the linking of THERMO-K with a crack growth prediction software, MODGRO. Four appendices are attached at the end of this report to provide some frequently used results. Appendix A discusses the effects of crack surface heat conductance on stress intensity factors. A general methodology of using distributed thermal dipoles at the crack region for treating a partially heat conductive crack is developed in this appendix. Appendix B shows a numerical integration scheme for calculating stress intensity for the two-dimensional crack models through the influence function approach. Appendix C gives an analytical solution for an edge loaded plate for use in crack Models 4 and 5. Appendix D provides a numerical integration scheme for calculating stress intensity factors for three-dimensional crack models through the

influence function approach. Appendix E contains the calculation procedure for the coefficients of an approximated mapping function used in Section 4 for crack Model 3.



$Q_i = F_i(t)$ - Point Heat Sources at Various Locations in Structure

Figure 1-1. Schematic of Cracked Plate Subjected to Rapid Thermal Pulses

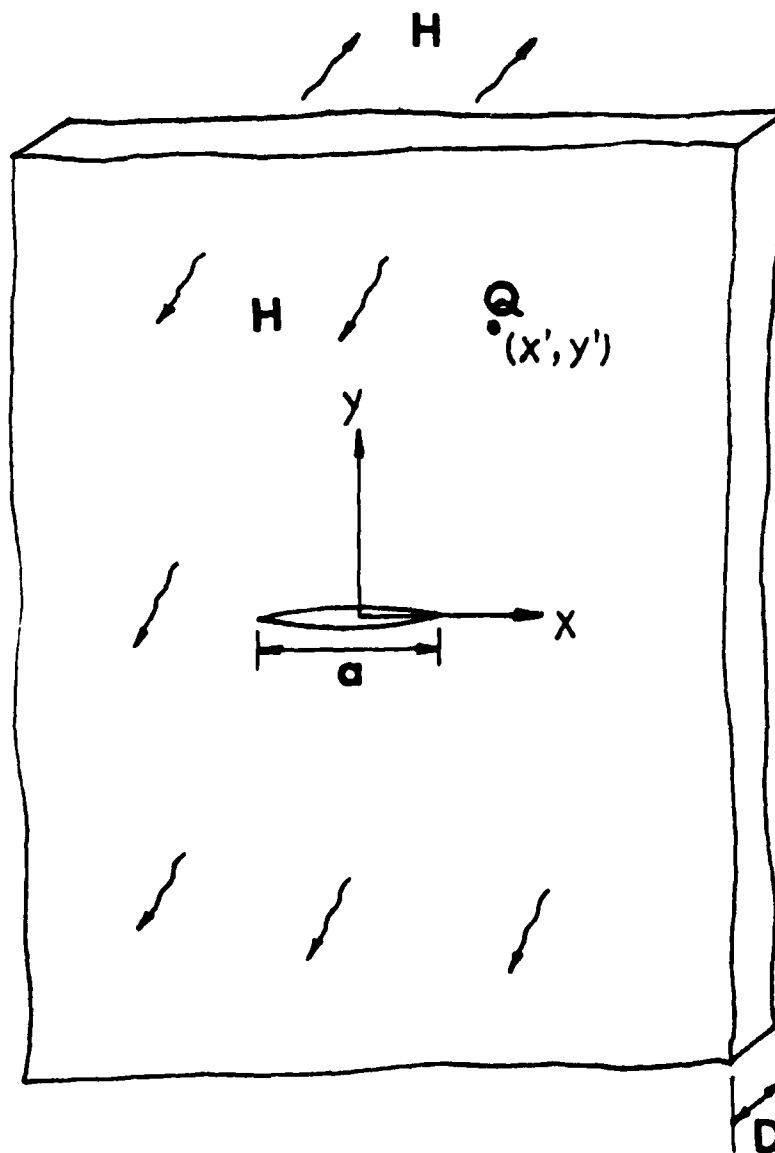


Figure 1-2. Crack Model 1 - A Finite Crack in an Infinite Plate

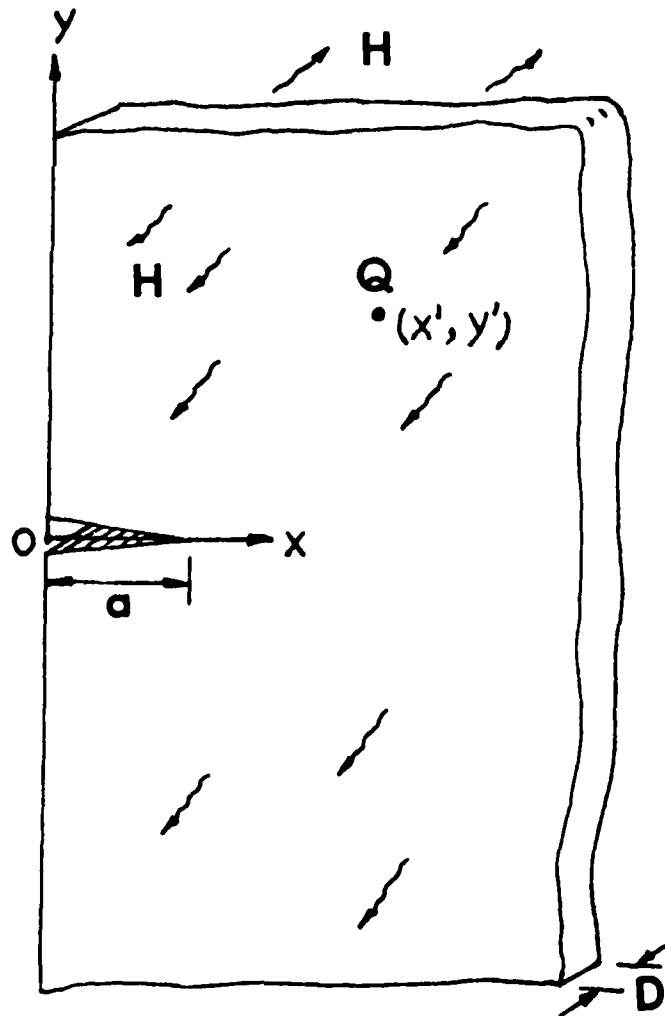


Figure 1-3. Crack Model 2 - A Single-edge-crack in a Semi-infinite Plate

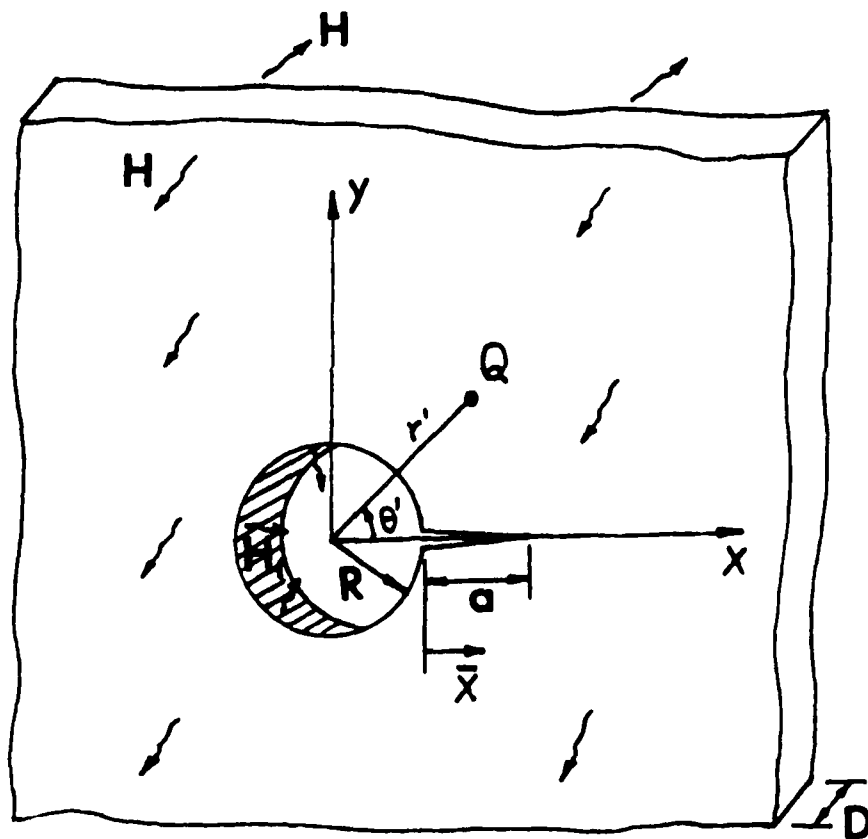


Figure 1-4. Crack Model 3 - A Radial Crack Emanating From a Circular Hole in an Infinite Plate

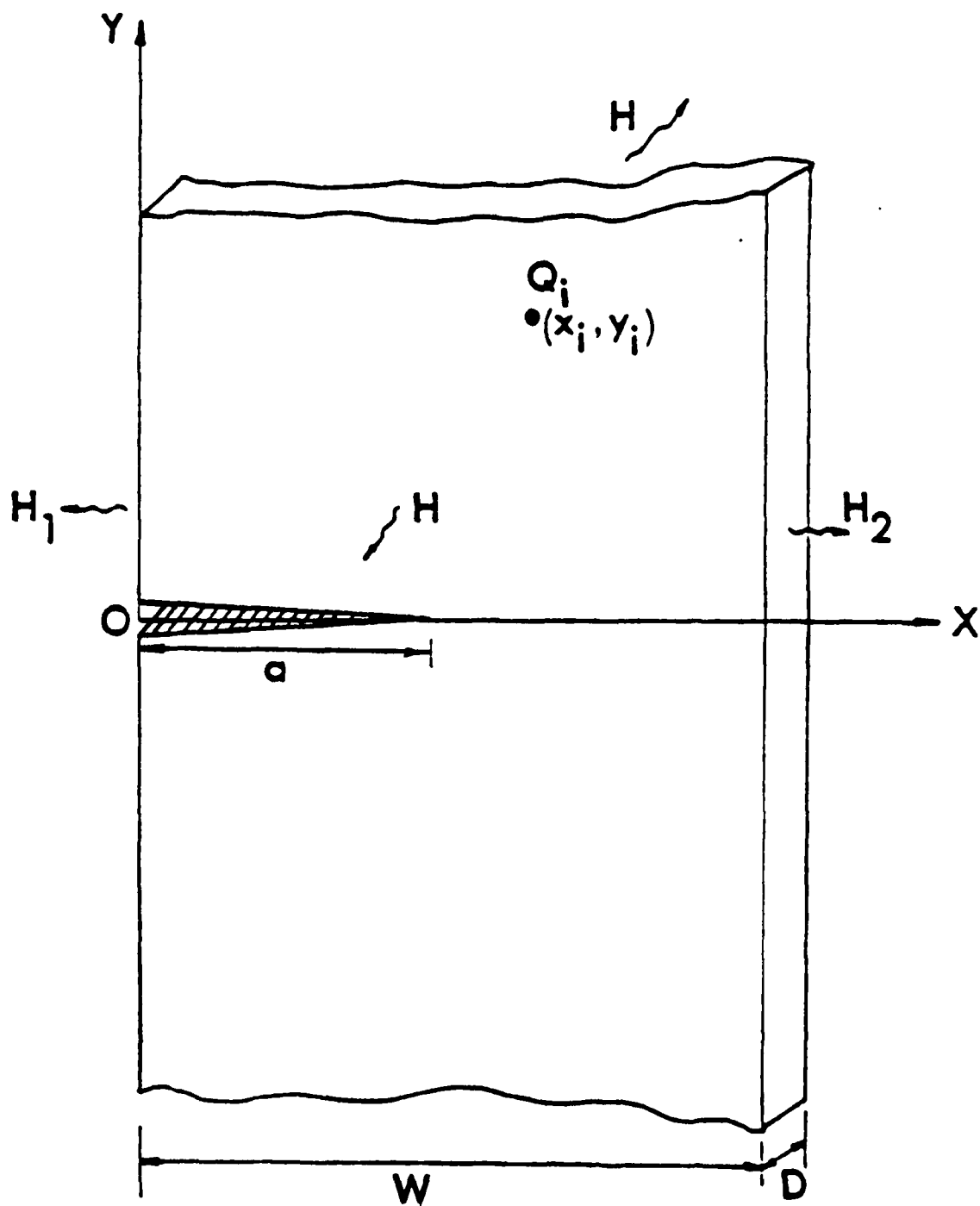


Figure 1-5. Crack Model 4 - A Single-edge-crack in an Infinitely Long, Finite Width Plate Strip

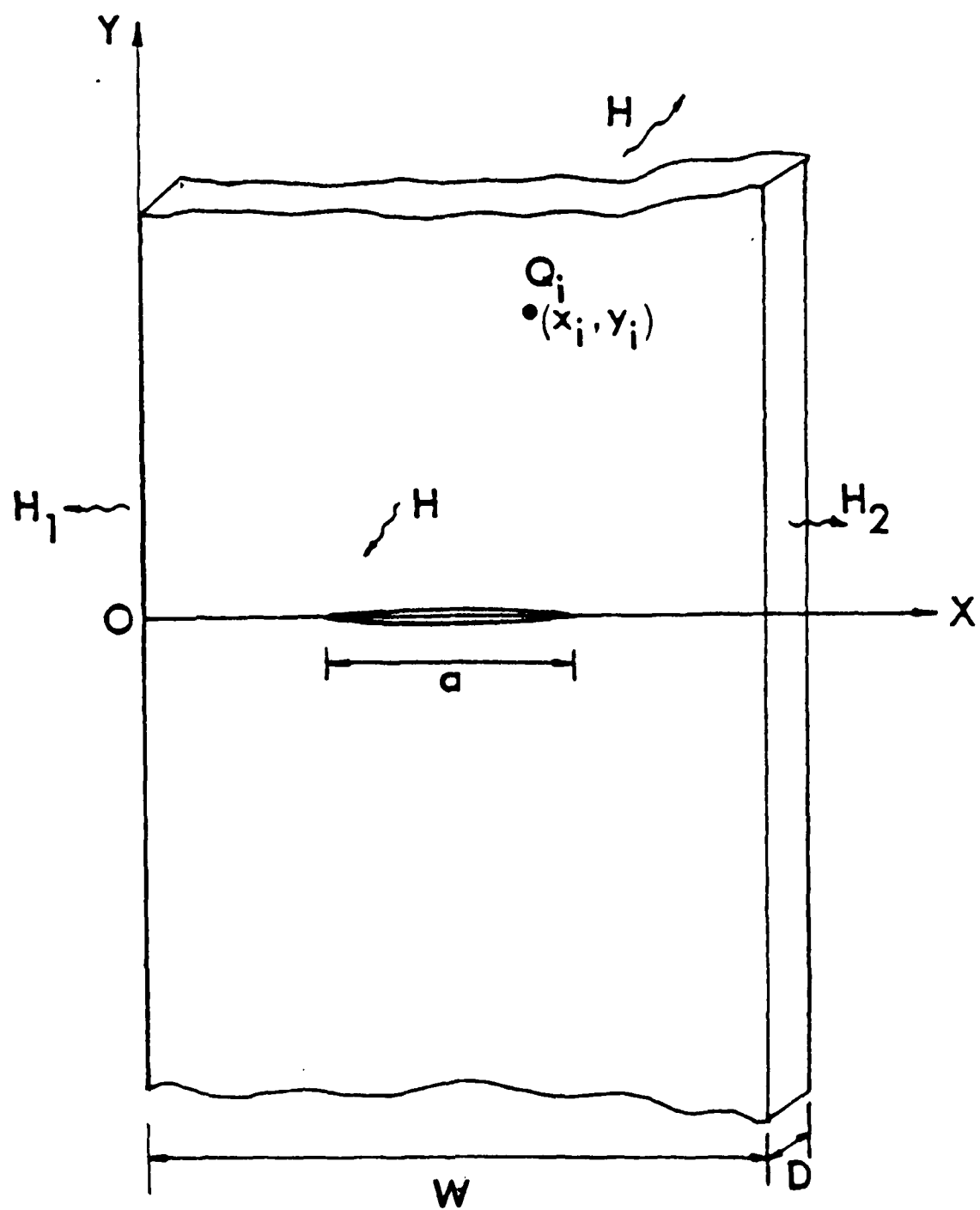


Figure 1-6. Crack Model 5 - A Center Crack in an Infinitely Long, Finite Width Plate Strip

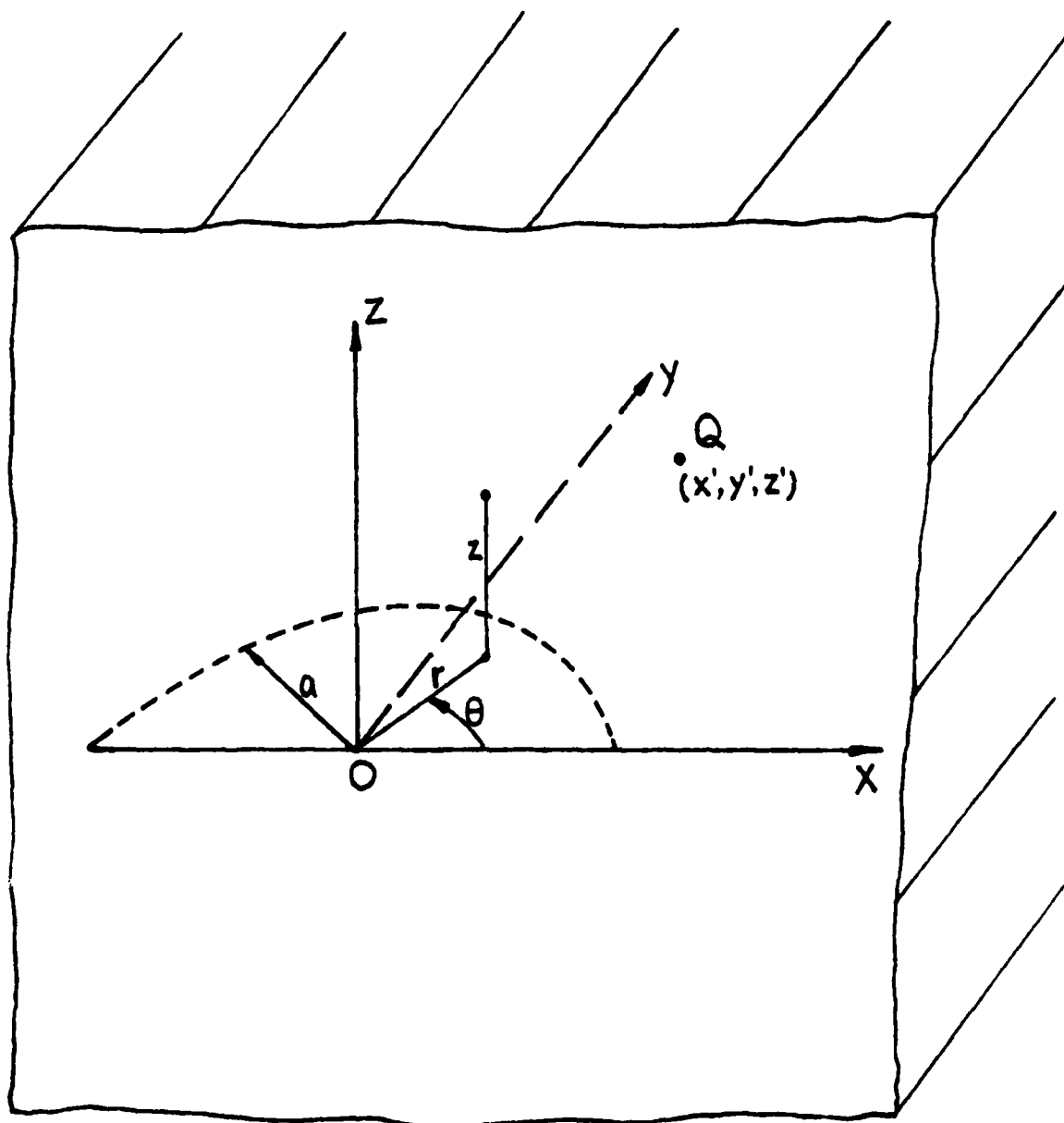


Figure 1-7. Crack Model 6 - A Semi-circular Surface Crack in a Half-space

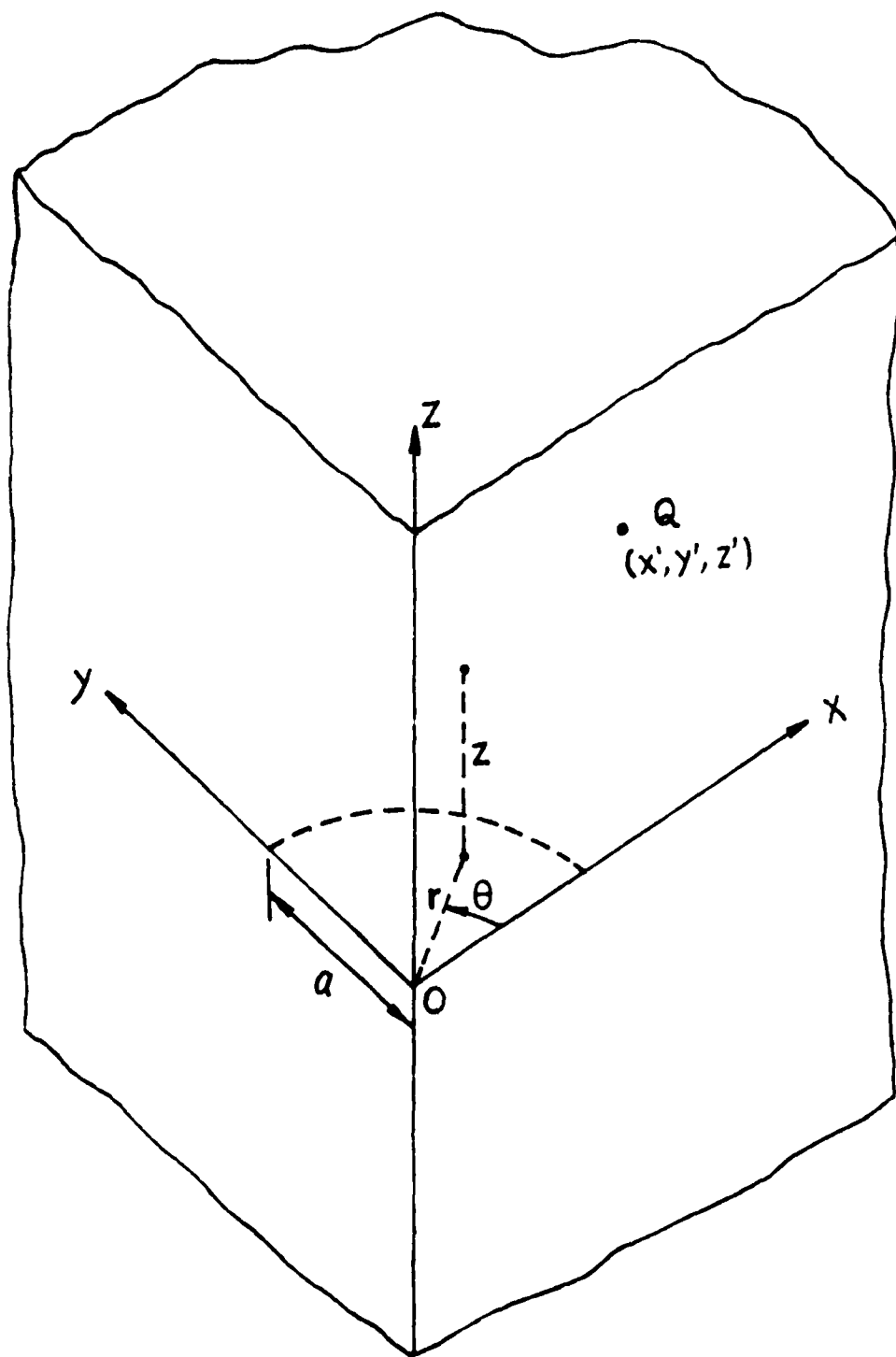


Figure 1-8. Crack Model 7 - A Quarter-circular Crack at the Corner of a Quarter-space

2.0 THEORETICAL BACKGROUND OF CRACK MODEL 1 - A FINITE CRACK IN AN INFINITE PLATE

This section describes the theoretical basis for crack Model 1 - a finite crack in an infinite plate, i.e., as illustrated in Figure 2-1, a crack of length a in an infinite plate of thickness D . The cracked plate is subjected to point heat sources with arbitrary time history at any points in the plate.

2.1 Assumptions

The following assumptions were made to simplify the problem:

- (a) The problem is assumed to be a plane stress problem. In other words, the thickness D shown in Figure 2-1 is assumed to be small enough that the temperature distribution in the thickness direction can be treated as uniform and the stress components in the thickness direction are negligible compared with the in-plane stress components.
- (b) The metallic materials are assumed to be isotropic, homogeneous, and linear elastic. Material properties are assumed to be temperature independent.
- (c) The rate of heat application is slow enough that the coupling terms and inertia terms in the general thermoelasticity equations can be neglected, i.e., it is assumed that the decoupled, quasi-static thermoelasticity applies.
- (d) The crack surfaces are assumed to be stress free. The crack surfaces can be completely insulated, fully heat conductive, or partially heat conductive. Heat conductance coefficient h at the crack surfaces is also assumed to be constant throughout the entire temperature range.

- (e) It is assumed that the heat convection coefficient, H , at the plate surfaces (see Figure 2-1) remain constant.

2.2 Governing Equations

For a plane stress thermoelasticity problem as illustrated in Figure 2-1, the governing equations are

$$\xi \nabla^2 T = T_{,t} + \xi \eta^2 T \quad (2-1)$$

$$\sigma_{ij,j} = 0 \quad (2-2)$$

$$\sigma_{ij} = 2G \left[\epsilon_{ij} + \left(\frac{\nu}{1-\nu} \right) \delta_{ij} \epsilon_{kk} - \alpha \left(\frac{1+\nu}{1-\nu} \right) \delta_{ij} T \right] \quad (2-3)$$

$$\epsilon_{ij} = (U_{i,j} + U_{j,i})/2 \quad (2-4)$$

and

$$\nabla^2 U_i + \left(\frac{1+\nu}{1-\nu} \right) U_{j,ji} = 2 \left(\frac{1+\nu}{1-\nu} \right) \alpha T \quad (2-5)$$

where $T=T(x,y;t)$ is temperature distribution, t , x and y are time and Cartesian coordinates, respectively, $\xi=(k/\rho c)$, k is heat conduction coefficients, ρ is mass density, c is heat capacity, $\eta^2=(2H)/k/D$, H is heat convection coefficient from the plate surfaces to the environment (see Figure 2-1), D is plate thickness, U_i are displacements, α is coefficient of thermal expansion, and G and ν are shear modulus and Poisson's ratio, respectively.

Nominal stress distributions generated with these equations are used to develop stress intensity factors via the influence function approach described below.

2.3 Influence Functions for Stress Intensity Factor

For any plate/crack geometry, cracktip stress intensity factors can be determined by integrating the product of the stresses at the crack location in an uncracked structure and an influence function (or weight function), (Buecker, 1973). That is, for a crack as shown in Figure 2-2, the stress intensity factor can be calculated by

$$K_I = \int_{-a/2}^{a/2} \sigma_{yy}(x,0) m_1(x) dx \quad (2-6)$$

$$K_{II} = \int_{-a/2}^{a/2} \sigma_{xy}(x,0) m_2(x) dx \quad (2-7)$$

where $m_1(x)$ and $m_2(x)$ are influence functions, x is a local coordinate shown in Figure 2-1 or Figure B-2 of Appendix B, and σ_{yy} and σ_{xy} are the normal and shear stress distributions on the crack surface in an identical but uncracked plate which is under the same temperature distribution as the cracked plate.

For a finite crack in an infinite plate, as illustrated in Figure 2-1, the influence functions have been shown (see e.g., Tada, et al., 1973) to be

$$m_1^R(x) = m_2^R(x) = \sqrt{\frac{(A+x)}{\pi A(A-x)}} \quad (2-8)$$

$$m_1^L(x) = m_2^L(x) = \sqrt{\frac{(A-x)}{\pi A(A+x)}} \quad (2-9)$$

where $A=a/2$ is one half of the crack length, influence functions with superscript "R" are for the crack tip on the right hand side ($x=a/2$), and influence functions with superscript "L" are for the crack tip on the left hand side ($x=-a/2$).

2.4 Principle of Superposition

In general, as shown in Figure 2-1, there may be multiple heat sources (or sinks) within the plate which will cause thermal stresses and stress intensity factors at the crack tip in the structure. Since the problem is linear, it is easily demonstrated that total stress intensity factor can be calculated as the sum of the stress intensity factors caused by each individual heat source or sink, acting independently. That is

$$K(t) = \sum_i [K(t)]_i \quad (2-10)$$

where $K(t)$ is the total stress intensity factor and $[K(t)]_i$ is the stress intensity factor due to the i^{th} heat source.

2.5 Green's Function Concept for Time Integration

In Equation (2-10), the stress intensity factor $[K(t)]_i$ caused by each individual heat source can be solved with the concept of Green's function integration. As illustrated in Figure 2-3, the stress intensity factor due to a heat source of intensity $Q_i(t)$ can be calculated by

$$[K(t)]_i = \int_0^t Q_i(\tau) G_i(t-\tau) d\tau \quad (\text{no summation}) \quad (2-11)$$

where $G_i(t)$ is the stress intensity factors due to a Delta function $\delta(t)$ heat source at the i^{th} heat source location.

As shown in Figure 2-3, generally, the Green's function $G_i(t)$ will decay and approach to zero after a decay period t_d . Therefore, the integration range in Equation (2-11) can be reduced from $(t-t_d)$ to t . Such a reduction in the integration range greatly increases the speed of the calculation because, instead of integrating for the entire time history, it is only necessary to integrate backwards from the present time t to $(t-t_d)$ as follows

$$[K(t)]_i = \int_{t-t_d}^t Q_i(\tau) G_i(t-\tau) d\tau \quad (2-12)$$

2.6 Green's Function for Fully Heat Conductive Cracks

Previous sections of this section show that the stress intensity factors for this crack models can be easily obtained by Equations (2-6), (2-7), (2-10), and (2-11) if the temperature and stress distributions and thereby the stress intensity factors at the crack tips, resulting from a delta function heat source (or sink) $Q\delta(t)$ at any arbitrary location (x',y') in the uncracked plate (refer to Figure 2-4), can be solved. The uncracked plate shares the same temperature distribution as the cracked plate. As the first step, we consider the problem of a fully heat conductive edge crack, i.e., in this subsection, it is assumed that heat flux can flow across the crack surfaces without any heat loss or resistance. Solutions for a more general, partially heat conductive crack will be discussed in the next subsection.

However, as will be seen in the next subsection and as shown in Appendix A of this report, for a crack model with symmetry about its crack plane such as this crack model, crack surface heat conductance will affect Mode II stress intensity factor solutions but not Mode I or Mode III stress intensity factor solutions. In other words, whether the crack surfaces are fully heat conductive, insulated, or partially heat conductive, the K_I solution will remain the same for a finite crack in an infinite plate. Thus, if only Mode I fracture is of major interest, the stress intensity factor solutions can be obtained by assuming the crack surfaces are fully heat conductive. The assumption of a fully heat conductive crack will greatly shorten the computation time for temperatures, thermal stresses, and stress intensity factors.

Since thermal stresses and stress intensity factors do not depend on the initial, stress free temperature of the plate, it is conveniently assumed that the initial temperature of the plate is zero, i.e., $T(x,y;0)=0$. To solve for the Green's function of this crack model, the following boundary conditions need to be satisfied in addition to the governing equations listed in Equations (2-1) to (2-5):

at infinity,

$$T(x,y;t) = 0 \quad (2-13)$$

$$\sigma_{xx}(x,y;t) = \sigma_{yy}(x,y;t) = \sigma_{xy}(x,y;t) = 0 \quad (2-14)$$

at $y=0$, $-a \leq x \leq a$,

$$T(x,0^+;t) = T(x,0^-;t) \quad (2-15)$$

$$\sigma_{yy}(x,0^+;t) = \sigma_{yy}(x,0^-;t) \quad (2-16)$$

$$\sigma_{xy}(x, 0^+; t) = \sigma_{xy}(x, 0^-; t) \quad (2-17)$$

$$U_i(x, 0^+; t) = U_i(x, 0^-; t) \quad , \quad i = x, y \quad (2-18)$$

Temperature solution to the uncracked plate problem can be obtained by solving Equation (2-1) along with boundary condition Equation (2-15). An analytical form of the temperature solution has been given by Carslaw and Jaeger (1959) as follows:

$$T(x, y; t) = \frac{Q}{4\pi\xi t \rho c D} \exp(-\xi\eta^2 t - \frac{R^2}{4\xi t}) \quad (2-19)$$

where ξ and η are defined in Equation (2-1), and

$$R^2 = (x-x')^2 + (y-y')^2 \quad (2-20)$$

The next step is to solve the stress distribution due to the temperature distribution of Equation (2-19). Boley and Weiner (1960) and Parkus (1968) have shown that a particular solution to the thermal stress problem can be expressed in terms of a thermoelastic potential ϕ as follows

$$U_i = \phi_{,i} \quad (i = x, y) \quad (2-21)$$

$$\sigma_{xx} = -2G \phi_{,yy} \quad (2-22)$$

$$\sigma_{yy} = -2G \phi_{,xx} \quad (2-23)$$

$$\sigma_{xy} = 2G \phi_{,xy} \quad (2-24)$$

$$\phi(x, y; t) = \alpha(1+\nu)\xi e^{-\xi\eta^2 t} \int_0^t e^{\xi\eta^2 \tau} T(x, y; \tau) d\tau + \phi_0 \quad (2-25)$$

where ϕ_0 is a function of x , y , and t such that ϕ would remain finite as t approaches infinity. Substitution of Equation (2-19) into Equation (2-25) yields

$$\phi(x, y; t) = \frac{\alpha(1+\nu)Q}{4\pi\rho c D} \exp(-\xi\eta^2 t) \left[\int_0^t \exp\left(-\frac{R^2}{4\xi\tau}\right) \frac{d\tau}{\tau} + \ln(R) \right] \quad (2-26)$$

Therefore, by substituting Equation (2-26) into Equations (2-22) to (2-24), it can be shown that

$$\sigma_{xx}(x, y; t) = \frac{Ga(1+\nu)Q}{\pi\rho c D R^2} e^{-\xi\eta^2 t} \left(\left[1 - \frac{2(y-y')^2}{R^2} \left(1 + \frac{R^2}{4\xi t} \right) \right] \exp\left(-\frac{R^2}{4\xi t}\right) - 1 + \frac{2(y-y')^2}{R^2} \right) \quad (2-27)$$

$$\sigma_{yy}(x, y; t) = \frac{Ga(1+\nu)Q}{\pi\rho c D R^2} e^{-\xi\eta^2 t} \left(\left[1 - \frac{2(x-x')^2}{R^2} \left(1 + \frac{R^2}{4\xi t} \right) \right] \exp\left(-\frac{R^2}{4\xi t}\right) - 1 + \frac{2(x-x')^2}{R^2} \right) \quad (2-28)$$

$$\sigma_{xy}(x, y; t) = \frac{2Ga(1+\nu)Q(x-x')(y-y')}{\pi\rho c D R^4} e^{-\xi\eta^2 t} \left[\left(1 + \frac{R^2}{4\xi t} \right) \exp\left(-\frac{R^2}{4\xi t}\right) - 1 \right] \quad (2-29)$$

where R is defined in Equation (2-20). It can also be shown that the displacements and stresses resulting from $\phi(x, y; t)$ satisfy

the boundary conditions specified in Equation (2-14), and (2-16) to (2-18).

To sum up this section, the Green's functions for the stress intensity factors are calculated by substituting the stress solutions $\sigma_{yy}(x,0;t)$ and $\sigma_{xy}(x,0;t)$ given in Equations (2-28) and (2-29) and the influence functions given in Equations (2-8) and (2-9) into Equations (2-6) and (2-7) and integrating Equations (2-6) and (2-7) by the numerical integration scheme depicted in Appendix B.

2.7 Green's Function for Partially Heat Conductive Cracks

In subsection 2.6 the Green's function solution for a single point heat source at any arbitrary point in an infinite plate with a finite crack is discussed. The crack surfaces in subsection 2.6 are assumed to be fully heat conductive. In reality, the crack surface is expected to be somewhere between completely insulated and fully heat conductive, i.e., crack surfaces are expected to be partially heat conductive. A general approach to treat a partially heat conductive crack is studied in detail in Appendix A of this report. Application of the concept given in Appendix A to a finite crack in an infinite plate is discussed in this section.

Governing heat transfer equation for a partially heat conductive crack in an infinite plate is still Equation (2-1), and the boundary conditions at infinity, Equation (2-13), remain unchanged. The only difference will be the boundary condition at $y=0$, $-\frac{a}{2} \leq x \leq \frac{a}{2}$, i.e., Equation (2-15) is replaced by

$$T_{,y}(x,0) = \frac{\lambda}{A} [T(x,0^+) - T(x,0^-)] \quad -\frac{a}{2} \leq x \leq \frac{a}{2} \quad (2-30)$$

where λ is defined as (Ah/k) in which $A=a/2$, h is crack surface heat conductance coefficient and k is material thermal conductivity. From Equation (2-30), it can be easily seen that the crack surfaces are fully heat conductive when $\lambda=\infty$ and the crack surfaces are completely insulated when $\lambda=0$. Any λ values between 0 and ∞ are corresponding to a partially heat conductive crack.

As discussed in Appendix A, when a crack is completely insulated or partially heat conductive, the resulting temperatures on both sides of a crack will be different, i.e., there is a temperature jump across the crack surface when λ equals to zero or a finite number. This temperature jump is analogous to the temperature jump created by a series of distributed heat dipoles (Carslaw and Jaeger, 1959) situated at the crack location. Thus, the overall temperature distribution for the partially heat conductive crack problem can be obtained as the superposition of the fully conductive solution, Equation (2-19), and a solution for the distributed heat dipoles. From Equation (2-19), it can be shown, by summing temperature solutions for a point heat source and a point heat sink with infinitesimally small distance in between, that temperature solution for an instantaneous heat dipole of strength M situated at $y=0$, $x=\bar{x}$ in an infinite plate is

$$T(x,y;t) = - \frac{M y}{8\pi\xi^2\rho c D t^2} \exp\left[-\frac{(x-\bar{x})^2+y^2}{4\xi^2 t} - \xi^2 t\right] \quad (2-31)$$

Thus, resulting temperature from distributed heat dipoles of strength $M(x,t)$ situated at $y=0$, $-\frac{a}{2} \leq x \leq \frac{a}{2}$ of the plate is

$$\hat{T}(x,y;t) = \frac{-y}{8\pi\rho c D \xi^2} \int_0^t \int_{-a/2}^{a/2} \frac{M(\bar{x},\tau)}{(t-\tau)^2} \exp[-\xi^2 t]$$

$$- \frac{(x-\bar{x})^2 + y^2}{4\xi(t-\tau)}] d\bar{x} d\tau \quad (2-32)$$

Substitution of the sum of Equations (2-19) and (2-32) into Equation (2-30) yields a Fredholm integral equation for the heat dipole distribution $M(x,t)$ as follows:

$$\int_0^t \int_{-a/2}^{a/2} \frac{M(\bar{x}, \tau)}{(t-\tau)^2} \exp\left[-\frac{(x-\bar{x})^2}{4\xi(t-\tau)}\right] d\bar{x} d\tau = \frac{Qy'}{t^2} \exp\left[-\frac{(x-\bar{x})^2 + y^2}{4\xi t}\right] - 8\pi\xi \frac{\lambda}{a} M(x,t) \quad (2-33)$$

A numerical approximation method is used in the computer program to solve Equation (2-33). Since the temperature-jump between two adjacent crack surfaces has to be zero at the crack tips, $x=\pm\frac{a}{2}$, we assume that

$$M(x,t) = \sqrt{1-\left(\frac{2x}{a}\right)^2} \sum_{m=1}^L b_m(t) \left(\frac{2x}{a}\right)^{m-1} \quad (2-34)$$

where L is the maximum number of terms included in the calculation and $b_m(t)$ is a time function, which is determined by substituting Equation (2-34) into Equation (2-33).

Similar to the fully heat conductive case, a thermoelastic potential $\hat{\phi}$ due to the distributed thermal dipoles at the crack region can be derived by integrating the temperature solution, Equation (2-32). That is,

$$\hat{\phi}(x,y;t) = a\xi(1+\nu) \int_0^t \hat{T}(x,y;\tau) \exp[-\xi\eta^2(t-\tau)] d\tau + \hat{\phi}_0 \quad (2-35)$$

where $\hat{T}(x,y;t)$ is the temperature solution given in Equation (2-32) and $\hat{\phi}_0$ is an analytic function to make $\hat{\phi}$ remain finite at infinity.

It can be shown that stresses at the crack region, $y=0$ and $-a/2 \leq x \leq a/2$, due to the thermoelastic potential $\hat{\phi}$ given in Equation (2-35) are

$$\hat{\sigma}_{yy}(x,0;t) = 0 \quad (2-36)$$

$$\begin{aligned} \hat{\sigma}_{xy}(x,0;t) = \frac{8Ga(1+\nu)}{\pi\rho cD} \int_{-a/2}^{a/2} \int_0^t \frac{M(\bar{x},\tau)}{(x-\bar{x})^3} \left[1 + \frac{(x-\bar{x})^2}{4\xi(t-\tau)} \right] \\ \exp[-\xi\eta^2 t - \frac{(x-\bar{x})^2}{4\xi(t-\tau)}] d\tau d\bar{x} \end{aligned} \quad (2-37)$$

Results shown in Equations (2-36) and (2-37) reiterate the fact, deduced in Appendix A, that for a cracked structure with symmetry, with respect to the crack plane such as the current crack model, crack surface heat conductance will not affect Mode I fracture solution ($\hat{\sigma}_{yy}=0$ in Equation (2-36)) but will change Mode II fracture solution ($\hat{\sigma}_{xy} \neq 0$ in Equation (2-37)).

To sum up, for a partially heat conductive crack in an infinite plate subjected to an instantaneous heat source of intensity Q at (x',y') , its overall temperature solution is the sum of Equation (2-19) and Equation (2-32). Stresses in the uncracked plate

strip, which share the same overall temperature distribution as the cracked plate, are the sum of Equations (2-28), (2-29), (2-36), and (2-37). Green's function solutions for stress intensity factors, K_I and K_{II} , at the crack tip are then calculated by substituting the above stresses at the crack region into Equations (2-6) and (2-7), respectively.

2.8 Finite Element Verification of Crack Model 1

To verify the formulation for stresses and stress intensity factors for crack Model 1, a finite element program, FEM2D (1986), was used to provide a numerical reference solution. A 1 inch long finite crack in a 1 inch thick infinite plate is selected as an example problem. The plate is assumed to be insulated on both front and back surfaces, i.e., $H=0$ in Figure 2-1, and is made of Aluminum 7075-T651 with the following material properties:

$$E=10.3 \times 10^6 \text{ psi}$$

$$\nu=0.33, \alpha=13 \times 10^{-6}$$

$$\rho=0.0978 \text{ Lbm/in}^3$$

$$c=0.23 \frac{\text{Btu}}{\text{Lbm-F}}$$

$$k=0.0017361 \frac{\text{Btu}}{\text{sec-in-F}}$$

As shown in Figure 2-5, a finite element model with 704 eight-node isoparametric elements and 768 nodal points is constructed for the heat transfer and thermal stress analyses of the example problem. In this finite element model, the adjacent nodal points at the crack surfaces are tied together in the

thermal stress analysis so that they will have the same displacements. However, in the heat transfer analysis, the adjacent nodes at the crack region may or may not be constrained together depending on whether the crack surface is fully heat conductive or completely insulated.

2.8.1 Fully Heat Conductive Crack

We first consider the following four cases for a fully heat conductive crack in the plate:

Case 1: A heat source of $\delta(t)$ Btu is applied at (2 inch, 0 inch)

Case 2: A heat source of $\delta(t)$ Btu is applied at (0 inch, 1 inch)

Case 3: A heat source of $\delta(t)$ Btu is applied at (1.4 inch,
0.4 inch)

Case 4: A heat source of $\delta(t)$ Btu is applied at (0.6 inch,
0.6 inch)

As discussed in the previous sections of this section, stress intensity factors for this crack model are equal to the integration of the product of influence functions and stresses at the crack region in an uncracked plate which shares the same temperature distribution as the cracked plate. Since the crack surface is assumed to be fully heat conductive, the adjacent nodes at the crack region are constrained together such that they share the same temperature as well as displacements and stresses. To obtain the reference solutions, temperatures and thermal stresses in the uncracked plate resulting from the single heat of cases 1 to 4 are first calculated by the finite element program, FEM2D (1986). Thermal stresses at the crack region are then substituted into Equations (2-6) and (2-7) for stress intensity factor calculations.

As shown in Figure 2-6, normal stresses σ_{yy} at (-0.9 inch, 0 inch), (0.1 inch, 0 inch), and (0.9 inch, 0 inch) predicted by THERMO-K for Case 1 of the example problem are plotted as functions of time and are compared with corresponding finite element solutions. It is seen from this figure that temperatures predicted by THERMO-K are in good agreement with the reference finite element solutions. Resulting stress intensity factors for the same case, Case 1, are illustrated in Figure 2-7. Again, very good agreement between THERMO-K results and finite element solutions is observed. Similarly, resulting stress intensity factors for the rest of the loading cases for this example problem are illustrated in Figures 2-8 to 2-10. From Figures 2-6 to 2-10, it is concluded that temperature, thermal stress, and thus stress intensity factor solutions predicted by THERMO-K are very accurate compared with finite element solutions.

2.8.2 Insulated Crack

In this subsection, the crack surfaces of the example crack problem are assumed to be completely insulated. The same finite element mesh, as is illustrated in Figure 2-5, is also used for the reference solution calculation for the insulated crack case. The adjacent nodal points at the crack region, however, are assumed to be independent in the heat transfer analysis but are tied together in the following thermal stress analysis. In other words, the adjacent nodes at the crack region have different temperatures but share the same displacements and stresses in the finite element analyses for the insulated crack problem. An instantaneous heat source of strength $\delta(t)$ applied at (0.6 inch, 0.6 inch) is the thermal loading for this problem. Comparison of the resulting stress intensity factors are shown in Figure 2-11. Again, good agreement between THERMO-K's predictions and finite element solutions is observed.

2.9 References

Boley, B. A., and Weiner, J. H., (1960), Theory of Thermal Stresses, Wiley & Sons, New York, New York.

Bueckner, H. F., (1973), "Field Singularities and Related Integral Representations," in Methods of Analysis and Solutions of Crack Problems, Vol 1, ed. G. C. Sih, pp. 239-314, Noordhoff, Holland.

Carslaw, H. S., and Jaeger, J. C., (1959), Conduction of Heat in Solids, 2nd edition, Oxford University Press, London.

FEM2D - A Two Dimensional Finite Element Computer Program for Two-Dimensional Heat Transfer/Thermal Stress Analysis. Users Manual, (1986), Structural Integrity Associates, San Jose, CA.

Parkus, H., (1968), Thermoelasticity, Blaisdell Publishing Co..

Tada, H., Paris, P., and Irwin, G., (1973), The Stress Analysis of Cracks Handbook, Del Research Co., Pennsylvania.

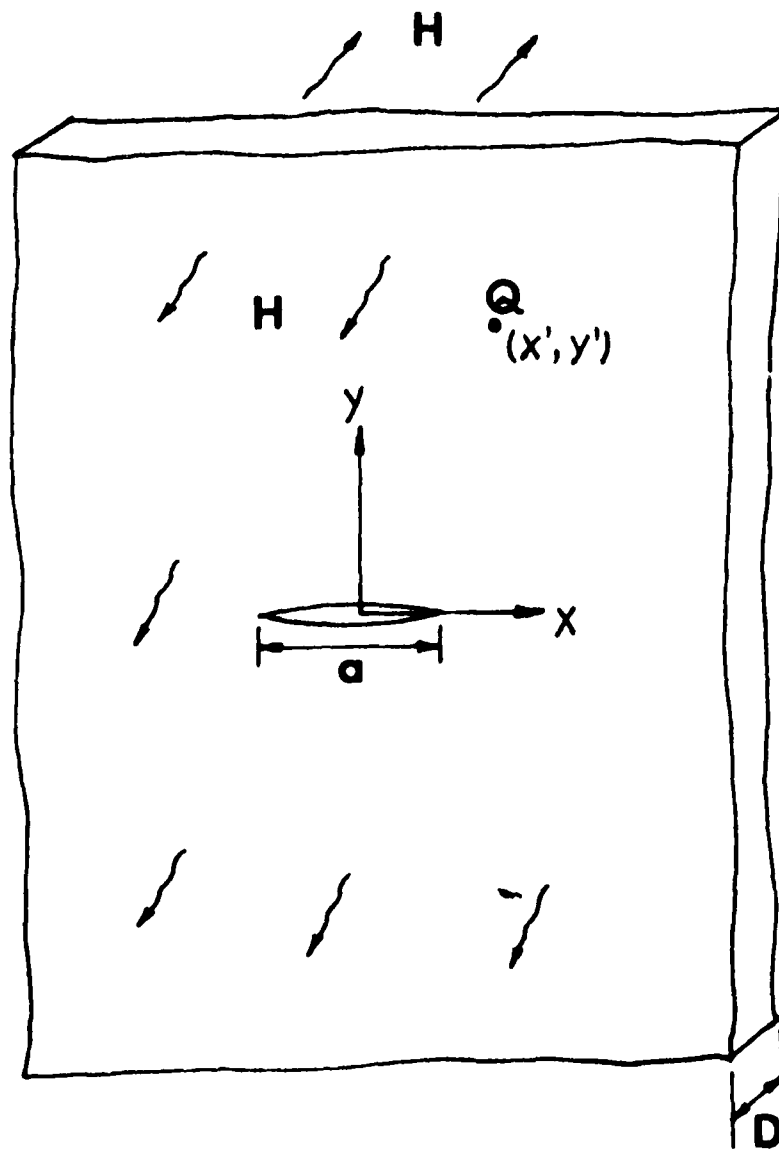


Figure 2-1. A Finite Crack in an Infinite Plate Subjected to Heat Sources

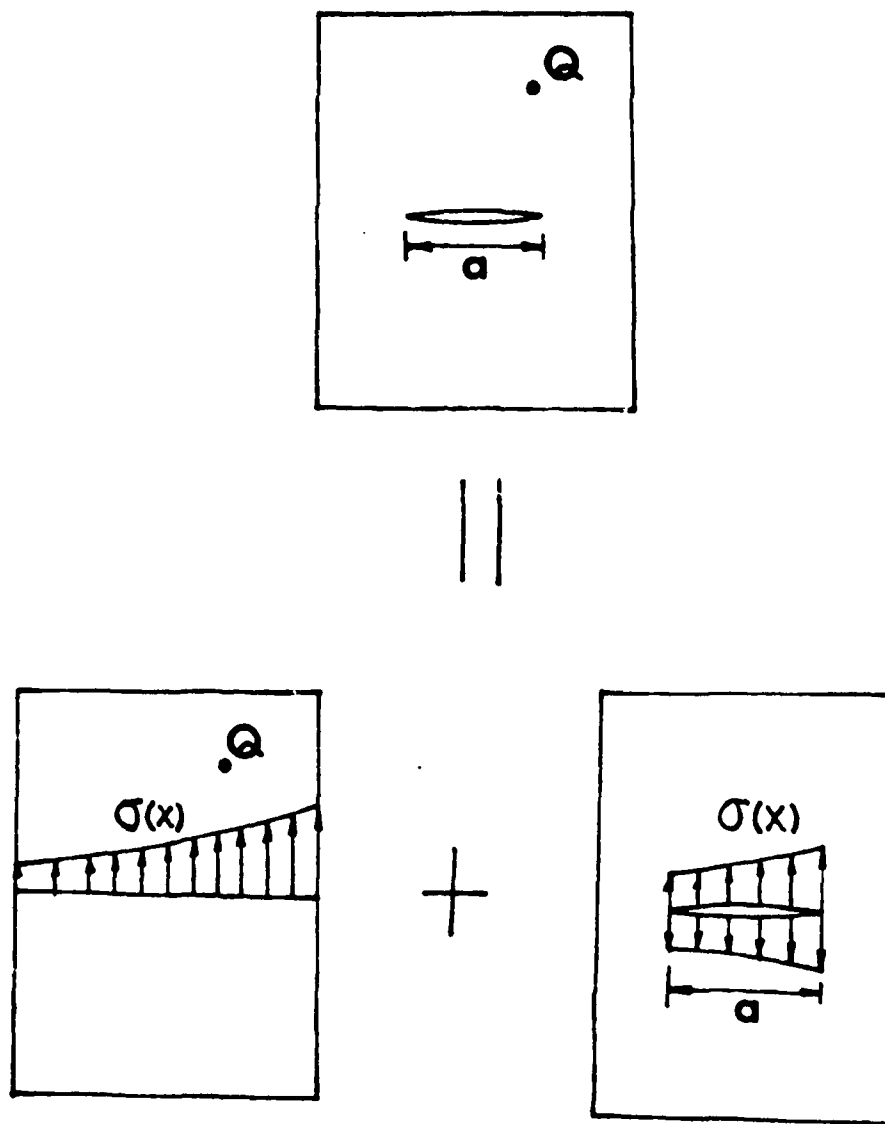
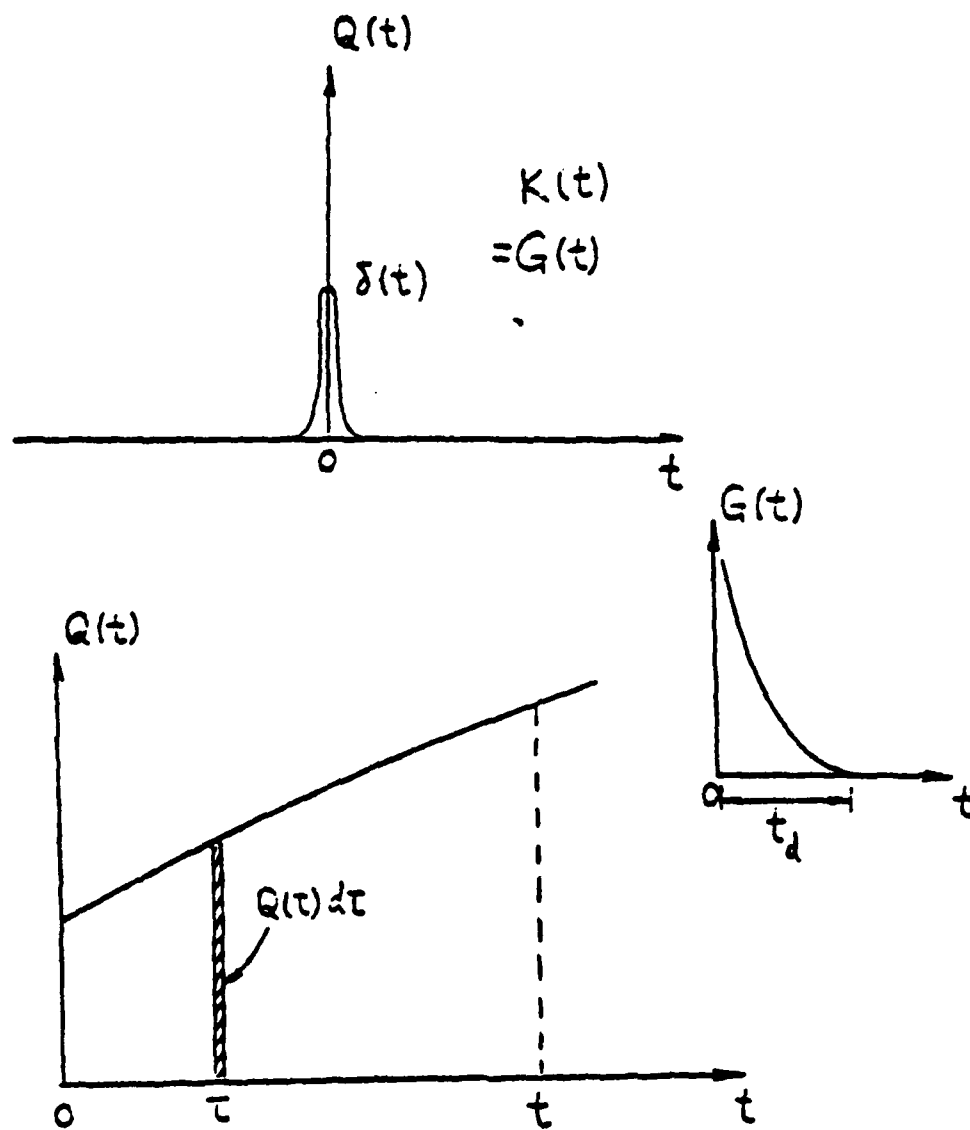


Figure 2-2. Concept of Influence Function



$$K(t) = \int_0^t Q(\tau) G(t-\tau) d\tau$$

$$= \int_{t-t_d}^t Q(\tau) G(t-\tau) d\tau$$

Figure 2-3. Concept of Green's Function

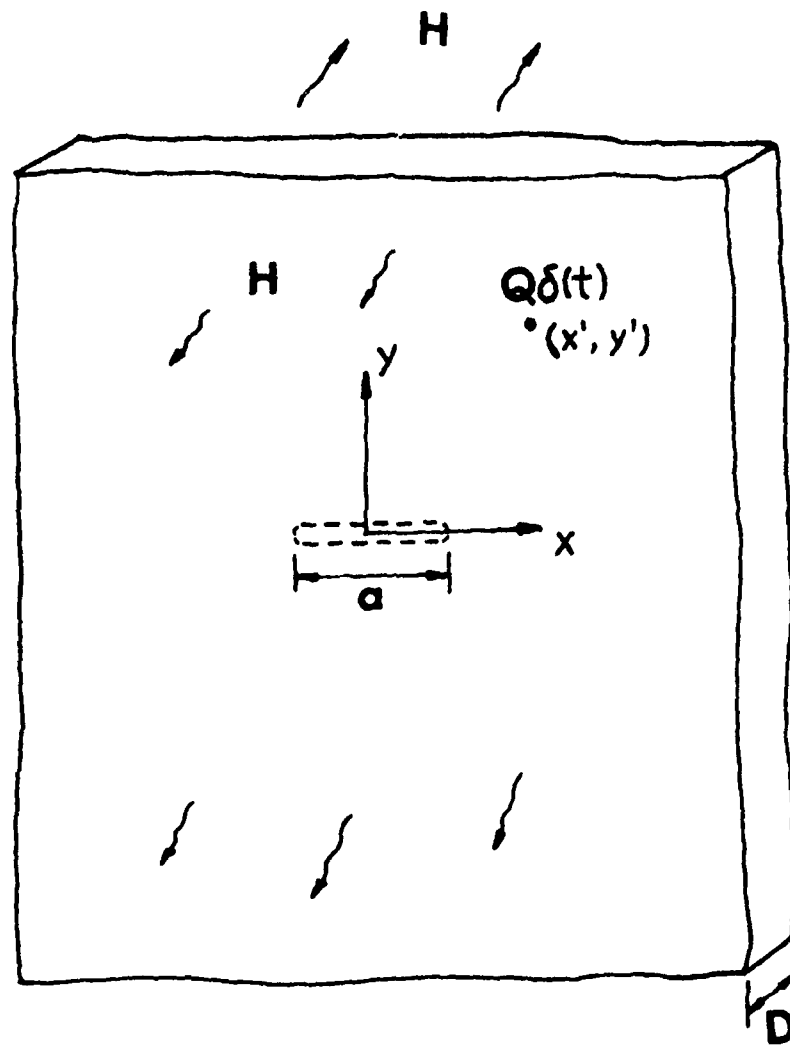


Figure 2-4. A Point Heat Source in an Uncracked Plate

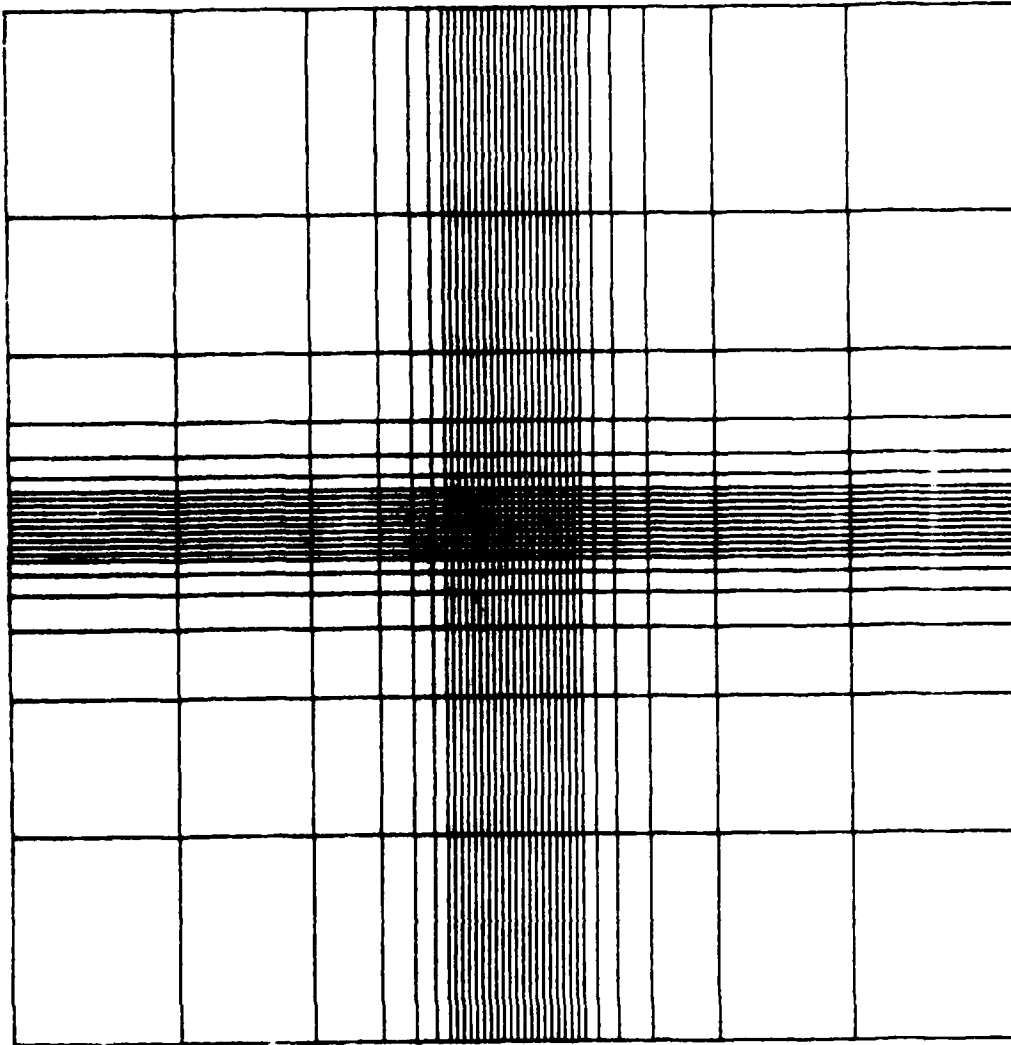


Figure 2-5(a). Finite Element Mesh for a Finite Crack in an Infinite Plate

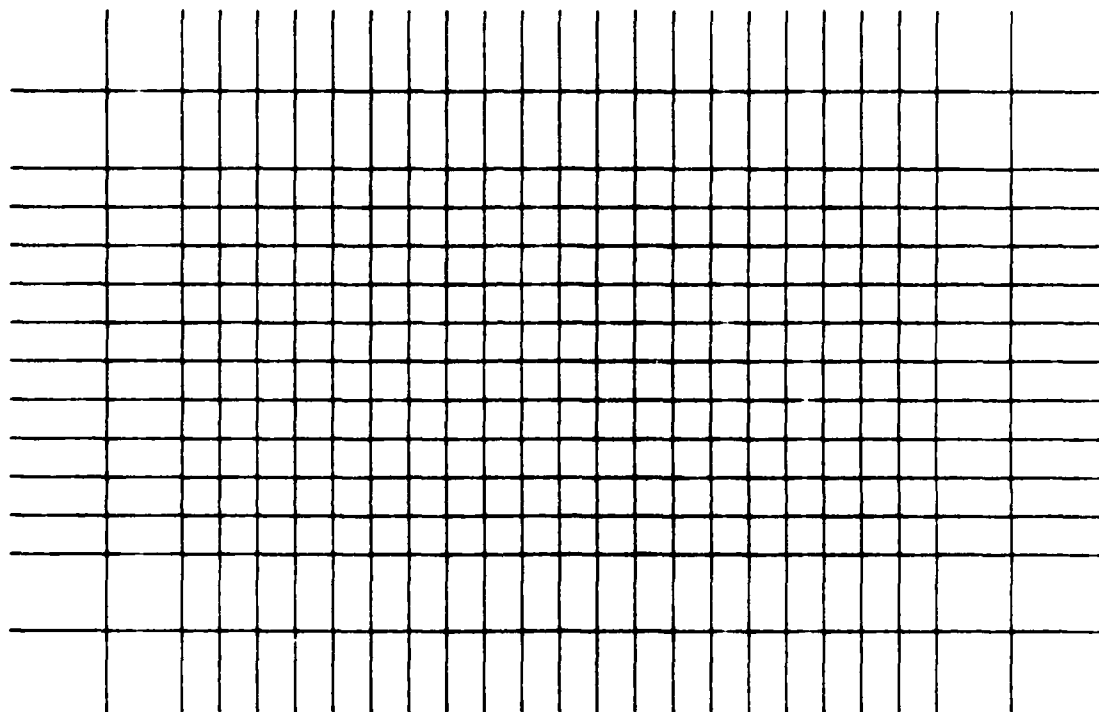


Figure 2-5(b). Finite Element Mesh Near the Crack Region

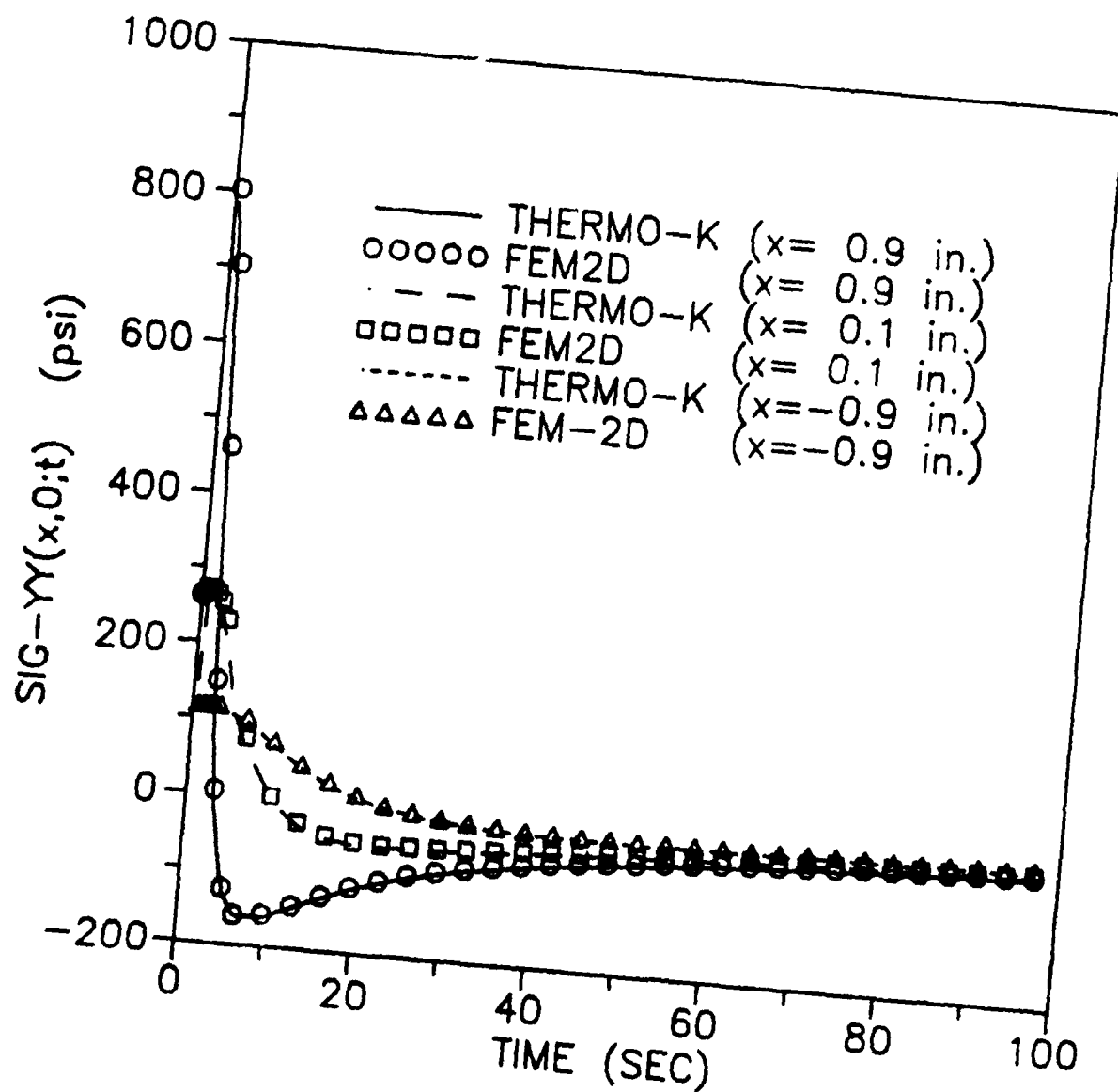


Figure 2-6. Normal Stresses Due to an Instantaneous Heat Source at (2 inch, 0 inch) (Fully Conductive Crack)

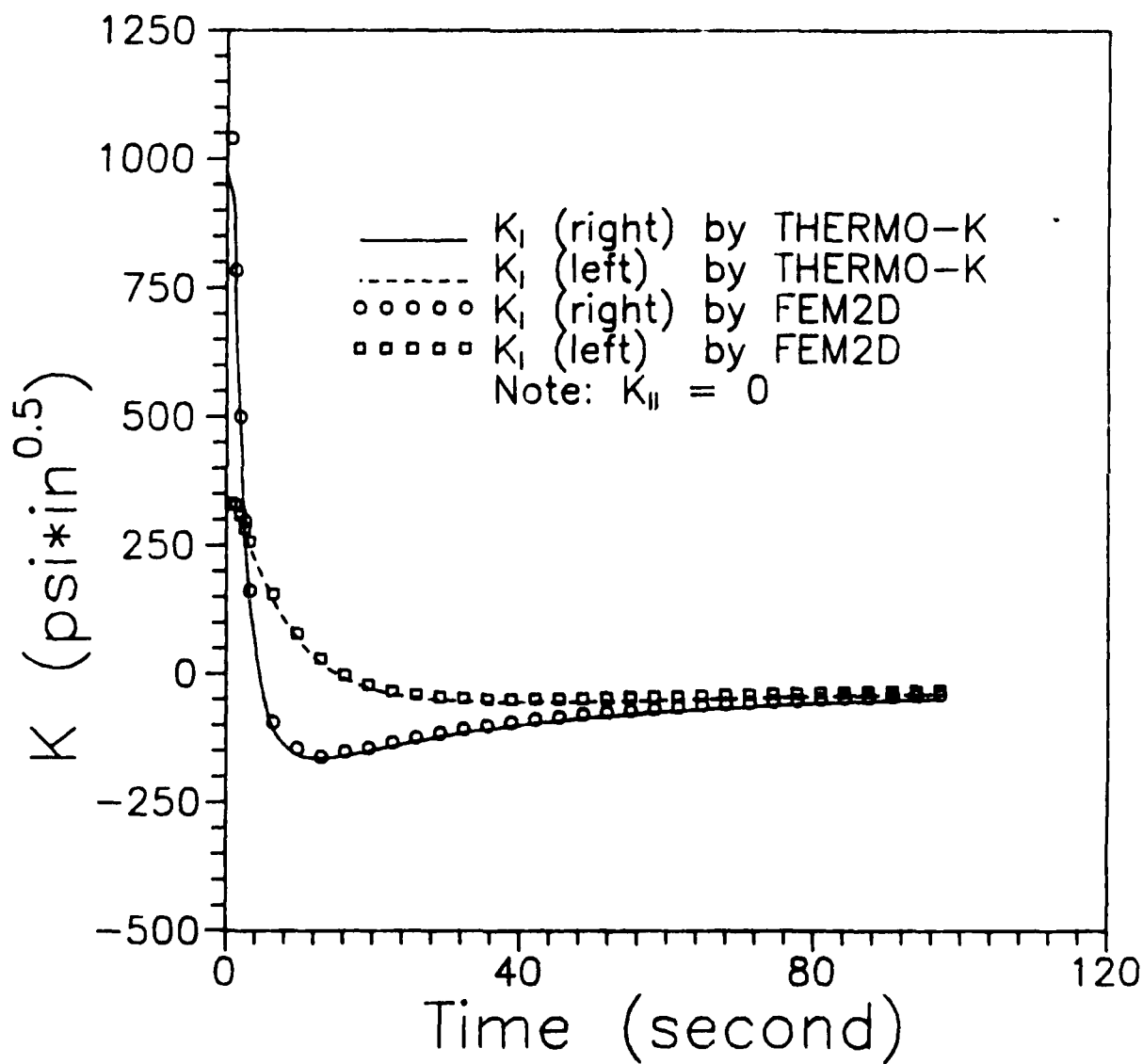


Figure 2-7. Stress Intensity Factors Due to an Instantaneous Heat Source at (2",0") (Fully Conductive Crack)

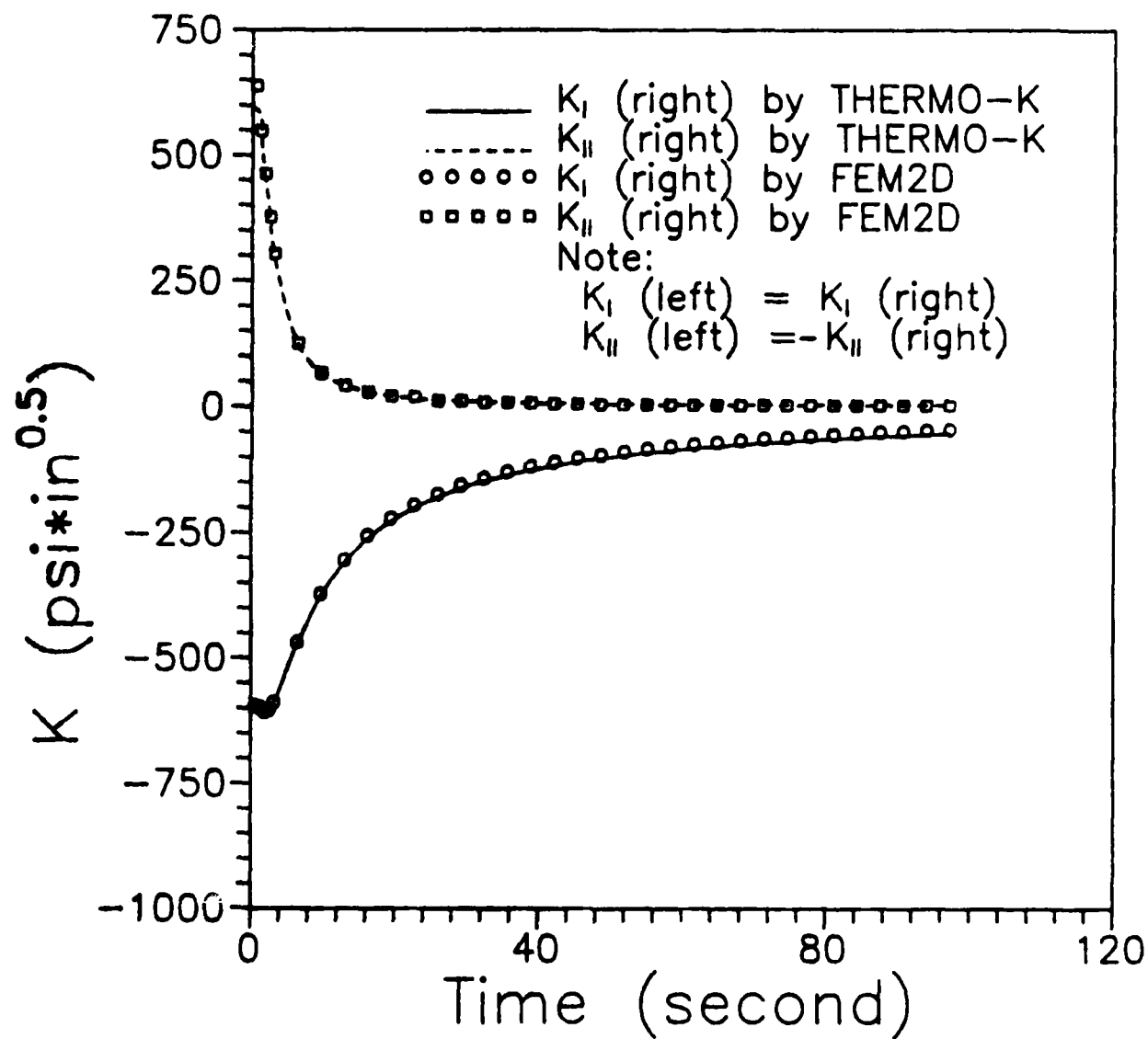


Figure 2-8. Stress Intensity Factor Due to an Instantaneous Heat Source at (0",1") (Fully Conductive Crack)

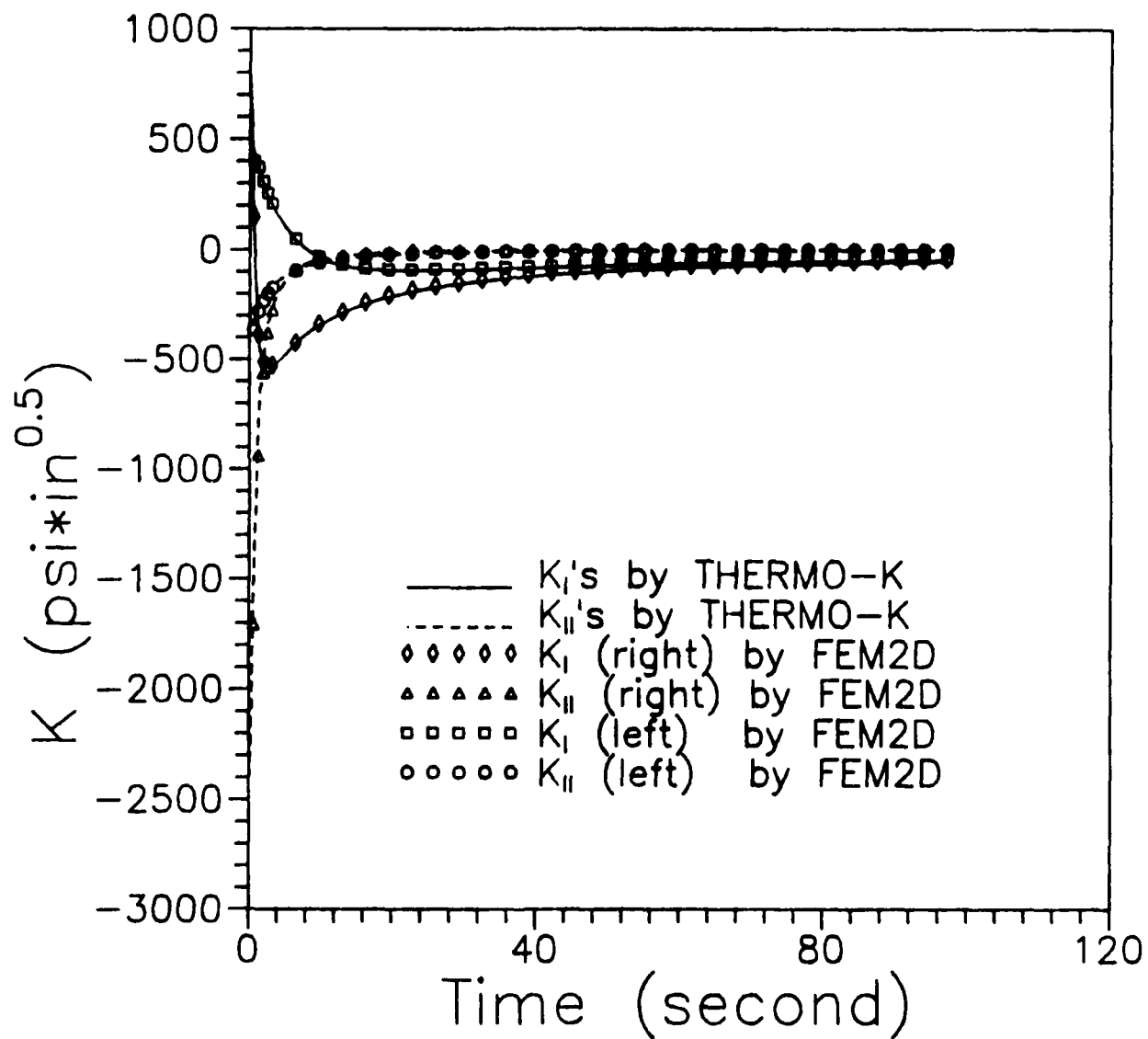


Figure 2-9. Stress Intensity Factors Due to an Instantaneous Heat Source at (1.4",0.4") (Fully Conductive Crack)

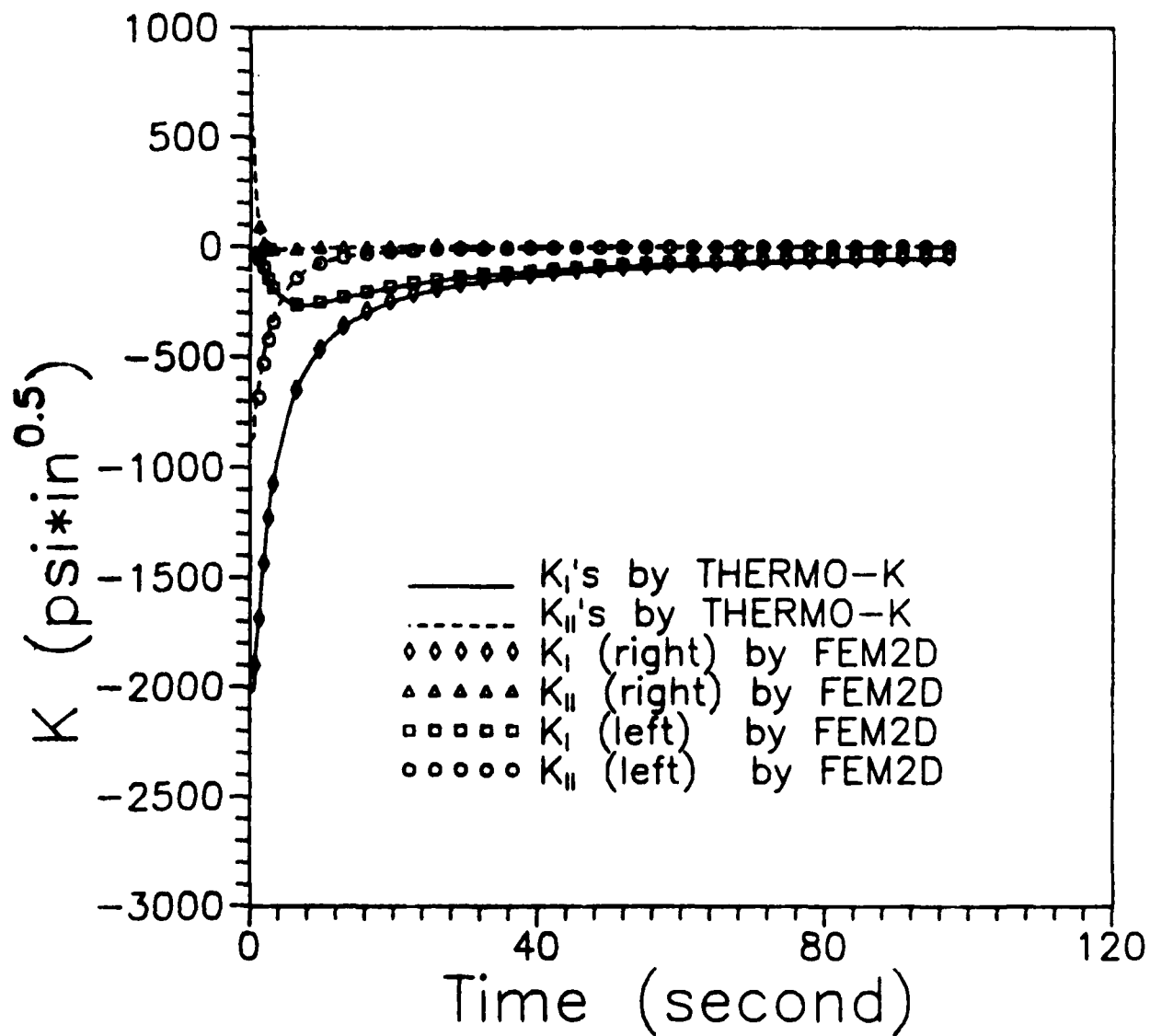


Figure 2-10. Stress Intensity Factors Due to an Instantaneous Heat Source at (0.6",0.6") (Fully Conductive Crack)

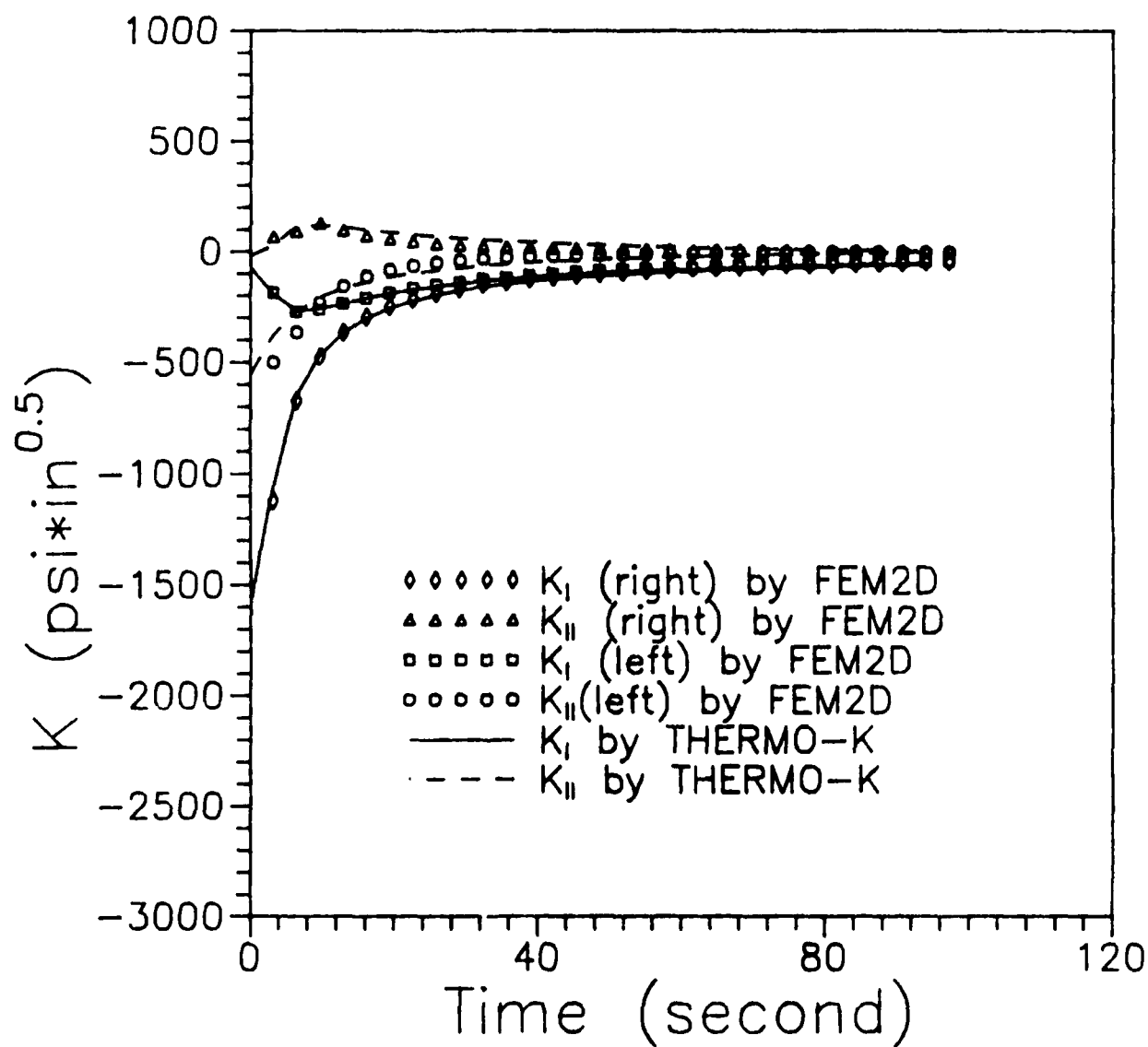


Figure 2-11. Stress Intensity Factors Due to an Instantaneous Heat Source at (0.6 inch, 0.6 inch) (Insulated Crack)

3.0 THEORETICAL BACKGROUND OF CRACK MODEL 2 - A SINGLE-EDGE CRACK IN A SEMI-INFINITE PLATE

This section describes the theoretical basis for crack Model 2 - a single-edge crack in a semi-infinite plate, i.e., as illustrated in Figure 3-1, a crack of length a in a semi-infinite plate of thickness D . The cracked plate is subjected to point heat sources with arbitrary time history at any points in the plate.

3.1 Assumptions

The following assumptions were made to simplify the problem:

- (a) The problem is assumed to be a plane stress problem. In other words, the thickness D shown in Figure 3-1 is assumed to be small enough that the temperature distribution in the thickness direction can be treated as uniform and the stress components in the thickness direction are negligible compared with the in-plane stress components.
- (b) The metallic materials are assumed to be isotropic, homogeneous, and linear elastic. Material properties are assumed to be temperature independent.
- (c) The rate of heat application is slow enough that the coupling terms and inertia terms in the general thermoelasticity equations can be neglected, i.e., it is assumed that the decoupled, quasi-static thermoelasticity applies.
- (d) The crack surfaces are assumed to be stress free. The crack surfaces can be completely insulated, fully heat conductive, or partially heat conductive. Heat conductance coefficient h at the crack surfaces is also assumed to be constant throughout the entire temperature range. The edge of the

semi-infinite plate, i.e., $x=0$ in Figure 3-1, is assumed to be insulated and stress free.

- (e) It is assumed that the heat convection coefficient, H , at the plate surfaces (see Figure 3-1) remain constant.

3.2 Governing Equations

For a plane stress thermoelasticity problem as illustrated in Figure 3-1, the governing equations are

$$\xi \nabla^2 T = T_{,t} + \xi \eta^2 T \quad (3-1)$$

$$\sigma_{ij,j} = 0 \quad (3-2)$$

$$\sigma_{ij} = 2G [\epsilon_{ij} + (\frac{\nu}{1-\nu}) \delta_{ij} \epsilon_{kk} - \alpha (\frac{1+\nu}{1-\nu}) \delta_{ij} T] \quad (3-3)$$

$$\epsilon_{ij} = (U_{i,j} + U_{j,i})/2 \quad (3-4)$$

and

$$\nabla^2 U_i + (\frac{1+\nu}{1-\nu}) U_{j,ji} = 2(\frac{1+\nu}{1-\nu}) \alpha T \quad (3-5)$$

where $T=T(x,y;t)$ is temperature distribution, t , x and y are time and Cartesian coordinates respectively, $\xi=(k/\rho c)$, k is heat conduction coefficients, ρ is mass density, c is heat capacity, $\eta^2=(2H)/k/D$, H is heat convection coefficient from the plate

surfaces to the environment (see Figure 3-1), D is plate thickness, U_i are displacements, α is coefficient of thermal expansion, and G and ν are shear modulus and Poisson's ratio respectively.

Nominal stress distributions generated with these equations are used to develop stress intensity factors via the influence function approach described below.

3.3 Influence Functions for Stress Intensity Factor

For any plate/crack geometry, cracktip stress intensity factors can be determined by integrating the product of the stresses at the crack location in an uncracked plate and an influence function (or weight function) (Buecker, 1973). That is, for a crack, as shown in Figure 3-2, the stress intensity factor can be calculated by

$$K_I = \int_0^a \sigma_{yy}(x,0) m_1(x) dx \quad (3-6)$$

$$K_{II} = \int_0^a \sigma_{xy}(x,0) m_2(x) dx \quad (3-7)$$

where $m_1(x)$ and $m_2(x)$ are influence functions, x is a local coordinate shown in Figure 3-1 or Figure B-1 of Appendix B, and σ_{yy} and σ_{xy} are the normal and shear stress distributions on the crack surface in an identical but uncracked plate which is under the same temperature distribution as the cracked plate.

For an edge crack in a semi-infinite plate, as illustrated in Figure 3-1, the influence functions have been provided by Sih (1973) as

$$m_1(x) = m_2(x) = \frac{1 + F(x/a)}{\sqrt{\pi a} (1-x/a)} \quad (3-8)$$

where

$$F\left(\frac{x}{a}\right) = \left(1 - \frac{x}{a}\right) \left[0.2945 - 0.3912\left(\frac{x}{a}\right)^2 + 0.7685\left(\frac{x}{a}\right)^4 - 0.9942\left(\frac{x}{a}\right)^6 + 0.5094\left(\frac{x}{a}\right)^8 \right] \quad (3-9)$$

Sih (1973) has indicated that the influence function given by Equations (3-8) and (3-9) are very accurate for all crack lengths.

3.4 Principle of Superposition

In general, as shown in Figure 3-1, there may be multiple heat sources (or sinks) within the plate which will cause thermal stresses and stress intensity factors at the crack tip in the structure. Since the problem is linear, it is easily demonstrated that total stress intensity factor can be calculated as the sum of the stress intensity factors caused by each individual heat source (or sink), acting independently. That is

$$K(t) = \sum_i [K(t)]_i \quad (3-10)$$

where $K(t)$ is the total stress intensity factor and $[K(t)]_i$ is the stress intensity factor due to the i^{th} heat source.

3.5 Green's Function Concept for Time Integration

In Equation (3-10), the stress intensity factor $[K(t)]_i$ caused by each individual heat source can be solved with the concept of

Green's function integration. As illustrated in Figure 3-3, the stress intensity factor due to a heat source of intensity $Q_i(t)$ can be calculated by

$$[K(t)]_i = \int_0^t Q_i(\tau) G_i(t-\tau) d\tau \quad (\text{no summation}) \quad (3-11)$$

where $G_i(t)$ is the stress intensity factors due to a delta function $\delta(t)$ heat source at the i^{th} heat source location.

As shown in Figure 3-3, generally, the Green's function $G_i(t)$ will decay and approach zero after a decay period t_d . Therefore, the integration range in Equation (3-11) can be reduced to from $(t-t_d)$ to t . Such a reduction in the integration range greatly increases the speed of the calculation because, instead of integrating for the entire time history, it is only necessary to integrate backwards from the present time t to $(t-t_d)$ as follows

$$[K(t)]_i = \int_{t-t_d}^t Q_i(\tau) G_i(t-\tau) d\tau \quad (3-12)$$

3.6 Green's Function for Fully Heat Conductive Cracks

Previous sections of this section show that the stress intensity factors for these crack models can be easily obtained by using Equations (3-6), (3-7), (3-10), and (3-12) if the temperature and stress distributions and thereby the stress intensity factors at the crack tip, resulting from a delta function heat source (or sink) $Q\delta(t)$ at any arbitrary location (x',y') in the uncracked plate (refer to Figure 3-4), can be solved. The uncracked plate shares the same temperature distribution as the cracked plate. As the first step, we consider the problem of a fully heat

conductive edge crack, i.e., in this subsection, it is assumed that heat flux can flow across the crack surfaces without any heat loss or resistance. Solutions for a more general, partially heat conductive crack will be discussed in the next section. However, as will be seen in the next subsection and as shown in Appendix A of this report, for a crack model with symmetry about its crack plane such as this crack model, crack surface heat conductivity will affect Mode II stress intensity factor solutions but not Mode I or Mode III stress intensity factor solutions. In other words, whether the crack surfaces are fully heat conductive, insulated, or partially heat conductive, the K_I solution will remain the same for an edge crack in a semi-infinite plate. Thus, if only the Mode I fracture is of major interest, the stress intensity factor solutions can be obtained by assuming the crack surfaces are fully heat conductive. The assumption of a fully heat conductive crack will greatly shorten the computation time for temperatures, thermal stresses, and stress intensity factors.

Since thermal stresses and stress intensity factors do not depend on the initial, stress-free temperature of the plate, it is conveniently assumed that the initial temperature of the plate is zero, i.e., $T(x,y;0)=0$. To solve the Green's function of this crack model, the following boundary conditions need to be satisfied in addition to the governing equations listed in Equations (3-1) to (3-5):

at infinity,

$$T(x,y;t) = 0 \quad (3-13)$$

$$\sigma_{xx}(x,y;t) = \sigma_{yy}(x,y;t) = \sigma_{xy}(x,y;t) = 0 \quad (3-14)$$

at $y=0$, $0 \leq x \leq a$,

$$T(x, 0^+; t) = T(x, 0^-; t) \quad (3-15)$$

$$\sigma_{yy}(x, 0^+; t) = \sigma_{yy}(x, 0^-; t) \quad (3-16)$$

$$\sigma_{xy}(x, 0^+; t) = \sigma_{xy}(x, 0^-; t) \quad (3-17)$$

$$U_i(x, 0^+; t) = U_i(x, 0^-; t) \quad , \quad i = x, y \quad (3-18)$$

at $x=0$

$$T_{,x}(0, y; t) = 0 \quad (3-19)$$

$$\sigma_{xx}(0, y; t) = \sigma_{xy}(0, y; t) = 0 \quad (3-20)$$

Temperature solution to the uncracked plate problem can be obtained by solving Equation (3-1) along with boundary conditions in Equations (3-15) and (3-19). An analytical form of the temperature solution has been derived by Carslaw and Jaeger (1959) as follows:

$$T(x, y; t) = \frac{Q}{4\pi\xi t \rho c D} \left[\exp(-\xi\eta^2 t - \frac{R^2}{4\xi t}) + \exp(-\xi\eta^2 t - \frac{\hat{R}^2}{4\xi t}) \right] \quad (3-21)$$

where ξ and η are defined in Equation (3-1), and

$$R^2 = (x-x')^2 + (y-y')^2 \quad (3-22)$$

$$\hat{R}^2 = (x+x')^2 + (y-y')^2 \quad (3-23)$$

Physically, Equation (3-21) represents the superposition of the temperature solutions for two instantaneous heat sources of strength Q situated at (x', y') and $(-x', y')$ in an infinite plate.

The next step is to solve the stress distribution due to the temperature distribution of Equation (3-21). Boley and Weiner (1960) and Parkus (1968) have shown that a particular solution to the thermal stress problem can be expressed in terms of a thermoelastic potential ϕ as follows:

$$U_i = \phi_{,i} \quad (i = x, y) \quad (3-24)$$

$$\sigma_{xx} = -2G \phi_{,yy} \quad (3-25)$$

$$\sigma_{yy} = -2G \phi_{,xx} \quad (3-26)$$

$$\sigma_{xy} = 2G \phi_{,xy} \quad (3-27)$$

$$\phi(x, y; t) = \alpha(1+\nu) \xi e^{-\xi \eta^2 t} \int_0^t e^{\xi \eta^2 \tau} T(x, y; \tau) d\tau + \phi_0 \quad (3-28)$$

where ϕ_0 is a function of x , y , and t such that ϕ would remain finite as t approaches infinity. Substitution of Equation (3-21) into Equation (3-28) yields

$$\begin{aligned}\phi(x,y;t) = & \frac{a(1+\nu)Q}{4\pi\rho cD} \exp(-\xi\eta^2 t) \left[\int_0^t \exp\left(-\frac{R^2}{4\xi\tau}\right) \frac{d\tau}{\tau} + \ln(R) \right. \\ & \left. + \int_0^t \exp\left(-\frac{\hat{R}^2}{4\xi\tau}\right) \frac{d\tau}{\tau} + \ln(\hat{R}) \right] \quad (3-29)\end{aligned}$$

Therefore, by substituting Equation (3-29) into Equations (3-25) to (3-27), it can be shown that

$$\begin{aligned}\sigma'_{xx}(x,y;t) = & \frac{Ga(1+\nu)Q}{\pi\rho cDR^2} e^{-\xi\eta^2 t} \left(\left[1 - \frac{2(y-y')^2}{R^2} \left(1 + \frac{R^2}{4\xi t} \right) \right] \right. \\ & \left. \exp\left(-\frac{R^2}{4\xi t}\right) - 1 + \frac{2(y-y')^2}{R^2} \right) \\ & + \frac{Ga(1+\nu)Q}{\pi\rho cD\hat{R}^2} e^{-\xi\eta^2 t} \left(\left[1 - \frac{2(y-y')^2}{\hat{R}^2} \left(1 + \frac{\hat{R}^2}{4\xi t} \right) \right] \right. \\ & \left. \exp\left(-\frac{\hat{R}^2}{4\xi t}\right) - 1 + \frac{2(y-y')^2}{\hat{R}^2} \right) \quad (3-30)\end{aligned}$$

$$\begin{aligned}\sigma'_{yy}(x,y;t) = & \frac{Ga(1+\nu)Q}{\pi\rho cDR^2} e^{-\xi\eta^2 t} \left(\left[1 - \frac{2(x-x')^2}{R^2} \left(1 + \frac{R^2}{4\xi t} \right) \right] \right. \\ & \left. \exp\left(-\frac{R^2}{4\xi t}\right) - 1 + \frac{2(x-x')^2}{R^2} \right) \\ & + \frac{Ga(1+\nu)Q}{\pi\rho cD\hat{R}^2} e^{-\xi\eta^2 t} \left(\left[1 - \frac{2(x-x')^2}{\hat{R}^2} \left(1 + \frac{\hat{R}^2}{4\xi t} \right) \right] \right. \\ & \left. \exp\left(-\frac{\hat{R}^2}{4\xi t}\right) - 1 + \frac{2(x-x')^2}{\hat{R}^2} \right) \quad (3-31)\end{aligned}$$

$$\begin{aligned}
\sigma'_{xy}(x,y;t) = & \frac{2Ga(1+\nu)Q(x-x')(y-y')}{\pi\rho cDR^4} e^{-\xi\eta^2t} \\
& \left[\left(1 + \frac{R^2}{4\xi t}\right) \exp\left(-\frac{R^2}{4\xi t}\right) - 1 \right] \\
& + \frac{2Ga(1+\nu)Q(x-x')(y-y')}{\pi\rho cD\hat{R}^4} e^{-\xi\eta^2t} \\
& \left[\left(1 + \frac{\hat{R}^2}{4\xi t}\right) \exp\left(-\frac{\hat{R}^2}{4\xi t}\right) - 1 \right]
\end{aligned} \tag{3-32}$$

where R is defined in Equation (3-22) and \hat{R} is defined in Equation (3-23). It can be shown that the displacements and stresses resulting from $\phi(x,y;t)$ satisfy the boundary conditions specified in Equations (3-14) and (3-16) to (3-18) but not in Equation (3-20). In fact, at the edge $x=0$, stress components resulting from the thermoelastic potential ϕ are

$$\begin{aligned}
\sigma'_{xx}(0,y;t) = & \frac{2Ga(1+\nu)Q}{\pi\rho cD\bar{R}^2} \left(\left[1 - \frac{2(y-y')^2}{\bar{R}^2} \left(1 + \frac{\bar{R}^2}{4\xi t} \right) \right] \exp\left(-\frac{\bar{R}^2}{4\xi t}\right) \right. \\
& \left. - 1 + \frac{2(y-y')^2}{\bar{R}^2} \right)
\end{aligned} \tag{3-33}$$

$$\sigma'_{xy}(0,y;t) = 0 \tag{3-34}$$

where $\bar{R}^2 = x'^2 + (y-y')^2$.

The non-zero stress components at the edge $x=0$, given by Equation (3-33), can easily be cancelled out by superimposing a set of complementary stress components σ''_{ij} , which are stresses in an edge loaded, isothermal semi-infinite plate. Of course, the edge

loading in the complementary problem is the negative of that resulting from ϕ , i.e., $\sigma''_{xx}(0,y;t) = -\sigma'_{xx}(0,y;t)$, and $\sigma''_{xy}(0,y;t) = 0$. Therefore, by using the classical solution for stresses in a semi-infinite plate subjected to a concentrated edge load (see e.g., Timoshenko, 1970), it can be shown that the complementary stresses at the crack region are

$$\sigma''_{yy}(x,0;t) = -\frac{2x}{\pi} \int_{-\infty}^{\infty} \sigma'_{xx}(0,\hat{y};t) \frac{\hat{y}^2}{(x^2+\hat{y}^2)^2} d\hat{y} \quad (3-35)$$

$$\sigma''_{xy}(x,0;t) = -\frac{2x^2}{\pi} \int_{-\infty}^{\infty} \sigma'_{xx}(0,\hat{y};t) \frac{\hat{y}}{(x^2+\hat{y}^2)^2} d\hat{y} \quad (3-36)$$

To sum up this subsection, the Green's functions for the stress intensity factors are calculated by substituting the sum of stress solutions $\sigma'_{yy}(x,0;t)$ and $\sigma'_{xy}(x,0;t)$ given in Equation (3-31) and (3-32) and complementary stress solutions $\sigma''_{yy}(x,0;t)$ and $\sigma''_{xy}(x,0;t)$ given in Equations (3-35) and (3-36) and the influence functions given in Equations (3-8) and (3-9) into Equations (3-6) and (3-7) and integrating Equations (3-6) and (3-7) by the numerical integration scheme depicted in Appendix B.

3.7 Green's Function for Partially Heat Conductive Cracks

In subsection 3.6, the Green's function solution for a single point heat source at any arbitrary point in a semi-infinite plate with a fully heat conductive edge crack is derived. In reality, the crack surface is expected to be somewhere between completely insulated and fully heat conductive, i.e., crack surfaces are expected to be partially heat conductive. A general approach to treat a partially heat conductive crack is studied in detail in Appendix A of this report. Application of the concept given in Appendix A to an edge crack in a semi-infinite plate is discussed in this subsection.

Governing heat transfer equation for a partially heat conductive crack in an infinite plate is still Equation (3-1), and the boundary conditions at infinity, Equation (3-13), and the boundary conditions at the edge, Equation (3-19), remain unchanged. The only difference will be the boundary condition at $y=0$, $0 \leq x \leq a$, i.e., Equation (3-15) is replaced by

$$T_{,y}(x,0) = \frac{\lambda}{a} [T(x,0^+) - T(x,0^-)] \quad 0 \leq x \leq a \quad (3-37)$$

where λ is defined as (ah/k) in which h is crack surface heat conductance coefficient and k is material thermal conductivity. From Equation (4-37), it can be easily seen that the crack surfaces are fully heat conductive when $\lambda=\infty$ and the crack surfaces are completely insulated when $\lambda=0$. Any λ values between 0 and ∞ are corresponding to a partially heat conductive crack.

As discussed in Appendix A, when a crack is completely insulated or partially heat conductive, the resulting temperatures on both sides of a crack will be different, i.e., there is a temperature jump across the crack surface when λ equals to zero or a finite number. This temperature jump is analogous to the temperature jump created by a series of distributed heat dipoles (Carslaw and Jaeger, 1959) situated at the crack location. Thus, the overall temperature distribution for the partially heat conductive crack problem can be obtained as the superposition of the fully conductive solution, Equation (3-21), and a solution for the distributed heat dipoles. From Equation (3-21), it can be shown, by summing temperature solutions for a point heat source and a point heat sink with infinitesimally small distance in-between, that temperature solution for an instantaneous heat dipole of strength M situated at $y=0$, $x=\bar{x}$ in a semi-infinite plate is

$$T(x,y;t) = - \frac{M y}{8\pi\xi^2 \rho c D t^2} \left(\exp\left[-\frac{(x-\bar{x})^2 + y^2}{4\xi t} - \xi\eta^2 t\right] + \exp\left[-\frac{(x+\bar{x})^2 + y^2}{4\xi t} - \xi\eta^2 t\right] \right) \quad (3-38)$$

Thus, resulting temperature from distributed heat dipoles of strength $M(x,t)$ situated at $y=0$, $0 \leq x \leq a$ of the plate is

$$\hat{T}(x,y;t) = \frac{-y}{8\pi\rho c D \xi^2} \int_0^t \int_0^a \frac{M(\bar{x},\tau)}{(t-\tau)^2} \left(\exp\left[-\xi\eta^2 t - \frac{(x-\bar{x})^2 + y^2}{4\xi(t-\tau)}\right] + \exp\left[-\xi\eta^2 t - \frac{(x+\bar{x})^2 + y^2}{4\xi(t-\tau)}\right] \right) d\bar{x} d\tau \quad (3-39)$$

Substitution of the sum of Equations (3-21) and (3-39) into Equation (3-37) yields a Fredholm integral equation for the heat dipole distribution $M(x,t)$ as follows:

$$2 \int_0^t \int_0^a \frac{M(\bar{x},\tau)}{(t-\tau)^2} \left(\exp\left[-\frac{(x-\bar{x})^2}{4\xi(t-\tau)}\right] + \exp\left[-\frac{(x+\bar{x})^2}{4\xi(t-\tau)}\right] \right) d\bar{x} d\tau =$$

$$\frac{Qy'}{t^2} \left(\exp\left[-\frac{(x-\bar{x})^2 + y^2}{4\xi t}\right] + \exp\left[-\frac{(x+\bar{x})^2 + y^2}{4\xi t}\right] \right)$$

$$- 8\pi\xi \frac{\lambda}{a} M(x,t) \quad (3-40)$$

A numerical approximation method is used in the computer program to solve Equation (3-40). Since the temperature jump between two adjacent crack surfaces has to be zero at the crack tip, $x=a$, we assume that

$$M(x,t) = \sum_{m=1}^L b_m(t) \sin\left(\frac{m\pi x}{a}\right) \quad (3-41)$$

where L is the maximum number of terms included in the calculation and $b_m(t)$ is a time function, which is determined by substituting Equation (3-41) into Equation (3-40).

Similar to the fully heat conductive case, a thermoelastic potential due to the distributed thermal dipoles at the crack region can be derived by integrating the temperature solution, Equation (3-39). That is,

$$\hat{\phi}(x,y;t) = \alpha\xi(1+\nu) \int_0^t \hat{T}(x,y;\tau) \exp[-\xi\eta^2(t-\tau)] d\tau + \hat{\phi}_0 \quad (3-42)$$

where $\hat{T}(x,y;t)$ is the temperature solution given in Equation (3-39) and $\hat{\phi}_0$ is an analytic function to make $\hat{\phi}$ remain finite at infinity.

It can be shown that stresses at the crack region, $y=0$ and $0 \leq x \leq a$, due to the thermoelastic potential $\hat{\phi}$ given in Equation (3-42) are

$$\hat{\sigma}'_{yy}(x,0;t) = 0 \quad (3-43)$$

$$\begin{aligned} \hat{\sigma}'_{xy}(x,0;t) = & \frac{16Ga(1+\nu)}{\pi\rho cD} \int_0^a \int_0^t M(\bar{x},\tau) \exp(-\xi\eta^2 t) \\ & \left(\frac{1}{(\bar{x}-\bar{\lambda})^3} \left[1 + \frac{(x-\bar{x})^2}{4\xi(t-\tau)} \right] \exp\left[-\frac{(x-\bar{x})^2}{4\xi(t-\tau)}\right] + \right. \\ & \left. \frac{1}{(x+\bar{x})^3} \left[1 + \frac{(x+\bar{x})^2}{4\xi(t-\tau)} \right] \exp\left[-\frac{(x+\bar{x})^2}{4\xi(t-\tau)}\right] \right) d\tau d\bar{x} \end{aligned} \quad (3-44)$$

Similar to last section, a set of complementary stresses is required to make stresses at the edge $x=0$ vanish. The complementary stresses are

$$\hat{\sigma}_{yy}''(x,0;t) = - \frac{2x}{\pi} \int_{-\infty}^{\infty} \hat{\sigma}_{xx}'(0,\hat{y};t) \frac{\hat{y}^2}{(x^2+\hat{y}^2)^2} d\hat{y} = 0 \quad (3-45)$$

$$\hat{\sigma}_{xy}''(x,0;t) = - \frac{2x^2}{\pi} \int_{-\infty}^{\infty} \hat{\sigma}_{xx}'(0,\hat{y};t) \frac{\hat{y}}{(x^2+\hat{y}^2)^2} d\hat{y} \quad (3-46)$$

where

$$\begin{aligned} \hat{\sigma}_{xx}'(0,y;t) = & - \frac{4Ga(1+\nu)}{\pi\rho cD} \int_0^a \int_0^t M(\bar{x},\tau) \frac{y}{(\bar{x}^2+y^2)^2} \left(1 + \right. \\ & \left. \frac{\bar{x}^2+y^2}{4\xi(t-\tau)} + \frac{4y^2}{(\bar{x}^2+y^2)} \left[1 + \frac{\bar{x}^2+y^2}{4\xi(t-\tau)} + \frac{(\bar{x}^2+y^2)^2}{32\xi^2(t-t')^2} \right] \right) \\ & \exp[-\xi\eta^2t - \frac{\bar{x}^2+y^2}{4\xi(t-\tau)}] d\tau d\bar{x} \end{aligned} \quad (3-47)$$

Results shown in Equations (3-43) to (3-47) reiterate the fact, deduced in Appendix A, that for a cracked structure with symmetry with respect to the crack plane such as the current crack model, crack surface heat conductivity will not affect Mode I fracture solution ($\hat{\sigma}_{yy}'(x,0;t) = \hat{\sigma}_{yy}''(x,0;t) = 0$ in Equations (3-43) and (3-45)) but will change Mode II fracture solution ($\sigma_{xy}(x,0;t) \neq 0$ in Equations (3-44) and (3-46)).

To sum up, for a partially heat conductive edge crack in a semi-infinite plate subjected to an instantaneous heat source of intensity Q at (x', y') , its overall temperature solution is the sum of Equation (3-21) and Equation (3-39). Stresses in the uncracked plate strip, which share the same overall temperature distribution as the cracked plate, are the sum of Equations (3-31), (3-32), (3-35), (3-36), and (3-43) to (3-46). Green's function solutions for stress intensity factors, K_I and K_{II} , at the crack tip are then calculated by substituting the above stresses at the crack region into Equations (3-6) and (3-7), respectively.

3.8 Finite Element Verification of Crack Model 2

Since stress intensity factors are calculated by integrating the product of influence functions and stresses at the crack region in an uncracked plate (see Equations (3-6) and (3-7)), it is necessary to verify both the influence function shown in subsection 3.3 and the temperature and thermal stress solution shown in subsections 3.6 and 3.7.

3.8.1 Verification of Influence Functions

To verify the influence functions given in Equations (3-8) and (3-9), the problem of a single edge crack in a semi-infinite plate subjected to a uniform tensile stress σ_0 and an uniform shear stress τ_0 at infinity. Stress intensity factors solutions for this problem has been shown (see e.g., Sih, 1973) to be

$$K_I = 1.1215 \sigma_0 \sqrt{\pi a}$$

$$K_{II} = 1.1215 \tau_0 \sqrt{\pi a}$$

K_I and K_{II} solutions obtained by substituting $\sigma_{yy}(x,0)=\sigma_o$ into Equation (3-6) and $\sigma_{xy}(x,0)=\tau_o$ into Equation (3-7) and going through a numerical integration are

$$K_I = 1.1214 \sigma_o \sqrt{\pi a}$$

$$K_{II} = 1.1214 \tau_o \sqrt{\pi a}$$

Therefore, the influence functions shown in Equations (3-8) and (3-9) are very accurate.

3.8.2 Fully Heat Conductive Crack

To verify the formulation for stresses and stress intensity factors for crack Model 2, a finite element program, FEM2D (1986), was used to provide a numerical reference solution. A 1 inch long edge crack in a 1 inch thick semi-infinite plate is selected as an example problem. The plate is assumed to be insulated on front and back surfaces with normal vectors in the out of paper directions, i.e., $H=0$ in Figure 3-1, and is made of Aluminum 7075-T651 with the following material properties:

$$E=10.3 \times 10^6 \text{ psi}$$

$$\nu=0.33, \alpha=13 \times 10^{-6}$$

$$\rho=0.0978 \text{ Lbm/in}^3$$

$$c=0.23 \frac{\text{Btu}}{\text{Lbm-F}}$$

$$k=0.0017361 \frac{\text{Btu}}{\text{sec-in-F}}$$

As shown in Figure 3-5, a finite element model with 330 eight-node isoparametric elements and 372 nodal points is constructed for the heat transfer and thermal stress analyses of the example problem. In this finite element model, the adjacent nodal points at the crack surfaces are tied together in the thermal stress analysis so that they will have the same displacements. However, in the heat transfer analysis, the adjacent nodes at the crack region may or may not be constrained together depending on whether the crack surface is fully heat conductive or completely insulated.

We then consider the case of an instantaneous unit heat source applied at (0.6 inch, 0.6 inch). As discussed in the previous subsections of this section, stress intensity factors for this crack model equal to the integration of the product of influence functions and stresses at the crack region in an uncracked plate which shares the same temperature distribution as the cracked plate. Since the crack surface is assumed to be fully heat conductive, the adjacent nodes at the crack region are constrained together such that they share the same temperature as well as displacements and stresses. To obtain the reference solutions, temperatures and thermal stresses in the uncracked plate resulting from the single heat source at (0.6 inch, 0.6 inch) are first calculated by the finite element program, FEM2D (1986). Thermal stresses at the crack region are then substituted in to Equations (3-6) and (3-7) for stress intensity factor calculations.

As shown in Figure 3-6, stresses at (0.1 inch, 0 inch), and (0.9 inch, 0 inch) predicted by THERMO-K for the example problem are plotted as functions of time and are compared with corresponding finite element solutions. It is seen from this figure that

temperatures predicted by THERMO-K are in good agreement with the reference finite element solutions. Resulting stress intensity factors for the same problem are illustrated in Figure 3-7. Again, very good agreement between THERMO-K results and finite element solutions is observed. From Figures 3-6 and 3-7, it is concluded that temperature, thermal stress, and thus stress intensity factor solutions predicted by THERMO-K are very accurate compared with finite element solutions.

3.8.3 Insulated Crack

In this subsection, the crack surfaces of the example crack problem are assumed to be completely insulated. The same finite element mesh as is illustrated in Figure 3-5 is also used for reference solution calculation for the insulated crack case. The adjacent nodal points at the crack region, however, are assumed to be independent in the heat transfer analysis but are tied together in the following thermal stress analysis. In other words, the adjacent nodes at the crack region have different temperatures but share the same displacements and stresses in the finite element analyses for the insulated crack problem. An instantaneous heat source of strength $\delta(t)$ applied at (0.6 inch, 0.6 inch) is the thermal loading for this problem. Comparison of the resulting stress intensity factors are shown in Figure 4-8. Again, good agreement between THERMO-K's predictions and finite element solutions is observed.

3.9 References

Boley, B. A., and Weiner, J. H., (1960), Theory of Thermal Stresses, Wiley & Sons, New York, New York.

Bueckner, H. F., (1973), "Field Singularities and Related Integral Representations," in Methods of Analysis and Solutions of Crack Problems, Vol 1, ed. G. C. Sih, pp. 239-314, Noordhoff, Holland.

Carslaw, H. S., and Jaeger, J. C., (1959), Conduction of Heat in Solids, 2nd edition, Oxford University Press, London.

FEM2D User's Manual- A Two Dimensional Finite Element Computer Program for Two-Dimensional Heat Transfer/Thermal Stress Analysis, (1986), Structural Integrity Associates, San Jose, CA.

Parkus, H., (1968), Thermoelasticity, Blaisdell Publishing Co..

Sih, G. C. (1973), Handbook of Stress Intensity Factors, Institute of Fracture and Solid Mechanics, Lehigh University, Bethlehem, PA.

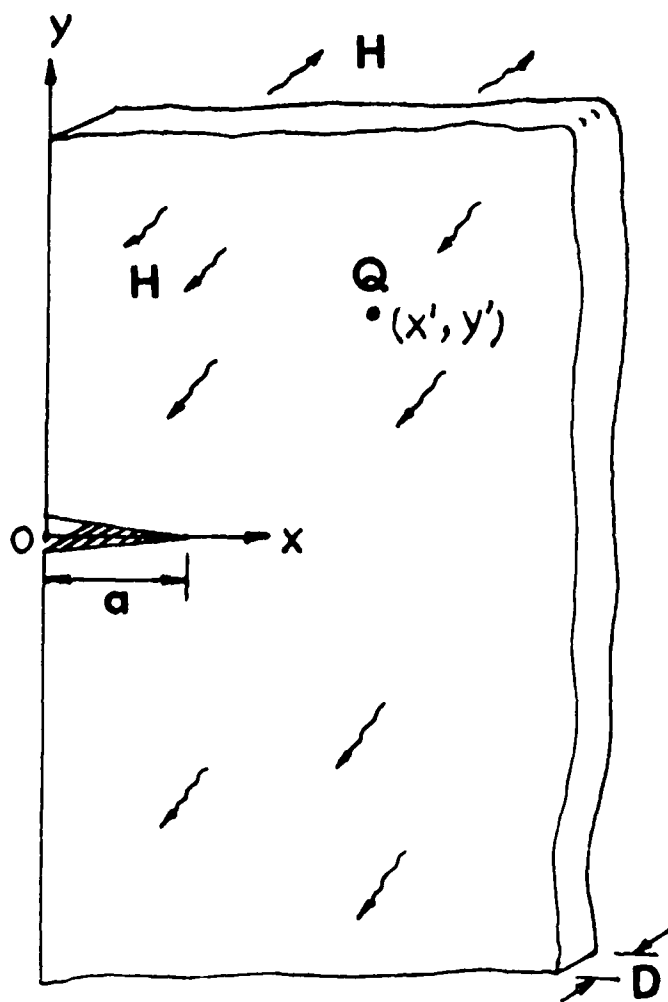


Figure 3-1. A Semi-Infinite Plate with a Single-Edge Crack Subjected to Heat Sources

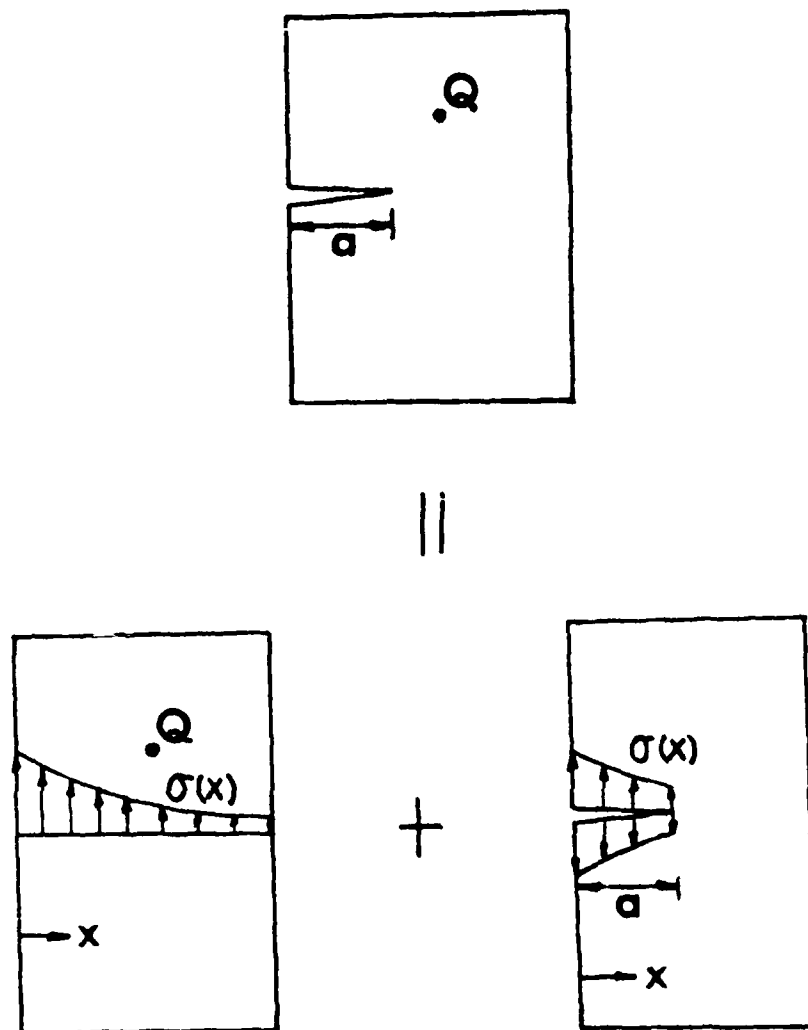
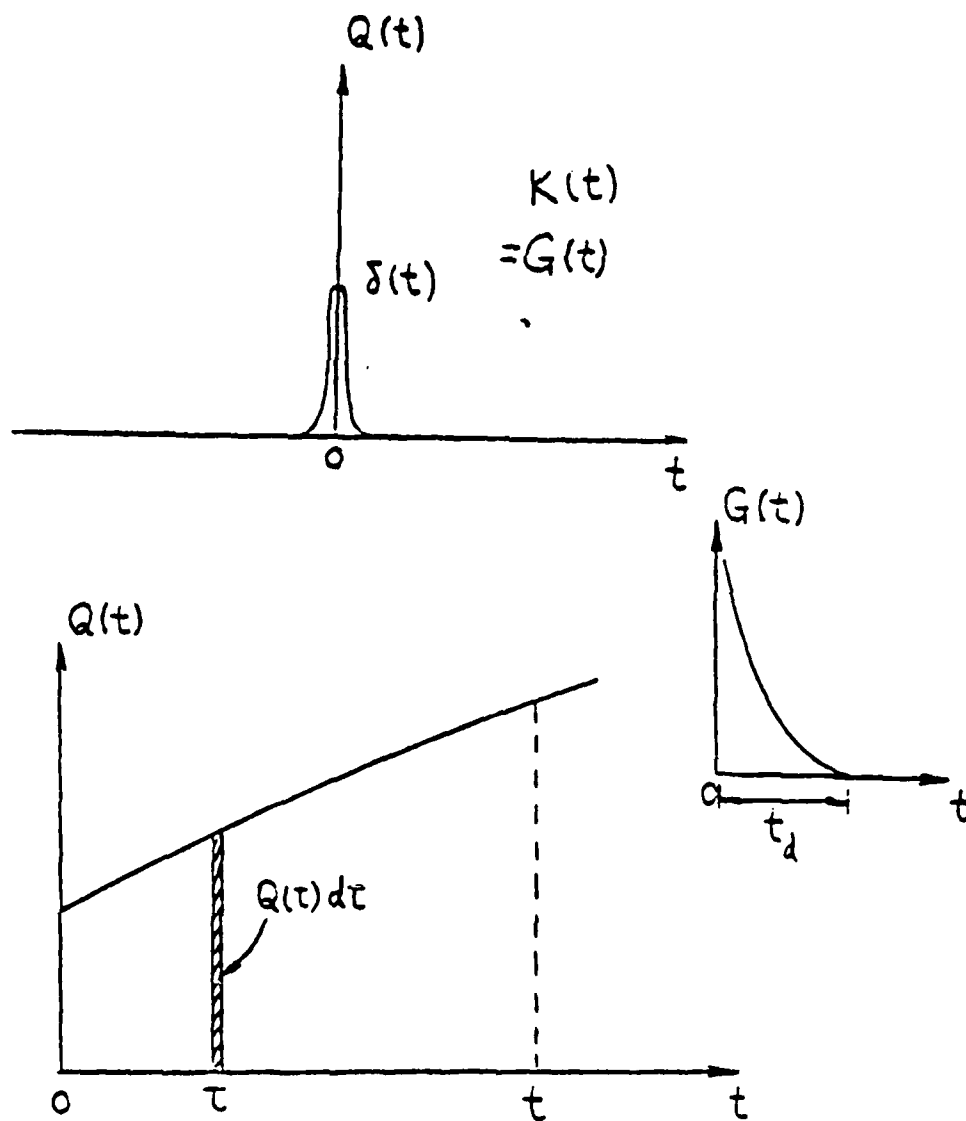


Figure 3-2. Concept of Influence Function



$$\begin{aligned}
 K(t) &= \int_0^t Q(\tau) G(t-\tau) d\tau \\
 &= \int_{t-t_d}^t Q(\tau) G(t-\tau) d\tau
 \end{aligned}$$

Figure 3-3. Concept of Green's Function

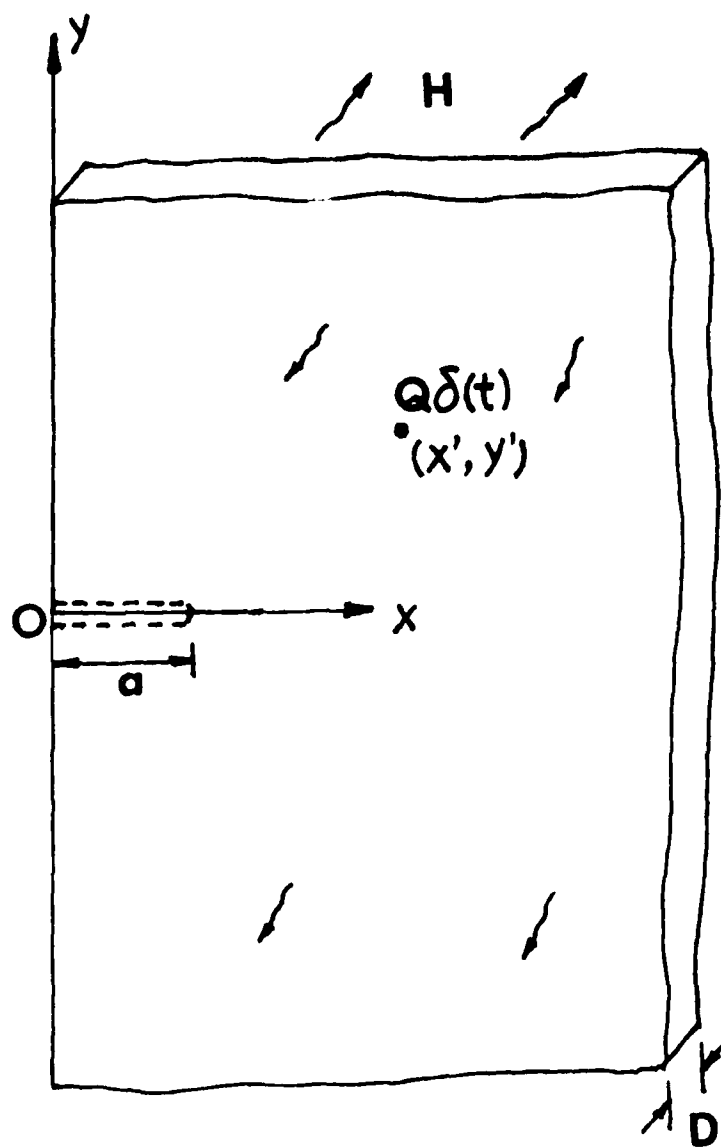


Figure 3-4. A Point Heat Source in an Uncracked Plate

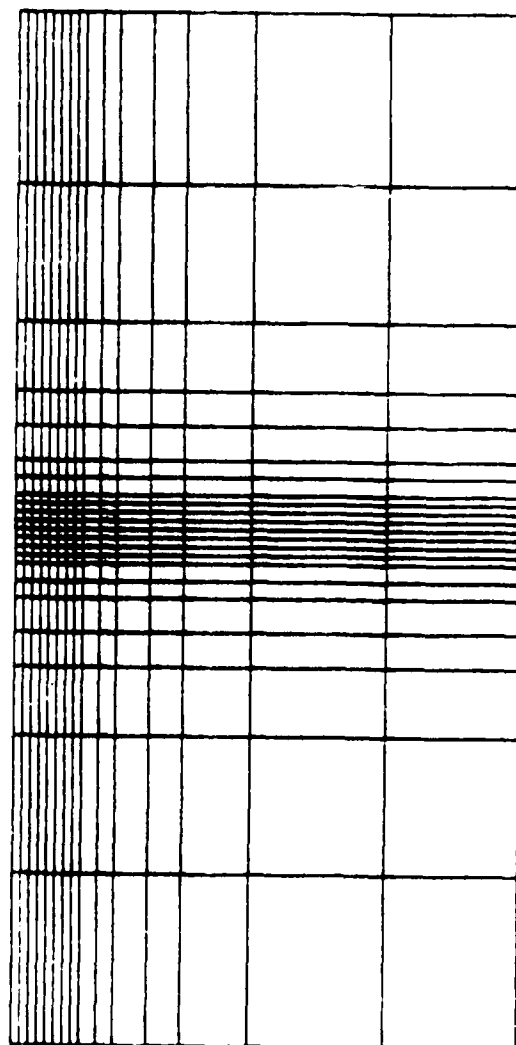


Figure 3-5(a). Finite Element Mesh for Crack Model 2
Verification Problems

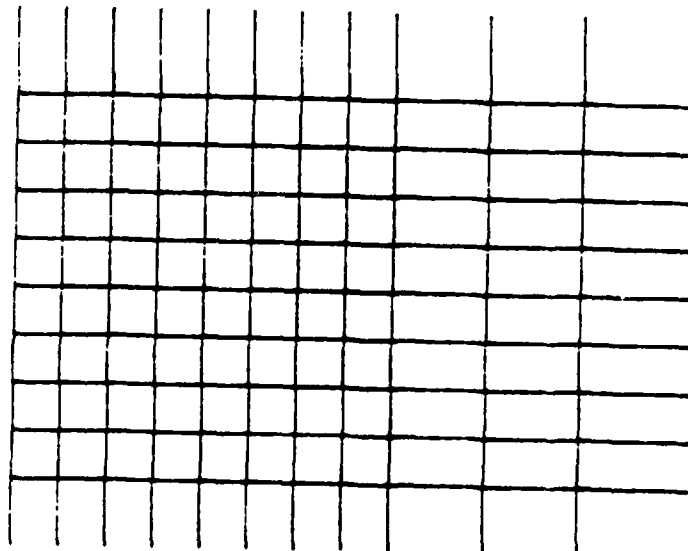


Figure 3-5(b). Finite Element Mesh Near Crack Region

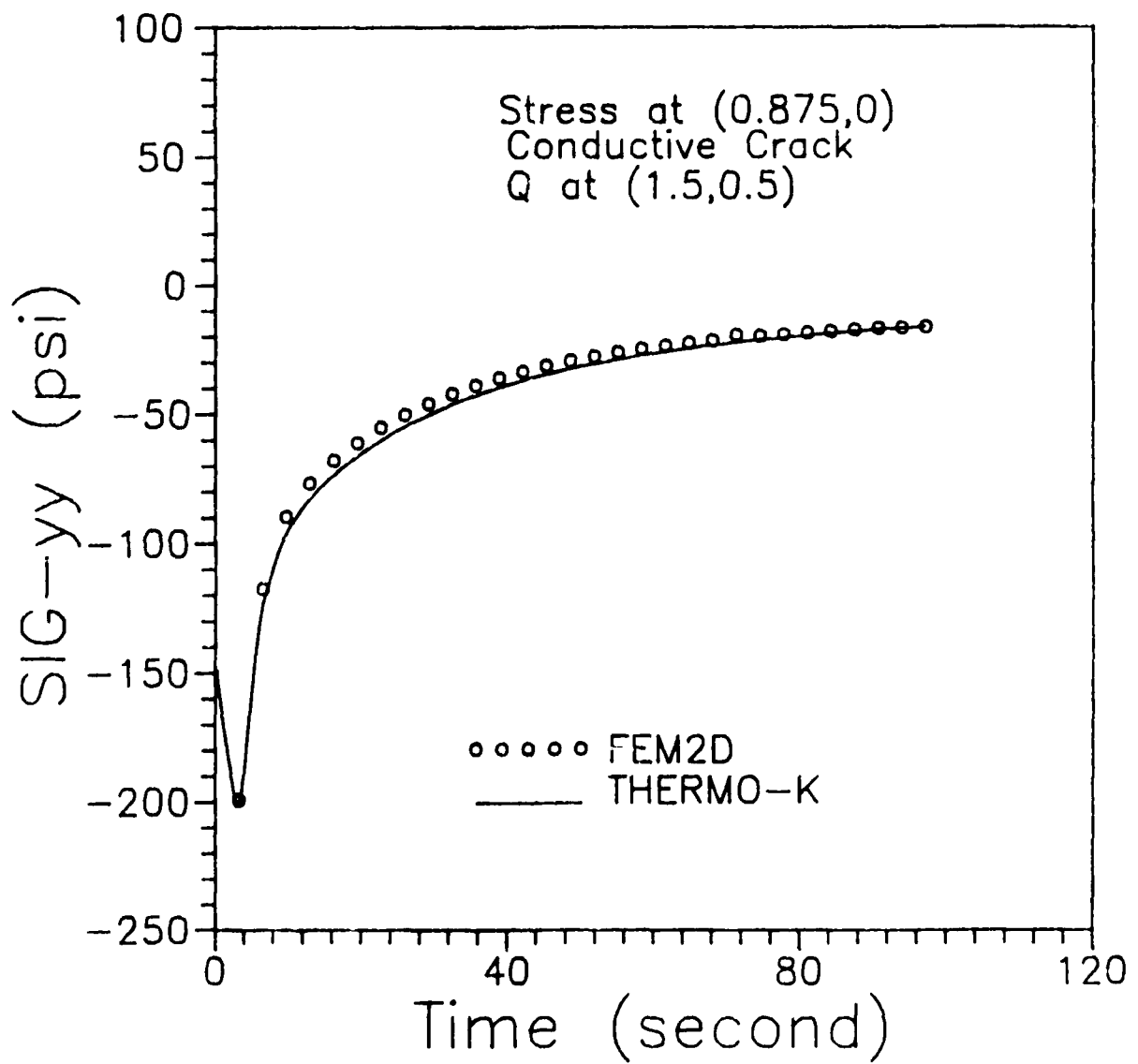


Figure 3-6. Normal Stresses Due to an Instantaneous Heat Source
at (1.5 inch, 0.5 inch) (Fully Conductive Crack)

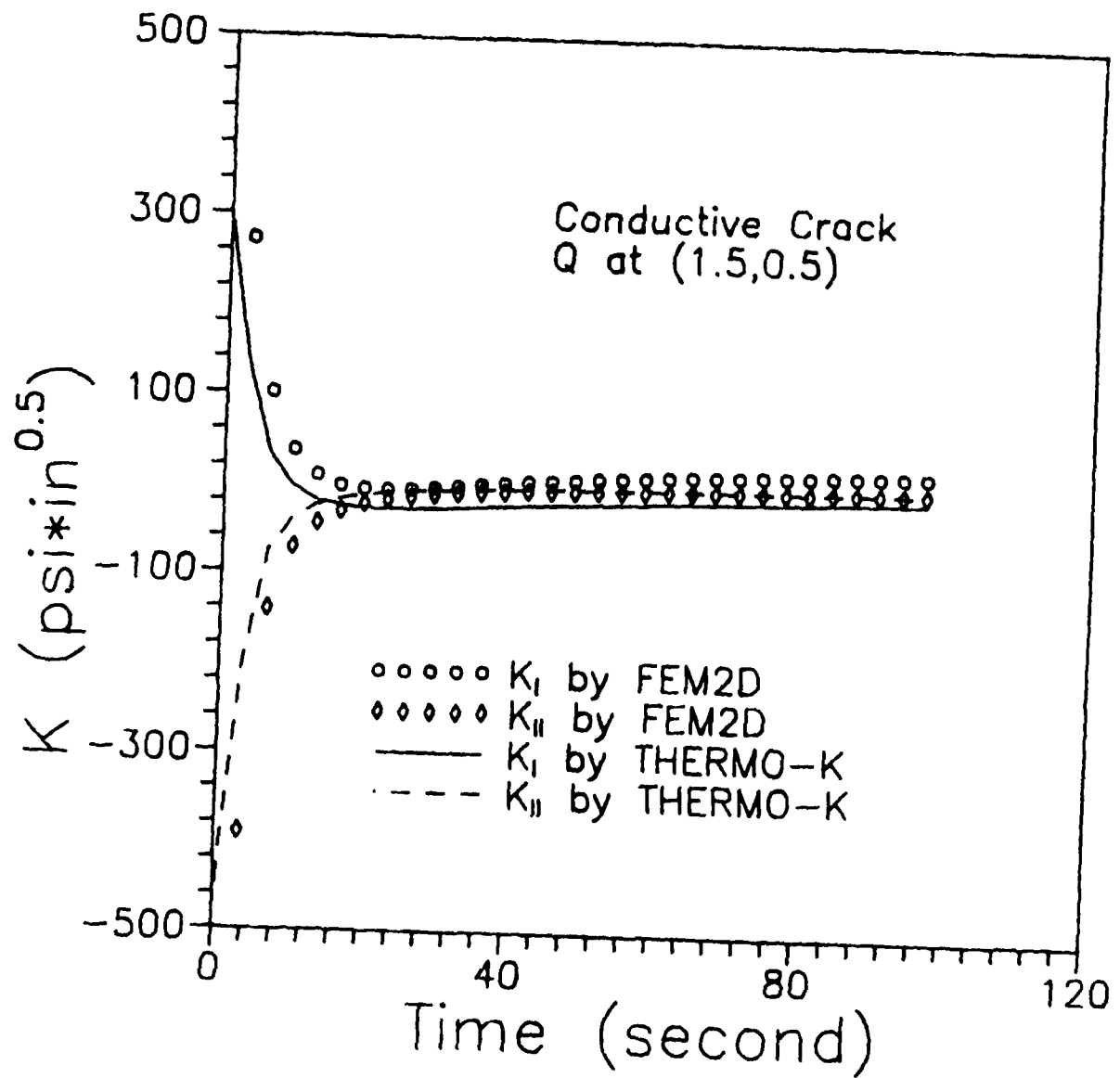


Figure 3-7. Stress Intensity Factors Due to an Instantaneous Heat Source at (1.5 inch, 0.5 inch) (Fully Conductive Crack)

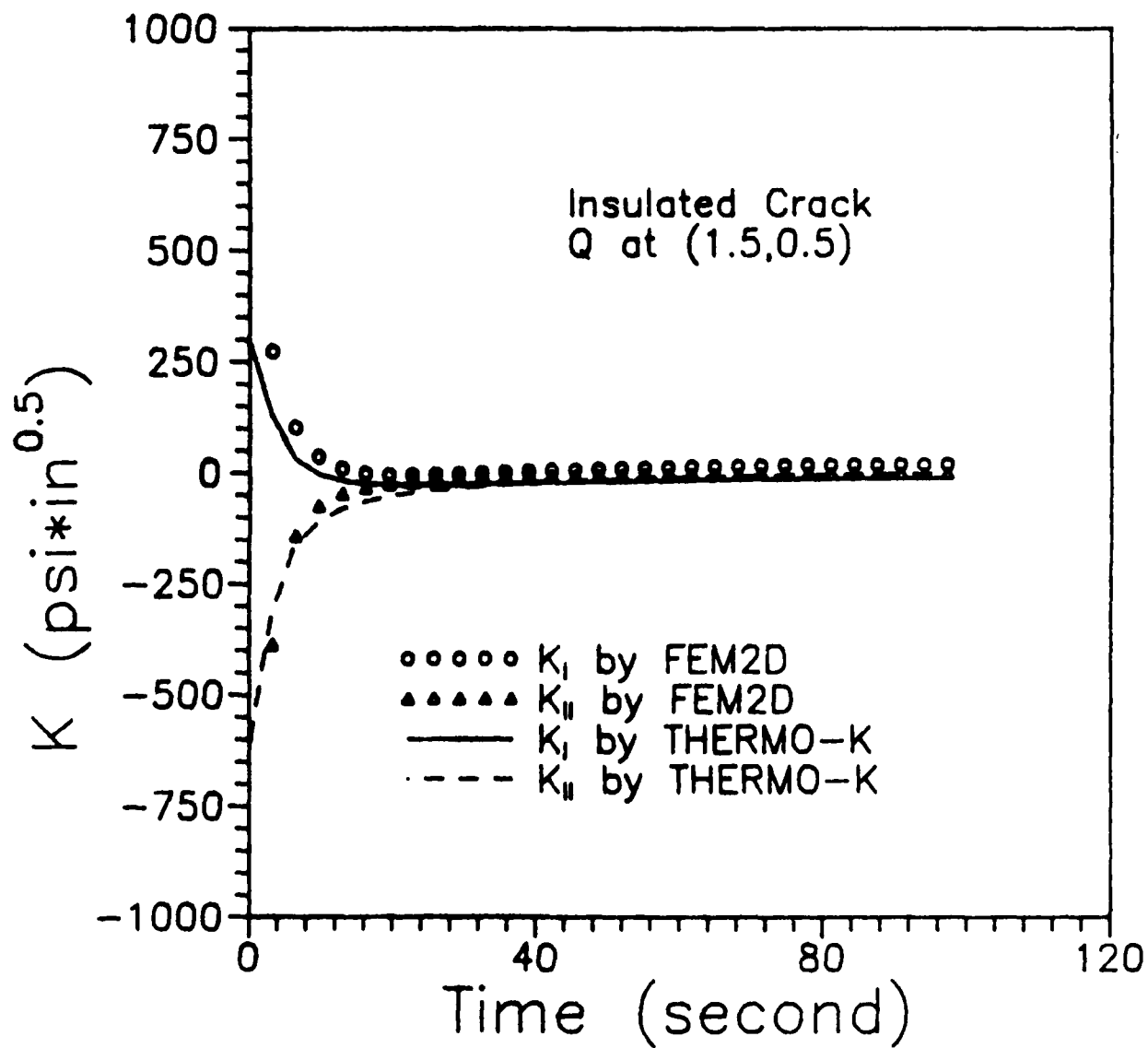


Figure 3-8. Stress Intensity Factors Due to an Instantaneous Heat Source at (1.5 inch, 0.5 inch) (Insulated Crack)

4.0 THEORETICAL BACKGROUND OF CRACK MODEL 3 - A RADIAL CRACK EMANATING FROM A CIRCULAR HOLE

This section describes the theoretical basis for crack Model 3 - a radial crack emanating from a circular hole, i.e., as illustrated in Figure 4-1, a radial crack of length a emanating from a circular hole of radius R in an infinite plate of thickness D . The cracked plate is subjected to point heat sources with arbitrary time history at any points in the plate region.

4.1 Assumptions

The following assumptions were made to simplify the problem:

- (a) The problem is assumed to be a plane stress problem. In other words, the thickness D shown in Figure 4-1 is assumed to be small enough so that the temperature distribution in the thickness direction can be treated as uniform and the stress components in the thickness direction are negligible compared with the in-plane stress components.
- (b) The metallic materials are assumed to be isotropic, homogeneous, and linear elastic. Material properties are assumed to be temperature independent.
- (c) The rate of heat application is slow enough that the coupling terms and inertia terms in the general thermoelasticity equations can be neglected, i.e., it is assumed that the decoupled, quasi-static thermoelasticity applies.
- (d) The crack surfaces are assumed to be stress-free. The crack surfaces can be completely insulated, fully heat conductive, or partially heat conductive. Heat conductance coefficient

h at the crack surfaces is also assumed to be constant throughout the entire temperature range.

- (e) It is assumed that the heat convection coefficients at the edge of the hole, H_1 , and at the plate surfaces, H , (see Figure 4-1) remain constant.

4.2 Governing Equations

For a plane stress thermoelasticity problem as illustrated in Figure 4-1, the governing equations are

$$\xi \nabla^2 T = T_{,t} + \xi \eta^2 T \quad (4-1)$$

$$\sigma_{ij,j} = 0 \quad (4-2)$$

$$\sigma_{ij} = 2G [\epsilon_{ij} + (\frac{\nu}{1-\nu}) \delta_{ij} \epsilon_{kk} - \alpha (\frac{1+\nu}{1-\nu}) \delta_{ij} T] \quad (4-3)$$

$$\epsilon_{ij} = (U_{i,j} + U_{j,i})/2 \quad (4-4)$$

and

$$\nabla^2 U_i + (\frac{1+\nu}{1-\nu}) U_{j,ji} = 2(\frac{1+\nu}{1-\nu}) \alpha T \quad (4-5)$$

where $T=T(r, \theta, t)$ is temperature distribution, t , r and θ are time and polar coordinates respectively, $\xi=(k/\rho c)$, k is heat conduction coefficients, ρ is mass density, c is heat capacity,

$\eta^2 = (2H)/k/D$, H is heat convection coefficient from the plate surfaces to the environment (see Figure 4-1), D is plate thickness, U_i are displacements, α is coefficient of thermal expansion, and G and ν are shear modulus and Poisson's ratio, respectively.

Nominal stress distributions generated with these equations are used to develop stress intensity factors via the influence function approach described below.

4.3 Influence Functions for Stress Intensity Factor

For any plate/crack geometry, cracktip stress intensity factors can be determined by integrating the product of the stresses at the crack location in an uncracked structure and an influence function (or weight function) (Buecker, 1973). That is, for a crack as shown in Figure 4-2, the stress intensity factor can be calculated by

$$K_I = \int_R^{R+a} \sigma_{\theta\theta}(r,0) m_1(r) dr \quad (4-6)$$

$$K_{II} = \int_R^{R+a} \sigma_{r\theta}(r,0) m_2(r) dr \quad (4-7)$$

where $m_1(r)$ and $m_2(r)$ are influence functions, $r=R+\bar{x}$, \bar{x} is a local coordinate shown in Figure B-1 of Appendix B, and $\sigma_{\theta\theta}$ and $\sigma_{r\theta}$ are the hoop and shear stress distributions on the crack surface in an identical but uncracked plate which is under the same temperature distribution as the cracked plate.

For a radial crack emanating from a circular hole in an infinite plate, as illustrated in Figure 4-1, the influence function (or weight function) can be evaluated by using the conformal mapping-collocation technique presented by Bowie (1956) and Bowie and Neal (1970).

As shown in Figure 4-3, influence functions for this crack model is the stress intensity factor solutions for the cracked plate subjected to a pair of horizontal forces and a pair of vertical forces which are both equal in magnitude by opposite in direction. As discussed in the papers by Bowie (1956) and Bowie and Neal (1970), this problem can be solved by employing the classical stress functions methods with conformal mapping technique. As illustrated in Figure 4-3, the cracked plate can be mapped into an infinite plate with a unit circle by a conformal mapping function. Bowie (1956) has shown that

$$z = \omega(\zeta) = \frac{R}{1-\epsilon} \left[\zeta + \frac{1}{\zeta} + 1 + \epsilon + (1 + \frac{1}{\zeta}) (\zeta^2 + 2\epsilon\zeta + 1) \right]^{1/2} \quad (4-8a)$$

$$\approx \frac{R}{1-\epsilon} \left[\zeta + \sum_{n=1}^{M+2} A_n \zeta^{1-n} \right] \quad (4-8b)$$

is the mapping function for the mapping shown in Figure 4-3, where coefficients A_n 's are defined in Appendix E, $(M+2)$ is the total number of terms used in Equation (4-8b), and

$$z = x + i y \quad (4-9)$$

$$\epsilon = \frac{\beta^4 - 4(\beta+1)}{(\beta+2)^2} \quad (4-10)$$

$$\beta = \frac{a}{R} \quad (4-11)$$

Equation (4-8) has two branch points at $\zeta = \exp(\pm i\lambda)$ where λ is the solution of

$$\cos(\lambda) = -\epsilon, \quad \sin(\lambda) = \sqrt{(1+\epsilon)(1-\epsilon)} \quad (4-12)$$

Physically, these two branch points correspond to point A and point C shown in Figure 4-3. It is easy to see that, for a constant hole radius R , $\epsilon = -1, 0$, and 1 correspond to $a = 0, R$, and ∞ , respectively. Unfortunately, as was pointed out by Bowie (1973), the mapping function shown in Equation (4-3a) are discontinuous across the cut A-B-C in Figure 4-3 and, thus, are not suitable for this application. Instead, as suggested by Bowie (1973), a polynomial approximation of the mapping function, Equation (4-8b), is used in this study. Stresses and displacements for the problem can then be expressed in terms of the mapping function $\omega(\zeta)$ and two stress functions, $\phi(z)$ and $\Psi(z)$ as follows:

$$\sigma_{xx} + \sigma_{yy} = 4 \operatorname{Re} \left[\frac{\phi'(\zeta)}{\omega'(\zeta)} \right] \quad (4-13)$$

$$\sigma_{yy} - \sigma_{xx} + 2i\sigma_{xy} = \frac{2}{\omega'(\zeta)} \left(\overline{\omega(\zeta)} \left[\frac{\phi'(\zeta)}{\omega'(\zeta)} \right]' + \Psi'(\zeta) \right) \quad (4-14)$$

$$2G(u + iv) = \kappa\phi(\zeta) - \omega(\zeta) \frac{\overline{\phi'(\zeta)}}{\overline{\omega'(\zeta)}} - \overline{\Psi(\zeta)} \quad (4-15)$$

$$f_1 + i f_2 = \kappa\phi(\zeta) + \omega(\zeta) \frac{\overline{\phi'(\zeta)}}{\overline{\omega'(\zeta)}} + \overline{\Psi(\zeta)} \quad (4-16)$$

where $\kappa = \frac{3-\nu}{1+\nu}$ for plane stress problem, $G = \frac{E}{2(1+\nu)}$, E is Young's modulus, ν is Poisson's ratio, and f_1 and f_2 are resulting forces in x - and y -directions, respectively. It has been shown by Bowie (1956) that stress intensity factors at the crack tip are

$$K = K_I - K_{II} = 2 \sqrt{\frac{\pi}{\omega''(s_0)}} \phi'(s_0) \quad (4-17)$$

where $s_0=1$ is the mapping point of the crack tip in the ζ -plane, i. e., point B in Figure 4-3. For mapping function of Equation (4-8b), it can be shown that

$$\omega''(s_0) = \omega''(1) = \frac{R}{1-\epsilon} [2 + \sqrt{(1+\epsilon)/2} + \sqrt{2/(1+\epsilon)}] \quad (4-18)$$

As shown in Figure 4-3, the loading conditions for the influence problem are two pairs of unit forces applied at a distance s away from the edge of the circle, that is

$$f_1(\gamma) + i f_2(\gamma) = (1 - i) [H(\gamma + \lambda^*) - H(\gamma - \lambda^*)] \quad (4-19)$$

where $-\pi \leq \gamma \leq \pi$ is the angular coordinate as shown in Figure 4-3, $H(x)$ is a Heaviside step function, and λ^* is the solution of

$$\cos(\lambda^*) = q, \quad \sin(\lambda^*) = \sqrt{(1+q)(1-q)}$$

$$q = \frac{p^2 - \epsilon}{4(1+\epsilon+p)}, \quad p = \frac{s}{R}(1-\epsilon) - 2\epsilon \quad (4-20)$$

By letting

$$\psi(\zeta) = -\bar{\phi}(1/\zeta) - \frac{\bar{\omega}(1/\zeta)}{\omega'(\zeta)} \phi'(\zeta) \quad (4-21)$$

and substituting Equations (4-21) and (4-19) into Equation (4-16), one obtains the following equation

$$\phi^-(s) - \phi^+(s) = f_1(\gamma) + i f_2(\gamma) \quad (4-22)$$

where $s = \exp(i\gamma)$. Equation (4-22) is a typical equation for a Hilbert arc problem. Thus

$$\begin{aligned} \phi(\zeta) &= \frac{1}{2\pi} \int_{-\pi}^{\pi} \left[\frac{f_1(\gamma) + i f_2(\gamma)}{\exp(i\gamma) - \zeta} \right] d\gamma \\ &= \frac{1-i}{2\pi i} \operatorname{Ln} \left[\frac{\exp(i\lambda^*) - \zeta}{\exp(-i\lambda^*) - \zeta} \right] \end{aligned} \quad (4-23)$$

Substitution of Equations (4-17) and (4-23) in Equation (4-18) yields the solutions for the influence functions m_1 and m_2 as follows:

$$m_1(r) - i m_2(r) = K_I - i K_{II} = \frac{1-i}{\sqrt{\pi} \omega''(1)} \left[\frac{1 + \operatorname{Sin}(\lambda^*)}{1 - \operatorname{Cos}(\lambda^*)} \right] \quad (4-24)$$

4.4 Principle of Superposition

In general, as shown in Figure 4-1, there may be multiple heat sources (or sinks) within the plate which will cause thermal stresses and stress intensity factors at the crack tip in the structure. Since the problem is linear, it is easily demonstrated that total stress intensity factor can be calculated as the sum of the stress intensity factors caused by each individual heat source or sink, acting independently. That is

$$K(t) = \sum_i [K(t)]_i \quad (4-25)$$

where $K(t)$ is the total stress intensity factor and $[K(t)]_i$ is the stress intensity factor due to the i^{th} heat source.

4.5 Green's Function Concept for Time Integration

In Equation (4-25), the stress intensity factor $[K(t)]_i$ caused by each individual heat source can be solved with the concept of Green's function integration. As illustrated in Figure 4-4, the stress intensity factor due to a heat source of intensity $Q_i(t)$ can be calculated by

$$[K(t)]_i = \int_0^t Q_i(\tau) G_i(t-\tau) d\tau \quad (\text{no summation}) \quad (4-26)$$

where $G_i(t)$ is the stress intensity factors due to a Delta function $\delta(t)$ heat source at the i^{th} heat source location.

As shown in Figure 4-4, generally, the Green's function $G_i(t)$ will decay and approach to zero after a decay period t_d . Therefore, the integration range in Equation (4-26) can be

reduced to from $(t-t_d)$ to t . Such a reduction in the integration range greatly increases the speed of the calculation because, instead of integrating for the entire time history, it is only necessary to integrate backwards from the present time t to $(t-t_d)$ as follows

$$[K(t)]_i = \int_{t-t_d}^t Q_i(\tau) G_i(t-\tau) d\tau \quad (4-27)$$

4.6 Green's Function for Fully Heat Conductive Cracks

Previous subsections of this section show that the stress intensity factors for this crack models can be easily obtained by Equations (4-6), (4-7), (4-25), and (4-27) if the temperature and stress distributions and thereby the stress intensity factors at the crack tip, resulting from a delta function heat source (or sink) $Q\delta(t)$ at any arbitrary location (r', θ') in the uncracked plate (refer to Figure 4-5), can be solved. The uncracked plate shares the same temperature distribution as the cracked plate. As the first step, we consider the problem of a fully heat conductive edge crack, i.e., in this subsection, it is assumed that heat flux can flow across the crack surfaces without any heat loss or resistance. Solutions for a more general, partially heat conductive crack will be discussed in the next subsection. However, as will be seen in the next subsection and as shown in Appendix A of this report, for a crack model with symmetry about its crack plane such as this crack model, crack surface heat conductivity will affect Mode II stress intensity factor solutions but not Mode I or Mode III stress intensity factor solutions. In other words, whether the crack surfaces are fully heat conductive, insulated, or partially heat conductive, the K_I solution will remain the same for a radial crack emanating from a circular hole in an infinite plate. Thus, if only Mode I or Mode

III fracture is of major interest, the stress intensity factor solutions can be obtained by assuming the crack surfaces are fully heat conductive. The assumption of a fully heat conductive crack will greatly shorten the computation time for temperatures, thermal stresses, and stress intensity factors.

Since thermal stresses and stress intensity factors do not depend on the initial, stress-free temperature of the plate, it is conveniently assumed that the initial temperature of the plate is zero, i.e., $T(r, \theta; 0) = 0$. To solve the Green's function of this crack model, the following boundary conditions need to be satisfied in addition to the governing equations listed in Equations (4-1) to (4-5):

at $r = R$,

$$kT_{,r}(R, \theta; t) = -H_1 T(R, \theta; t) \quad (4-28)$$

$$\sigma_{rr}(R, \theta; t) = \sigma_{r\theta}(R, \theta; t) = 0 \quad (4-29)$$

at $r = \infty$,

$$T(r, \theta; t) = 0 \quad (4-30)$$

$$\sigma_{rr}(r, \theta; t) = \sigma_{\theta\theta}(r, \theta; t) = \sigma_{r\theta}(r, \theta; t) = 0 \quad (4-31)$$

at $\theta = 0$, $R \leq r \leq (R+a)$,

$$T(r, 0^+; t) = T(r, 0^-; t) \quad (4-32)$$

$$\sigma_{\theta\theta}(r, 0^+; t) = \sigma_{\theta\theta}(r, 0^-; t) \quad (4-33)$$

$$\sigma_{r\theta}(r, 0^+; t) = \sigma_{r\theta}(r, 0^-; t) \quad (4-34)$$

$$U_{\beta}(r, 0^{+}; t) = U_{\beta}(r, 0^{-}; t) \quad \beta = r, \theta \quad (4-35)$$

Temperature solution to the uncracked plate problem can be obtained by solving Equation (4-1) along with boundary conditions Equations (4-28), (4-30), and (4-32). An analytical form of the temperature solution has been given by Carslaw and Jaeger (1959) as follows:

$$T(r, \theta; t) = \frac{Q}{2\pi\rho cD} \sum_{n=-\infty}^{\infty} \{ \cos[n(\theta - \theta')] \int_0^{\infty} [C_n(ur) C_n(ur') u \exp(-\xi u^2 t - \eta^2 t)] du \} \quad (4-36)$$

where ξ and η are defined in Equation (4-1),

$$C_n(ur) = \frac{J_n(ur) [uY'_n(uR) - (H_1/k)Y_n(uR)] - Y_n(ur) [uJ'_n(uR) - (H_1/k)J_n(uR)]}{\sqrt{[uJ'_n(uR) - (H_1/k)J_n(uR)]^2 + [uY'_n(uR) - (H_1/k)Y_n(uR)]^2}} \quad (4-37)$$

and $J_n(z)$ and $Y_n(z)$ are Bessel functions of the first and second kinds, respectively.

The next step is to solve the stress distribution due to the temperature distribution of Equation (4-36). Boley and Weiner (1960) and Parkus (1968) have shown that a particular solution to the thermal stress problem can be expressed in terms of a thermoelastic potential ϕ as follows

$$u_{\beta} = \phi_{,\beta} \quad (\beta = x, y) \quad (4-38)$$

$$\sigma_{rr} = -2G \left[\frac{\phi_{,r}}{r} + \frac{\phi_{,\theta\theta}}{r^2} \right] \quad (4-39)$$

$$\sigma_{\theta\theta} = -2G \phi_{,rr} \quad (4-40)$$

$$\sigma_{r\theta} = 2G \left[-\frac{\phi_{,\theta}}{r^2} + \frac{\phi_{,r\theta}}{r} \right] \quad (4-41)$$

$$\phi(r, \theta; t) = a(1+\nu) \xi e^{-\xi \eta^2 t} \int_0^t e^{\xi \eta^2 \tau} T(r, \theta; \tau) d\tau + \phi_0 \quad (4-42)$$

where ϕ_0 is a function of r , θ , and t such that ϕ would remain finite as t approaches infinity. Substitution of Equation (4-36) into Equation (4-42) yields

$$\begin{aligned} \phi(r, \theta; t) = & -\frac{a(1+\nu)kQ}{2\pi\rho^2 c^2 D} \sum_{n=-\infty}^{\infty} \{ \cos[n(\theta-\theta')] \} \int_0^{\infty} \\ & [C_n(ur) C_n(ur') \exp(-\xi u^2 t - \xi \eta^2 t)] \frac{du}{\xi u} \quad (4-43) \end{aligned}$$

By Equations (4-43), and (4-39) to (4-41), stress components σ_{rr} , $\sigma_{\theta\theta}$ and $\sigma_{r\theta}$ can be written as

$$\sigma_{rr}(r, \theta; t) = \sum_{n=-\infty}^{\infty} E_n(r, t) \cos[n(\theta-\theta')] \quad (4-44)$$

$$\sigma_{00}(r, \theta; t) - i \sigma_{r\theta}(r, \theta; t) = - \sum_{n=-\infty}^{\infty} A_n(r, t) \exp(in\theta) \quad (4-45)$$

where

$$A_n(r, t) = [B_n(r, t) - D_n(r, t) + B_{-n}(r, t) + D_{-n}(r, t)] e^{-in\theta'} \quad (4-46)$$

$$B_n(r, t) = - \frac{\alpha(1+\nu)kQG}{\pi\rho^2 c^2 D} \int_0^{\infty} \left(\left[\frac{C'_n(uR)}{R} - \frac{n^2}{uR^2} C_n(uR) \right] C_n(ur') \right. \\ \left. \exp(-\xi u^2 t - \xi \eta^2 t) \right) \frac{du}{\xi} \quad (4-47)$$

$$D_n(r, t) = - \frac{\alpha(1+\nu)kQG}{\pi\rho^2 c^2 D} \int_0^{\infty} \left(n \left[\frac{C'_n(uR)}{R} - \frac{1}{uR^2} C_n(uR) \right] C_n(ur') \right. \\ \left. \exp(-\xi u^2 t - \xi \eta^2 t) \right) \frac{du}{\xi} \quad (4-48)$$

$$E_n(r, t) = \frac{\alpha(1+\nu)kQG}{\pi\rho^2 c^2 D} \int_0^{\infty} C''_n(ur) C_n(ur') e^{-\xi u^2 t - \xi \eta^2 t} \frac{du}{\xi} \quad (4-49)$$

In general, the particular solution ϕ shown in Equation (4-43) satisfies the stress boundary conditions of Equations (4-31) and (4-33) to (4-35) but does not fulfill the stress-free conditions

at $r=R$, i.e., Equation (4-29) is not satisfied. In fact, it can be shown that, at $r=R$, coefficients B_n 's and D_n 's in Equations (4-47) and (4-48), A_n 's in Equation (4-46), and thus, $(\sigma_{rr} - i \sigma_{r\theta})$ do not equal to zero, in general.

Therefore, two complementary stress functions ϕ_c and ψ_c , which are analytic functions, must be included to make the edge of the hole, $r=R$, stress-free. In other words, stresses generated by ϕ_c and ψ_c at $r=R$ are the negative values of those given in Equation (4-45) and stresses generated by the two complementary stress functions vanish as r approaches infinity. Relationships between the complementary stress functions $\phi_c(z)$ and $\psi_c(z)$ and the resulting stress components $\hat{\sigma}_{\alpha\beta}$ are

$$\hat{\sigma}_{rr} + \hat{\sigma}_{\theta\theta} = 4 \operatorname{Re}[\phi_c(z)] \quad (4-50)$$

$$\hat{\sigma}_{\theta\theta} - \hat{\sigma}_{rr} + 2i\hat{\sigma}_{r\theta} = e^{2i\theta} [\bar{z} \phi'_c(z) + \psi_c(z)] \quad (4-51)$$

where $z = x + iy = r e^{i\theta}$.

Solution to this complementary problem has been obtained in §56 of Muskhelishvili (1954) as

$$\phi_c(z) = \sum_{k=0}^{\infty} a_k z^{-k}, \quad \psi_c(z) = \sum_{k=0}^{\infty} a'_k z^{-k} \quad (4-52)$$

where

$$a_1 = \frac{\bar{A}_1 R}{1+\kappa}, \quad a_2 = \bar{A}_2 R^2, \quad a_n = \bar{A}_n R^n \quad (n \geq 3) \quad (4-53)$$

$$a'_1 = - \frac{\kappa A_1 R}{1+\kappa} , \quad a'_2 = - A_0 R^2 ,$$

$$a'_n = (n-1)R^2 a_{n-2} - R^n A_{-n+2} \quad (n \geq 3) \quad (4-54)$$

Therefore, at the cross section of $\theta=0$, the total stresses caused by a Delta function heat source $Q\delta(t)$ at (r', θ') can be obtained by adding the stresses given in Equations (4-40), (4-41), (4-50), and (4-51) as follows:

$$\begin{aligned} \sigma_{\theta\theta}(r, 0; t) + i\sigma_{r\theta}(r, 0; t) = \\ \sum_{n=-\infty}^{\infty} [F_n \cos(n\theta') + i G_n \sin(n\theta')] \\ + \sum_{k=1}^{\infty} \{ [(1-k)a_k + \bar{a}_k + a'_k] r^{-k} \} \end{aligned} \quad (4-55)$$

where a_k and a'_k are defined in Equations (4-51) and (4-52),

$$\begin{aligned} F_n = \frac{\alpha(1+\nu)kQG}{\pi\rho^2 c^2 D} \int_0^{\infty} [C_n''(ur) C_n(ur')] \\ \exp(-\xi u^2 t - \xi \eta^2 t) \frac{du}{\xi} \end{aligned} \quad (4-56)$$

$$\begin{aligned} G_n = - \frac{\alpha(1+\nu)kQG}{\pi\rho^2 c^2 D} \int_0^{\infty} \left(n \left[\frac{C_n'(ur)}{r} - \frac{1}{ur^2} C_n(ur) \right] C_n(ur') \right. \\ \left. \exp(-\xi u^2 t - \xi \eta^2 t) \right) \frac{du}{\xi} \end{aligned} \quad (4-57)$$

To sum up this subsection, the Green's functions for the stress intensity factors are calculated by substituting the stress solutions given in Equations (4-45) and (4-55) and the influence functions given in Equation (4-24) into Equations (4-6) and (4-7) and integrating Equations (4-6) and (4-7) by the numerical integration scheme depicted in Appendix B.

4.7 Green's Function for Partially Heat Conductive Cracks

In subsection 4.6 the Green's function solution for a single point heat source at any arbitrary point in a plate with a radial crack emanating from a circular hole is discussed. The crack surfaces in subsection 4.6 are assumed to be fully heat conductive. In reality, the crack surface is expected to be somewhere between complete insulation and fully heat conductive, i.e., crack surfaces are expected to be partially heat conductive. A general approach to treat a partially heat conductive crack is studied in detail in Appendix A of this report. Application of the concept given in Appendix A to the model of a radial crack emanating from a circular hole in an infinite plate is discussed in this subsection.

Governing heat transfer equation for an infinite plate with a partially heat conductive radial crack emanating from a circular hole is still Equation (4-1), and the boundary conditions at $r=R$ and $r=0$, Equations (4-28) and (4-30), respectively, remain unchanged. The only difference will be the boundary condition at $\theta=0$, $a \leq r \leq (R+a)$, i.e. Equation (4-30), is replaced by

$$T_{,\theta}(r,0) = \frac{\lambda}{a} [T(r,0^+) - T(r,0^-)] , \quad a \leq r \leq (R+a) \quad (4-58)$$

where λ is defined as (ah/k) in which h is crack surface heat

conductance coefficient and k is material thermal conductivity. From Equation (4-58), it can be easily seen that the crack surfaces are fully heat conductive when $\lambda=\infty$ and the crack surfaces are completely insulated when $\lambda=0$. Any λ values between 0 and ∞ are corresponding to a partially heat conductive crack.

As discussed in Appendix A, when a crack is completely insulated or partially heat conductive, the resulting temperatures on both sides of a crack will be different, i.e., there is a temperature jump across the crack surface when λ equals to zero or a finite number. This temperature jump is analogous to the temperature jump created by a series of distributed heat dipoles (Carslaw and Jaeger, 1959) situated at the crack location. Thus, the overall temperature distribution can be obtained as the superposition of the fully conductive solution, Equation (4-36), and a solution for the distributed heat dipoles. From Equation (4-36), it can be shown, by summing temperature solutions for a point heat source and a point heat sink with infinitesimally small distance in between, that temperature solution for an instantaneous heat dipole of strength M situated at $\theta=0$, $r=\bar{r}$ in an infinite plate with a circular hole of radius R and thickness of D is

$$T(r, \theta; t) = - \frac{M}{2\pi\rho c D \bar{r}} \left(\sum_{n=-\infty}^{\infty} n \sin(n\theta) \int_0^{\infty} [C_n(ur) C_n(u\bar{r}) u \exp(-\xi u^2 t - \xi \eta^2 t)] du \right) \quad (4-59)$$

Thus resulting temperature from distributed heat dipoles of strength $M(r, t)$ situated at $\theta=0$, $a \leq r \leq (R+a)$ of the plate is

$$T(r, \theta; t) = - \frac{1}{2\pi\rho c D \bar{r}} \int_0^t \int_R^{R+a} (M(\bar{r}, \tau) \sum_{n=-\infty}^{\infty} n \sin(n\theta))$$

$$\int_0^{\infty} [C_n(ur) C_n(u\bar{r}) u \exp(-\xi u^2(t-\tau) - \xi \eta^2 t)] du \frac{d\bar{r}}{r} d\tau \quad (4-60)$$

Substitution of the sum of Equations (4-36) and (4-60) into Equation (4-58) yields a Fredholm integral equation for the heat dipole distribution $M(r, t)$ as follows:

$$\begin{aligned} \int_0^t \int_R^{R+a} \{M(\bar{r}, \tau) \sum_{n=-\infty}^{\infty} [n^2 \int_0^{\infty} C_n(ur) C_n(u\bar{r}) u \exp(-\xi u^2(t-\tau)) du] \\ (\frac{d\bar{r}}{r} d\tau = - \frac{2\pi r \lambda}{a \xi} M(r, t) + Q \sum_{n=-\infty}^{\infty} (n \sin(n\theta')) \int_0^{\infty} \\ [C_n(ur) C_n(ur') u \exp(-\xi u^2 t)] du\} \end{aligned} \quad (4-61)$$

A numerical approximation method is used in the computer program to solve Equation (4-61). Since the temperature jump between two adjacent crack surfaces has to be zero at the crack tip, $r=(R+a)$, we assume that

$$M(r, t) = \sum_{m=1}^L b_m(t) \cos\left[\frac{(2m-1)(r-R)\pi}{2a}\right] \quad (4-62)$$

where L is the maximum number of terms included in the calculation and $b_m(t)$ is a time function, which is determined by substituting Equation (4-62) into Equation (4-61).

Similar to the fully heat conductive case, a thermoelastic

potential due to the distributed thermal dipoles at the crack region can be derived by integrating the temperature solution, Equation (4-60). That is,

$$\phi(r, \theta; t) = a\xi(1+\nu) \int_0^t T(r, \theta; \tau) \exp[-\xi\eta^2(t-\tau)] d\tau + \phi_0 \quad (4-63)$$

where $T(r, \theta; t)$ is the temperature solution given in Equation (4-60) and ϕ_0 is an analytic function to make ϕ remain finite at infinity. Substituting Equation (4-62) into Equation (4-60) and thereafter into Equation (4-63), one obtains

$$\begin{aligned} \phi(r, \theta; t) = & \frac{a(1+\nu)}{2\pi\rho cD} \int_R^{R+a} \int_0^t \frac{1}{\bar{r}} \left[\sum_{m=1}^L b_m(t) \cos\left(\frac{(2m-1)(r-R)\pi}{2a}\right) \right] \\ & \left[\sum_{n=-\infty}^{\infty} n \sin(n\theta) \int_0^{\infty} C_n(ur) C_n(u\bar{r}) \exp(-\xi u^2(t-\tau) - \xi\eta^2 t) \frac{du}{u} \right] d\tau d\bar{r} \end{aligned} \quad (4-64)$$

where ξ and η are defined in Equation (4-1), $C_n(ur)$ are eigen functions defined in Equation (4-37), $b_m(t)$'s are the time functions defined in Equation (4-62), and L is the maximum number of terms included in the series expansions in Equation (4-62). Again, stresses resulting from the thermoelastic potential for the distributed thermal dipoles at the edge of the hole are not zero, in general. In fact, it can be shown that stresses at the edge of the hole due to the thermoelastic potential of Equation (4-64) can also be calculated by Equation (4-45) except that definitions of A_n 's in Equation (4-45) are now defined as

$$A_n(R, t) = \frac{i}{2} [-R_n(R, t) + T_n(R, t) + R_{-n}(R, t) + T_{-n}(R, T)] \quad (4-65)$$

where

$$R_n(R, t) = \frac{Ga(1+\nu)}{\rho cDR} \int_0^t \int_0^\infty \left[\int_R^{R+a} M(\bar{r}, t) C_n(u\bar{r}) \frac{d\bar{r}}{\bar{r}} \right] \\ [n C'_n(uR) - \frac{n^3}{uR} C_n(uR)] e^{-\xi u^2(t-\tau) - \xi \eta^2 t} du d\tau \quad (4-66)$$

$$T_n(R, t) = - \frac{Ga(1+\nu)}{\rho cDR} \int_0^t \int_0^\infty \left[\int_R^{R+a} M(\bar{r}, t) C_n(u\bar{r}) \frac{d\bar{r}}{\bar{r}} \right] n^2 \\ \left[\frac{1}{uR} C_n(uR) - C'_n(uR) \right] e^{-\xi u^2(t-\tau) - \xi \eta^2 t} du d\tau \quad (4-67)$$

To cancel out the above non-zero stresses at the edge of the hole, two more complementary stress functions are needed. With a derivation procedure very similar to one used in the last section for the fully conductive crack problem, total stresses at the crack region, $\theta=0$, $R \leq r \leq (R+a)$, resulting from the distributed thermal dipoles are

$$\sigma_{\theta\theta}(r, 0; t) = 0 \quad (4-68)$$

$$\sigma_{r\theta}(r, 0; t) = - \frac{Ga(1+\nu)}{\rho cDR} \sum_{n=-\infty}^{\infty} n^2 \int_0^t \int_0^\infty \left[\int_R^{R+a} M(\bar{r}, \tau) C_n(u\bar{r}) \right. \\ \left. \frac{d\bar{r}}{\bar{r}} \right] \left[\frac{1}{uR} C_n(ur) - C'_n(ur) \right] \exp(-\xi u^2(t-\tau) - \xi \eta^2 t) du d\tau + \\ \sum_{j=1}^{\infty} [(1-j)a_j + \bar{a}_j + a'_j] \quad (4-69)$$

where a_j and a'_j are calculated by substituting A_n 's defined in Equations (4-65) to (4-67) into Equations (4-53) and (4-54).

Results shown in Equations (4-68) and (4-69) reiterate the fact, deduced in Appendix A, that, for a cracked structure with symmetry with respect to the crack plane such as the current crack model, crack surface heat conductivity will not affect Mode I fracture solution ($\sigma_{\theta\theta}=0$ in Equation (4-68)) but will change Mode II fracture solution ($\sigma_{r\theta}\neq 0$ in Equation (4-69)).

To sum up, for a partially heat conductive radial crack emanating from a circular hole in an infinite plate, its overall temperature solution is the sum of Equation (4-36) and Equation (4-60). Total stresses in the uncracked plate, which share the same overall temperature distribution as the cracked plate, are the sum of Equations (4-55) and (4-69). Green's function solutions for stress intensity factors, K_I and K_{II} , at the crack tip are then calculated by substituting the total stresses at the crack region into Equations (4-6) and (4-7), respectively.

4.8 Finite Element Verification of Crack Model 3

Since stress intensity factors are calculated by integrating the product of influence functions and stresses at the crack location in a uncracked plate (see Equations (4-6) and (4-7)), it is necessary to verify both the influence functions shown in subsection 4.3 and the temperature and thermal stresses obtained in subsections 4.6 and 4.7.

4.8.1 Verification of Influence Functions

To verify the Mode I influence function given in Equation (4-24), the problem of a radial crack of length a emanating from a

circular hole of radius $R=1$ inch subjected to an uniform tension of 1 ksi perpendicular to the crack, as illustrated in Figure 4-6, is chosen a reference problem. Mode I stress intensity factors for various crack lengths for this problem has been obtained by Bowie (1956). Another reference solution for the same problem was obtained by running a commercially available fracture mechanics software, **pc-CRACK** (1986). As illustrated in Figure 4-6, K_I solutions obtained by integrating the influence functions derived in this report are in excellent agreement with the two reference solutions. Also illustrated in Figure 4-6 is the exact K_I solution ($=\sigma_0\sqrt{\pi a/2}$) for a finite crack of length a in an infinite plate. As shown in Figure 4-6, it is seen that as the crack length to the hole radius ratio (a/R) approaches a large number, stress intensity factor solutions predicted by the influence function integration technique approaches the exact solution. This asymptotic behavior at large (a/R) ratio is anticipated and thus provide further confirmation to the influence functions derived in this report.

4.8.2 Verification of Temperature and Stresses for Fully Heat Conductive Crack Surfaces

To verify the temperature and stress calculation procedures for a fully heat conductive radial crack of 5 inches long emanating from a circular hole of radius 5 inches in an infinite plate is considered. An instantaneous point heat source of strength $\delta(t)$ Btu is applied at $(r', \theta') = (12 \text{ inch}, 7.5^\circ)$. The plate is made of 7075-T651 Aluminum. Material properties for this reference problem are

$$E = 10.3 \times 10^6 \text{ psi}, \quad \nu = 0.33, \quad \alpha = 13 \times 10^{-6} / ^\circ\text{F}$$

$$k = 0.0017361 \frac{\text{Btu}}{\text{in-sec-F}}, \quad \rho = 0.0978 \frac{\text{lbm}}{\text{in}^3}, \quad c = 0.23 \frac{\text{Btu}}{\text{lbm-F}}$$

$$H = H_1 = 0 \frac{\text{Btu}}{\text{in}^2\text{-sec-F}} \quad (4-70)$$

A two-dimensional finite element program, FEM2D (1986), was used to analyze the problem. The finite element mesh for this problem are shown in Figure 4-7. All the elements in Figure 4-7 are eight-node isoparametric elements. Resulting temperatures are plotted in Figure 4-8 and resulting stresses are depicted in Figures 4-9 and 4-10 at five different time. The time increment, Δt , in Figures 4-8 to 4-10 are 86 seconds. Good agreements between the finite element results and solutions obtained by THERMO-K are observed in these three figures.

4.8.3 Verification of Temperature and Stresses for Insulated Crack Surfaces

This subsection is to check the accuracy of the temperatures and thermal stresses predicted by using the analytical approach described in this section. The same radial crack problem as subsection 4.8.2 is chosen as a reference problem. Material properties and heat transfer constants are the same as those given in Equation (4-70). Also, in this sample problem, the crack surfaces are assumed to be completely insulated, i.e., it is assumed that $\frac{\partial T}{\partial \theta} = 0$ at $\theta=0$, $a \leq r \leq (R+a)$. The same finite element mesh is also used here. However, in the crack region of the finite element model, the crack surfaces are set to be insulated for heat transfer analysis but are set to have continuous displacements in the following thermal stress analysis, i.e., the adjacent nodes on both sides of the crack are treated as independent points in the heat transfer analysis but are constrained together in the thermal stress analysis so that they will have the same displacements but different temperatures. Resulting temperature and stress distributions at cross section

$\theta=0$ are illustrated in Figures 4-11 to 4-13. Again, good agreement between finite element solutions and solutions calculated by the analytical approach discussed in this section.

4.9 References

Bowie, O.L., (1973) Solution of Plane Crack Problem by Mapping Technique", in Method of Analysis and Solutions of Crack Problems, Vol. 1, ed. G. C. Sih, pp. 1-55, Noordhoff, Holland.

Boley, B. A., and Weiner, J. H., (1960), Theory of Thermal Stresses, Wiley & Sons, New York, New York.

Bowie, O. L., (1956), "Analysis of an Infinite Plate Containing Radial Cracks Originating at the Boundary of an Internal Circular Hole," Journal of Mathematics and Physics, Vol. 35, No. 1, pp. 60-71.

Bowie, O. L., and Neal, D. M. (1970), "A Modified Mapping-Collocation Technique for Accurate Calculation of Stress Intensity Factors," Internal Journal of Fracture Mechanics, Vol. 6, No.2, pp. 199-206).

Bueckner, H. F., (1973), "Field Singularities and Related Integral Representations," in Methods of Analysis and Solutions of Crack Problems, Vol 1, ed. G. C. Sih, pp. 239-314, Noordhoff, Holland.

Carslaw, H. S., and Jaeger, J. C., (1959), Conduction of Heat in Solids, 2nd edition, Oxford University Press, London.

FEM2D - A Two-Dimensional Finite Element Computer Program for Two-Dimensional Heat Transfer/Thermal Stress Analysis. Users Manual, (1986), Structural Integrity Associates, San Jose, CA.

Muskhelishvili, N. I., (1954), Some Basic Problems of the Mathematical Theory of Elasticity.

pc-CRACK - Fracture Mechanics Software for Personal Computers. Users Manual, Version 1.1, Revision 1, (1986), Structural Integrity Associates, San Jose, CA.

Parkus, H., (1968), Thermoelasticity, Blaisdell Publishing Co..

Tada, H., Paris, P., and Irwin, G., (1973), The Stress Analysis of Cracks Handbook, Del Research Co., Pennsylvania.

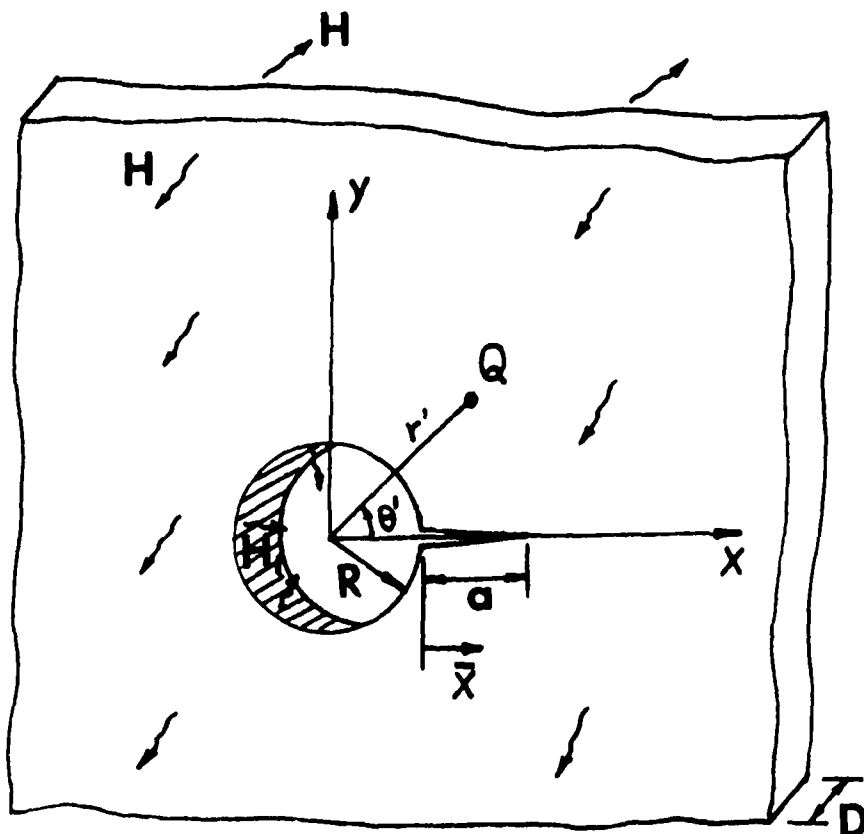


Figure 4-1. A Radial Crack Emanating From a Circular Hole in an Infinite Plate Subjected to Point Heat Sources

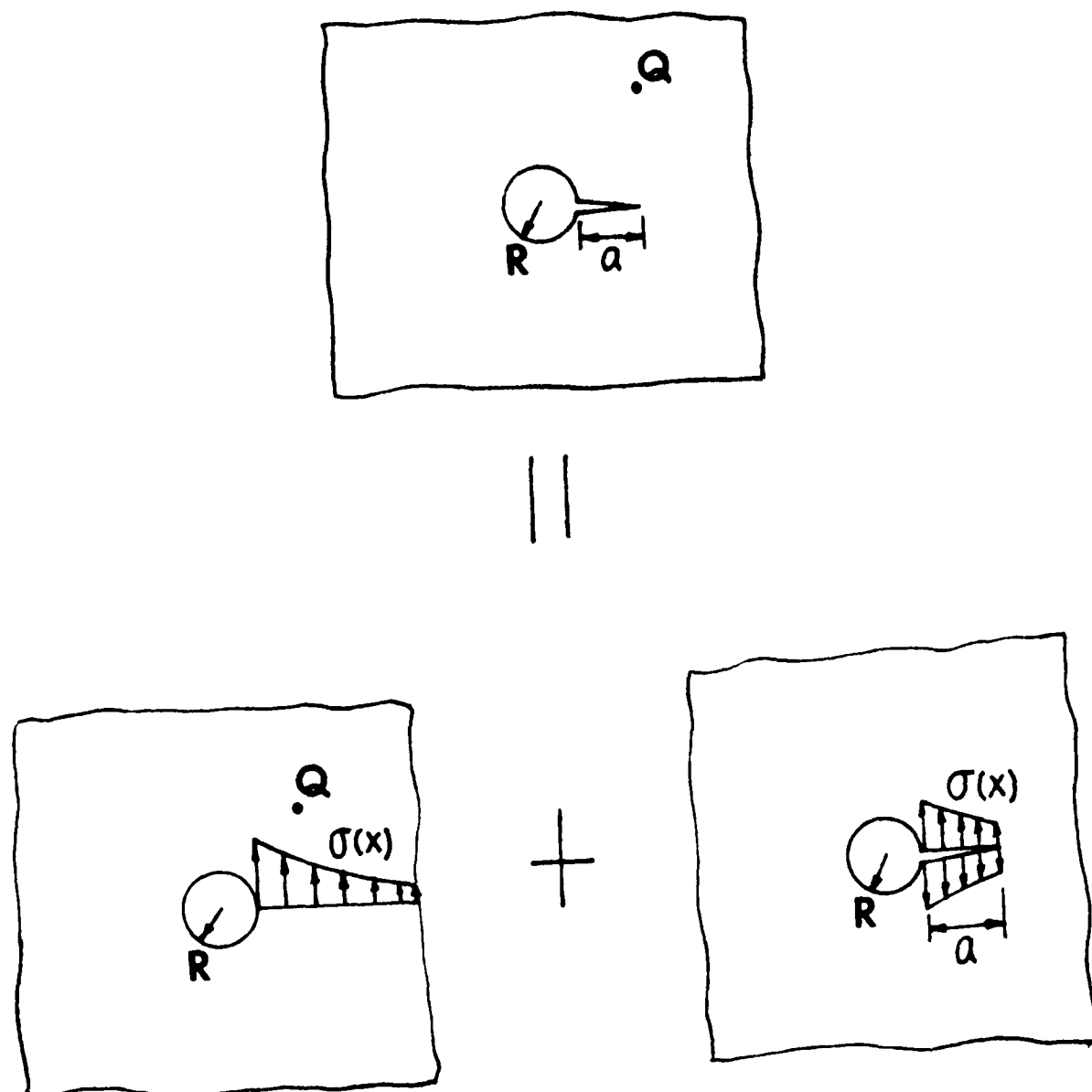


Figure 4-2. Concept of Influence Function Approach

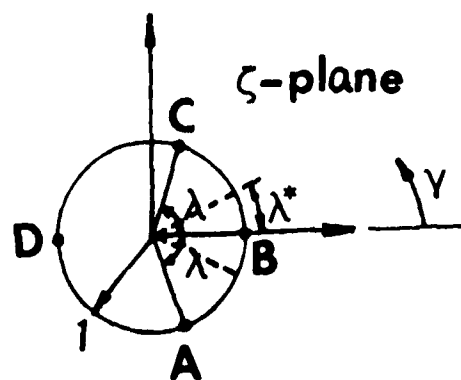
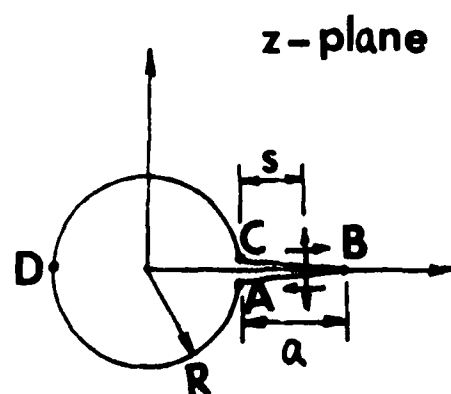
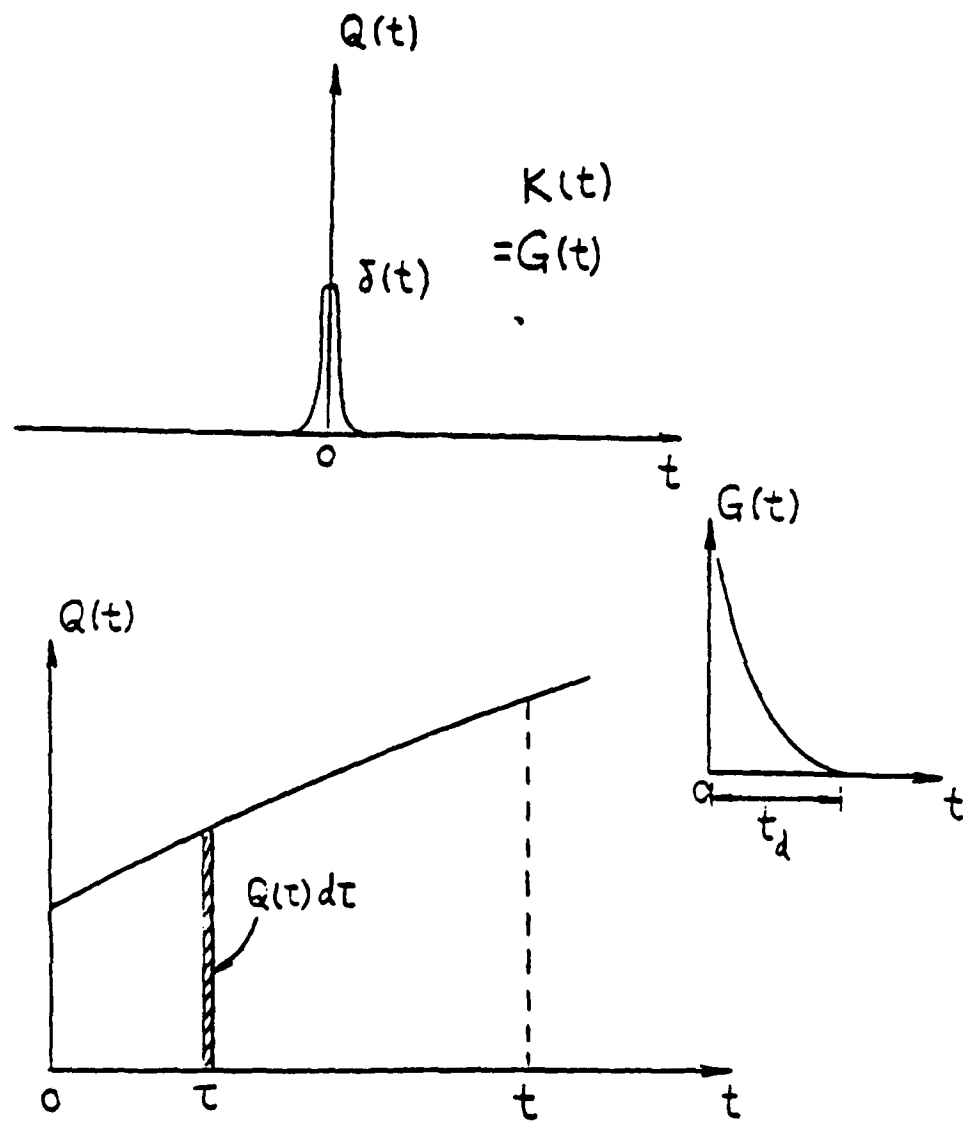


Figure 4-3. Conformal Mapping for Influence Function Solutions



$$K(t) = \int_0^t Q(\tau) G(t-\tau) d\tau$$

$$= \int_{t-t_d}^t Q(\tau) G(t-\tau) d\tau$$

Figure 4-4. Concept of Green's Function Approach

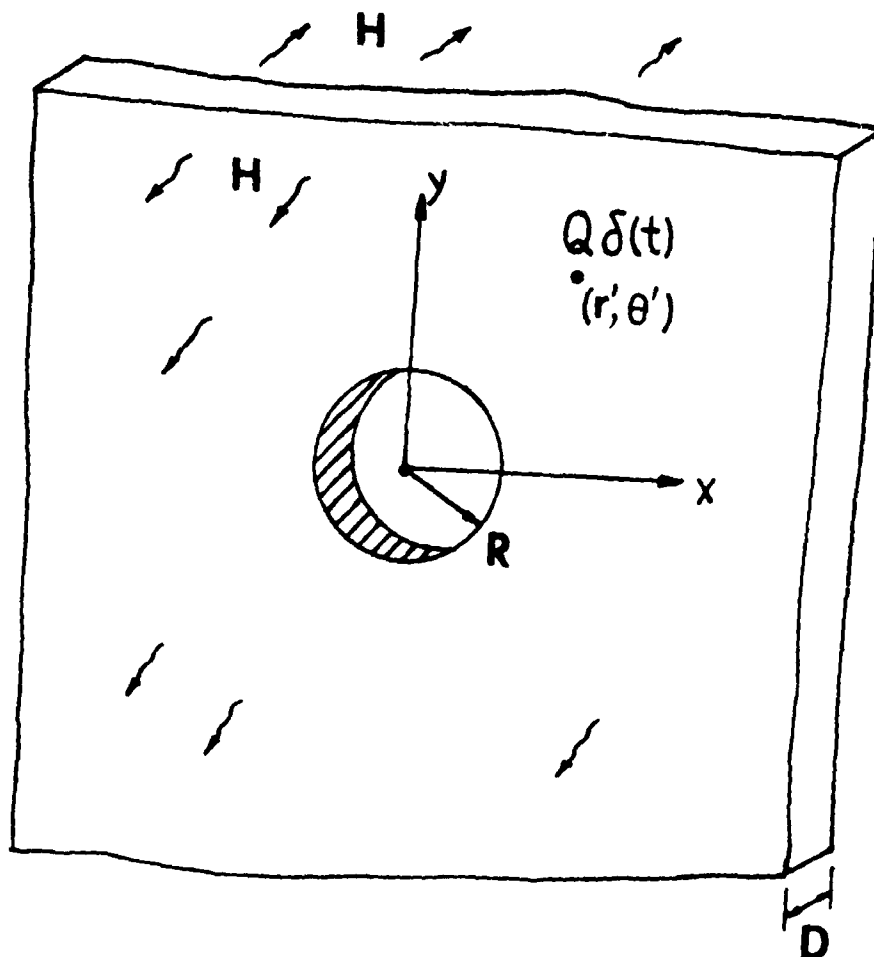


Figure 4-5. An Uncracked Plate with a Circular Hole
Subjected to a Point Heat Source at (r', θ')

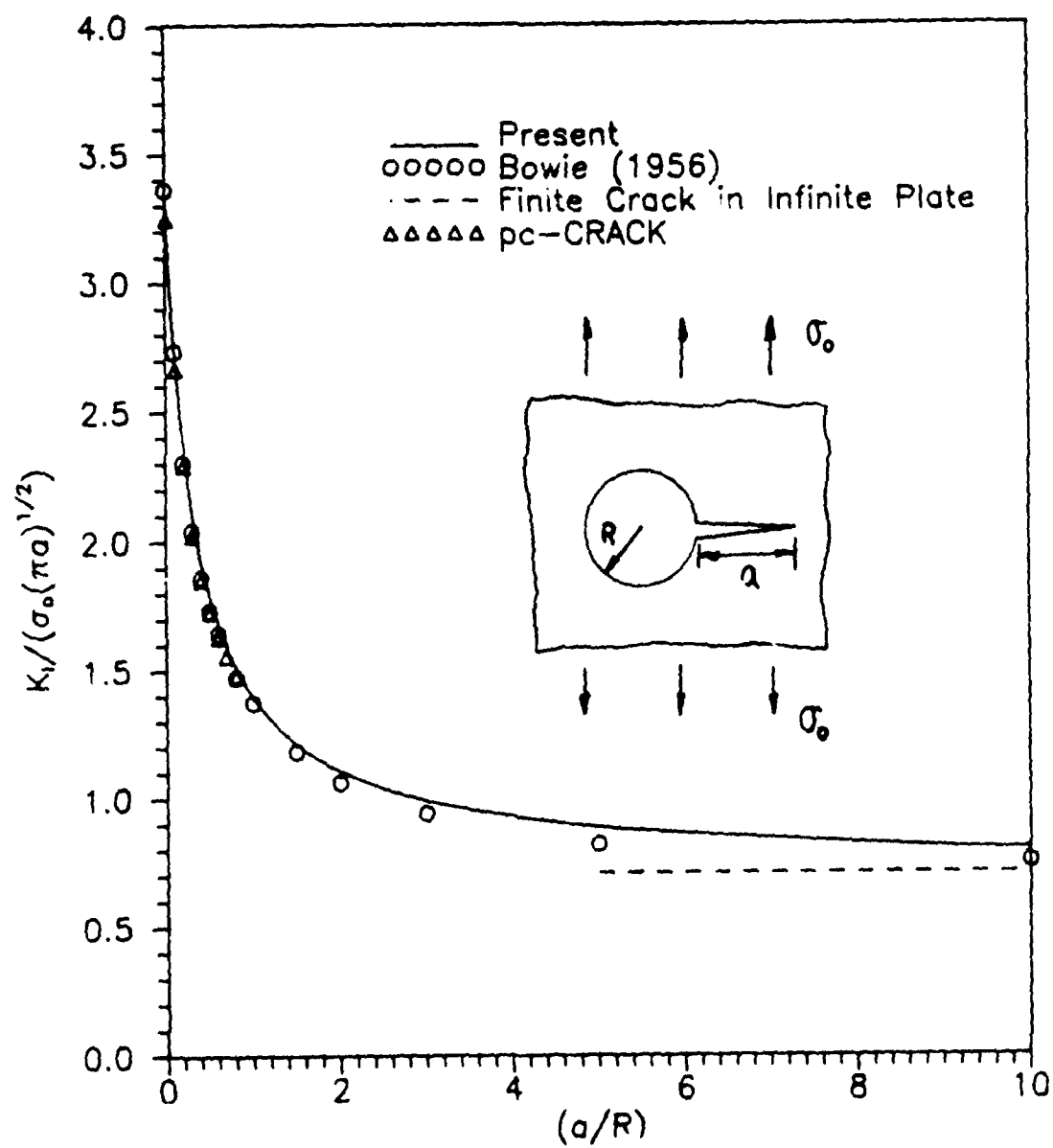


Figure 4-6. Verification of Mode I Influence Function

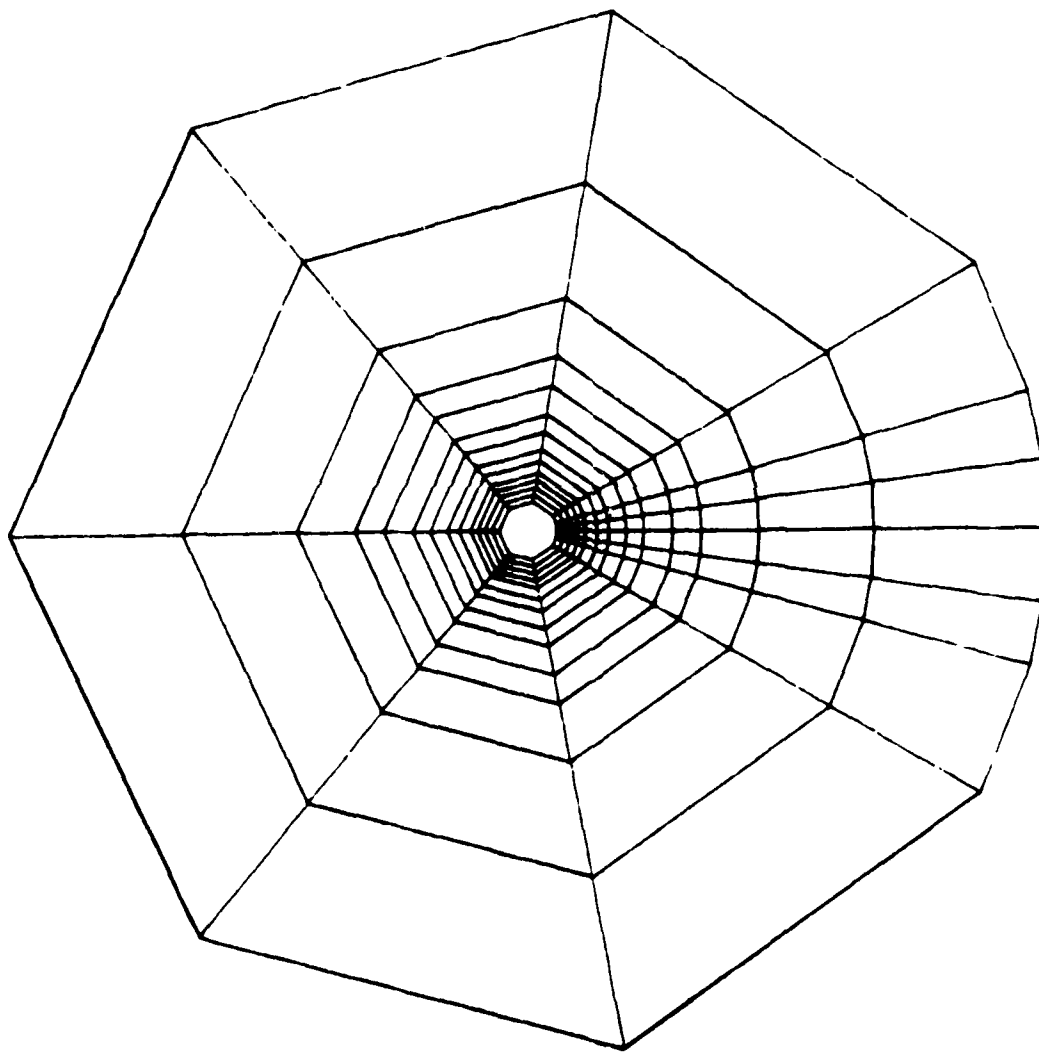


Figure 4-7(a). FEM-2D Mesh for a Radial Crack Emanating From a Hole

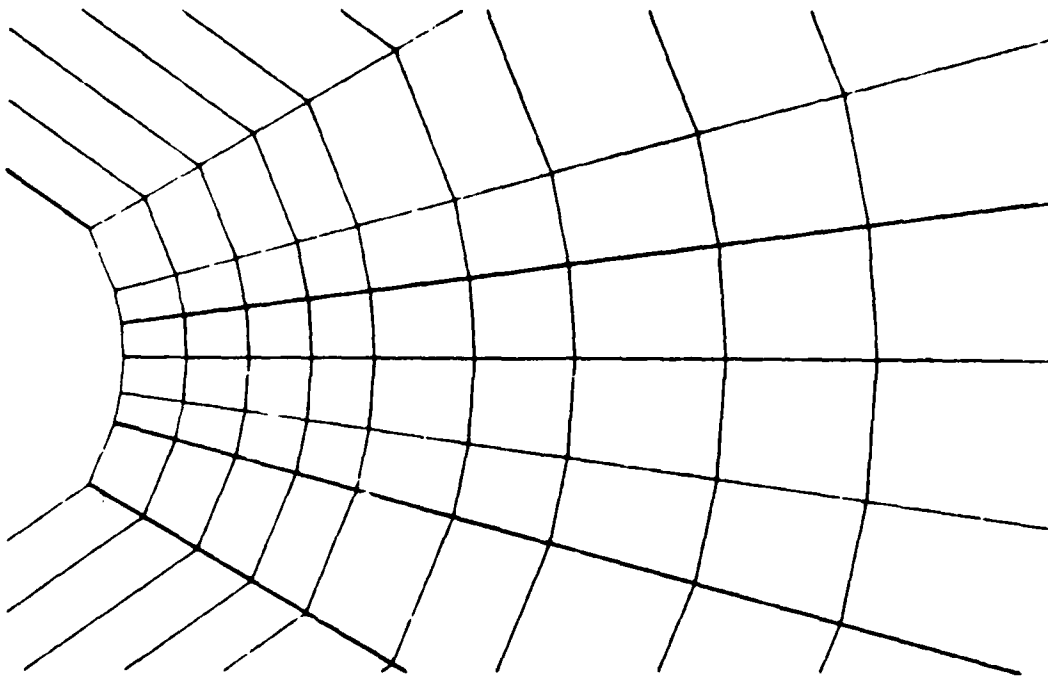


Figure 4-7(b). Finite Element Mesh Near the Crack Region

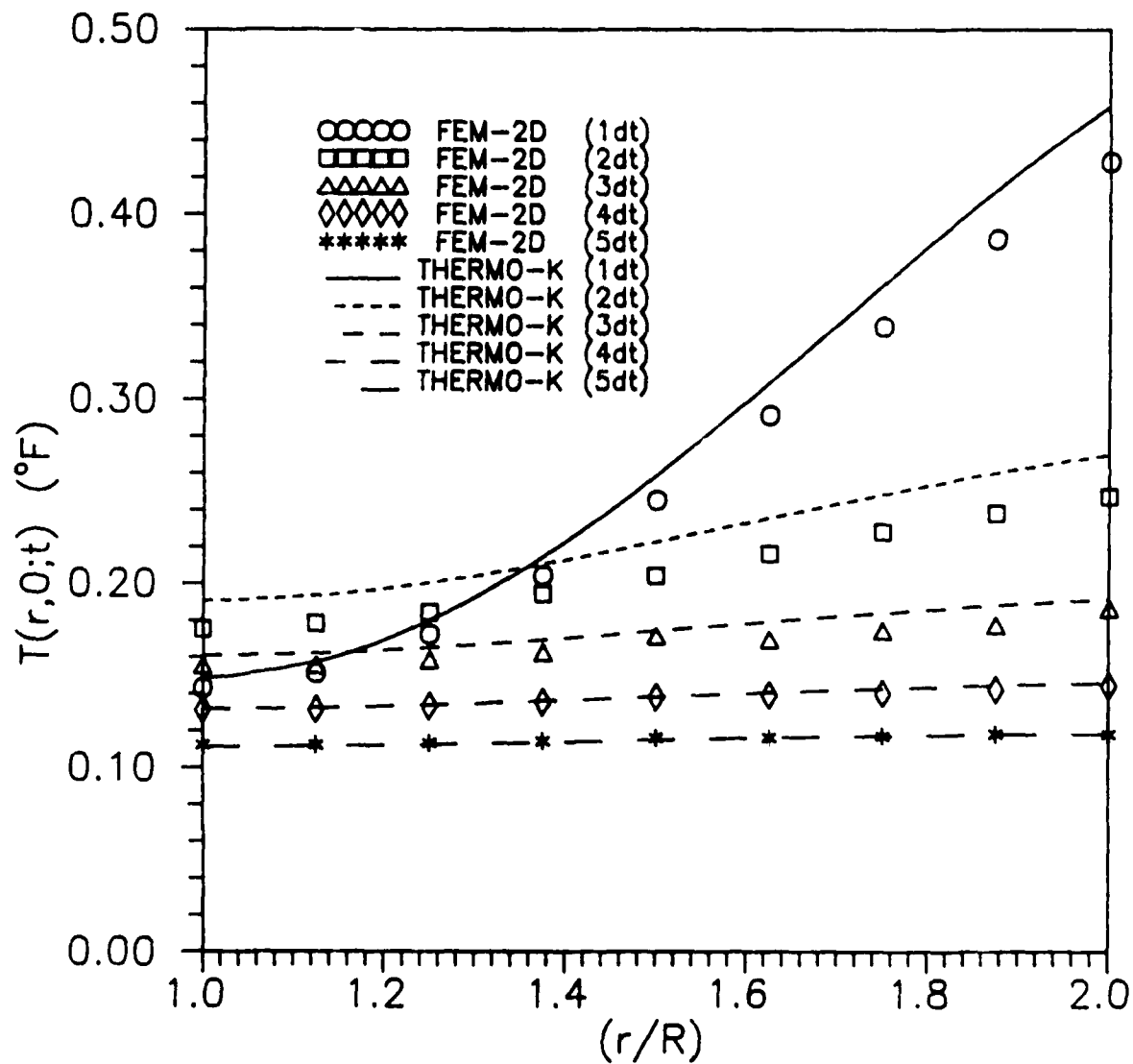


Figure 4-8. Comparison of Temperatures at $\theta = 0$ (Fully Conductive Crack)

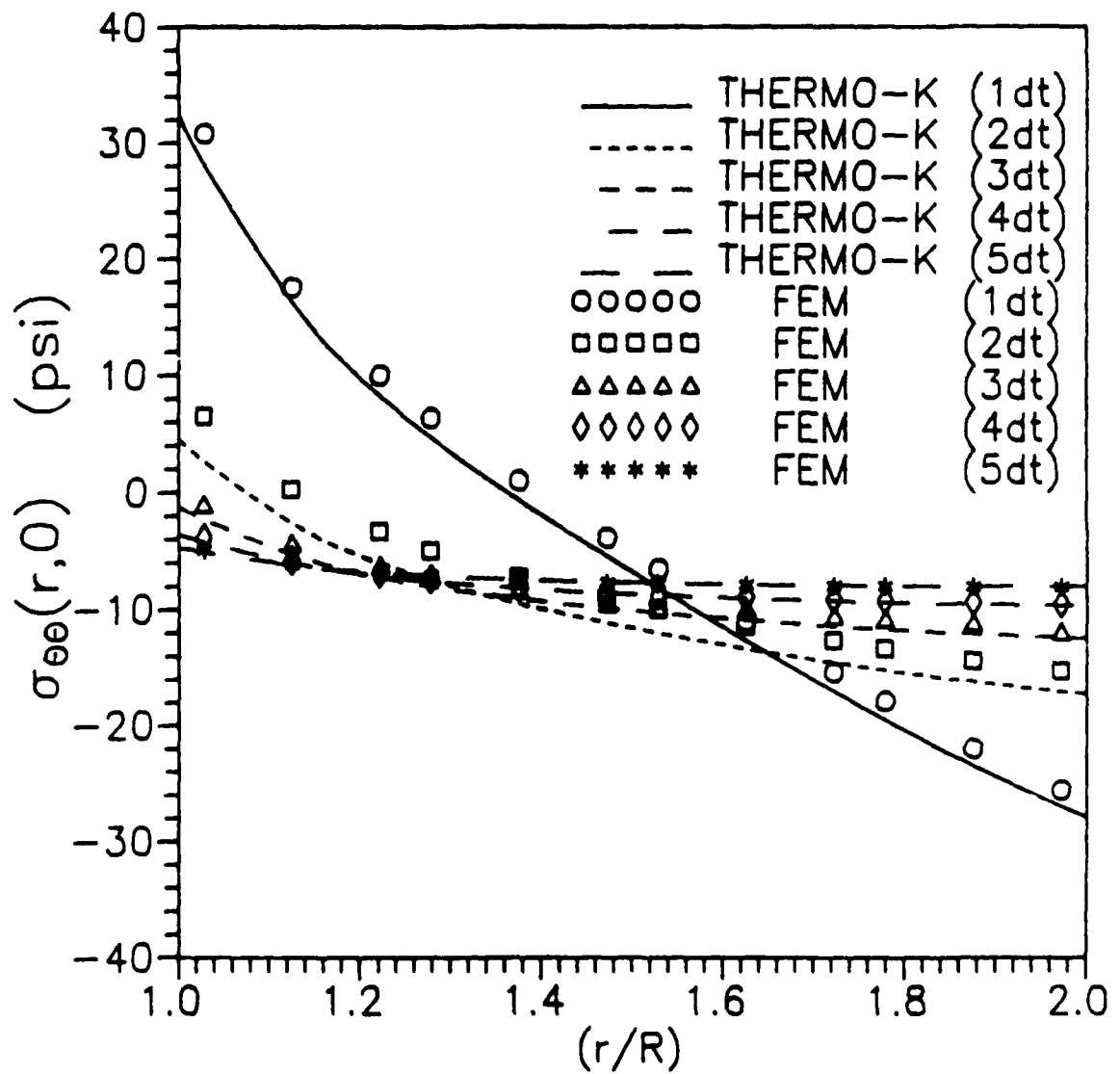


Figure 4-9. Comparison of Normal Stresses at $\theta = 0$
(Fully Conductive Crack)

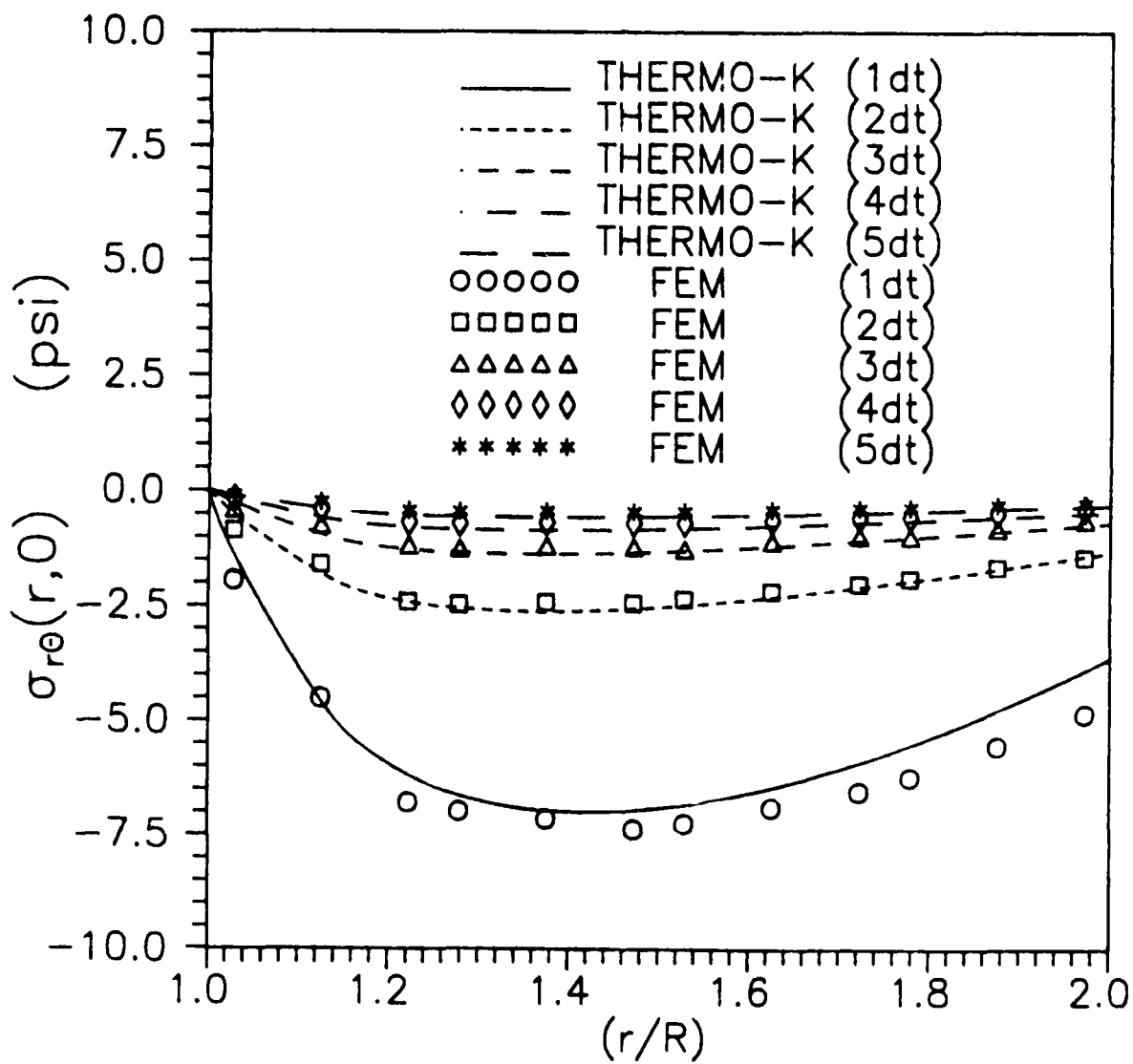


Figure 4-10. Comparison of Shear Stresses at $\theta = 0$
(Fully Conductive Crack)

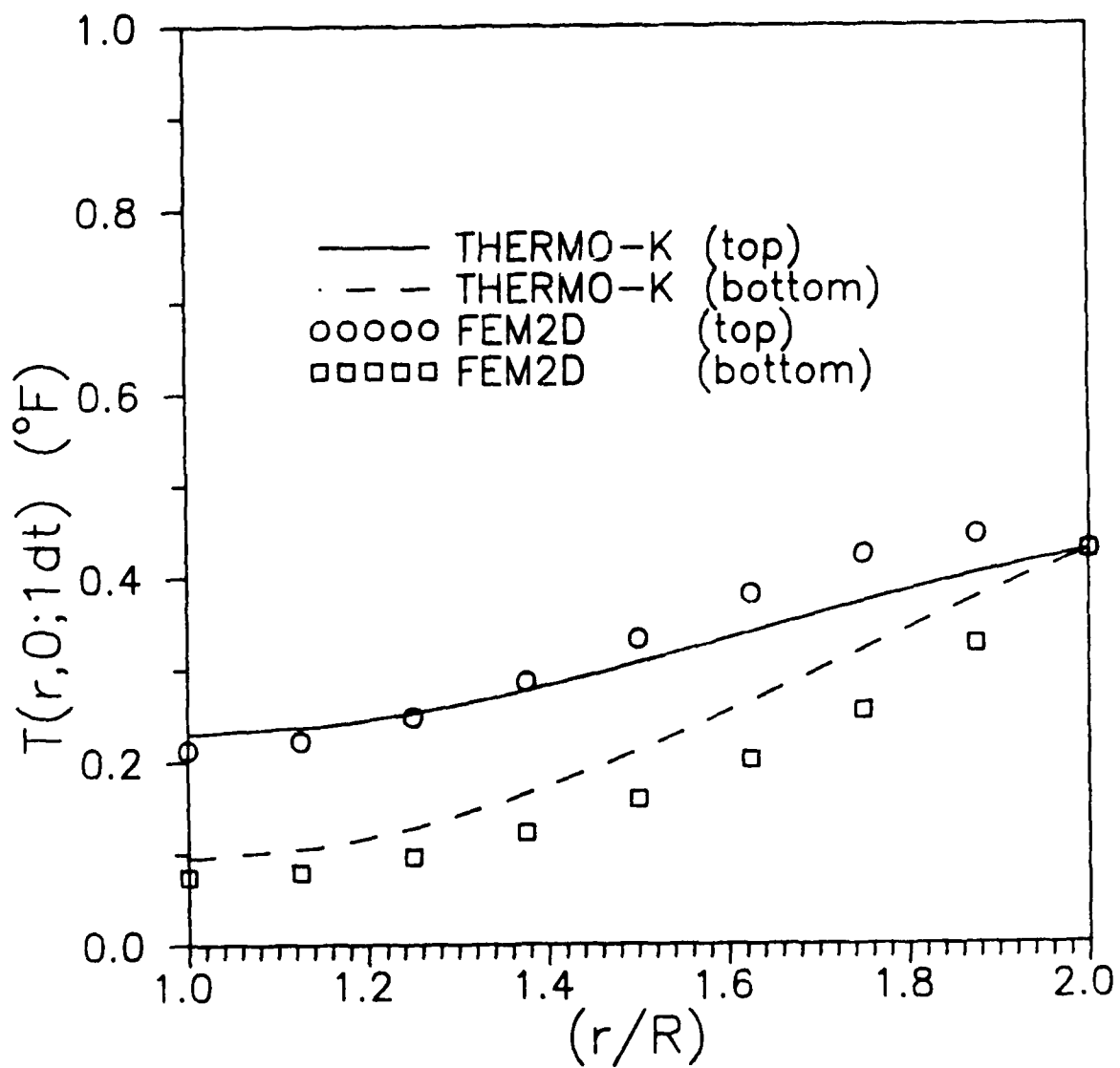


Figure 4-11(a). Comparison of Temperature at $\theta = 0$
(Insulated Crack $t = dt = 86$ sec)

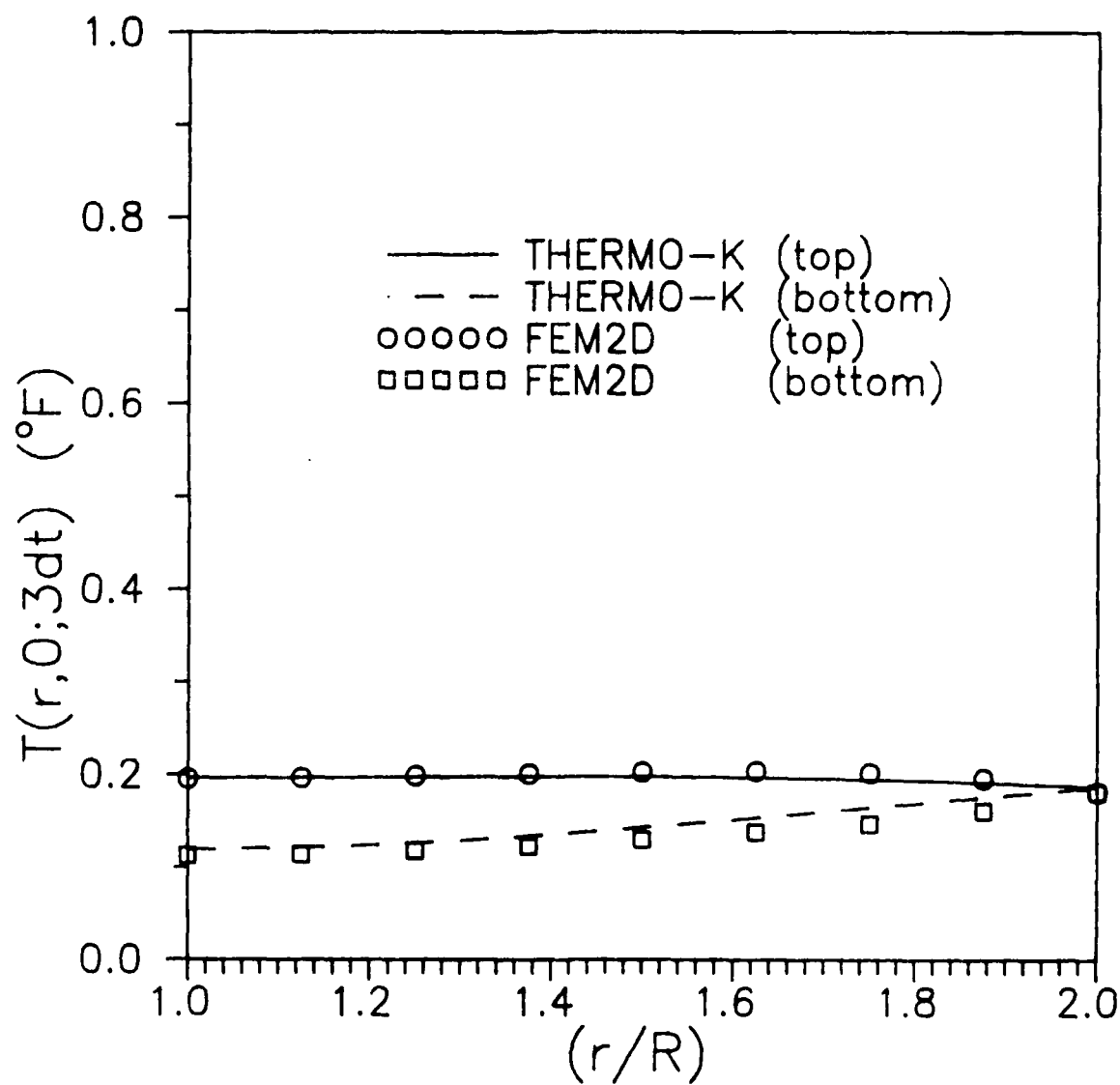


Figure 4-11(b). Comparison of Temperature at $\theta = 0$
(Insulated Crack $t = 3dt = 258$ sec)

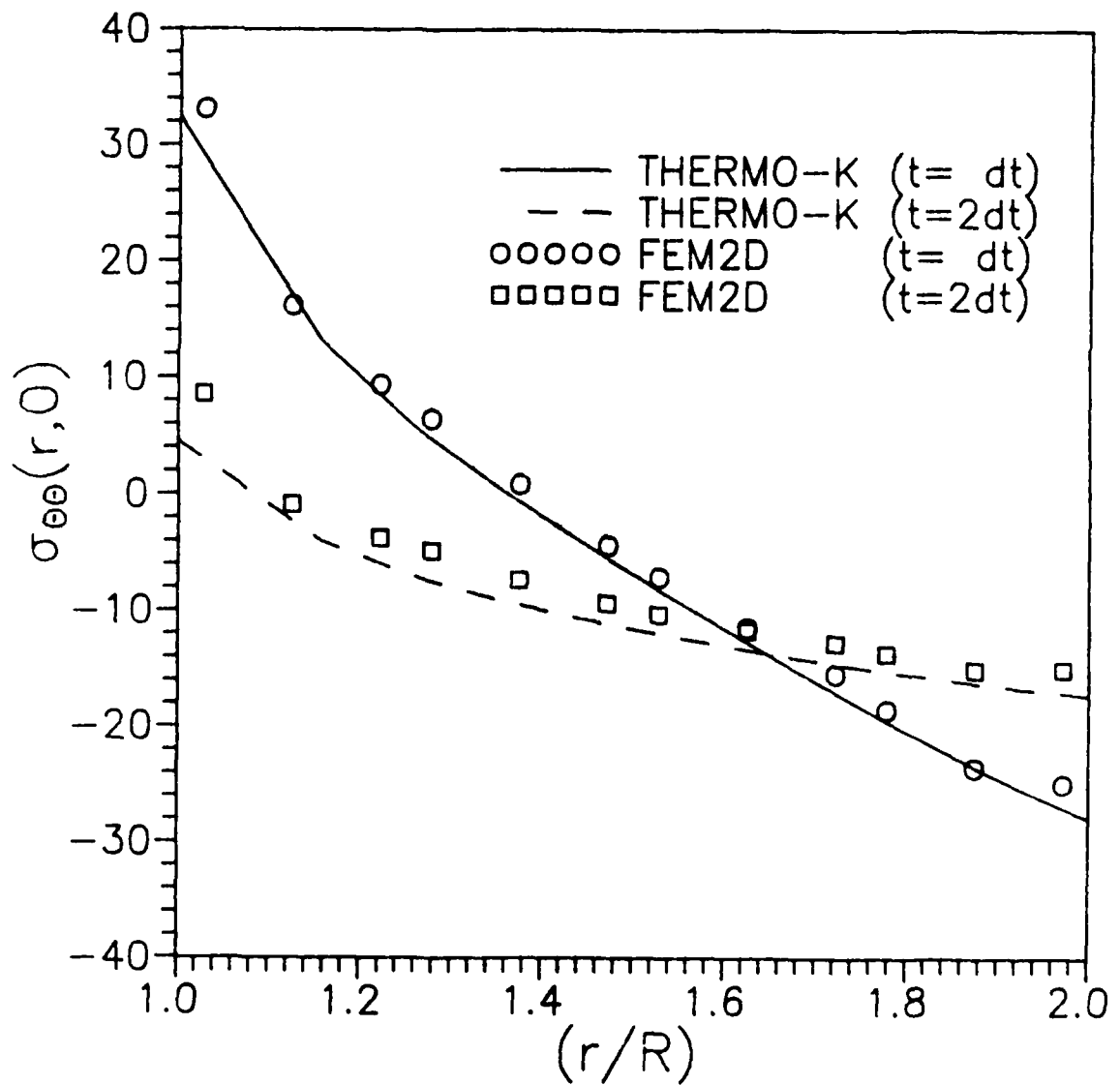


Figure 4-12. Comparison of Normal Stresses at $\theta = 0$ (Insulated Crack)

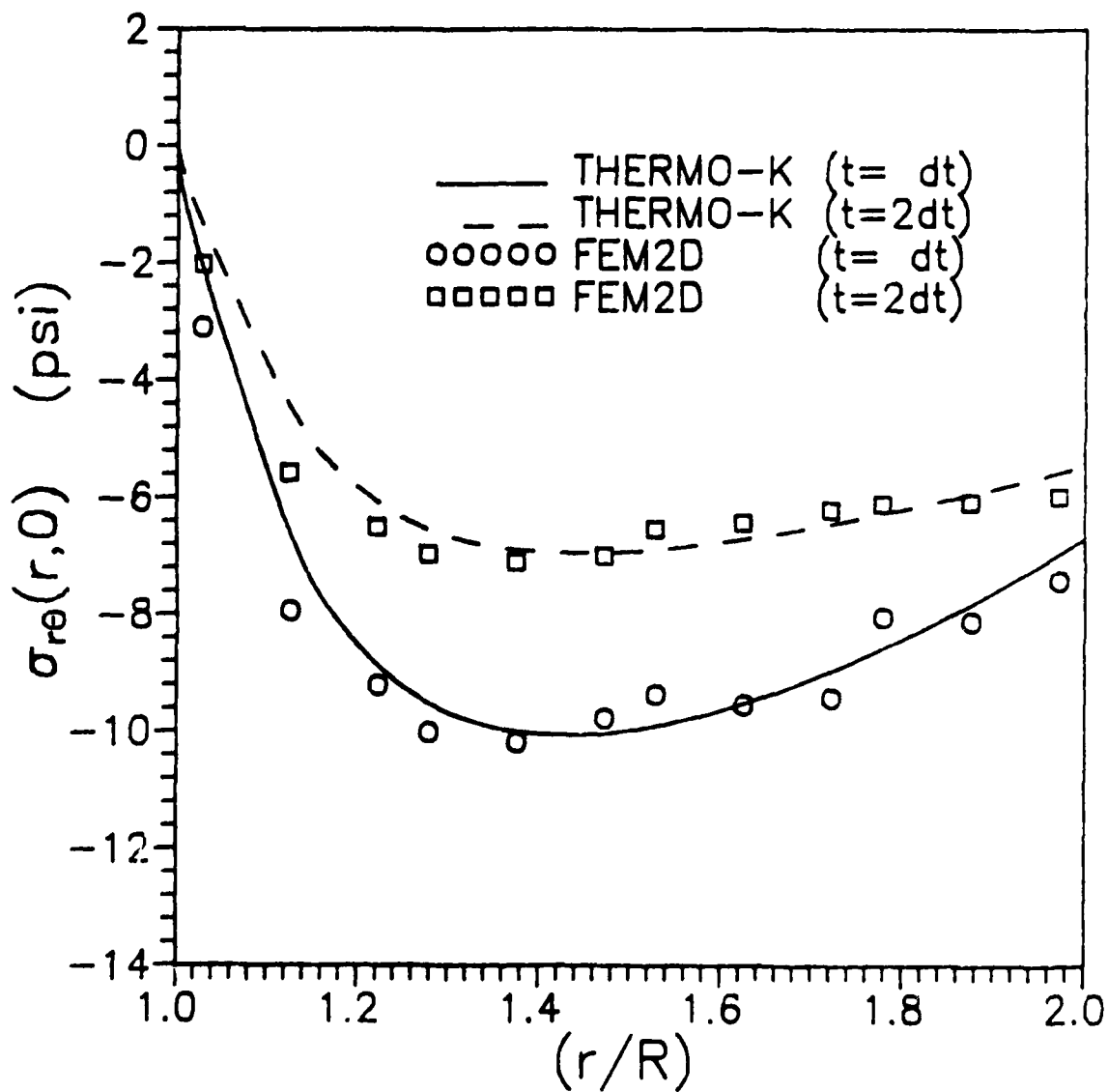


Figure 4-13. Comparison of Shear Stresses at $\theta = 0$
(Insulated Crack)

5.0 THEORETICAL BACKGROUND OF CRACK MODEL 4 - A SINGLE-EDGE CRACK PLATE

This section describes the theoretical basis for crack Model 4 - a single-edge crack plate, i.e., as illustrated in Figure 5-1, an edge crack of length a in an infinitely long plate strip of thickness D and width W . The cracked plate strip is subjected to point heat sources with arbitrary time history at any points in the plate region.

5.1 Assumptions

The following assumptions were made to simplify the problem:

- (a) The problem is assumed to be a plane stress problem. In other words, the thickness D shown in Figure 5-1 is assumed to be small enough that the temperature distribution in the thickness direction can be treated as uniform and the stress components in the thickness direction are negligible compared with the in-plane stress components.
- (b) The metallic materials are assumed to be isotropic, homogeneous, and linear elastic. Material properties are assumed to be temperature independent.
- (c) The rate of heat application is slow enough that the coupling terms and inertia terms in the general thermoelasticity equations can be neglected, i.e., it is assumed that the decoupled, quasi-static thermoelasticity applies.
- (d) The crack surfaces are assumed to be stress free. The crack surfaces can be completely insulated, fully heat conductive, or partially heat conductive. Heat conductance coefficient h at the crack surfaces is also assumed to be constant throughout the entire temperature range.

- (e) It is assumed that the heat convection coefficients at the two edges, H_1 and H_2 , and at the plate surfaces, H , (see Figure 5-1) remain constant.

5.2 Governing Equations

For a plane stress thermoelasticity problem as illustrated in Figure 5-1, the governing equations are

$$\xi \nabla^2 T = T_{,t} + \xi \eta^2 T \quad (5-1)$$

$$\sigma_{ij,j} = 0 \quad (5-2)$$

$$\sigma_{ij} = 2G [\epsilon_{ij} + (\frac{\nu}{1-\nu}) \delta_{ij} \epsilon_{kk} - a(\frac{1+\nu}{1-\nu}) \delta_{ij} T] \quad (5-3)$$

$$\epsilon_{ij} = (U_{i,j} + U_{j,i})/2 \quad (5-4)$$

and

$$\nabla^2 U_i + (\frac{1+\nu}{1-\nu}) U_{j,ji} = 2(\frac{1+\nu}{1-\nu}) a T \quad (5-5)$$

where $T=T(x_1, x_2, t)$ is temperature distribution, t and x_i are time and Cartesian coordinates respectively, $\xi=(k/\rho c)$, k is heat conduction coefficients, ρ is mass density, c is heat capacity, $\eta^2=(2H)/k/D$, H is heat convection coefficient from the plate surfaces to the environment (see Figure 5-1), D is plate thickness, U_i are displacements, a is coefficient of thermal expansion, and G and ν are shear modulus and Poisson's ratio respectively.

Nominal stress distributions generated with these equations are used to develop stress intensity factors via the influence function approach described below.

5.3 Influence Functions for Stress Intensity Factors

For any plate/crack geometry, cracktip stress intensity factors can be determined by integrating the product of the stresses at the crack location in an uncracked structure and an influence function (or weight function) (Buecker, 1973). That is, for a crack as shown in Figure 5-2, the stress intensity factor can be calculated by

$$K_I = \int_0^a \sigma_{yy}(x) m_1(x) dx \quad (5-6)$$

$$K_{II} = \int_0^a \sigma_{xy}(x) m_2(x) dx \quad (5-7)$$

where $m_1(x)$ and $m_2(x)$ are influence functions, x is a local coordinate shown in Figure 5-1 or Figure B-1 of Appendix B, and σ_{yy} and σ_{xy} are the normal and shear stress distributions on the crack surface in an identical but uncracked plate which is under the same temperature distribution as the cracked plate.

For a single edge crack in an infinitely long plate strip, as illustrated in Figure 5-1, the influence function (or weight function) for Mode I cracking has been provided by Bueckner (1973) as follows:

$$m_1(x) = \frac{\sqrt{2}}{\sqrt{\pi(a-x)}} \left[1 + p_1 \left(\frac{a-x}{a} \right) + p_2 \left(\frac{a-x}{a} \right)^2 \right] \quad (5-8)$$

where

$$p_1 = 0.6147 + 17.1844 R^2 + 8.8722 R^6 \quad (5-9)$$

$$p_3 = 0.2502 + 3.2889 R^2 + 70.0444 R^6 \quad (5-10)$$

$$R = a/W \quad (5-11)$$

and x , a , and W are defined in Figure 5-1.

Bueckner (1973) has stated that the above equations for the weight function $m_1(x)$ are very accurate for crack length up to one half of the plate width, i.e., Equation (5-8) is very accurate in the range of $0 \leq (a/W) \leq 0.5$.

With the use of boundary element method, Aliabadi et al. (1987) have obtained an influence function $m_2(x)$ for mode II cracking in a single-edge crack plate as follows:

$$m_2(x) = \frac{g(x/a)}{\sqrt{\pi a}} \frac{\sqrt{a+x}}{\sqrt{a-x}} \quad (5-12)$$

where

$$g(r) = 3.4948 - 4.1909r + 2.7506r^2 - 1.0684r^3 \quad (5-13)$$

when $a/W=0.6$, and

$$g(r) = 22.7041 - 2.7218r + 1.1381r^2 - 0.1146r^3 \quad (5-14)$$

when $a/W=0.3$. Also, results by Hartranft and Sih (1973) for an edge crack in a semi-infinite plate implies that

$$g(r) = 2.5909 - 2.6500r + 1.3515r^2 - 0.2910r^3 \quad (5-15)$$

when $a/W=0$. Linear interpolation among Equations (5-13) to (5-15) is used to calculate $m_2(x)$ for $r=a/W$ between 0 and 0.6.

The numerical integration scheme described in Appendix B of this report is used in the computer program.

5.4 Principle of Superposition

In general, as shown in Figure 5-1, there may be multiple heat sources (or sinks) within the plate which will cause thermal stresses and stress intensity factors at crack tips in the structure. Since the problem is linear, it is easily demonstrated that total stress intensity factor can be calculated as the sum of the stress intensity factors caused by each individual heat source or sink, acting independently. That is

$$K(t) = \sum_i [K(t)]_i \quad (5-16)$$

where $K(t)$ is the total stress intensity factor and $[K(t)]_i$ is the stress intensity factor due to the i^{th} heat source.

5.5 Green's Function Concept for Time Integration

In Equation (5-16), the stress intensity factor $[K(t)]_i$ caused by each individual heat source can be solved with the concept of Green's function integration. As illustrated in Figure 5-3, the stress intensity factor due to a heat source of intensity $Q_i(t)$ can be calculated by

$$[K(t)]_i = \int_0^t Q_i(\tau) G_i(t-\tau) d\tau \quad (\text{no summation}) \quad (5-17)$$

where $G_i(t)$ is the stress intensity factors due to a Delta function $\delta(t)$ heat source at the i^{th} heat source location.

As shown in Figure 5-3, generally, the Green's function $G_i(t)$ will decay and approach to zero after a decay period t_d . Therefore, the integration range in Equation (5-17) can be reduced to from $(t-t_d)$ to t . Such a reduction in the integration range greatly increases the speed of the calculation because, instead of integrating for the entire time history, it is only necessary to integrate backwards from the present time t to $(t-t_d)$ as follows

$$[K(t)]_i = \int_{t-t_d}^t Q_i(\tau) G_i(t-\tau) d\tau \quad (5-18)$$

5.6 Green's Function for Fully Heat Conductive Cracks

Previous subsections of this section show that the stress intensity factors for this crack models can be easily obtained by Equations (5-6), (5-7), (5-16), and (5-18) if the temperature and stress distributions and thereby the stress intensity factors at the crack tip, resulting from a delta function heat source (or sink) $Q\delta(t)$ at any arbitrary location (x',y') in the uncracked plate (Figure 5-4), can be solved. The uncracked plate shares the same temperature distribution as the cracked plate. As the first step, we consider the problem of a fully heat conductive edge crack, i.e., in this subsection, it is assumed that heat flux can flow across the crack surfaces without any heat loss or resistance. Solutions for a more general, partially heat conductive crack will be discussed in the next subsection. However, as will be seen in the next subsection and as shown in Appendix A of this report, for a crack model with symmetry about its crack plane such as this crack model, crack surface heat conductivity will affect Mode II stress intensity factor solutions but not Mode I or Mode III stress intensity factor solutions. In other words, whether the crack surfaces are fully heat conductive, insulated, or partially heat conductive, the K_I solution will remain the same for a single-edge crack in an infinitely long plate strip of finite width and thickness. Thus, if only Mode I or Mode III fracture is of major interest, the stress intensity factor solutions can be obtained by assuming the crack surfaces are fully heat conductive. The assumption of a fully heat conductive crack will greatly shorten the computation time for temperatures, thermal stresses, and stress intensity factors.

Since thermal stresses and stress intensity factors do not depend on the initial, stress free temperature of the plate, it is conveniently assumed that the initial temperature of the plate is zero, i.e., $T(x,y;0)=0$. To solve for the Green's function of this crack model, the following boundary conditions need to be

satisfied in addition to the governing equations listed in Equations (5-1) to (5-5):

at $x = 0$,

$$kT_{,x}(0,y;t) = -H_1 T(0,y;t) \quad (5-19)$$

$$\sigma_{xx}(0,y;t) = \sigma_{xy}(0,y;t) = 0 \quad (5-20)$$

at $x=W$,

$$kT_{,x}(W,y;t) = H_2 T(W,y;t) \quad (5-21)$$

$$\sigma_{xx}(W,y;t) = \sigma_{xy}(W,y;t) = 0 \quad (5-22)$$

at $y = \pm \infty$,

$$T(x,y;t) = 0 \quad (5-23)$$

$$\sigma_{xx}(x,y;t) = \sigma_{yy}(x,y;t) = \sigma_{xy}(x,y;t) = 0 \quad (5-24)$$

at $y=0$, $x \leq a$,

$$T(x,0^+;t) = T(x,0^-;t) \quad (5-25)$$

$$\sigma_{yy}(x, 0^+; t) = \sigma_{yy}(x, 0^-; t) \quad (5-26)$$

$$\sigma_{xy}(x, 0^+; t) = \sigma_{xy}(x, 0^-; t) \quad (5-27)$$

$$U_i(x, 0^+; t) = U_i(x, 0^-; t) \quad i = 1, 2 \quad (5-28)$$

Temperature solution to the uncracked plate problem can be obtained by solving Equation (5-1) along with boundary conditions Equations (5-19), (5-21), (5-23), and (5-25). An analytical form of the temperature solution has been given by Carslaw and Jaeger (1959) as follows:

$$T(x, y, t) = \frac{Q}{2\rho c D \sqrt{\pi \xi t}} \sum_{n=1}^{\infty} (Z_n(x) Z_n(x')) \exp\left[-\xi a_n^2 t - \xi \eta^2 t - \frac{(y-y')^2}{4\xi t}\right] \quad (5-29)$$

where ξ and η are defined in Equation (5-1), and

$$\tan a_n W = \frac{a_n k (H_1 + H_2)}{k^2 a_n^2 - H_1 H_2} \quad (5-30)$$

$$Z_n(x) = (k a_n \cos a_n x + H_1 \sin a_n x) Y_n \quad (5-31)$$

$$Y_n^2 = \frac{2(k^2 a_n^2 + H_2^2)}{(k^2 a_n^2 + H_1^2) [W(k^2 a_n^2 + H_2^2) + k H_2] + k H_1 (k^2 a_n^2 + H_2^2)} \quad (5-32)$$

The next step is to solve for the stress distribution due to the temperature distribution of Equation (5-29). Boley and Weiner (1960) and Parkus (1968) have shown that a particular solution to the thermal stress problem can be expressed in terms of a thermoelastic potential ϕ as follows

$$U_i = \phi_{,i} \quad (5-33)$$

$$\sigma_{xx} = -2G \phi_{,yy} \quad (5-34)$$

$$\sigma_{yy} = -2G \phi_{,xx} \quad (5-35)$$

$$\sigma_{xy} = 2G \phi_{,xy} \quad (5-36)$$

$$\phi(x,y,t) = \alpha(1+\nu) \xi e^{-\xi \eta^2 t} \int_0^t e^{\xi \eta^2 \tau} T(x,y,\tau) d\tau + \phi_0 \quad (5-37)$$

where ϕ_0 is a function of x , y , and t such that ϕ would remain finite as t approaches infinity. Substitution of Equation (5-29) into equation (5-37) yields

$$\phi(x,y;t) = e^{-\xi \eta^2 t} \sum_{n=1}^{\infty} \phi_n(x,y;t) \quad (5-38)$$

where

$$\phi_n = \frac{-\alpha(1+\nu)Q}{4\rho c D \alpha_n} z_n(x) z_n(x') [e^{-\alpha_n(y-y')} \operatorname{erfc}(\omega_1) +$$

$$e^{\alpha_n(y-y')} \operatorname{erfc}(w_2)] \quad (5-39)$$

$$w_{1,2} = (\alpha_n^2 \xi t)^{1/2} \pm \frac{(y-y')}{\sqrt{4\xi t}} \quad (5-40)$$

and $\operatorname{erfc}(x)$ is a complementary error function (see e.g., Abramowitz and Stegun, 1965 for definition).

In general, the particular solution ϕ shown in Equations (5-38) to (5-40) satisfies the stress free boundary of Equations (5-24), (5-26) to (5-28) but does not fulfill the stress boundary conditions at $x=0$ and $x=W$, i.e., Equations (5-20), (5-22) are not satisfied. For instance, typical edge stresses at $x=0$ due to ϕ for an instantaneous heat source situated at center of the plate strip are illustrated in Figures 5-5 and 5-6. Therefore, a complementary solution ψ , which is an analytic function, must be included to make the two edges $x=0$ and $x=W$ stress free. The overall stresses are then calculated by

$$\sigma_{xx} = 2G (\psi - \phi)_{,yy} \quad (5-41)$$

$$\sigma_{yy} = 2G (\psi - \phi)_{,xx} \quad (5-42)$$

and

$$\sigma_{xy} = -2G (\psi - \phi)_{,xy} \quad (5-43)$$

where Ψ is the solution of

$$\nabla^2 \nabla^2 \Psi = 0 \quad (5-44)$$

$$\Psi_{,yy} = \phi_{,yy} \quad \text{at } x=0 \text{ and } x=W \quad (5-45)$$

and

$$\Psi_{,xy} = \phi_{,xy} \quad \text{at } x=0 \text{ and } x=W \quad (5-46)$$

Solution to Equations (5-44) to (5-46) can be obtained by the methods described by Timoshenko and Goodier (1970) for the problem of an infinitely plate strip of width W and thickness D subjected to arbitrary tractions at both edges (as illustrated in Figure 5-7). Detailed derivations of Ψ are given in Appendix C of this report. From Appendix C, stresses resulting from the stress function Ψ at crack plane, $y=0$, are evaluated by

$$\begin{aligned} \hat{\sigma}_{yy}(x,0;t) = & 4G \int_{-\infty}^{\infty} \left(-[\phi_{,yy}(-\frac{W}{2},y;t) \beta_{yy}(\frac{x}{W}, \frac{|y|}{W})] \right. \\ & + [\phi_{,xy}(-\frac{W}{2},y;t) \gamma_{yy}(\frac{x}{W}, \frac{|y|}{W}) \operatorname{sgn}(y)] \\ & - [\phi_{,yy}(\frac{W}{2},y;t) \beta_{yy}(1 - \frac{x}{W}, \frac{|y|}{W})] \\ & \left. + [\phi_{,xy}(\frac{W}{2},y;t) \gamma_{yy}(1 - \frac{x}{W}, \frac{|y|}{W}) \operatorname{sgn}(y)] \right) \frac{dy}{W} \quad (5-47) \end{aligned}$$

$$\hat{\sigma}_{xy}(x,0;t) = 4G \int_{-\infty}^{\infty} ([\phi_{,yy}(-\frac{W}{2},y;t) \beta_{xy}(\frac{x}{W}, \frac{|y|}{W}) \operatorname{sgn}(y)]$$

$$\begin{aligned}
& - [\phi_{,xy}(-\frac{W}{2}, y; t) \gamma_{xy}(\frac{x}{W}, \frac{|y|}{W})] \\
& - [\phi_{,yy}(\frac{W}{2}, y; t) \beta_{xy}(1 - \frac{x}{W}, \frac{|y|}{W}) \operatorname{sgn}(y)] \\
& - [\phi_{,xy}(\frac{W}{2}, y; t) \gamma_{xy}(1 - \frac{x}{W}, \frac{|y|}{W})] \} \frac{dy}{W}
\end{aligned} \tag{5-48}$$

where $\phi(x, y; t)$ is the thermoelastic potential function given in Equations (5-38) to (5-40), $\operatorname{sgn}(y)$ is a sign function, and β_{yy} , β_{xy} , γ_{yy} , and γ_{xy} are edge effect functions shown in Figures C-3 to C-16) of Appendix B at the end of this report.

Therefore, at the cross section of $y=0$, the stresses caused by a Delta function heat source $Q\delta(t)$ at (x', y') are

$$\sigma_{yy} = \hat{\sigma}_{yy} + \sum (P_n \cos \alpha_n x + Q_n \sin \alpha_n x) + \frac{F}{W} + \frac{12Nx}{W^3} \tag{5-49}$$

$$\sigma_{xy} = \hat{\sigma}_{xy} + \sum (R_n \cos \alpha_n x + S_n \sin \alpha_n x) \tag{5-50}$$

where $\hat{\sigma}_{yy}$ and $\hat{\sigma}_{xy}$ are stresses calculated by Equations (5-47), (5-48), F and N are constants to maintain the condition of zero forces and moments at cross section $y=0$, and

$$P_n = \frac{G\alpha(1+\nu)Q}{2\rho cD} Y_n k \alpha_n^2 M Z_n(x') \tag{5-51}$$

$$Q_n = \frac{G\alpha(1+\nu)Q}{2\rho cD} Y_n H_1 \alpha_n M Z_n(x') \tag{5-52}$$

$$R_n = \frac{Ga(1+\nu)Q}{2\rho cD} Y_n H_1 N Z_n(x') \quad (5-53)$$

$$S_n = - \frac{Ga(1+\nu)Q}{2\rho cD} Y_n K a_n N Z_n(x') \quad (5-54)$$

$$M = - [\exp(a_n y') \operatorname{erfc}(\omega_2) + \exp(-a_n y') \operatorname{erfc}(\omega_1)] \quad (5-55)$$

$$N = - \left(\exp(a_n y') \left[a_n \operatorname{erfc}(\omega_2) + \frac{\exp(-\omega_2^2)}{\sqrt{\pi \xi t}} \right] - \exp(-a_n y') \left[a_n \operatorname{erfc}(\omega_1) + \frac{\exp(-\omega_1^2)}{\sqrt{\pi \xi t}} \right] \right) \quad (5-56)$$

To sum up this subsection, the Green's functions for the stress intensity factors are calculated by substituting the stress solutions given in Equations (5-49) and (5-50) and the influence functions given in Equations (5-8) and (5-12) into Equations (5-6) and (5-7) and integrating Equations (5-6) and (5-7) by the numerical integration scheme depicted in Appendix B.

5.7 Green's Function for Partially Heat Conductive Cracks

In subsection 5.6 the Green's function solution for a single point heat source at any arbitrary point in a single-edge crack plate is discussed. The crack surfaces in subsection 5.6 is assumed to be fully heat conductive. In reality, the crack surface is expected to be somewhere between complete insulation and fully heat conductive, i.e., crack surfaces are expected to be partially heat conductive. A general approach to treat a partially heat conductive crack is studied in detail in Appendix A of this report. Application of the concept given in Appendix A to the single-edge crack model is discussed in this subsection.

Governing heat transfer equation for a single-edge crack plate with partially heat conductive crack surfaces is still Equation (5-1), and the boundary conditions at $x=0$, $x=W$, and $y=\pm\infty$, Equations (5-19), (5-21), and (5-23), respectively, remain unchanged. The only difference will be the boundary condition at $y=0$, $0 \leq x \leq a$, i.e., Equation (5-25) is replaced by

$$T_{,y}(x,0) = \frac{\lambda}{a} [T(x,0^+) - T(x,0^-)] \quad 0 \leq x \leq a \quad (5-57)$$

where λ is defined as (ah/k) in which h is crack surface heat conductance coefficient and k is material thermal conductivity. From Equation (5-57), it can be easily seen that the crack surfaces are fully heat conductive when $\lambda=\infty$ and the crack surfaces are completely insulated when $\lambda=0$. Any λ values between 0 and ∞ are corresponding to a partially heat conductive crack.

As discussed in Appendix A, when a crack is completely insulated or partially heat conductive, the resulting temperatures on both sides of a crack will be different, i.e., there is a temperature jump across the crack surface when λ equals to zero or a finite number. This temperature jump is analogous to the temperature jump created by a series of distributed heat dipoles (Carslaw and Jaeger, 1959) situated at the crack location. Thus, the overall temperature distribution can be obtained as the superposition of the fully conductive solution, Equation (5-29), and a solution for the distributed heat dipoles. From Equation (5-29), it can be shown, by summing temperature solutions for a point heat source and a point heat sink with infinitesimally small distance in between, that temperature solution for an instantaneous heat dipole of strength M situated at $y=0$, $x=\bar{x}$ in an infinitely long plate strip is

$$T(x, y; t) = - \frac{M Y}{4 \rho c D \sqrt{\pi \xi t}} \left[\sum \exp(-\xi \eta^2 t - \xi a_n^2 t - \frac{y^2}{4 \xi t}) Z_n(x) \right. \\ \left. Z_n(\bar{x}) \right] \quad (5-58)$$

Thus resulting temperature from distributed heat dipoles of strength $M(x, t)$ situated at $y=0$, $0 \leq x \leq a$ of the plate strip is

$$T(x, y, ; t) = - \frac{Y}{4 \rho c D \sqrt{\pi \xi}^{1.5}} \int_0^t \int_0^a \left(\frac{M(\bar{x}, t')}{(t-t')^{3/2}} \exp\left[\frac{-y^2}{4 \xi (t-t')}\right] \right. \\ \left. [\sum \exp(-\xi \eta^2 t - \xi a_n(t-t')) Z_n(x) Z_n(\bar{x})] \right) d\bar{x} dt' \quad (5-59)$$

Substitution of the sum of Equations (5-29) and (5-59) into Equation (5-57) yield a Fredholm integral equation for the heat dipole distribution $M(x, t)$ as follows:

$$\frac{Q Y'}{4 R c D \sqrt{\pi \xi t} \xi t} \left[\sum \exp(-\xi a_n^2 t - \frac{y'^2}{4 \xi t}) - \frac{1}{4 \rho c D \sqrt{\pi \xi}^{3/2}} \int_0^t \int_0^a \right. \\ \left. \left(\frac{M(\bar{x}, t')}{(t-t')^{3/2}} [\sum \exp(-\xi a_n(t-t')) Z_n(x) Z_n(\bar{x})] \right) d\bar{x} dt' \right] \\ = \frac{\lambda}{a} \frac{M(x, t)}{\rho c D \xi} e^{\xi \eta^2 t} \quad (5-60)$$

A numerical approximation method is used in the computer program to solve Equation (5-60). Since the temperature jump between two adjacent crack surfaces has to be zero at the crack tip, $x=a$, we assume that

$$M(x,t) = \sum_{m=1}^L b_m(t) \cos\left[\frac{(2m-1)\pi x}{2a}\right] \quad (5-61)$$

where L is the maximum number of terms included in the calculation and $b_m(t)$ is a time function, which is determined by substituting Equation (5-61) into Equation (5-60).

Similar to the fully heat conductive case, a thermoelastic potential due to the distributed thermal dipoles at the crack region can be derived by integrating the temperature solution, Equation (5-59). That is,

$$\phi(x,y;t) = \alpha\xi(1+\nu) \int_0^t T(x,y;\tau) e^{-\xi\eta^2(t-\tau)} d\tau + \phi_0 \quad (5-62)$$

where $T(x,y;t)$ is the temperature solution given in Equation (5-59) and ϕ_0 is an analytic function to make ϕ remain finite at infinity. Substituting Equation (5-61) into Equation (5-59) and thereafter into Equation (5-62), one obtains

$$\phi(x,y;t) = \frac{-\alpha(1+\nu)}{4\rho c D \sqrt{\pi\xi}} \sum_{m=1}^L \sum_{n=1}^N (r_{mn} z_n(x) \int_0^t \int_0^\tau \frac{b_m(t') y}{(\tau-t')^{1.5}} \exp(-\xi\eta^2 t - \frac{y^2}{4\xi(\tau-t')} - \xi a_n^2(\tau-t')) dt' d\tau) \quad (5-63)$$

where

$$r_{mn} = kY_n a_n \left[\frac{\sin(\delta_m - \alpha_n)a}{2(\delta_m - \alpha_n)} + \frac{\sin(\delta_m + \alpha_n)a}{2(\delta_m + \alpha_n)} \right] +$$

$$Y_n H_1 \left[\frac{\cos(\delta_m - \alpha_n)a}{2(\delta_m - \alpha_n)} - \frac{\cos(\delta_m + \alpha_n)a}{2(\delta_m + \alpha_n)} \right] \quad (5-64)$$

$\delta_m = \frac{(2m-1)\pi}{2a}$, ξ and η are defined in Equation (5-1), α_n 's are the eigen values defined in Equation (5-30), $Z_n(x)$ are eigen functions defined in Equation (5-31), Y_n 's are constants defined in Equation (5-32), $b_m(t)$'s are the time functions defined in Equation (5-62), and N and L are the maximum number of terms included in the series expansions in Equation (5-29) and Equation (5-62), respectively. Stresses at the crack region, $y=0$, $0 \leq x \leq a$, due to the distributed thermal dipoles can then be evaluated by substituting Equation (5-64) into Equations (5-42), and (5-43). After some algebraic manipulation, it can be shown that stresses at section $y=0$ due to the thermoelastic potential ϕ of Equation (5-63) are as follows:

$$\sigma_{yy}(x, 0; t) = 0 \quad (5-65)$$

$$\sigma_{xy}(x, 0; t) = 2G\phi_{,xy}(x, 0; t)$$

$$= \sum_{m=1}^L \sum_{n=1}^N [r_{mn} Z'_n(x) F_n(0, t)] \quad (5-66)$$

$$\begin{aligned}
F_n(y, t) = & \frac{E\alpha}{4\rho CD} e^{-\xi\eta^2 t} \int_0^t \left\{ b_m(t') a_n [\exp(\alpha_n y) \operatorname{erfc}(\omega_1) \right. \\
& + \exp(-\alpha_n y) \operatorname{erfc}(\omega_2) - \frac{\omega_1 \exp(\alpha_n y - \omega_1^2)}{a_n \pi \xi (t-t')} \\
& \left. - \frac{\omega_2 \exp(-\alpha_n y - \omega_2^2)}{a_n \pi \xi (t-t')} \right\} dt' \quad (5-67)
\end{aligned}$$

where ω_1 and ω_2 are defined in Equation (5-40). Results shown in Equations (5-65) and (5-66) reiterate the fact, deduced in Appendix A, that, for a cracked structure with symmetry with respect to the crack plane such as the current crack model, crack surface heat conductivity will not affect Mode I fracture solution ($\sigma_{yy}=0$ in Equation (5-65)) but will change Mode II fracture solution ($\sigma_{xy} \neq 0$ in Equation (5-66)).

To sum up, for a single-edge crack plate with partially heat conductive or completely insulated crack surfaces, its overall temperature solution is the sum of Equation (5-29) and Equation (5-59). Stresses in the uncracked plate strip, which share the same overall temperature distribution as the cracked plate, are still given by Equations (5-49) and (5-50) except that the thermoelastic potential ϕ in Equations (5-41) to (5-48) now equal to the sum of Equations (5-38) and (5-63) and R_n 's in Equation (5-50) equal to the sum of the right hand side of Equation (5-53) and

$$\sum_{m=1}^L r_{mn} F_n a_n Y_n H_1 \quad (5-68)$$

and S_n 's in Equation (5-50) equal to the sum of the right hand side of Equation (5-54) and

$$- \sum_{m=1}^L r_{mn} F_n k a_n^2 Y_n \quad (5-69)$$

Green's function solutions for stress intensity factors, K_I and K_{II} , at the crack tip are then calculated by substituting the above stresses at the crack region into Equations (5-6) and (5-7), respectively.

5.8 Finite Element Verification of Crack Model 4

Since stress intensity factors are calculated by integrating the product of influence functions and stresses at the crack location in a uncracked plate (see Equations (5-6) and (5-7)), it is necessary to verify both the influence functions shown in subsection 5.3 and the temperature and thermal stresses obtained in subsections 5.6 and 5.7.

5.8.1 Verification of Influence Functions

To verify the Mode I influence function given in Equations (5-8) to (5-11), the problem of a single-edge crack plate of width 10 inches subjected to an uniform tension of 1 ksi, as illustrated in Figure 5-8, is chosen a reference problem. Mode I stress intensity factors for various crack lengths for this problem has been obtained by Tada, et al (1973) as well as pc-CRACK (1986). As illustrated in Figure 5-8, K_I solutions obtained by substituting Equations (5-8) to (5-11) and $\sigma_{yy}(x) = 1$ ksi into Equation (5-6) are in excellent agreement with the reference solutions given by Tada, et al (1973) and pc-CRACK (1986) up to $a/W=0.6$. Next, another loading case of a constant applied moment of 3000 in-lb at infinity is considered for a single-edge crack

plate of width 3 inches, i.e., as shown in Figure 5-9, the single-edge crack plate is subjected to a linear normal stress distribution of $\sigma_{yy}(x) = (2 - \frac{4}{3}x)$ ksi at infinity. Resulting K_I solutions, which are obtained by substituting this stress distribution and Equations (5-8) to (5-11) into Equation (5-6), are plotted in Figure 5-9. It is seen from this figure that current stress intensity factor solutions are in good agreement with the reference solutions obtained by Tada, et al (1973) up to $a/W=0.6$.

Similarly, a single-edge crack plate of width 10 inches under an uniform shear stress of 1 ksi, as illustrated in Figure 5-10, is chosen as a reference problem for verifying the Mode II influence function. As shown in Figure 5-10, stress intensity factor solutions obtained by substituting Equations (5-12) to (5-15) and $\sigma_{xy}(x) = 1$ ksi into Equation (5-7) are very close to the stress intensity factors given by Tada et al. (1973) and pc-CRACK (1986) up to $a/W=0.6$.

Therefore, it is concluded that the influence functions shown in Equations (5-8) to (5-15) for the crack model of a single-edge crack plate are quite accurate up to $a/W=0.6$, i.e., the influence functions are very accurate up to crack length of 60 percent of the plate width..

5 8.2 Verification of Temperature and Stresses for Fully Heat Conductive Crack Surfaces

To verify the temperature and stress calculation procedures for a fully heat conductive single-edge crack in an infinitely long plate strip, a commercially available finite element program, NASTRAN (NASTRAN, 1973) is used. The reference problem chosen is an infinitely long plate of width $W=5$ inches and thickness $D=0.5$

inch. The plate is made of 7075-T651 Aluminum. Material properties for this reference problem are

$$E = 10.3 \times 10^6 \text{ psi}, \quad \nu = 0.33, \quad \alpha = 13 \times 10^{-6} / ^\circ\text{F}$$

$$k = 0.0017361 \frac{\text{Btu}}{\text{in-sec-F}}, \quad \rho = 0.0978 \frac{\text{lbm}}{\text{in}^3}, \quad c = 0.23 \frac{\text{Btu}}{\text{lbm-F}}$$

$$H = H_1 = H_2 = 0 \frac{\text{Btu}}{\text{in}^2\text{-sec-F}} \quad (5-70)$$

As shown in Figures 5-11 and 5-12, a finite element mesh with 452 nodes and 394 four-node quadrilateral elements is constructed for one half of the plate strip. Loading heat sources are applied at the symmetry plane ($y=0$ plane in Figure 5-12) of the half model. The overall vertical dimension of the finite element is chosen to be 52 inches to simulate the infinite length of the plate strip. A total seven loading cases is considered in the temperature and thermal stress benchmarking analyses. Applied point heat sources for these seven cases are as follows:

$$\text{Case 5-1: } (x', y') = (2.5 \text{ inch}, 0 \text{ inch}), \quad \dot{Q}(t) = H(t) \text{ Btu/sec}$$

$$\text{Case 5-2: } (x', y') = (2.5 \text{ inch}, -1 \text{ inch}), \quad \dot{Q}(t) = H(t) \text{ Btu/sec}$$

$$\text{Case 5-3: } (x', y') = (2.5 \text{ inch}, -1.75 \text{ inch}), \quad \dot{Q}(t) = H(t) \text{ Btu/sec}$$

$$\text{Case 5-4: } (x', y') = (4 \text{ inch}, 0 \text{ inch}), \quad \dot{Q}(t) = H(t) \text{ Btu/sec}$$

$$\text{Case 5-5: } (x', y') = (4 \text{ inch}, -1 \text{ inch}), \quad \dot{Q}(t) = H(t) \text{ Btu/sec}$$

Case 5-6: $(x', y') = (4 \text{ inch}, -1.75 \text{ inch})$, $\dot{Q}(t) = H(t) \text{ Btu/sec}$

Case 5-7: $(x', y') = (4 \text{ inch}, -1.75 \text{ inch})$, $\dot{Q}_1(t) = 0.5H(t) \text{ Btu/sec}$

$(x', y') = (4", 1.75")$, $\dot{Q}_2(t) = 0.5 H(t) \text{ Btu/sec}$

Temperatures and stresses at cross section $y=0$ resulting from this study are plotted as solid or dash lines in Figures 5-13 to 5-30. Corresponding solutions obtained from the finite element analyses using NASTRAN are also plotted as symbols in these figures for comparison. It is seen that temperature and thereby thermal stress solutions generated by the analytical approach discussed in this subsection agree well with finite element solutions.

To further investigate the accuracy of the analysis, the displacement method is considered here (Chan, et al, 1970). Equation 5-71 defines K_1 as a function crack opening displacement (v) and radial distance from the crack tip (r).

$$K_1 = \left(\frac{\pi}{8}\right)^{1/2} \cdot E \cdot \frac{v}{r^{1/2}} \quad (5-71)$$

In Figure 5-31, K_1 calculated using the above equation is plotted as data points (with dashed line). The 'true' value of K_1 corresponds to the limiting value ($r \rightarrow 0$) in Equation (5-71). According to Chan, et al (1970), this limiting value can be obtained by fitting the linear portion of the data with a straight line and extrapolating to r equal to 0.0. The linear fits are shown as solid lines in Figure 5-32. These limiting values are then compared with the THERMO-K prediction (solid line) in Figure 5-32. Chan, et al (1970) also concluded that K_1 determined using this method is lower than the actual value, and that a coarse mesh comparable to the mesh used in this study

would yield K_1 values which are in error by about 10%. To check this, the THERMO-K prediction decreased by 10% is also plotted as dashed line in Figure 5-32. Interestingly, this value of K_1 coincides with the finite element results.

5.8.3 Verification of Temperature and Stresses for Insulated Crack Surfaces

This subsection is to check the accuracy of the temperatures and thermal stresses predicted by using the analytical approach described in this section. The same single-edge crack plate with a width of 5 inches and thickness 0.5 inch is chosen as a reference problem. The edge crack is set to be 1.25 inches long and a single heat source of strength $\dot{Q}(t) = H(t)$ Btu/sec is applied at $(x', y') = (3.75 \text{ inch}, -1.25 \text{ inch})$. Material properties and heat transfer constants are the same as those given in Equation (5-70) except that $H_2 = 0.0004 \frac{\text{Btu}}{\text{in}^2 \cdot \text{sec} \cdot \text{F}}$ is used in this sample problem. Also, in this sample problem, the crack surfaces are assumed to be completely insulated, i.e., it is assumed that $\frac{\partial T}{\partial y} = 0$ at $y=0$, $0 \leq x \leq a$. As shown in Figure 5-33, the plate is modeled with another finite element program, FEM2D (1986). In this finite element model, there is a total of 594 nodes and 176 eight-node isoparametric elements. In the crack region of the finite element model, the crack surfaces are set to be insulated for heat transfer analysis but are set to have continuous displacements in the subsequent thermal stress analysis, i.e., the adjacent nodes on both sides of the crack are treated as independent points in the heat transfer analysis but are constrained together in the thermal stress analysis so that they will have the same displacements but different temperatures. Resulting temperature and stress distributions at cross section $y=0$ are illustrated in Figures 5-34 to 5-37. Again, good agreement between finite element solutions and solutions calculated by the analytical approach discussed in this section.

5.9 References

- Abramowitz, M., and Stegun, I., (1965), Handbook of Mathematical Functions, Dover, New York, New York.
- Aliabadi, M. H., Rooke, D. P., and Cartwright, D. J., (1987), "Mixed-Mode Bueckner Weight Functions Using Boundary Element Analysis," Internal Journal of Fracture, Vol. 34, pp. 131-147.
- Boley, B. A., and Weiner, J. H., (1960), Theory of Thermal Stresses, Wiley & Sons, New York, New York.
- Bueckner, H. F., (1973), "Field Singularities and Related Integral Representations," in Methods of Analysis and Solutions of Crack Problems, Vol 1, ed. G. C. Sih, pp. 239-314, Noordhoff, Holland.
- Carslaw, H. S., and Jaeger, J. C., (1959), Conduction of Heat in Solids, 2nd edition, Oxford University Press, London.
- FEM2D - A Two Dimensional Finite Element Computer Program for Two-Dimensional Heat Transfer/Thermal Stress Analysis, Users Manual, (1986), Structural Integrity Associates, San Jose, CA.
- Hartranft, R. J., and Sih, G. C., (1973), "Alternating Method Applied to Edge and Surface Crack Problems," in Methods of Analysis and Solutions of Crack Problems, Vol 1, ed. G. C. Sih, pp. 179-238, Noordhoff, Holland.
- NASTRAN User Manuals, (1972), MSC Co..
- pc-CRACK - Fracture Mechanics Software for Personal Computers, Users Manual, Version 1.1, Revision 1, (1986), Structural Integrity Associates, San Jose, CA.
- Parkus, H., (1968), Thermoelasticity, Blaisdell Publishing Co..
- Tada, H., Paris, P., and Irwin, G., (1973), The Stress Analysis of Cracks Handbook, Del Research Co., Pennsylvania.
- Timoshenko, S. P., and Goodier, J. N., (1970), Theory of Elasticity, 3rd edition, McGraw Hill, New York, New York.

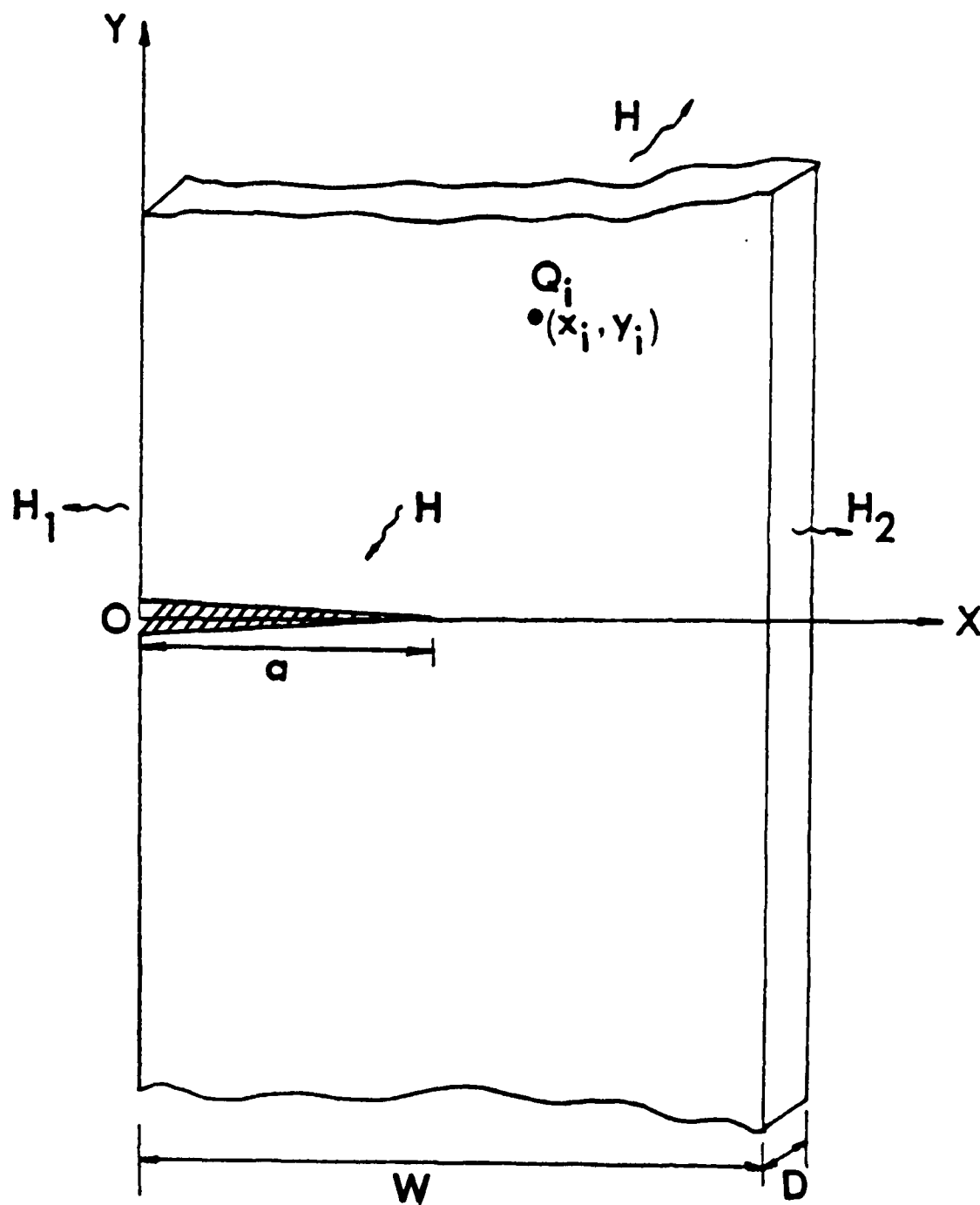


Figure 5-1. A Single-edge-crack Plate Strip Subjected to Point Heat Sources

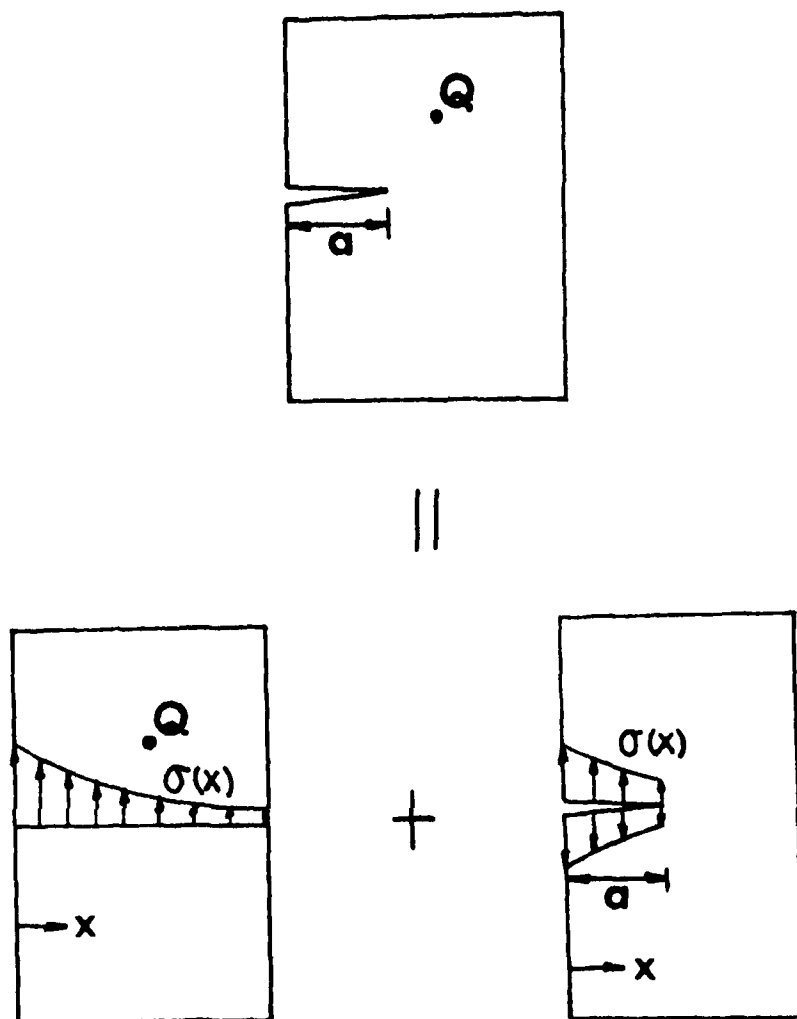
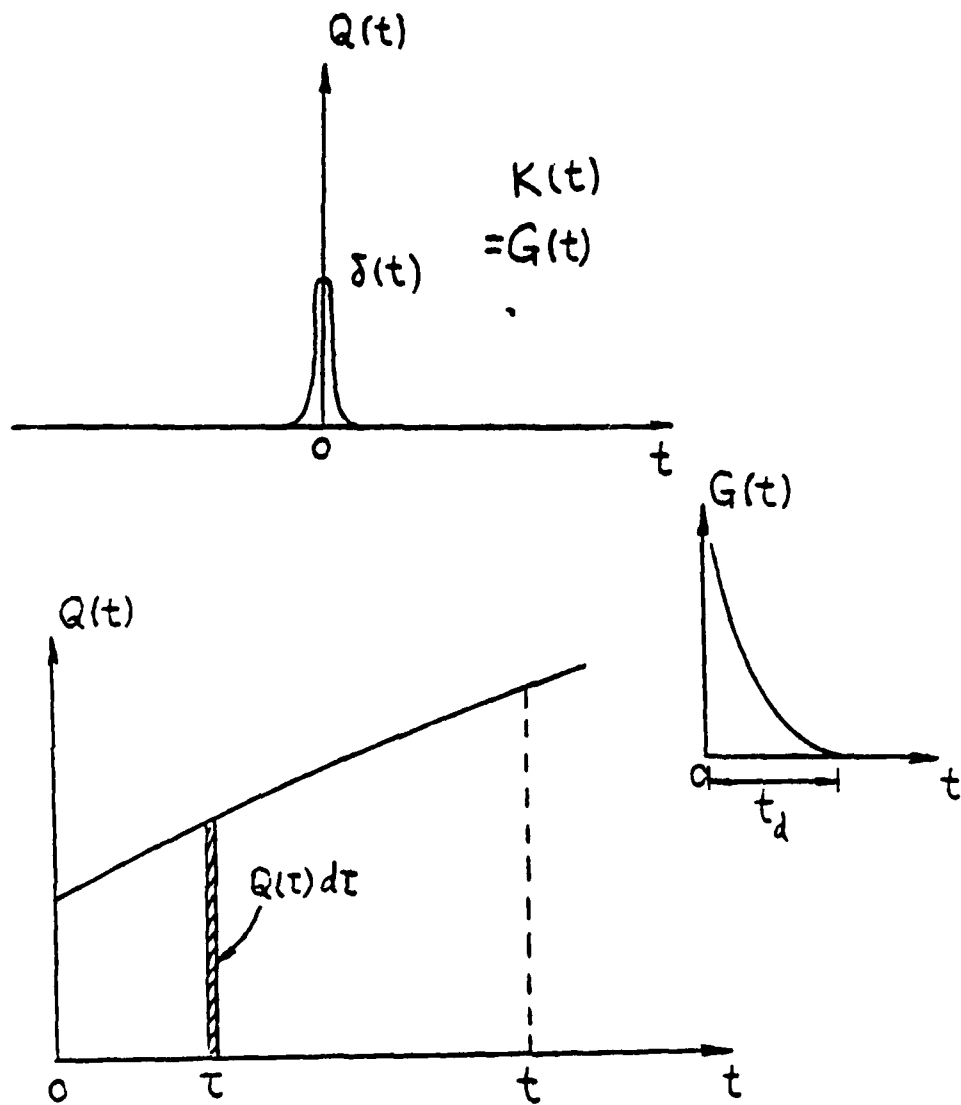


Figure 5-2. Concept of Influence Function



$$K(t) = \int_0^t Q(\tau) G(t-\tau) d\tau$$

$$= \int_{t-t_d}^t Q(\tau) G(t-\tau) d\tau$$

Figure 5-3. Concept of Green's Function

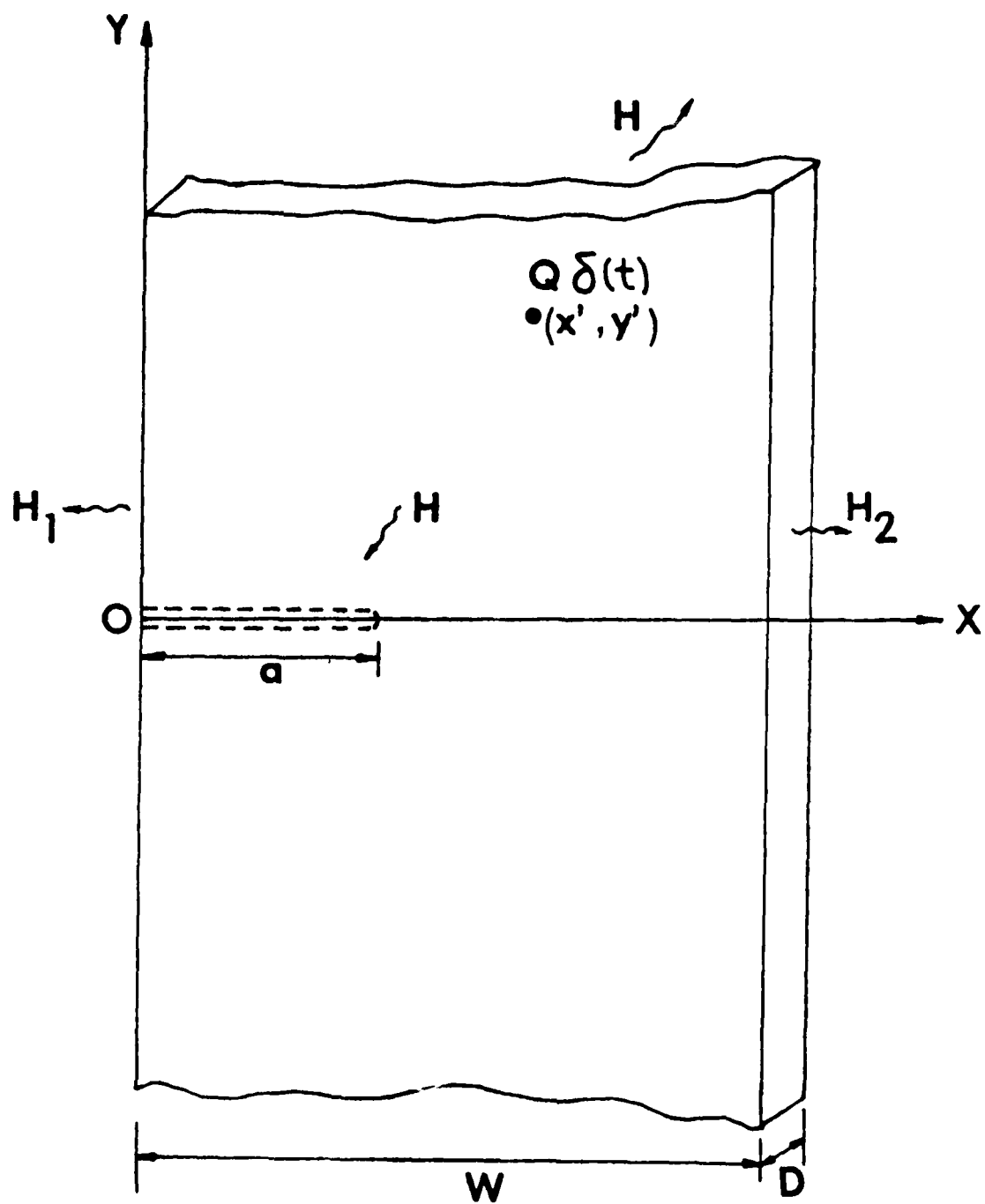


Figure 5-4. A Point Heat Source in an Uncracked Plate

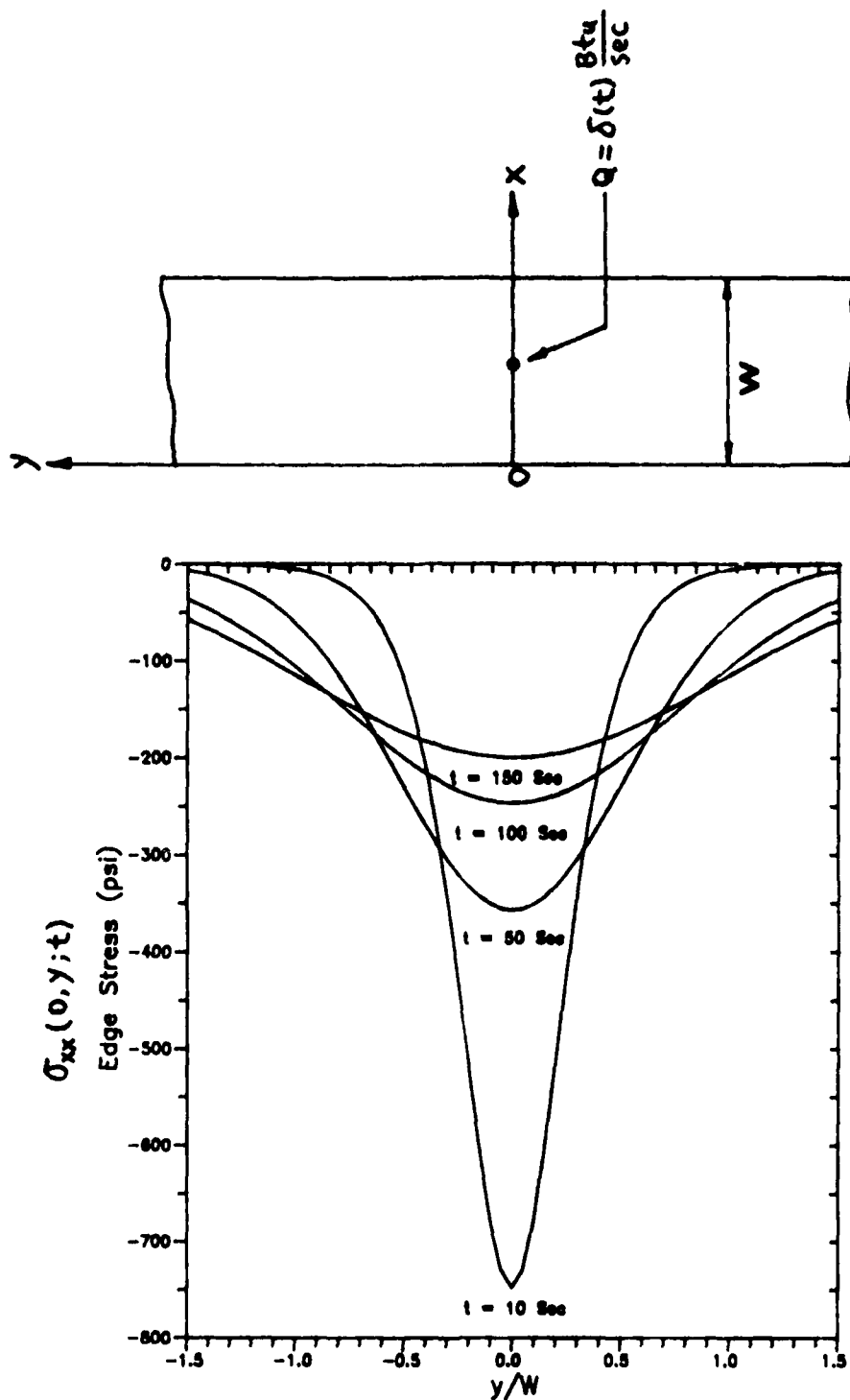


Figure 5-5. Edge Stress $\sigma_{xx}(0, y; t)$ Due to an Instantaneous Heat Source

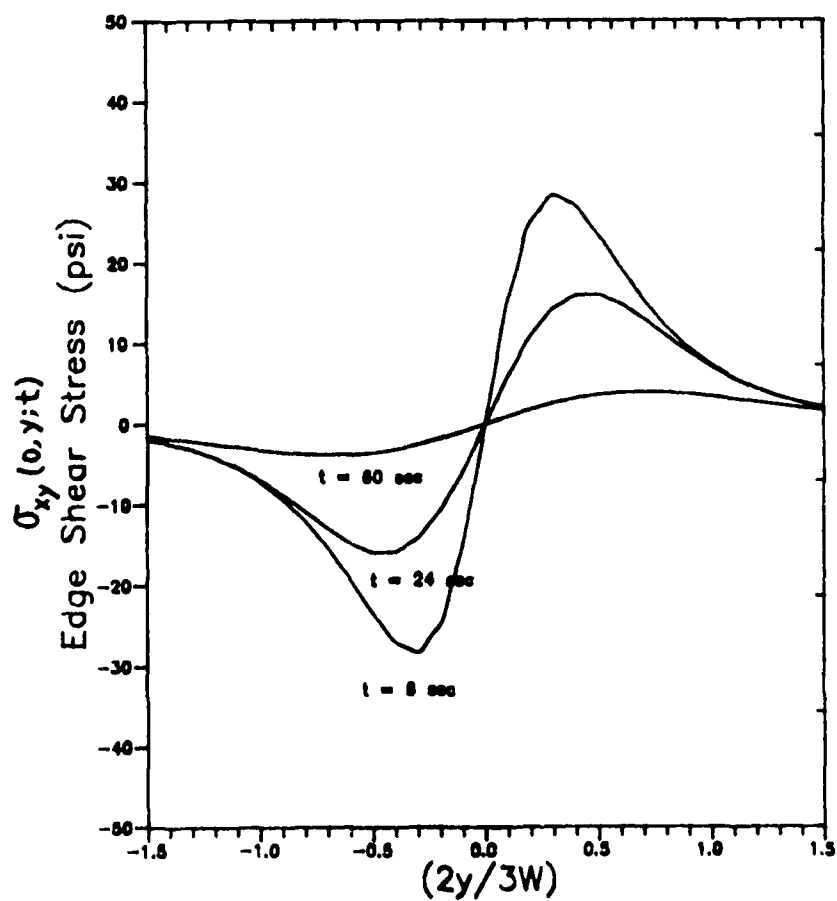
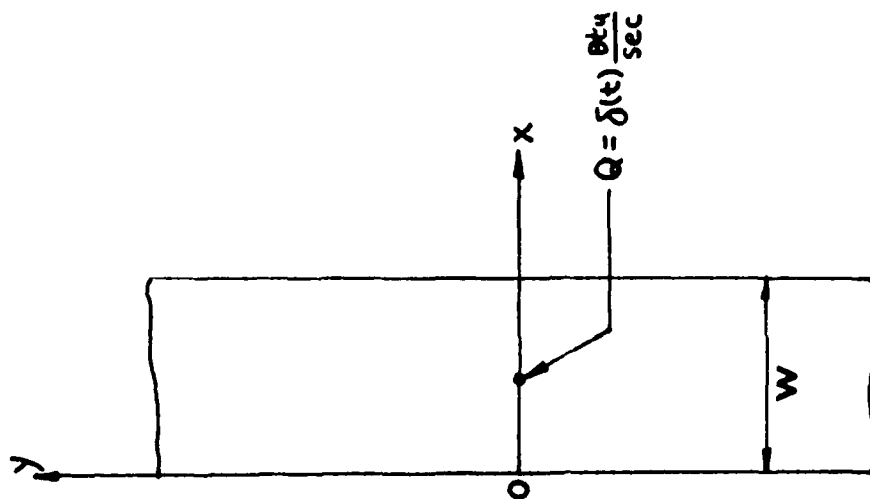


Figure 5-6. Edge Stress $\sigma_{xy}(0, y; t)$ Due to an Instantaneous Heat Source

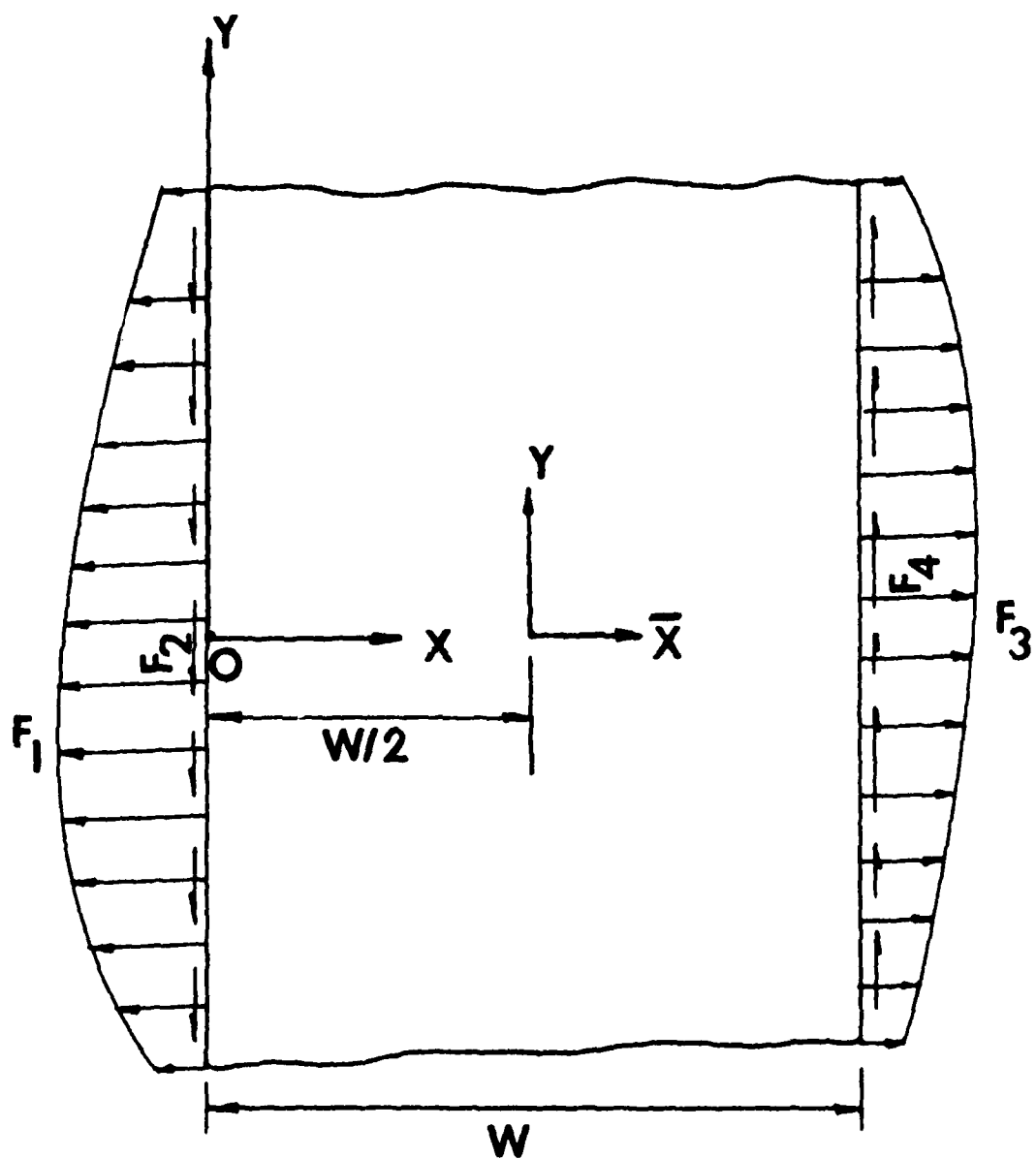


Figure 5-7. A Plate Strip Subjected to Arbitrary Edge Loads

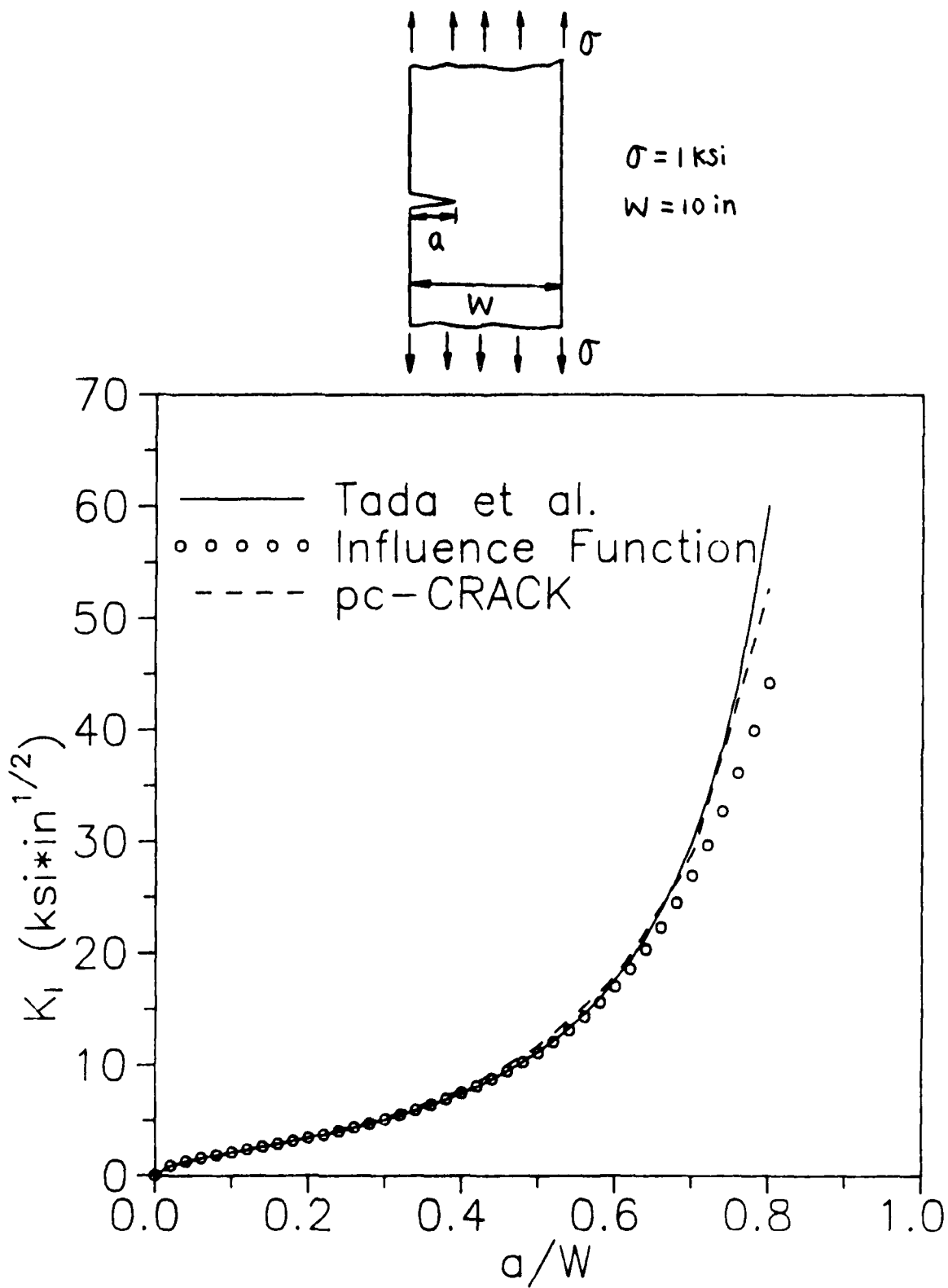


Figure 5-8. A Single-edge-crack Plate Under Uniform Tension

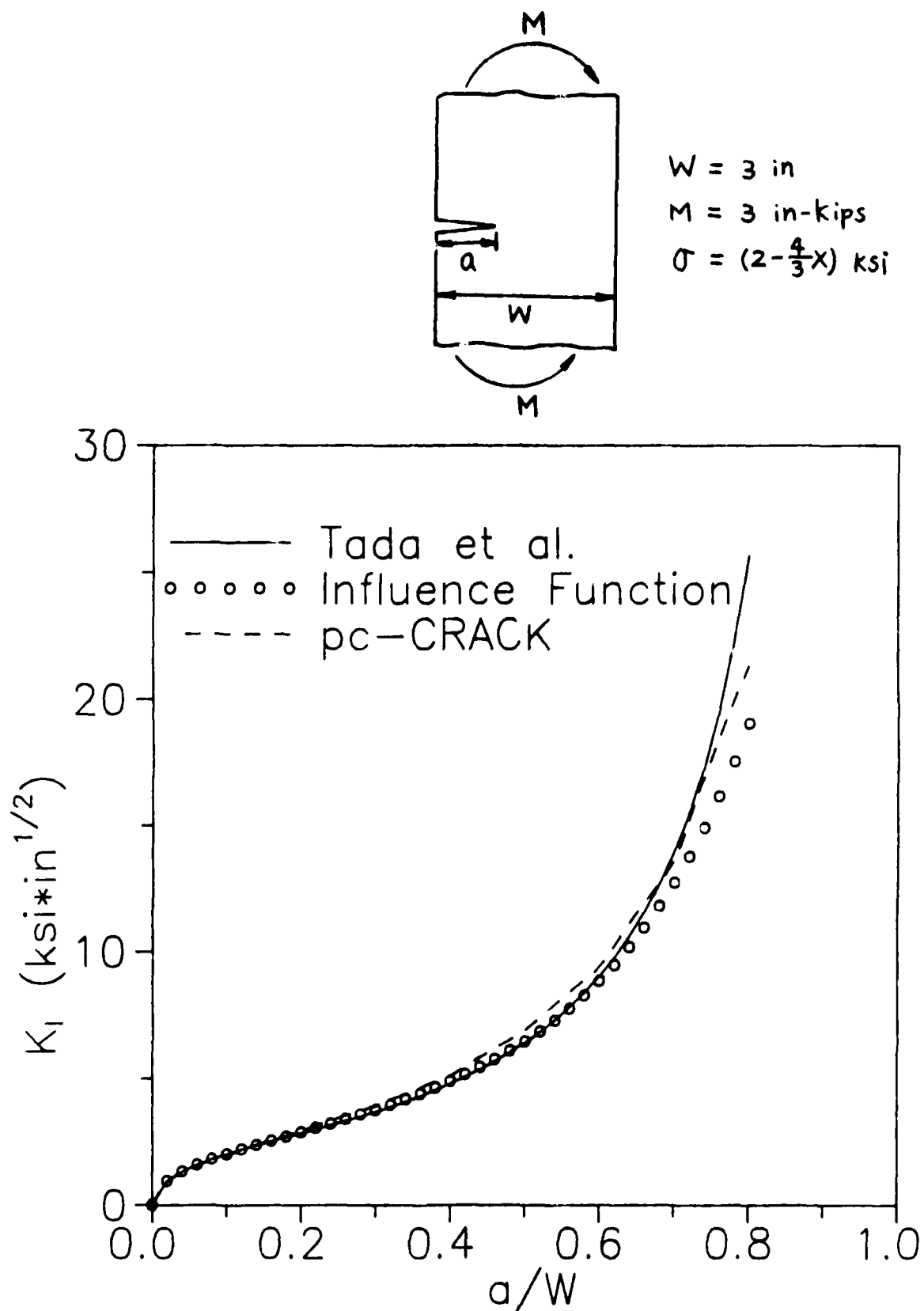


Figure 5-9. A Single-edge-crack Plate Under Remote Bending

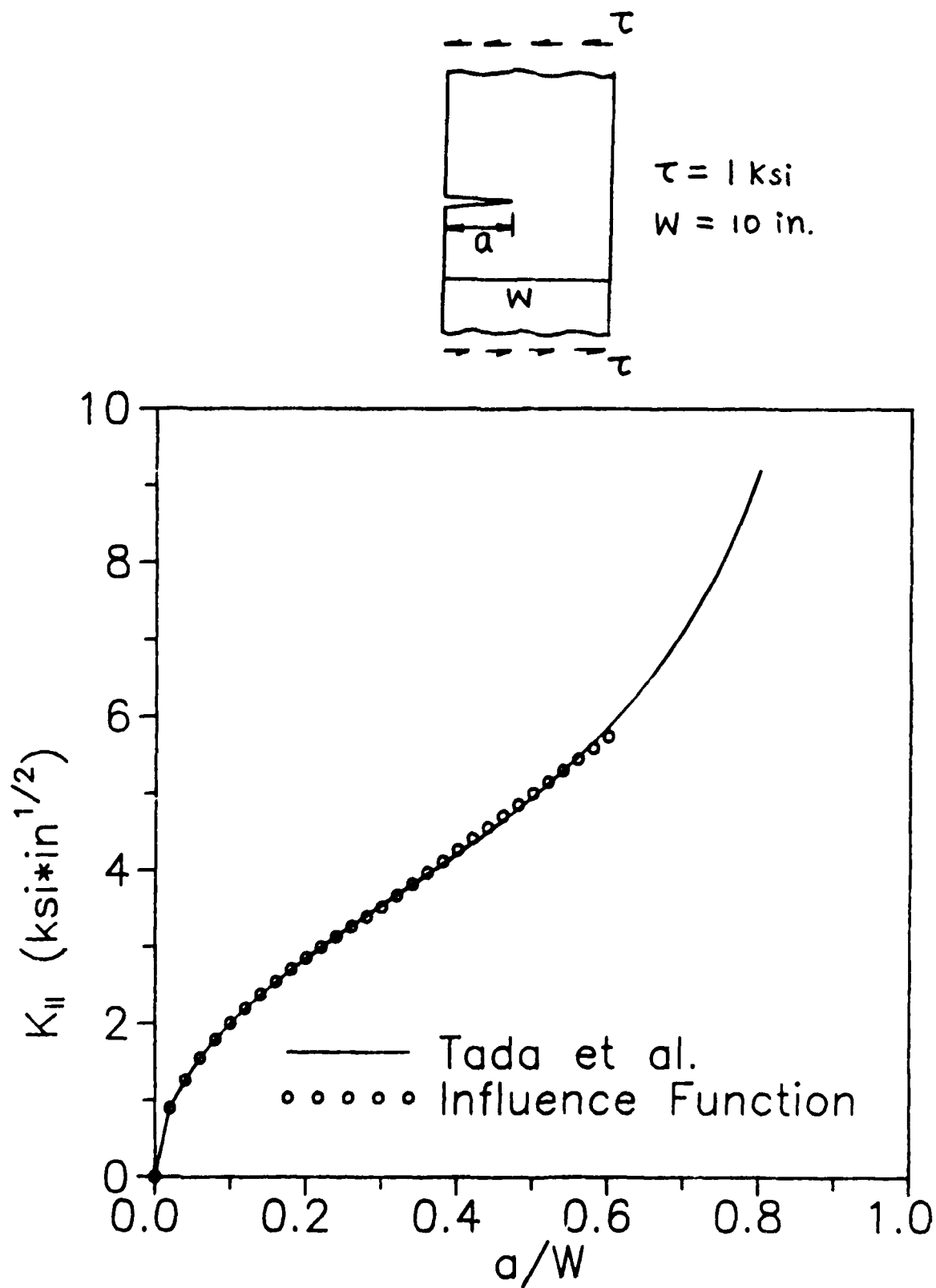


Figure 5-10. A Single-edge Plate Under Uniform Shear

Nastran Mesh for Heat Transfer and Mechanical Analysis

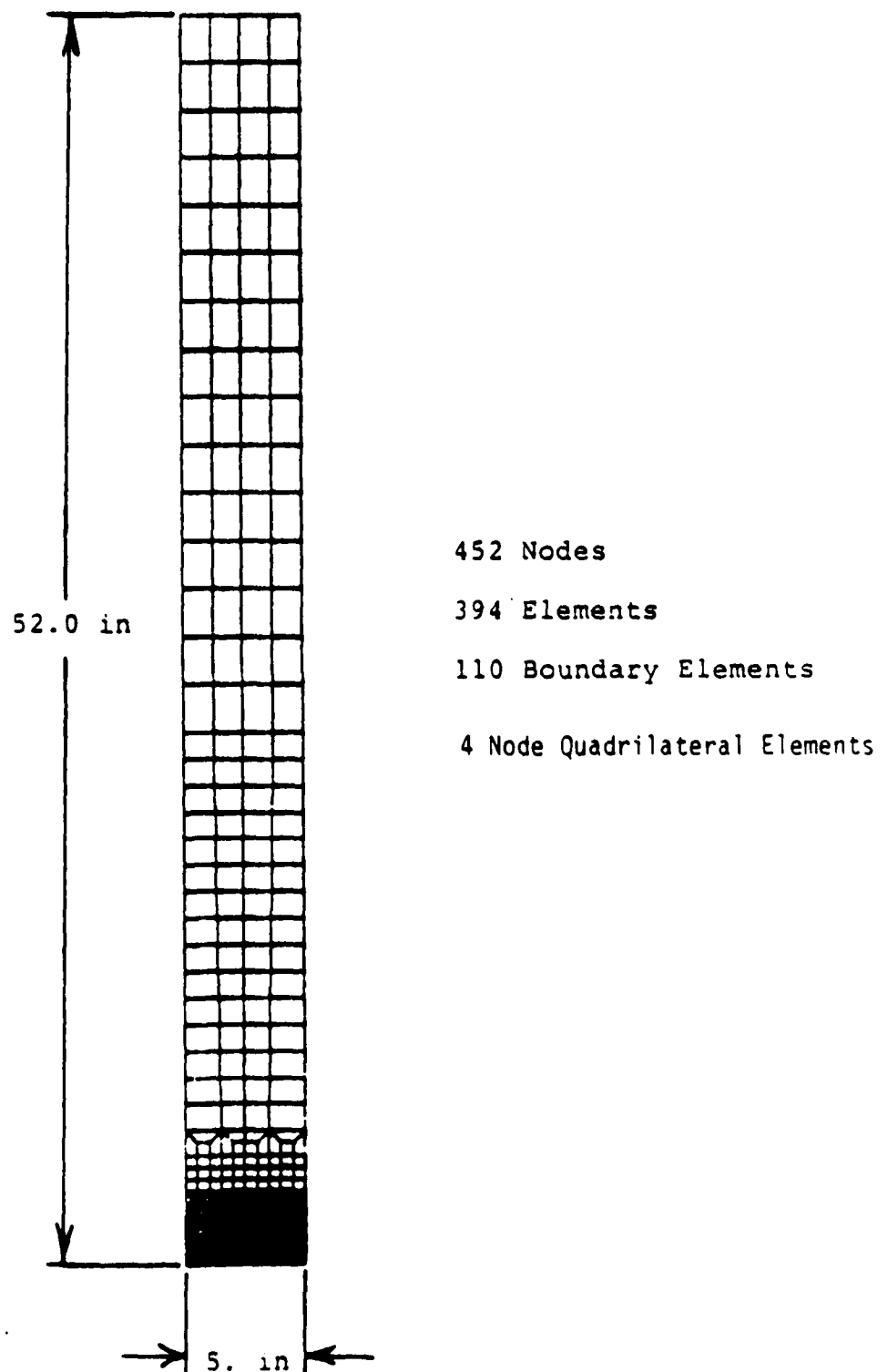


Figure 5-11. NASTRAN Mesh for Heat Transfer and Thermal Stress Analyses for a Fully Heat Conductive Single-edge Crack

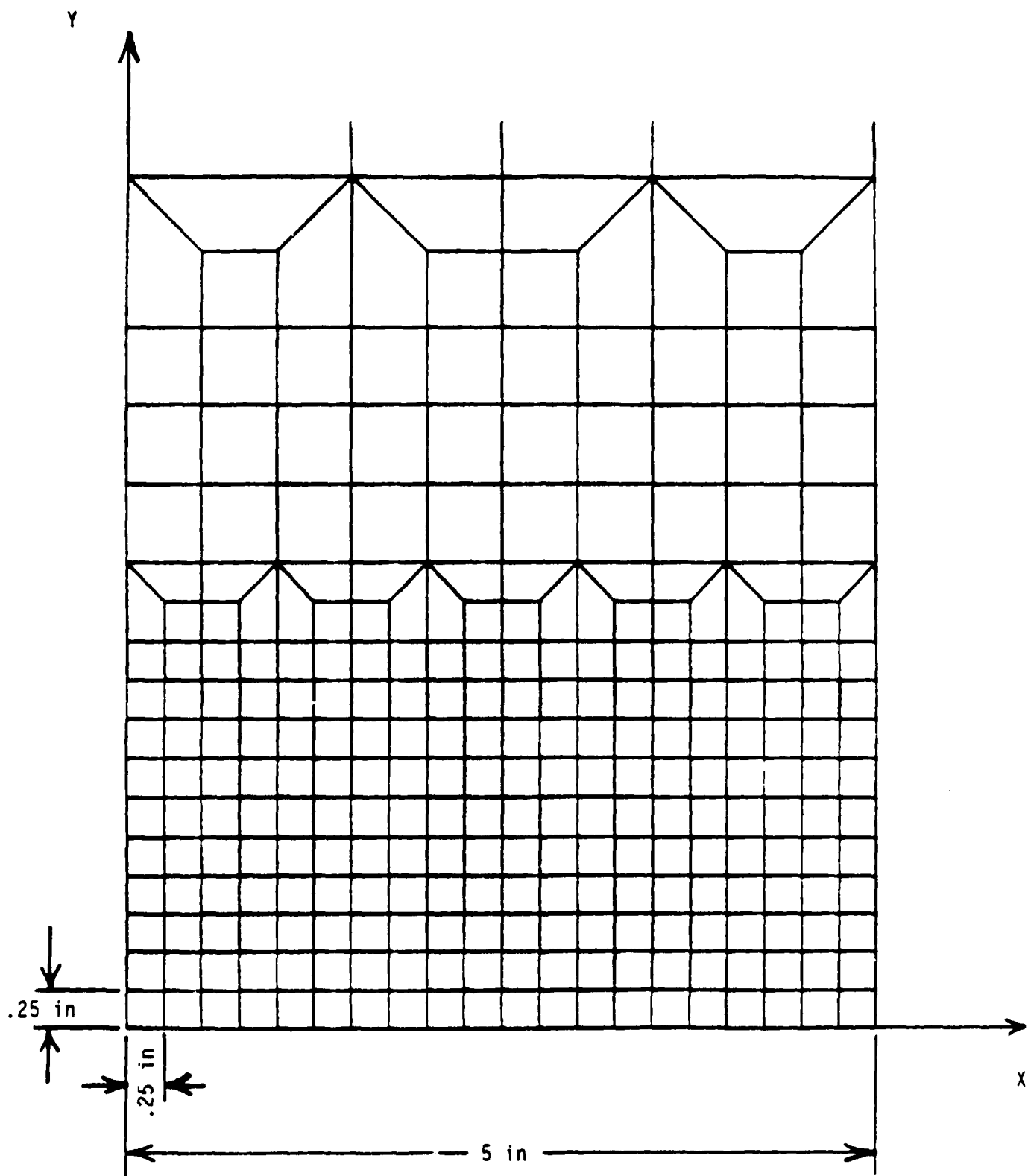


Figure 5-12. NASTRAN Mesh Near Heat Source

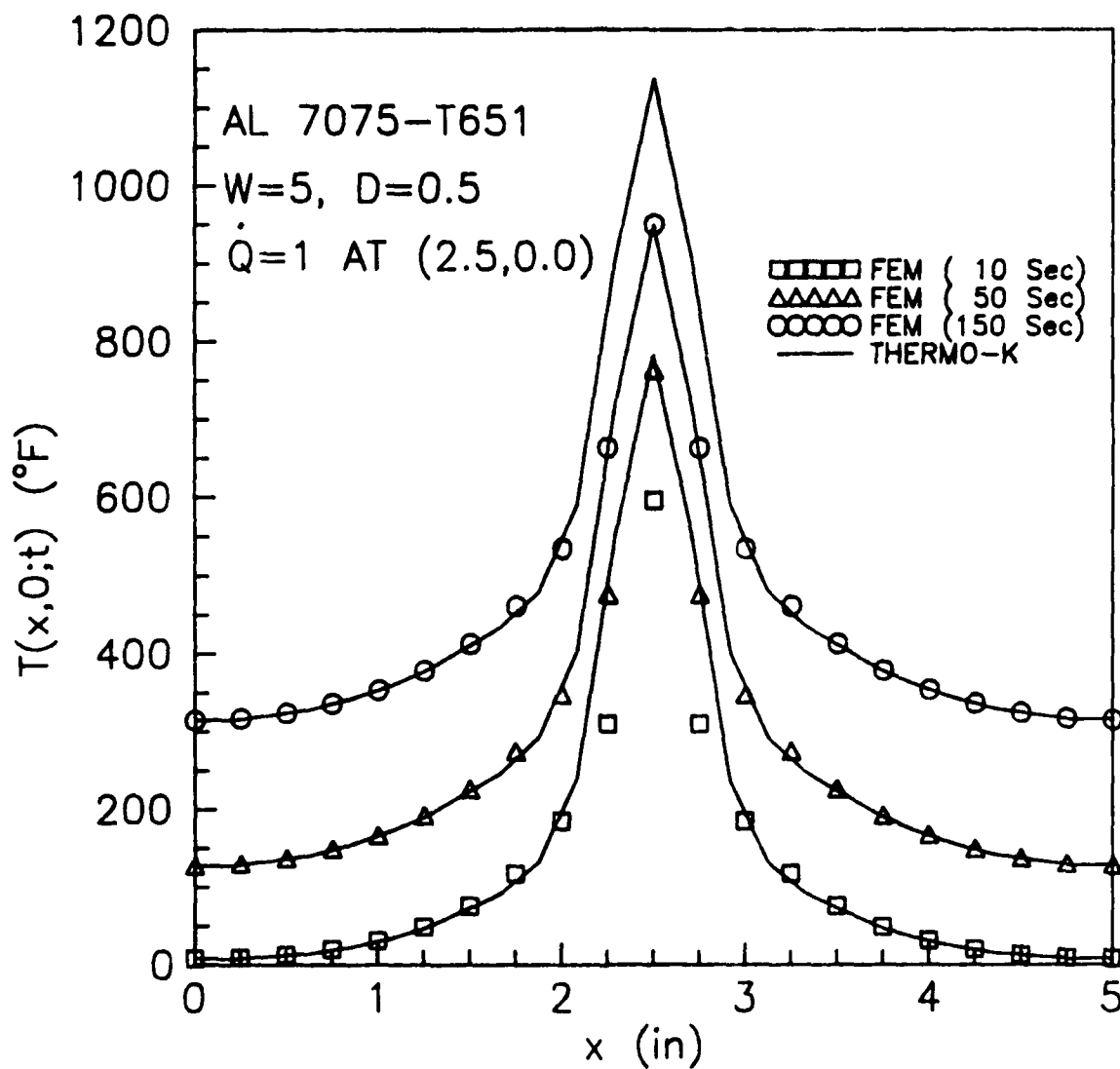


Figure 5-13. Comparison of Temperatures at $y = 0$ for Case 5-1

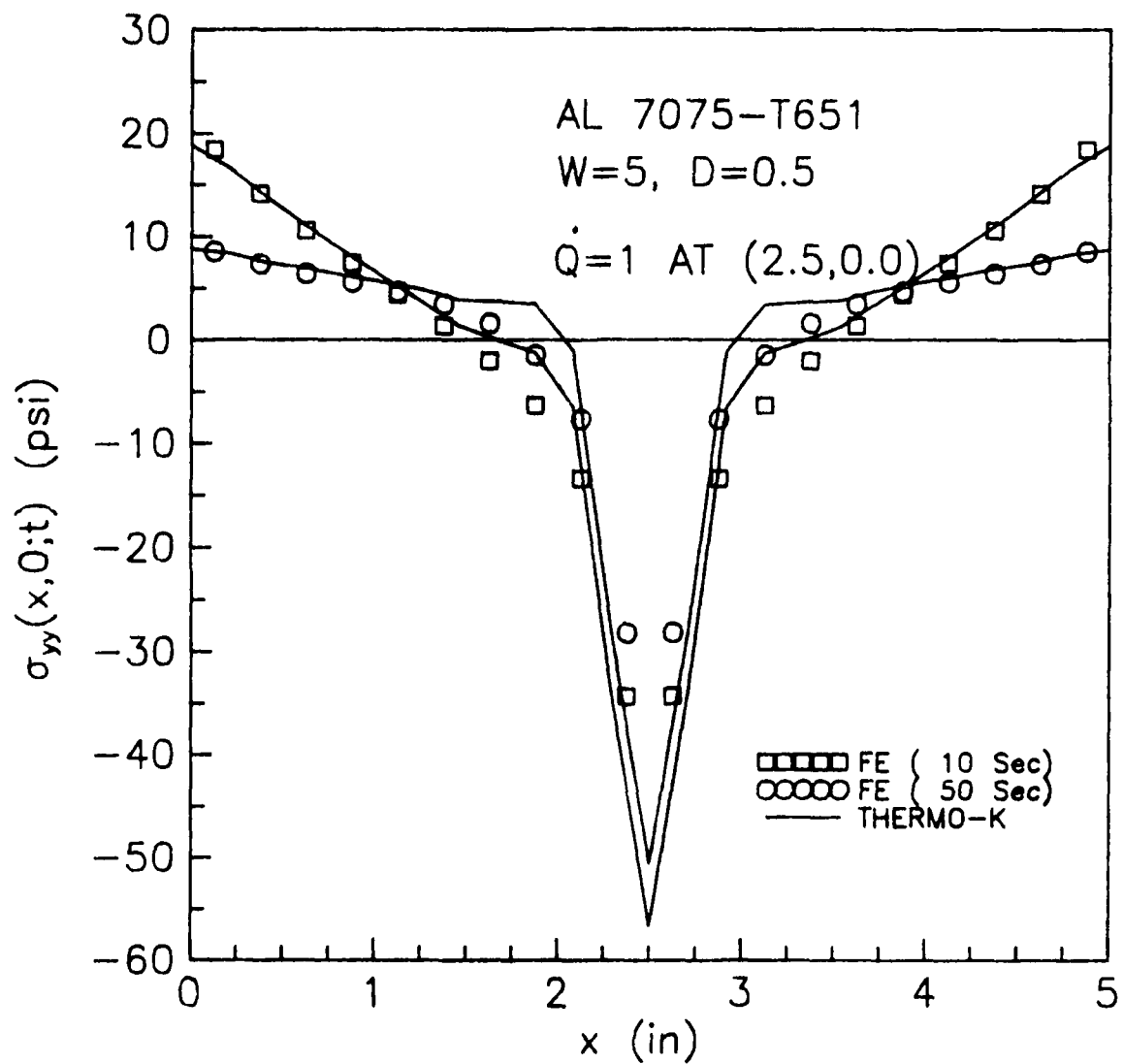


Figure 5-14. Comparison of Normal Stresses at $y = 0$ for Case 5-1

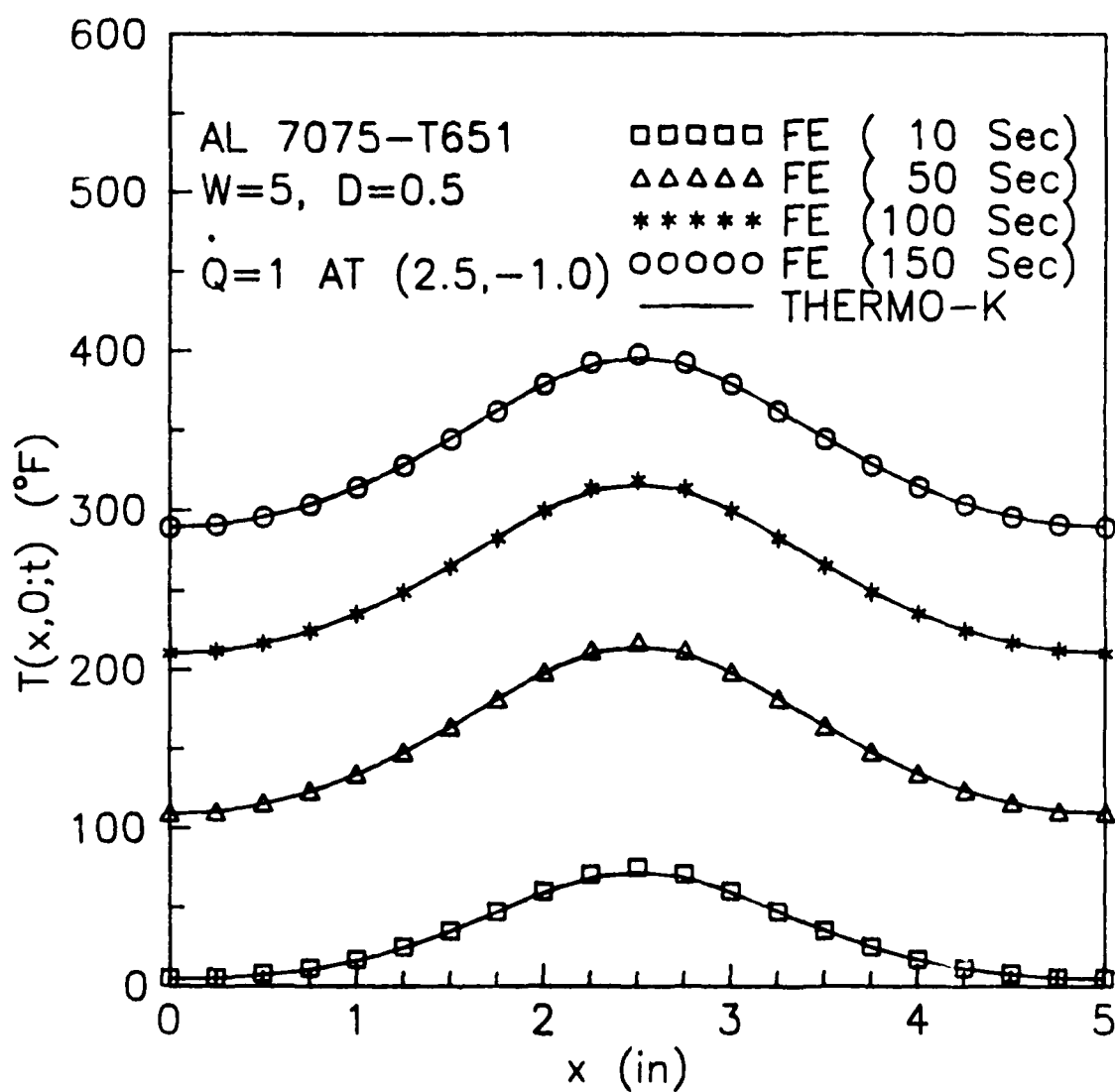


Figure 5-15. Comparison of Temperatures at $y = 0$ for Case 5-2

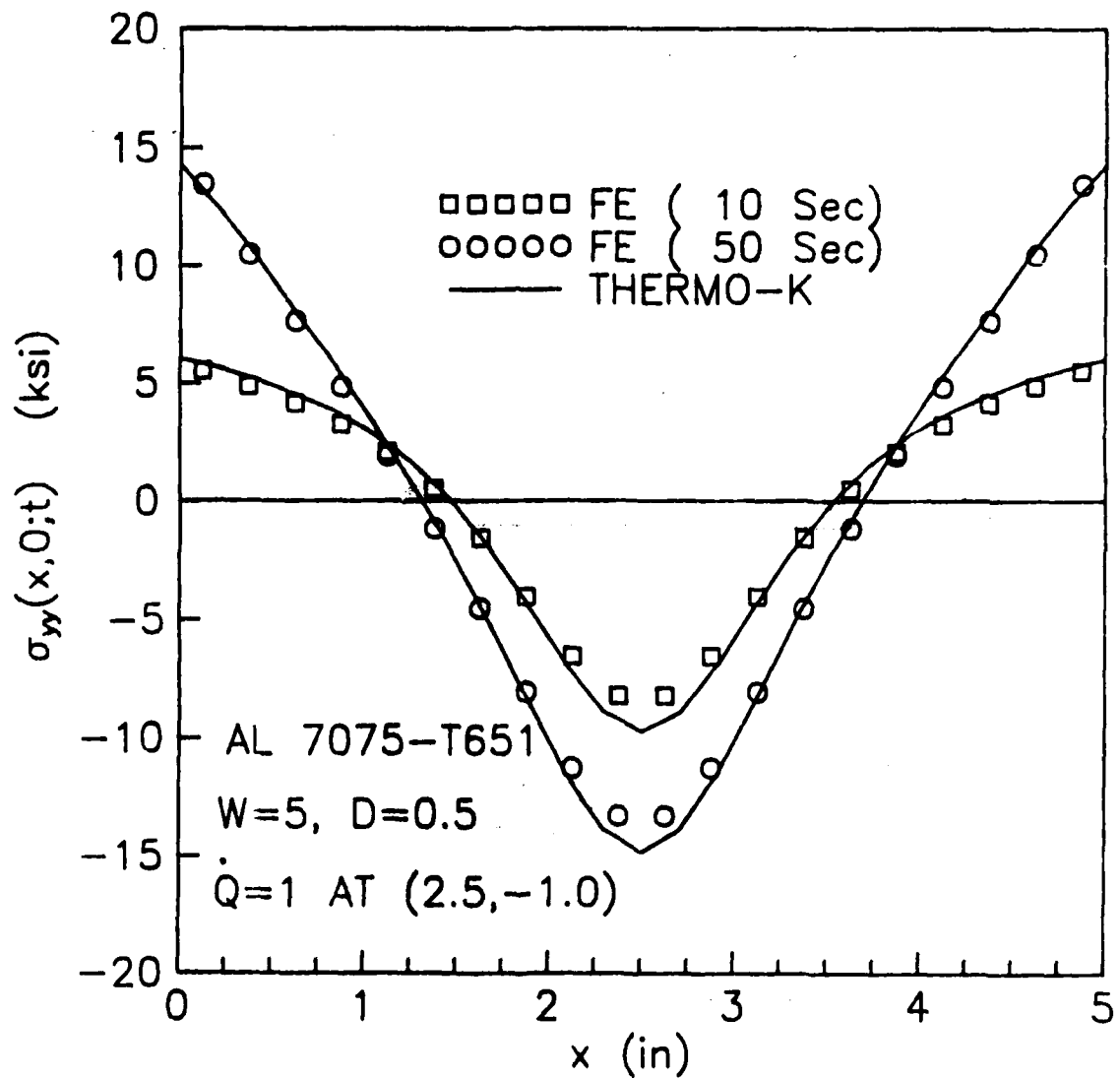


Figure 5-16. Comparison of Normal Stresses at $y = 0$ for Case 5-2

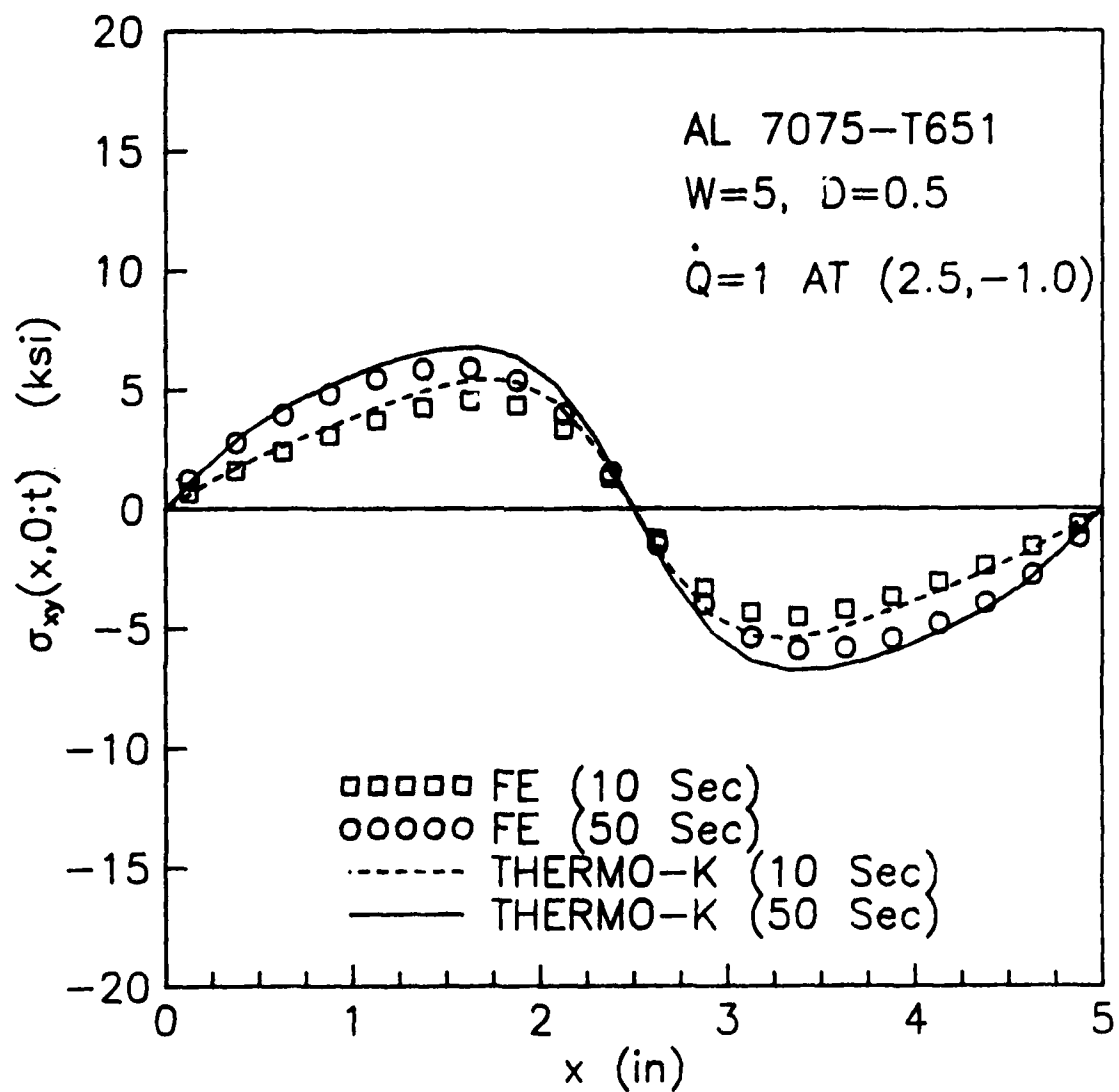


Figure 5-17. Comparison of Shear Stresses at $y = 0$ for Case 5-2

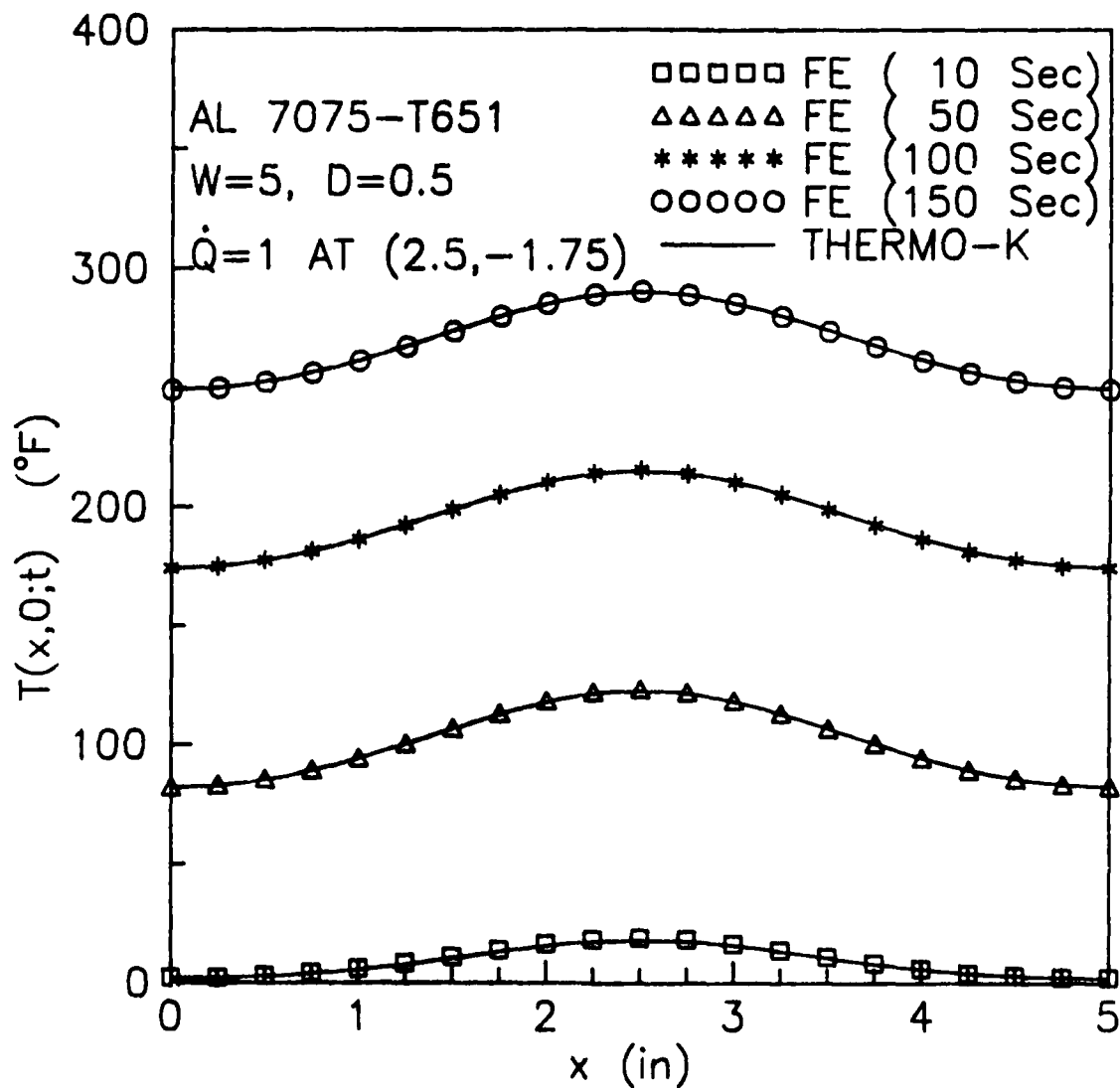


Figure 5-18. Comparison of Temperatures at $y = 0$ for Case 5-3

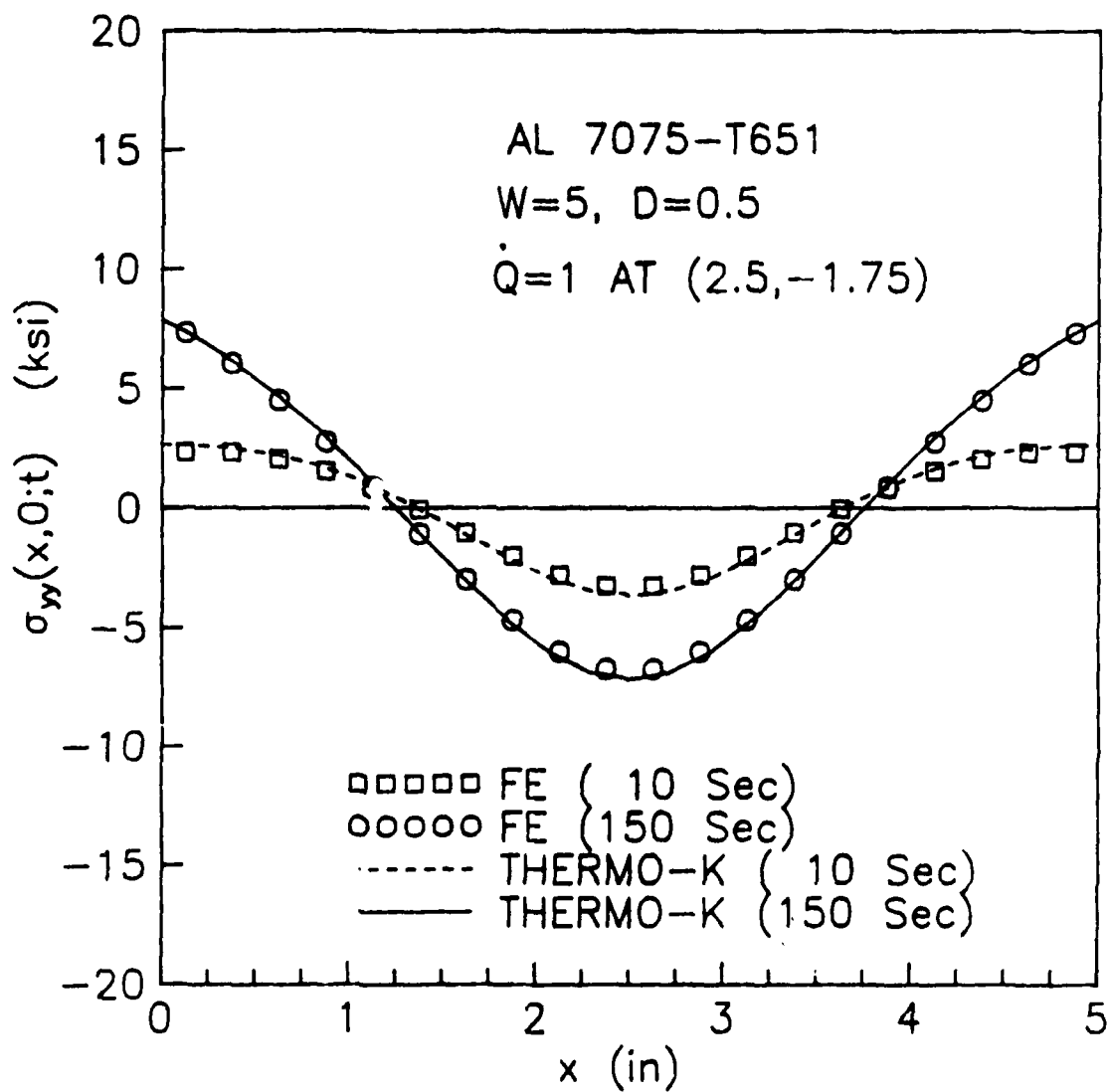


Figure 5-19. Comparison of Normal Stresses at $y = 0$ for Case 5-3

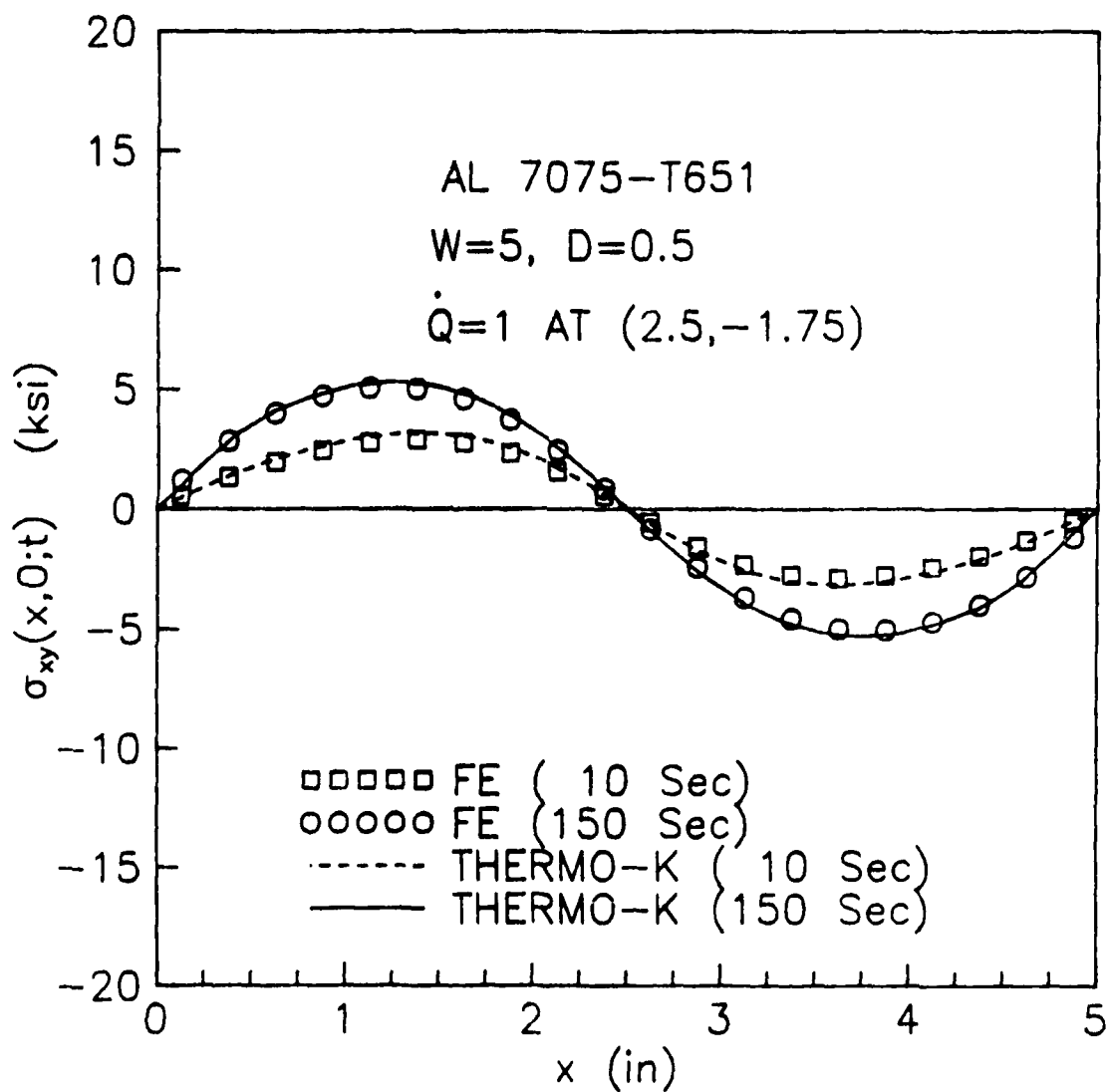


Figure 5-20. Comparison of Shear Stresses at $y = 0$ for Case 5-3

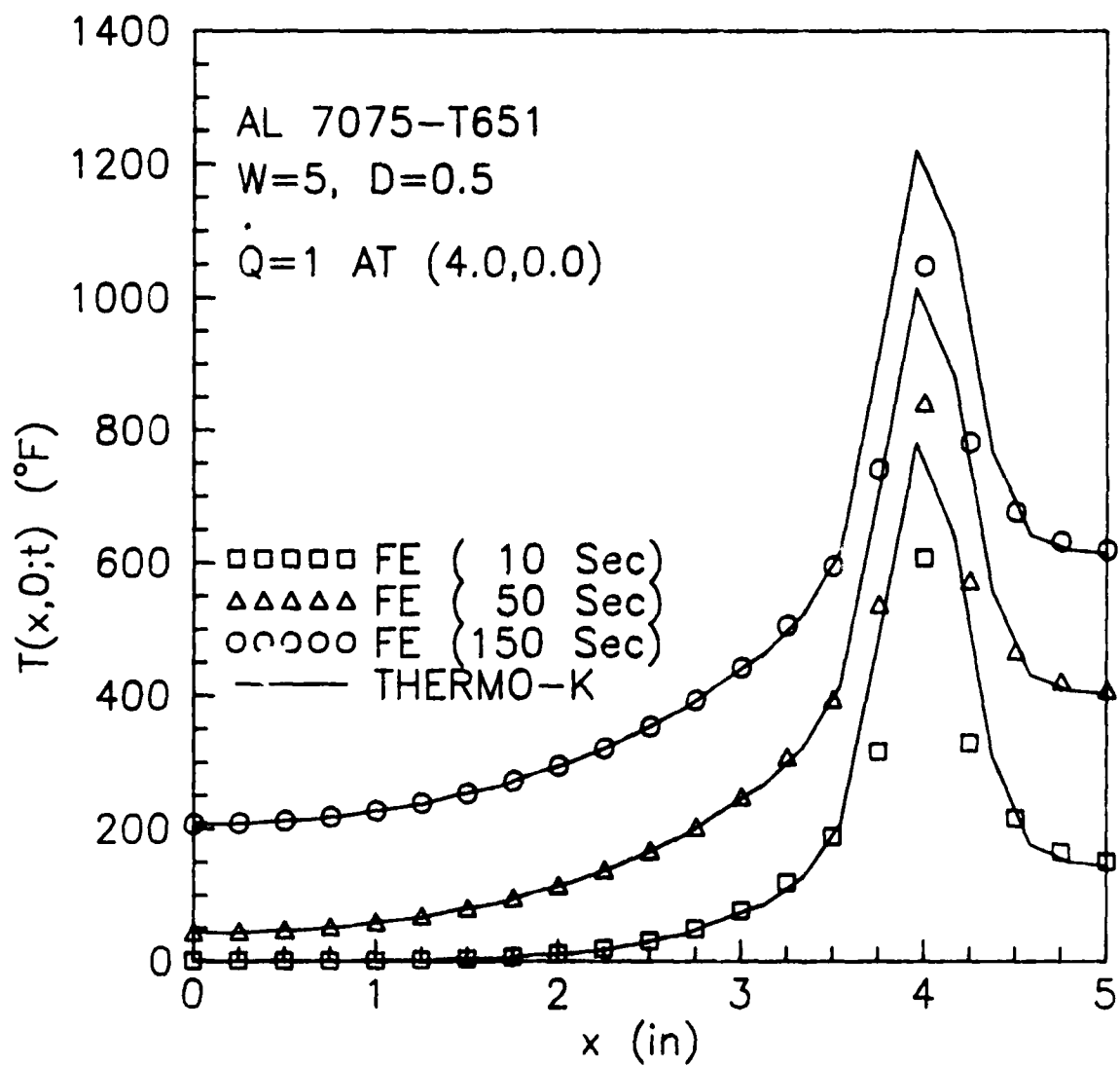


Figure 5-21. Comparison of Temperatures at $y = 0$ for Case 5-4

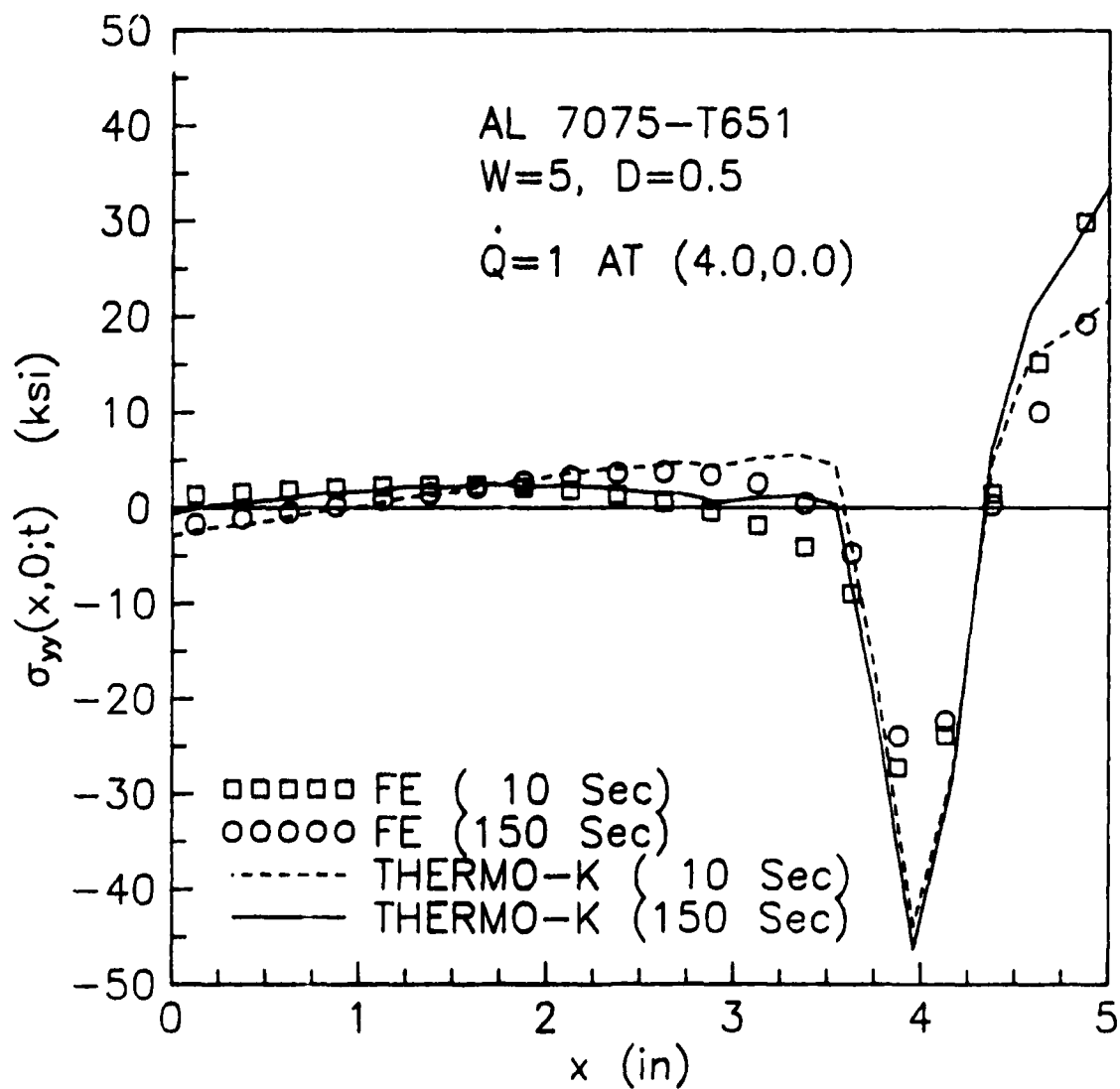


Figure 5-22. Comparison of Normal Stresses at $y = 0$ for Case 5-4

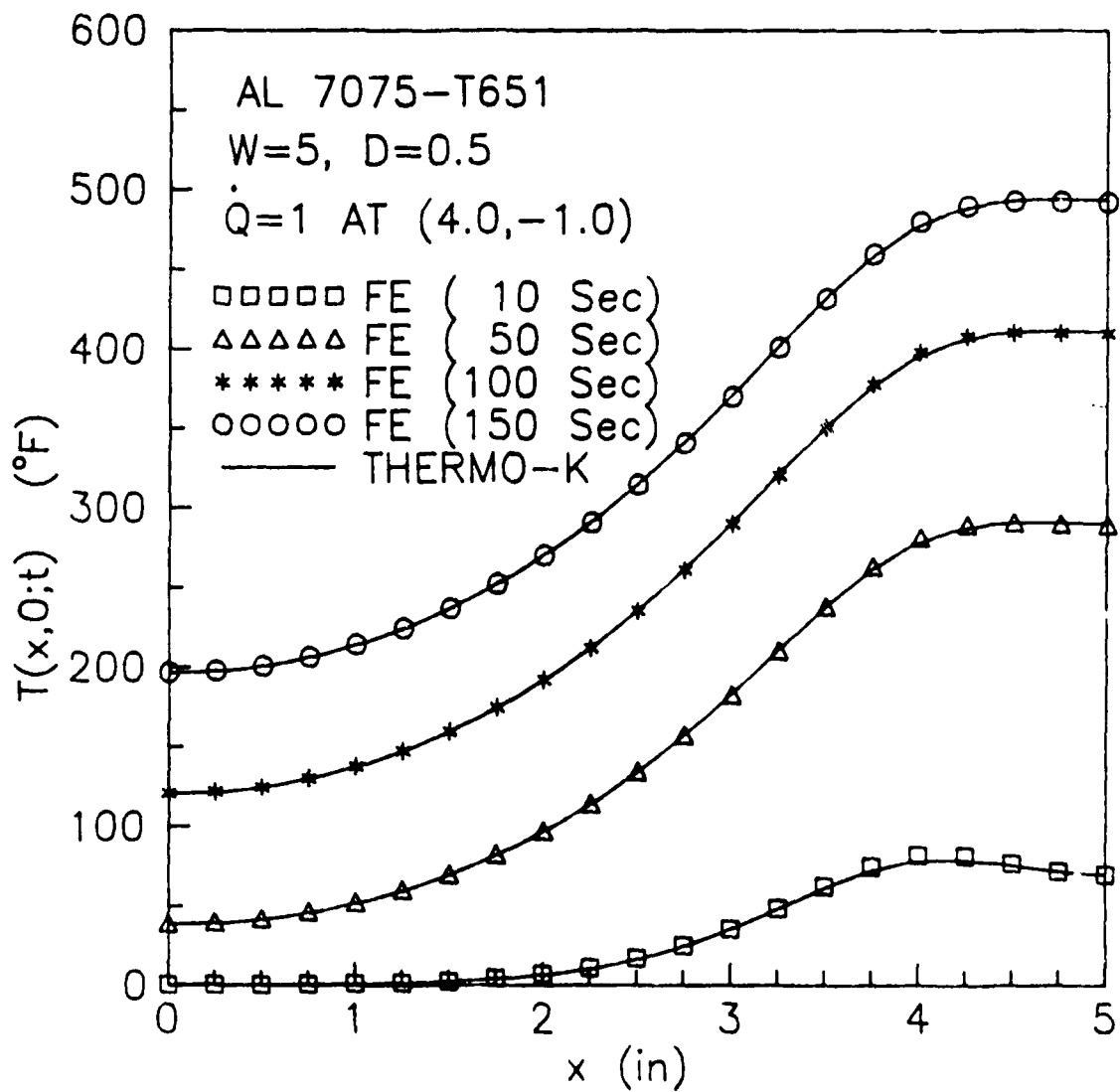


Figure 5-23. Comparison of Temperatures at $y = 0$ for Case 5-5

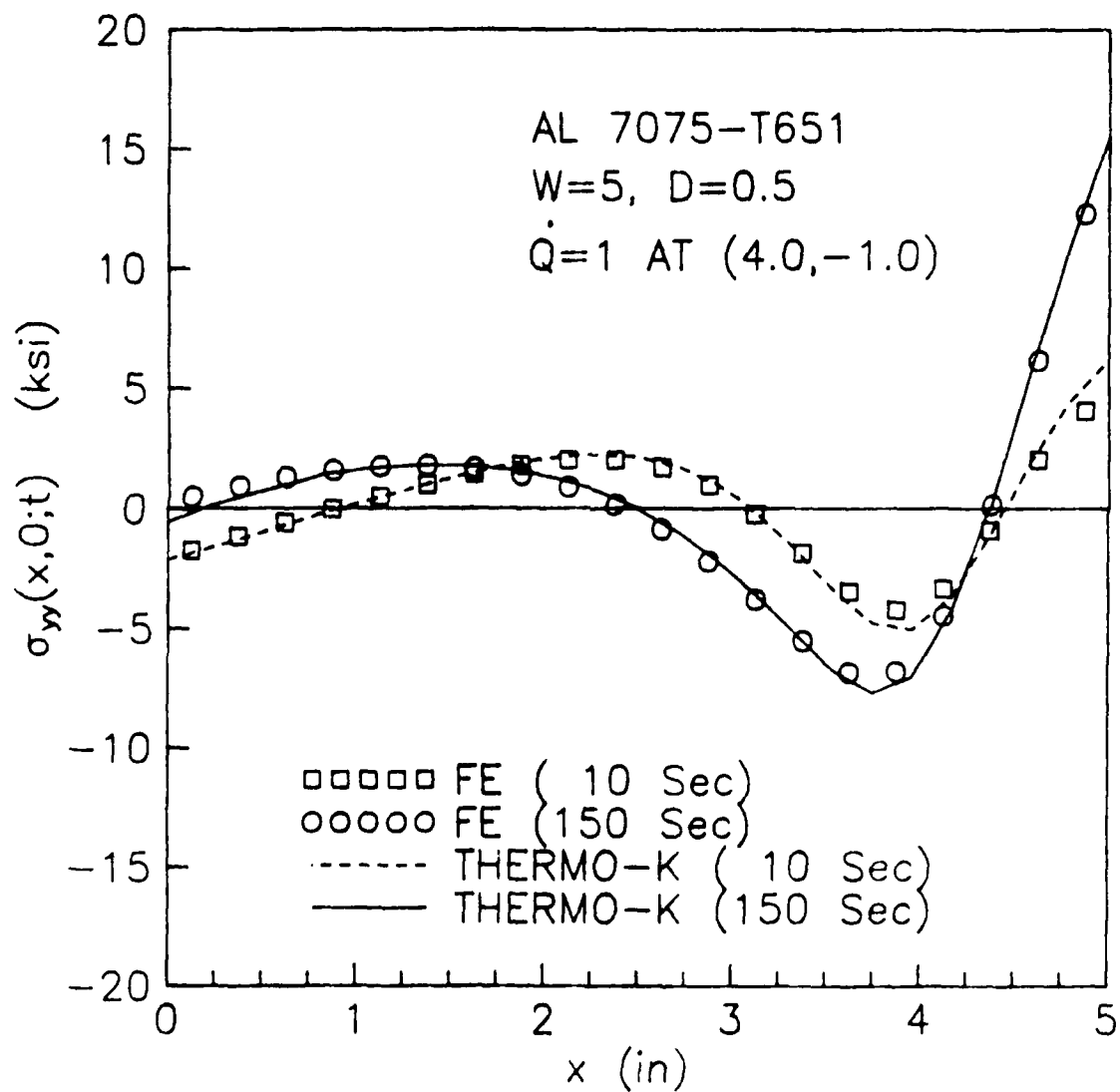


Figure 5-24. Comparison of Normal Stresses at $y = 0$ for Case 5-5

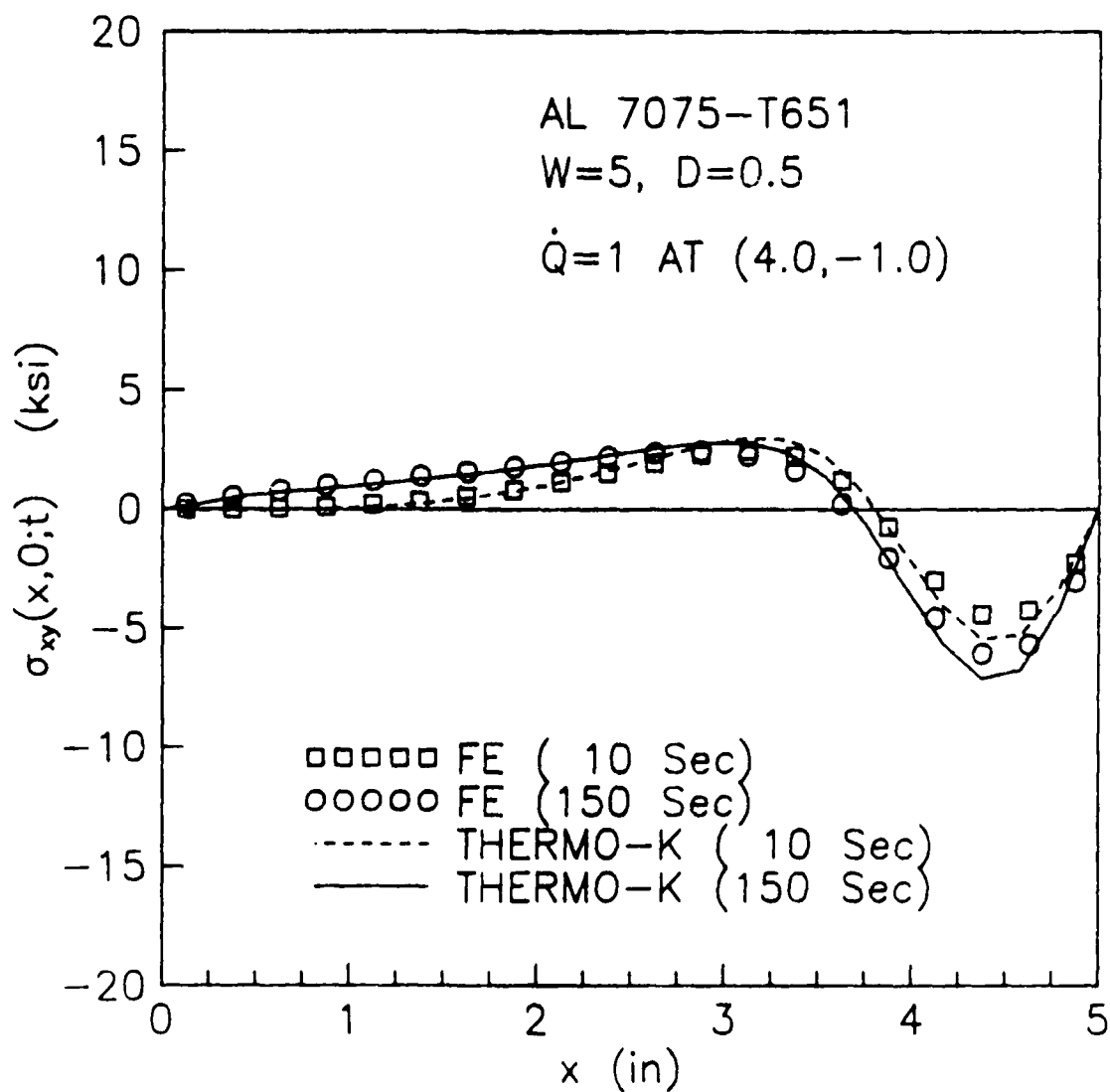


Figure 5-25. Comparison of Shear Stresses at $y = 0$ for Case 5-5

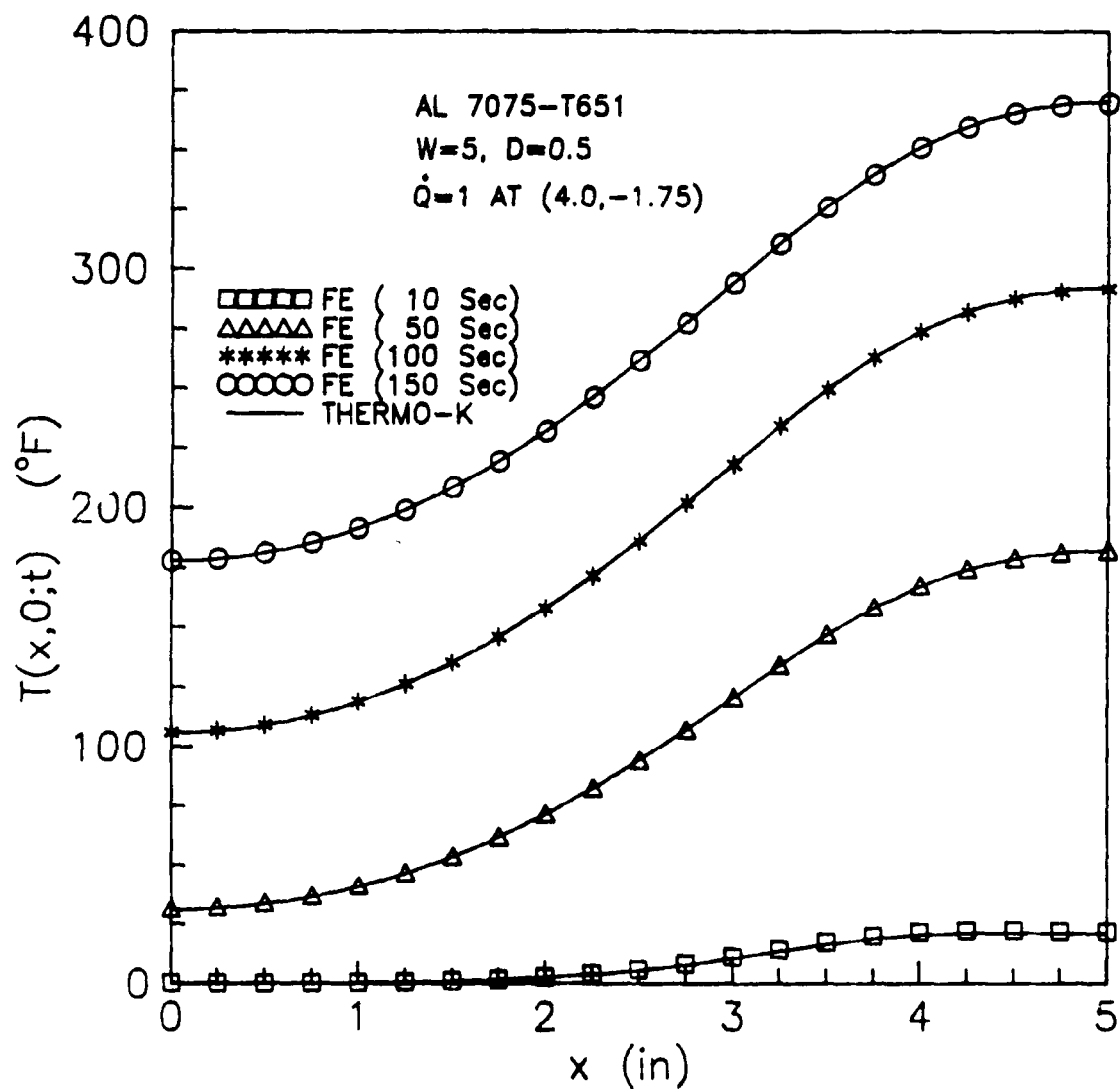


Figure 5-26. Comparison of Temperatures at $y = 0$ for Case 5-6

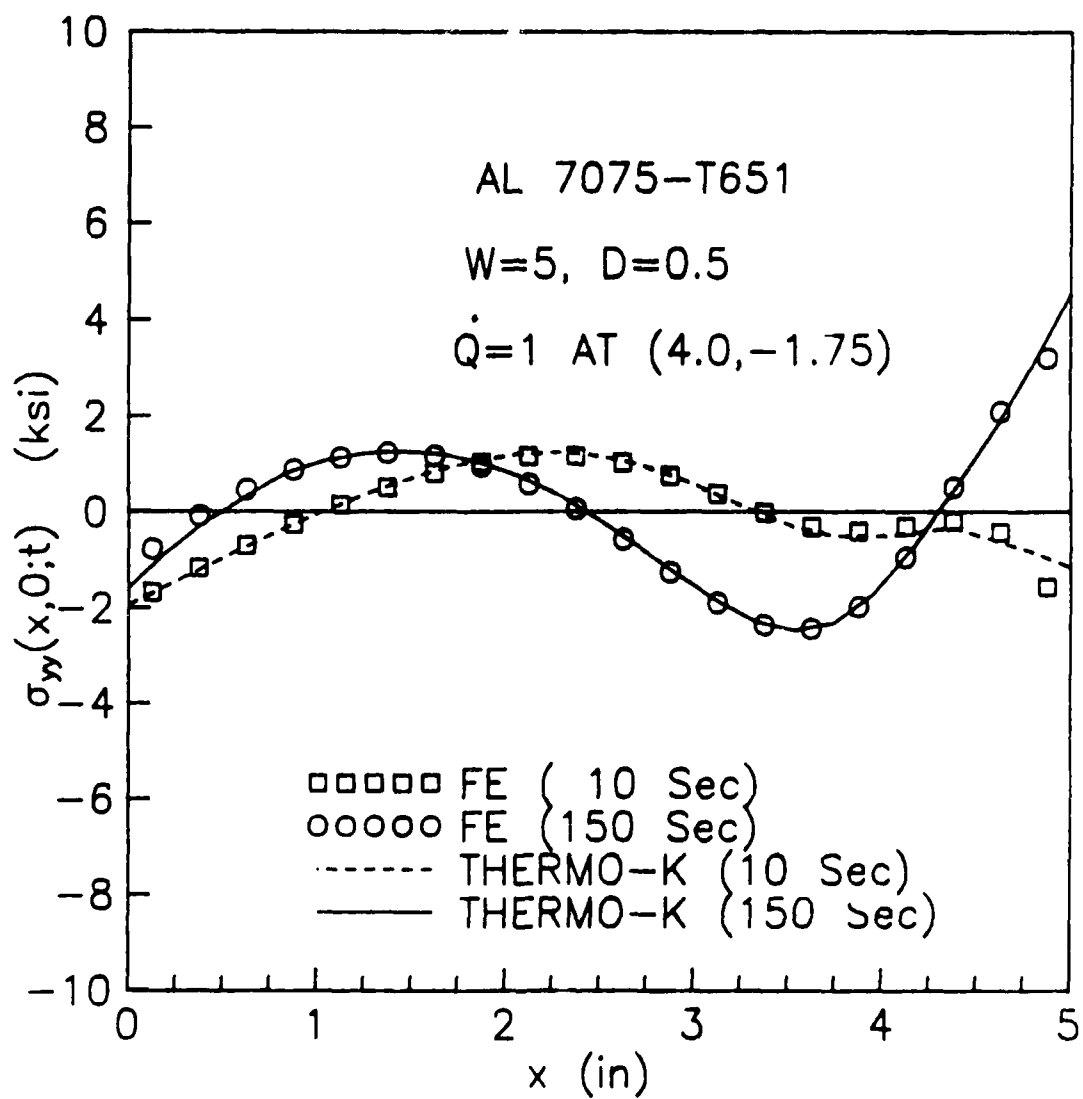


Figure 5-27. Comparison of Normal Stresses at $y = 0$ for Case 5-6

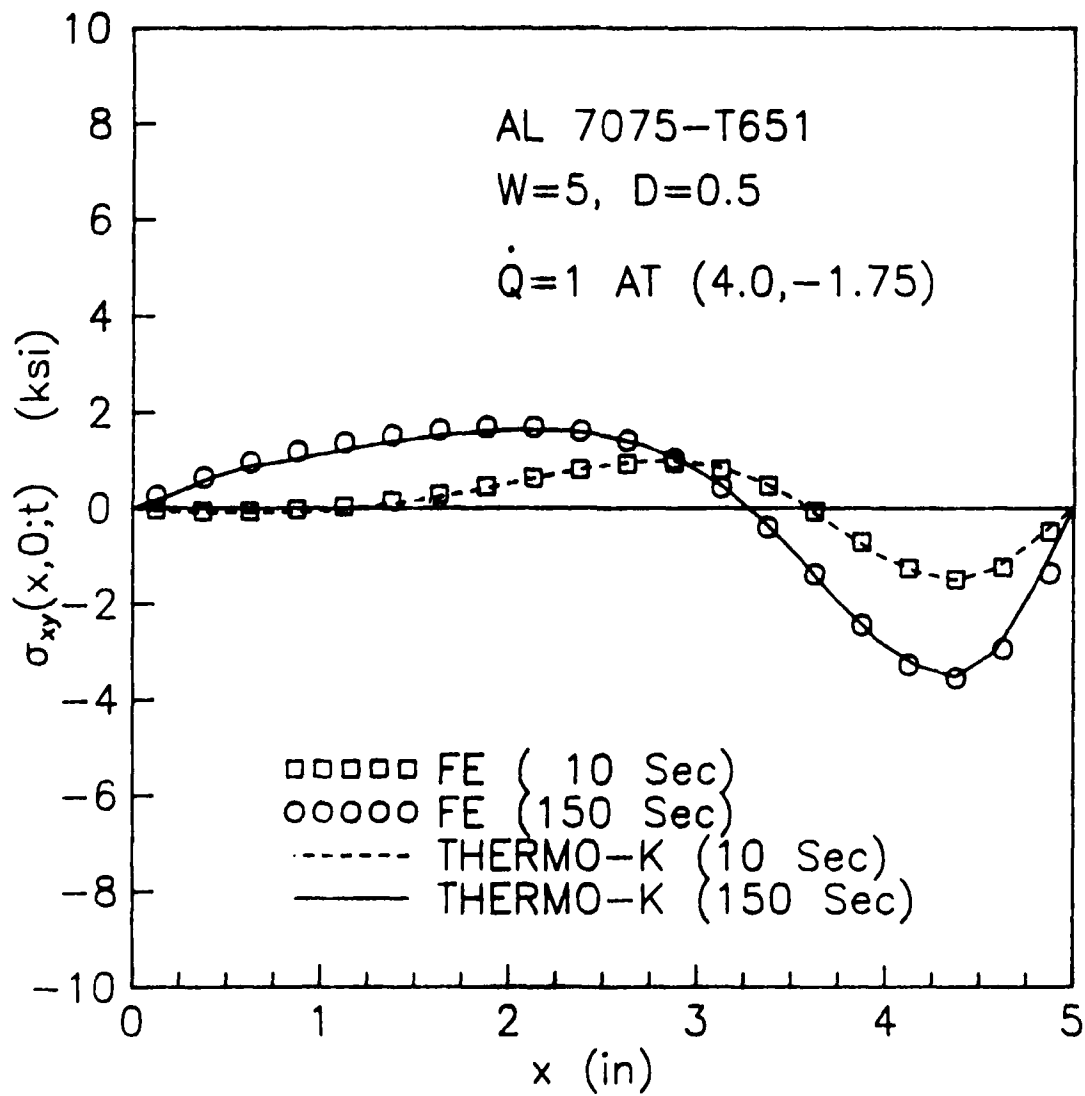


Figure 5-28. Comparison of Shear Stresses at $y = 0$ for Case 5-6

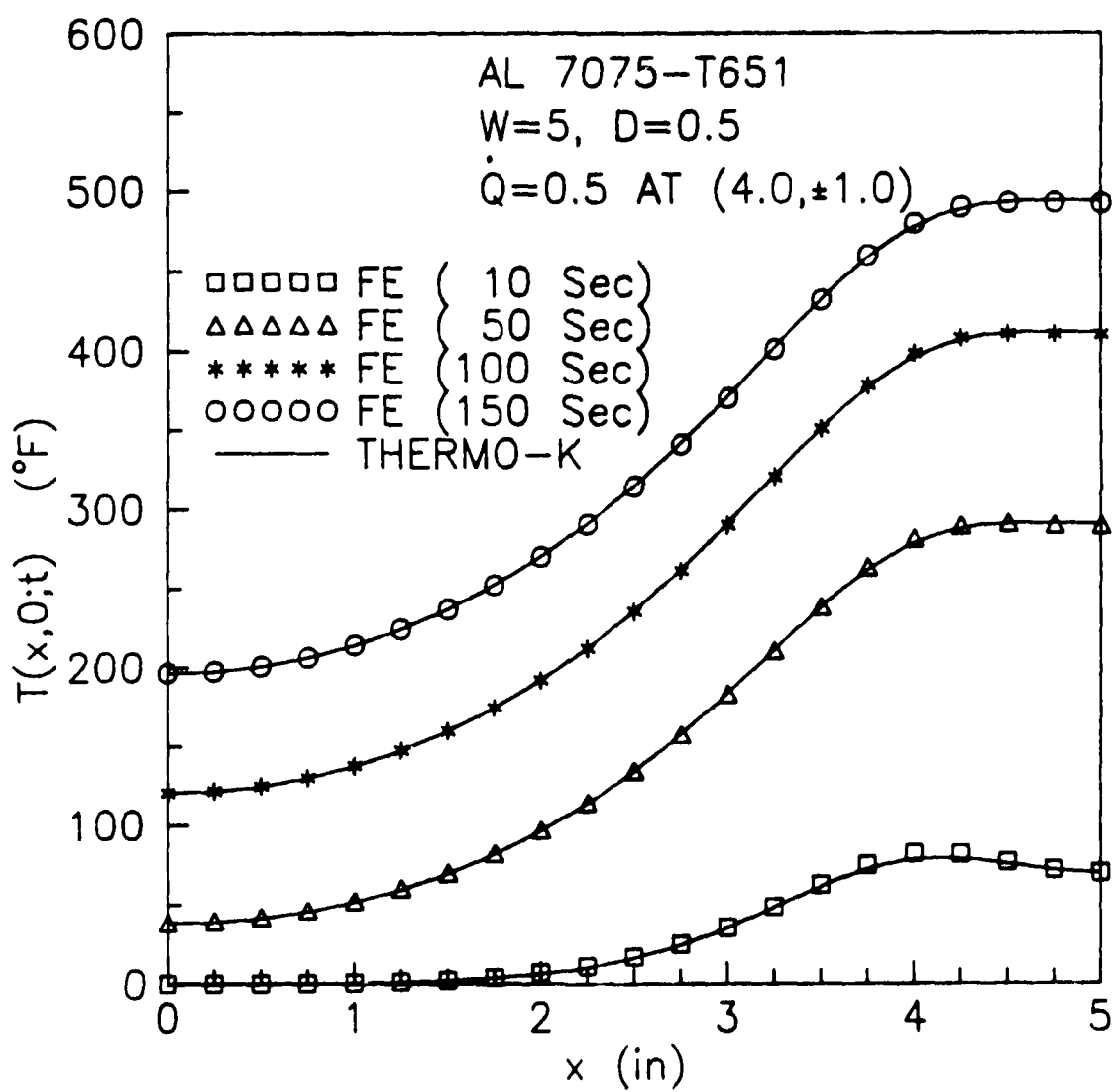


Figure 5-29. Comparison of Temperatures at $y = 0$ for Case 5-7

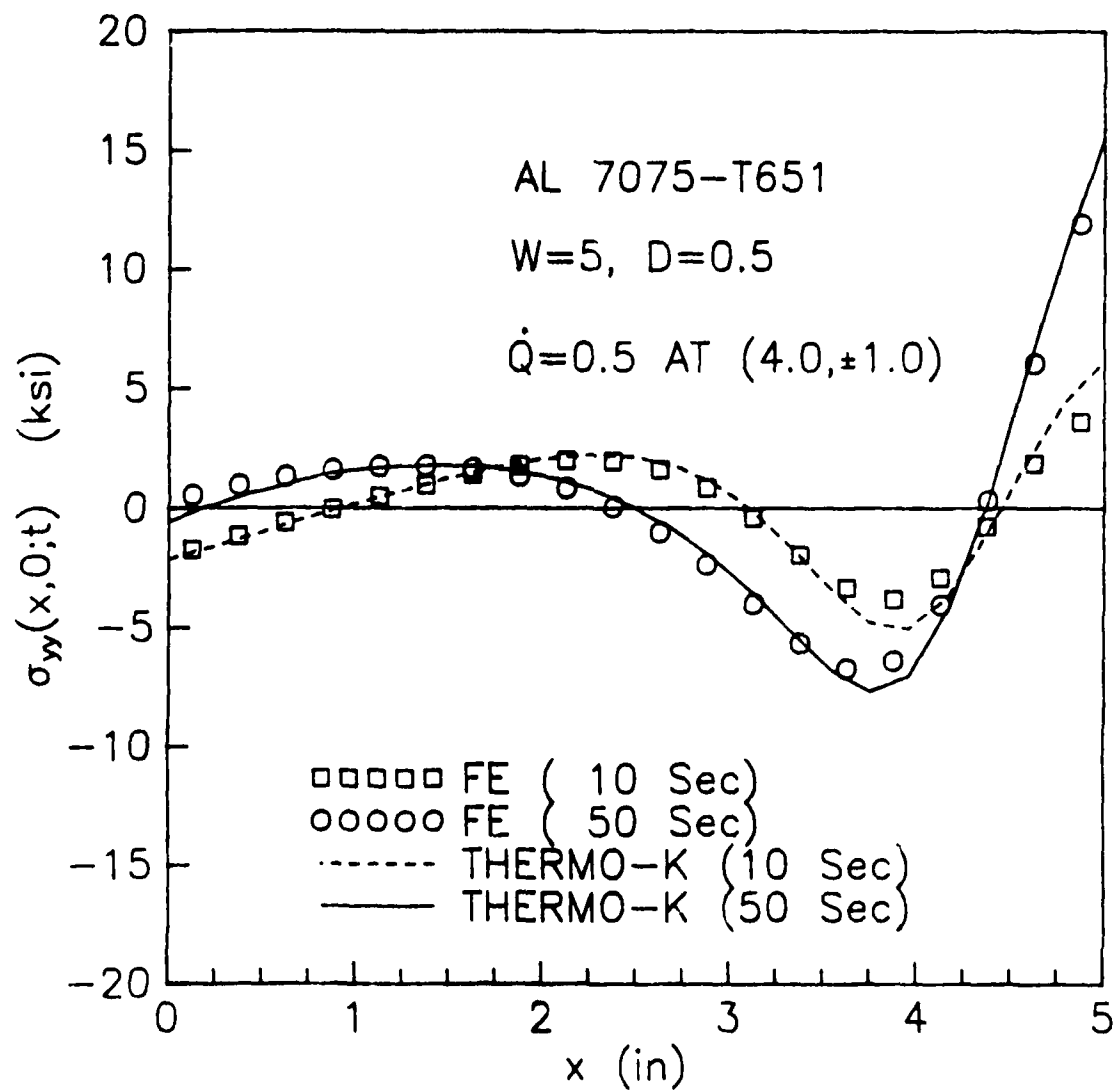


Figure 5-30. Comparison of Normal Stresses at $y = 0$ for Case 5-7

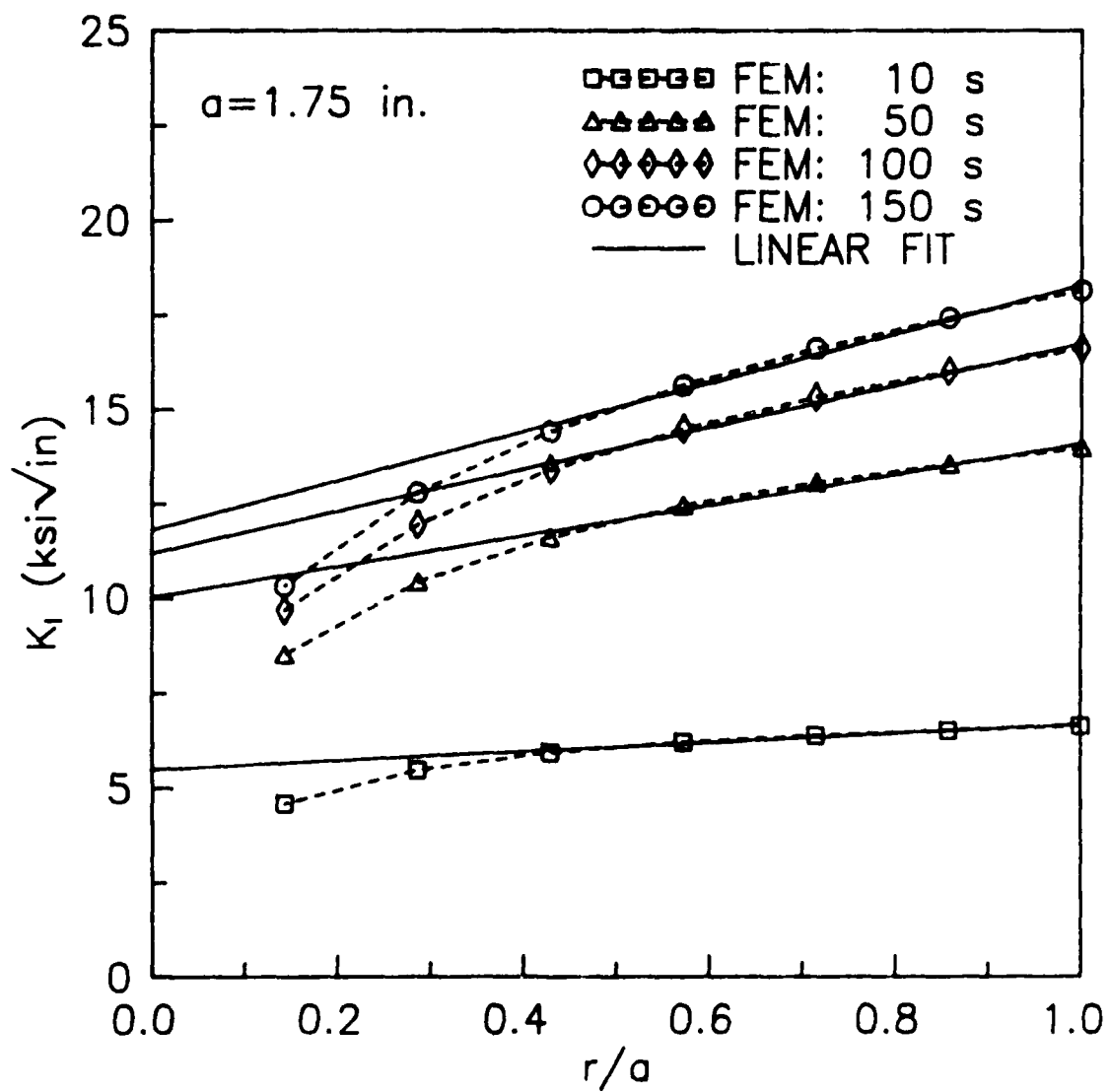


Figure 5-31. Variation of K_I Calculated Using the Displacement Method With Distance from the Crack Tip

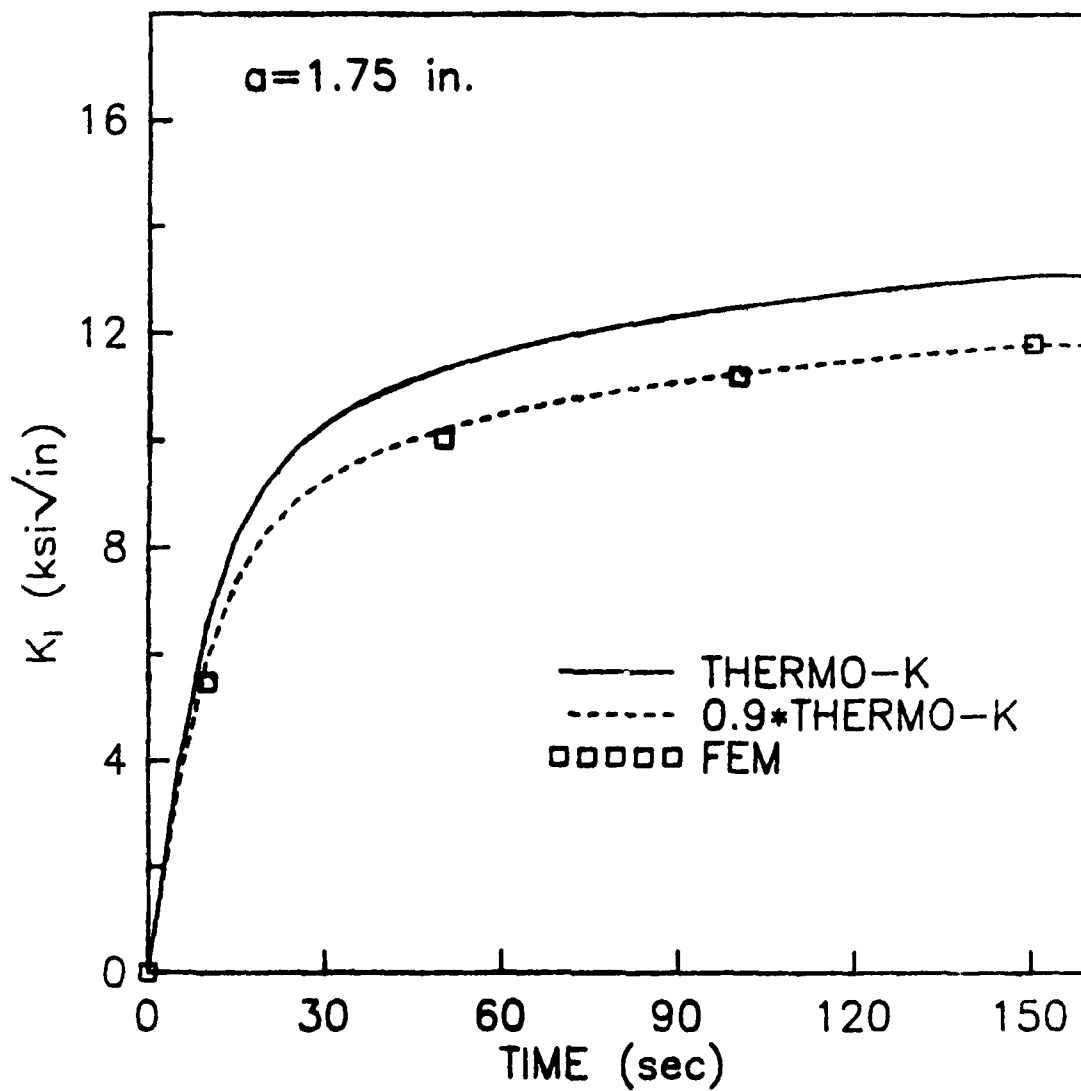


Figure 5-32. Comparison of Transient K_I Predicted by THERMO-K With the Finite Element Results



Figure 5-33(a). Finite Element Mesh (FEM2D) for Crack Model 4

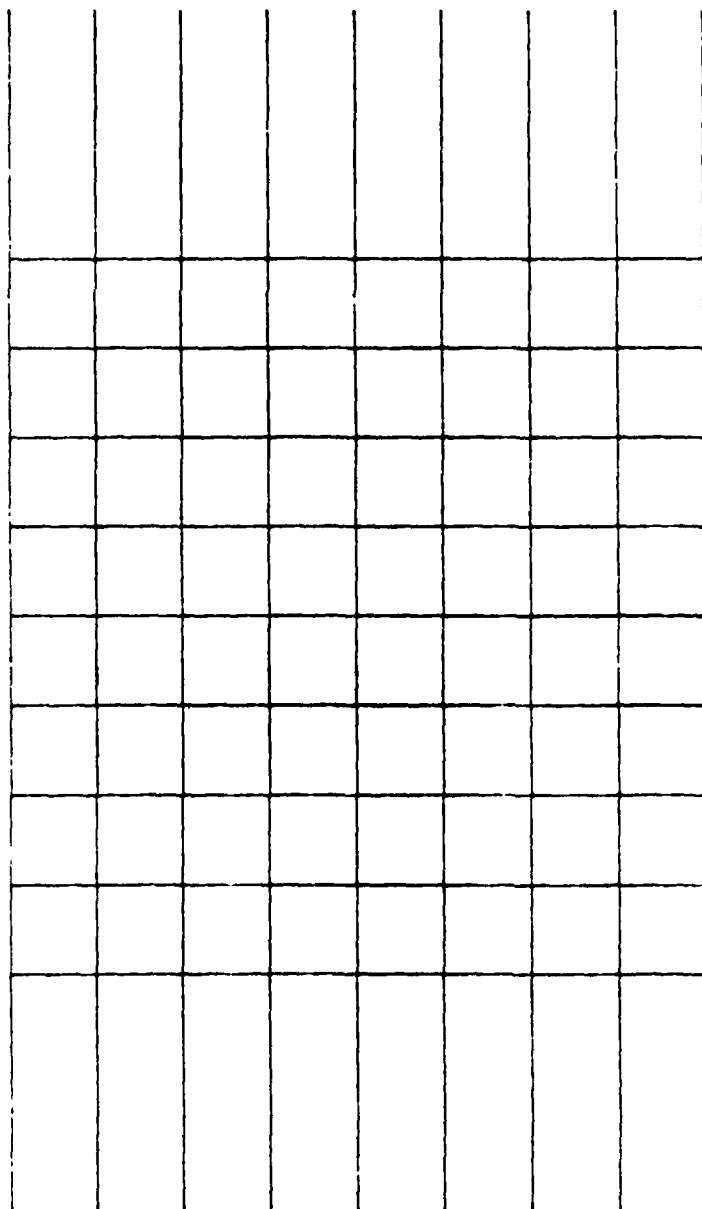


Figure 5-33(b). Finite Element Mesh Near the Crack Region

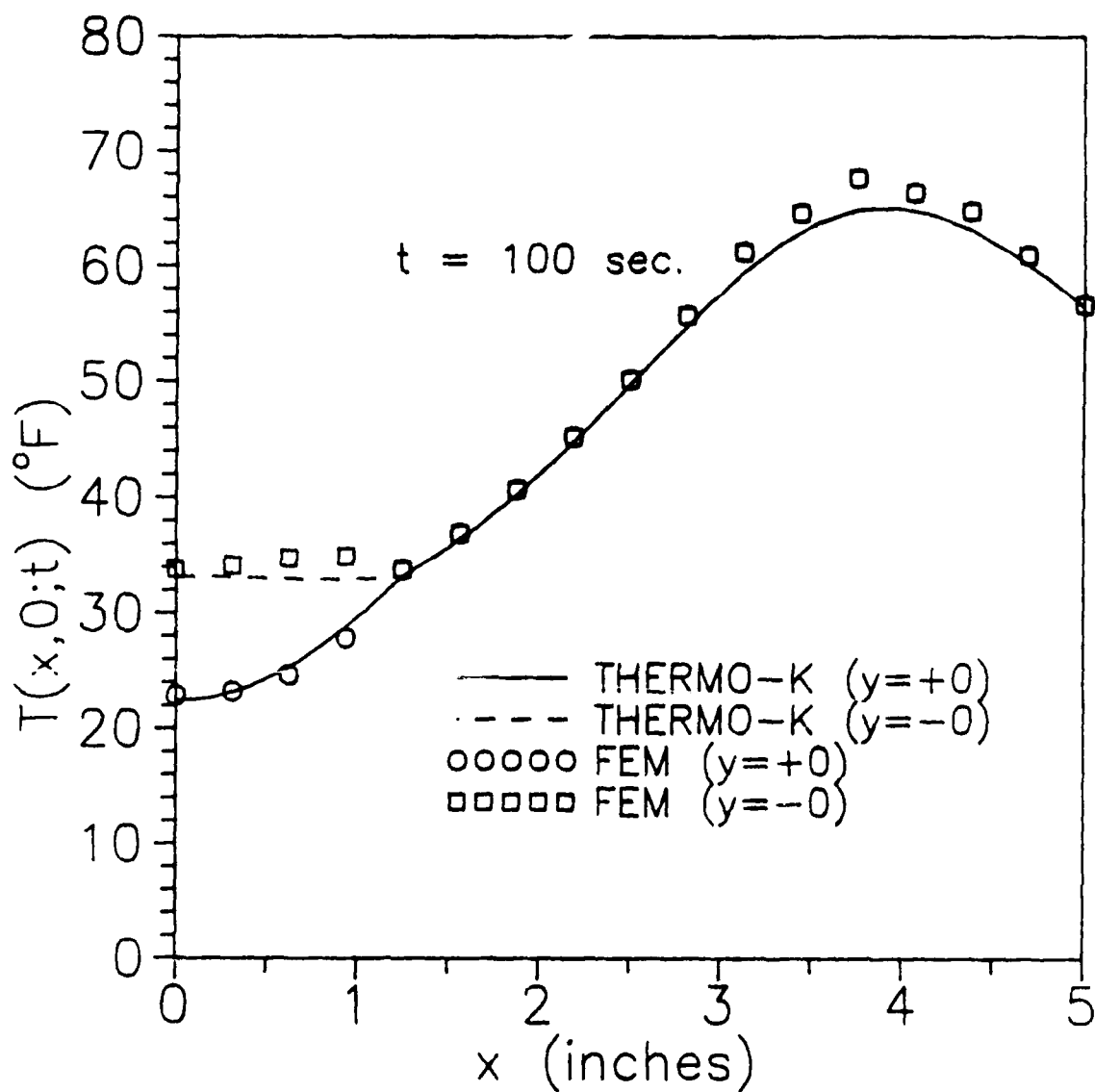


Figure 5-34. Comparison of Temperatures at $y = 0$ for an Insulated Single-edge-crack Plate (time = 100 sec)

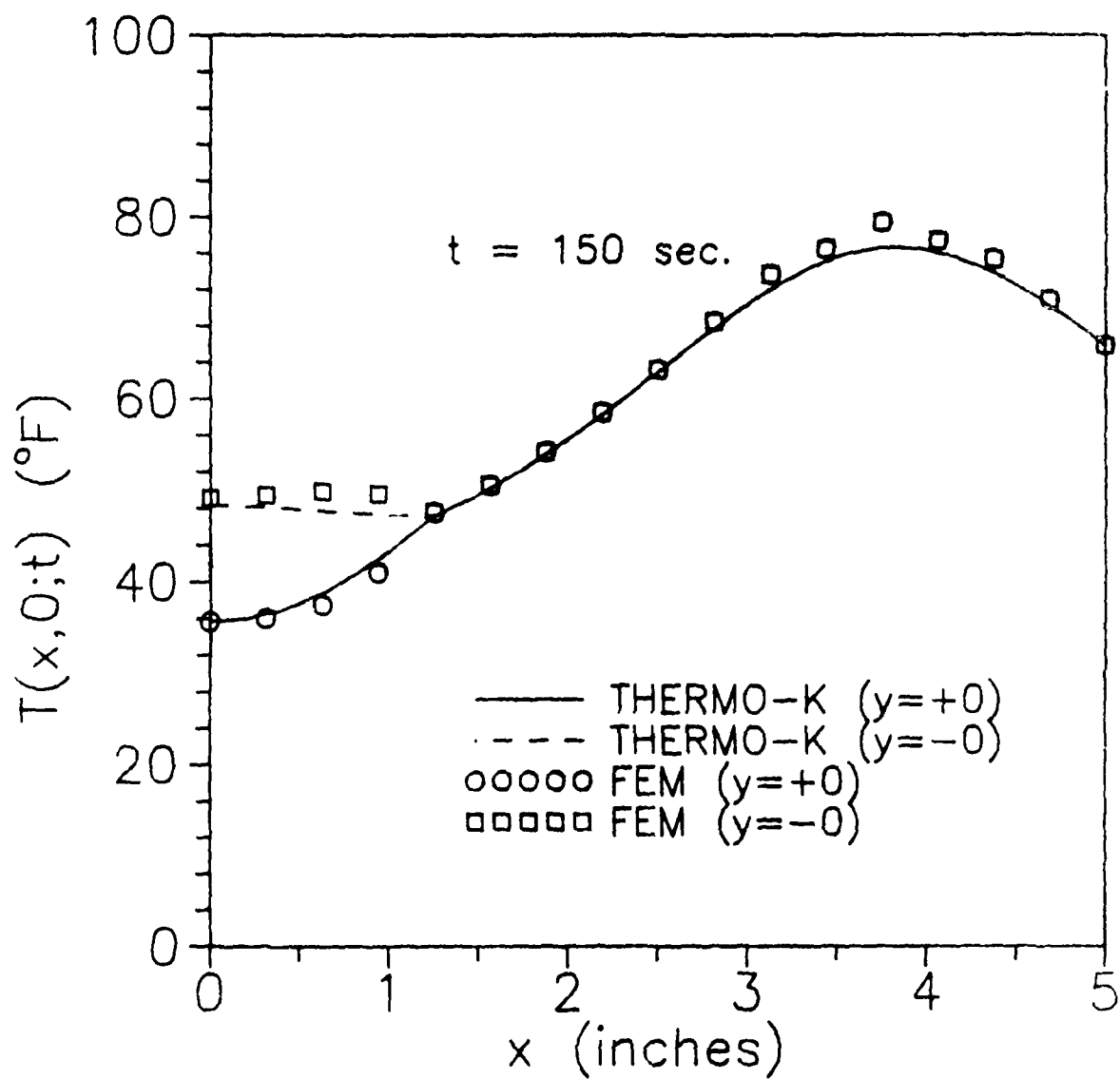


Figure 5-35. Comparison of Temperatures of $y = 0$ for an Insulated Single-edge-crack Plate (time = 150 sec)

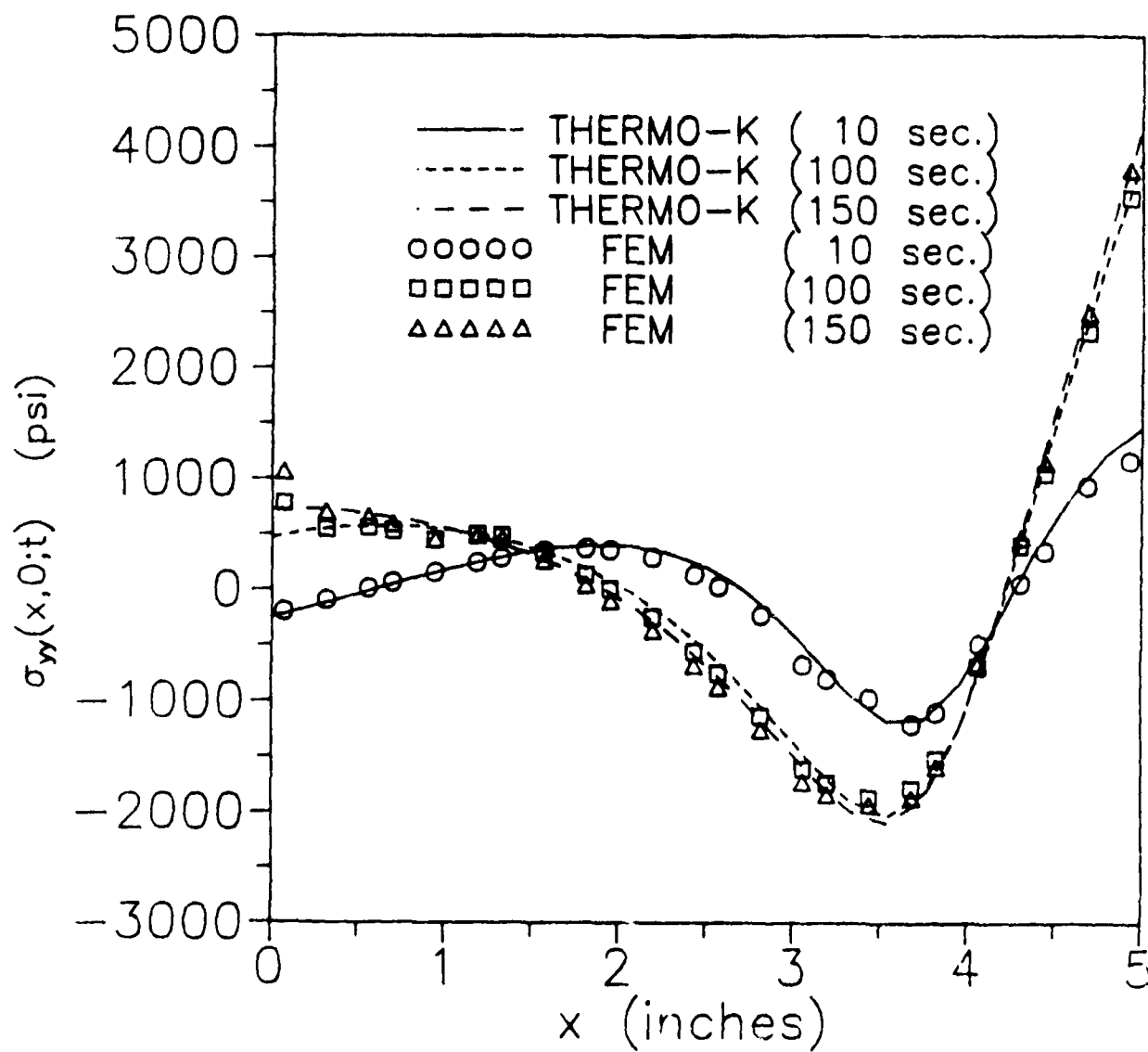


Figure 5-36. Comparison of Normal Stresses at $y = 0$ for an Insulated Single-edge-crack Plate

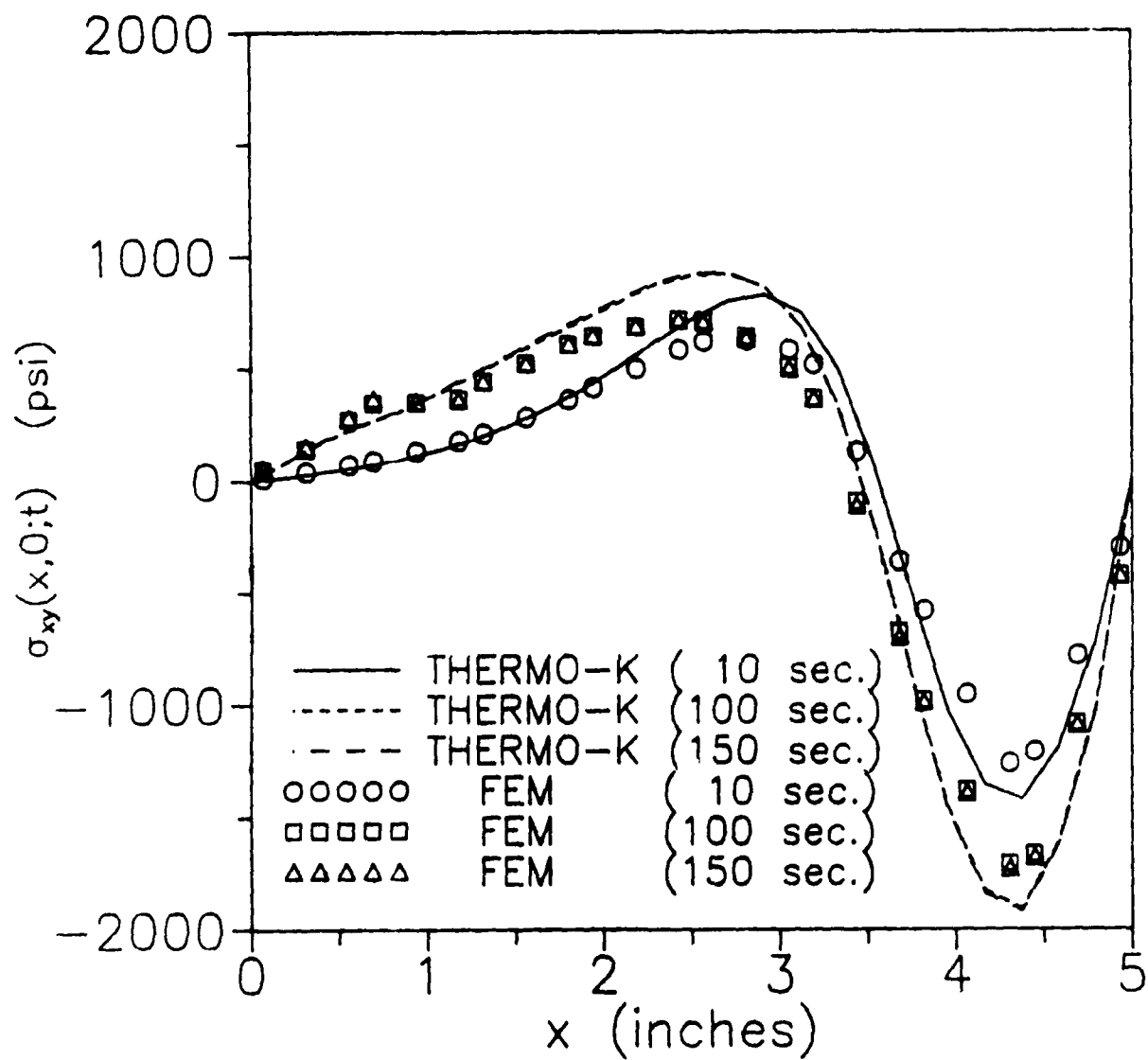


Figure 5-37. Comparison of Shear Stresses at $y = 0$ for an Insulated Single-edge-crack Plate

6.0 THEORETICAL BACKGROUND OF CRACK MODEL 5 - A CENTER-CRACK PLATE

This section describes the theoretical basis for crack Model 5 - a center-crack plate, i.e., as illustrated in Figure 6-1, a center crack of length a in an infinitely long plate strip of thickness D and width W . The cracked plate strip is subjected to point heat sources with arbitrary time history at any points in the plate region.

6.1 Assumptions

The following assumptions were made to simplify the problem:

- (a) The problem is assumed to be a plane stress problem. In other words, the thickness D shown in Figure 6-1 is assumed to be small enough that the temperature distribution in the thickness direction can be treated as uniform and the stress components in the thickness direction are negligible compared with the in-plane stress components.
- (b) The metallic materials are assumed to be isotropic, homogeneous, and linear elastic. Material properties are assumed to be temperature independent.
- (c) The rate of heat application is slow enough that the coupling terms and inertia terms in the general thermoelasticity equations can be neglected, i.e., it is assumed that the decoupled, quasi-static thermoelasticity applies.
- (d) The crack surfaces are assumed to be stress free. The crack surfaces can be completely insulated, fully heat conductive, or partially heat conductive. Heat conductance coefficient h at the crack surfaces is also assumed to be constant throughout the entire temperature range.

- (e) It is assumed that the heat convection coefficients at the two edges, H_1 and H_2 , and at the plate surfaces, H , (see Figure 6-1) remain constant.

6.2 Governing Equations

For a plane stress thermoelasticity problem as illustrated in Figure 6-1, the governing equations are

$$\xi \nabla^2 T = T_{,t} + \xi \eta^2 T \quad (6-1)$$

$$\sigma_{ij,j} = 0 \quad (6-2)$$

$$\sigma_{ij} = 2G [\epsilon_{ij} + (\frac{\nu}{1-\nu}) \delta_{ij} \epsilon_{kk} - \alpha (\frac{1+\nu}{1-\nu}) \delta_{ij} T] \quad (6-3)$$

$$\epsilon_{ij} = (U_{i,j} + U_{j,i})/2 \quad (6-4)$$

and

$$\nabla^2 U_i + (\frac{1+\nu}{1-\nu}) U_{j,ji} = 2(\frac{1+\nu}{1-\nu}) \alpha T \quad (6-5)$$

where $T=T(x_1, x_2, t)$ is temperature distribution, t and x_i are time and Cartesian coordinates respectively, $\xi=(k/\rho c)$, k is heat conduction coefficients, ρ is mass density, c is heat capacity, $\eta^2=(2H)/k/D$, H is heat convection coefficient from the plate surfaces to the environment (see Figure 6-1), D is plate thickness, U_i are displacements, α is coefficient of thermal expansion, and G and ν are shear modulus and Poisson's ratio respectively.

Nominal stress distributions generated with these equations are used to develop stress intensity factors via the influence function approach described in the next subsection.

6.3 Influence Functions for Stress Intensity Factors

For any plate/crack geometry, cracktip stress intensity factors can be determined by integrating the product of the stresses at the crack location in an uncracked structure and an influence function (or weight function) (Buecker, 1973). That is, for a crack as shown in Figure 6-2, the stress intensity factor can be calculated by

$$K_I = \int_0^a \sigma_{yy}(\bar{x}) m_1(\bar{x}) d\bar{x} \quad (6-6)$$

$$K_{II} = \int_0^a \sigma_{xy}(\bar{x}) m_2(\bar{x}) d\bar{x} \quad (6-7)$$

where $m_1(\bar{x})$ and $m_2(\bar{x})$ are influence functions, $\bar{x} = x - \frac{W}{2} + \frac{a}{2}$, x is a local coordinate shown in Figure 7-1 and Figure B-2 of Appendix B, and σ_{yy} and σ_{xy} are the normal and shear stress distributions on the crack surface in an identical but uncracked plate which is under the same temperature distribution as the cracked plate.

For a center crack in an infinitely long plate strip, as illustrated in Figure 6-1, the influence function (or weight function) for Mode I cracking has been provided by Tada, et al. (1973) as follows:

$$m_1(x) = m_2(x) = \frac{1}{\sqrt{2W}} F_A\left(\frac{a}{W}, \frac{2x-W}{a}\right) F_B\left(\frac{a}{W}, \frac{2x-W}{a}\right) \quad (6-8)$$

where

$$F_A(\xi, \eta) = 1 + 0.297 (1 - \cos \frac{\pi \xi}{2}) \sqrt{(1+\eta)(1-\eta)} \quad (6-9)$$

$$F_B(\xi, \eta) = \sqrt{\tan(\pi \xi / 2)} \frac{1 \pm (\sin \frac{\pi \xi \eta}{2} / \sin \frac{\pi \xi}{2})}{\sqrt{1 - (\cos \frac{\pi \xi}{2} / \cos \frac{\pi \xi \eta}{2})^2}} \quad (6-10)$$

and x , a , and W are defined in Figure 6-1. In Equation (6-10), the plus sign is for the right cracktip and the minus sign is for the left crack tip. Tada, et al. (1973) have shown that the influence functions shown in Equation (6-8) to (6-10) are accurate within 1% for all crack sizes.

6.4 Principle of Superposition

In general, as shown in Figure 6-1, there may be multiple heat sources (or sinks) within the plate which will cause thermal stresses and stress intensity factors at crack tips in the structure. Since the problem is a linear elastic problem, it is easily demonstrated that total stress intensity factor can be calculated as the sum of the stress intensity factors caused by each individual heat source or sink, acting independently. That is

$$K(t) = \sum_i [K(t)]_i \quad (6-11)$$

where $K(t)$ is the total stress intensity factor and $[K(t)]_i$ is the stress intensity factor due to the i^{th} heat source.

6.5 Green's Function Concept for Time Integration

In Equation (6-11), the stress intensity factor $[K(t)]_i$ caused by each individual heat source can be solved with the concept of

Green's function integration. As illustrated in Figure 6-3, the stress intensity factor due to a heat source of intensity $Q_i(t)$ can be calculated by

$$[K(t)]_i = \int_0^t Q_i(\tau) G_i(t-\tau) d\tau \quad (\text{no summation}) \quad (6-12)$$

where $G_i(t)$ is the stress intensity factors due to a Delta function $\delta(t)$ heat source at the i^{th} heat source location.

As shown in Figure 6-3, generally, the Green's function $G_i(t)$ will decay and approach to zero after a decay period t_d . Therefore, the integration range in Equation (6-12) can be reduced to from $(t-t_d)$ to t . Such a reduction in the integration range greatly increases the speed of the calculation because, instead of integrating for the entire time history, it is only necessary to integrate backwards from the present time t to $(t-t_d)$ as follows

$$[K(t)]_i = \int_{t-t_d}^t Q_i(\tau) G_i(t-\tau) d\tau \quad (6-13)$$

6.6 Green's Function for Fully Heat Conductive Cracks

Previous subsections of this chapter show that the stress intensity factors for this crack models can be easily obtained by Equations (6-6), (6-7), (6-11), and (6-13) if the temperature and stress distributions and thereby the stress intensity factors at the crack tip, resulting from a delta function heat source (or sink) $Q\delta(t)$ at any arbitrary location (x',y') in the uncracked plate (Figure 6-4), can be solved. The uncracked plate shares the same temperature distribution as the cracked plate. As the first step, we consider the problem of a fully heat conductive center crack in a plate strip, i.e., in this subsection, it is assumed that heat flux can flow across the crack surfaces without

any heat loss or resistance. Solutions for a more general, partially heat conductive crack will be discussed in the next subsection. However, as will be seen in the next subsection and as shown in Appendix A of this report, for a crack model with symmetry about its crack plane such as this crack model, crack surface heat conductivity will affect Mode II stress intensity factor solutions but not Mode I or Mode III stress intensity factor solutions. In other words, whether the crack surfaces are fully heat conductive, insulated, or partially heat conductive, the K_I solution will remain the same for a center crack in an infinitely long plate strip of finite width and thickness. Thus, if only Mode I or Mode III fracture is of major interest, the stress intensity factor solutions can be obtained by assuming the crack surfaces are fully heat conductive. The assumption of a fully heat conductive crack will greatly shorten the computation time for temperatures, thermal stresses, and stress intensity factors.

Since thermal stresses and stress intensity factors do not depend on the initial, stress-free temperature of the plate, it is conveniently assumed that the initial temperature of the plate is zero, i.e., $T(x,y;0)=0$. To solve for the Green's function of this crack model, the following boundary conditions need to be satisfied in addition to the governing equations listed in Equations (6-1) to (6-5):

at $x=0$,

$$kT_{,x}(0,y;t) = -H_1 T(0,y;t) \quad (6-14)$$

$$\sigma_{xx}(0,y;t) = \sigma_{xy}(0,y;t) = 0 \quad (6-15)$$

at $x=W$,

$$kT_{,x}(W,y;t) = H_2 T(W,y;t) \quad (6-16)$$

$$\sigma_{xx}(W,y;t) = \sigma_{xy}(W,y;t) = 0 \quad (6-17)$$

at $y = \pm w$,

$$T(x,y;t) = 0 \quad (6-18)$$

$$\sigma_{xx}(x,y;t) = \sigma_{yy}(x,y;t) = \sigma_{xy}(x,y;t) = 0 \quad (6-19)$$

at $y=0$, $\frac{W-a}{2} \leq x \leq \frac{W+a}{2}$,

$$T(x,0^+;t) = T(x,0^-;t) \quad (6-20)$$

$$\sigma_{yy}(x,0^+;t) = \sigma_{yy}(x,0^-;t) \quad (6-21)$$

$$\sigma_{xy}(x,0^+;t) = \sigma_{xy}(x,0^-;t) \quad (6-22)$$

$$U_i(x,0^+;t) = U_i(x,0^-;t) \quad i = 1,2 \quad (6-23)$$

Temperature solution to the uncracked plate problem can be obtained by solving Equation (6-1) along with boundary conditions Equations (6-14), (6-16), (6-18), and (6-20). An analytical form of the temperature solution has been given by Carslaw and Jaeger (1959) as follows:

$$T(x,y,t) = \frac{Q}{2\rho c D \sqrt{\pi \xi t}} \sum_{n=1}^{\infty} (Z_n(x) Z_n(x')) \exp\left[-\xi a_n^2 t - \xi \eta^2 t - \frac{(y-y')^2}{4\xi t}\right] \quad (6-24)$$

where ξ and η are defined in Equation (6-1), and

$$\tan \alpha_n W = \frac{\alpha_n k (H_1 + H_2)}{k^2 a_n^2 - H_1 H_2} \quad (6-25)$$

$$Z_n(x) = (k \alpha_n \cos \alpha_n x + H_1 \sin \alpha_n x) Y_n \quad (6-26)$$

$$Y_n^2 = \frac{2(k^2 a_n^2 + H_2^2)}{(k^2 a_n^2 + H_1^2) [W(k^2 a_n^2 + H_2^2) + k H_2] + k H_1 (k^2 a_n^2 + H_2^2)} \quad (6-27)$$

The next step is to solve for the stress distribution due to the temperature distribution of Equation (6-24). Boley and Weiner (1960) and Parkus (1968) have shown that a particular solution to the thermal stress problem can be expressed in terms of a thermoelastic potential ϕ as follows

$$U_i = \phi_{,i} \quad (6-28)$$

$$\sigma_{xx} = -2G \phi_{,yy} \quad (6-29)$$

$$\sigma_{yy} = -2G \phi_{,xx} \quad (6-30)$$

$$\sigma_{xy} = 2G \phi_{,xy} \quad (6-31)$$

$$\phi(x, y, t) = \alpha(1+\nu) \xi e^{-\xi \eta^2 t} \int_0^t e^{\xi \eta^2 \tau} T(x, y, \tau) d\tau + \phi_0 \quad (6-32)$$

where ϕ_0 is a function of x , y , and t such that ϕ would remain finite as t approaches infinity. Substitution of Equation (6-24) into Equation (6-32) yields

$$\phi(x, y; t) = e^{-\xi \eta^2 t} \sum_{n=1}^{\infty} \phi_n(x, y; t) \quad (6-33)$$

where

$$\begin{aligned} \phi_n = \frac{-a(1+\nu)Q}{4\rho c D a_n} z_n(x) z_n(x') [e^{-a_n(Y-Y')} \operatorname{erfc}(\omega_1) + \\ e^{a_n(Y-Y')} \operatorname{erfc}(\omega_2)] \end{aligned} \quad (6-34)$$

$$\omega_{1,2} = (a_n^2 \xi t)^{1/2} \pm \frac{(Y-Y')}{\sqrt{4\xi t}} \quad (6-35)$$

and $\operatorname{erfc}(x)$ is a complementary error function (see e.g., Abramowitz and Stegun, 1965 for definition).

In general, the particular solution ϕ shown in Equations (6-33) to (6-35) satisfies the stress free boundary of Equations (6-19), (6-21) to (6-23) but does not fulfill the stress boundary conditions at $x=0$ and $x=W$, i.e., Equations (6-15) and (6-17) are not satisfied. Therefore, a complementary solution Ψ , which is an analytic function, must be included to make the two edges $x=0$ and $x=W$ stress free. The overall stresses are then calculated by

$$\sigma_{xx} = 2G (\Psi - \phi)_{,yy} \quad (6-36)$$

$$\sigma_{yy} = 4G (\Psi - \phi)_{,xx} \quad (6-37)$$

and

$$\sigma_{xy} = -2G (\Psi - \phi)_{,xy} \quad (6-38)$$

where Ψ is the solution of

$$\nabla^2 \nabla^2 \Psi = 0 \quad (6-39)$$

$$\Psi_{,yy} = \phi_{,yy} \quad \text{at } x=0 \text{ and } x=W \quad (6-40)$$

and

$$\Psi_{,xy} = \phi_{,xy} \quad \text{at } x=0 \text{ and } x=W \quad (6-41)$$

Solution to Equations (6-39) to (6-41) can be obtained by the methods described by Timoshenko and Goodier (1970) for the problem of an infinite plate strip of width W and thickness D subjected to arbitrary tractions at both edges (as illustrated in Figure 6-5). Detailed derivations of Ψ are given in Appendix C of this report. From Appendix C, stresses resulting from the stress function Ψ at crack plane, $y=0$, are evaluated by

$$\hat{\sigma}_{yy}(x, 0; t) = 4G \int_{-\infty}^{\infty} \left(-[\phi_{,yy}(-\frac{W}{2}, y; t) \beta_{yy}(\frac{x}{W}, \frac{|y|}{W})] \right)$$

$$\begin{aligned}
& + [\phi_{,xy}(-\frac{W}{2}, y; t) \gamma_{yy}(\frac{x}{W}, \frac{|y|}{W}) \operatorname{sgn}(y)] \\
& - [\phi_{,yy}(\frac{W}{2}, y; t) \beta_{yy}(1 - \frac{x}{W}, \frac{|y|}{W})] \\
& + [\phi_{,xy}(\frac{W}{2}, y; t) \gamma_{yy}(1 - \frac{x}{W}, \frac{|y|}{W}) \operatorname{sgn}(y)] \Big) \frac{dy}{W} \quad (6-42)
\end{aligned}$$

$$\begin{aligned}
\hat{\sigma}_{xy}(x, 0; t) = 4G \int_{-\infty}^{\infty} & ([\phi_{,yy}(-\frac{W}{2}, y; t) \beta_{xy}(\frac{x}{W}, \frac{|y|}{W}) \operatorname{sgn}(y)] \\
& - [\phi_{,xy}(-\frac{W}{2}, y; t) \gamma_{xy}(\frac{x}{W}, \frac{|y|}{W})] \\
& - [\phi_{,yy}(\frac{W}{2}, y; t) \beta_{xy}(1 - \frac{x}{W}, \frac{|y|}{W}) \operatorname{sgn}(y)] \\
& - [\phi_{,xy}(\frac{W}{2}, y; t) \gamma_{xy}(1 - \frac{x}{W}, \frac{|y|}{W})] \Big) \frac{dy}{W} \quad (6-43)
\end{aligned}$$

where $\phi(x, y; t)$ is the thermoelastic potential function given in Equations (6-33) to (6-35), $\operatorname{sgn}(y)$ is a sign function, and β_{yy} , β_{xy} , γ_{yy} , and γ_{xy} are edge effect functions shown in Figures C-3 to C-16) of Appendix C at the end of this report.

Therefore, at the cross section of $y=0$, the stresses caused by a Delta function heat source $Q\delta(t)$ at (x', y') are

$$\sigma_{yy} = \hat{\sigma}_{yy} + \sum (P_n \cos \alpha_n x + Q_n \sin \alpha_n x) + \frac{F}{W} + \frac{12Nx}{W^3} \quad (6-44)$$

$$\sigma_{xy} = \hat{\sigma}_{xy} + \sum (R_n \cos \alpha_n x + S_n \sin \alpha_n x) \quad (6-45)$$

where $\hat{\sigma}_{yy}$ and $\hat{\sigma}_{xy}$ are stresses calculated by Equations (6-42) and (6-43), F and N are constants to maintain the condition of zero forces and moments at cross section $y=0$, and

$$P_n = \frac{Ga(1+\nu)Q}{2\rho cD} Y_n k a_n^2 M Z_n(x') \quad (6-46)$$

$$Q_n = \frac{Ga(1+\nu)Q}{2\rho cD} Y_n H_1 a_n M Z_n(x') \quad (6-47)$$

$$R_n = \frac{Ga(1+\nu)Q}{2\rho cD} Y_n H_1 N Z_n(x') \quad (6-48)$$

$$S_n = - \frac{Ga(1+\nu)Q}{2\rho cD} Y_n K a_n N Z_n(x') \quad (6-49)$$

$$M = - [\exp(a_n y') \operatorname{erfc}(\omega_2) + \exp(-a_n y') \operatorname{erfc}(\omega_1)] \quad (6-50)$$

$$N = - \left(\exp(a_n y') \left[a_n \operatorname{erfc}(\omega_2) + \frac{\exp(-\omega_2^2)}{\sqrt{\pi \xi t}} \right] - \exp(-a_n y') \left[a_n \operatorname{erfc}(\omega_1) + \frac{\exp(-\omega_1^2)}{\sqrt{\pi \xi t}} \right] \right) \quad (6-51)$$

To sum up this subsection, the Green's functions for the stress intensity factors are calculated by substituting the stress solutions given in Equations (6-44) and (6-45) and the influence functions given in Equation (6-8) into Equations (6-6) and (6-7) and integrating Equations (6-6) and (6-7) by the numerical integration scheme depicted in Appendix B.

6.7 Green's Function for Partially Heat Conductive Cracks

In subsection 6.6 the Green's function solution for a single point heat source at any arbitrary point in a center-crack plate is discussed. The crack surfaces in subsection 6.6 are assumed to be fully heat conductive. In reality, the crack surface is expected to be somewhere between complete insulation and fully heat conductive, i.e., crack surfaces are expected to be partially heat conductive. A general approach to treat a partially heat conductive crack is studied in detail in Appendix A of this report. Application of the concept given in Appendix A to the single-edge-crack model is discussed in this subsection.

Governing heat transfer equation for a single-edge-crack plate with partially heat conductive crack surfaces is still Equation (6-1), and the boundary conditions at $x=0$, $x=W$, and $y=\pm\infty$, Equations (6-14), (6-16), and (6-18), respectively, remain unchanged. The only difference will be the boundary condition at $y=0$, $\frac{W-a}{2} \leq x \leq \frac{W+a}{2}$, i.e., Equation (6-20) is replaced by

$$T_{,y}(x,0) = \frac{\lambda}{a} [T(x,0^+) - T(x,0^-)] \quad \frac{W-a}{2} \leq x \leq \frac{W+a}{2} \quad (6-52)$$

where λ is defined as (ah/k) in which h is crack surface heat conductance coefficient and k is material thermal conductivity. From Equation (6-52), it can be easily seen that the crack surfaces are fully heat conductive when $\lambda=\infty$ and the crack surfaces are completely insulated when $\lambda=0$. Any λ values between 0 and ∞ are corresponding to a partially heat conductive crack.

As discussed in Appendix A, when a crack is completely insulated or partially heat conductive, the resulting temperatures on both sides of a crack will be different, i.e., there is a temperature jump across the crack surface when λ equals to zero or a finite number. This temperature jump is analogous to the temperature

jump created by a series of distributed heat dipoles (Carslaw and Jaeger, 1959) situated at the crack location. Thus, the overall temperature distribution can be obtained as the superposition of the fully conductive solution, Equation (6-24), and a solution for the distributed heat dipoles. From Equation (6-24), it can be shown, by summing temperature solutions for a point heat source and a point heat sink with infinitesimally small distance in between, that temperature solution for an instantaneous heat dipole of strength M situated at $y=0$, $x=\bar{x}$ in an infinitely long plate strip is

$$T(x,y;t) = -\frac{M y}{4\rho c D \sqrt{\pi \xi t} \xi t} [\sum \exp(-\xi \eta^2 t - \xi a_n^2 t - \frac{y^2}{4\xi t}) Z_n(x) Z_n(\bar{x})] \quad (6-53)$$

Thus resulting temperature from distributed heat dipoles of strength $M(x,t)$ situated at $y=0$, $\frac{W-a}{2} \leq x \leq \frac{W+a}{2}$ of the plate strip is

$$T(x,y;t) = -\frac{y}{4\rho c D \sqrt{\pi \xi}^{1.5}} \int_0^t \int_0^a \left(\frac{M(\bar{x},t')}{(t-t')^{1.5}} \exp\left[\frac{-y^2}{4\xi(t-t')}\right] \right. \\ \left. [\sum \exp(-\xi \eta^2 t - \xi a_n(t-t')) Z_n(x) Z_n(\bar{x})] \right) d\bar{x} dt' \quad (6-54)$$

Substitution of the sum of Equations (6-24) and (6-54) into Equation (6-52) yield a Fredholm integral equation for the heat dipole distribution $M(x,t)$ as follows:

$$\frac{Q y'}{4R c D \sqrt{\pi \xi t} \xi t} \left[\sum \exp\left[-\xi a_n^2 t - \frac{y'^2}{4\xi t}\right] - \frac{1}{4\rho c D \sqrt{\pi \xi}^{1.5}} \int_0^t \int_{\frac{W-a}{2}}^{\frac{W+a}{2}} \right]$$

$$\begin{aligned}
& \left(\frac{M(\bar{x}, t')}{(t-t')^{1.5}} \left[\sum \exp(-\xi \alpha_n(t-t')) z_n(x) z_n(\bar{x}) \right] \right) d\bar{x} dt' \\
& = \frac{\lambda}{a} \frac{M(x, t)}{\rho c D \xi} e^{\xi \eta^2 t} \quad (6-55)
\end{aligned}$$

A numerical approximation method is used in the computer program to solve Equation (6-55). Since the temperature jump between two adjacent crack surfaces has to be zero at the crack tips, $x = \frac{W-a}{2}$ and $x = \frac{W+a}{2}$, we assume that

$$M(x, t) = \sum_{m=1}^L [b_m(t) \cos \delta_m \bar{x} + \hat{b}_m(t) \sin(\delta_m + \frac{\pi}{a}) \bar{x}] \quad (6-56)$$

where $\bar{x} = x - \frac{W}{2}$, $\delta_m = \frac{(2m-1)\pi}{a}$, L is the maximum number of terms included in the calculation, and $b_m(t)$ and $\hat{b}_m(t)$ are time functions, which are determined by substituting Equation (6-56) into Equation (6-55).

Similar to the fully heat conductive case, a thermoelastic potential due to the distributed thermal dipoles at the crack region can be derived by integrating the temperature solution, Equation (6-54). That is,

$$\phi(x, y; t) = a\xi(1+\nu) \int_0^t e^{-\xi \eta^2(t-\tau)} T(x, y; \tau) d\tau + \phi_0 \quad (6-57)$$

where $T(x, y; t)$ is the temperature solution given in Equation (6-54) and ϕ_0 is an analytic function to make ϕ remain finite at infinity. Substituting Equation (6-56) into Equation (6-54) and thereafter into Equation (6-57), one obtains

$$\phi(x, y; t) = \frac{-a(1+\nu)}{4\rho c D \sqrt{\pi \xi}} \sum_{m=1}^L \sum_{n=1}^N z_n(x) \int_0^t \int_0^{\tau} ([r_{mn} b_m(t') + v_{mn} \hat{b}_m(t')] \left[\frac{y}{(\tau-t')^{1.5}} \exp(-\xi \eta^2 t - \frac{y^2}{4\xi(\tau-t')}) - \xi a_n^2(\tau-t') \right]) dt' d\tau \quad (6-58)$$

where

$$r_{mn} = C_n \left(\frac{\sin[(\delta_m - a_n)a/2]}{(\delta_m - a_n)} + \frac{\sin[(\delta_m + a_n)a/2]}{(\delta_m + a_n)} \right) \quad (6-59)$$

$$v_{mn} = D_n \left(\frac{-\cos[(\delta_m - a_n)a/2]}{[\delta_m - a_n + (\pi/a)]} + \frac{\cos[(\delta_m + a_n)a/2]}{[\delta_m + a_n + (\pi/a)]} \right) \quad (6-60)$$

$$C_n = k Y_n a_n \cos(W a_n / 2) + Y_n H_1 \sin(W a_n / 2) \quad (6-61)$$

$$D_n = -k Y_n a_n \sin(W a_n / 2) + Y_n H_1 \cos(W a_n / 2) \quad (6-62)$$

a_n 's are eigen values defined in Equation (6-25), $z_n(x)$'s are eigen functions defined in Equation (6-26), $b_m(t)$'s and $\hat{b}_m(t)$'s are time functions defined in Equation (6-56), Y_n 's are constants defined in Equation (6-27), δ_m 's are defined in Equation (6-56), ξ and η are defined in Equation (6-1), and N and L are the maximum number of terms included in the series expansions in Equation (6-24) and Equation (6-56), respectively. Stresses at the crack region, $y=0$, $\frac{W-a}{2} \leq x \leq \frac{W+a}{2}$, due to the distributed thermal dipoles can then be evaluated by substituting Equation (6-58)

into Equations (6-37) and (6-38). After some algebraic manipulation, it can be shown that stresses at section $y=0$ due to the thermoelastic potential ϕ of Equation (6-58) are as follows:

$$\sigma_{yy}(x,0;t) = 0 \quad (6-63)$$

$$\begin{aligned} \sigma_{xy}(x,0;t) &= 2G\phi_{,xy}(x,0;t) \\ &= \sum_{m=1}^L \sum_{n=1}^N z'_n(x) [r_{mn} E_n(0,t) + v_{mn} F_n(0,t)] \end{aligned} \quad (6-64)$$

$$\begin{aligned} E_n(y,t) &= \frac{Ea}{4\rho cD} e^{-\xi\eta^2 t} \int_0^t \left(b_m(t') a_n [\exp(a_n y) \operatorname{erfc}(\omega_1) \right. \\ &\quad + \exp(-a_n y) \operatorname{erfc}(\omega_2) - \frac{\omega_1 \exp(a_n y - \omega_1^2)}{a_n \pi \xi(t-t')} \\ &\quad \left. - \frac{\omega_2 \exp(-a_n y - \omega_2^2)}{a_n \pi \xi(t-t')} \right] dt' \end{aligned} \quad (6-65)$$

$$\begin{aligned} F_n(y,t) &= \frac{Ea}{4\rho cD} e^{-\xi\eta^2 t} \int_0^t \left(\hat{b}_m(t') a_n [\exp(a_n y) \operatorname{erfc}(\omega_1) \right. \\ &\quad + \exp(-a_n y) \operatorname{erfc}(\omega_2) - \frac{\omega_1 \exp(a_n y - \omega_1^2)}{a_n \pi \xi(t-t')} \\ &\quad \left. - \frac{\omega_2 \exp(-a_n y - \omega_2^2)}{a_n \pi \xi(t-t')} \right] dt' \end{aligned} \quad (6-66)$$

where ω_1 and ω_2 are defined in Equations (6-35). Results shown in Equations (6-63) and (6-64) reiterate the fact, deduced in Appendix A that, for a cracked structure with symmetry with respect to the crack plane such as the current crack model, crack surface heat conductivity will not affect Mode I fracture solution ($\sigma_{yy}=0$ in Equation (6-63)) but will change Mode II fracture solution ($\sigma_{xy} \neq 0$ in Equation (6-64)).

To sum up, for a center-crack plate with partially heat conductive or completely insulated crack surfaces, its overall temperature solution is the sum of Equation (6-24) and Equation (6-54). Stresses in the uncracked plate strip, which share the same overall temperature distribution as the cracked plate, are still given by Equations (6-44) and (6-45) except that the thermoelastic potential ϕ in Equations (6-36) to (6-43) now equal to the sum of Equations (6-33) and (6-58) and R_n 's in Equation (6-45) equal to the sum of the right hand side of Equation (6-48) and

$$\sum_{m=1}^L [(r_{mn} E_n + v_{mn} F_n) a_n Y_n H_1] \quad (6-67)$$

and S_n 's in Equation (6-45) equal to the sum of the right hand side of Equation (6-49) and

$$- \sum_{m=1}^L [(r_{mn} E_n + v_{mn} F_n) k a_n^2 Y_n] \quad (6-68)$$

Green's function solutions for stress intensity factors, K_I and K_{II} , at the crack tips are then calculated by substituting the above stresses at the crack region into Equations (6-6) and (6-7), respectively.

6.8 Finite Element Verification of Crack Model 5

Since stress intensity factors are calculated by integrating the product of influence functions and stresses at the crack location in a uncracked plate (see Equations (6-6) and (6-7)), it is necessary to verify both the influence functions shown in subsection 6.3 and the temperature and thermal stresses obtained in subsections 6.6 and 6.7.

6.8.1 Verification of Influence Functions

Since the influence functions are identical for both Mode I and Mode II fracture in a center-crack plate, only one numerical case is needed to verifying the influence functions. As shown in Figure 6-6, an infinitely long plate strip of width 10 inch with a center crack of length ranging from 0 inch to 8 inch. The center-crack plate is subjected to an uniform tensile as well as shear stresses of 1 ksi at infinity. Stress intensity factors resulting from influence function integration are compared with reference solutions provided by Tada, et al. (1973) and pc-CRACK (1986). It is seen from this figure that results by influence function integration agree well with the reference solutions.

6.8.2 Verification of Temperature and Stresses for Fully Heat Conductive Crack Surfaces

For a fully heat conductive crack, the temperature and thereby thermal stress solutions resulting from a heat source applied at an arbitrary location within the center-crack plate are identical to those for a fully heat conductive crack in a single-edge-crack plate. This can be easily deduced by comparing the equations and solutions in subsections 5.6 and 6.6. Therefore, the verification problems discussed in subsection 6.8.2 are also applicable to this crack model.

6.8.3 Verification of Temperature and Stresses for Insulated Crack Surfaces

This subsection is to check the accuracy of the temperatures and thermal stresses predicted by using the analytical approach described in this subsection. A center-crack plate with a width of 5 inches and thickness 0.5 inch is chosen as a reference problem. The center crack is set to be 1.25 inches long and a single heat source of strength $\dot{Q}(t) = H(t)$ Btu/sec is applied at $(x', y') = (3.75 \text{ inch}, -1.25 \text{ inch})$. Material properties and heat transfer constants are as follows:

$$E = 10.3 \times 10^6 \text{ psi}, \quad \nu = 0.33, \quad \alpha = 13 \times 10^{-6} / ^\circ\text{F}$$

$$k = 0.0017361 \frac{\text{Btu}}{\text{in-sec-F}}, \quad \rho = 0.0978 \frac{\text{lbm}}{\text{in}^3}, \quad c = 0.23 \frac{\text{Btu}}{\text{lbm-F}}$$

$$H = H_1 = 0 \frac{\text{Btu}}{\text{in}^2\text{-sec-F}}, \quad H_2 = 0.004 \frac{\text{Btu}}{\text{in}^2\text{-sec-F}} \quad (6-69)$$

The crack surfaces are assumed to be completely insulated, i.e., it is assumed that $\frac{\partial T}{\partial y} = 0$ at $y=0$, $\frac{W-a}{2} \leq x \leq \frac{W+a}{2}$. As shown in Figure 6-7, the plate is modeled with a finite element program, FEM2D (1986). In this finite element model, there is a total of 594 nodes and 176 eight-node isoparametric elements. In the crack region of the finite element model, the crack surfaces are set to be insulated for heat transfer analysis but are set to have continuous displacements in the subsequent thermal stress analysis, i.e., the adjacent nodes on both sides of the crack are treated as independent points in the heat transfer analysis but are constrained together in the thermal stress analysis so that they will have the same displacements but different temperatures. Resulting temperature and stress distributions at cross section $y=0$ are illustrated in Figures 6-8 to 6-11. Again, good

agreement between finite element solutions and solutions calculated by the analytical approach discussed in this subsection.

6.9 References

Boley, B. A., and Weiner, J. H., (1960), Theory of Thermal Stresses, Wiley & Sons, New York, New York.

Bueckner, H. F., (1973), "Field Singularities and Related Integral Representations," in Methods of Analysis and Solutions of Crack Problems, Vol 1, ed. G. C. Sih, pp. 239-314, Noordhoff, Holland.

Carslaw, H. S., and Jaeger, J. C., (1959), Conduction of Heat in Solids, 2nd edition, Oxford University Press, London.

FEM2D - A Two Dimensional Finite Element Computer Program for Two-Dimensional Heat Transfer/Thermal Stress Analysis, Users Manual, (1986), Structural Integrity Associates, San Jose, CA.

pc-CRACK - Fracture Mechanics Software for Personal Computers, Users Manual, Version 1.1, Revision 1, (1986), Structural Integrity Associates, San Jose, CA.

Parkus, H., (1968), Thermoelasticity, Blaisdell Publishing Co..

Tada, H., Paris, P., and Irwin, G., (1973), The Stress Analysis of Cracks Handbook, Del Research Co., Pennsylvania.

Timoshenko, S. P., and Goodier, J. N., (1970), Theory of Elasticity, 3rd edition, McGraw Hill, New York, New York.

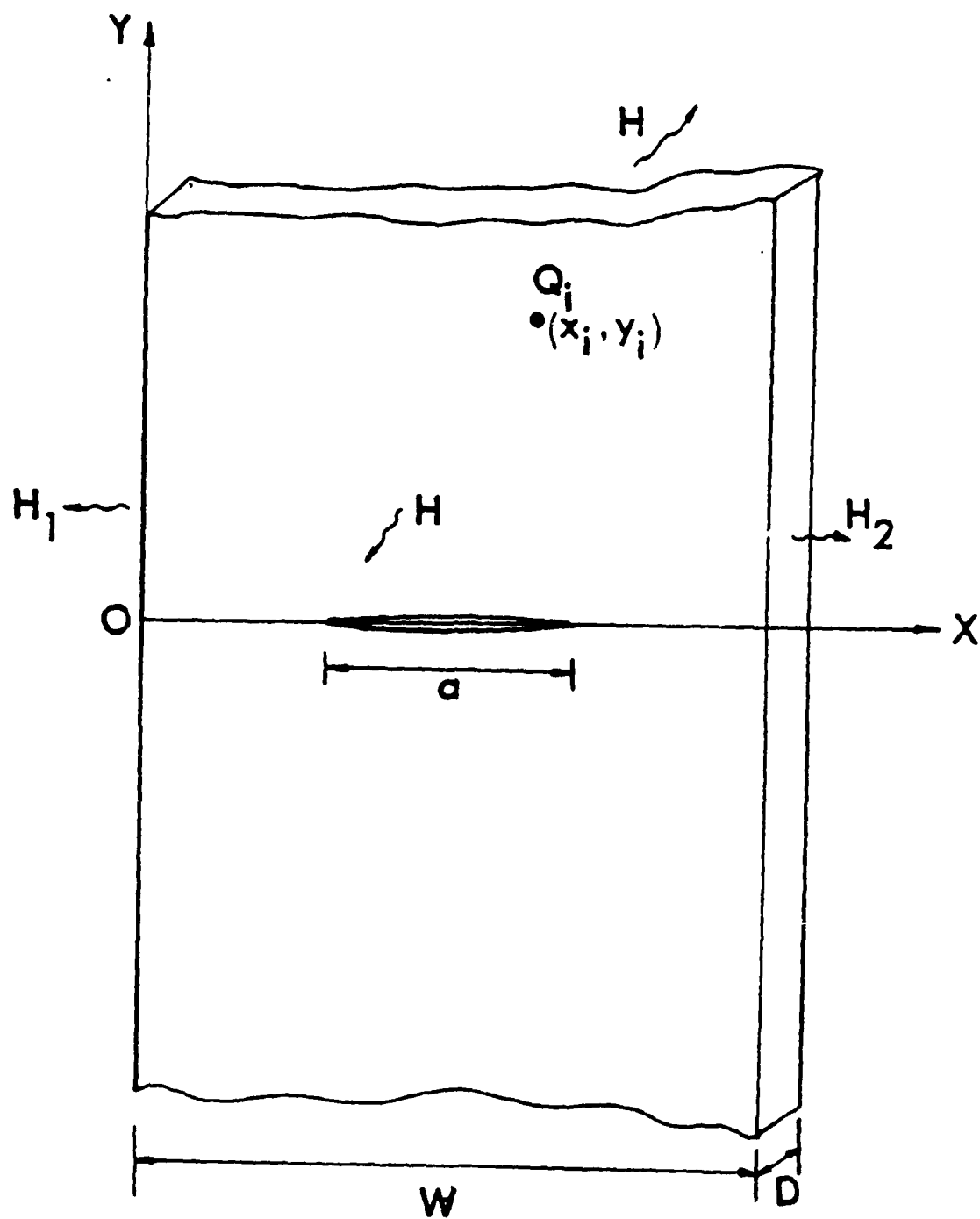


Figure 6-1. A Center-Crack Plate Subjected to Point Heat Sources

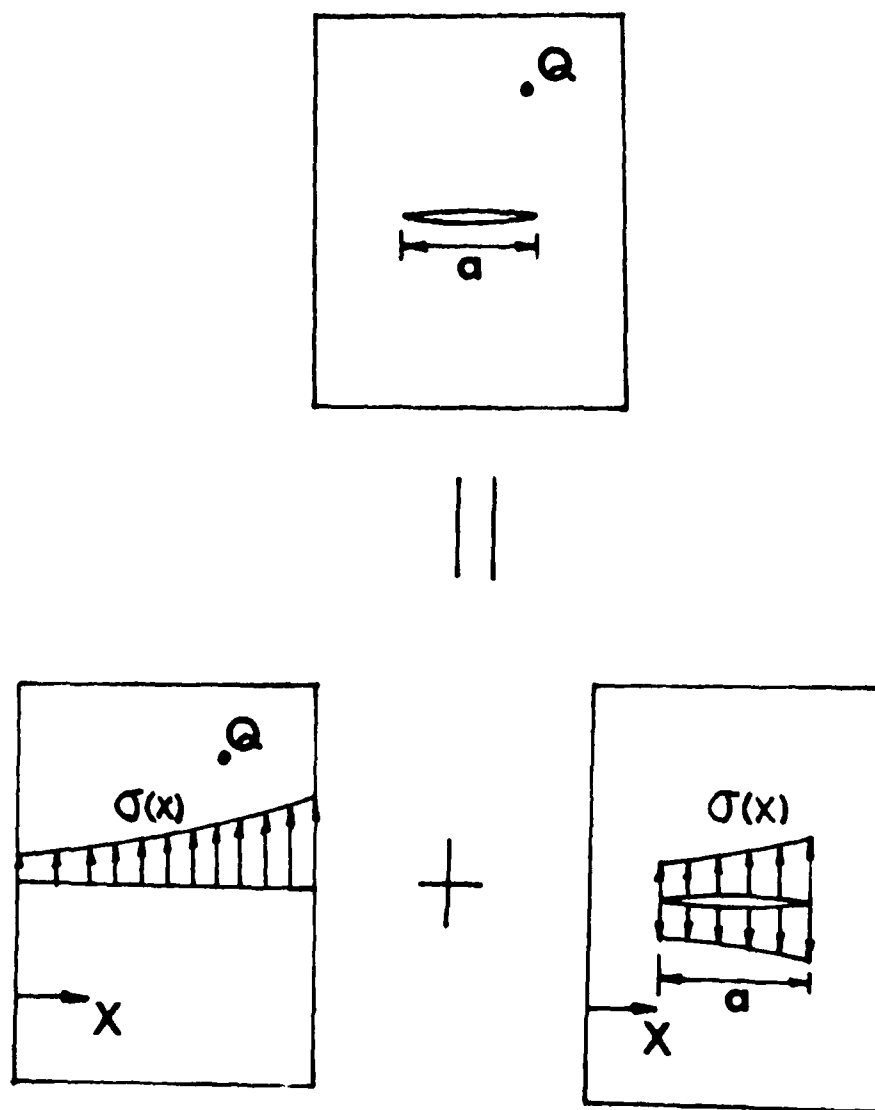
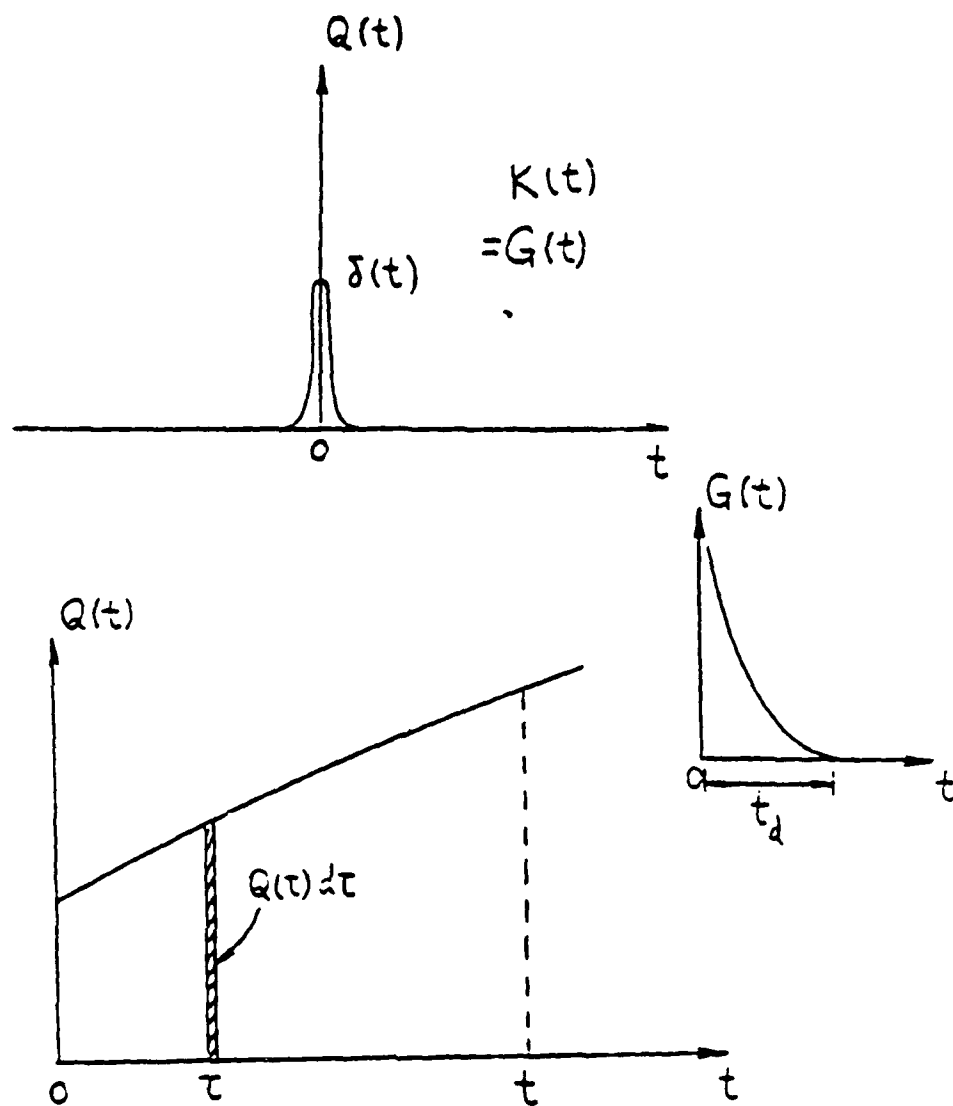


Figure 6-2. Concept of Influence Function



$$K(t) = \int_0^t Q(\tau) G(t-\tau) d\tau$$

$$= \int_{t-t_d}^t Q(\tau) G(t-\tau) d\tau$$

Figure 6-3. Concept of Green's Function

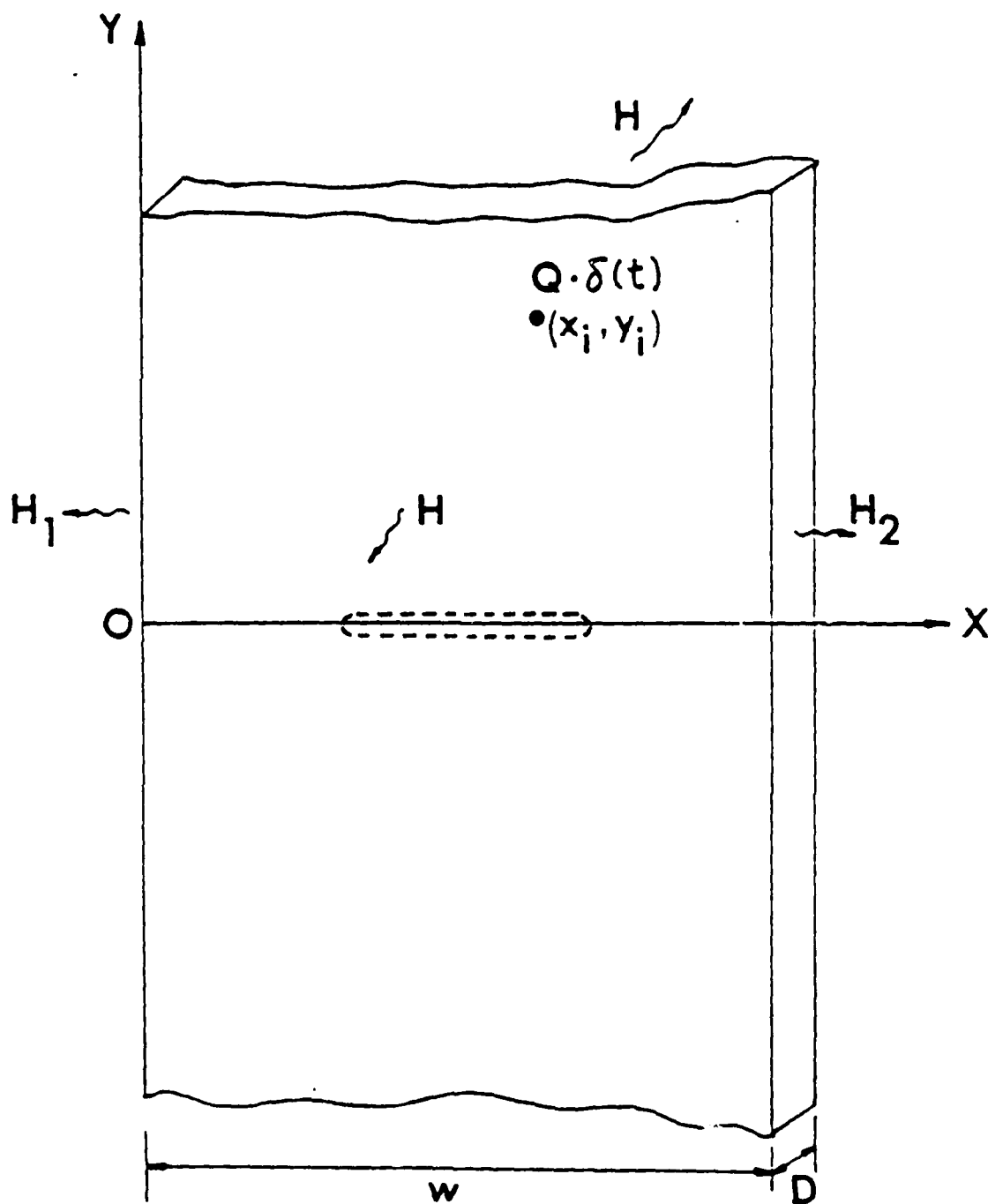


Figure 6-4. A Point Heat Source in an Uncracked Plate

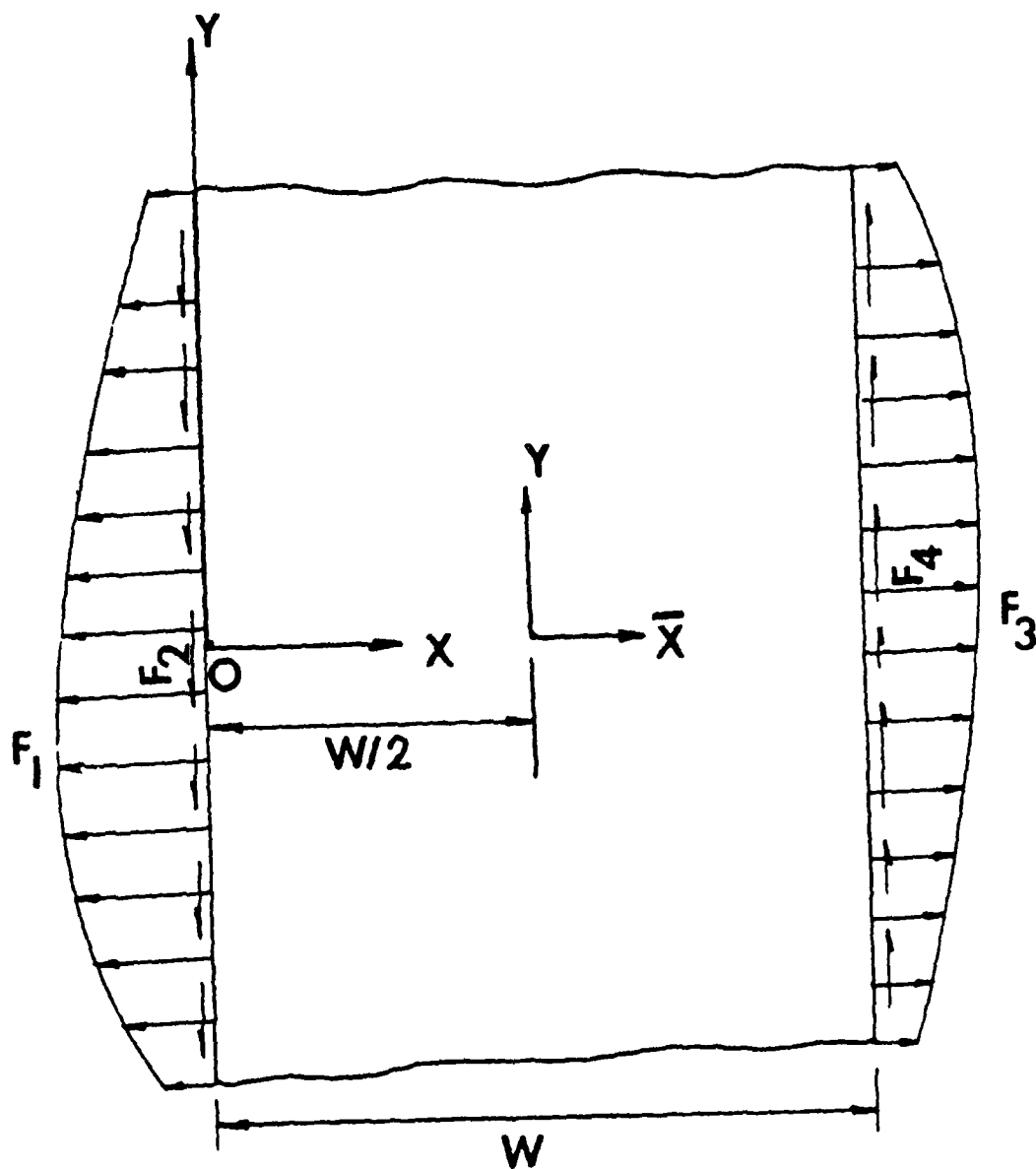


Figure 6-5. A Plate Strip Subjected to Arbitrary Edge Loads

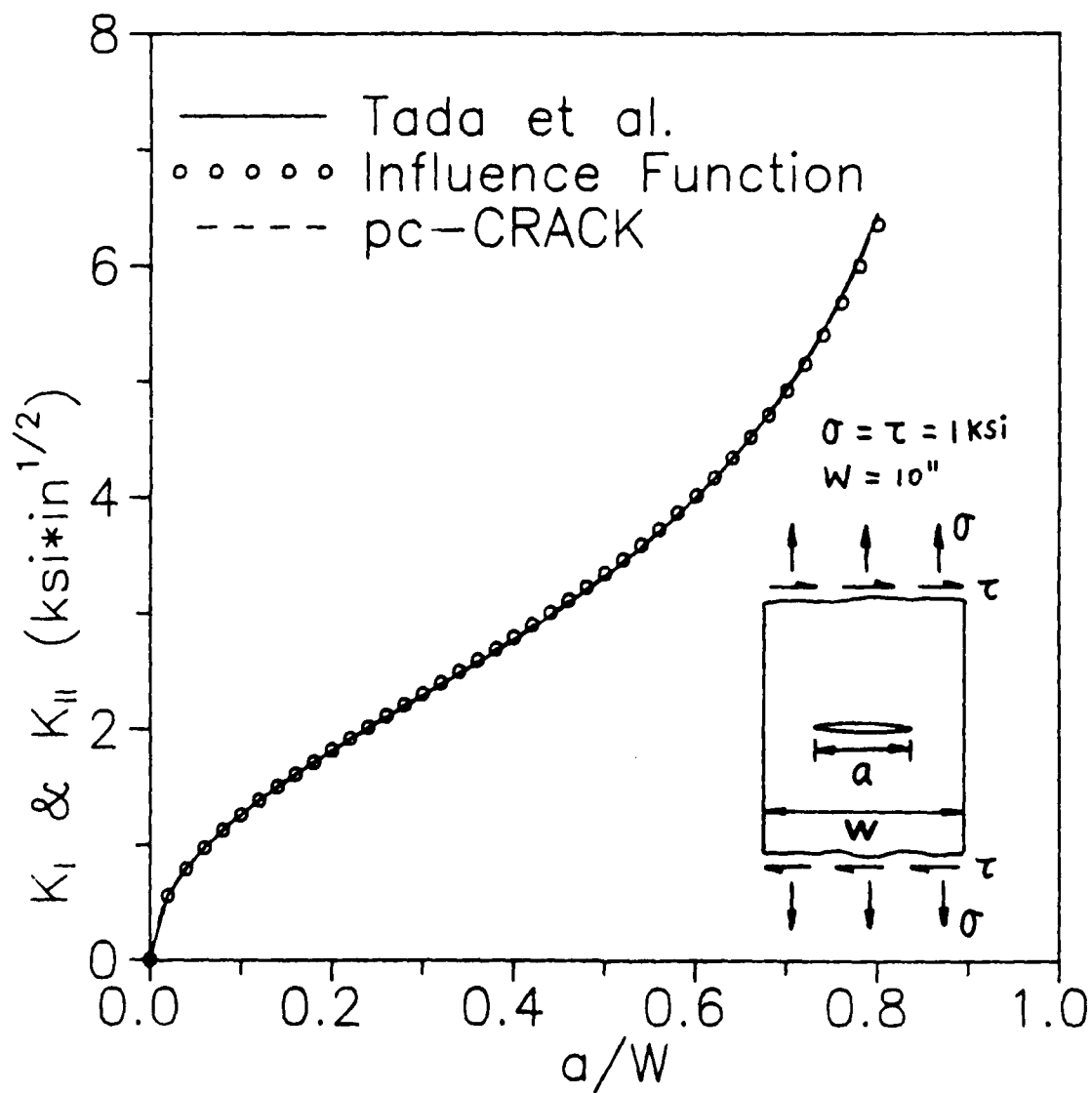


Figure 6-6. A Center-Crack Plate Under Combined Uniform Tension and Shear



Figure 6-7(a). Finite Element Mesh (FEM2D) for Crack Model 5

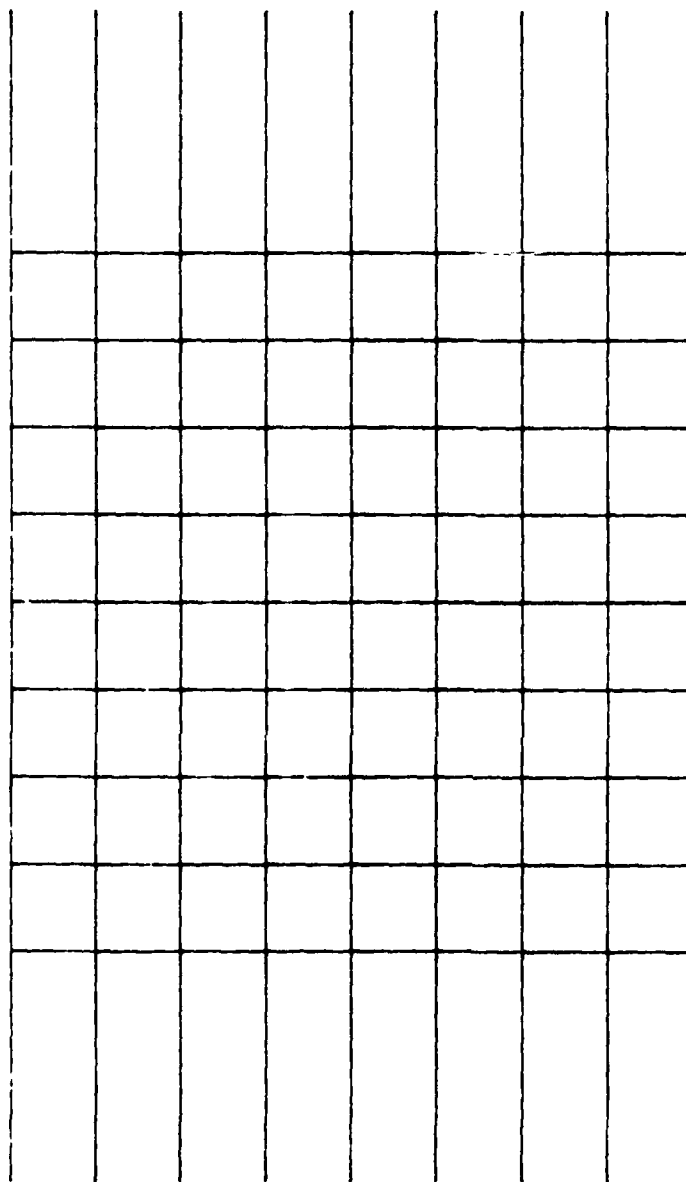


Figure 6-7 (b). Finite Element Mesh Near the Crack Region

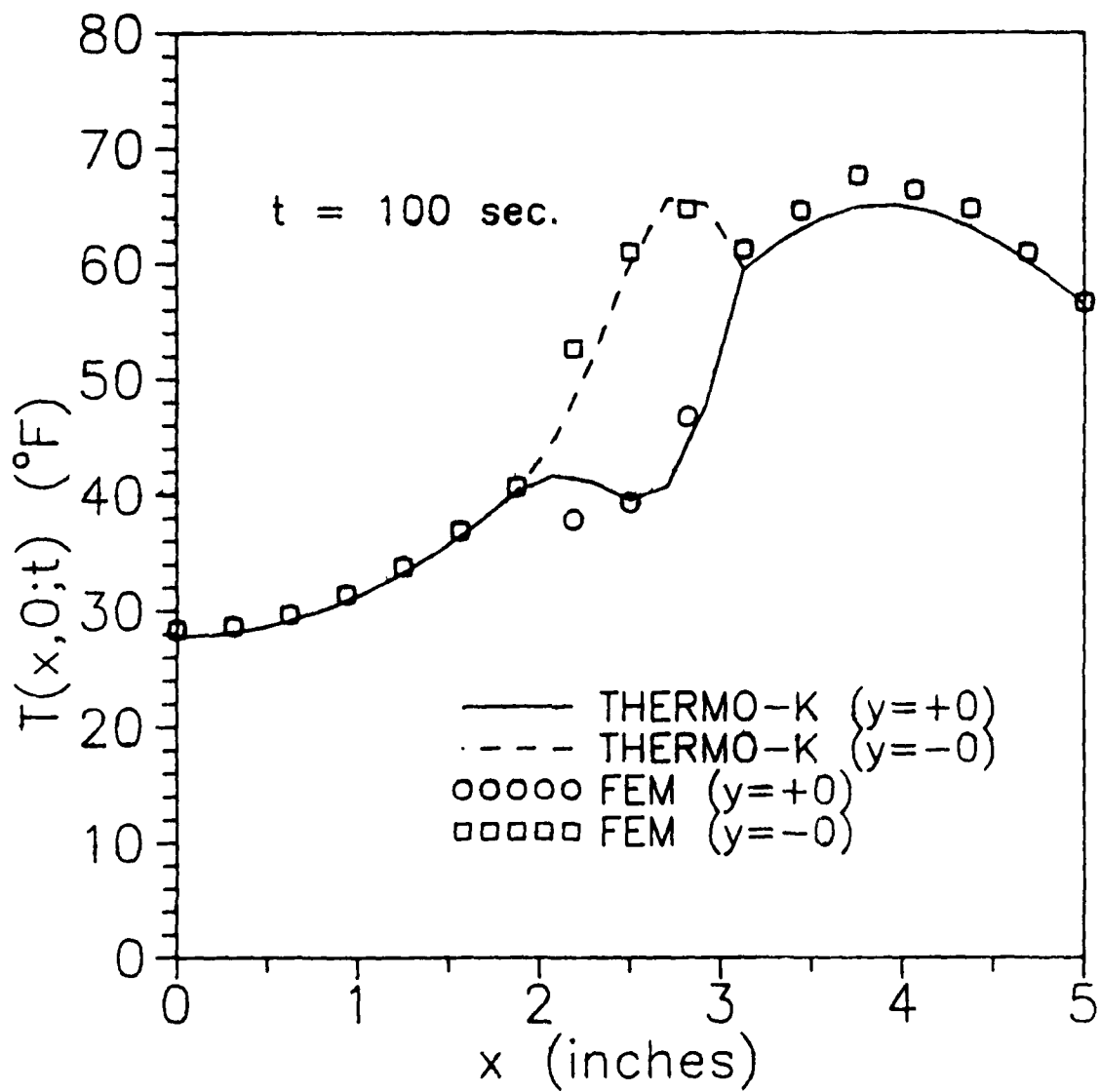


Figure 6-8. Comparison of Temperature at $y = 0$, $t = 100$ sec

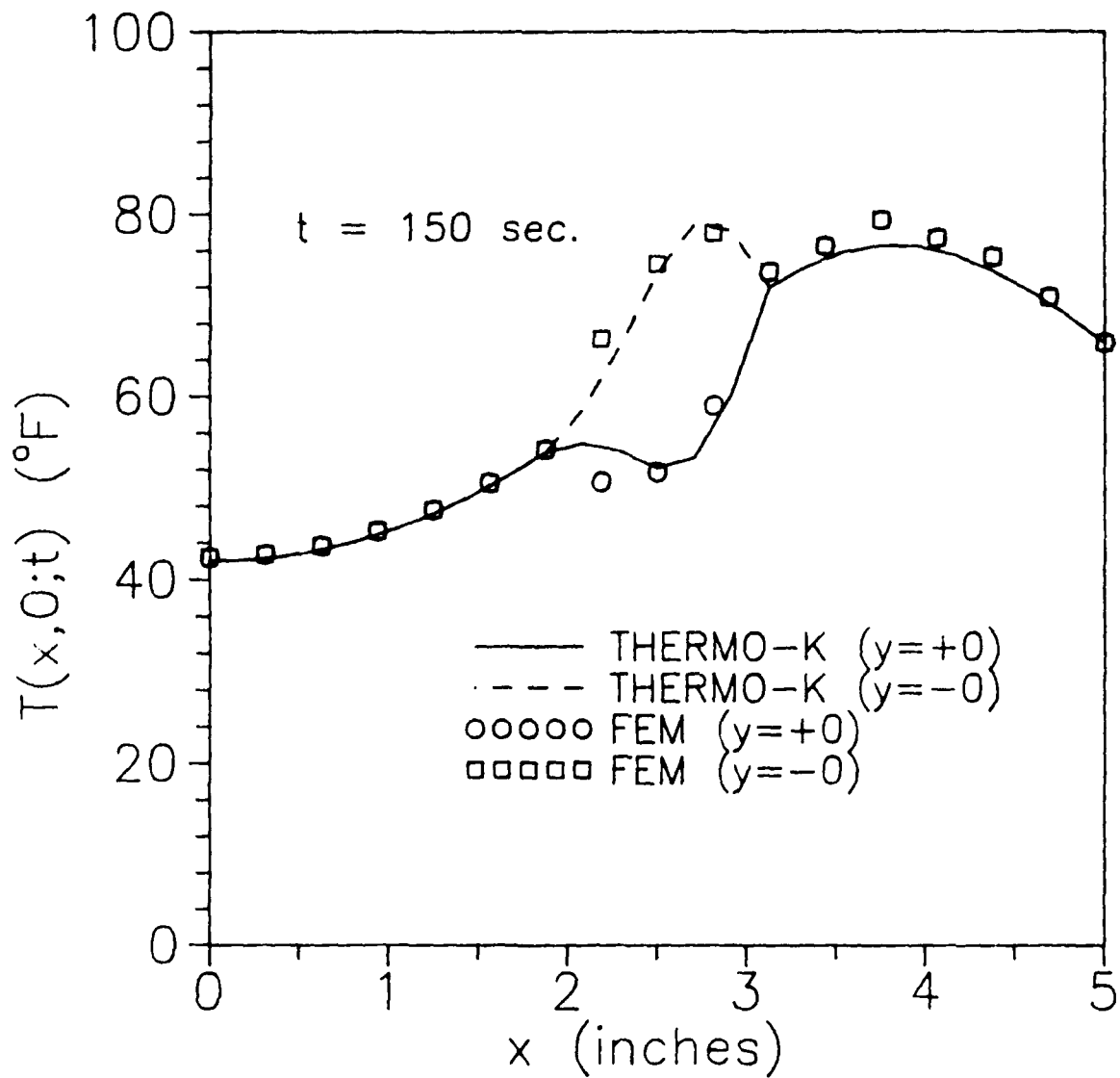


Figure 6-9. Comparison of Temperatures at $y = 0$, $t = 150 \text{ sec}$

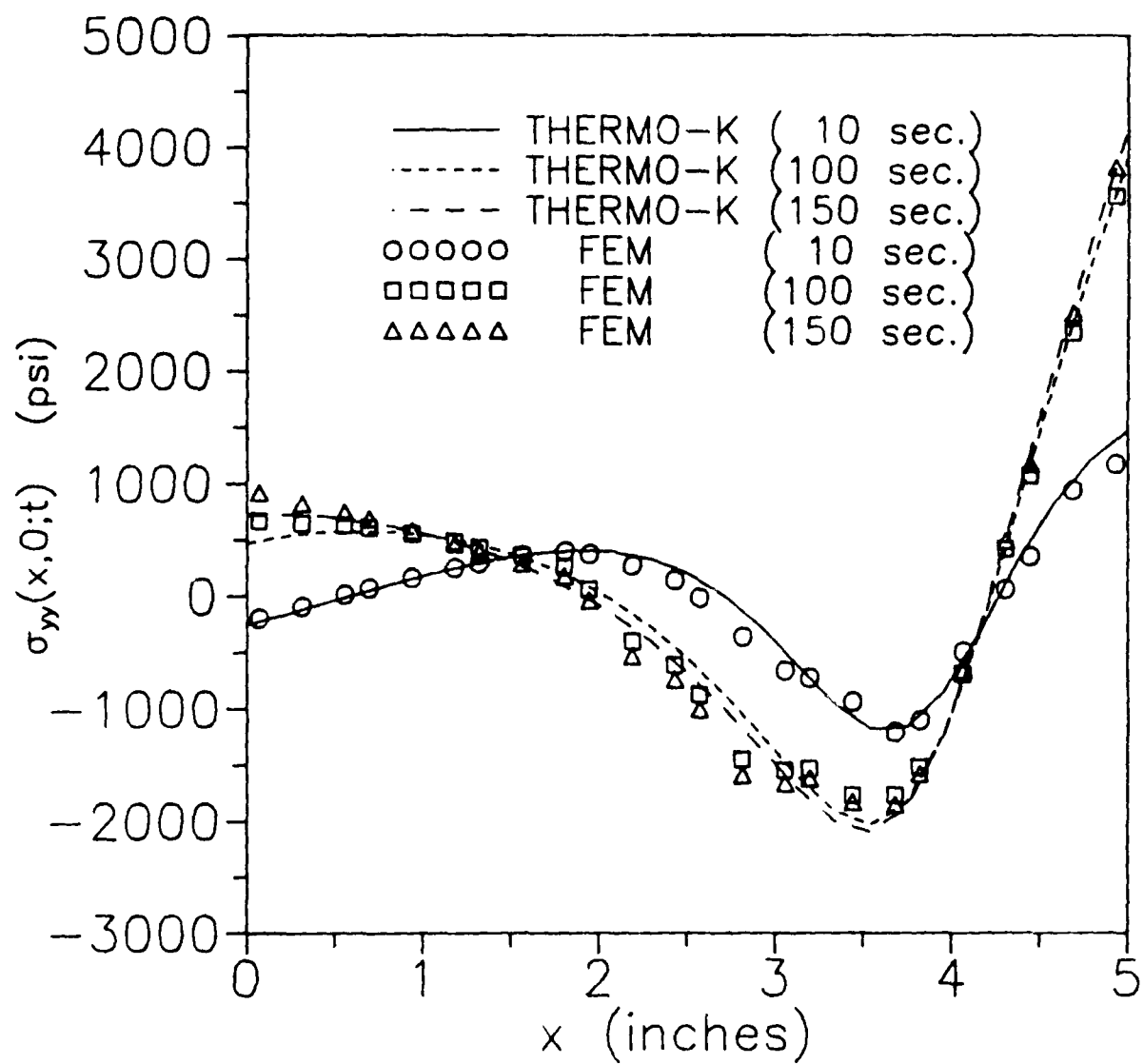


Figure 6-10. Comparison of Normal Stresses at $y = 0$

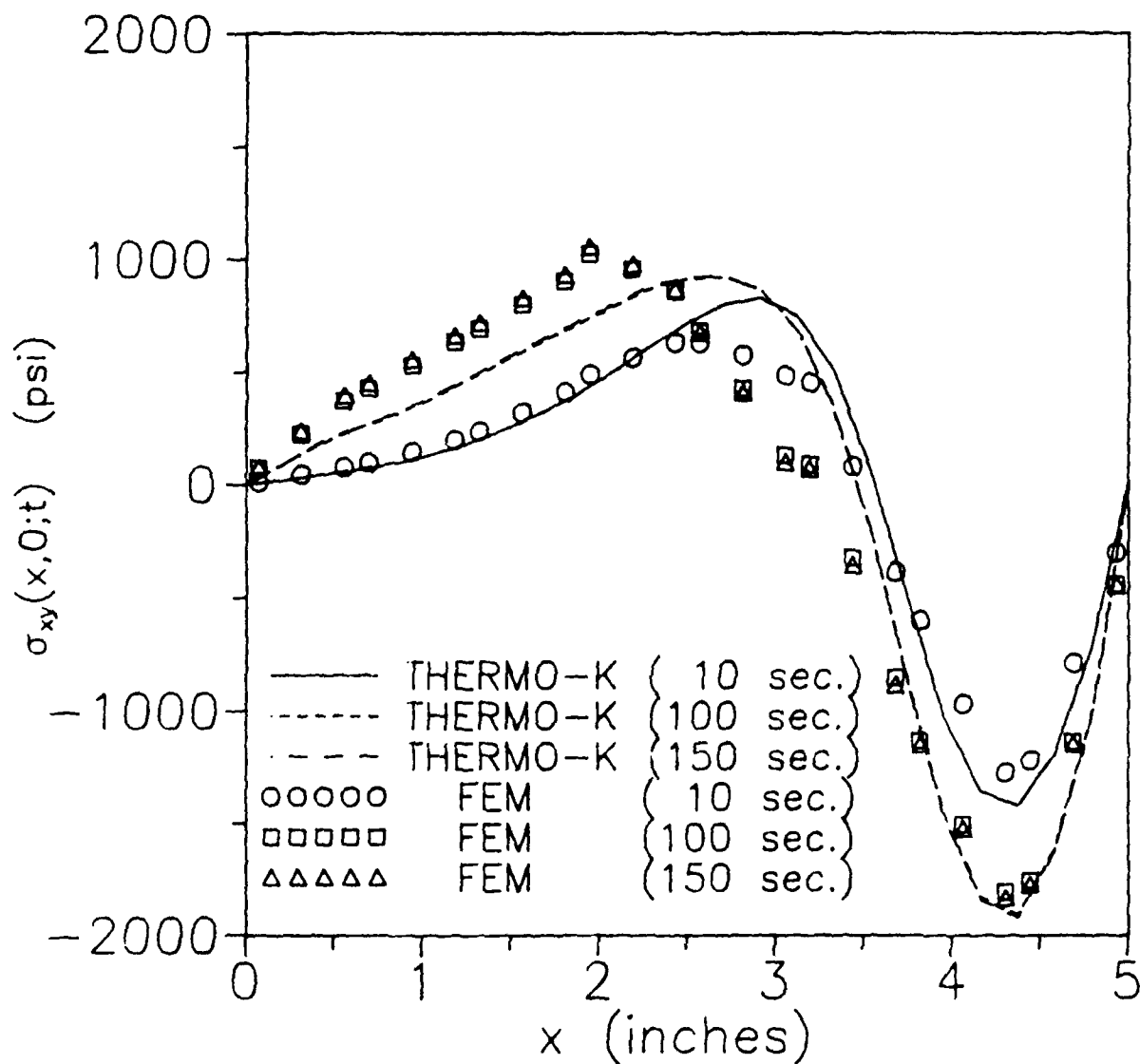


Figure 6-11. Comparison of Shear Stresses at $y = 0$

7.0 THEORETICAL BACKGROUND OF CRACK MODEL 6 - A SEMICIRCULAR SURFACE CRACK IN A HALF-SPACE

This section describes the theoretical basis for crack Model 6 - a semicircular surface crack in a semi-infinite space, i.e., as illustrated in Figure 7-1, a semicircular crack of radius a in a semi-infinite space, $y \geq 0$. The cracked semi-infinite space is subjected to point heat sources with arbitrary time history $Q(t)$ at any points (x', y', z') in the region of $y \geq 0$.

7.1 Assumptions

The following assumptions were made to simplify the problem:

- (a) The metallic materials are assumed to be isotropic, homogeneous, and linear elastic. Material properties are assumed to be temperature independent.
- (b) The rate of heat application is slow enough that the coupling terms and inertia terms in the general thermoelasticity equations can be neglected, i.e., it is assumed that the decoupled, quasi-static thermoelasticity applies.
- (c) The crack surfaces are assumed to be stress-free. The crack surfaces can be completely insulated, fully heat conductive, or partially heat conductive. Heat conductance coefficient h at the crack surfaces is also assumed to be constant throughout the entire temperature range.
- (d) It is assumed that the boundary surface of the semi-infinite space, $y=0$, is insulated.

7.2 Governing Equations

For a three-dimensional thermoelasticity problem as illustrated in Figure 7-1, the governing equations are

$$\xi \nabla^2 T = T_{,t} \quad (7-1)$$

$$\sigma_{ij,j} = 0 \quad (7-2)$$

$$\sigma_{ij} = 2G [\epsilon_{ij} + (\frac{\nu}{1-\nu}) \delta_{ij} \epsilon_{kk} - \alpha (\frac{1+\nu}{1-\nu}) \delta_{ij} T] \quad (7-3)$$

$$\epsilon_{ij} = (U_{i,j} + U_{j,i})/2 \quad (7-4)$$

and

$$\nabla^2 U_i + (\frac{1+\nu}{1-\nu}) U_{j,ji} = 2(\frac{1+\nu}{1-\nu}) \alpha T \quad (7-5)$$

where $T=T(x_1, x_2, x_3; t)$ is temperature distribution, t and x_i are time and Cartesian coordinates respectively, $\xi=(k/\rho c)$, k is heat conduction coefficients, ρ is mass density, c is heat capacity, U_i are displacements, α is coefficient of thermal expansion, and G and ν are shear modulus and Poisson's ratio, respectively.

Nominal stress distributions derived from these equations are used to develop stress intensity factors via the influence function approach described in the next subsection.

7.3 Influence Functions for Stress Intensity Factors

For any cracked structure, crack tip stress intensity factors can be determined by integrating the product of the stresses at the crack location in an uncracked structure and an influence function (or weight function) (Buecker, 1973). That is, for a

surface crack as shown in Figure 7-1, the stress intensity factor can be calculated by

$$K_I(\theta) = \int_0^\pi \int_0^a \sigma_{zz}(\bar{r}, \bar{\theta}, 0; t) m_1(\bar{r}, \bar{\theta}; \theta) \bar{r} d\bar{r} d\bar{\theta} \quad (7-6)$$

$$K_{II}(\theta) = \int_0^\pi \int_0^a [\sigma_{zr}(\bar{r}, \bar{\theta}, 0; t) m_{2r}(\bar{r}, \bar{\theta}; \theta) + \sigma_{z\theta}(\bar{r}, \bar{\theta}, 0; t) m_{2\theta}(\bar{r}, \bar{\theta}; \theta)] \bar{r} d\bar{r} d\bar{\theta} \quad (7-7)$$

$$K_{III}(\theta) = \int_0^\pi \int_0^a [\sigma_{zr}(\bar{r}, \bar{\theta}, 0; t) m_{3r}(\bar{r}, \bar{\theta}; \theta) + \sigma_{z\theta}(\bar{r}, \bar{\theta}, 0; t) m_{3\theta}(\bar{r}, \bar{\theta}; \theta)] \bar{r} d\bar{r} d\bar{\theta} \quad (7-8)$$

where $m_1(\bar{r}, \bar{\theta}; \theta)$, $m_{2r}(\bar{r}, \bar{\theta}; \theta)$, $m_{2\theta}(\bar{r}, \bar{\theta}; \theta)$, $m_{3r}(\bar{r}, \bar{\theta}; \theta)$, and $m_{3\theta}(\bar{r}, \bar{\theta}; \theta)$ are influence functions, (r, θ, z) are cylindrical coordinates shown in Figure 7-1, and σ_{zz} , σ_{zr} , and $\sigma_{z\theta}$ are the normal stress and shear stresses at the crack region in an identical but uncracked half-space which is under the same temperature distribution as the cracked structure. Physically, as illustrated in Figure 7-2(a), $m_1(\bar{r}, \bar{\theta}; \theta)$ is the Mode I stress intensity factor at crack tip location (a, θ) due to a pair of equal in magnitude but opposite in direction unit normal forces (in z -direction) applied at point $(\bar{r}, \bar{\theta})$ of the crack surface. Similarly, as illustrated in Figures 7-2(b), $m_{2r}(\bar{r}, \bar{\theta}; \theta)$ and $m_{3r}(\bar{r}, \bar{\theta}; \theta)$ are, respectively, Mode II and Mode III stress intensity factors at crack tip location (a, θ) due to a pair of equal in magnitude but opposite in direction unit radial shear forces (in the r -direction) applied at point $(\bar{r}, \bar{\theta})$ of the crack

surface. And, as shown in Figure 7-2(c), $m_{2\theta}(\bar{r}, \bar{\theta}; \theta)$ and $m_{3\theta}(\bar{r}, \bar{\theta}; \theta)$ are, respectively, Mode II and Mode III stress intensity factors at crack tip location (a, θ) due to a pair of equal in magnitude but opposite in direction unit tangential shear forces (in the θ -direction) applied at point $(\bar{r}, \bar{\theta})$ of the crack surface.

7.3.1 Influence Function m_1

To derive the influence functions $m_1(\bar{r}, \bar{\theta}; \theta)$, the following iterative procedure has been developed:

Step I-0 - Initiation

We first let $L=0$, and

$$\bar{\sigma}_{zz}^{(L)}(r, \theta, 0) = \frac{1}{r} \delta(r-\bar{r}) \delta(\theta-\bar{\theta}) \quad (7-9)$$

$$\bar{\sigma}_{rz}^{(L)}(r, \theta, 0) = \bar{\sigma}_{\theta z}^{(L)}(r, \theta, 0) = 0 \quad (7-10)$$

where $\delta(r)$ and $\delta(\theta)$ are Delta functions in r - and θ -directions, respectively.

Step I-1 - Penny-Shaped Crack Solutions

We then calculate stress intensity factors for a penny-shaped crack in an infinite space subjected to two symmetric pairs of concentrated normal forces on its crack surface. That is, we consider a problem which consists of the cracked half-space shown in Figure 7-2(a) as well as its mirror image with respect to the x - z plane. Stress intensity factor solution for a penny-shaped crack in an infinite space subjected to symmetric pairs of

concentrated normal forces, i.e., if one pair is at $(\bar{r}, \bar{\theta})$, another pair of the same magnitude must be at $(\bar{r}, -\bar{\theta})$, has been given by Sih (1973) as

$$K_I^{(L)}(\theta) = \int_0^\pi \int_0^a \hat{m}_1(\hat{r}, \hat{\theta}; \theta) \bar{\sigma}_{zz}^{(L)}(\hat{r}, \hat{\theta}, 0) \hat{r} d\hat{r} d\hat{\theta} \quad (7-11)$$

$$K_{II}^{(L)}(\theta) = K_{III}^{(L)}(\theta) = 0 \quad (7-12)$$

where

$$\hat{m}_1(\hat{r}, \hat{\theta}; \theta) = \frac{2}{\pi a \sqrt{\pi a (1-r_o)(1+r_o)}} (1 + 2 \sum_{n=1}^{\infty} [r_o^n \cos(n\hat{\theta}) \cos(n\theta)]) \quad (7-13)$$

$$r_o = \frac{\hat{r}}{a} \quad (7-14)$$

Step I-2 - Stresses at Surface, $y=0$, (increase L by 1)

It is obvious that stress solutions for a penny-shaped crack in an infinite space subjected to the concentrated crack surface normal loads do not satisfy the stress-free boundary at the free surface $y=0$ for the semicircular surface crack problem. In fact, by using the methodology developed by Bell (1979), it can be shown that, for a penny-shaped crack in an infinite space subjected to crack surface loads symmetric to x - z plane, stresses at the symmetry plane $y=0$ are

$$\bar{\sigma}_{yx}^{(L)}(x, 0, z) = \bar{\sigma}_{yz}^{(L)}(x, 0, z) = 0 \quad (7-15)$$

$$\bar{\sigma}_{YY}^{(L)}(x, 0, z) = \int_0^\pi \int_0^a \Omega_1(x, z; \hat{r}, \hat{\theta}) \bar{\sigma}_{zz}^{(L-1)}(\hat{r}, \hat{\theta}, 0) \hat{r} d\hat{r} d\hat{\theta} \quad (7-16)$$

where G and ν are shear modulus and Poisson's ratio, respectively, of the material,

$$\Omega_i(x, z; \hat{r}, \hat{\theta}) = \sum_{m=0}^{\infty} \sum_{k=0}^{\infty} \left[\left(\frac{x}{|x|} \right)^m a_{m,k,i} F_{m,k,i}^{\theta\theta} \left(\frac{|x|}{a}, \frac{z}{a} \right) \right] \quad (7-17)$$

$$a_{m,k,1} = 2(m+2k+\frac{3}{2}) \sum_{n=1}^{\infty} \frac{\alpha_{m,n}}{j_{m,n}^{3/2}} J_{m+2k+3/2}(j_{m,n}) \quad (7-18)$$

$$a_{m,k,2} = 2(m+2k+\frac{5}{2}) \sum_{n=1}^{\infty} \frac{\beta_{m,n}}{j_{m+1,n}^{3/2}} J_{m+2k+5/2}(j_{m+1,n}) \quad (7-19)$$

$$a_{m,k,3} = 2(m+2k+\frac{1}{2}) \sum_{n=1}^{\infty} \frac{\gamma_{m,n}}{j_{m-1,n}^{3/2}} J_{m+2k+1/2}(j_{m-1,n}) \quad (7-20)$$

$$\alpha_{m,n} = \frac{4}{\pi a^2 J_{m+1}^2(j_{m,n})} J_m(j_{m,n} r_0) \cos(m\hat{\theta}) \quad (7-21)$$

$$\beta_{m,n} = \frac{4}{\pi a J_{m+1}^2(j_{m,n})} J_m(j_{m,n} r_0) \sin(m\hat{\theta}) \quad (7-22)$$

$$\gamma_{m,n} = \alpha_{m,n} \quad (7-23)$$

$$F_{m,k,1}^{\theta\theta}(\rho, \zeta) = -2\nu I_{m,m+2k+1}^1 + \frac{m-1}{\rho} U_{m,k,1} + \frac{m+1}{\rho} V_{m,k,1} \quad (7-24)$$

$$F_{m,k,2}^{\theta\theta}(\rho, \zeta) = \frac{\zeta}{|\zeta|} \nu I_{m,m+2k+2}^1 + \frac{m+1}{\rho} U_{m,k,2} + \frac{m-1}{\rho} V_{m,k,2} \quad (7-25)$$

$$F_{m,k,3}^{\theta\theta}(\rho, \zeta) = \frac{\zeta}{|\zeta|} b_k \nu I_{m,m+2k}^1 + \frac{m+1}{\rho} U_{m,k,3} + \frac{m-1}{\rho} V_{m,k,3} \quad (7-26)$$

$$U_{m,k,1}(\rho, \zeta) = -\frac{1}{2} [(1-2\nu) I_{m+1,m+2k+1}^0 - |\zeta| I_{m+1,m+2k+1}^1] \quad (7-27)$$

$$U_{m,k,2}(\rho, \zeta) = \frac{\zeta}{2|\zeta|} [(2-\nu) I_{m+1,m+2k+2}^0 - \frac{1}{2} |\zeta| I_{m+1,m+2k+2}^1] \quad (7-28)$$

$$U_{m,k,3}(\rho, \zeta) = -\frac{\zeta}{|\zeta|} I_{m+1,m+2k}^0 + \frac{\zeta}{2|\zeta|} b_k [(2-\nu) I_{m+1,m+2k}^0 - \frac{|\zeta|}{2} I_{m+1,m+2k}^1] \quad (7-29)$$

$$V_{m,k,1}(\rho, \zeta) = -\frac{1}{2} [(1-2\nu) I_{m-1,m+2k+1}^0 - |\zeta| I_{m-1,m+2k+1}^1] \quad (7-30)$$

$$V_{m,k,2}(\rho, \zeta) = \frac{-\zeta}{2|\zeta|} [\nu I_{m-1,m+2k+2}^0 + \frac{1}{2} |\zeta| I_{m-1,m+2k+2}^1] \quad (7-31)$$

$$V_{m,k,3}(\rho, \zeta) = \frac{\zeta}{|\zeta|} I_{m-1,m+2k}^0 - \frac{\zeta}{2|\zeta|} b_k [(2-\nu) I_{m-1,m+2k}^0 + \frac{|\zeta|}{2} I_{m-1,m+2k}^1] \quad (7-32)$$

$$b_0 = \frac{2}{2-\nu}, \quad b_k = 1 \quad (k \geq 1) \quad (7-33)$$

$$I_{M,N}^n(\rho, \zeta) = \int_0^\infty e^{-t|\zeta|} t^{n-1/2} J_M(\rho t) J_{N+1/2}(t) dt \quad (7-34)$$

$r_0 = \frac{r}{a}$, $\rho = \frac{|x|}{a}$, $\zeta = \frac{z}{a}$, and $j_{m,n}$ is the n -th positive root of $J_m(z)$, i.e.,

$$J_m(j_{m,n}) = 0, \quad j_{m,n} > 0 \quad (7-35)$$

It is seen from the above equations that calculation of the stresses at the symmetry plane $y=0$ for the penny-shaped crack problem hinges on the evaluation of the integral $I_{M,N}^n$ given in Equation (7-34). By formula 6.626 of Gradshteyn and Ryzhik (1980), Equation (7-34) can be rewritten as

$$I_{M,N}^n(\rho, \zeta) = \frac{\rho^M}{\Gamma(N+3/2)} 2^{-N-M-1/2} |\zeta|^{-n-M-N-1} \sum_{m=0}^{\infty} [(-1)^m \cdot \left(\frac{\rho}{4\zeta}\right)^{2m} \frac{\Gamma(2m+n+M+N+1)}{m! \Gamma(m+M+1)} F(-m, -M-m; N+\frac{3}{2}; \frac{1}{\rho^2})] \quad (7-36)$$

where $\Gamma(z)$ is a Gamma function and F is a hypergeometric function defined as

$$F(\alpha, \beta; \gamma; z) = 1 + \frac{\alpha \cdot \beta}{\gamma \cdot 1} z + \frac{\alpha(\alpha+1)\beta(\beta+1)}{\gamma(\gamma+1) \cdot 1 \cdot 2} z^2 + \frac{\alpha(\alpha+1)(\alpha+2)\beta(\beta+1)(\beta+2)}{\gamma(\gamma+1)(\gamma+2) \cdot 1 \cdot 2 \cdot 3} z^3 + \dots \quad (7-37)$$

Step I-3 - Stresses in an Uncracked Half-Space

The non-zero stresses on the symmetry plane $y=0$ given in Equation (7-16) can be eliminated by adding a complementary stress solution for an uncracked half-space subjected to normal loads, which are the negative of the normal stresses given by Equation (7-16), at its surface $y=0$. This complementary problem is often called as the Boussinesq's problem, of which solution can usually be found in the text books (e.g., Timoshenko and Goodier, 1970). It can be shown that the resulting complementary stresses $\bar{\sigma}_{ij}^{(L)}$ at plane $z=0$ are as follows:

$$\begin{aligned} \bar{\sigma}_{zz}^{(L)}(x, y, 0) = & \frac{(1-2\nu)}{2\pi} \int_{-\infty}^{\infty} \int_{-\infty}^{\infty} \bar{\sigma}_{yy}^{(L)}(\hat{x}, 0, \hat{z}) \left(\left[\frac{(x-\hat{x})^2 - \hat{z}^2}{r^4} \right] \right. \\ & \left. [-1 + (r^2 + y^2)^{-1/2}] + \frac{(x-\hat{x})^2 y}{r^2} (r^2 + y^2)^{-3/2} \right) d\hat{x} d\hat{z} \\ & - \frac{3}{2\pi} \int_{-\infty}^{\infty} \int_{-\infty}^{\infty} \bar{\sigma}_{yy}^{(L)}(\hat{x}, 0, \hat{z}) y \hat{z}^2 (r^2 + y^2)^{-5/2} d\hat{x} d\hat{z} \end{aligned} \quad (7-38)$$

$$\begin{aligned} \bar{\sigma}_{xz}^{(L)}(x, y, 0) = & \frac{(1-2\nu)}{2\pi} \int_{-\infty}^{\infty} \int_{-\infty}^{\infty} \bar{\sigma}_{yy}^{(L)}(\hat{x}, 0, \hat{z}) \left(\frac{-2(x-\hat{x})\hat{z}}{r^4} \right) \\ & [1 - y(r^2 + y^2)^{-1/2}] + \frac{(x-\hat{x}) y \hat{z}}{r^2} (r^2 + y^2)^{-3/2} d\hat{x} d\hat{z} \\ & + \frac{3}{2\pi} \int_{-\infty}^{\infty} \int_{-\infty}^{\infty} \bar{\sigma}_{yy}^{(L)}(\hat{x}, 0, \hat{z}) (x-\hat{x}) y \hat{z} (r^2 + y^2)^{-5/2} d\hat{x} d\hat{z} \end{aligned} \quad (7-39)$$

$$\bar{\sigma}_{yz}^{(L)}(x, y, 0) = \frac{3}{2\pi} \int_{-\infty}^{\infty} \int_{-\infty}^{\infty} \left[\bar{\sigma}_{yy}^{(L)}(\hat{x}, 0, \hat{z}) y^2 \hat{z} (r^2 + y^2)^{-5/2} \right] d\hat{x} d\hat{z} \quad (7-40)$$

where $\bar{\sigma}_{yy}^{(L)}(\hat{x}, 0, \hat{z})$ are the normal stresses calculated from Equation (7-16), and

$$r^2 = (x - \hat{x})^2 + \hat{z}^2 \quad (7-41)$$

Step I-4 Check Convergence

If the residual crack surface stresses $\bar{\sigma}_{ij}^{(L)}$ calculated in Step I-3 satisfy the preset convergence criterion (1% difference is used in this study as the convergence criterion), then calculate the influence functions m_1 as follows:

$$m_1(\bar{r}, \bar{\theta}; \theta) = \sum_{j=0}^{L-1} K_I^{(j)} \quad (7-42)$$

and stop the iteration here, otherwise go to Step I-1 and repeat Step I-1 to Step I-4.

7.3.2 Influence Functions m_{2r} and m_{3r}

Similarly, an iterative procedure for calculating m_{2r} , and m_{3r} can be developed as follows.

Step II-0 - Initiation

We first let $L=0$, and

$$\bar{\sigma}_{rz}^{(L)}(r, \theta, 0) = \frac{1}{r} \delta(r - \bar{r}) \delta(\theta - \bar{\theta}) \quad (7-43)$$

$$\bar{\sigma}_{zz}^{(L)}(r, \theta, 0) = \bar{\sigma}_{\theta z}^{(L)}(r, \theta, 0) = 0 \quad (7-44)$$

where $\delta(r)$ and $\delta(\theta)$ are Delta functions in r - and θ directions, respectively.

Step II-1 - Penny-Shaped Crack Solutions

We then calculate stress intensity factors for a penny-shaped crack in an infinite space subjected to two pairs of concentrated radial shear forces on its crack surface. That is, we consider a problem which consists of the cracked half-space shown in Figure 7-2(b) as well as its mirror image with respect to the x - z plane. Stress intensity factor solution for a penny-shaped crack in an infinite space subjected to pairs of symmetric concentrated radial shear forces, i.e., if one pair is at $(\hat{r}, \hat{\theta})$, another pair of the same magnitude must be at $(\hat{r}, -\hat{\theta})$, has been given by Sih (1973) as

$$K_I^{(L)}(\theta) = 0 \quad (7-45)$$

$$K_{II}^{(L)}(\theta) = \int_0^{2\pi} \int_0^a \hat{m}_{2r}(\hat{r}, \hat{\theta}; \theta) \bar{\sigma}_{zr}^{(L)}(\hat{r}, \hat{\theta}, 0) \hat{r} d\hat{r} d\hat{\theta} \quad (7-46)$$

$$K_{III}^{(L)}(\theta) = \int_0^{2\pi} \int_0^a \hat{m}_{3r}(\hat{r}, \hat{\theta}; \theta) \bar{\sigma}_{zr}^{(L)}(\hat{r}, \hat{\theta}, 0) \hat{r} d\hat{r} d\hat{\theta} \quad (7-47)$$

where

$$\hat{m}_{2r}(\hat{r}, \hat{\theta}; \theta) = \frac{2}{\pi a(2-\nu) \sqrt{\pi a(1-r_o)(1+r_o)}} \left((2-\nu)r_o + \right. \\ \left. 2 \sum_{n=1}^{\infty} [1+n\nu+(1-\nu-n\nu)r_o^2] r_o^{n-1} \cos(n\hat{\theta}) \cos(n\theta) \right) \quad (7-48)$$

$$\hat{m}_{3r}(\hat{r}, \hat{\theta}; \theta) = \frac{-4\sqrt{(1+r_0)(1-r_0)}}{\pi a(2-\nu)\sqrt{\pi a}} \sum_{n=1}^{\infty} [1-(1+n)\nu] r_0^{n-1} \cos(n\hat{\theta}) \cos(n\theta) \quad (7-49)$$

and r_0 is defined in Equation (7-14).

Step II-2 - Stresses at Surface, $y=0$, (increase L by 1)

It is obvious that stress solutions for a penny-shaped crack in an infinite space subjected to concentrated crack surface loads do not satisfy the stress-free boundary condition at the free surface $y=0$ for the semicircular surface crack problem. In fact, by using the methodology developed by Bell (1979), it can be shown that, for a penny-shaped crack in an infinite space subjected to crack surface radial shear loads symmetric to x - z plane loads on crack surface, stresses at the symmetry plane $y=0$ are

$$\bar{\sigma}_{yx}^{(L)}(x, 0, z) = \bar{\sigma}_{yz}^{(L)}(x, 0, z) = 0 \quad (7-50)$$

$$\bar{\sigma}_{yy}^{(L)}(x, 0, z) = \int_0^{2\pi} \int_0^a \Omega_3(x, z; \hat{r}, \hat{\theta}) \bar{\sigma}_{zr}^{(L-1)}(\hat{r}, \hat{\theta}, 0) \hat{r} d\hat{r} d\hat{\theta} \quad (7-51)$$

where G and ν are shear modulus and Poisson's ratio, respectively, of the material, and $\Omega_3(x, z; \hat{r}, \hat{\theta})$ is defined in Equation (7-17).

Step II-3 - Stresses in an Uncracked Half-Space

It can be shown that complementary stresses $\bar{\sigma}_{ij}^{(L)}$ at plane $z=0$ are evaluated by Equations (7-38) to (7-40) in which $\bar{\sigma}_{yy}^{(L)}(\hat{x}, 0, \hat{z})$ are the normal stresses calculated from Equation (7-51).

Step II-4 Check Convergence

If the residual crack surface stresses $\bar{\sigma}_{ij}^{(L)}$ calculated in Step II-3 satisfy the preset convergence criterion (1% difference is used in this study as the convergence criterion), then calculate the influence functions m_{2r} and m_{3r} as follows:

$$m_{2r}(\bar{r}, \bar{\theta}; \theta) = \sum_{j=0}^{L-1} K_{II}^{(j)} \quad (7-52)$$

$$m_{3r}(\bar{r}, \bar{\theta}; \theta) = \sum_{j=0}^{L-1} K_{III}^{(j)} \quad (7-53)$$

and stop iteration here, otherwise go to Step II-1 and repeat Step II-1 to Step II-4.

7.3.3 Influence Functions $m_{2\theta}$ and $m_{3\theta}$

An iterative procedure for calculating $m_{2\theta}$ and $m_{3\theta}$ can be developed as follows.

Step III-0 - Initiation

We first let $L=0$, and

$$\bar{\sigma}_{z\theta}^{(L)}(r, \theta, 0) = \frac{1}{r} \delta(r-\bar{r}) \delta(\theta-\bar{\theta}) \quad (7-54)$$

$$\bar{\sigma}_{zz}^{(L)}(r, \theta, 0) = \bar{\sigma}_{zr}^{(L)}(r, \theta, 0) = 0 \quad (7-55)$$

where $\delta(r)$ and $\delta(\theta)$ are Delta functions in r - and θ -directions, respectively.

Step III-1 - Penny-Shaped Crack Solutions

We then calculate stress intensity factors for a penny-shaped crack in an infinite space subjected to two pairs of concentrated tangential shear forces on its crack surface. That is, we consider a problem which consists of the cracked half-space shown in Figure 7-2(c) as well as its mirror image with respect to the x - z plane. Stress intensity factor solution for a penny-shaped crack in an infinite space subjected to pairs of symmetric concentrated tangential shear forces, (i.e., if one pair is at $(\hat{r}, \hat{\theta})$, another pair of the same magnitude but in reverse direction must be at $(\hat{r}, -\hat{\theta})$, has been given by Sih (1973) as:

$$K_I^{(L)}(\theta) = 0 \quad (7-56)$$

$$K_{II}^{(L)}(\theta) = \int_0^{2\pi} \int_0^a \hat{m}_{2\theta}(\hat{r}, \hat{\theta}; \theta) \bar{\sigma}_{z\theta}^{(L)}(\hat{r}, \hat{\theta}, 0) \hat{r} \, d\hat{r} \, d\hat{\theta} \quad (7-57)$$

$$K_{III}^{(L)}(\theta) = \int_0^{2\pi} \int_0^a \hat{m}_{3\theta}(\hat{r}, \hat{\theta}; \theta) \bar{\sigma}_{z\theta}^{(L)}(\hat{r}, \hat{\theta}, 0) \hat{r} \, d\hat{r} \, d\hat{\theta} \quad (7-58)$$

where

$$\hat{m}_{2\theta}(\hat{r}, \hat{\theta}; \theta) = \frac{4}{\pi a(2-\nu) \sqrt{\pi a(1-r_0)(1+r_0)}}$$

$$\sum_{n=1}^{\infty} [1-n\nu+(1+n\nu)r_0^2]r_0^{n-1}\sin(n\hat{\theta})\cos(n\theta) \quad (7-59)$$

$$\hat{m}_{3\theta}(\hat{r}, \hat{\theta}; \theta) = \frac{4}{\pi a(2-\nu)\sqrt{\pi a(1-r_0)(1+r_0)}}$$

$$\sum_{n=1}^{\infty} [1+(1+n)\nu+(1+n\nu)r_0^2]r_0^{n-1}\sin(n\hat{\theta})\sin(n\theta) \quad (7-60)$$

where r_0 is defined in Equation (7-14).

Step III-2 - Stresses at Surface, $y=0$, (increase L by 1)

It is obvious that stress solutions for a penny-shaped crack in an infinite space subjected to concentrated crack surface loads do not satisfy the stress-free boundary condition at the free surface $y=0$ for the semicircular surface crack problem. In fact, by using the methodology developed by Bell (1979), it can be shown that, for a penny-shaped crack in an infinite space subjected to crack surface tangential shear loads symmetric to x-z plane, stresses at the symmetry plane $y=0$ are

$$\bar{\sigma}_{yx}^{(L)}(x, 0, z) = \bar{\sigma}_{yz}^{(L)}(x, 0, z) = 0 \quad (7-61)$$

$$\bar{\sigma}_{yy}^{(L)}(x, 0, z) = \int_0^{2\pi} \int_0^a \Omega_2(x, z; \hat{r}, \hat{\theta}) \bar{\sigma}_{z\theta}^{(L-1)}(\hat{r}, \hat{\theta}, 0) \hat{r} d\hat{r} d\hat{\theta} \quad (7-62)$$

where G and ν are shear modulus and Poisson's ratio, respectively, of the material, and $\Omega_2(x, z; \hat{r}, \hat{\theta})$ is defined in Equation (7-17).

Step III-3 - Stresses in an Uncracked Half-Space

It can be shown that complementary stresses $\bar{\sigma}_{ij}^{(L)}$ at plane $z=0$ are evaluated by Equations (7-38) to (7-40) in which $\bar{\sigma}_{yy}^{(L)}(\hat{x}, 0, \hat{z})$ are the normal stresses calculated by Equation (7-62).

Step III-4 Check Convergence

If the residual crack surface stresses $\bar{\sigma}_{ij}^{(L)}$ calculated in Step III-3 satisfy the preset convergence criterion (1% difference is used in this study as the convergence criterion), then calculate the influence functions m_{2r} and m_{3r} as follows:

$$m_{2\theta}(\bar{r}, \bar{\theta}; \theta) = \sum_{j=0}^{L-1} K_{II}^{(j)} \quad (7-63)$$

$$m_{3\theta}(\bar{r}, \bar{\theta}; \theta) = \sum_{j=0}^{L-1} K_{III}^{(j)} \quad (7-64)$$

and stop the iteration here, otherwise go to Step III-1 and repeat Step III-1 to Step III-4.

7.4 Principle of Superposition

In general, as shown in Figure 7-1, there may be multiple heat sources (or sinks) within the half-space which will cause thermal stresses and stress intensity factors at crack tips in the structure. Since the problem is linear, it is easily demonstrated that total stress intensity factor can be calculated as the sum of the stress intensity factors caused by each individual heat source or sink, acting independently. That is

$$K(t) = \sum_i [K(t)]_i \quad (7-65)$$

where $K(t)$ is the total stress intensity factor and $[K(t)]_i$ is the stress intensity factor due to the i^{th} heat source.

7.5 Green's Function Concept for Time Integration

In Equation (7-65), the stress intensity factor $[K(t)]_i$ caused by each individual heat source can be solved with the concept of Green's function integration. As illustrated in Figure 7-3, the stress intensity factor due to a heat source of intensity $Q_i(t)$ can be calculated by

$$[K(t)]_i = \int_0^t Q_i(\tau) G_i(t-\tau) d\tau \quad (\text{no summation}) \quad (7-66)$$

where $G_i(t)$ is the stress intensity factors due to a Delta function $\delta(t)$ heat source at the i^{th} heat source location.

As shown in Figure 7-3, in general, the Green's function $G_i(t)$ will decay and approach to zero after a decay period t_d . Therefore, the integration range in Equation (7-66) can be reduced from $(t-t_d)$ to t . Such a reduction in the integration range greatly increases the speed of the calculation because, instead of integrating for the entire time history, it is only necessary to integrate backwards from the present time t to $(t-t_d)$ as follows

$$[K(t)]_i = \int_{t-t_d}^t Q_i(\tau) G_i(t-\tau) d\tau \quad (7-67)$$

7.6 Green's Function for Fully Heat Conductive Cracks

Previous subsections of this section show that the stress intensity factors for these crack models can be easily obtained by Equations (7-6), (7-7), (7-8), (7-65), and (7-67) if the temperature and stress distributions and thereby the stress intensity factors at the crack tip, resulting from an instantaneous heat source (or sink) $Q\delta(t)$ at any arbitrary location (x',y',z') in the uncracked half-space (Figure 7-4), can be solved. The uncracked half-space shares the same temperature distribution as the cracked half-space. As the first step, we consider the problem of a fully heat conductive surface crack, i.e., in this subsection, it is assumed that heat flux can flow across the crack surfaces without any heat loss or resistance. Solutions for a more general, partially heat conductive crack will be discussed in the next subsection. However, as will be seen in the next subsection and as shown in Appendix A of this report, for a crack model with symmetry about its crack plane such as this crack model, crack surface heat conductivity will affect Mode II stress intensity factor solutions but not Mode I or Mode III stress intensity factor solutions. In other words, whether the crack surfaces are fully heat conductive, insulated, or partially heat conductive, the K_I and K_{III} solutions will remain the same for a semicircular surface crack in a half-space. Thus, if only Mode I or Mode III fractures are of major interest, the stress intensity factor solutions can be obtained by assuming the crack surfaces are fully heat conductive. The assumption of a fully heat conductive crack will greatly shorten the computation time for temperatures, thermal stresses, and stress intensity factors.

Since thermal stresses and stress intensity factors do not depend on the initial temperature of the solid, it is conveniently assumed that the initial temperature of the half-space is zero, i.e., $T(x,y,z;0)=0$. To solve for the Green's function of this crack model, the following boundary conditions need to be

satisfied in addition to the governing equations listed in Equations (7-1) to (7-5):

at $y = 0$,

$$kT_{,y}(x, 0, z; t) = 0 \quad (7-68)$$

$$\sigma_{yy}(x, 0, z; t) = 0 \quad (7-69)$$

$$\sigma_{yx}(x, 0, z; t) = \sigma_{yz}(x, 0, z; t) = 0 \quad (7-70)$$

at infinity

$$T(x, y, z; t) = 0 \quad (7-71)$$

$$\sigma_{ij}(x, y, z; t) = 0 \quad (7-72)$$

at $z=0$, $(x^2+y^2) \leq a^2$,

$$T(x, y, 0^+; t) = T(x, y, 0^-; t) \quad (7-73)$$

$$\sigma_{zz}(x, y, 0^+; t) = \sigma_{zz}(x, y, 0^-; t) \quad (7-74)$$

$$\sigma_{zx}(x, y, 0^+; t) = \sigma_{zx}(x, y, 0^-; t) \quad (7-75)$$

$$\sigma_{zy}(x, y, 0^+; t) = \sigma_{zy}(x, y, 0^-; t) \quad (7-76)$$

$$U_i(x, y, 0^+; t) = U_i(x, y, 0^-; t) \quad i = 1, 2, 3 \quad (7-77)$$

Temperature solution to the problem of a half-space with a fully heat conductive surface crack can be obtained by solving Equation (7-1) along with boundary conditions Equations (7-68), (7-71),

and (7-73). An analytical form of the temperature solution has been given by Carslaw and Jaeger (1959) as follows:

$$T(x,y,z;t) = \frac{Q}{8\rho c(\pi\xi t)^{3/2}} \sum_{i=1}^2 \exp\left(\frac{-R_i^2}{4\xi t}\right) \quad (7-78)$$

where ρ is mass density, c is heat capacity (specific heat), ξ is defined in Equation (7-1) and

$$R_1^2 = (x-x')^2 + (y-y')^2 + (z-z')^2 \quad (7-79)$$

$$R_2^2 = (x-x')^2 + (y+y')^2 + (z-z')^2 \quad (7-80)$$

Physically, Equation (7-78) represents the temperature solution in an infinite space due to two symmetric instantaneous heat sources, one at (x',y',z') and the other at $(x',-y',z')$. The next step is to solve for the stress distribution due to the temperature distribution of Equation (7-78) in an uncracked half-space. Boley and Weiner (1960) and Parkus (1968) have shown that a particular solution to the thermal stress problem can be expressed in terms of a thermoelastic potential ϕ as follows

$$\sigma_{xx} = 2G (\phi_{,xx} - \nabla^2 \phi) \quad (7-81)$$

$$\sigma_{yy} = 2G (\phi_{,yy} - \nabla^2 \phi) \quad (7-82)$$

$$\sigma_{zz} = 2G (\phi_{,zz} - \nabla^2 \phi) \quad (7-83)$$

$$\sigma_{xy} = 2G \phi_{,xy} \quad \sigma_{yz} = 2G \phi_{,yz} \quad \sigma_{zx} = 2G \phi_{,zx} \quad (7-84)$$

$$\phi(x,y,t) = \alpha\left(\frac{1+\nu}{1-\nu}\right)\xi \int_0^t T(x,y,z;\tau) d\tau + \phi_0 \quad (7-85)$$

where ϕ_0 is a function of x, y, z and t such that ϕ would remain finite as t approaches infinity. Substitution of Equation (7-78) into Equation (7-85) yields

$$\phi(x, y, z; t) = -\frac{\alpha Q(1+\nu)}{4\pi\rho cR(1-\nu)} \sum_{i=1}^2 \operatorname{erf}\left(\frac{R_i}{2\sqrt{\xi t}}\right) \quad (7-86)$$

where $\operatorname{erf}(z)$ is an error function and

$$R_{2,1}^2 = (x-x')^2 + (y\pm y')^2 + (z-z')^2 \quad (7-87)$$

In general, the particular solution ϕ shown in Equation (7-86) satisfies boundary conditions of Equations (7-70), (7-72), (7-74) (7-75), (7-76) and (7-77) but does not fulfill the stress-free boundary condition of Equation (7-69) at $y=0$. In other words, $\sigma_{yy}(x, 0, z; t)$ derived from the thermoelastic potential ϕ of Equation (7-86) does not vanish but equals to

$$\begin{aligned} \sigma'_{yy}(x, 0, z; t) = & \frac{(1+\nu) \alpha G Q}{(1-\nu) \pi \rho c R^2} \left(\left[1 - 3\left(\frac{y'}{R}\right)^2 \right] \left[\frac{1}{R} \operatorname{erf}\left(\frac{R}{2\sqrt{\xi t}}\right) - \right. \right. \\ & \left. \left. \frac{1}{\sqrt{\pi \xi t}} \exp\left(\frac{-R^2}{4\xi t}\right) \right] + \frac{(y'^2 - R^2)}{2\xi t \sqrt{\pi \xi t}} \exp\left(\frac{-R^2}{4\xi t}\right) \right) \end{aligned} \quad (7-88)$$

where

$$R^2 = (x-x')^2 + y'^2 + (z-z')^2 \quad (7-89)$$

Stresses at plane $z=0$ resulting from the thermoelastic potential ϕ given in Equation (7-86) are

$$\begin{aligned} \sigma'_{zz}(x, y, 0; t) = & \frac{(1+\nu) a G Q}{2(1-\nu) \pi \rho c} \sum_{i=1}^2 \frac{1}{R_i^2} \left(\left[1 - 3 \left(\frac{z'}{R_i} \right)^2 \right] \cdot \right. \\ & \left[\frac{1}{R_i} \operatorname{erf} \left(\frac{R_i}{2\sqrt{\xi t}} \right) - \frac{1}{\sqrt{\pi \xi t}} \exp \left(\frac{-R_i^2}{4\xi t} \right) \right] + \\ & \left. \frac{(z'^2 - R_i^2)}{2\xi t \sqrt{\pi \xi t}} \exp \left(\frac{-R_i^2}{4\xi t} \right) \right) \end{aligned} \quad (7-90)$$

$$\begin{aligned} \sigma'_{xz}(x, y, 0; t) = & - \frac{3(1+\nu) a G Q}{2(1-\nu) \pi \rho c} \sum_{i=1}^2 \frac{1}{R_i^4} (x-x') z' \cdot \\ & \left[\frac{1}{\sqrt{\pi \xi t}} \left(1 + \frac{R_i^2}{6\xi t} \right) \exp \left(\frac{-R_i^2}{4\xi t} \right) - \frac{1}{R_i} \operatorname{erf} \left(\frac{R_i}{2\sqrt{\xi t}} \right) \right] \end{aligned} \quad (7-91)$$

$$\begin{aligned} \sigma'_{yz}(x, y, 0; t) = & - \frac{3(1+\nu) a G Q}{2(1-\nu) \pi \rho c} \sum_{i=1}^2 \frac{1}{R_i^4} (y-y') z' \cdot \\ & \left[\frac{1}{\sqrt{\pi \xi t}} \left(1 + \frac{R_i^2}{6\xi t} \right) \exp \left(\frac{-R_i^2}{4\xi t} \right) - \frac{1}{R_i} \operatorname{erf} \left(\frac{R_i}{2\sqrt{\xi t}} \right) \right] \end{aligned} \quad (7-92)$$

where

$$R_{2,1}^2 = (x-x')^2 + (y \pm y')^2 + z'^2 \quad (7-93)$$

A complementary set of stresses σ''_{ij} can then be added to cancel out the non-zero surface stresses at $y=0$, i.e., stresses given in Equation (7-88). Similar to the approach used in the last

subsection, solutions to the Boussinesq's problem can be used to derive the following complementary stresses σ''_{ij} :

$$\begin{aligned} \sigma''_{zz}(x, y, 0) = & \frac{(1-2\nu)}{2\pi} \int_{-\infty}^{\infty} \int_{-\infty}^{\infty} \sigma'_{yy}(\hat{x}, 0, \hat{z}) \left(\frac{(x-\hat{x})^2 - \hat{z}^2}{r^4} \right. \\ & [-1 + (r^2 + y^2)^{-1/2}] + \frac{(x-\hat{x})^2 y}{r^2} (r^2 + y^2)^{-3/2} \Big) d\hat{x} d\hat{z} \\ & - \frac{3}{2\pi} \int_{-\infty}^{\infty} \int_{-\infty}^{\infty} \sigma'_{yy}(\hat{x}, 0, \hat{z}) y \hat{z}^2 (r^2 + y^2)^{-5/2} d\hat{x} d\hat{z} \end{aligned} \quad (7-94)$$

$$\begin{aligned} \sigma''_{xz}(x, y, 0) = & \frac{(1-2\nu)}{2\pi} \int_{-\infty}^{\infty} \int_{-\infty}^{\infty} \sigma'_{yy}(\hat{x}, 0, \hat{z}) \left(\frac{-2(x-\hat{x})^2 \hat{z}}{r^4} \right. \\ & [1 - y(r^2 + y^2)^{-1/2}] + \frac{(x-\hat{x}) y \hat{z}}{r^2} (r^2 + y^2)^{-3/2} \Big) d\hat{x} d\hat{z} \\ & + \frac{3}{2\pi} \int_{-\infty}^{\infty} \int_{-\infty}^{\infty} \sigma'_{yy}(\hat{x}, 0, \hat{z}) (x-\hat{x}) y \hat{z} (r^2 + y^2)^{-5/2} d\hat{x} d\hat{z} \end{aligned} \quad (7-95)$$

$$\sigma''_{yz}(x, y, 0) = \frac{3}{2\pi} \int_{-\infty}^{\infty} \int_{-\infty}^{\infty} [\sigma'_{yy}(\hat{x}, 0, \hat{z}) y^2 \hat{z} (r^2 + y^2)^{-5/2}] d\hat{x} d\hat{z} \quad (7-96)$$

where $\sigma'_{yy}(\hat{x}, 0, \hat{z})$ are the normal stresses calculated from Equation (7-88), and

$$r^2 = (x-\hat{x})^2 + \hat{z}^2 \quad (7-97)$$

To sum up this subsection, the Green's function for the stress intensity factors of a fully heat conductive semicircular crack

in a half-space are calculated by substituting the sum of the stress solutions given in Equations (7-90) to (7-92) and (7-94) to (7-96) and the influence functions given in Equations (7-42), (7-52), (7-53), (7-63) and (7-64) into Equations (7-6) to (7-8) and integrating Equations (7-6) to (7-8) by the numerical integration scheme depicted in Appendix D.

7.7 Green's Function for Partially Heat Conductive Cracks

In subsection 7.6 of this report, the Green's function solution for a single instantaneous heat source at any arbitrary point in a half-space with a semicircular surface crack is discussed. The crack surfaces in subsection 7.6 are assumed to be fully heat conductive. In reality, the crack surfaces are expected to be somewhere between completely insulated and fully heat conductive, i.e., crack surfaces are expected to be partially heat conductive. A general approach to treat a partially heat conductive crack is studied in detail in Appendix A of this report. Application of the concept given in Appendix A to the problem of a semicircular surface crack in a half-space is discussed in this subsection.

Governing heat transfer equation for a half-space with a semicircular, partially heat conductive crack surfaces is still Equation (7-1), and the boundary conditions given in Equations (7-68) and (7-71) remain unchanged. The only difference will be that the boundary condition at $z=0$, $(x^2+y^2) \leq a^2$, i.e., Equation (7-73), is replaced by

$$T_{,z}(x,y,0;t) = \frac{\lambda}{a} [T(x,y,0^+;t) - T(x,y,0^-;t)] \quad (7-98)$$

where λ is defined as (ah/k) in which h is crack surface heat conductance coefficient and k is material thermal conductivity. From Equation (7-98), it can be easily seen that the crack

surfaces are fully heat conductive when $\lambda=\infty$ and the crack surfaces are completely insulated when $\lambda=0$. Any λ values between 0 and ∞ are corresponding to a partially heat conductive crack.

As discussed in Appendix A, when a crack is completely insulated or partially heat conductive, the resulting temperatures on both sides of a crack will be different, i.e., there is a temperature-jump across the crack surface when λ equals to zero or a finite number. This temperature jump is analogous to the temperature-jump created by a series of distributed heat dipoles (Carslaw and Jaeger, 1959) situated at the crack location. Thus, the overall temperature distribution can be obtained as the superposition of the fully conductive solution, Equation (7-78), and a solution for the distributed heat dipoles. From Equation (7-78), it can be shown, by summing temperature solutions for a point heat source and a point heat sink with infinitesimally small distance in-between, that temperature solution for an instantaneous heat dipole of strength M situated at $(x=\bar{x}, y=\bar{y}, z=0)$ in a insulated half space, $y \geq 0$, is

$$T(x, y, z; t) = \frac{M z}{16\pi^{3/2} (\xi t)^{5/2} \rho c} \sum_{i=1}^2 \exp\left(-\frac{R_{i,1}^2}{4\xi t}\right) \quad (7-99)$$

where

$$R_{2,1}^2 = (x-\bar{x})^2 + (y\pm\bar{y})^2 + z^2 \quad (7-100)$$

Physically, Equation (7-99) is the temperature response generated by two instantaneous dipoles of strength M situated at $(\bar{x}, \bar{y}, 0)$ and $(\bar{x}, -\bar{y}, 0)$, respectively, in an infinite solid. Thus, the resulting temperature from distributed heat dipoles of strength $M(x, y, t)$ situated at region $(z=0, y \geq 0, 0 \leq (x^2 + y^2) \leq a^2)$ of the half space is

$$T(x, y, z; t) = \frac{z}{16\pi^{3/2}(\xi)^{5/2}\rho c} \sum_{i=1}^2 \int_0^t \int_{S_c} \frac{M(\bar{x}, \bar{y}; \tau)}{(t-\tau)^{5/2}} \exp\left(\frac{R_i^2}{4\xi\tau}\right) dS_c d\tau \quad (7-101)$$

where $dS_c = d\bar{x} \cdot d\bar{y}$, S_c is the crack area, $z=0$, $(x^2+y^2) \leq a^2$, $y \geq 0$, and R_1 and R_2 are defined in Equation (7-100).

Substitution of the sum of Equations (7-78) and (7-101) into Equation (7-98) yield a Fredholm integral equation for the heat dipole distribution $M(x, y, t)$ as follows:

$$\begin{aligned} & \frac{Qz'}{t^{5/2}} \left(\exp\left[\frac{-(x-x')^2 - (y-y')^2 - z^2}{4\xi t}\right] + \exp\left[\frac{-(x-x')^2 - (y+y')^2 - z^2}{4\xi t}\right] \right) \\ & + \int_{S_c} \int_0^t \frac{M(\bar{x}, \bar{y}, \tau)}{(t-\tau)^{5/2}} \left(\exp\left[\frac{-(x-\bar{x})^2 - (y-\bar{y})^2}{4\xi(t-\tau)}\right] + \right. \\ & \left. \exp\left[\frac{-(x-\bar{x})^2 - (y+\bar{y})^2}{4\xi(t-\tau)}\right] \right) d\tau dS_c = \frac{16\pi^{3/2}\lambda k}{\rho c a^{1/2}} M(x, y, t) \end{aligned} \quad (7-102)$$

where dS_c , and S_c are defined in Equation (7-101), k , ρ , and c are thermal conductivity, mass density, and specific heat, respectively, of the material, a is the radius of the semicircular surface crack, and $\lambda = ah/k$ is the nondimensionalized crack surface conductance defined in Equation (7-98).

A numerical approximation method is used in the computer program to solve Equation (7-102). Since the temperature-jump between

two adjacent crack surfaces has to be zero at the crack tip, $z=0$, $(x^2+y^2)=a^2$, we assume that

$$M(x,y,t) = M(r,\theta,t) = \sum_{m=0}^L \sum_{n=1}^{L'} [b_{mn}(t) \cos(2m\theta) \cos[\frac{(2n-1)\pi r}{2a}]] \quad (7-103)$$

where L and L' are the maximum numbers of terms included in the calculation and $b_{mn}(t)$ are time functions, which are determined by substituting Equation (7-103) into Equation (7-102).

Similar to the fully heat conductive case, a thermoelastic potential due to the distributed thermal dipoles at the crack region in an uncracked half-space can be derived by integrating the temperature solution, Equation (7-101). That is,

$$\phi(x,y;t) = \alpha \xi \left(\frac{1+\nu}{1-\nu} \right) \int_0^t T(x,y,z;\tau) d\tau + \phi_0 \quad (7-104)$$

where $T(x,y,z;t)$ is the temperature solution given in Equation (7-101) and ϕ_0 is an analytic function to make ϕ remain finite at infinity. It can be shown that stresses at the crack region due to the thermoelastic potential ϕ of Equation (7-104) are as follows:

$$\sigma'_{zz}(x,y,0;t) = 0 \quad (7-105)$$

$$\sigma'_{zx}(x,y,0;t) = \int_{S_c} \int_0^t \sigma_{zx}^M(x,y,0;\tau;\bar{x},\bar{y}) M(\bar{x},\bar{y},\tau) d\tau dS_c \quad (7-106)$$

$$\sigma'_{zy}(x, y, 0; t) = \int_{S_C} \int_0^t \sigma_{zy}^M(x, y, 0; \tau; \bar{x}, \bar{y}) M(\bar{x}, \bar{y}, \tau) d\tau dS_C \quad (7-107)$$

where

$$\begin{aligned} \sigma_{zx}^M(x, y, 0; t; \bar{x}, \bar{y}) = & \frac{(1+\nu) a G}{(1-\nu) 2 \pi \rho c} \sum_{i=1}^2 \frac{(x-\bar{x})}{R_i^2} \left(\frac{3}{R_i^3} \operatorname{erf}\left(\frac{R_i}{\sqrt{4\xi(t-\tau)}}\right) \right. \\ & \left. - \frac{1}{\sqrt{\pi\xi(t-\tau)}} \left[\frac{3}{R_i^2} + \frac{1}{2\xi(t-\tau)} \right] \exp\left(\frac{-R_i^2}{4\xi(t-\tau)}\right) \right) \end{aligned} \quad (7-108)$$

$$\begin{aligned} \sigma_{zy}^M(x, y, 0; t; \bar{x}, \bar{y}) = & \frac{(1+\nu) a G}{(1-\nu) 2 \pi \rho c} \sum_{i=1}^2 \frac{(y-\bar{y}_i)}{R_i^2} \left(\frac{3}{R_i^3} \operatorname{erf}\left(\frac{R_i}{\sqrt{4\xi(t-\tau)}}\right) \right. \\ & \left. - \frac{1}{\sqrt{\pi\xi(t-\tau)}} \left[\frac{3}{R_i^2} + \frac{1}{2\xi(t-\tau)} \right] \exp\left(\frac{-R_i^2}{4\xi(t-\tau)}\right) \right) \end{aligned} \quad (7-109)$$

$$R_i^2 = (x-\bar{x})^2 + (y-\bar{y}_i)^2 \quad (7-110)$$

$$\bar{y}_1 = \bar{y} \quad , \quad \bar{y}_2 = -\bar{y} \quad (7-111)$$

and ξ is defined in Equation (7-1). Similarly, stresses at plane $y=0$ due to the thermoelastic potential of Equation (7-104) are

$$\sigma'_{yx}(x, 0, z; t) = \sigma'_{yz}(x, 0, z; t) = 0 \quad (7-112)$$

$$\sigma'_{yy}(x, y, 0; t) = \int_{S_C} \int_0^t \sigma_{yy}^M(x, 0, z; \tau; \bar{x}, \bar{y}) M(\bar{x}, \bar{y}, \tau) d\tau dS_C \quad (7-113)$$

where

$$\begin{aligned} \sigma_{yy}^M(x, 0, z; \bar{x}, \bar{y}) = & \frac{(1-\nu) \alpha G z}{(1+\nu) \pi \rho c} \left(\frac{1}{R^2} \left(\frac{5\bar{y}^2 - R^2}{R^4} \right) \left[\frac{-3}{R^3} \operatorname{erf} \left(\frac{R}{2\sqrt{\xi(t-\tau)}} \right) \right. \right. \\ & + \left. \left(\frac{3}{R^2 \sqrt{\pi \xi(t-\tau)}} + \frac{1}{2\xi(t-\tau) \sqrt{\pi \xi(t-\tau)}} \right) \exp \left(\frac{-R^2}{4\xi(t-\tau)} \right) \right] \\ & + \left. \frac{(\bar{y}^2 - R^2)}{4\sqrt{\pi} \xi^{5/2}(t-\tau)^{5/2} R^2} \exp \left(\frac{-R^2}{4\xi(t-\tau)} \right) \right] \end{aligned} \quad (7-114)$$

$$R^2 = (x - \bar{x})^2 + \bar{y}^2 + z^2 \quad (7-115)$$

Similar to Equations (7-94) to (7-96), the non-zero normal stresses at surface $y=0$ given by Equation (7-113) can be eliminated by adding a complementary set of stresses, $\sigma_{ij}''(x, y, z; t)$, which is calculated by substituting $\sigma'_{yy}(x, 0, z; t)$ of Equation (8-114) into Equations (7-94) to (7-96)

By substituting the sum of the aforementioned complementary stresses $\sigma_{ij}''(x, y, 0; t)$ and the stresses σ'_{ij} calculated from Equations (7-105) to (7-107) into Equations (7-6) to (7-8) and using the influence functions given in Equations (7-42), (7-48), (7-49), (7-52), and (7-53), it can be shown that, in general, the mode I and III stress intensity factors caused by the distributed heat dipoles at the crack region are zero while the Mode II stress intensity factor caused by the distributed heat dipoles is not zero. This observation reiterates the fact, deduced in Appendix A, that, for a cracked structure with symmetry with respect to the crack plane such as the current crack model, crack surface heat conductance will not affect Mode I and Mode III fracture solutions but will change Mode II fracture solution.

To sum up, for a semicircular surface crack with partially heat conductive or completely insulated crack surfaces in an insulated half-space, its overall temperature solution is the sum of Equation (7-78) and Equation (7-101). Total stresses in the uncracked half-space, which share the same overall temperature distribution as the cracked structure, equal to the sum of the aforementioned complementary stresses $\sigma''_{ij}(x,y,0;t)$ and stresses given in Equations (7-90) to (7-92), (7-94) to (7-96), and (7-105) to (7-107). Green's function solutions for stress intensity factors, K_I , K_{II} , and K_{III} , at the crack tip are then calculated by substituting the total stresses at the crack region into Equations (7-6) to (7-8).

7.8 Numerical Verification of Crack Model 6

Since stress intensity factors are calculated by integrating the product of influence functions and stresses at the crack location in an uncracked plate (see Equations (7-6) to (7-8)), it is necessary to verify both the influence functions derived in Subsection 7.3 and the temperature and thermal stresses obtained in subsections 7.6 and 7.7. The following sections describe, in detail, the verification of crack Model 6.

7.8.1 Verification of Influence Functions

7.8.1.1 Circular Crack in an Infinite Space

This section describes the verification of the influence functions as well as the numerical integration procedure for a single circular crack embedded in an infinite space. The formulation of the influence functions \hat{m}_1 , \hat{m}_{2r} , $\hat{m}_{2\theta}$, \hat{m}_{3r} and $\hat{m}_{3\theta}$ are described in subsection 7.3, Equations (7-13), (7-48), (7-49), (7-59) and (7-60), respectively. The numerical procedures used in calculating these influence functions are described in Appendix D-1.

Direct verification of the influence functions by itself is unlikely. The verification method employed in this section is to use the influence functions developed in subsection 7.3 to calculate the stress intensity factors for a simple problem and compare to the results obtained by other methods. A circular crack in an infinite space subjected to uniform stress distribution is selected for verification of the influence functions. The stress intensity factors for an embedded circular crack under combined uniform tension $\sigma_{zz}=\sigma$ and uniform shear $\sigma_{zx}=\tau$ at infinity are given by Hartranft and Sih (1973) as

$$K_I = \frac{2}{\sqrt{\pi}} \sigma \sqrt{a} \quad (7-116)$$

$$K_{II} = \frac{1-\nu}{2-\nu} \frac{4}{\sqrt{\pi}} \tau \sqrt{a} \cos \theta \quad (7-117)$$

$$K_{III} = \frac{1-\nu}{2-\nu} \frac{4}{\sqrt{\pi}} \tau \sqrt{a} \sin \theta \quad (7-118)$$

where σ , τ , a and θ are tension stress, shear stress, crack radius and crack angle, as defined in Figure 7-1, respectively.

Assuming unit stress on tension and shear and unit crack size, the stress intensity factors for all three modes K_I , K_{II} and K_{III} were calculated using Equations (7-6) to (7-8) and compared to that obtained from Equations (7-116) to (7-118). The comparison are shown in Figures 7-5 to 7-7. Using Equation (7-6), the K_I ranged from 1.09 to 1.175 compared to 1.128 obtained from Equation (7-116). The error is about $\pm 4\%$. The oscillating deviation of the numerical solutions from the exact solutions is believed to be caused by the relatively less number of integration points used in the numerical procedure. However, 4% error bound is deemed to be satisfactory for this application. Figure 7-5 shows the comparison on K_{II} using Equations (7-7) and (7-117). Figure 7-6 shows the comparison on K_{III} using Equations (7-8) and (7-118). They all show an error band of about $\pm 4\%$.

7.8.1.2 Semicircular Crack in a Semi-infinite Space

This subsection presents the verification of the semicircular crack in a semi-infinite space using the methodology described in subsection 7.3 and the numerical scheme delineated in Appendix D.

Due to the excessive computation time, as described in Appendix D, on the three-dimensional model, the stress intensity factors for the semicircular crack in a semi-infinite space are presented at three crack angles; $\theta = 0^\circ$, 90° , and 180° (see Figure 7-1 for the definition of θ). Figure 7-8 presents only the comparison of THERMO-K with those by Hartranft and Sih (1973) and Smith, Emery and Kobayashi (1967). At the deepest point of the crack, $\theta = 0^\circ$, THERMO-K calculates the normalized K to be 0.985 compared to the 1.05 from Hartranft and Sih (1973) and 1.03 from Smith, Emery and Kobayashi (1967). For the crack angle at the surface ($\theta = 0^\circ$ and 180°), the normalized value from THERMO-K is 1.279. It is about 7% higher than that of Hartranft and Sih (1973) and Smith, Emery and Kobayashi (1967). As described in Hartranft and Sih (1973), the solutions presented are by no means the exact solution of the problem but are represented by the best approximation solution as judged. In this model, the numerical solution to the problem was formulated by a combination of the methods used by Bell (1979) and Hartranft and Sih (1973). Also, as discussed in Appendix D, due to the excessive computer execution time, the number of Gaussian integration points on the crack surface is pared down to the bare minimum.

Newman (1979) presents a review and assessment of the stress intensity factors for surface crack in a finite plate. A total of 14 different solutions, (e.g., engineering estimate, alternating method, and finite element method) are compared. These results are presented as a boundary correction factor F verse a/t , where a is the crack depth and t is the plate thickness. For Mode I stress intensity factor for a crack in a finite plate, it is given as

$$K_I = \sigma \sqrt{\frac{\pi a}{Q}} F\left(\frac{a}{t}, \frac{a}{c}, \frac{c}{W}, \Phi\right) \quad (7-119)$$

where c , half-length of surface crack; W , plate width, Φ , complete elliptic integral of second kind and Q , the shape factor can be expressed as

$$Q = 1 + 1.464 \left(\frac{a}{c}\right)^{1.65} \quad \text{for } \frac{a}{c} \leq 1 \quad (7-120)$$

For the limiting case of a/t approaching zero, it can be essentially considered as a crack in an semi-infinite space. Thus it can be used to serve another comparison for the THERMO-K. Table 7-1 presents the comparison of the results

Table 7-1

Comparison of Results

θ	<u>THERMO-K</u>	<u>Newman</u>
$\frac{K_I}{\sigma \sqrt{a}}$		
0°	1.44	1.236 - 1.38
$90^\circ, 180^\circ$	1.11	1.129 - 1.24

The THERMO-K calculates a higher value of the stress intensity factor at the surface but lower value at the maximum depth point of the semicircular crack.

7.8.2 Verification Temperature and Stresses for Fully Heat Conductive Crack Surface

The verification of the transient temperature and stress distribution for a fully heat conductive crack surface, as described in subsection 7.6, are accomplished by a transient

analysis of the same model using finite element method. The problem of a 1 inch radius semicircular surface crack in a semi-infinite space of $y > 0$ (see Figure 7-1) subjected to a single heat source of intensity $\dot{Q} = H(t)$ Btu/sec at (0 inch, 1.4 inch, 0 inch) is considered. Due to the prohibited computing cost in a three-dimensional finite element analysis for the transient thermal stress problem and the inherent symmetry condition of the verification problem, a two-dimensional axisymmetric model is used instead.

The two-dimensional finite element model is shown in Figures 7-9 and 7-10. The model is defined in the R-Z coordinate. The half space surface of the semi-infinite solid is represented by a plane at $z=0$. The size of the axisymmetric model shown in Figure 7-9 is 100 inches x 100 inches which should be large enough to represent a semi-infinite solid. The model consists of 514 isoparametric, four-node elements and 534 nodes. The crack surface is assumed to be near the origin, (i.e., $r=0$, $z=0$). As shown in Figure 7-10, a fine mesh is used in this region with a coarse mesh at distance further away from the crack location. The size of this region is 5 inches x 5 inches with 135 elements.

The heat transfer boundary condition of the model is that an insulated surface is set at surface $z=0$, $z=100$ and $r=100$. A roller displacement boundary condition is imposed at plane $z=100$. The material properties used are 0.0978 lb/in³ for mass density, 0.23 Btu/lb-F for specific heat, 0.0017361 Btu/sec-F-in for thermal conductivity, 0.000013 in/in/F for thermal coefficient of expansion, 10.3×10^6 psi for Young's modulus and 0.33 for Poisson's ratio. A unit point heat source, 1 Btu/sec, is placed at $r=0$, $z=1.4$. This point heat source is a delta function in space and constant over time throughout the transient, unit step function in time $t=0$. It is equivalent to a location of $x=0$, $y=1.4$ and $z=0.0$ in the coordinate system of the three-dimensional model, Figure 7-1. An integration time step of 1.0 second is

used in the transient analysis for a time history of 500 seconds. The finite element program used in this verification is FEM2D (1986), developed by Structural Integrity Associates.

Analysis results of the three-dimensional semicircular crack in a semi-infinite space are also obtained using Equations (7-78) to (7-96).

7.8.2.1 Temperature Results

Figures 7-11 and Figure 7-12 present the comparison of the temperature results between the THERMO-K and the finite element analysis.

Figure 7-11 illustrates the temperature transient plot for three selected locations. The three locations are at origin ($x=0$, $y=0$, $z=0$; x , y , z as defined in Figure 7-1), at 1 inch away from the origin on the half surface, $y=0$ ($x=1$, $y=0$, $z=0$), and at 5 inches from the surface and 5 inches from the symmetry axis, ($x=5$, $y=5$, $z=0$). At the first two locations, the temperature rise is substantial because of the proximity to the point heat source. At location (0,0,0), temperature climbs up to over 45°F in about 100 seconds. At location (5,5,0), no temperature rise due to the point heat source has been observed during the first 100 seconds. Because of its location is further away from the point heat source, the time for temperature response would be longer and the magnitude of response would not be as high as the first two locations. In all three locations examined, the agreement between the finite element method and the THERMO-K are excellent.

Figure 7-12 presents the temperature distribution in the semi-infinite solid at three selected points of time, ($t = 10$ sec, 20 sec and 100 sec) during the transient. The temperature is plotted as a function of distance, y , from the insulated surface at the origin ($x=0$, $z=0$). As time increases, the temperature profile increases due to the constant supply of heat

from the heat source. The magnitude of temperature increase is higher at the surface, $y=0$, due to the insulated effect at the surface. At a distance of 5 inches from the surface, the temperature increase is not as significant. Near the heat source, $y=1.4$ inch, temperatures are as high as 100°F .

As evident in Figure 7-12, the agreement between the temperature predicted by THERMO-K and by finite element method is good. At the region near the heat source, $y=1.4$ inch, results from the FEM2D are higher compared to that obtained by THERMO-K using Equation (7-78). The overprediction in temperature by the finite element method is believed to result from the coarse mesh near the point heat source in the finite element model.

7.8.2.2 Stress Results

Figures 7-13 and 7-14 show the comparison of the thermal stress results between THERMO-K and FEM2D. The stress component presented in these two figures is σ_{zz} .

Figure 7-13 plots the stress transient for four selected locations. The four locations are $x, y, z = (0.1, 0.1, 0)$, $(1.9, 1.71, 0)$, $(4.75, 0.475, 0)$ and $(9.5, 9.5, 0)$. These locations are selected in random but with the intention to examine enough locations to study the effect of the heat sources on the stresses in the solid. The agreement between the THERMO-K and FEM2D is reasonable. The peak stress response in the transient matches fairly well between the two results. Further into the transient, the results at locations near the surface and the heat source differ from each other. It is as much as 18%. From Figure 7-14, it is also difficult to predict whether the results is over-predicted or under-predicted. It is difficult to provide any reason for that level of difference just from this figure alone. Figure 7-14 provides a little bit more of the insight.

Figure 7-14 presents a stress profile at a select section for $t=10$ sec., 20 sec. and 100 sec. in the transient. The stress is plotted versus y , distance from the insulated surface, with $z=0$ and x varied from 0.1 inch to 0.5 inch. It is a composite stress profile for a row of element near the z axis (i.e., $r \cong 0$) Figure 7-10. In Figure 7-14, stresses are in good agreement between THERMO-K and FEM2D except in the region near the heat source. As expected, stress is high near the location where the heat source exists. In addition, near the insulated surface, FEM2D analysis shows a peak in stress and it decreases again as it gets to the surface. This peak seems to increase as time increases. Similar results are also observed in the development of the two-dimensional crack models. One plausible explanation to this is that it is due to the surface correction in order to satisfy the displacement compatibility in the finite element analysis.

7.8.3 Verification of Temperature Distribution for Insulated Crack Surfaces

The verification of transient temperature distribution for a fully insulated crack surface is accomplished by a transient thermal analysis of a finite element model. The finite element model represents a problem of a semi-circular crack surface of one inch radius in a semi-infinite space of $y \geq 0$, (Figure 7-1) subject to a single heat source of intensity $Q=H(t)$ Btu/sec.

As mentioned in subsection 7.8.2, the cost of performing a transient analysis for a conductive crack model is prohibitive. A two-dimensional axisymmetric finite element model shown in Figures 7-15 and 7-16 is used. This model is used to verify the transient temperature distribution in the plane containing the crack surface, ($z=0$).

The model is defined in the R-Z coordinate. The size of the model is 100 inches in radius (R-axis) and 200 inches long

(Z-axis), (Figure 7-15). The models consists of 1035 isoparametric, four node elements and 1028 nodes. The crack surface is at the plane, $z=0$. A finer mesh is used in the region close to the crack surface, as shown in Figure 7-16. This region is 5 inches in the R axis and 10 inches in the Z axis.

For the heat transfer boundary condition, the crack surface, ($z=0^+$, 0^+ , $r=0$ to 1 inch) is insulated, (i.e., $h=0.0$). The surfaces at $z=100$ inches, -100 inches and $R=100$ inches are also insulated. The material properties are the same as the fully heat conductive crack surface case in subsection 7.8.2. A unit heat source, 1 Btu/sec, is placed at $(0, 0, 1.4)$. This point heat source is a delta function in space and constant over time throughout the transient, step at time $t=0$. An integration time step of 1.0 second is used in the transient analysis for a history of 100 seconds.

The comparison of temperature transient results between THERMO-K and finite element analysis is presented in Figure 7-17. Location $(1, 0, 0)$ is at the crack tip. Location $(0, 0^+, 0)$ is at the top surface at the crack mouth directly under the point heat source. Location $(0, 0^-, 0)$ is at the bottom surface of the crack. Temperature results are in very good agreement for the locations at the crack tip and at the top surface. The temperature responses at the bottom crack surface are also in good agreement except at the very beginning of the transient. This is due to the numerical procedure used in the determination of the heat dipoles to simulate the heat conductive condition of the crack surface, (Appendix D). At present, only one term is used in the equation representing the heat dipole.

Figures 7-18 and 7-19 presents the temperature profiles at different points of time in the transient. The temperature profiles are plotted for the plane containing the crack surface ($z=0$) and as temperature against the distance from the surface ($y=0$) in the semi-infinite solid. The temperature profiles

results are presented for time $t = 10, 20, 50$ and 100 seconds into the transient. For the distance within the crack surface, $r \leq 1.0$, both the top and bottom crack surface temperature are presented. The results from THERMO-K are, in general, overpredicting the temperature at the bottom crack surface except near the edge of the surface ($y=0$). This is due to the number of terms used in the heat dipole equation and the location used to determine the coefficients in the equation.

7.9 References

Bell, J. C., (1979), "Stresses from Arbitrary Loads on a Circular Crack," International Journal of Fracture, Vol. 15, No.1, pp. 85-104.

Boley, B. A., and Weiner, J. H., (1960), Theory of Thermal Stresses, Wiley & Sons, New York, New York.

Bueckner, H. F., (1973), "Field Singularities and Related Integral Representations," in Methods of Analysis and Solutions of Crack Problems, Vol 1, ed. G. C. Sih, pp. 239-314, Noordhoff, Holland.

Carslaw, H. S., and Jaeger, J. C., (1959), Conduction of Heat in Solids, 2nd edition, Oxford University Press, London.

FEM2D User's Manual (1986) - A Two-dimensional Finite Element Computer Program for Two-Dimensional Heat Transfer/Thermal Stress Analysis, Structural Integrity Associates, San Jose, CA.

Hartranft, R. J., and Sih, G. C., (1973), "Alternating Method Applied to Edge and Surface Crack Problems," in Methods of Analysis and Solutions of Crack Problems Vol 1, ed. G. C. Sih, pp. 179-238, Noordhoff, Holland.

Hartranft, R. J., and Sih, G. C., (1973), "Alternating Method Applied to Edge and Surface Crack Problems," in Methods of Analysis and Solution of Crack Problems, Vol. 1, ed. G. C. Sih, pp. 233-237, Noordhoff, Holland.

Newman, J. C., "A Review and Assessment of the Stress Intensity Factors for Surface Cracks," Part-Through Crack Fatigue Life Prediction, ASTM STP 687, J. B. Chang, Ed. American Society for Testing and Materials, 1979, pp. 16-42.

pc-CRACK - Fracture Mechanics Software for Personal Computers, Users Manual, Version 1.1, Revision 1, (1986), Structural Integrity Associates, San Jose, CA.

Parkus, H., (1968), Thermoelasticity, Blaisdell Publishing Co..

Sih, G. C., (1973), Handbook of Stress Intensity Factors, Institute of Fracture and Solid Mechanics, Lehigh University, Bethlehem, PA.

Smith, F. W., Emery, A. F., and Kobayashi, A. S., Journal of Applied Mechanics, Vol. 34, No. 4; Transactions, American Society of Mechanical Engineers, Vol. 89, Series E, Dec. 1967, pp 953-959.

Tada, H., Paris, P., and Irwin, G., (1973), The Stress Analysis of Cracks Handbook, Del Research Co., Pennsylvania.

Timoshenko, S. P., and Goodier, J. N., (1970), Theory of Elasticity, 3rd edition, McGraw Hill, New York, New York.

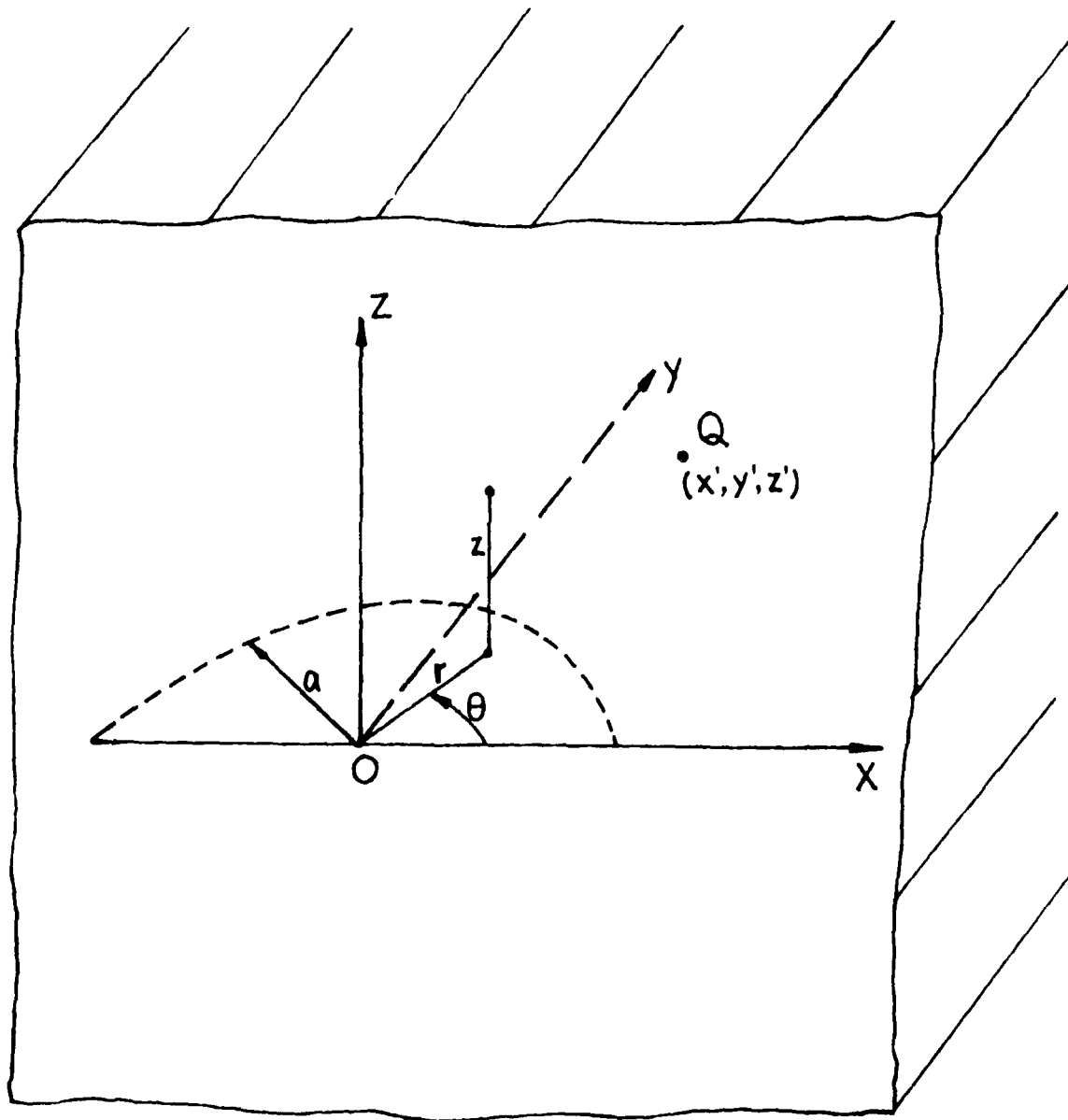


Figure 7-1. A Semi-circular Surface Crack in a Semi-infinite Space ($y \geq 0$)

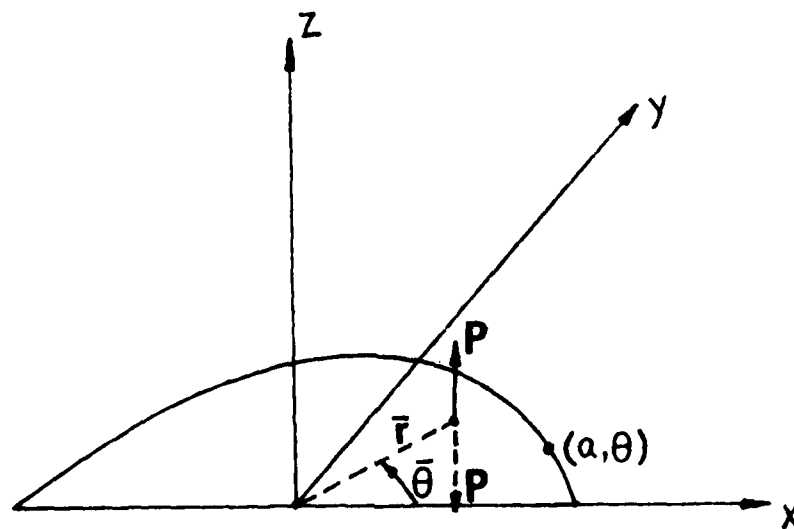


Figure 7-2(a). A Pair of Unit Normal Forces Applied at $(\bar{r}, \bar{\theta})$ of the Crack Surface

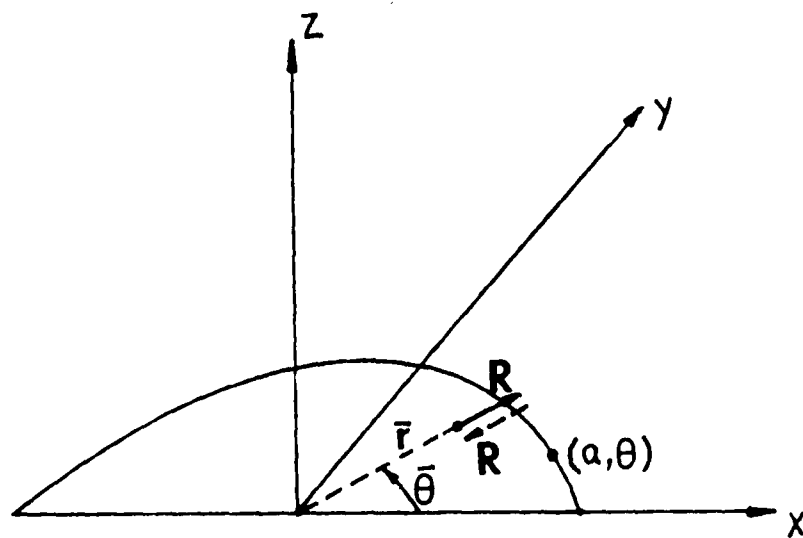


Figure 7-2(b). A Pair of Unit Radial Forces Applied at $(\bar{r}, \bar{\theta})$ of the Crack Surface

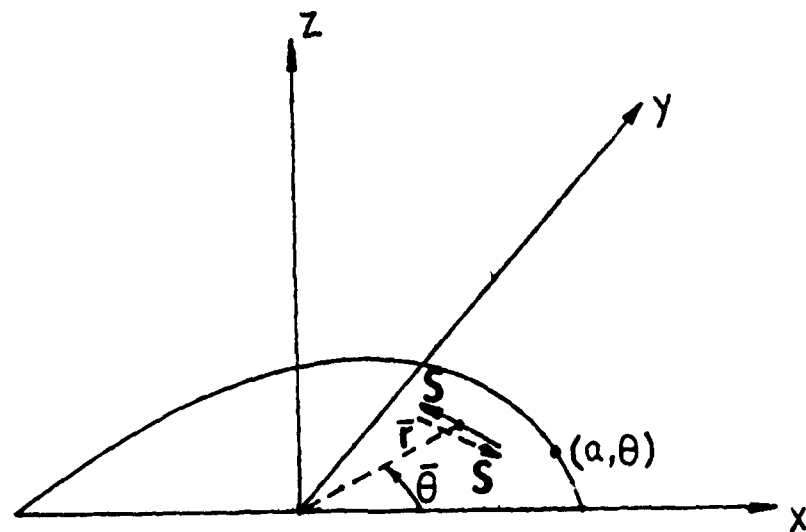
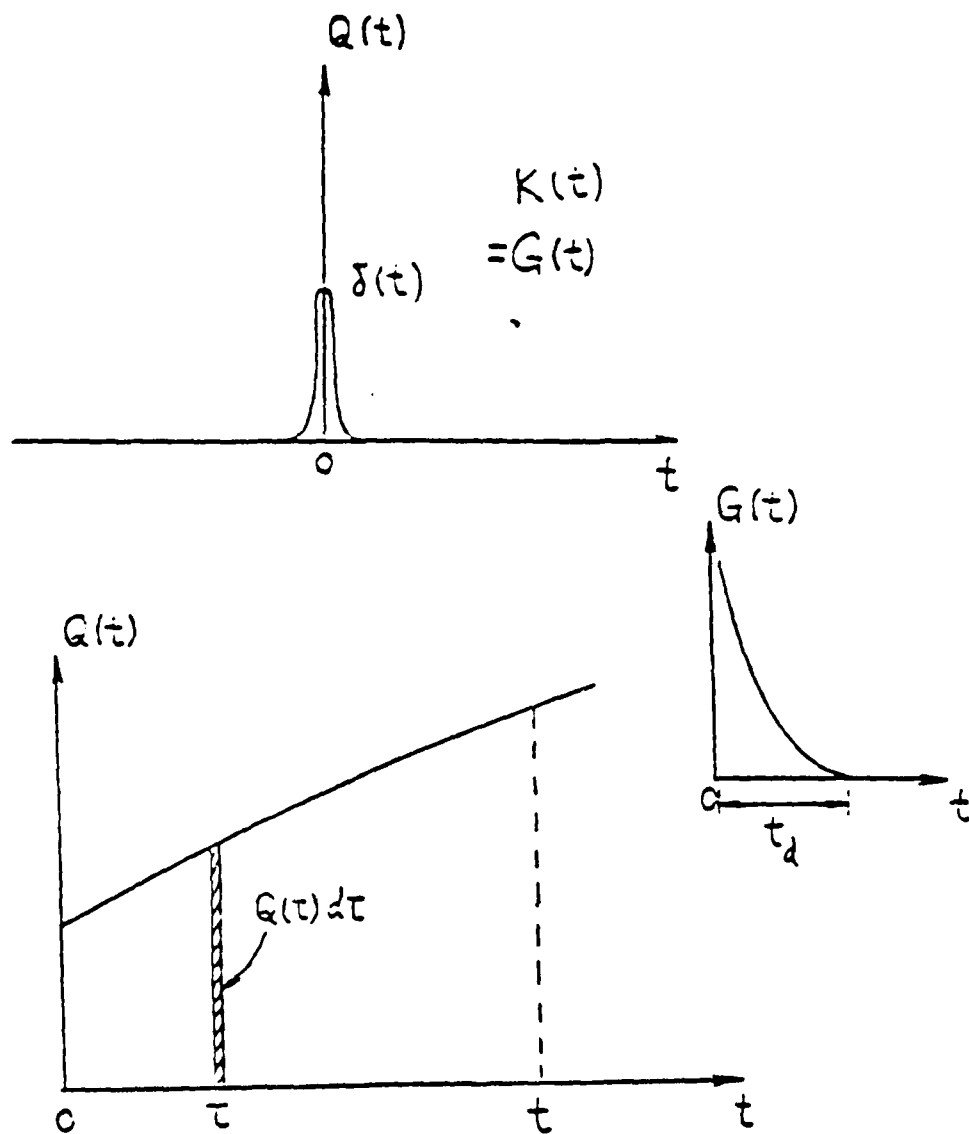


Figure 7-2(c). A Pair of Unit Tangential Forces Applied at $(\bar{r}, \bar{\theta})$ of the Crack Surface



$$K(t) = \int_0^t Q(\tau) G(t-\tau) d\tau$$

$$= \int_{t-t_d}^t Q(\tau) G(t-\tau) d\tau$$

Figure 7-3. Concept of Green's Function

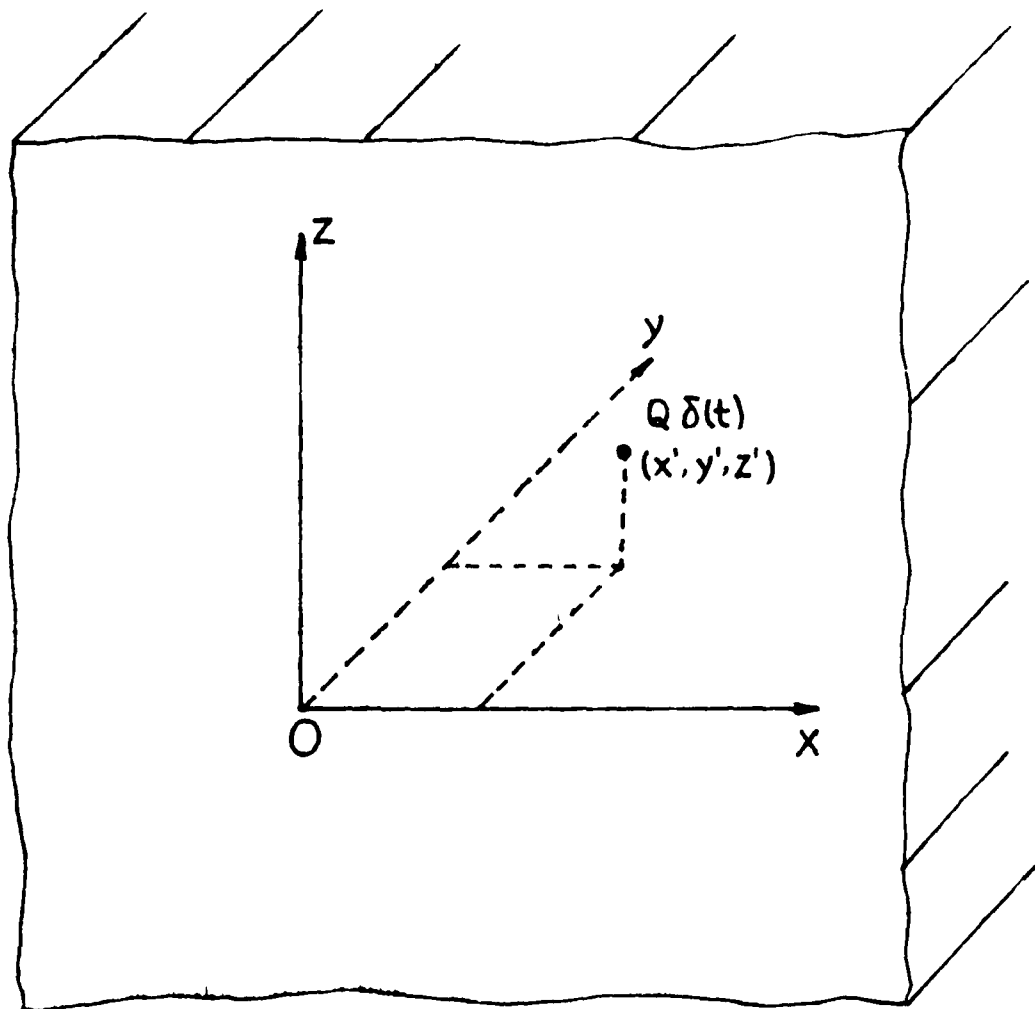


Figure 7-4. An Instantaneous Heat Source in a Half-space

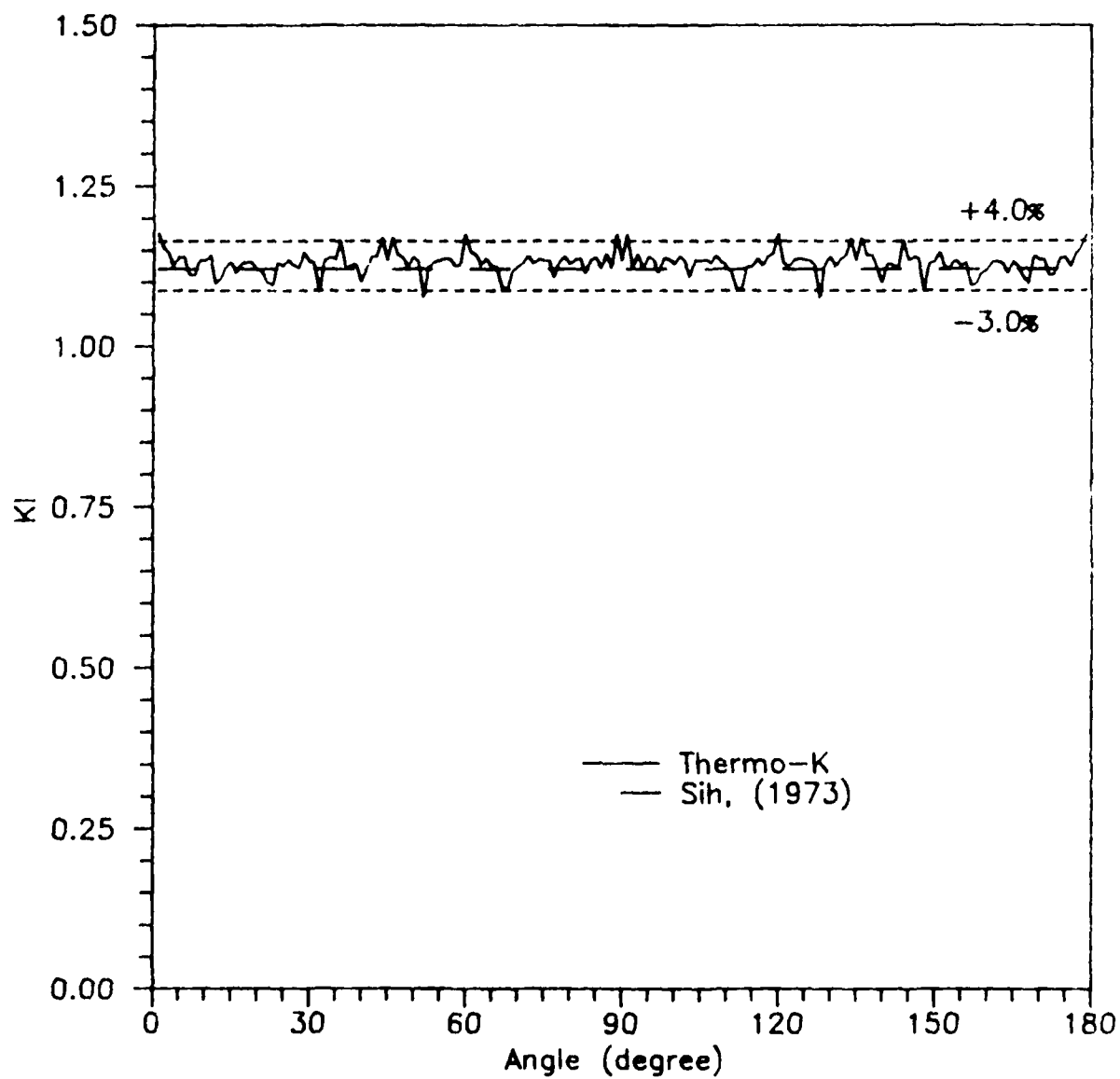


Figure 7-5. Verification of Mode I Stress Intensity Factor of Circular Crack in an Infinite Solid

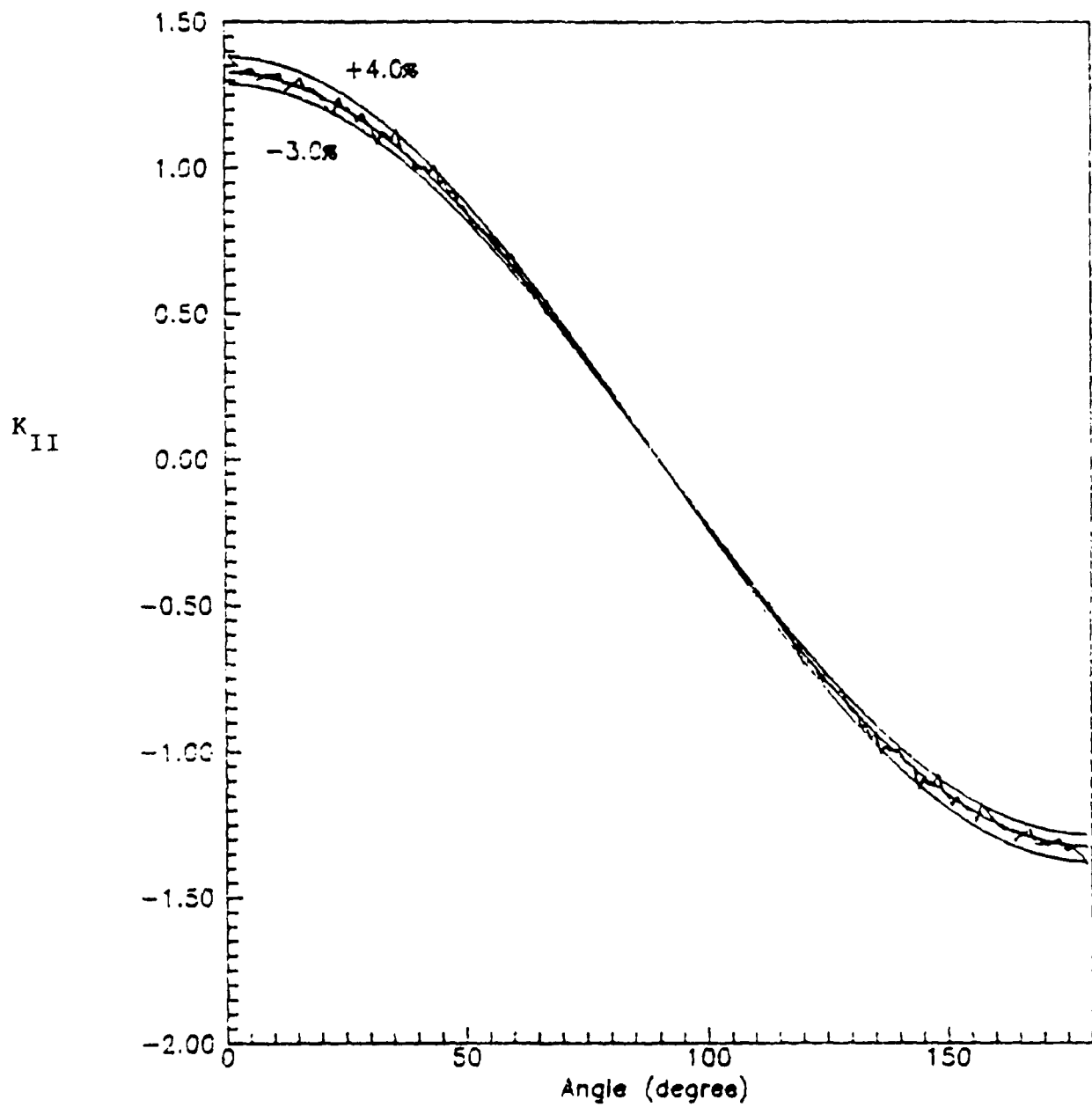


Figure 7-6. Verification of Mode II Stress Intensity Factor of Circular Crack in an Infinite Solid

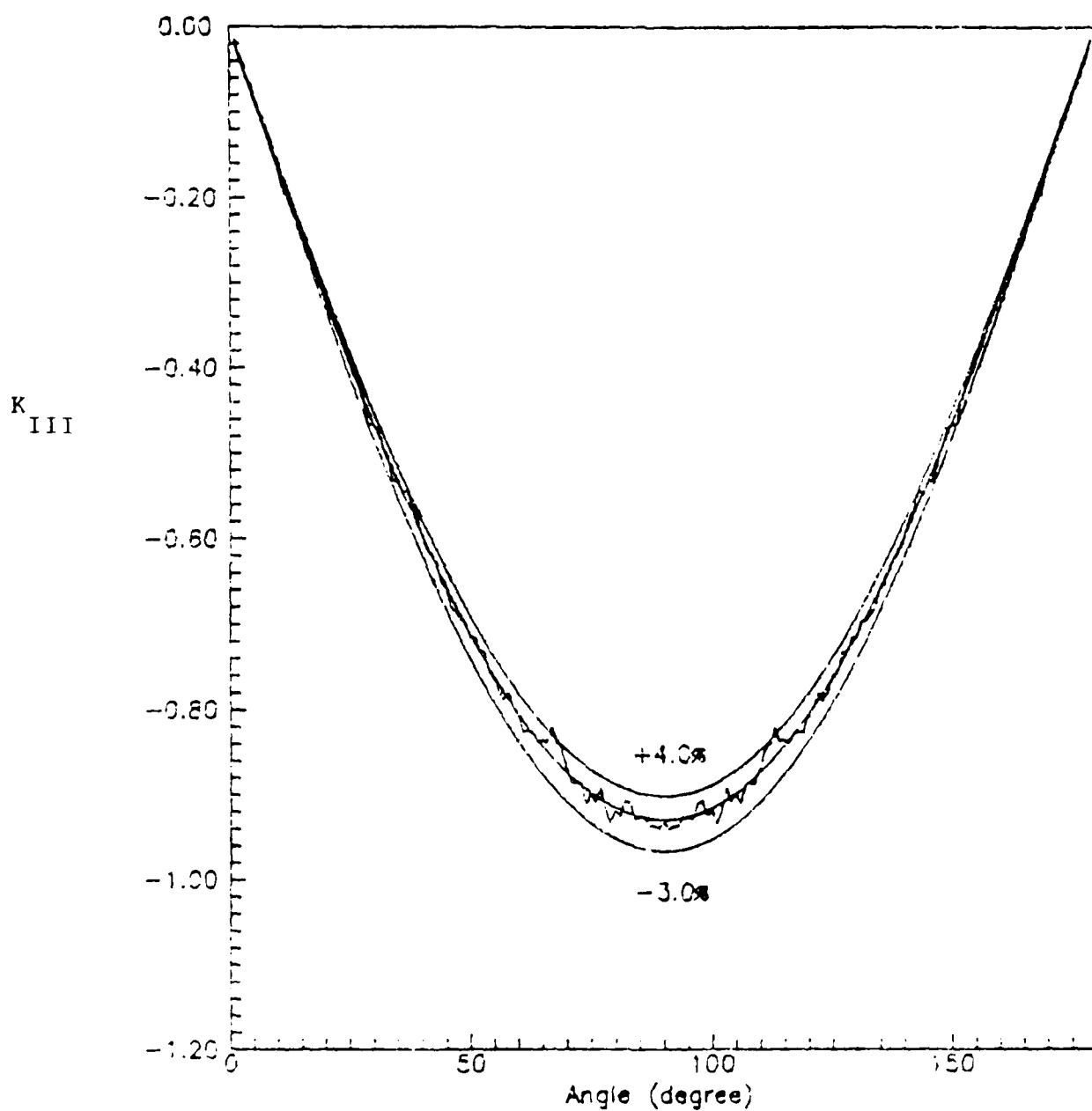


Figure 7 7. Verification of Mode III Stress Intensity Factor of Circular Crack in an Infinite Solid

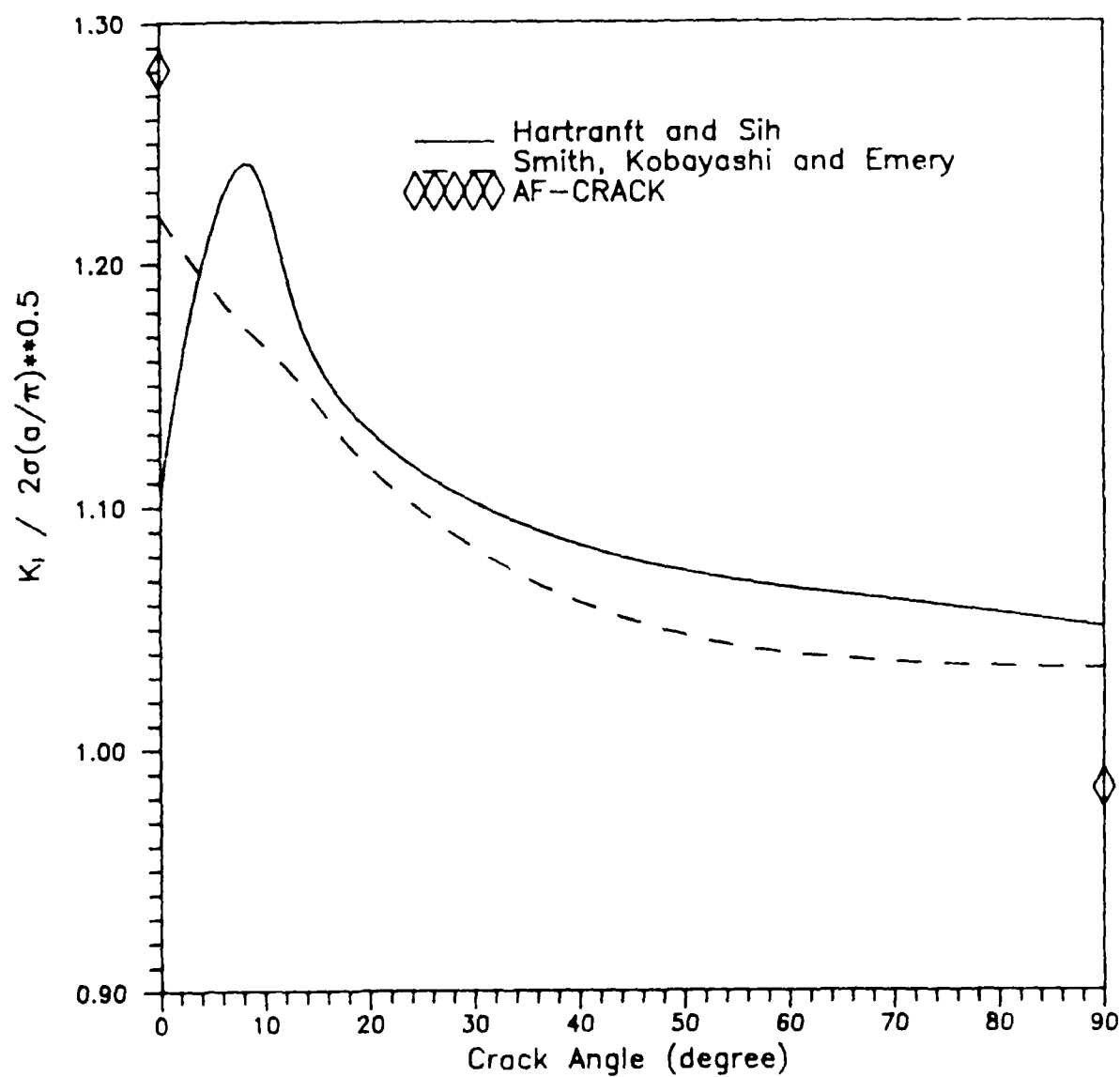


Figure 7-1. Comparison of Crack in a Semi-infinite Solid Results

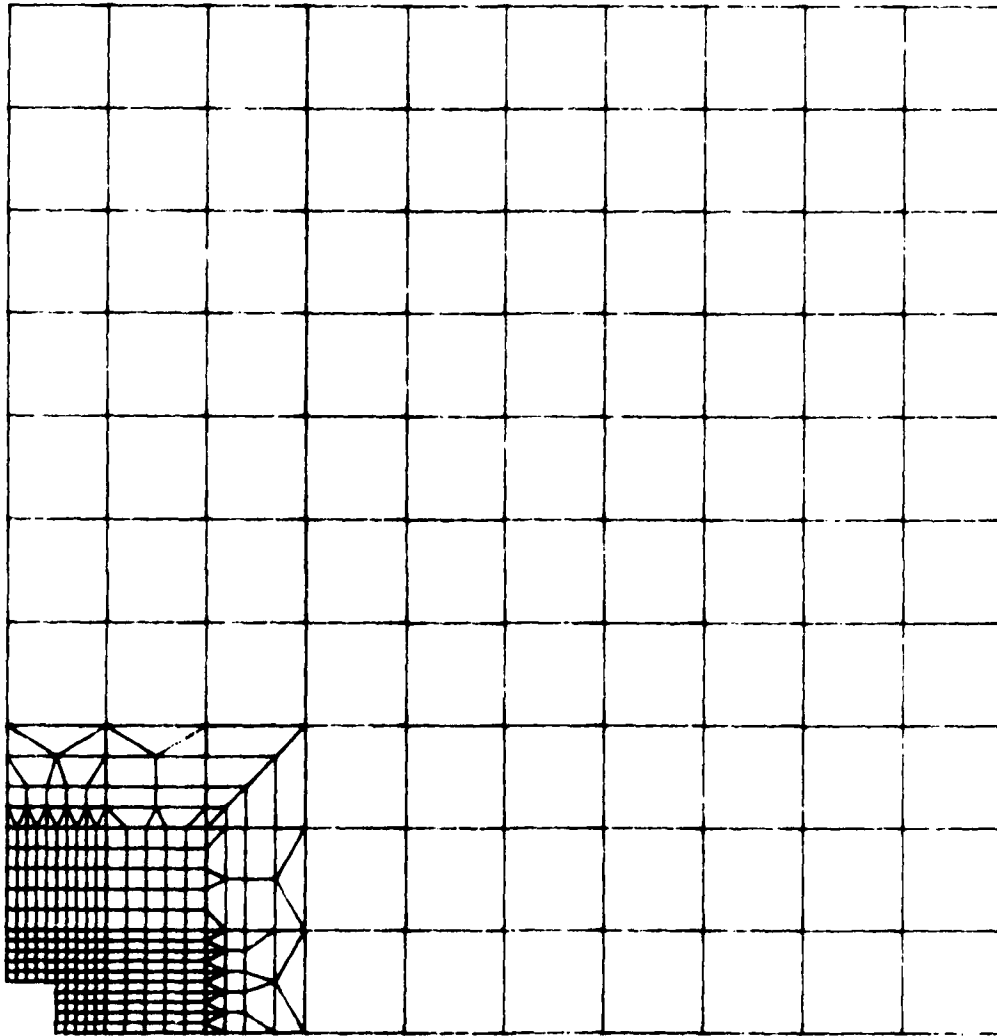


Figure 7-9. Axisymmetric Finite Element Model for Verification of Temperature and Stress

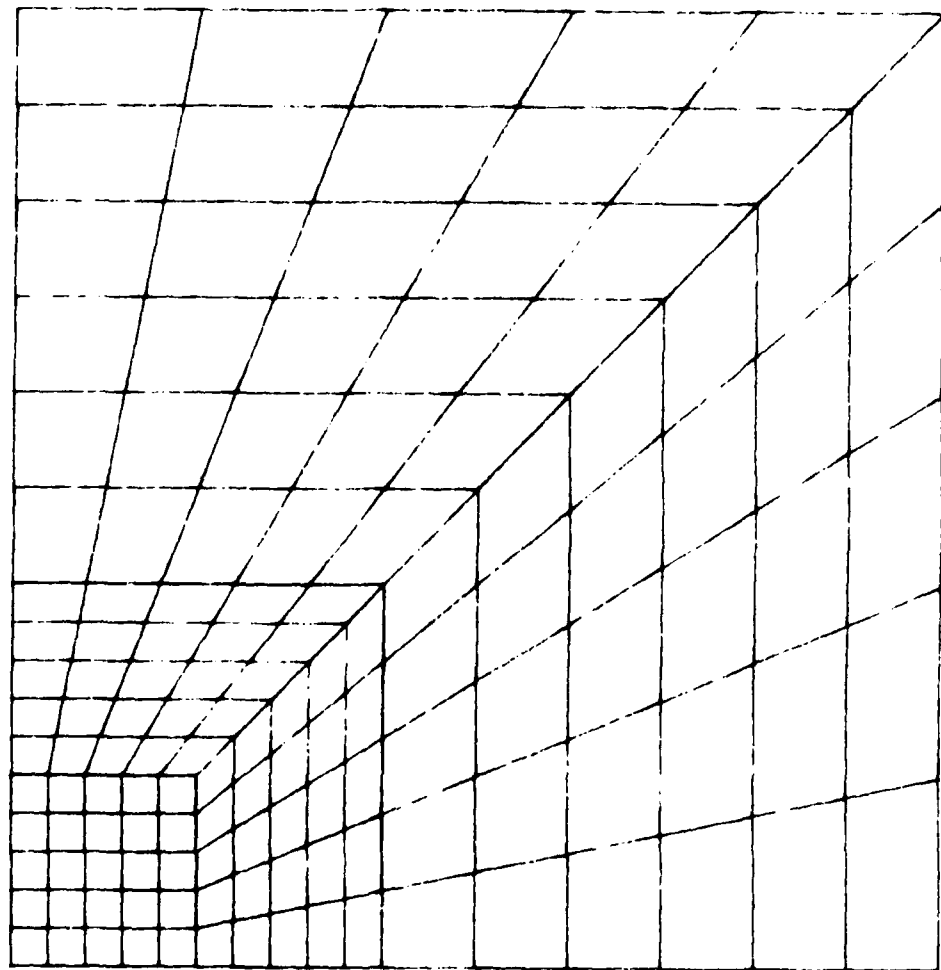


Figure 7-10. Axisymmetric Finite Element Mesh at the Crack Location

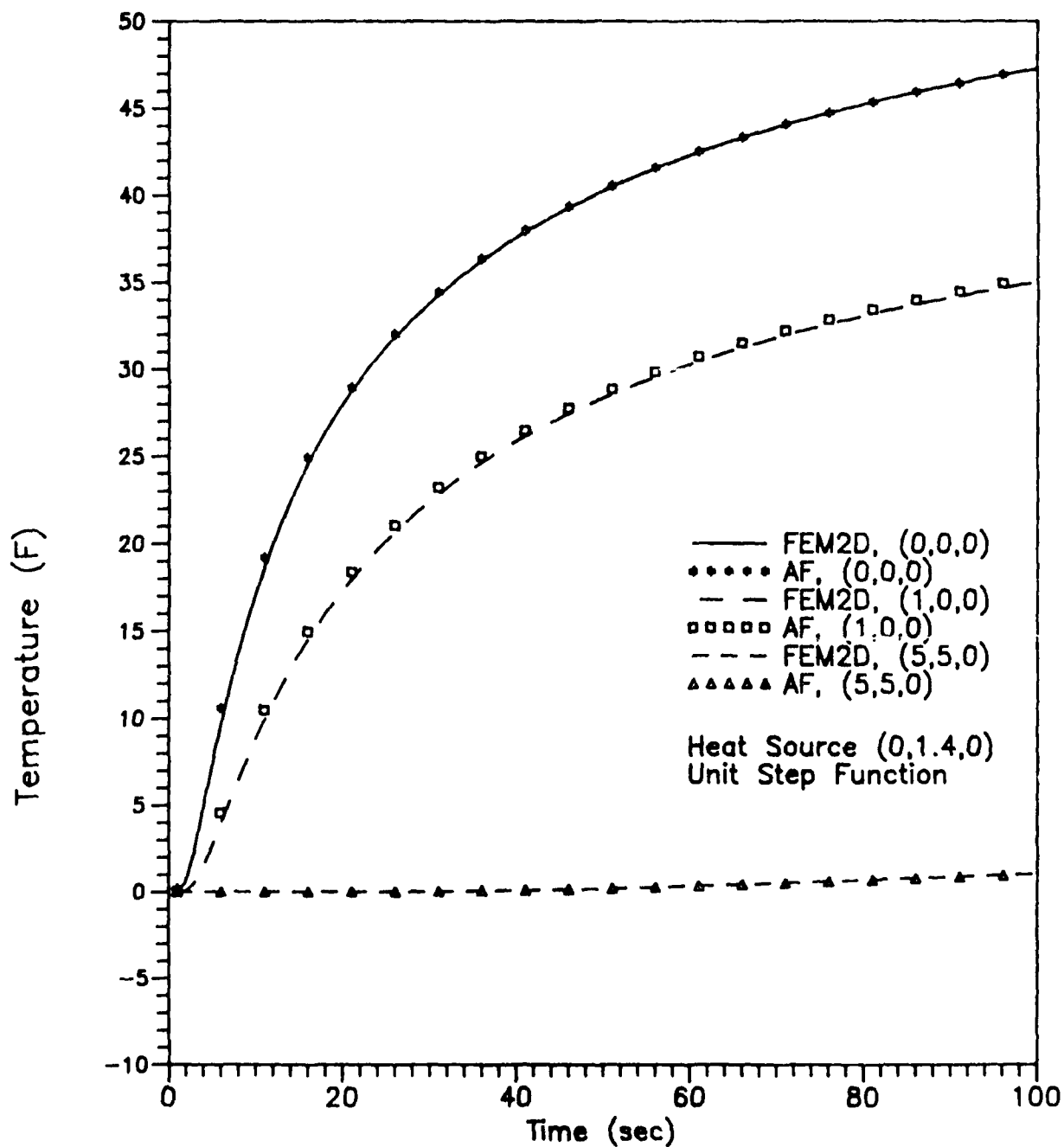


Figure 7-11. Comparison of Temperature Transients Due to a Unit Step Heat Source in a Semi-infinite Solid With a Fully Conductive Crack Surface

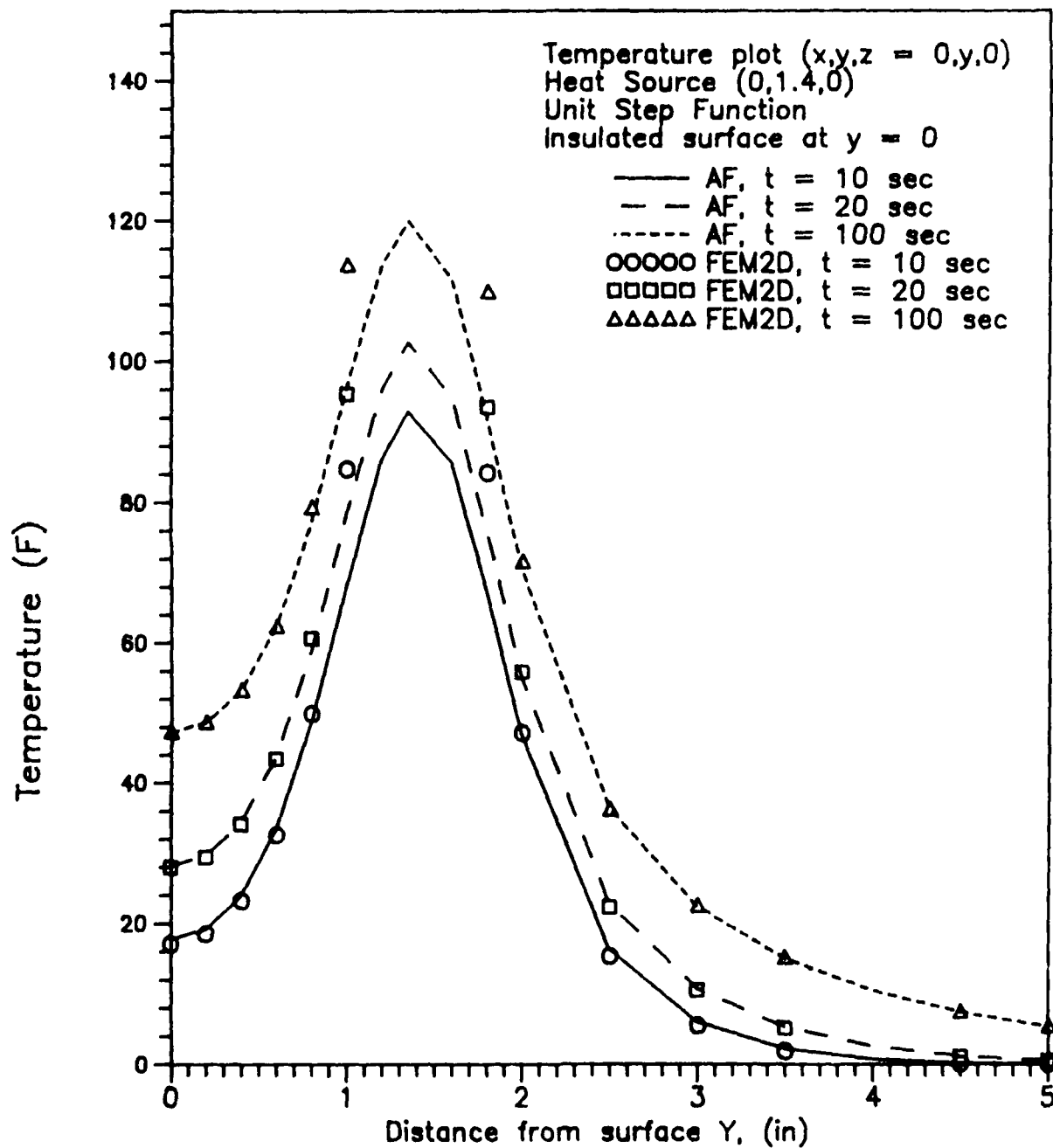


Figure 7-12. Comparison of Temperature Profiles Due to a Unit Step Heat Source in a Semi-infinite Solid With a Fully Conductive Crack Surface

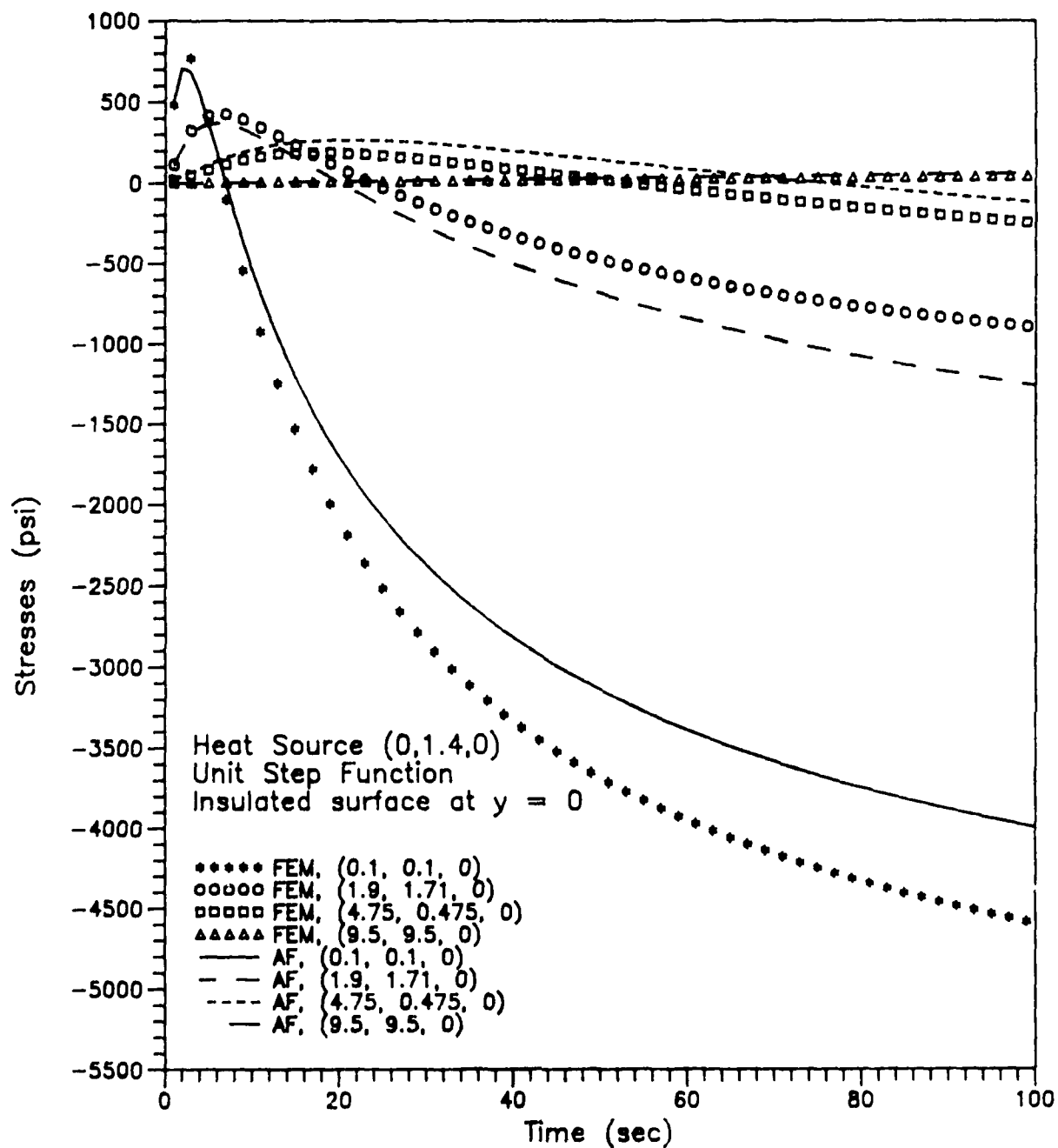


Figure 7-13. Comparison of σ_{zz} Stress Transient Due to a Unit Step Heat Source^{zz} in a Semi-infinite Solid with a Fully Conductive Crack Surface

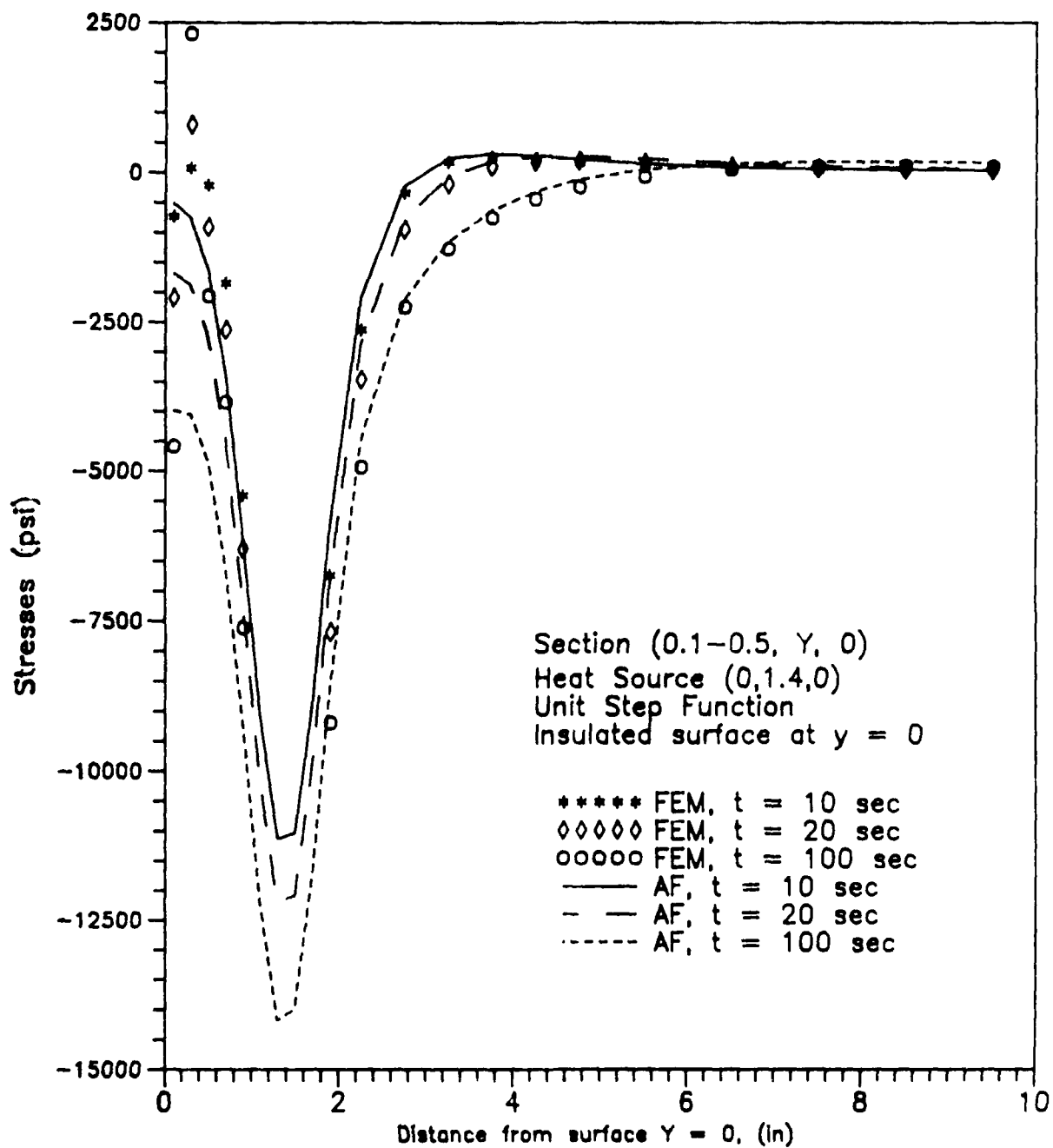


Figure 7-14. Comparison of σ_z Stress Profiles Due to a Unit Step Heat Source²² in a Semi-Infinite Solid With a Fully Conductive Crack Surface

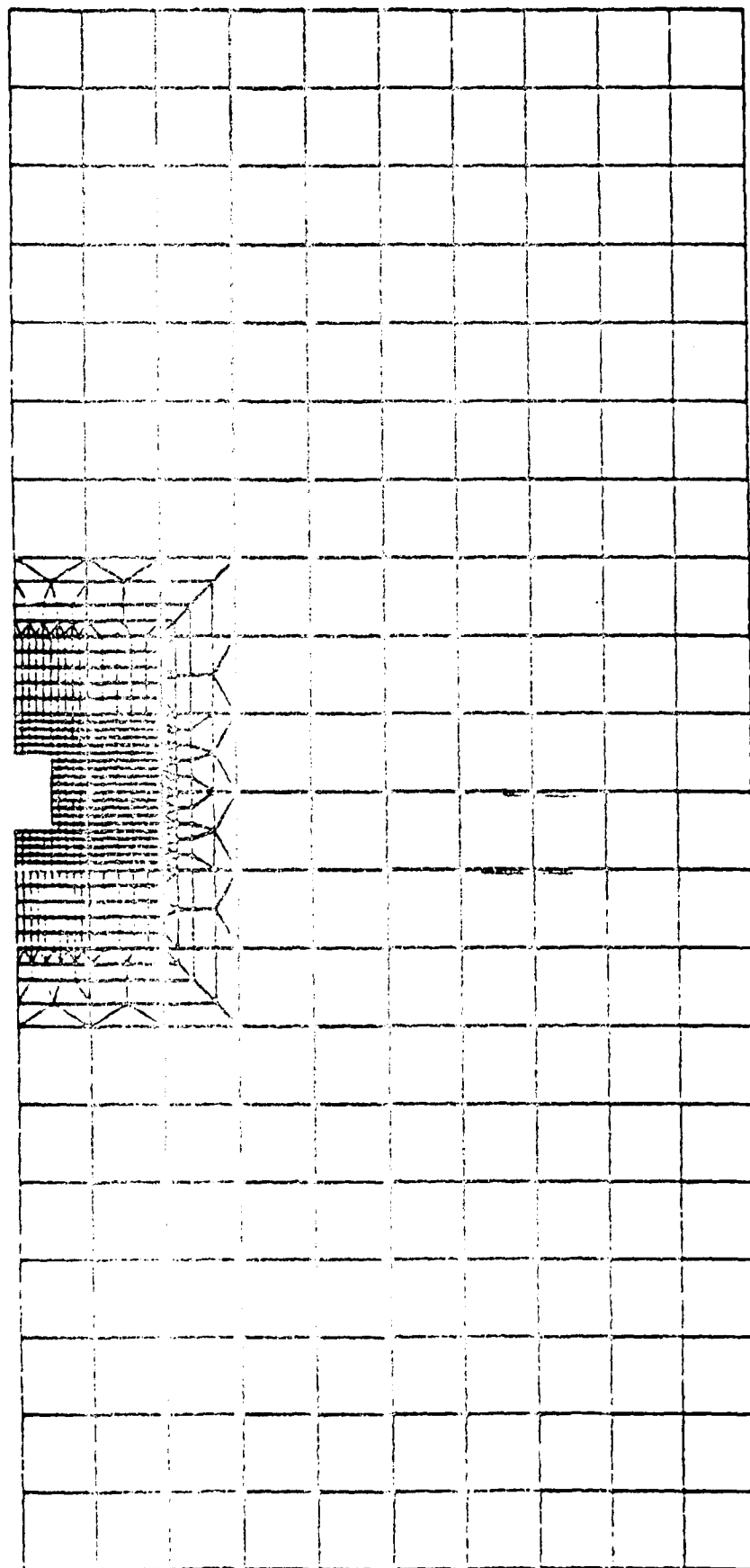


Figure 7-15. Axisymmetric Finite Element Model for Verification of Temperature for a Crack With Insulated Surface

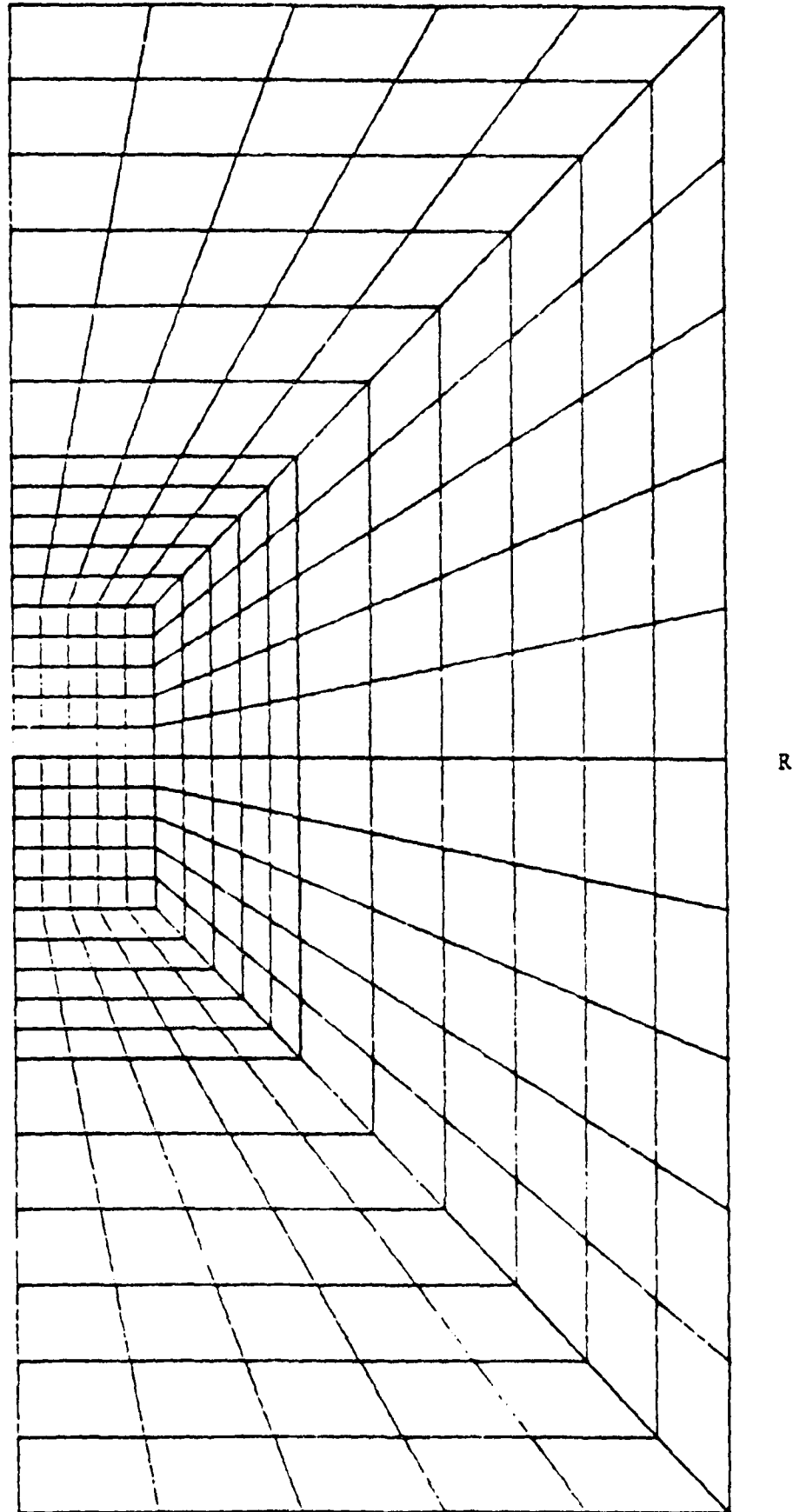


Figure 7-16. Finite Element Mesh at the Crack Region for Semicircular Crack in a Semi-Infinite Solid With Insulated Crack Surface

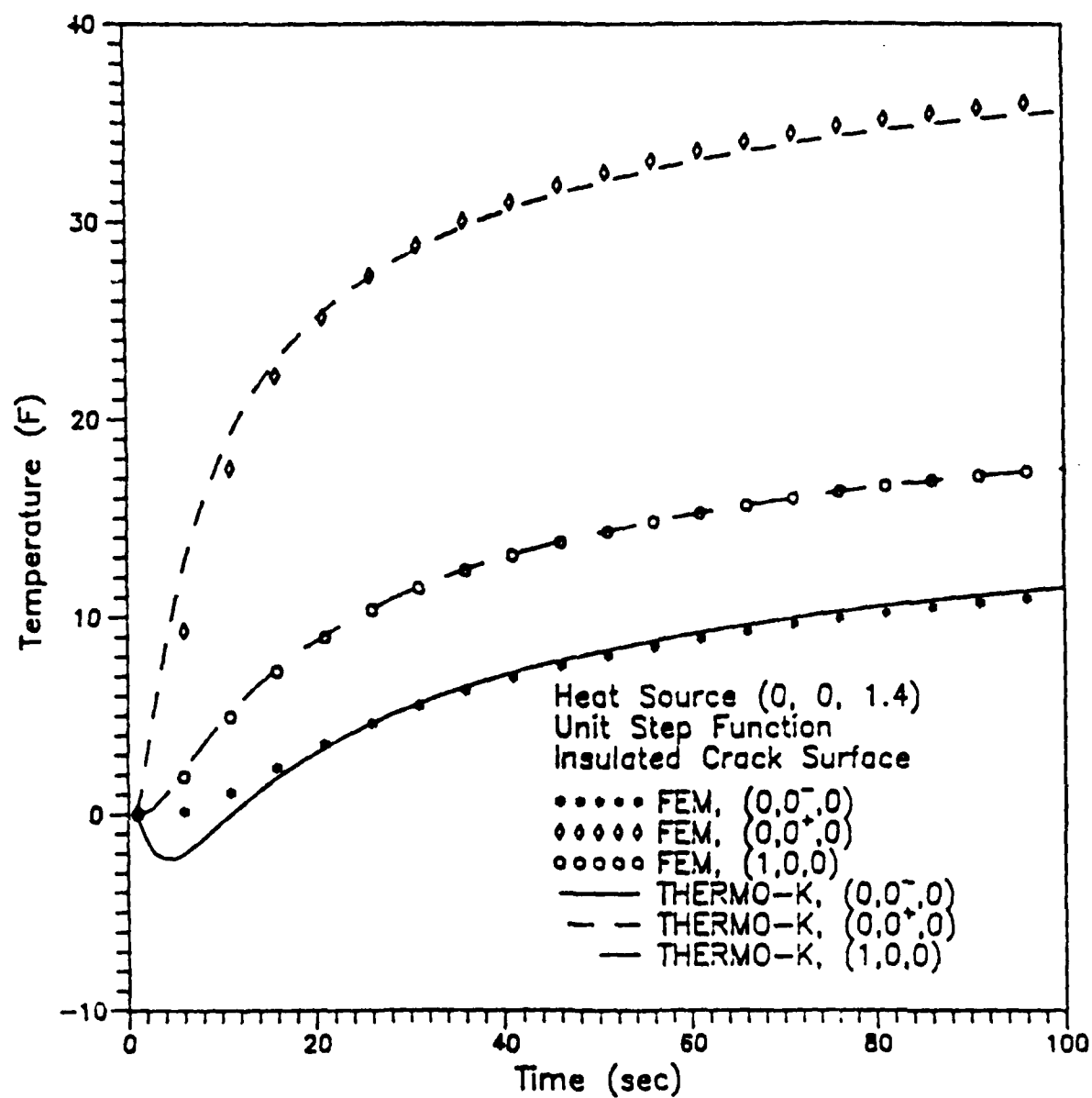


Figure 7-17. Comparison of Temperatures Predicted by THERMO-K and Finite Element Method (T vs. Time)

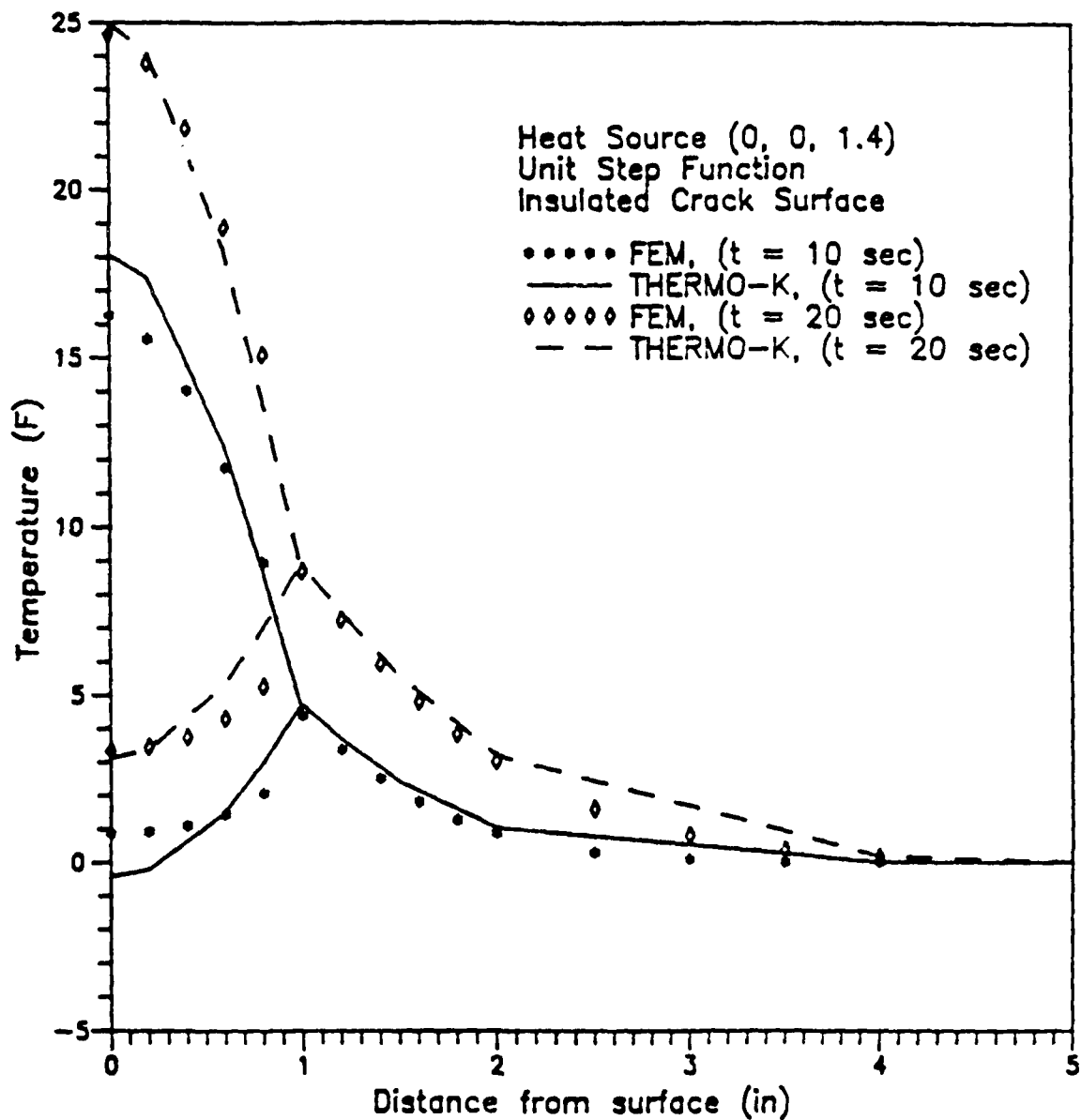


Figure 7-18. Comparison of Temperatures Predicted by THERMO-K and Finite Element Method (T vs. r)

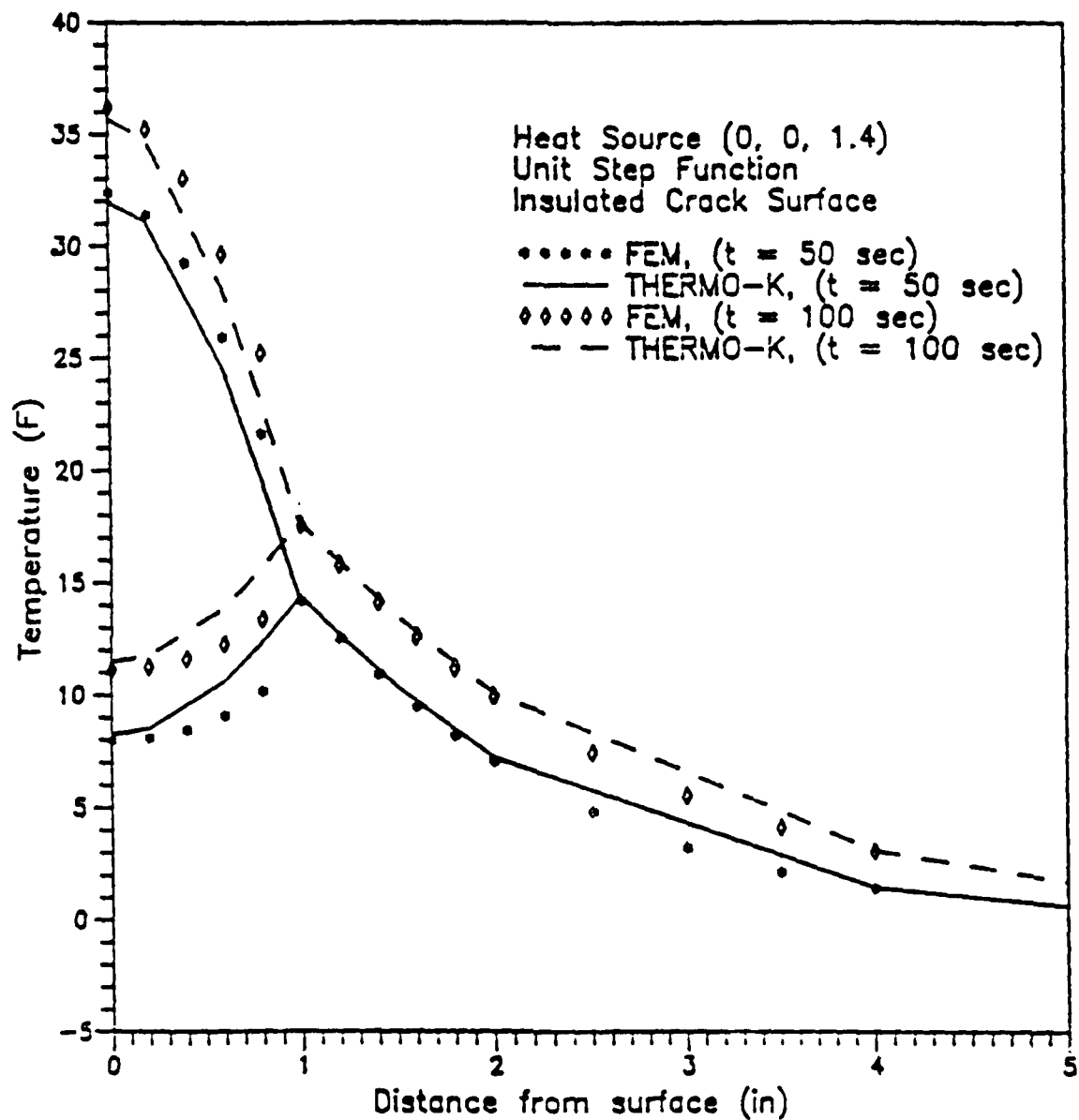


Figure 7-19. Comparison of Temperature Profiles Due to a Unit Step Heat Source in a Semi-infinite Solid With a Fully Insulated Crack Surface at t=50 and 100 Seconds

8.0 THEORETICAL BACKGROUND OF CRACK MODEL 7 -

A QUARTER-CIRCULAR SURFACE CRACK IN A QUARTER-SPACE

This section describes the theoretical basis for crack Model 7 - a quarter-circular surface crack in a quarter-space, i.e., as illustrated in Figure 8-1, a quarter-circular crack of radius a in a quarter-space, $x \geq 0$, $y \geq 0$. The cracked quarter-space is subjected to point heat sources with arbitrary time history $Q(t)$ at any points (x', y', z') in the region of $x \geq 0$, $y \geq 0$.

8.1 Assumptions

The following assumptions were made to simplify the problem:

- (a) The metallic materials are assumed to be isotropic, homogeneous, and linear elastic. Material properties are assumed to be temperature independent.
- (b) The rate of heat application is slow enough that the coupling terms and inertia terms in the general thermoelasticity equations can be neglected, i.e., it is assumed that the decoupled, quasi-static thermoelasticity applies.
- (c) The crack surfaces are assumed to be stress free. The crack surfaces can be completely insulated, fully heat conductive, or partially heat conductive. Heat conductance coefficient h at the crack surfaces is also assumed to be constant throughout the entire temperature range.
- (d) It is assumed that the boundary surfaces of the quarter, surface $y=0$ and surface $x=0$, are insulated.

8.2 Governing Equations

For a three-dimensional stress thermoelasticity problem as illustrated in Figure 8-1, the governing equations are

$$\xi \nabla^2 T = T_{,t} \quad (8-1)$$

$$\sigma_{ij,j} = 0 \quad (8-2)$$

$$\sigma_{ij} = 2G \left[\epsilon_{ij} + \left(\frac{\nu}{1-\nu} \right) \delta_{ij} \epsilon_{kk} - \alpha \left(\frac{1+\nu}{1-\nu} \right) \delta_{ij} T \right] \quad (8-3)$$

$$\epsilon_{ij} = (U_{i,j} + U_{j,i})/2 \quad (8-4)$$

and

$$\nabla^2 U_i + \left(\frac{1+\nu}{1-\nu} \right) U_{j,ji} = 2 \left(\frac{1+\nu}{1-\nu} \right) \alpha T \quad (8-5)$$

where $T=T(x_1, x_2, x_3; t)$ is temperature distribution, t and x_i are time and Cartesian coordinates respectively, $\xi=(k/\rho c)$, k is heat conduction coefficients, ρ is mass density, c is heat capacity, U_i are displacements, α is coefficient of thermal expansion, and G and ν are shear modulus and Poisson's ratio respectively.

Nominal stress distributions derived from these equations are used to develop stress intensity factors via the influence function approach described in the next section.

8.3 Influence Functions for Stress Intensity Factors

For any cracked structure, crack tip stress intensity factors can be determined by integrating the product of the stresses at the crack location in an uncracked structure and an influence function (or weight function) (Buecker, 1973). That is, for a

surface crack as shown in Figure 8-1, the stress intensity factor can be calculated by

$$K_I(\theta) = \int_0^{\pi/2} \int_0^a \sigma_{zz}(\bar{r}, \bar{\theta}, 0; t) m_1(\bar{r}, \bar{\theta}; \theta) \bar{r} d\bar{r} d\bar{\theta} \quad (8-6)$$

$$K_{II}(\theta) = \int_0^{\pi/2} \int_0^a [\sigma_{zr}(\bar{r}, \bar{\theta}, 0; t) m_{2r}(\bar{r}, \bar{\theta}; \theta) + \sigma_{z\theta}(\bar{r}, \bar{\theta}, 0; t) m_{2\theta}(\bar{r}, \bar{\theta}; \theta)] \bar{r} d\bar{r} d\bar{\theta} \quad (8-7)$$

$$K_{III}(\theta) = \int_0^{\pi/2} \int_0^a [\sigma_{zr}(\bar{r}, \bar{\theta}, 0; t) m_{3r}(\bar{r}, \bar{\theta}; \theta) + \sigma_{z\theta}(\bar{r}, \bar{\theta}, 0; t) m_{3\theta}(\bar{r}, \bar{\theta}; \theta)] \bar{r} d\bar{r} d\bar{\theta} \quad (8-8)$$

where $m_1(\bar{r}, \bar{\theta}; \theta)$, $m_{2r}(\bar{r}, \bar{\theta}; \theta)$, $m_{2\theta}(\bar{r}, \bar{\theta}; \theta)$, $m_{3r}(\bar{r}, \bar{\theta}; \theta)$, and $m_{3\theta}(\bar{r}, \bar{\theta}; \theta)$ are influence functions, (r, θ, z) are cylindrical coordinates shown in Figure 8-1, and σ_{zz} , σ_{zr} , and $\sigma_{z\theta}$ are the normal stress and shear stresses at the crack region in an identical but uncracked quarter-space which is under the same temperature distribution as the cracked structure. In this subsection, cylindrical coordinates (r, θ, z) and/or Cartesian coordinates (x, y, z) whichever is more convenient will be used.

Physically, as illustrated in Figure 8-2(a), $m_1(\bar{r}, \bar{\theta}; \theta)$ is the Mode I stress intensity factor at crack tip location (a, θ) due to a pair of equal in magnitude but opposite in direction unit normal forces (in z -direction) applied at point $(\bar{r}, \bar{\theta})$ of the crack surface. Similarly, as illustrated in Figures 8-2(b), $m_{2r}(\bar{r}, \bar{\theta}; \theta)$ and $m_{3r}(\bar{r}, \bar{\theta}; \theta)$ are, respectively, Mode II and Mode III stress intensity factors at crack tip location (a, θ) due to a pair of equal in magnitude but opposite in direction unit radial

shear forces (in the r -direction) applied at point $(\bar{r}, \bar{\theta})$ of the crack surface. And, as shown in Figure 8-2(c), $m_{2\theta}(\bar{r}, \bar{\theta}; \theta)$ and $m_{3\theta}(\bar{r}, \bar{\theta}; \theta)$ are, respectively, Mode II and Mode III stress intensity factors at crack tip location (a, θ) due to a pair of equal in magnitude but opposite in direction unit tangential shear forces (in the θ -direction) applied at point $(\bar{r}, \bar{\theta})$ of the crack surface.

To derive the influence functions $m_1(\bar{r}, \bar{\theta}; \theta)$, the following iterative procedure has been developed:

8.3.1 Influence Function m_1

Step I-0 - Initiation

We first let $L=0$, and

$$\bar{\sigma}_{zz}^{(L)}(r, \theta, 0) = \frac{1}{r} \delta(r - \bar{r}) \delta(\theta - \bar{\theta}) \quad (8-9)$$

$$\bar{\sigma}_{rz}^{(L)}(r, \theta, 0) = \bar{\sigma}_{\theta z}^{(L)}(r, \theta, 0) = 0 \quad (8-10)$$

$$\bar{\sigma}_{yy}^{(L)}(x, 0, z) = \bar{\sigma}_{yx}^{(L)}(x, 0, z) = \bar{\sigma}_{yz}^{(L)}(x, 0, z) = 0 \quad (8-11)$$

$$\bar{\sigma}_{xx}^{(L)}(0, y, z) = \bar{\sigma}_{xy}^{(L)}(0, y, z) = \bar{\sigma}_{zz}^{(L)}(0, y, z) = 0 \quad (8-12)$$

where $\delta(r)$ and $\delta(\theta)$ are Delta functions in r - and θ - directions, respectively.

Step I-1 - Penny-Shaped Crack Solutions

We then calculate stress intensity factors for a penny-shaped crack in an infinite space subjected to four pairs of symmetric

concentrated normal forces on its crack surface. That is, we consider a problem which consists of the cracked quarter-space shown in Figure 8-2(a) as well as its mirror images with respect to the x-z plane and y-z plane. Stress intensity factor solution for a penny-shaped crack in an infinite space subjected to symmetric pairs of concentrated normal forces, i.e., if one pair is at $(\hat{r}, \hat{\theta})$, other pairs of the same magnitude must be at $(\hat{r}, -\hat{\theta})$, $(\hat{r}, \pi - \hat{\theta})$, and $(\hat{r}, -\pi + \hat{\theta})$, has been given by Sih (1973) as

$$K_I^{(L)}(\theta) = \int_0^{\pi/2} \int_0^a \hat{m}_1(\hat{r}, \hat{\theta}; \theta) \bar{\sigma}_{zz}^{(L)}(\hat{r}, \hat{\theta}, 0) \hat{r} d\hat{r} d\hat{\theta} \quad (8-13)$$

$$K_{II}^{(L)}(\theta) = K_{III}^{(L)}(\theta) = 0 \quad (8-14)$$

where

$$\hat{m}_1(\hat{r}, \hat{\theta}; \theta) = \frac{4}{\pi a \sqrt{\pi a (1-r_0)(1+r_0)}} \left(1 + 2 \sum_{n=1}^{\infty} [r_0^n \cos(2n\hat{\theta}) \cos(2n\theta)] \right) \quad (8-15)$$

$$r_0 = \frac{\hat{r}}{a} \quad (8-16)$$

Equation (8-15) is derived by adding influence functions $\hat{m}_1(\hat{r}, \hat{\theta}; \theta)$ and $\hat{m}_1(\hat{r}, \pi - \hat{\theta}; \theta)$, which are defined in Equation (8-13) of section 8.

Step I-2 - Stresses at Surface, $y=0$, (increase L by 1)

It is obvious that stress solutions for a penny-shaped crack in an infinite space subjected to the symmetric concentrated crack surface normal loads do not satisfy the stress free boundary condition at the free surfaces $y=0$ and $x=0$ for the quarter-circular surface crack problem. In fact, by using the

methodology developed by Bell (1979), it can be shown that, for a penny-shaped crack in an infinite space subjected to surface loads symmetric to x-z plane loads on crack surface, stresses at the symmetry plane y=0 are

$$\bar{\sigma}_{yx}^{(L)}(x, 0, z) = \bar{\sigma}_{yz}^{(L)}(x, 0, z) = 0 \quad (8-17)$$

$$\bar{\sigma}_{yy}^{(L)}(x, 0, z) = \bar{\sigma}_{yy}^{(L-1)}(x, 0, z) +$$

$$\int_0^\pi \int_0^a \Omega_1(x, z; \hat{r}, \hat{\theta}) \bar{\sigma}_{zz}^{(L-1)}(\hat{r}, \hat{\theta}, 0) \hat{r} d\hat{r} d\hat{\theta} \quad (8-18)$$

where G and ν are shear modulus and Poisson's ratio, respectively, of the material, $\Omega_1(x, z; \hat{r}, \hat{\theta})$ is defined by Equation (7-17) in Section 7, and

$$\bar{\sigma}_{zz}^{(L-1)}(r, \pi-\theta, 0) = \bar{\sigma}_{zz}^{(L-1)}(r, \theta, 0) \quad 0 \leq \theta \leq \pi/2 \quad (8-19)$$

Step I-3 - Stresses at Surface, x=0

Also, the stress solutions for a penny-shaped crack in an infinite space subjected to the concentrated crack surface normal loads do not satisfy the stress free boundary condition at the free surface x=0 for the quarter-circular surface crack problem. Similar to the procedure used in last step, stresses at the symmetry plane x=0 are

$$\bar{\sigma}_{xy}^{(L)}(0, y, z) = \bar{\sigma}_{xz}^{(L)}(0, y, z) = 0 \quad (8-20)$$

$$\bar{\sigma}_{xx}^{(L)}(0, y, z) = \bar{\sigma}_{xx}^{(L-1)}(0, y, z) +$$

$$\int_0^\pi \int_0^a \Omega_1(-y, z; \hat{r}, \hat{\theta}) \bar{\sigma}_{zz}^{(L-1)}(\hat{r}, \hat{\theta}-\pi/2, 0) \hat{r} d\hat{r} d\hat{\theta} \quad (8-21)$$

where G and ν are shear modulus and Poisson's ratio, respectively, of the material, $\Omega_1(x, z; \hat{r}, \hat{\theta})$ is defined by Equation (7-17) in Section 7, and

$$\bar{\sigma}_{zz}^{(L-1)}(r, -\theta, 0) = \bar{\sigma}_{zz}^{(L-1)}(r, \theta, 0) \quad 0 \leq \theta \leq \pi/2 \quad (8-22)$$

Step I-4 - Stresses in an Uncracked Half-Space

Magnitude of the non-zero stresses on the symmetry planes $y=0$ and $x=0$ given by Equation (8-18) and (8-21) can be greatly reduced by adding two complementary stress solutions, one for an uncracked half-space, $y \geq 0$, subjected to normal loads which are the negative of the normal stresses given by Equation (8-18) at surface $y=0$ and the other for an uncracked half-space, $x \geq 0$, subjected to normal loads which are the negative of the normal stresses given by Equation (8-21) at surface $x=0$. Again, with the solution to the Boussinesq's problem (Timoshenko and Goodier, 1970), it can be shown that the resulting complementary stresses $\bar{\sigma}_{ij}^{(L)}$ at plane $z=0$ are as follows:

$$\begin{aligned} \bar{\sigma}_{zz}^{(L)}(x, y, 0) = & \frac{(1-2\nu)}{2\pi} \int_{-\infty}^{\infty} \int_{-\infty}^{\infty} \bar{\sigma}_{yy}^{(L)}(\hat{x}, 0, \hat{z}) \left(\left[\frac{(x-\hat{x})^2 - \hat{z}^2}{r^4} \right] \right. \\ & \left. [-1 + y(r^2 + y^2)^{-1/2}] + \frac{(x-\hat{x})^2 y}{r^2} (r^2 + y^2)^{-3/2} \right) d\hat{x} d\hat{z} \\ & - \frac{3}{2\pi} \int_{-\infty}^{\infty} \int_{-\infty}^{\infty} \bar{\sigma}_{yy}^{(L)}(\hat{x}, 0, \hat{z}) y \hat{z}^2 (r^2 + y^2)^{-5/2} d\hat{x} d\hat{z} \\ & - \frac{(1-2\nu)}{2\pi} \int_{-\infty}^{\infty} \int_{-\infty}^{\infty} \bar{\sigma}_{xx}^{(L)}(0, -\hat{y}, \hat{z}) \left(\left[\frac{(-y+\hat{y})^2 - \hat{z}^2}{r'^4} \right] \right. \\ & \left. [-1 + x(r'^2 + x^2)^{-1/2}] + \frac{(-y+\hat{y})^2 x}{r'^2} (r'^2 + x^2)^{-3/2} \right) d\hat{y} d\hat{z} \end{aligned}$$

$$+ \frac{3}{2\pi} \int_{-\infty}^{\infty} \int_{-\infty}^{\infty} \bar{\sigma}_{xx}^{(L)}(0, -\hat{y}, \hat{z}) \hat{x} \hat{z}^2 (r'^2 + x^2)^{-5/2} d\hat{y} d\hat{z} \quad (8-23)$$

$$\begin{aligned} \bar{\sigma}_{xz}^{(L)}(x, y, 0) &= \frac{(1-2\nu)}{2\pi} \int_{-\infty}^{\infty} \int_{-\infty}^{\infty} \bar{\sigma}_{yy}^{(L)}(\hat{x}, 0, \hat{z}) \left(\frac{-2(x-\hat{x})\hat{z}}{r^4} \right. \\ &\quad \left. [1 - y(r^2 + y^2)^{-1/2}] + \frac{(x-\hat{x})y\hat{z}}{r^2} (r^2 + y^2)^{-3/2} \right) d\hat{x} d\hat{z} \\ &\quad + \frac{3}{2\pi} \int_{-\infty}^{\infty} \int_{-\infty}^{\infty} \bar{\sigma}_{yy}^{(L)}(\hat{x}, 0, \hat{z}) (x-\hat{x}) y \hat{z} (r^2 + y^2)^{-5/2} d\hat{x} d\hat{z} \\ &\quad - \frac{3}{2\pi} \int_{-\infty}^{\infty} \int_{-\infty}^{\infty} [\bar{\sigma}_{xx}^{(L)}(0, -\hat{y}, \hat{z}) x^2 \hat{z} (r'^2 + x^2)^{-5/2}] d\hat{y} d\hat{z} \end{aligned} \quad (8-24)$$

$$\begin{aligned} \bar{\sigma}_{yz}^{(L)}(x, y, 0) &= \frac{3}{2\pi} \int_{-\infty}^{\infty} \int_{-\infty}^{\infty} [\bar{\sigma}_{yy}^{(L)}(\hat{x}, 0, \hat{z}) y^2 \hat{z} (r^2 + y^2)^{-5/2}] d\hat{x} d\hat{z} \\ &\quad + \frac{(1-2\nu)}{2\pi} \int_{-\infty}^{\infty} \int_{-\infty}^{\infty} \bar{\sigma}_{xx}^{(L)}(0, -\hat{y}, \hat{z}) \left(\frac{-2(-y+\hat{y})\hat{z}}{r'^4} \right. \\ &\quad \left. [1 - x(r^2 + x^2)^{-1/2}] + \frac{(-y+\hat{y})x\hat{z}}{r'^2} (r'^2 + x^2)^{-3/2} \right) d\hat{y} d\hat{z} \\ &\quad + \frac{3}{2\pi} \int_{-\infty}^{\infty} \int_{-\infty}^{\infty} \bar{\sigma}_{xx}^{(L)}(0, -\hat{x}, \hat{z}) (-y+\hat{y}) x \hat{z} (r'^2 + x^2)^{-5/2} d\hat{y} d\hat{z} \end{aligned} \quad (8-25)$$

where

$$r^2 = (x-\hat{x})^2 + \hat{z}^2 \quad (8-26)$$

$$r'^2 = (y - \hat{y})^2 + \hat{z}^2 \quad (8-27)$$

$\bar{\sigma}_{yy}^{(L)}(\hat{x}, 0, \hat{z})$ are the normal stresses calculated from Equation (8-18), and $\bar{\sigma}_{xx}^{(L)}(0, \hat{y}, \hat{z})$ are the normal stresses calculated by Equation (8-21).

Similarly, complementary stresses at surfaces $y=0$ and $x=0$ are

$$\begin{aligned} \bar{\sigma}_{yy}^{(L)}(x, 0, z) = & -\frac{(1-2\nu)}{2\pi} \int_{-\infty}^{\infty} \int_{-\infty}^{\infty} \bar{\sigma}_{xx}^{(L)}(0, -\hat{y}, \hat{z}) \left(\left[\frac{\hat{y}^2 - (z - \hat{z})^2}{r'^4} \right] \right. \\ & \left. [-1 + x(r'^2 + x^2)^{-1/2}] + \frac{(z - \hat{z})^2 x}{r'^2} (r'^2 + x^2)^{-3/2} \right) d\hat{y} d\hat{z} \\ & + \frac{3}{2\pi} \int_{-\infty}^{\infty} \int_{-\infty}^{\infty} \bar{\sigma}_{xx}^{(L)}(0, -\hat{y}, \hat{z}) x(-y + \hat{y})^2 (r'^2 + x^2)^{-5/2} d\hat{y} d\hat{z} \end{aligned} \quad (8-28)$$

$$\begin{aligned} \bar{\sigma}_{xx}^{(L)}(0, y, z) = & \frac{(1-2\nu)}{2\pi} \int_{-\infty}^{\infty} \int_{-\infty}^{\infty} \bar{\sigma}_{yy}^{(L)}(\hat{x}, 0, \hat{z}) \left(\left[\frac{\hat{x}^2 - (z - \hat{z})^2}{r^4} \right] \right. \\ & \left. [-1 + y(r^2 + y^2)^{-1/2}] + \frac{(z - \hat{z})^2 y}{r^2} (r^2 + y^2)^{-3/2} \right) d\hat{x} d\hat{z} \\ & - \frac{3}{2\pi} \int_{-\infty}^{\infty} \int_{-\infty}^{\infty} \bar{\sigma}_{yy}^{(L)}(\hat{x}, 0, \hat{z}) y(x - \hat{x})^2 (r^2 + y^2)^{-5/2} d\hat{x} d\hat{z} \end{aligned} \quad (8-29)$$

where

$$r^2 = \hat{x}^2 + (z - \hat{z})^2 \quad (8-30)$$

$$r'^2 = \hat{y}^2 + (z - \hat{z})^2 \quad (8-31)$$

Step I-5 Check Convergence

If the residual stresses $\bar{\sigma}_{ij}^{(L)}$ at the crack surface calculated from Equations (7-38) to (7-40) satisfy the preset convergence criterion (1% difference is used in this study as the convergence criterion), then calculate the influence functions m_1 as follows:

$$m_1(\bar{r}, \bar{\theta}; \theta) = \sum_{j=0}^{L-1} K_I^{(j)} \quad (8-32)$$

and stop the iteration here, otherwise go to Step I-1 and repeat Step I-1 to Step I-5.

8.3.2 Influence Functions m_{2r} and m_{3r}

Similarly, an iterative procedure for calculating m_{2r} , and m_{3r} can be developed as follows:

Step II-0 - Initiation

We first let $L=0$, and

$$\bar{\sigma}_{rz}^{(L)}(r, \theta, 0) = \frac{1}{r} \delta(r - \bar{r}) \delta(\theta - \bar{\theta}) \quad (8-33)$$

$$\bar{\sigma}_{zz}^{(L)}(r, \theta, 0) = \bar{\sigma}_{\theta z}^{(L)}(r, \theta, 0) = 0 \quad (8-34)$$

$$\bar{\sigma}_{yy}^{(L)}(x, 0, z) = \bar{\sigma}_{yx}^{(L)}(x, 0, z) = \bar{\sigma}_{yz}^{(L)}(x, 0, z) = 0 \quad (8-35)$$

$$\bar{\sigma}_{xx}^{(L)}(0, y, z) = \bar{\sigma}_{xy}^{(L)}(0, y, z) = \bar{\sigma}_{zz}^{(L)}(0, y, z) = 0 \quad (8-36)$$

where $\delta(r)$ and $\delta(\theta)$ are Delta functions in r - and θ - directions, respectively.

Step II-1 - Penny-Shaped Crack Solutions

We then calculate stress intensity factors for a penny-shaped crack in an infinite space subjected to four symmetric pairs of concentrated radial shear forces on its crack surface. That is, we consider a problem which consists of the cracked quarter-space shown in Figure 8-2(b) as well as its mirror images with respect to the x - z plane and the y - z plane. Stress intensity factor solution for a penny-shaped crack in an infinite space subjected to symmetric pairs of concentrated radial shear forces, i.e., if one pair is at $(\hat{r}, \hat{\theta})$, other pairs of the same magnitude must be at $(\hat{r}, -\hat{\theta})$, $(\hat{r}, \pi - \hat{\theta})$, and $(\hat{r}, -\pi + \hat{\theta})$, , has been given by Sih (1973) as

$$K_I^{(L)}(\theta) = 0 \quad (8-37)$$

$$K_{II}^{(L)}(\theta) = \int_0^{\pi/2} \int_0^a \hat{m}_{2r}(\hat{r}, \hat{\theta}; \theta) \bar{\sigma}_{2r}^{(L)}(\hat{r}, \hat{\theta}; \theta) \hat{r} d\hat{r} d\hat{\theta} \quad (8-38)$$

$$K_{III}^{(L)}(\theta) = \int_0^{\pi/2} \int_0^a \hat{m}_{3r}(\hat{r}, \hat{\theta}; \theta) \bar{\sigma}_{2r}^{(L)}(\hat{r}, \hat{\theta}; \theta) \hat{r} d\hat{r} d\hat{\theta} \quad (8-39)$$

where

$$\hat{m}_{2r}(\hat{r}, \hat{\theta}; \theta) = \frac{4}{\pi a (2-\nu) \sqrt{\pi a (1-r_0) (1+r_0)}} \{ (2-\nu) r_0 +$$

$$2 \sum_{n=1}^{\infty} [1+2n\nu+(1-\nu-2n\nu)r_o^2]r_o^{n-1}\cos(2n\hat{\theta}) \cos(2n\theta) \quad (8-40)$$

$$\hat{m}_{3r}(\hat{r}, \hat{\theta}; \theta) = \frac{-8\sqrt{(1+r_o)(1-r_o)}}{\pi a(2-\nu)\sqrt{\pi a}}$$

$$\sum_{n=1}^{\infty} [1-(1+2n)\nu]r_o^{2n-1}\cos(2n\hat{\theta})\cos(2n\theta) \quad (8-41)$$

and r_o is defined in Equation (8-16). Equation (8-40) is the sum of influence functions $m_{2r}(r, \theta; \theta)$ and $m_{2r}(r, \pi-\theta; \theta)$, which are defined by Equation (7-48) in Section 7. Equation (8-41) is derived from Equation (7-49) of section in a similar way.

Step II-2 - Stresses at Surface, $y=0$, (increase L by 1)

It is obvious that stress solutions for a penny-shaped crack in an infinite space subjected to the concentrated crack surface radial shear loads do not satisfy the stress free boundary condition at the free surfaces $y=0$ and $x=0$ for the quarter-circular surface crack problem. In fact, by using the methodology developed by Bell (1979), it can be shown that, for a penny-shaped crack in an infinite space subjected to crack surface radial loads symmetric to x-z plane loads on crack surface, stresses at the symmetry plane $y=0$ are calculated by

$$\bar{\sigma}_{yx}^{(L)}(x, 0, z) = \bar{\sigma}_{yz}^{(L)}(x, 0, z) = 0 \quad (8-42)$$

$$\bar{\sigma}_{yy}^{(L)}(x, 0, z) = \bar{\sigma}_{yy}^{(L-1)}(x, 0, z) +$$

$$\int_0^{\pi} \int_0^a \Omega_3(x, z; \hat{r}, \hat{\theta}) \bar{\sigma}_{zr}^{(L-1)}(\hat{r}, \hat{\theta}, 0) \hat{r} d\hat{r} d\hat{\theta} \quad (8-43)$$

where G and ν are shear modulus and Poisson's ratio, respectively, of the material, $\Omega_3(x, z; \hat{r}, \hat{\theta})$ is defined by Equation (7-17) in Section 7, and

$$\bar{\sigma}_{zr}^{(L-1)}(r, \pi-\theta, 0) = \bar{\sigma}_{zr}^{(L-1)}(r, \theta, 0) \quad 0 \leq \theta \leq \pi/2 \quad (8-44)$$

Step II-3 - Stresses at Surface, $x=0$

Also, the stress solutions for a penny-shaped crack in an infinite space subjected to the concentrated crack surface shear loads do not satisfy the stress free boundary at the free surface $x=0$ for the quarter-circular surface crack problem. Similar to the procedure used in last step, stresses at the symmetry plane $x=0$ are calculated by

$$\bar{\sigma}_{xy}^{(L)}(0, y, z) = \bar{\sigma}_{xz}^{(L)}(0, y, z) = 0 \quad (8-45)$$

$$\bar{\sigma}_{xx}^{(L)}(0, y, z) = \bar{\sigma}_{xx}^{(L-1)}(0, y, z) +$$

$$\int_0^\pi \int_0^a \Omega_3(-y, z; \hat{r}, \hat{\theta}) \bar{\sigma}_{zr}^{(L-1)}(\hat{r}, \hat{\theta}-\pi/2, 0) \hat{r} d\hat{r} d\hat{\theta} \quad (8-46)$$

where G and ν are shear modulus and Poisson's ratio, respectively, of the material, $\Omega_3(x, z; \hat{r}, \hat{\theta})$ is defined in Equation (7-17), and

$$\bar{\sigma}_{zr}^{(L-1)}(r, -\theta, 0) = \bar{\sigma}_{zr}^{(L-1)}(r, \theta, 0) \quad 0 \leq \theta \leq \pi/2 \quad (8-47)$$

Step II-4 - Stresses in an Uncracked Half-Space

The non-zero stresses on the symmetry planes $y=0$ and $x=0$ given by Equations (8-43) and (8-46) can be greatly reduced by adding two complementary stress solutions for an uncracked half-space, one for half-space $y \geq 0$ subjected to normal loads on its surface $y=0$ which equal to the negative of the normal stresses given by Equation (8-43), and the other for half-space $x \geq 0$ subjected to normal loads on its surface $x=0$, which equal to the negative of the normal stresses given by Equation (8-46). Again, with the solution to the Boussinesq's problem, it can be shown that the resulting complementary stresses $\bar{\sigma}_{ij}^{(L)}$ at plane $z=0$ are as calculated by the same equations as Equations (8-23)-(8-31).

Step II-5 Check Convergence

If the residual crack surface stresses $\bar{\sigma}_{ij}^{(L)}$ calculated from Equations (8-23) to (8-31) satisfy the preset convergence criterion (1% difference is used in this study as the convergence criterion), then calculate the influence functions m_{2r} and m_{3r} as follows:

$$m_{2r}(\bar{r}, \bar{\theta}; \theta) = \sum_{j=0}^{L-1} K_{II}^{(j)} \quad (8-48)$$

$$m_{3r}(\bar{r}, \bar{\theta}; \theta) = \sum_{j=0}^{L-1} K_{III}^{(j)} \quad (8-49)$$

and stop iteration here, otherwise go to Step II-1 and repeat Step II-1 to Step II-5.

8.3.3 Influence Functions $m_{2\theta}$ and $m_{3\theta}$

An iterative procedure for calculating $m_{2\theta}$, and $m_{3\theta}$ can be developed as follows.

Step III-0 - Initiation

We first let $L=0$, and

$$\bar{\sigma}_{z\theta}^{(L)}(r, \theta, 0) = \frac{1}{r} \delta(r-\bar{r}) \delta(\theta-\bar{\theta}) \quad (8-50)$$

$$\bar{\sigma}_{zz}^{(L)}(r, \theta, 0) = \bar{\sigma}_{zr}^{(L)}(r, \theta, 0) = 0 \quad (8-51)$$

$$\bar{\sigma}_{yy}^{(L)}(x, 0, z) = \bar{\sigma}_{yx}^{(L)}(x, 0, z) = \bar{\sigma}_{yz}^{(L)}(x, 0, z) = 0 \quad (8-52)$$

$$\bar{\sigma}_{xx}^{(L)}(0, y, z) = \bar{\sigma}_{xy}^{(L)}(0, y, z) = \bar{\sigma}_{zz}^{(L)}(0, y, z) = 0 \quad (8-53)$$

where $\delta(r)$ and $\delta(\theta)$ are Delta functions in r - and θ - directions, respectively.

Step III-1 - Penny-Shaped Crack Solutions

We then calculate stress intensity factors for a penny-shaped crack in an infinite space subjected to four pairs of concentrated tangential shear forces on its crack surface. That is, we consider a problem which consists of the cracked quarter-space shown in Figure 8-2(c) as well as its mirror images with respect to the x - z plane and the y - z plane. Stress intensity factor solution for a penny-shaped crack in an infinite space subjected to pairs of symmetric concentrated tangential shear forces, i.e., if one pair is at $(\hat{r}, \hat{\theta})$, another pair of the same

magnitude must be at $(\hat{r}, \hat{\theta} - \pi)$ and two other pairs of the same magnitude but reverse in direction must be at $(\hat{r}, -\hat{\theta})$ and $(\hat{r}, \pi - \hat{\theta})$, has been given by Sih (1973) as

$$K_I^{(L)}(\theta) = 0 \quad (8-54)$$

$$K_{II}^{(L)}(\theta) = \int_0^{\pi/2} \int_0^a \hat{m}_{2\theta}(\hat{r}, \hat{\theta}; \theta) \bar{\sigma}_{z\theta}^{(L)}(\hat{r}, \hat{\theta}; \theta) \hat{r} d\hat{r} d\hat{\theta} \quad (8-55)$$

$$K_{III}^{(L)}(\theta) = \int_0^{\pi/2} \int_0^a \hat{m}_{3\theta}(\hat{r}, \hat{\theta}; \theta) \bar{\sigma}_{z\theta}^{(L)}(\hat{r}, \hat{\theta}; \theta) \hat{r} d\hat{r} d\hat{\theta} \quad (8-56)$$

where

$$\hat{m}_{2\theta}(\hat{r}, \hat{\theta}; \theta) = \frac{8}{\pi a(2-\nu) \sqrt{\pi a(1-r_0)(1+r_0)}} \sum_{n=1}^{\infty} [1-2n\nu + (1+2n\nu)r_0^2] r_0^{2(n-1)} \sin(2n\hat{\theta}) \cos(2n\theta) \quad (8-57)$$

$$\hat{m}_{3\theta}(\hat{r}, \hat{\theta}; \theta) = \frac{8}{\pi a(2-\nu) \sqrt{\pi a(1-r_0)(1+r_0)}} \sum_{n=1}^{\infty} [1+(1+2n)\nu + (1+2n\nu)r_0^2] r_0^{2n-1} \sin(2n\hat{\theta}) \sin(2n\theta) \quad (8-58)$$

where r_0 is defined in Equation (8-16). Equation (8-57) is the difference of influence functions $m_{2\theta}(\hat{r}, \hat{\theta}; \theta)$ and $m_{2\theta}(\hat{r}, \pi - \hat{\theta}; \theta)$, which are defined by Equation (7-59) in Section 7. Equation (8-58) is derived by a similar way from Equation (7-60) of Section 7.

Step III-2 - Stresses at Surface, $y=0$, (increase L by 1)

It is obvious that stress solutions for a penny-shaped crack in an infinite space subjected to the concentrated crack surface tangential shear loads do not satisfy the stress free boundary at the free surfaces $y=0$ and $x=0$ for the quarter-circular surface crack problem. In fact, by using the methodology developed by Bell (1979), it can be shown that, for a penny-shaped crack in an infinite space subjected to surface loads symmetric to x-z plane loads on crack surface, stresses at the symmetry plane $y=0$ are calculated by

$$\bar{\sigma}_{yx}^{(L)}(x, 0, z) = \bar{\sigma}_{yz}^{(L)}(x, 0, z) = 0 \quad (8-59)$$

$$\bar{\sigma}_{yy}^{(L)}(x, 0, z) = \bar{\sigma}_{yy}^{(L-1)}(x, 0, z) +$$

$$\int_0^\pi \int_0^a \Omega_2(x, z; \hat{r}, \hat{\theta}) \bar{\sigma}_{z\theta}^{(L-1)}(\hat{r}, \hat{\theta}, 0) \hat{r} d\hat{r} d\hat{\theta} \quad (8-60)$$

where G and ν are shear modulus and Poisson's ratio, respectively, of the material, $\Omega_2(x, z; \hat{r}, \hat{\theta})$ is defined in Equation (7-17) of Section 7, and

$$\bar{\sigma}_{z\theta}^{(L-1)}(r, \pi-\theta, 0) = -\bar{\sigma}_{z\theta}^{(L-1)}(r, \theta, 0) \quad 0 \leq \theta \leq \pi/2 \quad (8-61)$$

Step III-3 - Stresses at Surface, $x=0$

Also, the stress solutions for a penny-shaped crack in an infinite space subjected to the concentrated crack surface shear loads do not satisfy the stress free boundary at the free surface $x=0$ for the quarter-circular surface crack problem. Similar to

the procedure used in last step, stresses at the symmetry plane $x=0$ are calculated by

$$\bar{\sigma}_{xy}^{(L)}(0, y, z) = \bar{\sigma}_{xz}^{(L)}(0, y, z) = 0 \quad (8-62)$$

$$\bar{\sigma}_{xx}^{(L)}(0, y, z) = \bar{\sigma}_{xx}^{(L-1)}(0, y, z) +$$

$$\int_0^\pi \int_0^a \Omega_2(-y, z; \hat{r}, \hat{\theta}) \bar{\sigma}_{z\theta}^{(L-1)}(\hat{r}, \hat{\theta} - \pi/2, 0) \hat{r} d\hat{r} d\hat{\theta} \quad (8-63)$$

where G and ν are shear modulus and Poisson's ratio, respectively, of the material, $\Omega_2(x, z; \hat{r}, \hat{\theta})$ is defined by Equation (8-17) in Section 8, and

$$\bar{\sigma}_{z\theta}^{(L-1)}(r, -\theta, 0) = -\bar{\sigma}_{z\theta}^{(L-1)}(r, \theta, 0) \quad 0 \leq \theta \leq \pi/2 \quad (8-64)$$

Step III-4 - Stresses in an Uncracked Half-Space

The non-zero stresses on the symmetry planes $y=0$ and $x=0$ given by Equations (8-60) and (8-63) can be greatly reduced by adding two complementary stress solutions, one for an uncracked half-space, $y \geq 0$, subjected to normal loads which are the negative of the normal stresses given by Equation (8-60) on its surface $y=0$, and the other for an uncracked half-space, $x \geq 0$, subjected to normal loads which are the negative of the normal stresses given by Equation (8-63) on its surface $x=0$. Again, with the solution to the Boussinesq's problem, it can be shown that the resulting complementary stresses $\bar{\sigma}_{ij}^{(L)}$ at plane $z=0$ are as calculated by the same equations as Equations (8-23) to (8-31).

Step III-5 Check Convergence

If the residual crack surface stresses $\bar{\sigma}_{ij}^{(L)}$ calculated from Equations (8-23) to (8-31) satisfy the preset convergence criterion (1% difference is used in this study as the convergence criterion), then calculate the influence functions m_{2r} and m_{3r} as follows:

$$m_{2\theta}(\bar{r}, \bar{\theta}; \theta) = \sum_{j=0}^{L-1} K_{II}^{(j)} \quad (8-65)$$

$$m_{3\theta}(\bar{r}, \bar{\theta}; \theta) = \sum_{j=0}^{L-1} K_{III}^{(j)} \quad (8-66)$$

and stop iteration here ,otherwise go to Step III-1 and repeat Step III-1 to Step III-5.

8.4 Principle of Superposition

In general, as shown in Figure 8-1, there may be multiple heat sources (or sinks) within the quarter-space which will cause thermal stresses and stress intensity factors at crack tips in the structure. Since the problem is linear, it is easily demonstrated that total stress intensity factor can be calculated as the sum of the stress intensity factors caused by each individual heat source or sink, acting independently. That is

$$K(t) = \sum_i [K(t)]_i \quad (8-67)$$

where $K(t)$ is the total stress intensity factor and $[K(t)]_i$ is the stress intensity factor due to the i^{th} heat source.

8.5 Green's Function Concept for Time Integration

In Equation (8-67), the stress intensity factor $[K(t)]_i$ caused by each individual heat source can be solved with the concept of Green's function integration. As illustrated in Figure 8-3, the stress intensity factor due to a heat source of intensity $Q_i(t)$ can be calculated by

$$[K(t)]_i = \int_0^t Q_i(\tau) G_i(t-\tau) d\tau \quad (\text{no summation}) \quad (8-68)$$

where $G_i(t)$ is the stress intensity factors due to a Delta function $\delta(t)$ heat source at the i^{th} heat source location.

As shown in Figure 8-3, in general, the Green's function $G_i(t)$ will decay and approach to zero after a decay period t_d . Therefore, the integration range in Equation (8-68) can be reduced from $(t-t_d)$ to t . Such a reduction in the integration range greatly increases the speed of the calculation because, instead of integrating for the entire time history, it is only necessary to integrate backwards from the present time t to $(t-t_d)$ as follows

$$[K(t)]_i = \int_0^t Q_i(\tau) G_i(t-\tau) d\tau \quad (8-69)$$

8.6 Green's Function for Fully Heat Conductive Cracks

Previous subsections of this section show that the stress intensity factors for this crack models can be easily obtained by Equations (8-6) to (8-8), (8-67), and (8-69) if the temperature and stress distributions and thereby the stress intensity factors at the crack tip, resulting from an instantaneous heat source (or

sink) $Q\delta(t)$ at any arbitrary location (x',y',z') in the uncracked quarter-space (Figure 8-4), can be solved. The uncracked quarter-space shares the same temperature distribution as the cracked quarter-space. As the first step, we consider the problem of a fully heat conductive surface crack, i.e., in this section, it is assumed that heat flux can flow across the crack surfaces without any heat loss or resistance. Solutions for a more general, partially heat conductive crack will be discussed in the next section. However, as will be seen in the next section and as shown in Appendix A of this report, for a crack model with symmetry about its crack plane such as this crack model, crack surface heat conductivity will affect Mode II stress intensity factor solutions but not Mode I or Mode III stress intensity factor solutions. In other words, whether the crack surfaces are fully heat conductive, insulated, or partially heat conductive, the K_I and K_{III} solutions will remain the same for a quarter-circular surface crack in a quarter-space. Thus, if only Mode I or Mode III fractures are of major interest, the stress intensity factor solutions can be obtained by assuming the crack surfaces are fully heat conductive. The assumption of a fully heat conductive crack will greatly shorten the computation time for temperatures, thermal stresses, and stress intensity factors.

Since thermal stresses and stress intensity factors do not depend on the initial stress-free temperature of the solid, it is conveniently assumed that the initial temperature of the plate is zero, i.e., $T(x,y,z;0)=0$. To solve for the Green's function of this crack model, the following boundary conditions need to be satisfied in addition to the governing equations listed in Equations (8-1) to (8-5):

at $y = 0, x \geq 0,$

$$kT_{,y}(x,0,z;t) = 0 \quad (8-70)$$

$$\sigma_{yy}(x,0,z;t) = 0 \quad (8-71)$$

$$\sigma_{yx}(x,0,z;t) = \sigma_{yz}(x,0,z;t) = 0 \quad (8-72)$$

at $x=0, y \geq 0,$

$$kT_{,x}(0,y,z;t) = 0 \quad (8-73)$$

$$\sigma_{xx}(0,y,z;t) = 0 \quad (8-74)$$

$$\sigma_{xy}(0,y,z;t) = \sigma_{xz}(0,y,z;t) = 0 \quad (8-75)$$

at infinity

$$T(x,y,z;t) = 0 \quad (8-76)$$

$$\sigma_{ij}(x,y,z;t) = 0 \quad (8-77)$$

at $z=0, (x^2+y^2) \leq a^2, x \geq 0, y \geq 0,$

$$T(x,y,0^+;t) = T(x,y,0^-;t) \quad (8-78)$$

$$\sigma_{zz}(x,y,0^+;t) = \sigma_{zz}(x,y,0^-;t) \quad (8-79)$$

$$\sigma_{zx}(x,y,0^+;t) = \sigma_{zx}(x,y,0^-;t) \quad (8-80)$$

$$\sigma_{zy}(x,y,0^+;t) = \sigma_{zy}(x,y,0^-;t) \quad (8-81)$$

$$U_i(x,y,0^+;t) = U_i(x,y,0^-;t) \quad i = 1,2,3 \quad (8-82)$$

Temperature solution to the problem of a quarter-space with a fully heat conductive surface crack can be obtained by solving

Equation (8-1) along with boundary conditions Equations (8-70), (8-73), (8-76), and (8-78). An analytical form of the temperature solution has been given by Carslaw and Jaeger (1959) as follows:

$$T(x,y,z;t) = \frac{Q}{8\rho c(\pi\xi t)^{3/2}} \sum_{i=1}^4 \exp\left(\frac{-R_i^2}{4\xi t}\right) \quad (8-83)$$

where ρ is density, c is heat capacity (specific heat), ξ is defined in Equation (8-1) and

$$R_1^2 = (x-x')^2 + (y-y')^2 + (z-z')^2 \quad (8-84)$$

$$R_2^2 = (x+x')^2 + (y-y')^2 + (z-z')^2 \quad (8-85)$$

$$R_3^2 = (x-x')^2 + (y+y')^2 + (z-z')^2 \quad (8-86)$$

$$R_4^2 = (x+x')^2 + (y+y')^2 + (z-z')^2 \quad (8-87)$$

Solution given by Equation (8-83) is the superposition of the temperature solution for four instantaneous heat sources of intensity Q situated at (x',y',z') , $(-x',y',z')$, $(x',-y',z')$, and $(-x',-y',z')$, respectively, in an infinite space.

The next step is to solve for the stress distribution due to the temperature distribution of Equation (8-83) in an uncracked quarter-space. Boley and Weiner (1960) and Parkus (1968) have shown that a particular solution to the thermal stress problem can be expressed in terms of a thermoelastic potential ϕ as follows

$$\sigma_{xx} = 2G (\phi_{,xx} - \nabla^2 \phi) \quad (8-88)$$

$$\sigma_{yy} = 2G (\phi_{,yy} - \nabla^2 \phi) \quad (8-89)$$

$$\sigma_{zz} = 2G (\phi_{,zz} - \nabla^2 \phi) \quad (8-90)$$

$$\sigma_{xy} = 2G \phi_{,xy} \quad \sigma_{yz} = 2G \phi_{,yz} \quad \sigma_{zx} = 2G \phi_{,zx} \quad (8-91)$$

$$\phi(x,y,z,t) = \alpha \left(\frac{1+\nu}{1-\nu} \right) \xi \int_0^t T(x,y,z;\tau) d\tau + \phi_0 \quad (8-92)$$

where ϕ_0 is a function of x, y, z and t such that ϕ would remain finite as t approaches infinity. Substitution of Equation (8-83) into Equation (8-92) yields

$$\phi(x,y,z;t) = -\frac{\alpha Q(1+\nu)}{4\pi\rho cR(1-\nu)} \sum_{i=1}^4 \operatorname{erf}\left(\frac{R_i}{2\sqrt{\xi t}}\right) \quad (8-93)$$

where $\operatorname{erf}(z)$ is an error function and R_i 's are defined in Equations (8-84) to (8-87).

In general, the particular solution ϕ shown in Equation (8-93) satisfies boundary conditions of Equations (8-72), (8-75), (8-77), and (8-79) to (8-82) but does not fulfill the stress free boundary conditions of Equations (8-71) at $y=0$ and (8-74) at $x=0$. In other words, $\sigma_{yy}(x,0,z;t)$ and $\sigma_{xx}(0,y,z;t)$ derived from the thermoelastic potential ϕ of Equation (8-93) does not vanish but equals to

$$\sigma'_{yy}(x,0,z;t) = \frac{(1+\nu)\alpha GQ}{(1-\nu)\pi\rho c} \sum_{i=1}^2 \frac{1}{R_i^2} \left[1 - 3\left(\frac{y'}{R_i}\right)^2 \right] \left[\frac{1}{R_i} \operatorname{erf}\left(\frac{R_i}{2\sqrt{\xi t}}\right) - \right.$$

$$\frac{1}{\sqrt{\pi\xi t}} \exp\left(\frac{-R_1^2}{4\xi t}\right) + \frac{(y'^2 - R_1^2)}{2\xi t \sqrt{\pi\xi t}} \exp\left(\frac{-R_1^2}{4\xi t}\right) \quad (8-94)$$

$$\sigma'_{xx}(0, y, z; t) = \frac{(1+\nu) \alpha G Q}{(1-\nu) \pi \rho c} \sum_{i=1}^2 \frac{1}{R_i^2} \left(\left[1 - 3 \left(\frac{x'}{R_i} \right)^2 \right] \left[\frac{1}{R_i} \operatorname{erf}\left(\frac{R_i}{2\sqrt{\xi t}}\right) - \frac{1}{\sqrt{\pi\xi t}} \exp\left(\frac{-R_i^2}{4\xi t}\right) \right] + \frac{(x'^2 - R_i^2)}{2\xi t \sqrt{\pi\xi t}} \exp\left(\frac{-R_i^2}{4\xi t}\right) \right) \quad (8-95)$$

where

$$R_{2,1}^2 = (x \pm x')^2 + y'^2 + (z - z')^2 \quad (8-96)$$

$$R_{2,1}^2 = x'^2 + (y \pm y')^2 + (z - z')^2 \quad (8-97)$$

Stresses at crack region, $z=0$, $x \geq 0$, $y \geq 0$, $(x^2 + y^2) \leq a^2$, resulting from the thermoelastic potential ϕ of Equation (8-93) are

$$\begin{aligned} \bar{\sigma}_{zz}^{(0)}(x, y, 0; t) &= \frac{(1+\nu) \alpha G Q}{2(1-\nu) \pi \rho c} \sum_{i=1}^4 \frac{1}{R_i^2} \left(\left[1 - 3 \left(\frac{z'}{R_i} \right)^2 \right] \cdot \right. \\ &\quad \left[\frac{1}{R_i} \operatorname{erf}\left(\frac{R_i}{2\sqrt{\xi t}}\right) - \frac{1}{\sqrt{\pi\xi t}} \exp\left(\frac{-R_i^2}{4\xi t}\right) \right] + \\ &\quad \left. \frac{(z'^2 - R_i^2)}{2\xi t \sqrt{\pi\xi t}} \exp\left(\frac{-R_i^2}{4\xi t}\right) \right) \quad (8-98) \end{aligned}$$

$$\bar{\sigma}_{xz}^{(0)}(x, y, 0; t) = - \frac{3(1+\nu) \alpha G Q}{2(1-\nu) \pi \rho c} \sum_{i=1}^4 \frac{1}{R_i^4} (x - x') z'.$$

$$\left[\frac{1}{\sqrt{\pi \xi t}} \left(1 + \frac{R_i^2}{6 \xi t} \right) \exp\left(-\frac{R_i^2}{4 \xi t}\right) - \frac{1}{R_i} \operatorname{erf}\left(\frac{R_i}{2 \sqrt{\xi t}}\right) \right] \quad (8-99)$$

$$\bar{\sigma}_{yz}^{(0)}(x, y, 0; t) = - \frac{3(1+\nu) a G Q}{2(1-\nu) \pi \rho c} \sum_{i=1}^4 \frac{1}{R_i^4} (y-y') z'.$$

$$\left[\frac{1}{\sqrt{\pi \xi t}} \left(1 + \frac{R_i^2}{6 \xi t} \right) \exp\left(-\frac{R_i^2}{4 \xi t}\right) - \frac{1}{R_i} \operatorname{erf}\left(\frac{R_i}{2 \sqrt{\xi t}}\right) \right] \quad (8-100)$$

where

$$R_1^2 = (x-x')^2 + (y-y')^2 + z'^2 \quad (8-101)$$

$$R_2^2 = (x+x')^2 + (y-y')^2 + z'^2 \quad (8-102)$$

$$R_3^2 = (x-x')^2 + (y+y')^2 + z'^2 \quad (8-103)$$

$$R_4^2 = (x+x')^2 + (y+y')^2 + z'^2 \quad (8-104)$$

A complementary set of stresses $\bar{\sigma}_{ij}$ can then be added to cancel out the non-zero surface stresses at $y=0$, and at $x=0$, i.e., stresses given by Equations (8-94) and (8-95). The procedures for calculating the complementary stresses $\bar{\sigma}_{ij}$ are as follows:

Step 0 Initiation

Set $L=1$, and

$$\bar{\sigma}_{yy}^{(L)}(\hat{x}, 0, \hat{z}) = \sigma'_{yy}(\hat{x}, 0, \hat{z}; t) \quad (8-105)$$

$$\bar{\sigma}_{xx}^{(L)}(0, \hat{y}, \hat{z}) = \sigma'_{xx}(0, \hat{y}, \hat{z}; t) \quad (8-106)$$

where σ'_{yy} and σ'_{xx} are calculated by Equations (8-94) and (8-95), respectively.

Step 1 Stresses at Crack Region

Calculate stresses $\bar{\sigma}_{zz}^{(L)}(x, y, 0)$, $\bar{\sigma}_{xz}^{(L)}(x, y, 0)$, and $\bar{\sigma}_{yz}^{(L)}(x, y, 0)$ by Equations (8-23), (8-24), and (8-25), respectively.

Step 2 Stresses at $y=0$ and at $x=0$ (increase L by 1)

Calculate stresses $\bar{\sigma}_{yy}^{(L)}(x, 0, z)$ and $\bar{\sigma}_{xx}^{(L)}(0, y, z)$ by

$$\begin{aligned} \bar{\sigma}_{yy}^{(L)}(x, 0, z) = & \int_0^\pi \int_0^a [\Omega_1(x, z; \hat{r}, \hat{\theta}) \bar{\sigma}_{zz}^{(L-1)}(\hat{r}, \hat{\theta}, 0) + \\ & \Omega_3(x, z; \hat{r}, \hat{\theta}) \bar{\sigma}_{zr}^{(L-1)}(\hat{r}, \hat{\theta}, 0) + \\ & \Omega_2(x, z; \hat{r}, \hat{\theta}) \bar{\sigma}_{z\theta}^{(L-1)}(\hat{r}, \hat{\theta}, 0)] \hat{r} d\hat{r} d\hat{\theta} \end{aligned} \quad (8-107)$$

$$\bar{\sigma}_{xx}^{(L)}(0, y, z) = \int_0^\pi \int_0^a [\Omega_1(-y, z; \hat{r}, \hat{\theta}) \bar{\sigma}_{zz}^{(L-1)}(\hat{r}, \hat{\theta} - \pi/2, 0) +$$

$$\Omega_3(-y, z; \hat{r}, \hat{\theta}) \bar{\sigma}_{zr}^{(L-1)}(\hat{r}, \hat{\theta} - \pi/2, 0) + \\ \Omega_2(-y, z; \hat{r}, \hat{\theta}) \bar{\sigma}_{z\theta}^{(L-1)}(\hat{r}, \hat{\theta} - \pi/2, 0)] \hat{r} d\hat{r} d\hat{\theta} \quad (8-108)$$

where $\bar{\sigma}_{ij}^{(L-1)}(r, \theta, 0)$ are polar components of the stresses

$\bar{\sigma}_{ij}^{(L-1)}(x, y, 0)$ and $\bar{\sigma}_{ij}^{(L-1)}(r, \theta, 0)$ satisfy the symmetry conditions of Equations (8-22), (8-47), and (8-61).

Step 3 Convergence Check

If the residual surface stresses, $\bar{\sigma}_{yy}^{(L)}(x, 0, z)$ and $\bar{\sigma}_{xx}^{(L)}(0, y, z)$, satisfy the preset convergence criterion (1% difference is used in this study as the convergence criterion), then calculate total stresses on crack surface by

$$\sigma_{zz}(x, y, 0) = \sum_{n=0}^L \bar{\sigma}_{zz}^{(n)}(x, y, 0) \quad (8-109)$$

$$\sigma_{zx}(x, y, 0) = \sum_{n=0}^L \bar{\sigma}_{zx}^{(n)}(x, y, 0) \quad (8-110)$$

$$\sigma_{zy}(x, y, 0) = \sum_{n=0}^L \bar{\sigma}_{zy}^{(n)}(x, y, 0) \quad (8-111)$$

and stop the iteration here, otherwise go to Step 1 and repeat Step 1 to Step 3.

To sum up this section, the Green's functions for the stress intensity factors of a fully heat conductive quarter-circular surface crack in a quarter-space are calculated by substituting the total stresses in crack region calculated from Equations (8-109) - (8-111) and the influence functions calculated by Equations (8-32), (8-48), (8-49), and (8-65)-(8-66) into Equations (8-6) to (8-8) and integrating Equations (8-6) to (8-8) by the numerical integration scheme depicted in Appendix D.

8.7 Green's Function for Partially Heat Conductive Cracks

In subsection 8.6 of this report, the Green's function solution for a single instantaneous heat source at any arbitrary point in a quarter-space with a quarter-circular surface crack is discussed. The crack surfaces in subsection 8.6 is assumed to be fully heat conductive. In reality, the crack surfaces are expected to be somewhere between completely insulated and fully heat conductive, i.e., crack surfaces are expected to be partially heat conductive. A general approach to treat a partially heat conductive crack is studied in detail in Appendix A of this report. Application of the concept given in Appendix A to the problem of a quarter-circular surface crack in a quarter-space is discussed in this section.

Governing heat transfer equation for a quarter-space with a quarter-circular, partially heat conductive crack surfaces is still Equation (8-1), and the boundary conditions given in Equations (8-70), (8-73), and (8-76) remain unchanged. The only difference will be that the the boundary condition at $z=0$, $(x^2+y^2) \leq a^2$, i.e., Equation (8-78), is replaced by

$$T_{,z}(x,y,0;t) = \frac{\lambda}{a} [T(x,y,0^+;t) - T(x,y,0^-;t)] \quad (8-112)$$

where λ is defined as (ah/k) in which h is crack surface heat conductance coefficient and k is material thermal conductivity. From Equation (8-112), it can be easily seen that the crack surfaces are fully heat conductive when $\lambda=\infty$ and the crack surfaces are completely insulated when $\lambda=0$. Any λ values between 0 and ∞ are corresponding to a partially heat conductive crack.

As discussed in Appendix A, when a crack is completely insulated or partially heat conductive, the resulting temperatures on both sides of a crack will be different, i.e., there is a temperature jump across the crack surface when λ equals to zero or a finite number. This temperature jump is analogous to the temperature jump created by a series of distributed heat dipoles (Carslaw and Jaeger, 1959) situated at the crack location. Thus, the overall temperature distribution can be obtained as the superposition of the fully conductive solution, Equation (8-83), and a solution for the distributed heat dipoles. From Equation (8-93), it can be shown, by summing temperature solutions for a point heat source and a point heat sink with infinitesimally small distance in between, that temperature solution for an instantaneous heat dipole of strength M situated at $(x=\bar{x}, y=\bar{y}, z=0)$ in a insulated quarter-space, $(x \geq 0, y \geq 0)$, is

$$T(x, y, z; t) = \frac{M z}{16\pi^{3/2} (\xi t)^{5/2} \rho c} \sum_{i=1}^4 \exp\left(\frac{R_i^2}{4\xi t}\right) \quad (8-113)$$

where

$$R_1^2 = (x-\bar{x})^2 + (y-\bar{y})^2 + z^2 \quad (8-114)$$

$$R_2^2 = (x+\bar{x})^2 + (y-\bar{y})^2 + z^2 \quad (8-115)$$

$$R_3^2 = (x-\bar{x})^2 + (y+\bar{y})^2 + z^2 \quad (8-116)$$

$$R_4^2 = (x+\bar{x})^2 + (y+\bar{y})^2 + z^2 \quad (8-117)$$

Physically, Equation (8-113) is the temperature response generated by four instantaneous dipoles of strength M situated at $(\bar{x}, \bar{y}, 0)$, $(\bar{x}, -\bar{y}, 0)$, $(-\bar{x}, \bar{y}, 0)$ and $(-\bar{x}, -\bar{y}, 0)$, respectively, in an infinite solid. Thus, resulting temperature from distributed heat dipoles of strength $M(x, y, t)$ situated at region $[z=0, x \geq 0, y \geq 0, 0 \leq (x^2 + y^2) \leq a^2]$ of the quarter-space is

$$T(x, y, z; t) = \frac{z}{16\pi^{3/2}(\xi)^{5/2}\rho c} \sum_{i=1}^4 \int_0^t \int_{S_c} \frac{M(\bar{x}, \bar{y}; \tau)}{(t-\tau)^{5/2}} \exp\left(\frac{R_i^2}{4\xi\tau}\right) dS_c d\tau \quad (8-118)$$

where $dS_c = d\bar{x} \cdot d\bar{y}$, S_c is the crack area, $z=0$, $(x^2 + y^2) \leq a^2$, $x \geq 0$, $y \geq 0$, and R_i 's are defined in Equations (8-114) to (8-117).

Substitution of the sum of Equations (8-83) and (8-118) into Equation (8-112) yield a Fredholm integral equation for the heat dipole distribution $M(x, y, t)$ as follows:

$$\begin{aligned} & \frac{Qz'}{t^{5/2}} \left(\exp\left[\frac{-(x-x')^2 - (y-y')^2 - z^2}{4\xi t}\right] + \exp\left[\frac{-(x-x')^2 - (y+y')^2 - z^2}{4\xi t}\right] \right) \\ & + \int_{S_c} \int_0^t \frac{M(\bar{x}, \bar{y}, \tau)}{(t-\tau)^{5/2}} \left(\exp\left[\frac{-(x-\bar{x})^2 - (y-\bar{y})^2}{4\xi(t-\tau)}\right] + \right. \end{aligned}$$

$$\begin{aligned} & \exp\left[\frac{-(x-\bar{x})^2 - (y+\bar{y})^2}{4\xi(t-\tau)}\right] + \exp\left[\frac{-(x+\bar{x})^2 - (y-\bar{y})^2}{4\xi(t-\tau)}\right] + \\ & \exp\left[\frac{-(x+\bar{x})^2 - (y+\bar{y})^2}{4\xi(t-\tau)}\right] d\tau dS_c = \frac{16\pi^{3/2}\lambda k}{\rho c a^{1/2}} M(x, y, t) \end{aligned} \quad (8-119)$$

where dS_c , and S_c are defined in Equation (8-118), k , ρ , and c are thermal conductivity, mass density, and specific heat, respectively, of the material, a is the radius of the semi-circular surface crack, and $\lambda = ah/k$ is the non-dimensionalized crack surface conductance defined in Equation (8-112).

A numerical approximation method is used in the computer program to solve Equation (8-119). Since the temperature jump between two adjacent crack surfaces has to be zero at the crack tip, $z=0$, $(x^2+y^2)=a^2$, we assume that

$$\begin{aligned} M(x, y, t) = M(r, \theta, t) = & \sum_{m=1}^L \sum_{n=1}^{L'} [b_{mn}(t) \sin(n\theta) + \\ & \hat{b}_{mn} \cos(n\theta)] \cos\left[\frac{(2m-1)\pi r}{2a}\right] \end{aligned} \quad (8-120)$$

where L and L' are the maximum numbers of terms included in the calculation and $\hat{b}_{mn}(t)$ and $b_{mn}(t)$ are time functions, which are determined by substituting Equation (8-120) into Equation (8-119).

Similar to the fully heat conductive case, a thermoelastic potential due to the distributed thermal dipoles at the crack

region in an uncracked quarter-space can be derived by integrating the temperature solution, Equation (8-118). That is,

$$\phi(x, y; t) = \alpha \xi \left(\frac{1+\nu}{1-\nu} \right) \int_0^t T(x, y, z; \tau) d\tau + \phi_0 \quad (8-121)$$

where $T(x, y, z; t)$ is the temperature solution given in Equation (8-118) and ϕ_0 is an analytic function to make ϕ remain finite at infinity. It can be shown that stresses at the crack region due to the thermoelastic potential ϕ of Equation (8-121) are as follows:

$$\bar{\sigma}_{zz}^{(0)}(x, y, 0; t) = 0 \quad (8-122)$$

$$\bar{\sigma}_{zx}^{(0)}(x, y, 0; t) = \int_{S_C} \int_0^t \sigma_{zx}^M(x, y, 0; \tau; \bar{x}, \bar{y}) M(\bar{x}, \bar{y}, \tau) d\tau dS_C \quad (8-123)$$

$$\bar{\sigma}_{zy}^{(0)}(x, y, 0; t) = \int_{S_C} \int_0^t \sigma_{zy}^M(x, y, 0; \tau; \bar{x}, \bar{y}) M(\bar{x}, \bar{y}, \tau) d\tau dS_C \quad (8-124)$$

where

$$\begin{aligned} \sigma_{zx}^M(x, y, 0; t; \bar{x}, \bar{y}) = & \frac{(1+\nu)\alpha G}{(1-\nu)2\pi\rho c} \sum_{i=1}^4 \frac{(x-\bar{x})}{R_i^2} \left(\frac{3}{R_i^3} \operatorname{erf}\left(\frac{R_i}{\sqrt{4\xi(t-\tau)}}\right) \right. \\ & \left. - \frac{1}{\sqrt{\pi\xi(t-\tau)}} \left[\frac{3}{R_i^2} + \frac{1}{2\xi(t-\tau)} \right] \exp\left(\frac{-R_i^2}{4\xi(t-\tau)}\right) \right) \end{aligned} \quad (8-125)$$

$$\begin{aligned} \sigma_{zy}^M(x, y, 0; t; \bar{x}, \bar{y}) = & \frac{(1+\nu) \alpha G}{(1-\nu) 2 \pi \rho c} \sum_{i=1}^4 \frac{(y - \bar{y}_i)}{R_i^2} \left(\frac{3}{R_i^3} \operatorname{erf}\left(\frac{R_i}{\sqrt{4\xi(t-\tau)}}\right) \right. \\ & \left. - \frac{1}{\sqrt{\pi\xi(t-\tau)}} \left[\frac{3}{R_i^2} + \frac{1}{2\xi(t-\tau)} \right] \exp\left(\frac{-R_i^2}{4\xi(t-\tau)}\right) \right) \end{aligned} \quad (8-126)$$

$$R_1^2 = (x - \bar{x})^2 + (y - \bar{y})^2 \quad (8-127)$$

$$R_2^2 = (x - \bar{x})^2 + (y + \bar{y})^2 \quad (8-128)$$

$$R_3^2 = (x + \bar{x})^2 + (y - \bar{y})^2 \quad (8-129)$$

$$R_4^2 = (x + \bar{x})^2 + (y + \bar{y})^2 \quad (8-130)$$

and ξ is defined in Equation (8-1). Similarly, stresses at planes $y=0$ and $x=0$ due to the thermoelastic potential of Equation (8-121) are

$$\sigma'_{yx}(x, 0, z; t) = \sigma'_{yz}(x, 0, z; t) = 0 \quad (8-131)$$

$$\sigma'_{yy}(x, y, 0; t) = \int_{S_c} \int_0^t \sigma_{yy}^M(x, 0, z; \tau; \bar{x}, \bar{y}) M(\bar{x}, \bar{y}, \tau) d\tau dS_c \quad (8-132)$$

$$\sigma'_{yx}(0, y, z; t) = \sigma'_{xz}(0, y, z; t) = 0 \quad (8-133)$$

$$\sigma'_{xx}(x, y, 0; t) = \int_{S_c} \int_0^t \sigma_{xx}^M(0, y, z; \tau; \bar{x}, \bar{y}) M(\bar{x}, \bar{y}, \tau) d\tau dS_c \quad (8-134)$$

where

$$\begin{aligned} \sigma_{yy}^M(x, 0, z; \bar{x}, \bar{y}) = & \frac{(1-\nu) \alpha G z}{(1+\nu) \pi \rho c} \sum_{i=1}^2 \left(\frac{1}{R_i^2} \left(\frac{5\bar{y}^2 - R_i^2}{R_i^4} \right) \left[\frac{-3}{R_i^3} \operatorname{erf} \left(\frac{R_i}{2\sqrt{\xi(t-\tau)}} \right) \right. \right. \\ & + \left. \left(\frac{3}{R_i^2 \sqrt{\pi \xi(t-\tau)}} + \frac{1}{2\xi(t-\tau) \sqrt{\pi \xi(t-\tau)}} \right) \exp \left(\frac{-R_i^2}{4\xi(t-\tau)} \right) \right] \\ & + \left. \frac{(\bar{y}^2 - R_i^2)}{4\sqrt{\pi} \xi^{5/2}(t-\tau)^{5/2} R_i^2} \exp \left(\frac{-R_i^2}{4\xi(t-\tau)} \right) \right] \end{aligned} \quad (8-135)$$

$$\begin{aligned} \sigma_{xx}^M(0, y, z; \bar{x}, \bar{y}) = & \frac{(1-\nu) \alpha G z}{(1+\nu) \pi \rho c} \sum_{i=1}^4 \left(\frac{1}{R_i^2} \left(\frac{5\bar{x}^2 - R_i^2}{R_i^4} \right) \left[\frac{-3}{R_i^3} \operatorname{erf} \left(\frac{R_i}{2\sqrt{\xi(t-\tau)}} \right) \right. \right. \\ & + \left. \left(\frac{3}{R_i^2 \sqrt{\pi \xi(t-\tau)}} + \frac{1}{2\xi(t-\tau) \sqrt{\pi \xi(t-\tau)}} \right) \exp \left(\frac{-R_i^2}{4\xi(t-\tau)} \right) \right] \\ & + \left. \frac{(\bar{x}^2 - R_i^2)}{4\sqrt{\pi} \xi^{5/2}(t-\tau)^{5/2} R_i^2} \exp \left(\frac{-R_i^2}{4\xi(t-\tau)} \right) \right] \end{aligned} \quad (8-136)$$

$$R_1^2 = (x - \bar{x})^2 + \bar{y}^2 + z^2 \quad (8-137)$$

$$R_2^2 = (x + \bar{x})^2 + \bar{y}^2 + z^2 \quad (8-138)$$

$$R_3^2 = \bar{x}^2 + (y - \bar{y})^2 + \bar{z}^2 \quad (8-139)$$

$$R_4^2 = \bar{x}^2 + (y + \bar{y})^2 + \bar{z}^2 \quad (8-140)$$

The following iterative procedure has been developed to calculate stresses at the crack region in an uncracked quarter-space, which shares the same temperature distribution as the cracked solid:

Step 0 Initiation

Set $L=1$, and

$$\bar{\sigma}_{yy}^{(L)}(\hat{x}, 0, \hat{z}) = \sigma'_{yy}(\hat{x}, 0, \hat{z}; t) \quad (8-141)$$

$$\bar{\sigma}_{xx}^{(L)}(0, \hat{y}, \hat{z}) = \sigma'_{xx}(0, \hat{y}, \hat{z}; t) \quad (8-142)$$

where σ'_{yy} and σ'_{xx} are calculated by Equations (8-132) and (8-134), respectively.

Step 1 Stresses at Crack Region

Calculate stresses $\bar{\sigma}_{zz}^{(L)}(x, y, 0)$, $\bar{\sigma}_{xz}^{(L)}(x, y, 0)$, and $\bar{\sigma}_{yz}^{(L)}(x, y, 0)$ by Equations (8-23), (8-24), and (8-25), respectively.

Step 2 Stresses at $y=0$ and at $x=0$ (increase L by 1)

Calculate stresses $\bar{\sigma}_{yy}^{(L)}(x, 0, z)$ and $\bar{\sigma}_{xx}^{(L)}(0, y, z)$ by Equations (8-107) and (8-108), respectively.

Step 3 Convergence Check

If the residual surface stresses, $\bar{\sigma}_{yy}^{(L)}(x_0, z)$ and $\bar{\sigma}_{xx}^{(L)}(0, y, z)$, satisfy the preset convergence criterion (1% difference is used in this study as the convergence criterion), then calculate total stresses on crack surface by

$$\sigma_{zz}(x, y, 0) = \sum_{n=0}^L \bar{\sigma}_{zz}^{(n)}(x, y, 0) \quad (8-143)$$

$$\sigma_{zx}(x, y, 0) = \sum_{n=0}^L \bar{\sigma}_{zx}^{(n)}(x, y, 0) \quad (8-144)$$

$$\sigma_{zy}(x, y, 0) = \sum_{n=0}^L \bar{\sigma}_{zy}^{(n)}(x, y, 0) \quad (8-145)$$

and stop the iteration here, otherwise go to Step 1 and repeat Step 1 to Step 3.

Stress intensity factors are then calculated by substituting the stresses at the crack region, i.e., stresses given by Equations (8-133) to (8-135), into Equations (8-6) to (8-8). It can be shown that, in general, the Modes I and III stress intensity factors caused by the distributed heat dipoles at the crack region are zero while the Mode II stress intensity factor caused by the distributed heat dipoles is not zero. This observation reiterates the fact, deduced in Appendix A, that, for a cracked structure with symmetry with respect to the crack plane such as the current crack model, crack surface heat conductivity will not affect Mode I and Mode III fracture solutions but will change Mode II fracture solution.

To sum up, for a quarter-circular surface crack with partially heat conductive or completely insulated crack surfaces in an insulated quarter-space subjected to an instantaneous heat source at (x', y', z') , its overall temperature solution is the sum of Equation (8-83) and Equation (8-118). Total stresses in the uncracked quarter-space, which share the same overall temperature distribution as the cracked structure, equal to the sum of the stresses given by Equations (8-143) to (8-145) and the stresses given in Equations (8-109) to (8-111). Green's function solutions for stress intensity factors, K_I , K_{II} , and K_{III} , at the crack tip are then calculated by substituting the total stresses at the crack region and the influence functions given by Equations (8-32), (8-48), (8-49), (8-65), and (8-66) into Equations (8-6) to (8-8).

8.8 Numerical Verification of Crack Model 7

Since stress intensity factors are calculated by integrating the product of influence functions and stresses at the crack location in a uncracked quarter-space (see Equations (8-6) to (8-8)), it is necessary to verify both the influence functions derived in Subsection 8.3 and the temperature and thermal stresses obtained in subsections 8.6 and 8.7.

8.8.1 Verification of Influence Functions

8.8.1.1 Circular Crack in an Infinite Space

This section describes the verification of the influence functions as well as the numerical integration procedure for a single circular crack embedded in an infinite space. The formulation of the influence functions \hat{m}_1 , \hat{m}_{2r} , $\hat{m}_{2\theta}$, \hat{m}_{3r} and $\hat{m}_{3\theta}$ are described in Subsection 8.3, Equations (8-15), (8-40),

(8-41), (8-57) and (8-58), respectively. The numerical procedures used in calculating these influence functions are described in Appendix D-1.

Direct verification of the influence functions by itself is unlikely. The verification method employed in this section is to use the influence functions developed in Subsection 8.3 to calculate the stress intensity factors for a simple problem and compare to the results obtained by other methods. A circular crack in an infinite space subjected to uniform stress distribution is selected for verification of the influence functions. The stress intensity factors for an embedded circular crack under combined uniform tension $\sigma_{zz}=\sigma$ and uniform shear $\sigma_{zx}=\tau$ at infinity are given by Hartranft and Sih (1973) as

$$K_I = \frac{2}{\sqrt{\pi}} \sigma \sqrt{a} \quad (8-146)$$

$$K_{II} = \frac{1-\nu}{2-\nu} \frac{4}{\sqrt{\pi}} \tau \sqrt{a} \cos \theta \quad (8-147)$$

$$K_{III} = \frac{1-\nu}{2-\nu} \frac{4}{\sqrt{\pi}} \tau \sqrt{a} \sin \theta \quad (8-148)$$

where σ , τ , a and θ are tension stress, shear stress, crack radius and crack angle, as defined in Figure 8-1, respectively.

Assuming unit stress on tension and shear and unit crack size, the stress intensity factors for all three modes K_I , K_{II} and K_{III} were calculated using Equations (8-6) to (8-8) and compared to that obtained from Equations (8-146) to (8-148). The comparison are shown in Figures 8-5 to 8-7. Using Equation (8-6), the K_I ranged from 1.09 to 1.175 compared to 1.128 obtained from Equation (8-146). The error is about $\pm 4\%$. The oscillating deviation of the numerical solutions from the exact solutions is believed to be caused by the relatively less number of

integration points used in the numerical procedure. However, 4% error bound is deemed to be satisfactory for this application. Figure 8-6 shows the comparison on K_{II} using Equations (8-7) and (8-147). Figure 8-7 shows the comparison on K_{III} using Equations (8-8) and (8-148). They all show an error band of about $\pm 4\%$.

8.8.1.2 Quarter-Circular Crack in a Quarter Space Under Uniform Tension

For a quarter-circular of radius 1 inch subjected to a uniform remote tension of 1 psi is chosen as the verification problem for the influence function of this crack model.

Stress intensity solution to the verification problem was calculated to be 1.2815 psi $\sqrt{\text{in}}$ by pc-CRACK (1986) and was predicted to be 1.3136 psi $\sqrt{\text{in}}$ by THERMO-K. The difference between the two solutions to the verification problem is only 2.5 percent.

8.8.2 Verification Temperature for Fully Heat Conductive Crack Surface

The verification of the transient temperature and stress distribution for a fully heat conductive crack surface, as described in subsection 8.6, are accomplished by a transient analysis of the same model using finite element method. The problem of a 1 inch radius quarter-circular surface crack in a quarter-infinite space of $x > 0$, $y > 0$ (see Figure 8-1 subjected to a single heat source of intensity $\dot{Q} = H(t)$ Btu/sec at (0 inch, 1.4 inch, 0 inch) is considered. Due to the prohibited computing cost in a three-dimensional finite element analysis for the transient thermal stress problem and the inherent symmetry condition of the verification problem, a two-dimensional axisymmetric model is used instead.

The two-dimensional finite element model is shown in Figures 8-8 and 8-9. The model is defined in the R-Z coordinate. The half space surface of the semi-infinite solid is represented by a plane at $z=0$. The size of the axisymmetric model shown in Figure 8-8 is 100 inches x 100 inches which should be large enough to represent a semi-infinite solid. The model consists of 514 isoparametric, four-node elements and 534 nodes. The crack surface is assumed to be near the origin, (i.e., $r=0$, $z=0$). As shown in Figure 8-9, a fine mesh is used in this region with a coarse mesh at distance further away from the crack location. The size of this region is 5 inches x 5 inches with 135 elements.

The heat transfer boundary condition of the model is that an insulated surface is set at surface $z=0$, $z=100$ and $r=100$. A roller displacement boundary condition is imposed at plane $z=100$. The material properties used are 0.0978 lb/in³ for mass density, 0.23 Btu/lb-F for specific heat, 0.0017361 Btu/sec-F-in for thermal conductivity, 0.000013 in/in/F for thermal coefficient of expansion, 10.3×10^6 psi for Young's modulus and 0.33 for Poisson's ratio. A unit point heat source, 1 Btu/sec, is placed at $r=0$, $z=1.4$. This point heat source is a delta function in space and constant over time throughout the transient, unit step function in time $t=0$. It is equivalent to a location of $x=0$, $y=1.4$ and $z=0.0$ in the coordinate system of the three-dimensional model, Figure 8-1. An integration time step of 1.0 second is used in the transient analysis for a time history of 500 seconds. The finite element program used in this verification is FEM2D (1986), developed by Structural Integrity Associates.

Analysis results of the three-dimensional quarter-circular crack in a quarter-infinite space are also obtained using Equations (8-113) to (8-135). Figures 8-10 and Figure 8-11 present the comparison of the temperature results between the THERMO-K and the finite element analysis.

Figure 8-10 illustrates the temperature transient plot for three selected locations. The three locations are at origin ($x=0$, $y=0$, $z=0$; x , y , z as defined in Figure 8-1), at 1 inch away from the origin on the half surface, $y=0$ ($x=1$, $y=0$, $z=0$), and at 5 inches from the surface and 5 inches from the symmetry axis, ($x=5$, $y=5$, $z=0$). At the first two locations, the temperature rise is substantial because of the proximity to the point heat source. At location (0,0,0), temperature climbs up to over 45°F in about 100 seconds. At location (5,5,0), no temperature rise due to the point heat source has been observed during the first 100 seconds. Because of its location is further away from the point heat source, the time for temperature response would be longer and the magnitude of response would not be as high as the first two locations. In all three locations examined, the agreement between the finite element method and the THERMO-K are excellent.

Figure 8-11 presents the temperature distribution in the quarter-infinite solid at three selected points of time, ($t=10$ sec, 20 sec and 100 sec) during the transient. The temperature is plotted as a function of distance, y , from the insulated surface at the origin ($x=0$, $z=0$). As time increases, the temperature profile increases due to the constant supply of heat from the heat source. The magnitude of temperature increase is higher at the surface, $y=0$, due to the insulated effect at the surface. At a distance of 5 inches from the surface, the temperature increase is not as significant. Near the heat source, $y=1.4$ inch, temperatures are as high as 100°F .

As evident in Figure 8-11, the agreement between the temperature predicted by THERMO-K and by finite element method is good. At the region near the heat source, $y=1.4$ inch, results from the FEM2D are higher compared to that obtained by THERMO-K using Equation (8-113). The overprediction in temperature by the finite element method is believed to result from the coarse mesh near the point heat source in the finite element model.

8.8.3 Verification of Temperature Distribution for Insulated Crack Surfaces

The verification of transient temperature distribution for a fully insulated crack surface is accomplished by a transient thermal analysis of a finite element model. The finite element model represents a problem of a quarter-circular crack surface of one inch radius in a quarter-infinite space of $x \geq 0$, $y \geq 0$, (Figure 8-1) subject to a single heat source of intensity $Q = H(t)$ Btu/sec.

As mentioned in subsection 8.8.2, the cost of performing a three-dimensional transient analysis for a conductive crack model is prohibitive. A two-dimensional axisymmetric finite element model shown in Figures 8-12 and 8-13 is used. This model is used to verify the transient temperature distribution in the plane containing the crack surface, ($z=0$).

The model is defined in the R-Z coordinate. The size of the model is 100 inches in radius (R-axis) and 200 inches long (Z-axis), (Figure 8-12). The models consists of 1035 isoparametric, four node elements and 1028 nodes. The crack surface is at the plane, $z=0$. A finer mesh is used in the region close to the crack surface, as shown in Figure 8-13. This region is 5 inches in the R axis and 10 inches in the Z axis.

For the heat transfer boundary condition, the crack surface, ($z=0^+$, 0^+ , $r=0$ to 1 inch) is insulated, (i.e., $h=0.0$). The surfaces at $z=100$ inches, -100 inches and $R=100$ inches are also insulated. The material properties are the same as the fully heat conductive crack surface case in subsection 8.8.2. A unit heat source, 1 Btu/sec, is placed at (0, 0, 1.4). This point heat source is a delta function in space and constant over time throughout the transient, step at time $t=0$. An integration time step of 1.0 second is used in the transient analysis for a history of 100 seconds.

The comparison of temperature transient results between THERMO-K and finite element analysis is presented in Figure 8-14. Location $(1, 0, 0)$ is at the crack tip. Location $(0, 0^+, 0)$ is at the top surface at the crack mouth directly under the point heat source. Location $(0, 0^-, 0)$ is at the bottom surface of the crack. Temperature results are in very good agreement for the locations at the crack tip and at the top surface. The temperature responses at the bottom crack surface are also in good agreement except at the very beginning of the transient. This is due to the numerical procedure used in the determination of the heat dipoles to simulate the heat conductive condition of the crack surface (Appendix D). At present, only one term is used in the equation representing the heat dipole.

Figures 8-15 and 8-16 presents the temperature profiles at different points of time in the transient. The temperature profiles are plotted for the plane containing the crack surface ($z=0$) and as temperature against the distance from the surface ($y=0$) in the semi-infinite solid. The temperature profiles results are presented for time $t = 10, 20, 50$ and 100 seconds into the transient. For the distance within the crack surface, $r \leq 1.0$, both the top and bottom crack surface temperature are presented. The results from THERMO-K are, in general, overpredicting the temperature at the bottom crack surface except near the edge of the surface ($y=0$). This is due to the number of terms used in the heat dipole equation and the location used to determine the coefficients in the equation.

8.9 References

Bell, J. C., (1979), "Stresses from Arbitrary Loads on a Circular Crack," International Journal of Fracture, Vol. 15, No.1, pp. 85-104.

Boley, B. A., and Weiner, J. H., (1960), Theory of Thermal Stresses, Wiley & Sons, New York, New York.

Bueckner, H. F., (1973), "Field Singularities and Related Integral Representations," in Methods of Analysis and Solutions of Crack Problems, Vol. 1, ed. G. C. Sih, pp. 239-314, Noordhoff, Holland.

Carslaw, H. S., and Jaeger, J. C., (1959), Conduction of Heat in Solids, 2nd edition, Oxford University Press, London.

FEM2D User's Manual (1986) - A Two-Dimensional Finite Element Computer Program for Two-Dimensional Heat Transfer/Thermal Stress Analysis, Structural Integrity Associates, San Jose, CA.

Hartranft, R. J., and Sih, G. C., (1973), "Alternating Method Applied to Edge and Surface Crack Problems," in Methods of Analysis and Solutions of Crack Problems, Vol. 1, ed. G. C. Sih, pp. 179-238, Noordhoff, Holland.

pc-CRACK - Fracture Mechanics Software for Personal Computers, Users Manual, Version 1.1, Revision 1, (1986), Structural Integrity Associates, San Jose, CA.

Parkus, H., (1968), Thermoelasticity, Blaisdell Publishing Co.

Sih, G. C., (1973), Handbook of Stress Intensity Factors, Institute of Fracture and Solid Mechanics, Lehigh University, Bethlehem, PA.

Tada, H., Paris, P., and Irwin, G., (1973), The Stress Analysis of Cracks Handbook, Del Research Co., Pennsylvania.

Timoshenko, S. P., and Goodier, J. N., (1970), Theory of Elasticity, 3rd edition, McGraw Hill, New York, New York.

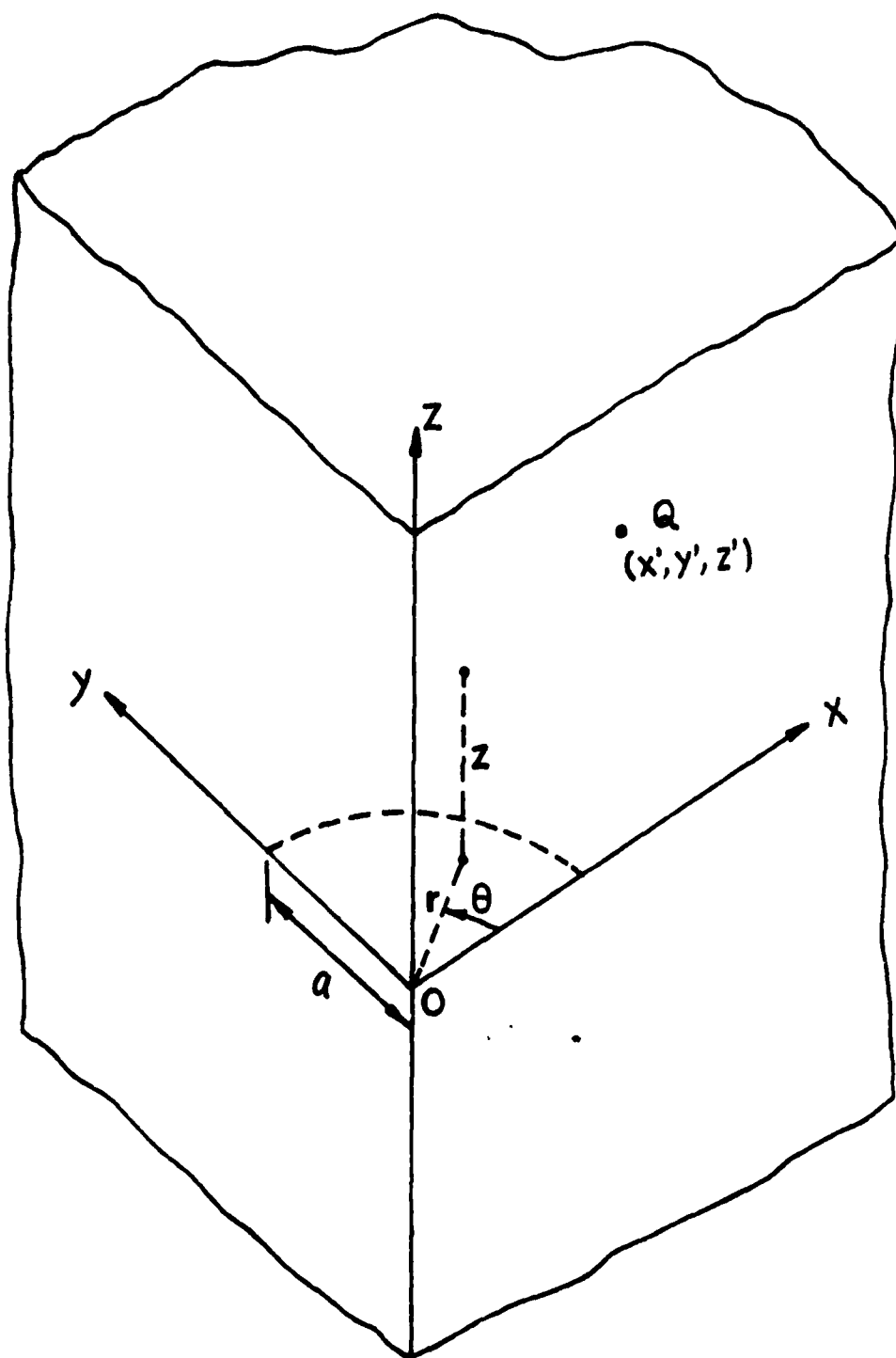


Figure 8-1. A Quarter-Circular Surface Crack in a Quarter-Space

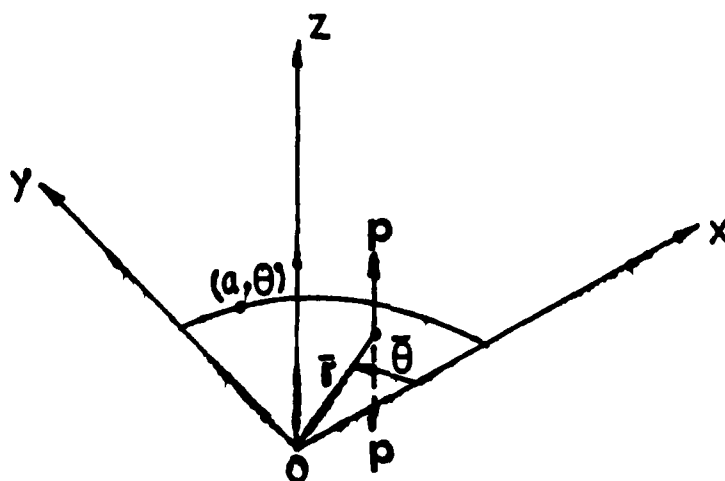


Figure 8-2 (a). A Pair of Unit Normal Forces Applied at (r, θ) of the Crack Surface

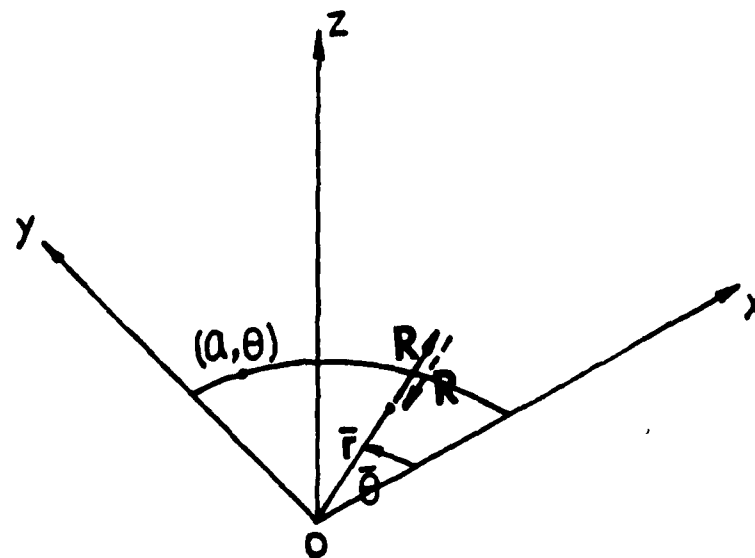


Figure 8-2 (b). A Pair of Unit Radial Forces Applied at $(\bar{r}, \bar{\theta})$ of the Crack Surface

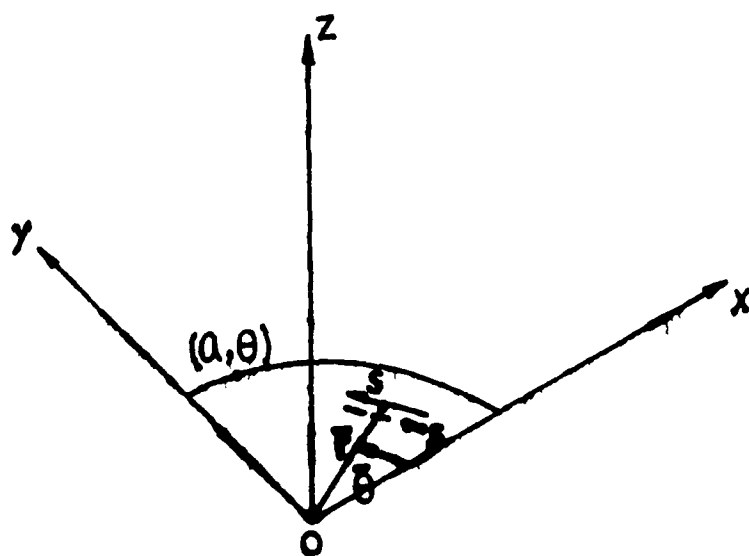
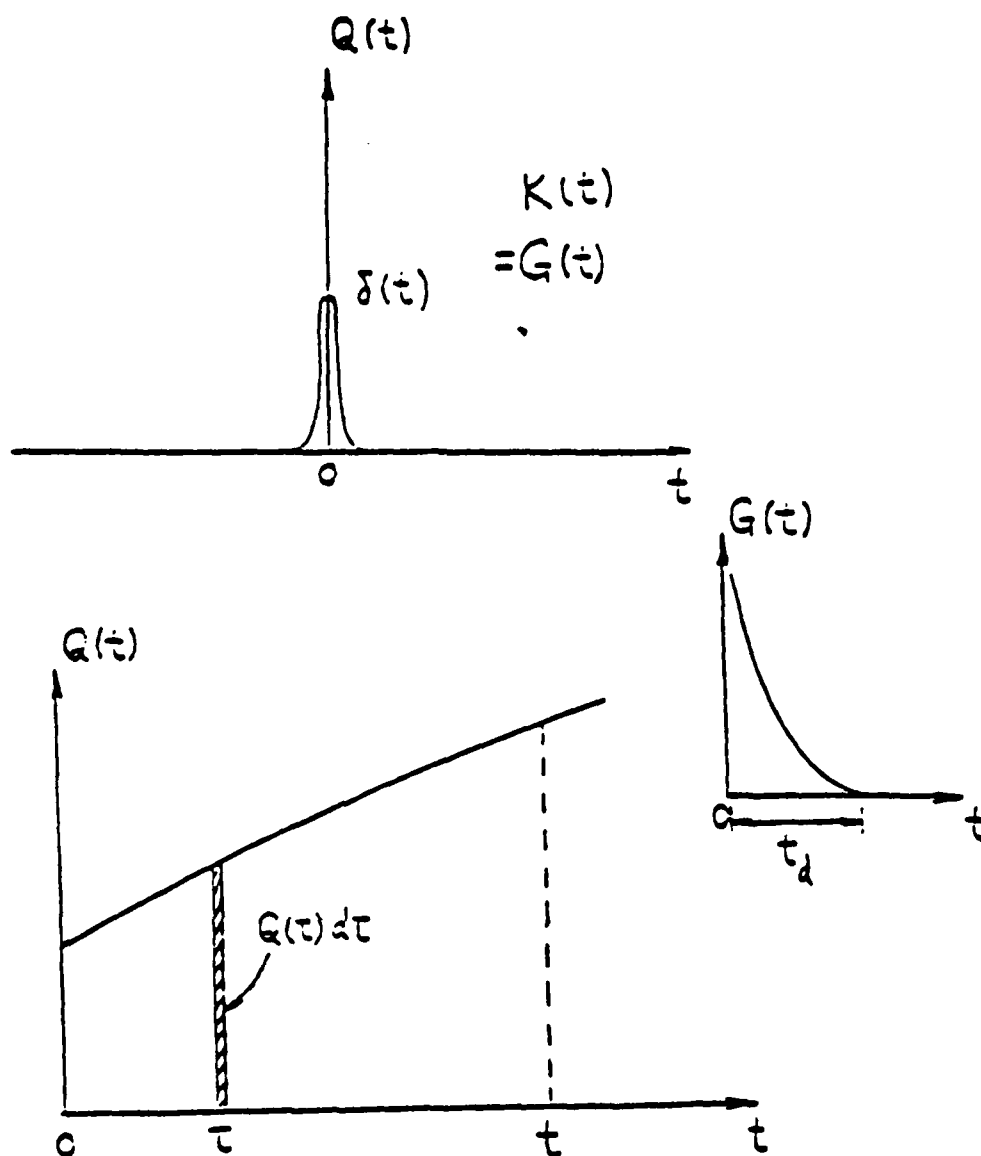


Figure 8-2 (c). A Pair of Unit Tangential Forces
Applied at (T, θ) of the Crack Surface



$$K(t) = \int_0^t Q(\tau) G(t-\tau) d\tau$$

$$= \int_{t-t_d}^t Q(\tau) G(t-\tau) d\tau$$

Figure 8-3. Concept of Green's Function

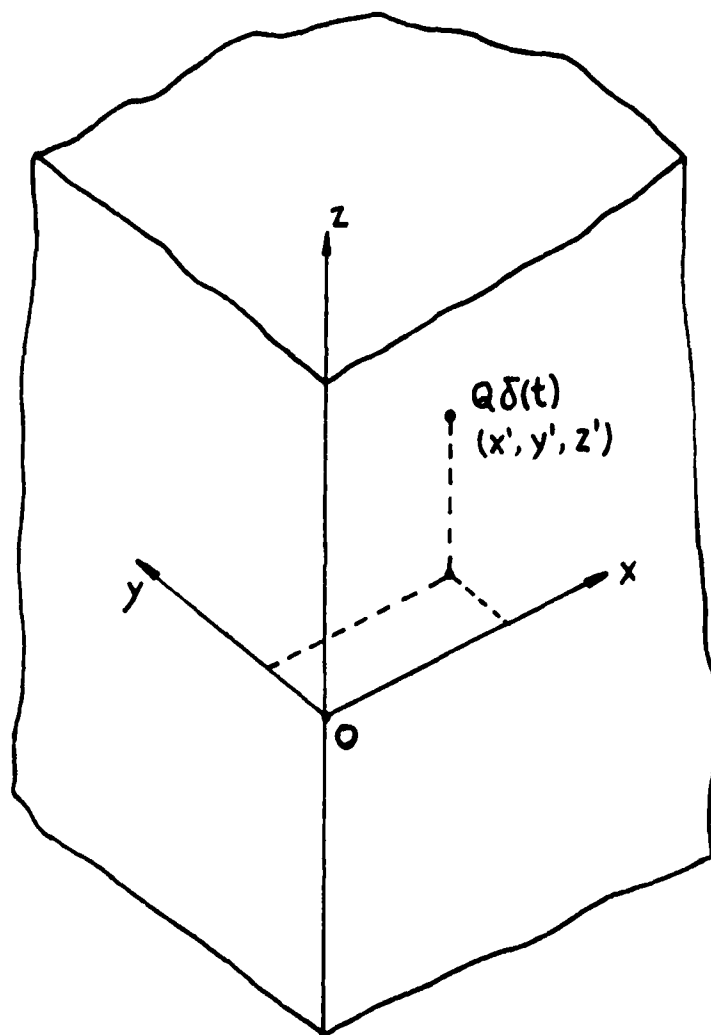


Figure 8-4. An Instantaneous Heat Source in A Quarter-Space

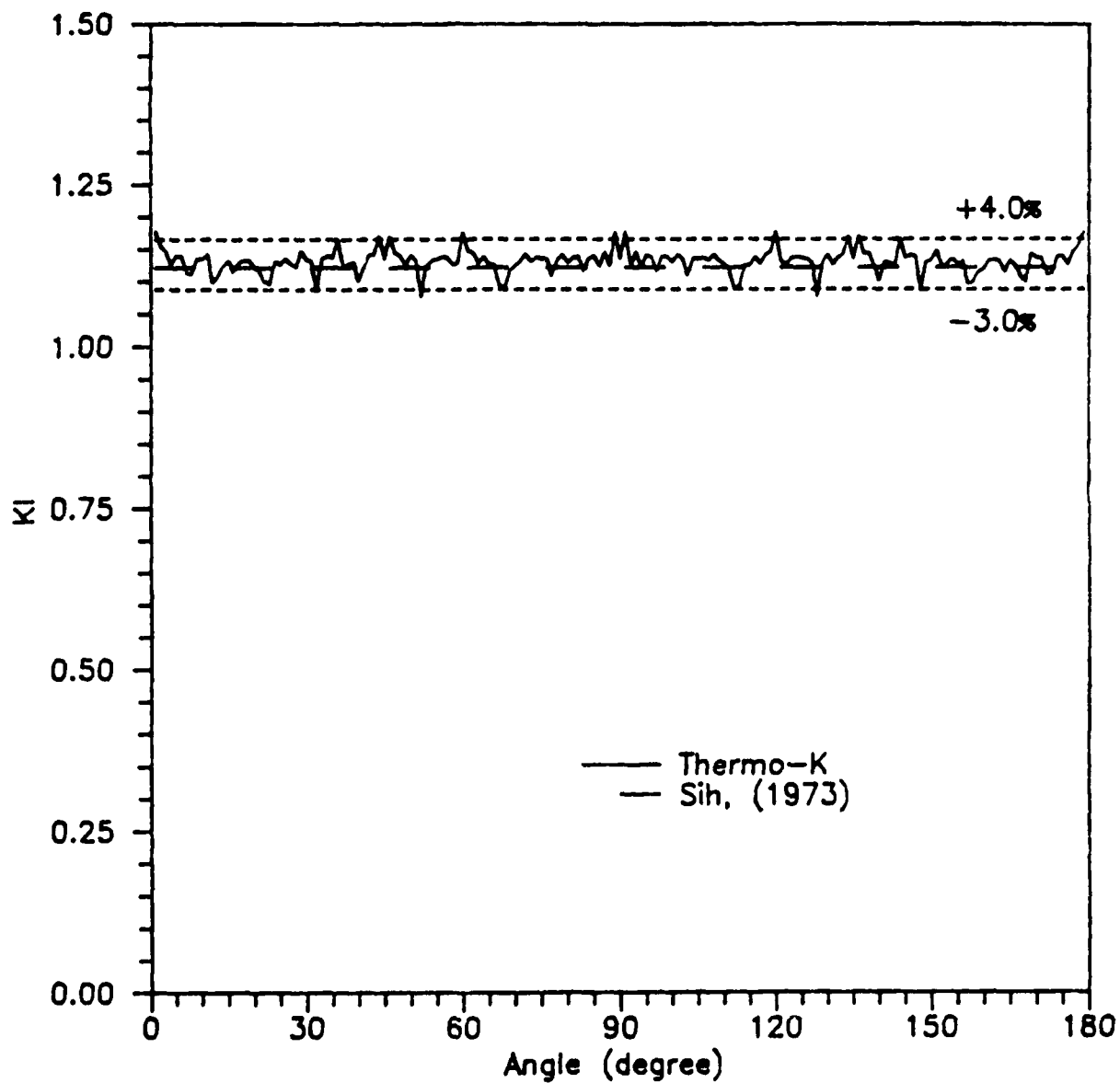


Figure 8-5. Verification of Mode I Stress Intensity Factor of Circular Crack in an Infinite Solid

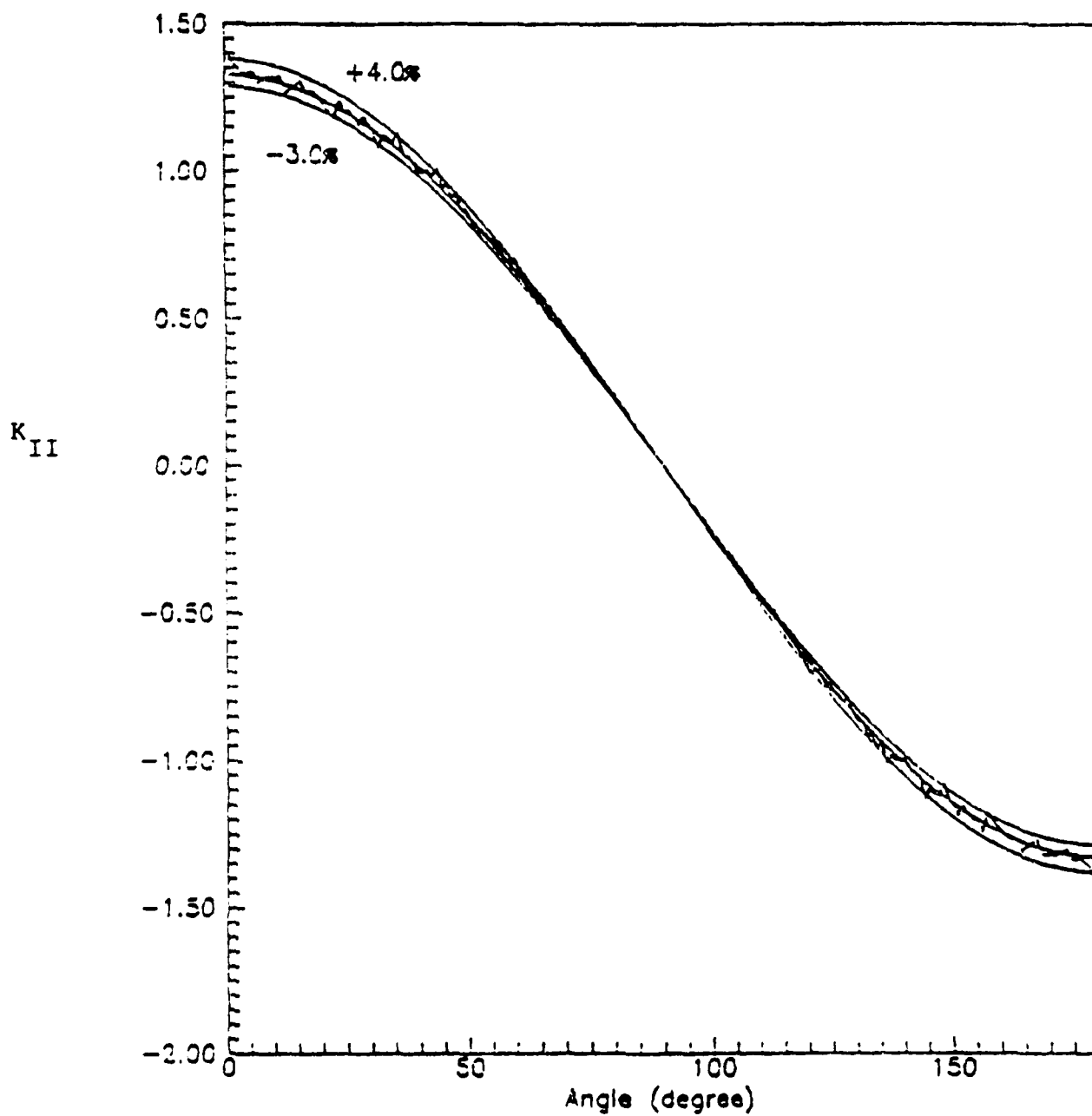


Figure 8-6. Verification of Mode II Stress Intensity Factor of Circular Crack in an Infinite Solid

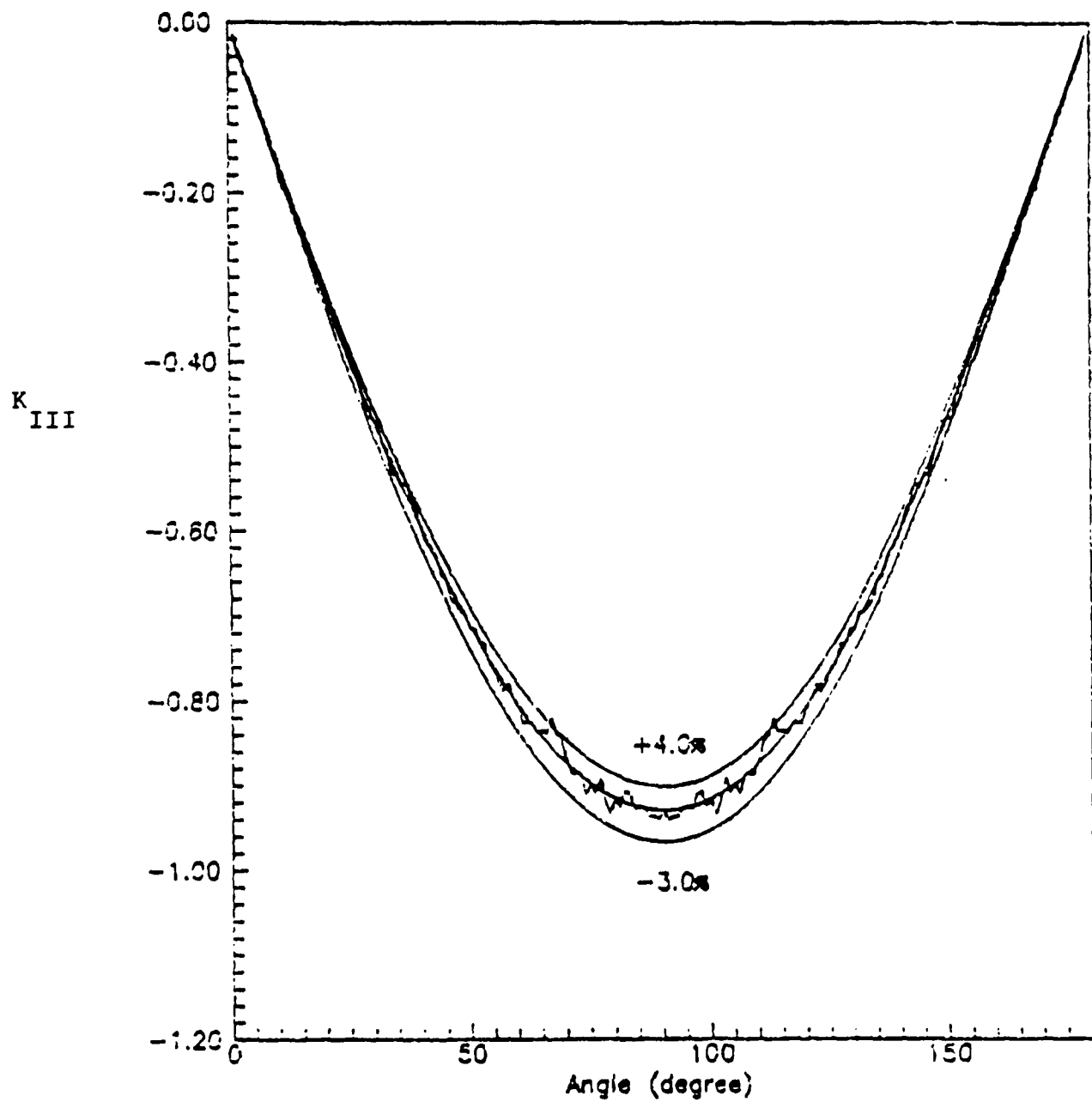


Figure 8-7. Verification of Mode III Stress Intensity Factor of Circular Crack in an Infinite Solid

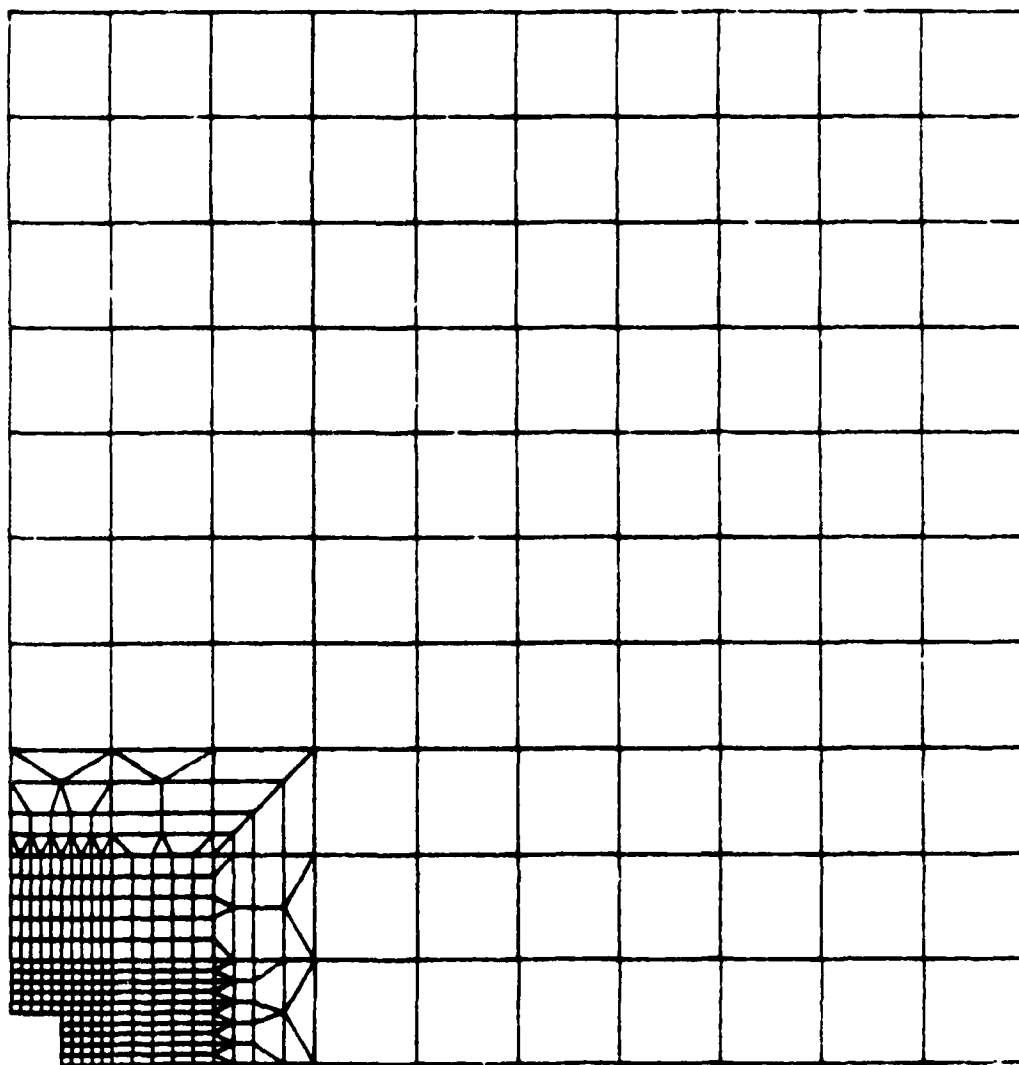


Figure 8-8. Axisymmetric Finite Element Model for Verification of Temperature and Stress

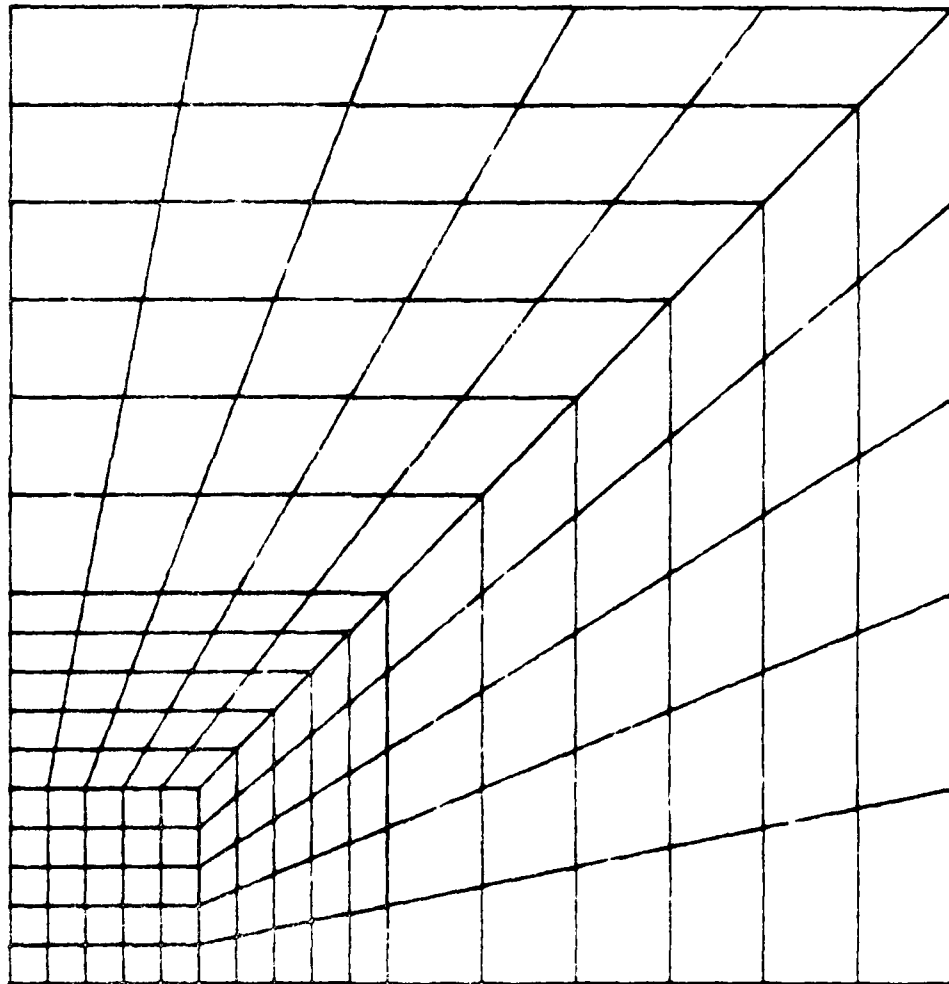


Figure 8-9. Axisymmetric Finite Element Mesh at the Crack Location

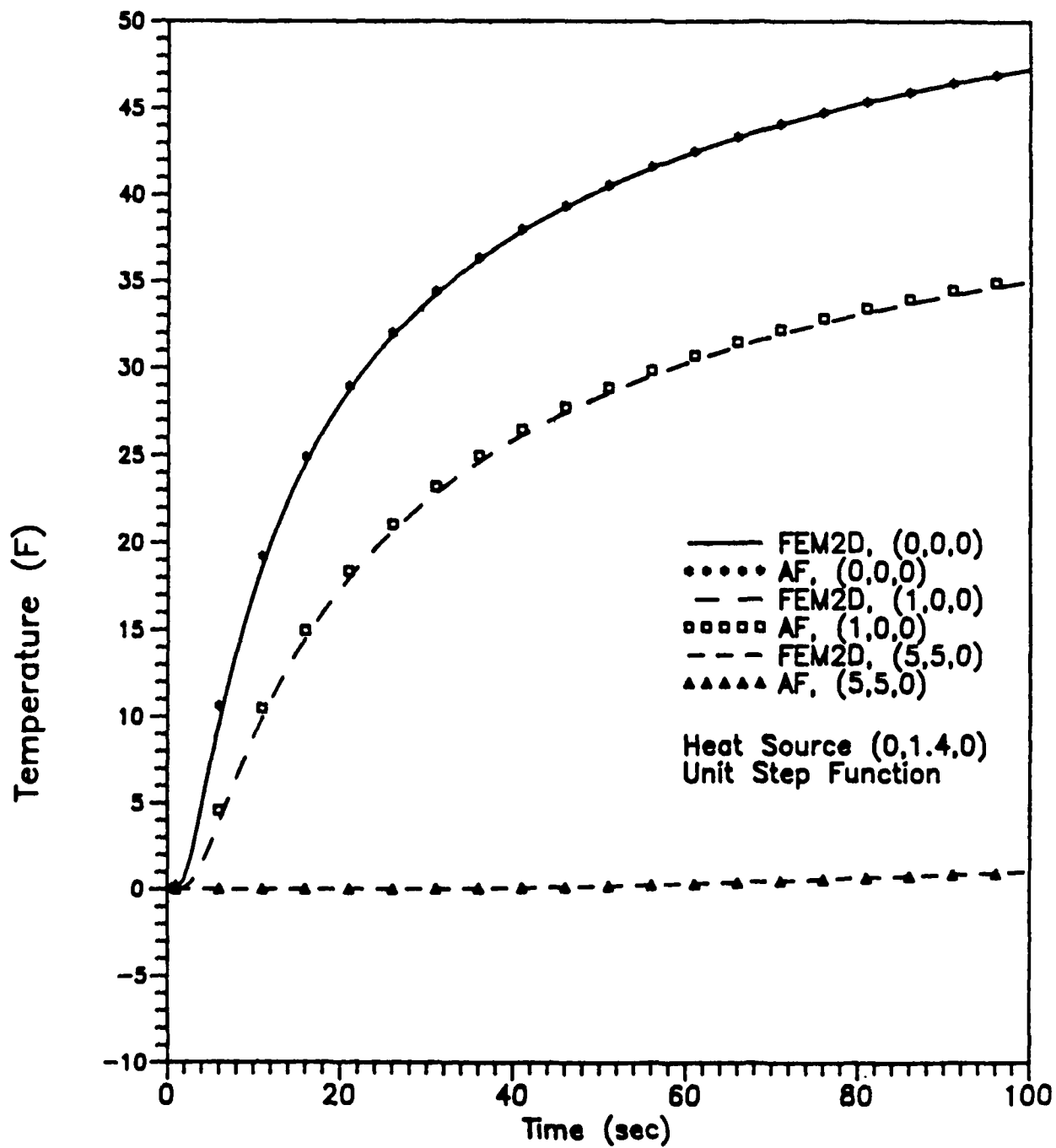


Figure 8-10. Comparison of Temperature Transients Due to a Unit Step Heat Source in a Quarter-infinite Solid With a Fully Conductive Crack Surface

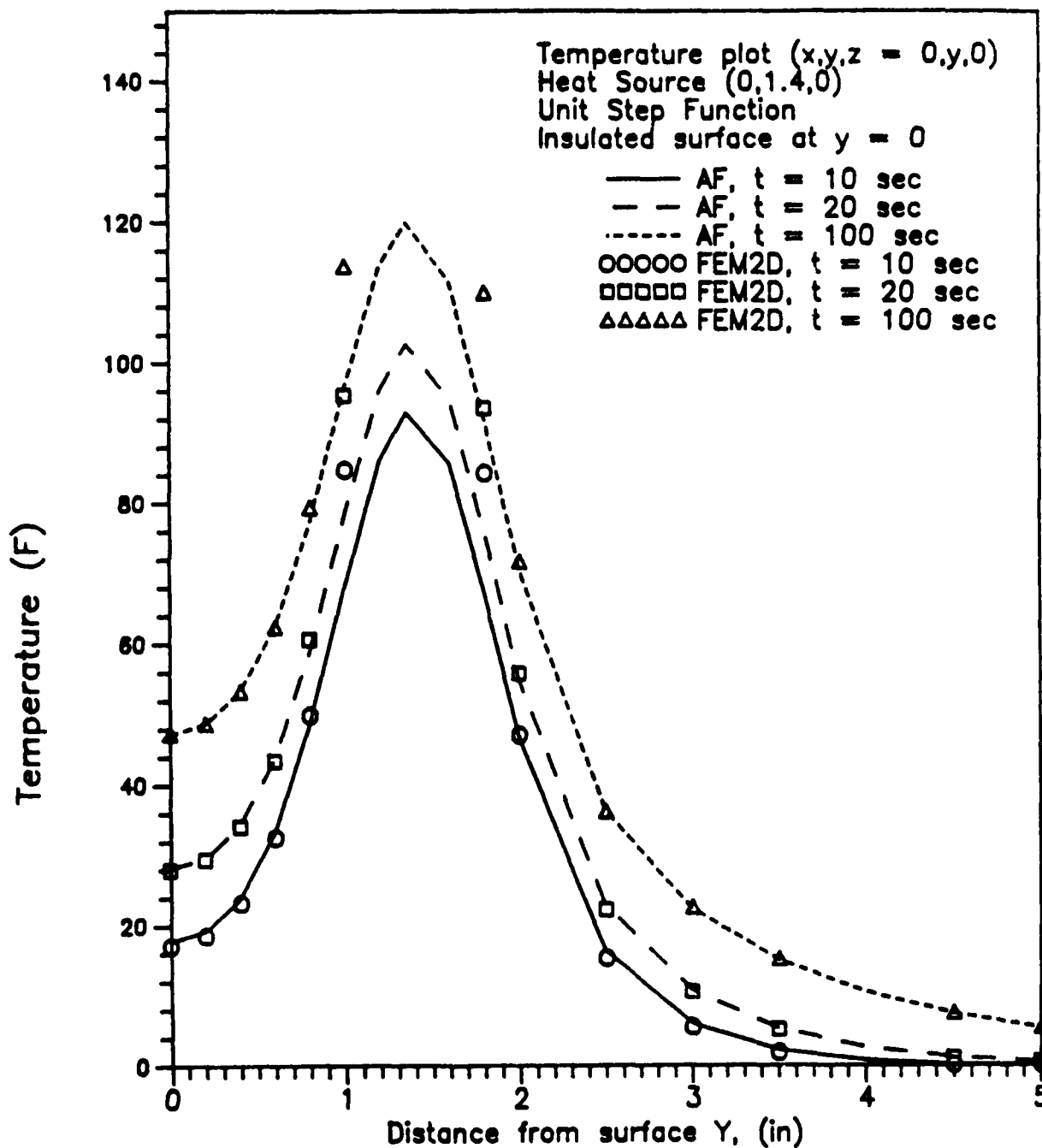


Figure 8-11. Comparison of Temperature Profiles Due to a Unit Step Heat Source in a Quarter-infinite Solid With a Fully Conductive Crack Surface

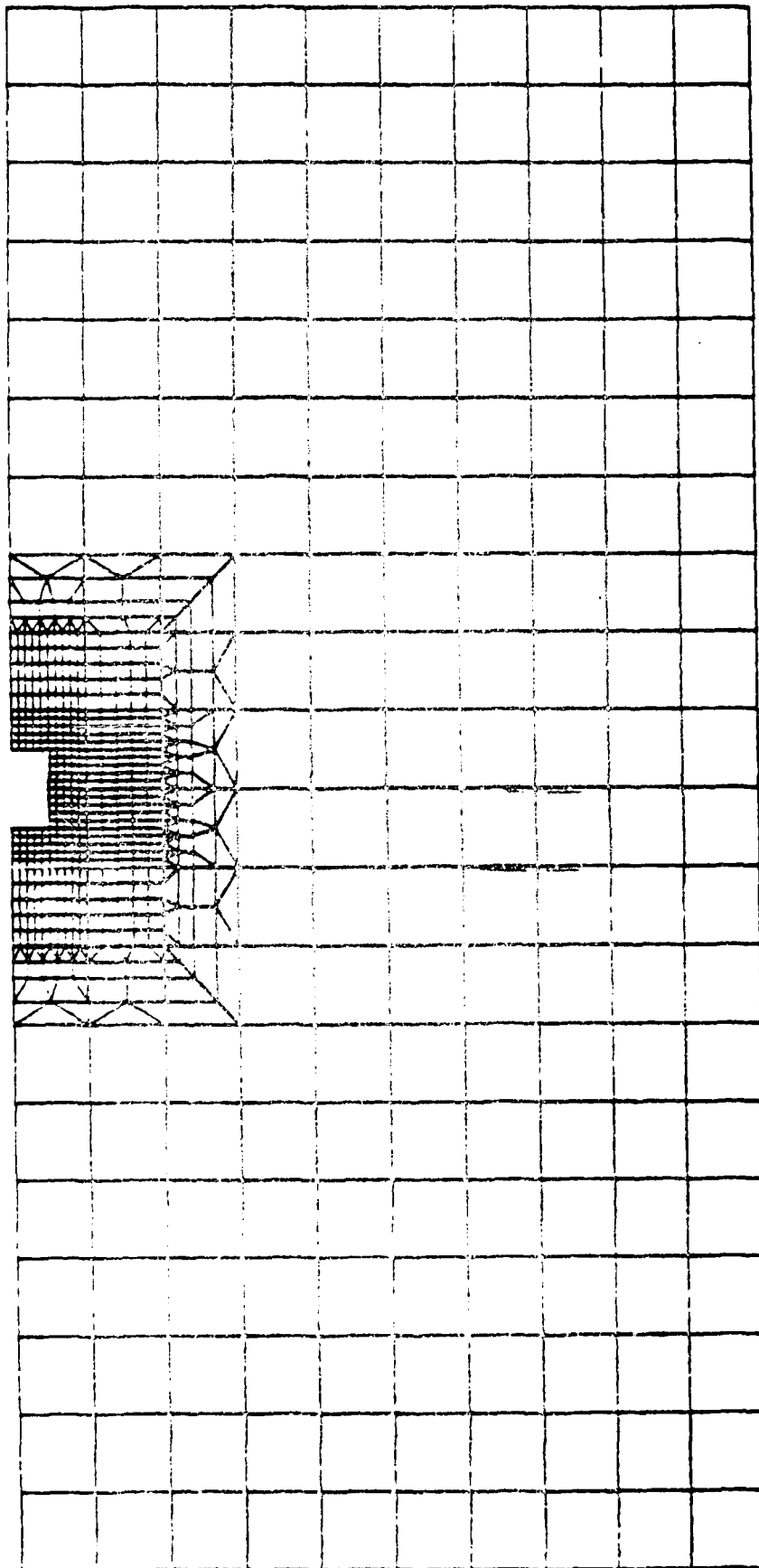


Figure 8-12. Axisymmetric Finite Element Model for Verification of Temperature for a Crack With Insulated Surface

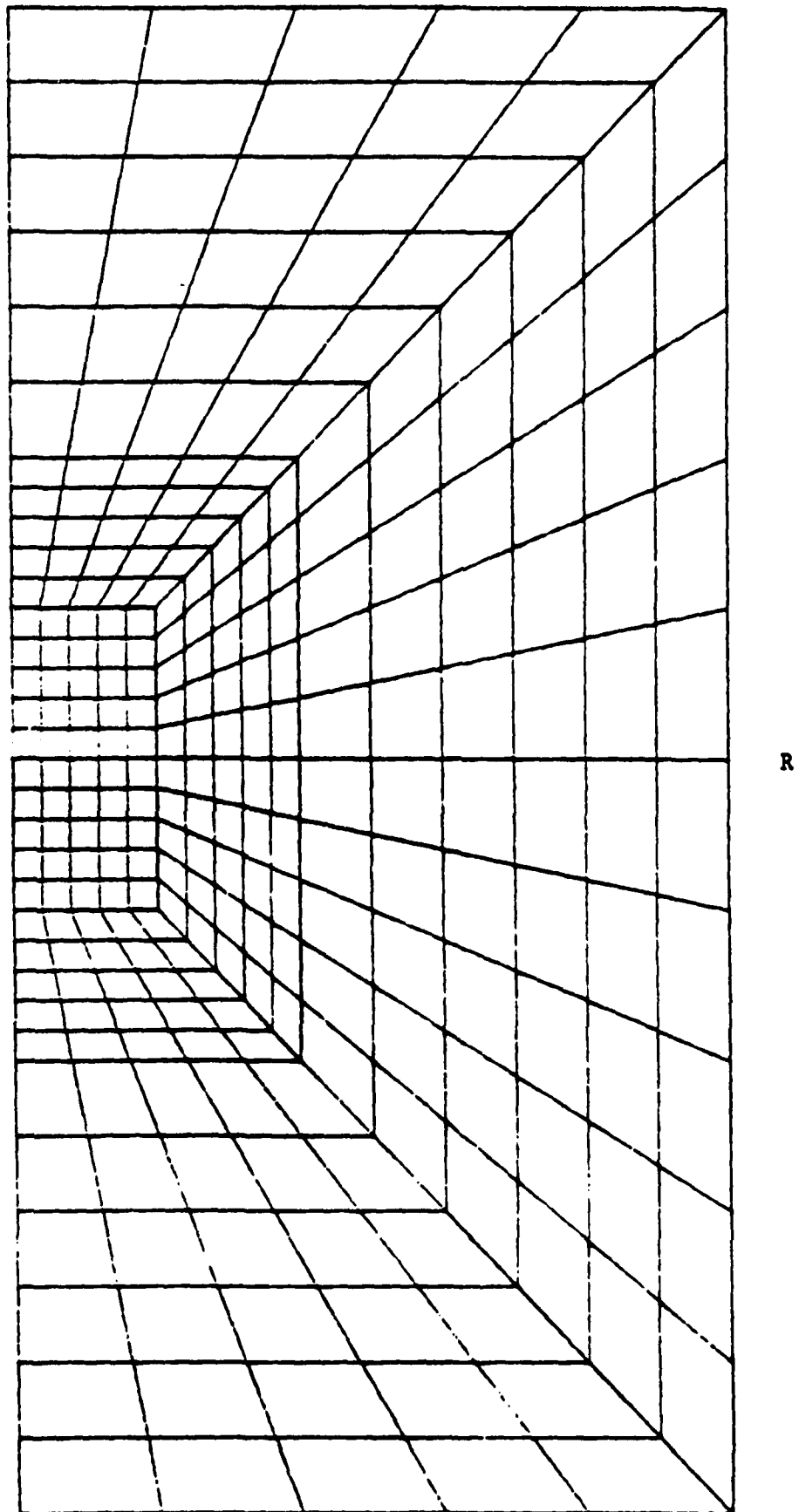


Figure 8-13. Finite Element Mesh at the Crack Region for Quarter-circular Crack in a Quarter-infinite Solid With Insulated Crack Surface

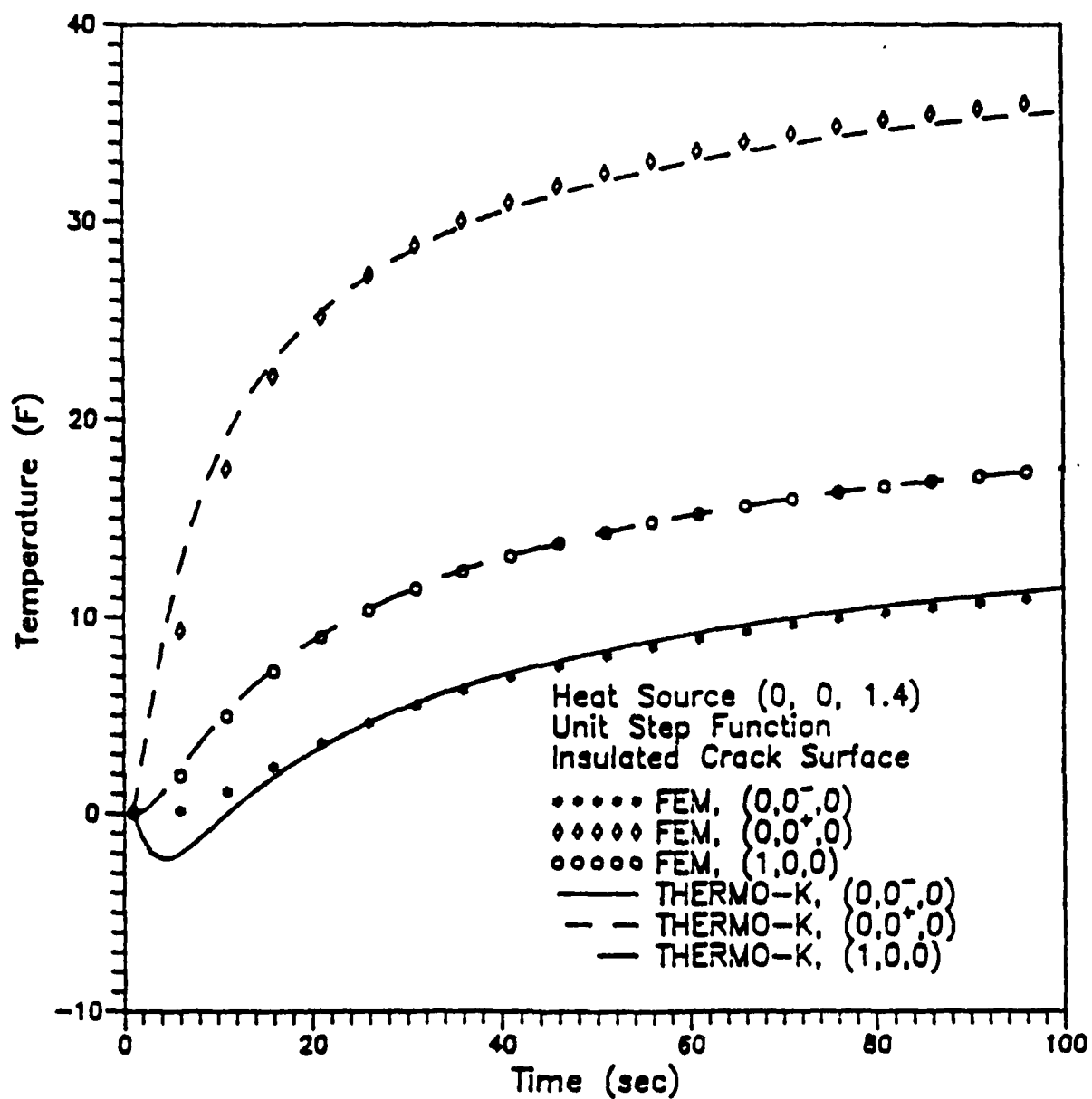


Figure 8-14. Comparison of Temperatures Predicted by THERMO-K and Finite Element Method (T vs. Time)

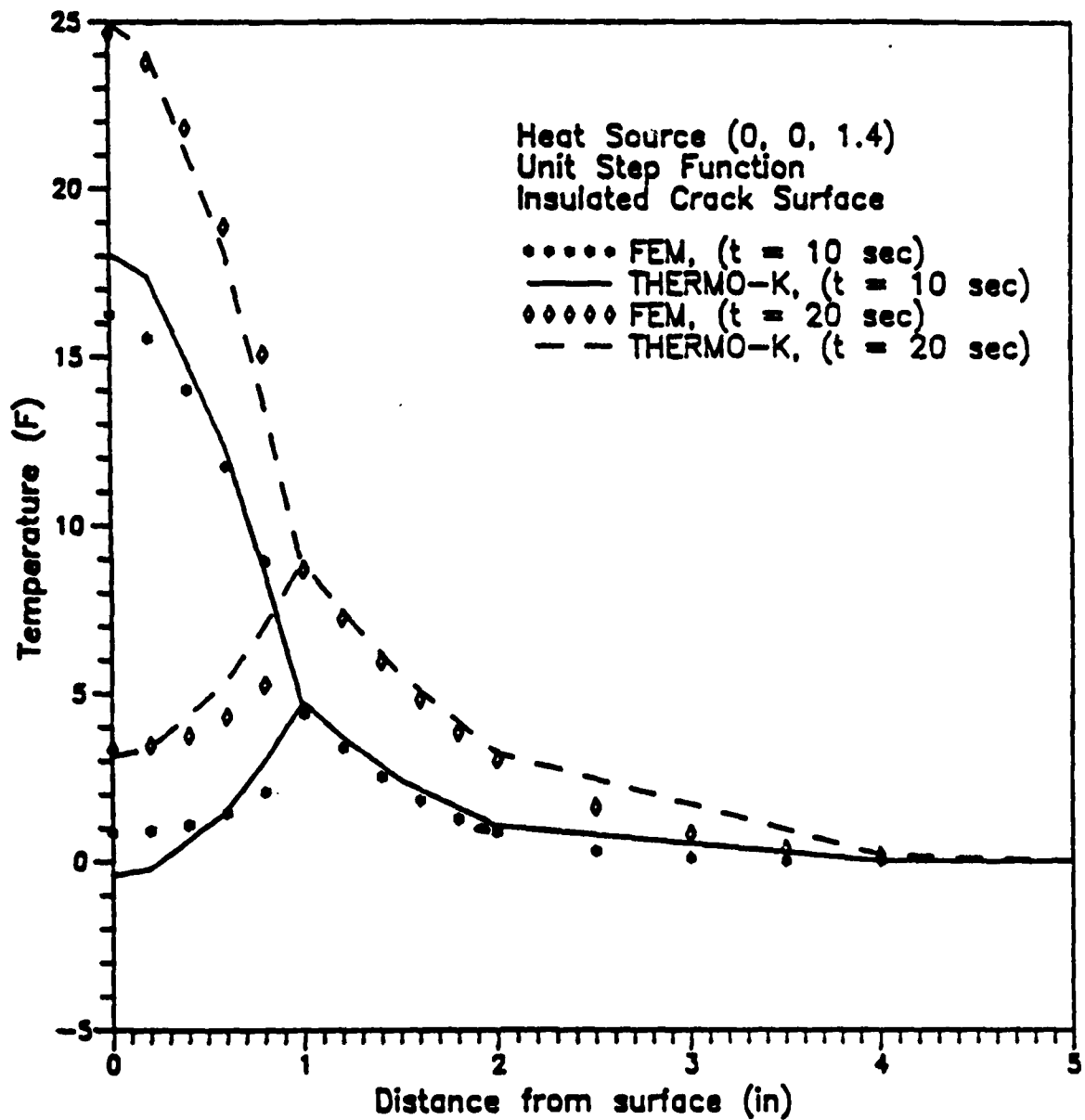


Figure 8-15. Comparison of Temperatures Predicted by THERMO-K and Finite Element Method (T vs. r)

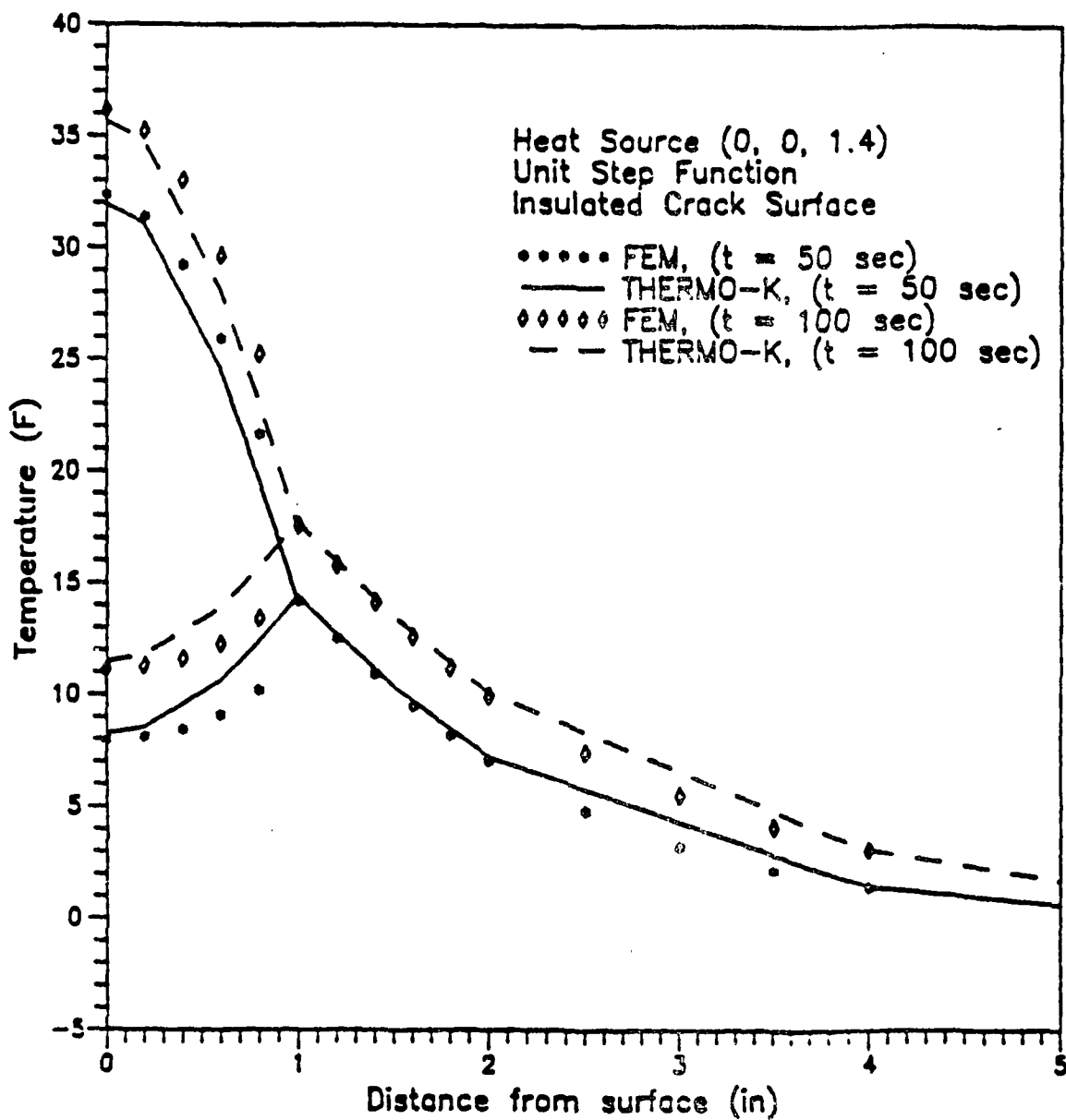


Figure 8-16. Comparison of Temperature Profiles Due to a Unit Step Heat Source in a Semi-infinite Solid With a Fully Insulated Crack Surface at $t=50$ and 100 Seconds

9.0 LIMITATIONS ON DECOUPLED, LINEARIZED THEORIES

Throughout this study, the uncoupled, quasi-static thermoelasticity and linear elastic fracture mechanics (LEFM) theories have been used for all crack models. However, under some extreme loading conditions, such as high loading rates and temperatures, the underline assumptions for the uncoupled, quasi-static thermoelasticity and/or LEFM may not be applicable. This section is to establish a set of conditions, under which the uncoupled, quasi-static thermoelasticity and LEFM can be used with good accuracy.

9.1 Limitation of Uncoupled, Quasi-Static Thermoelasticity Theory

The uncoupled, quasi-static thermoelasticity theory used in this study assumes that the temperature and displacement solutions are decoupled and the inertia terms in the equilibrium equation can be neglected. Thus the current version of THERMO-K is expected to be accurate only if heating rate and material constants fall within certain ranges, for which the effects of inertia term and the coupling between temperature and displacement are negligible.

9.1.1 Temperature-Displacement Coupling Effects

In general, it is known that, when an elastic body is subjected to external mechanical loading, temperature distribution within the elastic body will be altered slightly due to internal heating generated by the mechanical deformation. This phenomenon, known as thermoelastic dissipation, implies that temperature and displacement solutions are coupled. It has been shown by Boley and Weiner (1960) that governing heat conduction equation for the coupled thermoelasticity is

$$k\nabla^2 T = \rho c T_{,t} \left[1 + \delta \left(\frac{\lambda + G}{3\lambda + 2G} \right) \left(\frac{e}{aT} \right)_{,t} \right] \quad (9-1)$$

where $T=T(x,y,z;t)$ is temperature distribution, (x,y,z) are Cartesian coordinates, t is time, k is thermal conductivity, ρ is mass density, c is heat capacity (specific heat), α is coefficient of thermal expansion, e is dilatational strain defined as

$$e = \epsilon_{xx} + \epsilon_{yy} + \epsilon_{zz} \quad (9-2)$$

ϵ_{ij} is strain, λ and G are Lamé's constants defined as $\lambda = \frac{E\nu}{(1+\nu)(1-2\nu)}$ and $G = \frac{E}{2(1+\nu)}$, respectively, E is Young's modulus, ν is Poisson's ratio,

$$\delta = \frac{(3\lambda+2\mu)^2 \alpha^2 T_0}{\rho^2 c v_e^2} \quad (9-3)$$

T_0 is a reference temperature at which the elastic solid is stress free, and v_e is the propagation speed of dilatational waves in the elastic solid defined as

$$v_e = \sqrt{(\lambda+2\mu)/\rho} \quad (9-4)$$

Inside the bracket on the right hand side of Equation (9-1), the term proportional to δ is the coupling term. From Equation (9-1), it is seen that the effects of coupling between temperature and displacement are negligible if the second term inside the bracket of Equation (9-1) is much smaller than unity, i.e., use of the decoupled heat conduction equation (see e.g., Equations (2-1), (3-1), (4-1), ...etc.) is a very good approximation, if the following condition is satisfied:

$$\frac{e}{3\alpha T}, t \ll \left(\frac{\lambda+2\mu/3}{\lambda+2\mu} \right) \frac{1}{\delta} \quad (9-5)$$

Material properties for two most widely used metallic materials, aluminum and steel, will be used to check against the condition set by Equation (9-5). For aluminum, with

$$\lambda = 7.5 \times 10^6 \text{ psi}, \quad \mu = 3.9 \times 10^6 \text{ psi}, \quad \alpha = 13 \times 10^{-6} / ^\circ\text{F}$$

$$\rho = 0.0978 \frac{\text{lbm}}{\text{in}^3}, \quad c = 0.23 \frac{\text{Btu}}{\text{lbm-}^\circ\text{F}}, \quad (9-6)$$

$$k = 0.00174 \frac{\text{Btu}}{\text{in-sec-F}}, \quad T_o = 200 ^\circ\text{F} \text{ (about } 660 ^\circ\text{R)}$$

δ is found to be

$$\delta_{\text{Al}} = 0.010$$

Similarly, for steel, with

$$\lambda = 18 \times 10^6 \text{ psi}, \quad \mu = 12 \times 10^6 \text{ psi}, \quad \alpha = 6.5 \times 10^{-6} / ^\circ\text{F}$$

$$\rho = 0.283 \frac{\text{lbm}}{\text{in}^3}, \quad c = 0.11 \frac{\text{Btu}}{\text{lbm-}^\circ\text{F}}, \quad T_o = 200 ^\circ\text{F} \quad (9-7)$$

$$k = 0.00026 \frac{\text{Btu}}{\text{in-sec-F}}$$

δ is calculated to be

$$\delta_{\text{Steel}} = 0.004$$

Thus for both materials the coupling effects will be small if

$$\frac{e_{,t}}{3\alpha T_{,t}} \ll 65 \quad (9-8)$$

is satisfied. Equation (9-5) is the sufficient and necessary

condition for neglecting the coupling effects between displacements and temperature, which is usually met because, in most of the practical applications, the strain rate \dot{e}_t is about the same order of magnitude as the product of temperature rate and coefficient of thermal expansion αT_t , i.e. $(\frac{\dot{e}_t}{\alpha T_t}) \approx 1$. Particularly, if the inertia effects, which will be discussed in the next subsection of this section, can be neglected, it is anticipated that the time history of the displacements closely follows that of temperature, and thereby that, \dot{e}_t and αT_t are about the same order of magnitude.

9.1.2 Inertia Effects

As can be seen in sections 2 through 9 of this report, static equilibrium equations have been used to develop the stress and stress intensity factor solutions for all the crack models. Solutions by this approach is accurate only when the inertia effects are negligible. It has been pointed out by Boley and Weiner (1960) that the inertia effects can indeed be neglected if

$$C = \frac{t_M}{\sqrt{t_T \cdot t_0}} \ll 1 \quad (9-9)$$

where t_0 is the characteristic time for heat generation, and t_M and t_T are, respectively, the characteristic mechanical time and characteristic thermal time defined as

$$t_M = L/v_e \quad (9-10)$$

$$t_T = \rho c L^2 / k \quad (9-11)$$

in which L is a length characteristic of the geometry of the cracked body, v_e is defined in Equation (9-4), ρ , c , and k are mass density, heat capacity, and thermal conductivity,

respectively. For instance, in Crack Model 4 - a single-edge-crack plate (see Figure 6-1), the characteristic length L is equal to the plate width W , and the characteristic time for heat generation t_o is equal to $W^2 \rho c / k$ (from Equations (5-40), (5-49), and (5-56)). Thus, the condition of Equation (9-10) becomes

$$C = \frac{t_M}{\sqrt{t_T \cdot t_o}} = \frac{W k}{\sqrt{\rho(\lambda + 2\mu)} c} \ll 1 \quad (9-12)$$

For aluminum with material properties of Equation (9-6), condition of Equation (9-12) implies that

$$W \ll 3.11 \times 10^6 \text{ inches} \quad (9-13)$$

which is generally true. Similarly, for steel with material properties of Equation (9-7), condition of Equation (9-12) implies that

$$W \ll 2.87 \times 10^7 \text{ inches} \quad (9-14)$$

which is also true for most of the practical problems.

Similar to the derivation of Equations (9-13) and (9-14) for crack Model 5, it can be shown that condition of Equation (9-9) for neglecting the inertia terms is usually satisfied for most of the practical problem for all the other crack models.

9.2 Limitation of Linear Elastic Fracture Mechanics (LEFM)

Another major assumption used to derive stress and stress intensity factor solutions is that the plastic zone size created by the heat sources and the crack is small enough that the linear

elastic fracture mechanics (LEFM) theory can be applied. Quantitatively, LEFM theory is accurate only when the following condition is satisfied:

$$\frac{r_p}{L} \ll 1 \quad (9-15)$$

where L is the characteristic length of the geometry, and r_p is the plastic zone size around the crack tip defined as

$$r_p = \frac{1}{\pi} \left(\frac{K_I^2 + K_{II}^2 + K_{III}^2}{\sigma_y^2} \right) \quad (9-16)$$

in which σ_y is yield strength of the material and K_I , K_{II} , and K_{III} are peak stress intensity factors of Mode I, Mode II, and Mode III fractures, respectively, generated by the thermal loading. Again, consider an aluminum, single-edge-crack plate of width W (Figure 6-1) with material properties Equation (9-6), $\sigma_y = 72$ ksi, and $K = K_{IC} = 30 \text{ ksi}\sqrt{\text{in}}$, condition of Equation (9-15) implies that

$$W \gg 0.055 \text{ inch} \quad (9-17)$$

which is usually true for most of the practical examples. This equation along with Equation (9-13) set up a range of plate width for an aluminum, single-edge-crack plate, under which the decoupled, quasi-static thermoelasticity theory is accurate enough. Similarly, for a steel, single-edge-crack plate of width W (Figure 6-1) with material properties Equation (9-7), $\sigma_y = 200$ ksi, and $K = K_{IC} = 40 \text{ ksi}\sqrt{\text{in}}$, condition of Equation (9-15) implies that

$$W \gg 0.013 \text{ inch} \quad (9-18)$$

which can be met in most cases of interest.

9.3 Summary

To sum up this chapter, the decoupled, quasi-static thermoelasticity theory is quite accurate if conditions of Equations (9-9) and (9-10) are satisfied, and the LEFM theory is valid only when condition of Equation (9-16) is met. For most of the cracks in the metallic materials with a wide range of geometric dimensions of practical interest, these three conditions are usually satisfied.

9.4 References

Boley, B. A., and Weiner, J. H., (1960), Theory of Thermal Stresses, Wiley & Sons, New York, New York.

10.0 EXPERIMENTAL VERIFICATION OF THERMO-K

This section describes the University of Dayton's effort in the experimental verification of the temperature, strain and stress intensity factor predictions by THERMO-K. Subsection 10.1 describes the material used for the specimen and geometry adopted for the tests. The baseline fracture toughness tests conducted with the compact tension specimens are discussed in subsection 10.2. The infrared spot heaters used to apply the thermal loading and the calibration of these heat sources are explained in Sections 10.3 and 10.4, respectively. Subsections 10.5 and 10.6 describes the temperature and strain verification tests, respectively, conducted using uncracked plate specimens. Subsection 10.7 describes the thermal-mechanical tests conducted using single edge cracked specimens to verify the thermal stress intensity factors. The results of the experimental verification are then summarized in subsection 10.8.

10.1 Selection of Specimen Geometry and Material

The fracture specimens chosen is the single edge cracked geometry shown in Figure 10-1. For this geometry the heat sources used to apply the thermal loading should be located such that the maximum tensile stresses are generated near the edges, resulting in maximum K_I at the crack tip. Based on the analysis conducted in Subsection 5.8, we concluded that the heat source should be located along the centerline (mid-width) of the plate to generate maximum K_I for the edge crack. The aluminum specimen analyzed in Figure 5-11 correspond to this case. The maximum K_I generated is equal to about $38.0 \text{ ksi}\sqrt{\text{in}}$ for a 2.0 inch long crack loaded at a rate of $\dot{Q} = 1.0 \text{ BTU/sec}$ ($=1055 \text{ watt}$). This also corresponds to a temperature of about 1200°F (650°C) at the source location (see Figures 5-13 and 5-14). While the maximum K_I was just sufficient to meet the test needs, the temperature (1200°F , 650°C) and the heating rate ($\dot{Q} = 1.0 \text{ BTU/sec}$) were greater than the capability

of the aluminum and our heating system (to be described in subsection 10.3). So we had to chose an alternate material as discussed next.

The analytical procedure used in THERMO-K assumes that the mechanical properties of the material are independent of temperature. Hence for direct comparison with THERMO-K's predictions, the experimental procedure should be designed such that the material properties are not changed significantly during the test. This requires that the material chosen for the study must have the following properties: (1) low conductivity, (2) low fracture toughness, and (3) high temperature capability.

A survey of readily available metals indicated that AISI-SAE 1095 steel ('spring steel') would satisfy the above conditions. The typical thermophysical properties of this material are presented in Table 10-1. The AISI-SAE 1095 steel has relatively low fracture toughness ($= 60 \text{ ksi}\sqrt{\text{In}}$), high yield strength ($= 200 \text{ ksi}$), and significantly higher temperature capability than aluminum. As discussed in later subsections, this material proved to be an ideal candidate for verifying the theoretical predictions.

Based on the finite element analysis discussed in Section 3, a length of about 19.5 inches was sufficient to duplicate the infinitely long plate condition assumed by THERMO-K. The width of the plate ($= 6 \text{ in.}$) was chosen such that the experimental hot spot at the heat source location could be theoretically approximated as a point source, and the crack tip corresponding to maximum K_I was sufficiently removed from the high temperatures and compressive stresses generated near the heat source location. A very thin plate (thickness $= 0.0625 \text{ in.}$) was chosen to satisfy the following conditions: (1) uniform temperature should be maintained through the thickness, (2) plane stress conditions

assumed by THERMO-K, and (3) capability for generating high tensile stresses in the specimen with the available heat sources.

10.2 Baseline Fracture Toughness Tests

Baseline Mode I fracture toughness (K_{1f}) tests were conducted for the steel specimen using the compact tension, C(T) geometry shown in Figure 10-2. The geometry conforms to ASTM Standard E399 (1987) except for the thickness. The C-T specimen has a thickness of 0.0625 in., which was the same as that of the specimen shown in Figure 10-1, so that K_{1f} determined from the C-T sample could be compared directly with the thermal stress intensity factor generated in the thermal-mechanical fracture tests.

A servo-controlled MTS universal testing system was used for precracking and fracture toughness testing. An automated fatigue crack growth testing system developed at the University of Dayton was used for this purpose (Mate User's Manual, 1988). Three specimens were tested at room temperature (76°F, 24°C). Crack mouth opening displacement (CMOD) was measured using an MTS CMOD clip gage. Precracking was done according to the ASTM procedure E399. To obtain K_{1f} , the precracked specimen was subjected to a monotonically increasing load and the peak load versus crack mouth opening displacement was measured. K_{1f} was calculated at the peak load. These values are reported in Table 10-2. The average value of K_{1f} is equal to 58.1 ksi $\sqrt{\text{in.}}$.

10.3 Heat Sources - Infrared Spot Heaters

High intensity focused infrared spot heaters (Model 4085, Research, Inc., 1988) were used to apply thermal pulse at the desired location on the specimen. A schematic of the thermal loading test setup is shown in Figure 10-3. Temperature was measured on the specimen using K-type thermocouples. Preliminary

tests with temperature measurement on both sides of the specimen at the source location confirmed that uniform temperature through the thickness is achieved almost instantaneously. Hence, only one spot heater was used at each location. The size of the hot spot was about 0.20 inch in diameter. The heaters were controlled using a closed-loop process controller system (Micricon, Model 823, 1988) . The power to the heaters could be controlled in two ways: (1) heater output adjusted such that a desired temperature versus time profile is maintained at point of measurement and (2) constant heater output as percentage of the full capacity. The full rated capacity of the spot heater is 0.711 BTU/sec (750 W). Due to radiation losses, the actual thermal loading applied on the specimen can be expected to be less than this value. To check this, the spot heaters were calibrated as discussed in the next section.

10.4 Calibration of Heat Sources

The thermal loading system described in the previous section yields only the rate of heater output as percentage of full capacity versus time. As discussed earlier, THERMO-K requires the rate of thermal pulse, \dot{Q} applied at the source location on the specimen as the thermal load input for analysis. Hence, the heat sources were calibrated to obtain the relationship between the heater output and \dot{Q} as described below.

The calibration test setup is shown in Figure 10-4. The heat sources were located at $(x,y) = (3.0, \pm 1.0 \text{ in})$. Temperature was measured at locations 3 and 6. Constant levels of heater output varying from 5% to 45% were applied and the temperature versus time profile was obtained. Then the thermal load, \dot{Q} was calculated such that the THERMO-K predictions matched these measured values. The calculated values of \dot{Q} are shown versus the heater output in Figure 10-5. The power law fit is given by

$$\dot{Q} = 0.00249 (L_o) \quad (10-1)$$

where L_o = heater output in percentage (%), and \dot{Q} = rate of thermal load in BTU/sec. This relationship was used in all further calculations using THERMO-K.

In the above procedure, the temperature was measured at 1.0 to 2.0 inches removed from the source location. This involves heat conduction through the material. Hence, the calibration equation, Equation (10-1) is probably a function of the material. The system was not calibrated at output levels greater than 50% because such high thermal loads were introducing highly localized irreversible deformation at the source location ('dimpling' effect). Assuming that Equation (10-1) is valid over the entire range of the spot heater, the maximum rate of thermal load at 100% is equal to about 0.357 BTU/sec (376 W), which is only half the rated capacity of the heat sources.

10.5 Temperature Verification Tests

Temperature verification tests were conducted to verify the heat transfer analytical predictions by THERMO-K. Uncracked plates were used for this purpose. The test setup used is shown in Figure 10-6. Figure 10-6 shows that temperature was measured at thirteen different locations on the specimen including ten locations along the 'crack plane' ($y=0$), two locations of heat sources ('B' & 'C') and one location ('A') at the far end of the specimen. Two cases were tested as reported in Table 10-3; one was symmetric, the other asymmetric. For each case, two specimens were tested. An existing automated data acquisition system developed at the University of Dayton was used to collect the test results.

For the symmetric cases, the thermal loading, \dot{Q} was applied at $(x,y) = (4.5, \pm 1.0)$, i.e., at locations 'B' and 'C' in Figure 10-6. \dot{Q} was controlled that such the temperature profile shown in Figure 10-7 was maintained at each source location, i.e., the temperature at the source increased linearly with time reaching about 475°C above room temperature (500°C total) in 150 seconds and then held constant at that temperature for an additional 150 seconds. The corresponding rate of thermal loading pulse is shown in Figure 10-8. This was determined by measuring the heater output versus time and using Equation (10-1). The thermal pulse in Figure 10-8 was used as input loading for the THERMO-K analysis.

The measured temperature variation are compared with the THERMO-K predictions in Figures 10-9 to 10-12. The two dashed lines at each location correspond to the two specimens tested. The solid lines are the THERMO-K predictions. From these figures it can be seen that the measured transient heat transfer phenomenon is predicted very well by THERMO-K, across the entire width of the specimen.

In the next stage, the asymmetric tests were conducted with only one heat source located at 'C', i.e., $(x,y) = (4.0, -1.0)$ in Figure 10-6. The thermal loading applied at location 'C' was identical to Figure 10-8. The experimental results for the asymmetric tests are compared with the theoretical predictions in Figures 10-13 to 10-16. For this case also, the THERMO-K analytical results correlate well with the measured temperatures. Note that the temperatures in this case are half that of the symmetric case with two heat sources.

Figures 10-9 to 10-16 show that the highest temperature occurs close to the heat source, and the temperature decreases rapidly away from the heat source. Such steep temperature gradients can be expected to generate high stresses in the specimen. The

reader should note that in both the above cases, the farfield temperature at location 'A' did not increase more than 11°C above room temperature even after 300 seconds into the test as shown in Figures 10-12 and 10-16. Hence, the length of the specimen appears to be adequate for test durations less than 300 seconds.

10.6 Strain Verification Tests

After the heat transfer tests were completed, the University of Dayton conducted strain verification tests with strain gages glued on the specimen. The test setup is shown in Figure 10-17. Both symmetric and asymmetric tests were conducted as reported in Table 10-3. The test conditions were maintained identical to the temperature verification tests. Strains were measured at locations 3, 6, and 9 as marked in Figure 10-17. To eliminate the errors due to plate bending, strains in the y-direction (ϵ_{yy}) were measured on both sides of the specimen and the results averaged.

For the symmetric tests, only the normal strains ϵ_{yy} were measured. For the asymmetric tests, normal, transverse and shear strains (ϵ_{yy} , ϵ_{xx} , ϵ_{xy}) were measured at the three locations using strain rosettes. The measured strain values are shown in Figure 10-18 for the symmetrical tests and in Figures 10-19 to 10-21 for the asymmetrical tests. These strain values are the actual strain gage readings which include the thermal strains (= temperature x coefficient of thermal expansion).

As shown in Figures 10-18 to 10-21, the experimental results obtained in the strain verification tests are in good agreement with the THERMO-K predictions.

Very high compressive strains corresponding to high temperatures are observed under the heat sources at location 3 as shown in Figure 10-18. Tensile strains are observed away from the source location as indicated by the values measured at locations 6 and 9

in the same figure. The tensile strains close to the edge $x=0$ are less than 400 microstrains. These low values are consistent with the observations made during the finite element analysis in subsection 5.8. As the source is moved horizontally away from the vertical centerline of the specimen, the tensile strains close to the edges decrease rapidly (for example, compare Figures 5-14 and 5-22). In Figure 10-18 we also observe that the strains at location 9 are less than that at location 6. This trend is also shown in Figure 5-22, where the thermal loading configuration is comparable to that of the symmetrical strain verification tests.

10.7 Thermal-Mechanical Fracture Tests

The Mode I thermal-mechanical fracture tests were conducted using the single edge cracked specimen geometry detailed in Figure 10-22. An eccentric pin loaded geometry was chosen to facilitate generating higher K_I stress intensity factors with the same mechanical load. This geometry also prevented localized yielding and failure at the hole. For the combined tensile and bending loading, the principle of superposition was used to calculate the total stress intensity factor (K_I) as shown in Figure 10-23. To check the validity of this analysis, a linear elastic finite element analysis was performed for this geometry using SNAP (1982). K_I was calculated using the J-integral and quarter-point singular element methods. The results are presented in Table 10-4. It can be seen that the results obtained using the linear superposition principle are within about 2.5% of the finite element results for combined tensile and bending loading.

The mechanical loads were applied using the servo-controlled MTS testing system and the thermal loads using the infrared spot heaters as discussed earlier. All the specimens had an initial EDM (electrical discharge machined) notch equal to 1.20 inches. These specimens were precracked about 0.10 in. beyond the notch using a constant amplitude fatigue load equivalent to K_I of about

25 ksi $\sqrt{\text{in}}$. The final crack length at the end of precracking was equal to 1.30 inches.

The test procedure consisted of three steps as shown in Figure 10-24.

Step 1: Apply constant load corresponding to the desired mechanical K , see Figure 10-24(a).

Step 2: Begin applying thermal load (\dot{Q}) while simultaneously observing the crack tip. Note time to fracture, t_f , as shown in Figure 10-24(b).

Step 3: Using the THERMO-K predicted K_1 and K_2 versus time relationship corresponding to the above \dot{Q} , determine the thermal K_1 and K_2 ($K_{1,\text{ther}}$ and $K_{2,\text{ther}}$, respectively) which is generated at time t_f . These values of $K_{1,\text{ther}}$ and $K_{2,\text{ther}}$ are the thermal stress intensity factors required to fracture the specimen in addition to the applied mechanical K_1 .

The thermal-mechanical tests conducted during this study are shown in Table 10-5. Three levels of mechanical K_1 ($K_{1,\text{mech}}$) were chosen for this purpose. These values correspond to low, medium and high percentages of the K_{1f} determined from the compact tension tests. For all tests, temperatures were monitored close to the crack tip (end of precrack) and at the source location. Data was collected at 0.50 second intervals using the automated data acquisition system.

10.7.1 Mode I Tests

Mode I thermal-mechanical tests were conducted by applying thermal loads at $(x,y) = (3.0, +1.0)$ and $(3.0, -1.0)$, i.e.

locations 'E' and 'F' as shown in Figure 10.22. A constant \dot{Q} of 0.08763 BTU/sec (92.45 W) was applied at each source location. The thermal sources were located symmetrically about the crack tip resulting in only normal thermal stresses (σ_{yy}) generated at the crack tip. THERMO-K predicted the K versus time relationship that was used to determine $K_{1,ther}$ as shown in Figure 10-25. The results of the Mode I tests are reported in Table 10-6. It is worth noting that in all the Mode I tests, crack initiation was accompanied by a distinct 'pop' sound.

Figure 10-26 shows a plot of additional $K_{1,ther}$ required to fracture the specimen versus the applied $K_{1,mech}$. It is observed that as applied $K_{1,mech}$ decreases, the $K_{1,ther}$ required to fracture the specimen increases linearly. The sum ($K_{1,mech} + K_{1,ther}$) signifies the total stress intensity factor at the crack tip at the time of fracture. To check the correlation between the thermal and mechanical stress intensity factors, the total K_1 ($= K_{1,ther} + K_{1,mech}$) is plotted versus $K_{1,mech}$ in Figure 10-27. In this figure, it is seen that the ratio of total K_1 to K_{1f} is close to 1.0 for all cases. This implies that $K_{1,ther}$ can be used in fracture and fatigue analysis in combination with $K_{1,mech}$.

The THERMO-K predicted and measured temperatures at the crack tip, and the measured temperature at the source location are plotted in Figure 10-28. There is satisfactory correlation between the measured and predicted temperature at the crack tip. Even for the case with the lowest mechanical load, i.e., highest $K_{1,ther}$, the temperature at the crack tip was only about 50°C, and at the source about 215°F. At these temperatures the mechanical properties of the specimen is same as that at room temperature.

Figure 10-29 shows a plot of time to fracture, t versus $K_{1,mech}$. A linear relationship is observed similar to Figure 10-26.

Figure 10-29 implies that the specimen could have been fractured with pure thermal load (i.e., $K_{1,mech} = 0$) in about 35-40 seconds (also see Figure 10-25).

10.7.2 Mixed Mode Tests

Mixed mode thermal mechanical tests were conducted by applying the thermal load at $(x,y) = (3.0, -1.0)$, i.e., at location 'F' shown in Figure 10-22. A constant \dot{Q} of 0.0175 BTU/sec (184.63 W) was applied at this location. Since the thermal source was located asymmetrically about the crack tip, normal and shear thermal stresses (σ_{yy} and σ_{xy}) exist at the crack tip. This results in $K_{1,ther}$ and $K_{2,ther}$ at the crack tip. Figure 10-30 summarizes the THERMO-K predicted Mode I and II stress intensity factor versus time relationships that were used to determine $K_{1,ther}$ and $K_{2,ther}$ at fracture.

The results of the mixed mode tests are presented in Table 10-7. Figure 10-31 shows a plot of the total Mode II stress intensity factor ($=K_{2,ther}$) versus the total Mode I stress intensity factor ($=K_{1,ther} + K_{1,mech}$) at fracture. Due to the scatter in the test results, only the average values are plotted in this figure. For comparison purposes, two curves corresponding to Equation (10-2) are also plotted. Specific forms of this equation have been used extensively to represent mixed mode fracture envelopes for different materials.

$$\left(\frac{K_2}{K_{2f}}\right)^p + \left(\frac{K_1}{K_{1f}}\right)^p = 1 \quad (10-2)$$

where

$$K_2 = K_{2,ther}$$

$$K_1 = K_{1,ther} + K_{1,mech}$$

K_{2f} = Mode 2 fracture toughness

K_{1f} = Mode 1 fracture toughness

p = arbitrary exponent

Based on extensive experiments, Shah (1974) concluded that Equation (10-3) adequately describes the mixed mode fracture behavior of 4340 steel.

$$K_1 + K_2 = K_{1f} \quad (10-3)$$

where

$$K_1 = K_{1, \text{mech}} , \text{ and}$$

$$K_2 = K_{2, \text{mech}} .$$

Equation (10-3) is a special case of Equation (10-2) with K_{2f} equal to K_{1f} and the exponent 'p' equal to 1.0. In the present study, K_{2f} was not determined. Hence, we have two variables; namely K_{2f} and p , in Equation (10-2). So we considered the following two cases.

In the first case, K_{2f} was set equal to K_{1f} and p chosen such that Equation (10-2) fit the data. In this case p was equal to 1.45 and not 1.0 as suggested by Shah (1974). Equation (10-2) with $K_{2f} = K_{1f} = 58.1 \text{ ksi}\sqrt{\text{in}}$ and $p = 1.45$ is shown as the solid line in Figure 10-31. In the second case, p was set equal to 2.0 and K_{2f} chosen such that Equation (10-2) fit the data. In this case, K_{2f} equal to (0.5) K_{1f} represented the data well as shown by the dashed line in Figure 10-31. The second case with $p = 2$ approximates the relationship between K_1 and K_2 as obtained from energy principles (Brock, 1986).

The lack of a K_{2f} value, coupled with insufficient mixed mode data, made it impossible to reach a definitive conclusion about the mixed-mode thermal-mechanical fracture results. The reader might note that for most of the tests, the total K ($= K_{1,mech} + K_{1,ther}$) was close to K_{1f} . Thus one might also be able to use the Mode I failure criterion and neglect any Mode II contribution as long as K_2 is less than about 20% of K_{1f} .

We attempted to correlate the crack initiation angle with the linear elastic mixed mode fracture theories (Erdogan and Sih, 1963). These theories were developed for brittle materials. Even though the crack tip zone of plasticity was small for this material, the crack tip plastic deformation made this comparison impossible. The observation of crack initiation under mixed mode was difficult compared to the Mode I tests. There was no 'pop' sound heard like that heard in the Mode I tests. This may have contributed to the scatter in the test results. In addition, this uncertainty in crack initiation occurrence results in potentially longer times to fracture and thus higher predicted values of $K_{1,ther}$ and $K_{2,ther}$.

10.8 Summary

The good correlation between the temperature verification test results and THERMO-K predictions confirms the validity of the heat transfer theoretical approach used in THERMO-K. The strain verification test results also confirm the stress trends predicted by THERMO-K. The Mode I thermal-mechanical fracture test results indicated that the thermal stress intensity factor predicted by THERMO-K correlates well with the mechanical fracture toughness of the material. The mixed mode thermal-mechanical test results seem to validate THERMO-K's predictions within the available small range of data. Additional experiments are required to investigate the thermal-mechanical fracture behavior under a wide range of mixed mode loading conditions.

10.9 References

ASTM E-399, Annual Book of ASTM Standards, Sec. 3, Vol. 03.01, 1987.

Brockman, R. A., "SNAP: A Simple Nonlinear Analysis Program for Education and Research," UDR-TM-82-06, University of Dayton Research Institute, Dayton, OH, 1982.

Broek, D., Elementary Engineering Fracture Mechanics, Martinus Nijhoff Publishers, The Netherlands, 1986.

Erdogan, F. and Sih, G.C., "On the Crack Extension in Plates Under Plane Loading and Transverse Shear," Journal of Basic Engineering, ADME, Vol. 85, pp. 519-527, December, 1963.

Infrared Spot Heaters, Model 4085, Bulletin of Research, Inc., Minneapolis, MN.

MATE and MATE Modules, User Manuals - Version 2.22A, Crack Growth Analysis and Test Environment, UDR-TR-88-138, University of Dayton, Research Institute, Dayton, OH 45469.

Micricon 823, Distributed Controller, Bulletin of Research, Inc., Minneapolis, MN.

Shah, R. C., "Fracture Under Combined Modes in 4340 Steel," Fracture Analysis, ASTM STP 560, American Society for Testing and Materials, pp. 29-52, 1974.

TABLE 10-1

THERMOPHYSICAL PROPERTIES OF AISI-SAE 1095 STEEL*

Yield Strength, s	= 200 ksi
Plane Strain Fracture toughness, K	= 60 ksi $\sqrt{\text{in}}$
Specific heat, c	= 0.113 BTU/lb-°F
Density, p	= 0.2836 lb/in
Thermal conductivity, k	= 0.0005787 BTU/sec-in-°F
Thermal expansion coefficient**, a	= 6.5 x 10 in/in-°F
Young's modulus, E	= 30.0 x 10 psi
Poisson's ratio, n	= 0.28
Heat convection coefficient, H	= 5.00 x 10 BTU/in ² -sec-°F
H ₁	= 0
H ₂	= 0

Note:

* All the values were estimated from the handbook

** Average value of 'H' obtained from Structural Integrity Associates H₁ = H₂ = 0.0, since thin specimen was used

TABLE 10-2

RESULTS FROM BASELINE FRACTURE TOUGHNESS TESTS**

Specimen Number	Precrack Length a_p (in)	Total Crack Length $a = a_N^* + a_p$ (in)	Peak Load (kip)	Fracture Toughness K_{I_f} (ksi $\sqrt{\text{in}}$)
1	0.478	0.750	0.5058	58.0
2	0.486	0.758	0.4608	53.6
3	0.477	0.749	0.5480	62.7

Average = 58.1

Note:

* a_N = length of EDM notch = 0.272 in.

** all tests were conducted at room temperature (76°F, 24°C)

TABLE 10-3

TEST PROGRAM FOR TEMPERATURE AND STRAIN
VERIFICATION TESTS

Type of Thermal Loading	Number of Heat Sources	Location of Heat Sources (x,y) (in.)	Number of Specimens Tested
Symmetric	2	(4.5,±1.0)	2
Asymmetric	1	(4.5,-1.0)	2

TABLE 10-4
PLANE STRESS \bar{K}_1 VALUES CALCULATED USING
DIFFERENT METHODS

Method	\bar{K}_1
1. Principle of Superposition	8.21
2. Finite Element Analysis Quarter-Point Singular Element	7.96
3. Finite Element Analysis J-integral Method	8.03

Note:

* $\bar{K}_1 = K_1 W t / P \sqrt{\pi a}$

v, t, P, a are defined in Figure 10-22

TABLE 10-5
PROGRAM FOR THERMAL-MECHANICAL FRACTURE TESTS

Type of Test	K_I Mechanical	$K_{I, mech}$ K_{If} (%)	Thermal Loading			Number of Specimens Tested
			Numbers of Source	Location of Sources (x,y) (in.)	Heater Output (%)	
Mode 1	10	17			27.3	3
	25	43	2	(3.0, ± 1.0)		3
	40	69				3
Mixed Mode	10	17				3
	25	43	1	(3.0, -1.0)	51.9	3
	40	69				3

Note:

* $K_{I, mech} = K_I$ mechanical

$K_{If} = 58.1 \text{ ksi}\sqrt{\text{in}}$

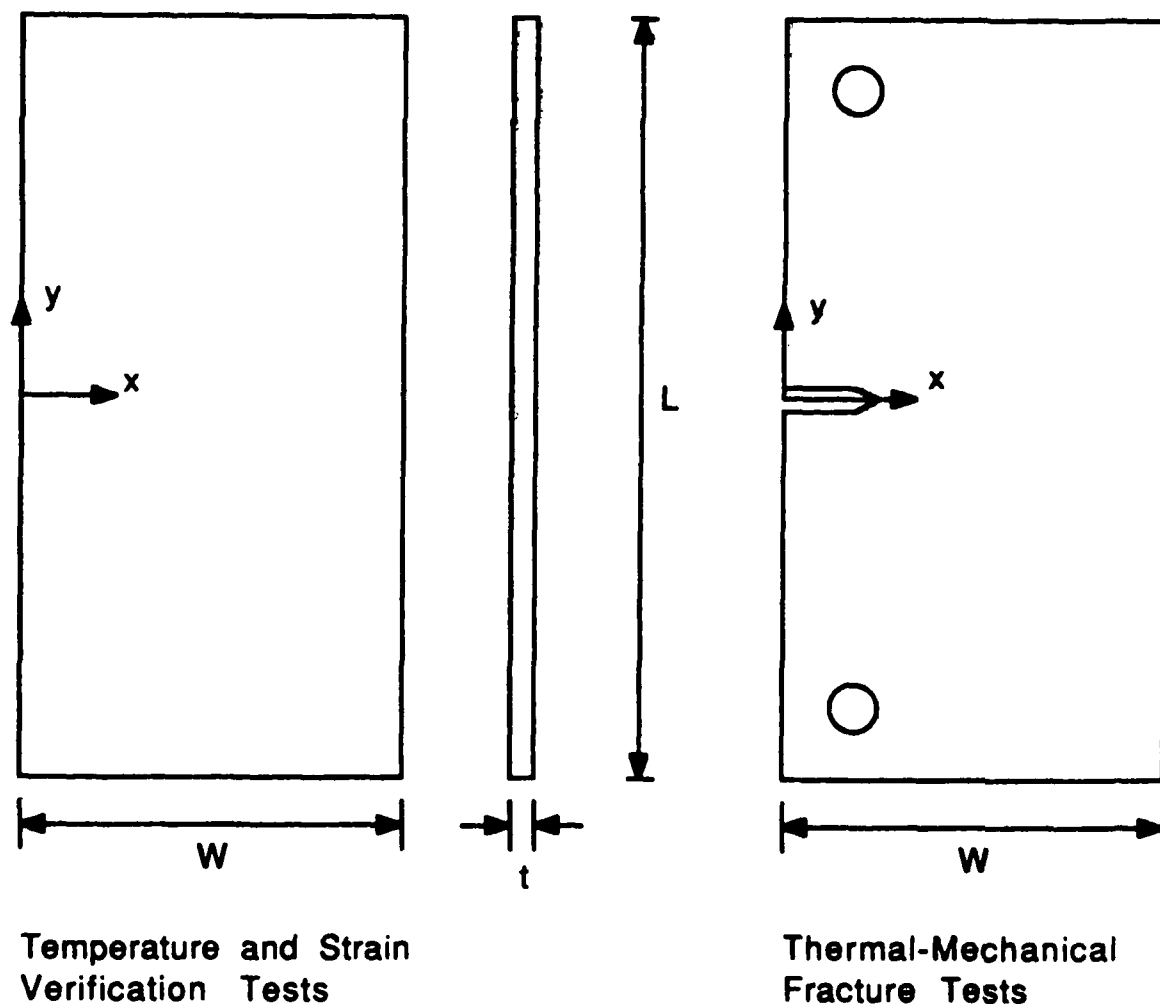
TABLE 10-6
TEST RESULTS FOR MODE 1 TESTS

K_I Mechanical ($\text{ksi}\sqrt{\text{in}}$)	Time to Fracture t_f (sec)	K_I Thermal ($\text{ksi}\sqrt{\text{in}}$)	K_I Total ($\text{ksi}\sqrt{\text{in}}$)
10.0	28.3	45.8	55.8
10.0	27.8	44.5	54.5
10.0	34.3	52.0	62.0
25.0	14.2	23.2	48.2
25.0	20.0	32.2	52.2
25.0	22.7	36.5	61.5
40.0	11.0	18.0	58.0
40.0	10.6	17.3	57.3
40.0	12.7	20.7	60.7

TABLE 10-7

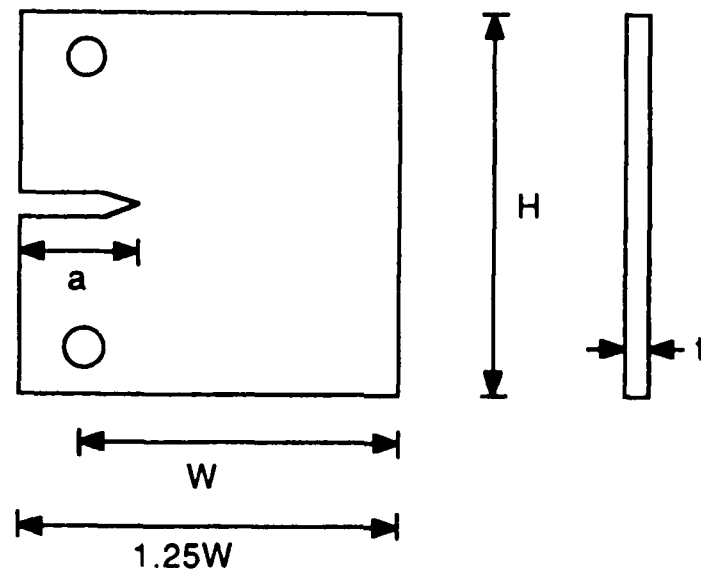
TEST RESULTS FOR MIXED MODE TESTS

K_1 Mechanical ($\text{ksi}\sqrt{\text{in}}$)	Time to Fracture t_f (sec)	K_1 Thermal ($\text{ksi}\sqrt{\text{in}}$)	K_2 Thermal ($\text{ksi}\sqrt{\text{in}}$)	K_1 Total ($\text{ksi}\sqrt{\text{in}}$)
10.0	22.2	35.7	11.97	45.7
10.0	-- crack initiation was not observed --			
10.0	29.5	46.7	15.39	56.7
25.0	18.4	29.4	9.96	54.4
25.0	17.2	27.9	9.45	52.9
25.0	20.6	33.2	11.16	58.2
40.0	18.19	18.2	6.25	58.2
40.0	17.12	17.1	5.88	57.1
40.0	17.29	17.3	5.94	57.3



Length (L) = 19.5 in., Width (W) = 6.0 in., Thickness (t) = 0.0625 in.

Figure 10-1. Overview of Specimen Geometries Used During the Experimental Verification of THERMO-K



$H = 1.875$ in.
 $W = 1.575$ in.
 $t = 0.0625$ in.

$a = \text{EDM notch} = 0.272$ in.

Figure 10-2. Compact Tension Specimens Used for Baseline Fracture Toughness Test

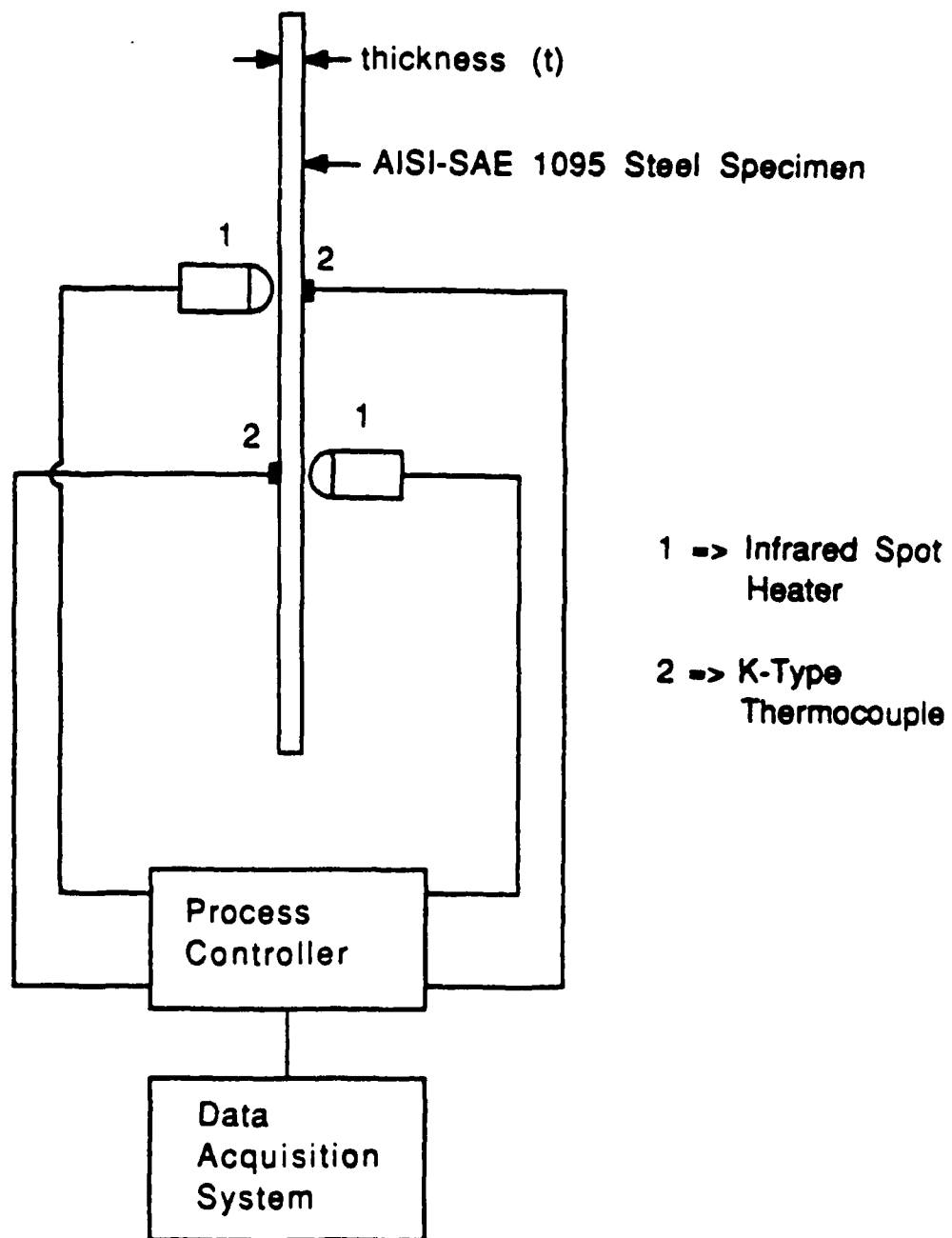
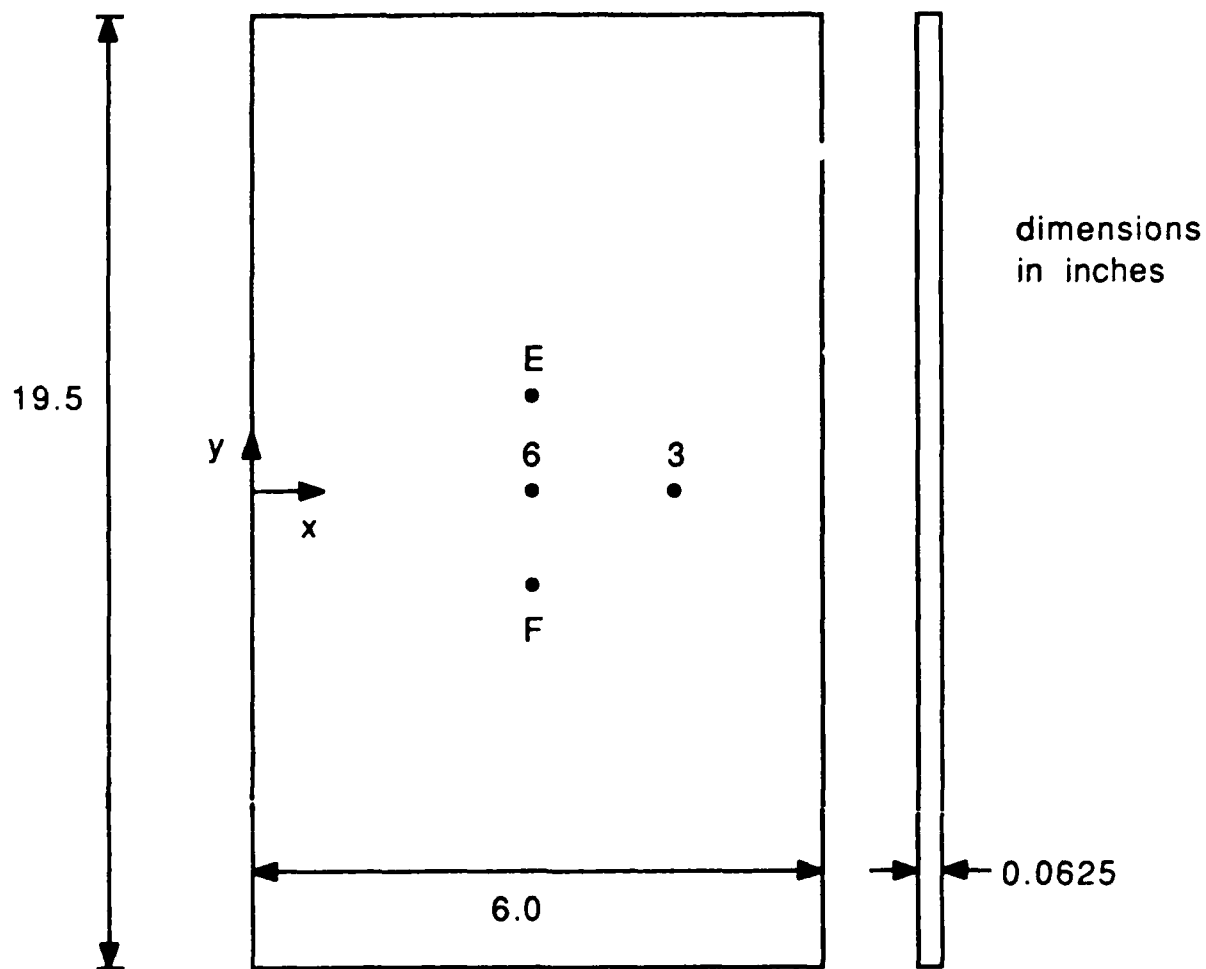


Figure 10-3. Schematic of Thermal Loading Test Setup



Location Number	(x,y) (in)	Remarks
E	(4.5,+1.0)	Thermal Load
F	(4.5,-1.0)	Thermal Load
3	(4.5, 0.0)	Temperature Measurement
6	(3.0, 0.0)	Temperature Measurement

Figure 10-4. Test Setup for Calibration of Heat Sources

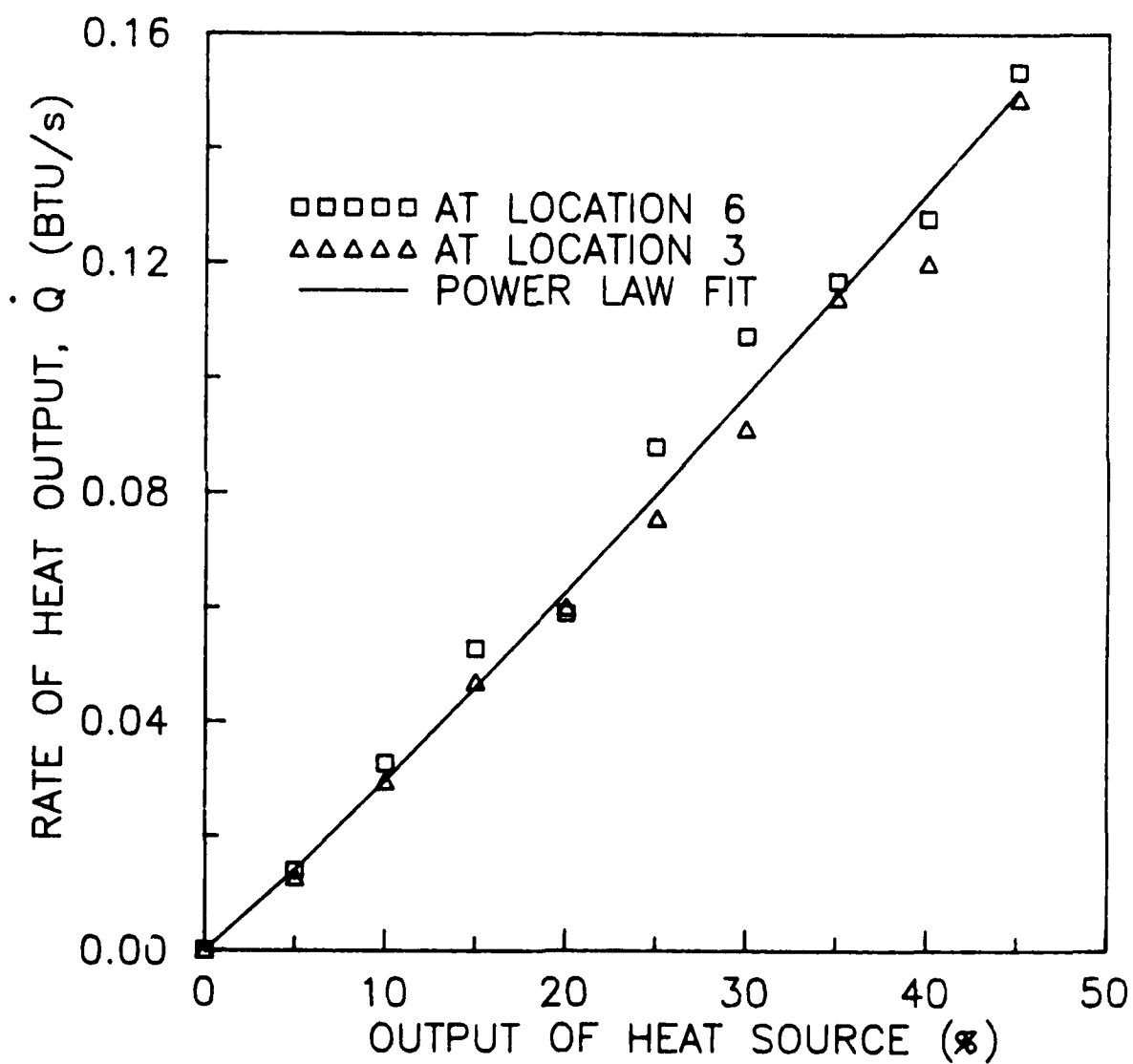
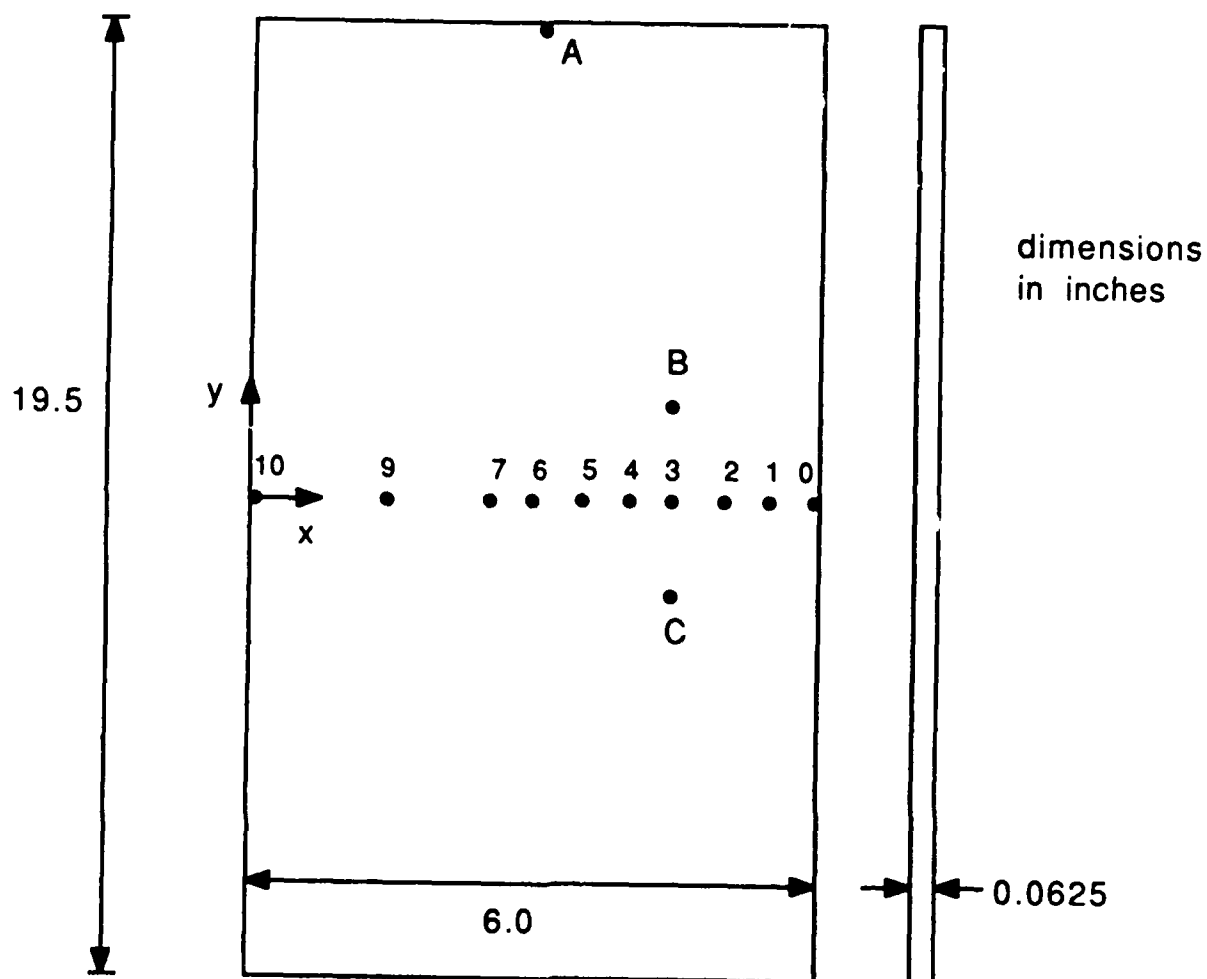


Figure 10-5. Calibration Data and Fit Curve for the Spot Heater



Location Number	(x,y) (in)	Location Number	(x,y) (in)
0	(5.95, 0.0)	7	(2.50, 0.0)
1	(5.50, 0.0)	8	(2.00, 0.0)
2	(5.00, 0.0)	9	(1.00, 0.0)
3	(4.50, 0.0)	10	(0.05, 0.0)
4	(4.00, 0.0)	A	(3.00, 9.7)
5	(3.50, 0.0)	B	(4.50,+1.0)
6	(3.00, 0.0)	C	(4.50,-1.0)

Figure 10-6. Test Setup for Temperature Verification Tests

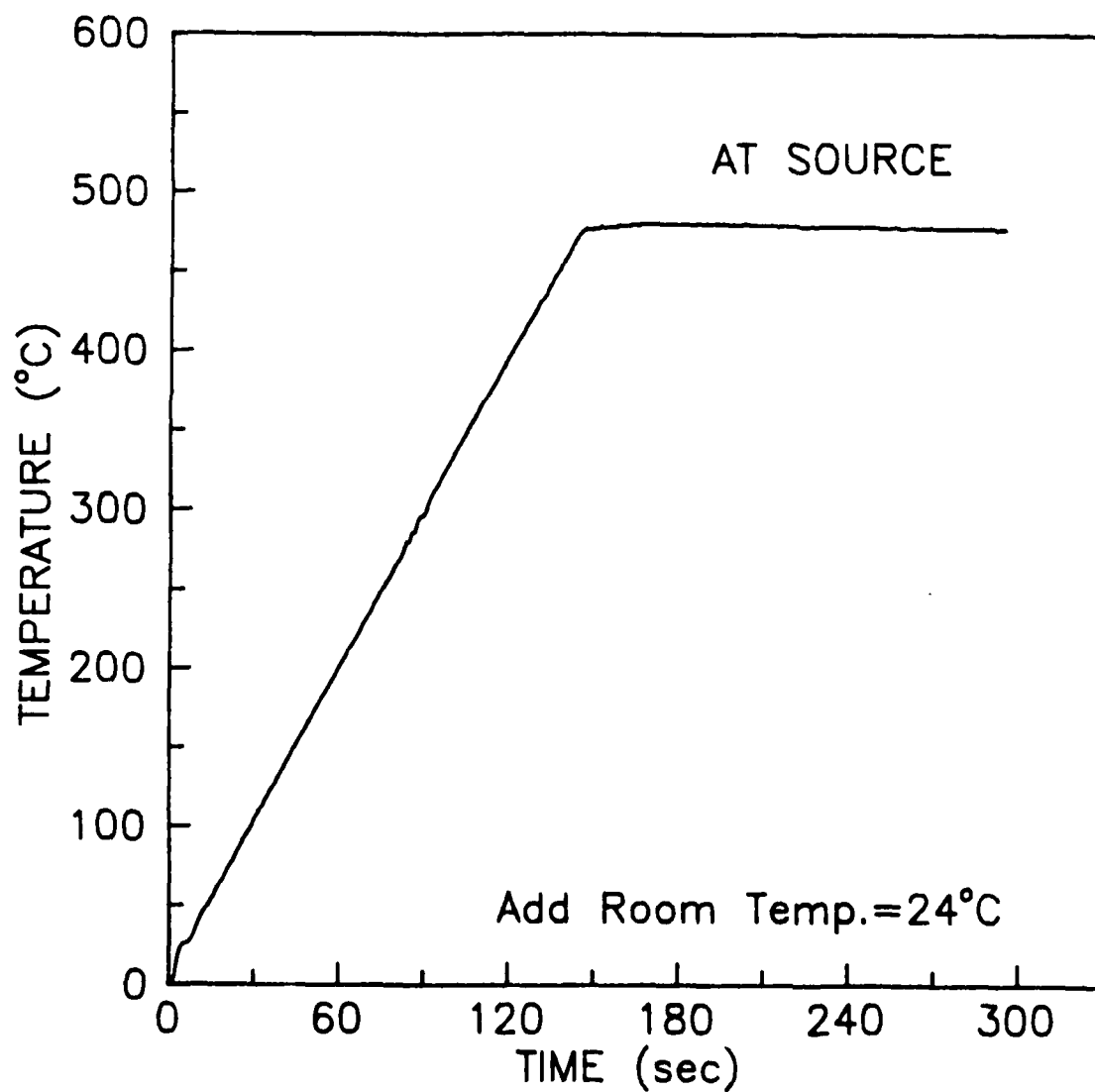


Figure 10-7. Temperature Profile Maintained at Source Location for Temperature and Strain Verification Tests

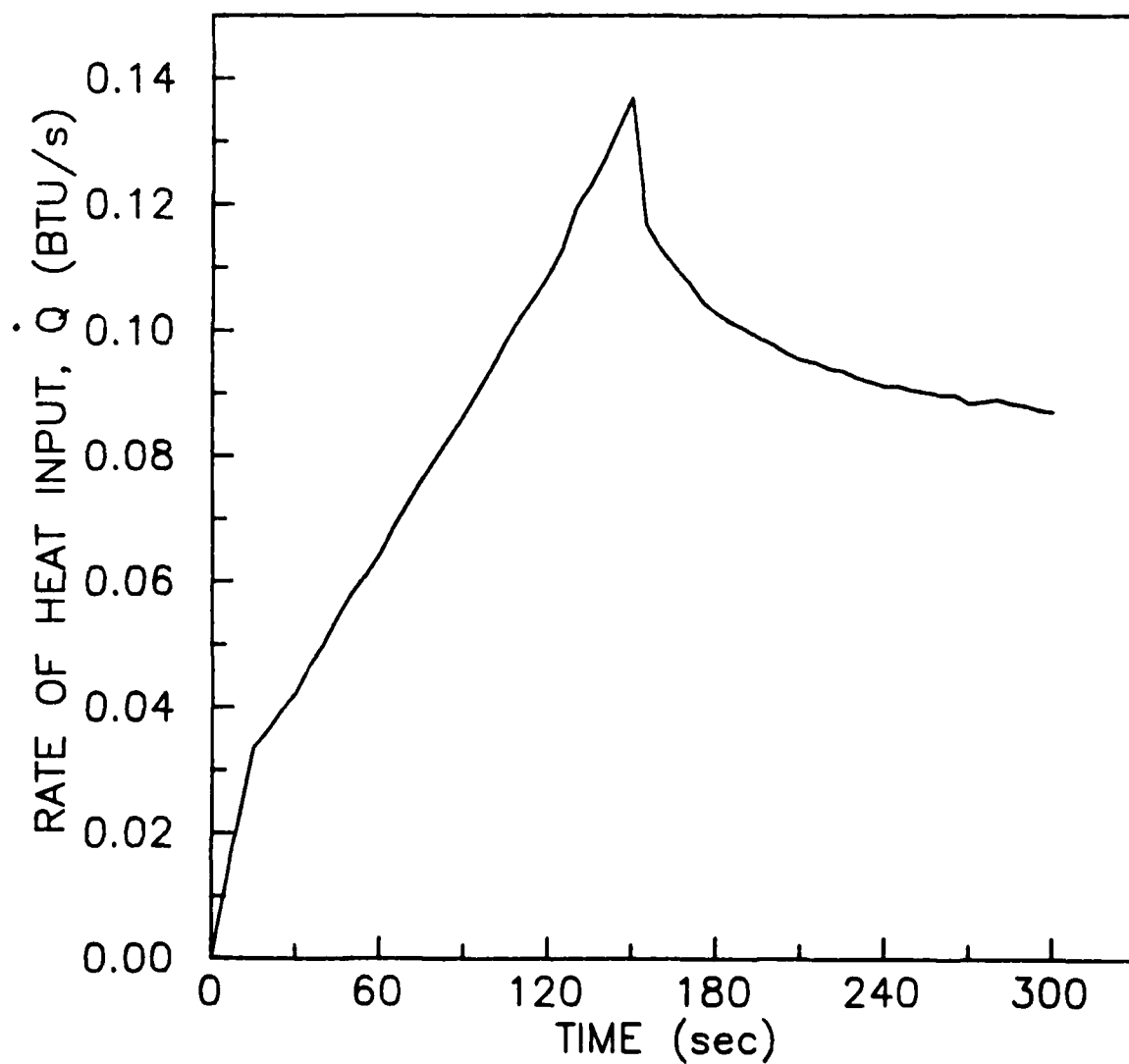


Figure 10-8. Rate of Heat Input at Source Location Corresponding to Temperature Profile in Figure 10-7.

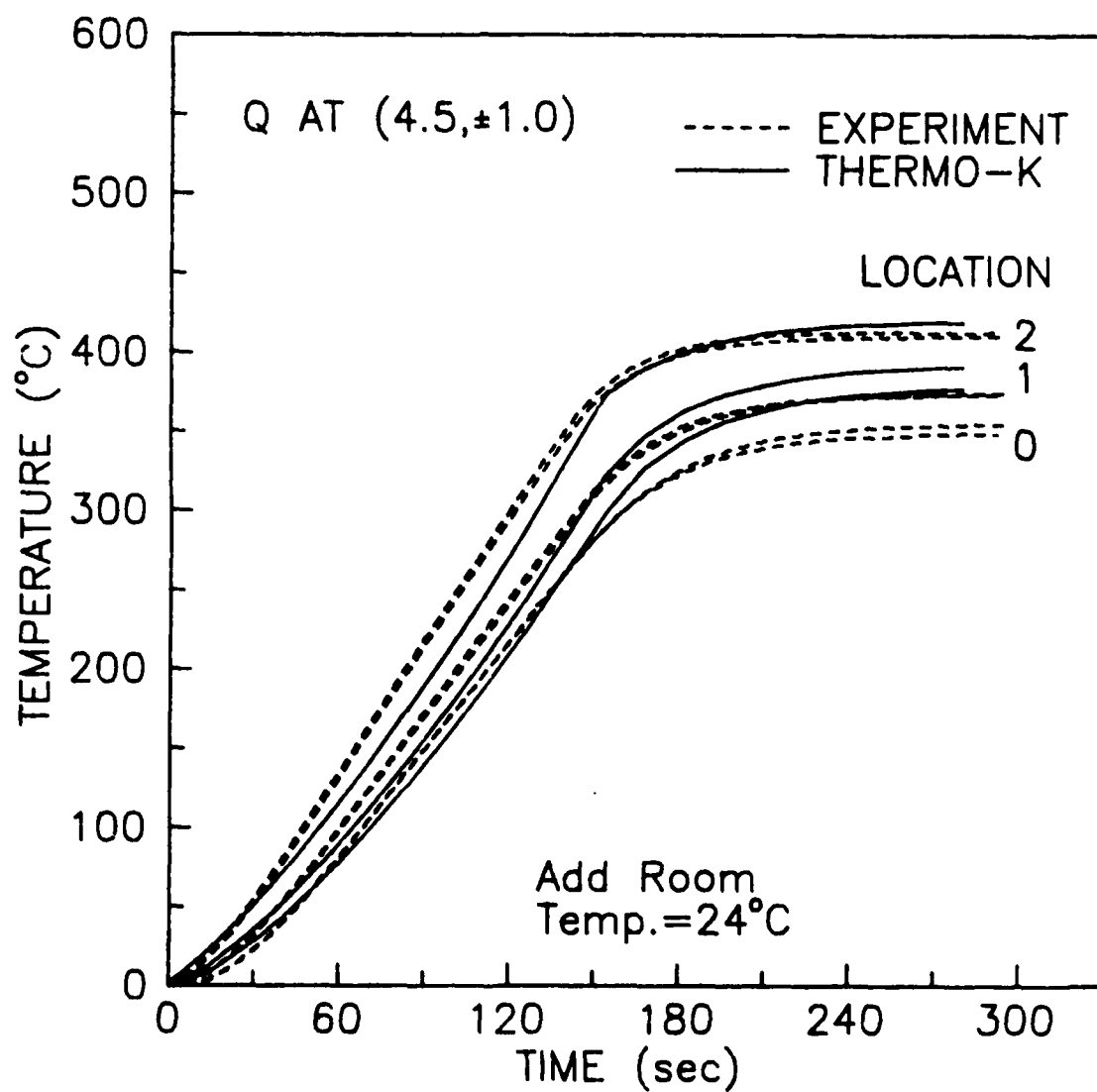


Figure 10-9. Results for Symmetrical Temperature Verification Tests at Locations 0, 1 and 2

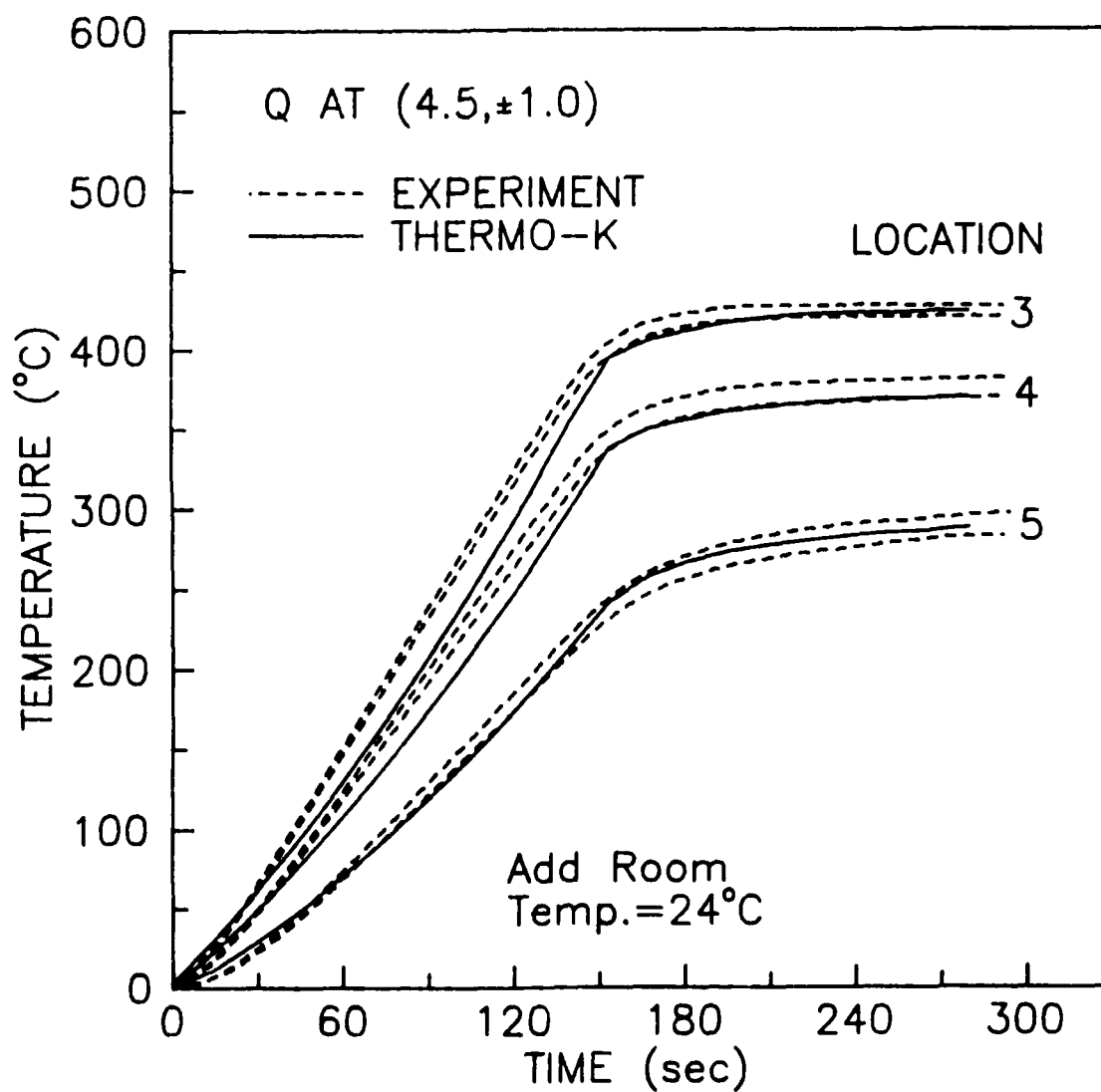


Figure 10-10. Results for Symmetrical Temperature Verification Tests at Locations 3, 4 and 5

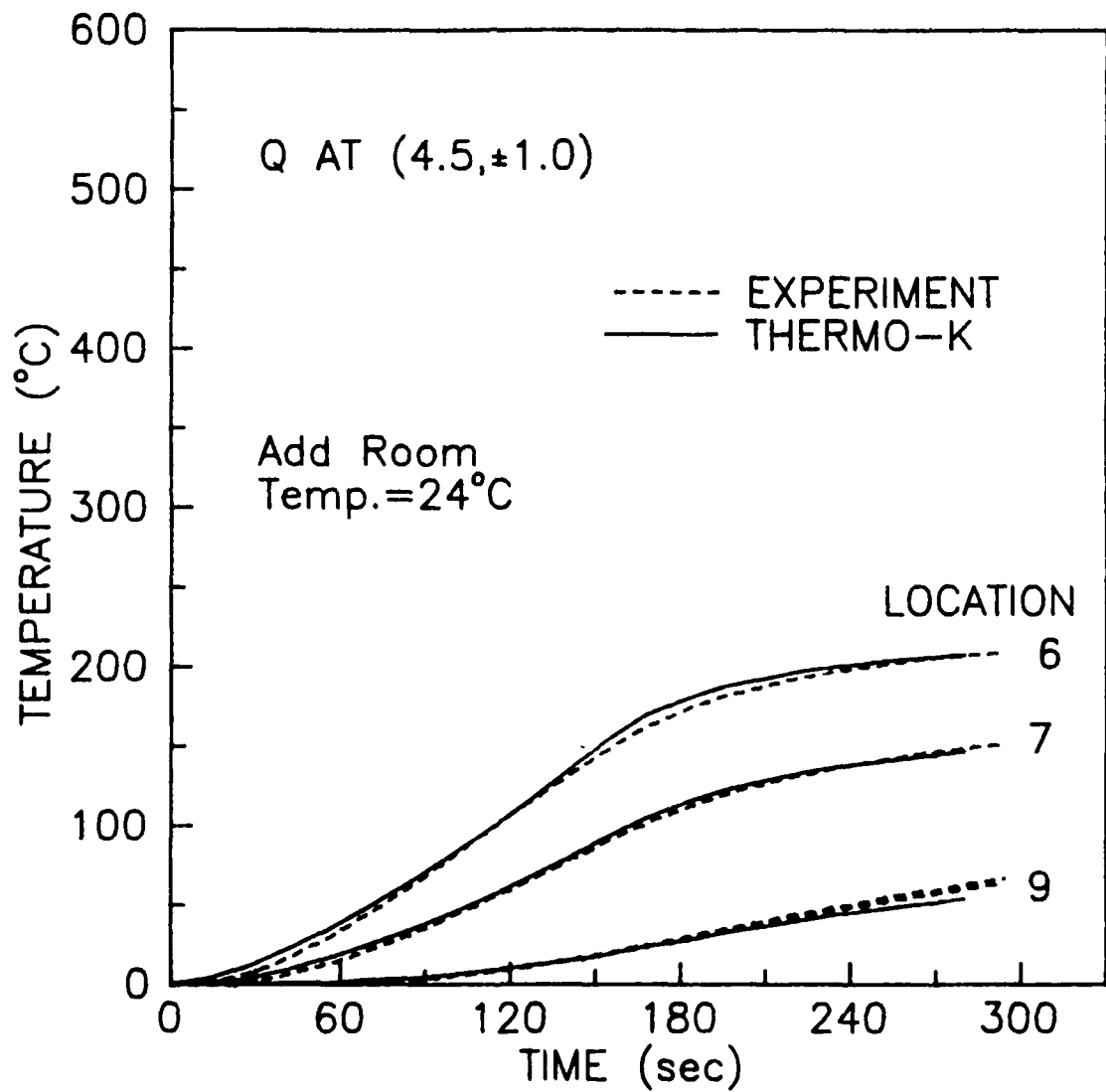


Figure 10-11. Results for Symmetrical Temperature Verification Tests at Locations 6, 7 and 9

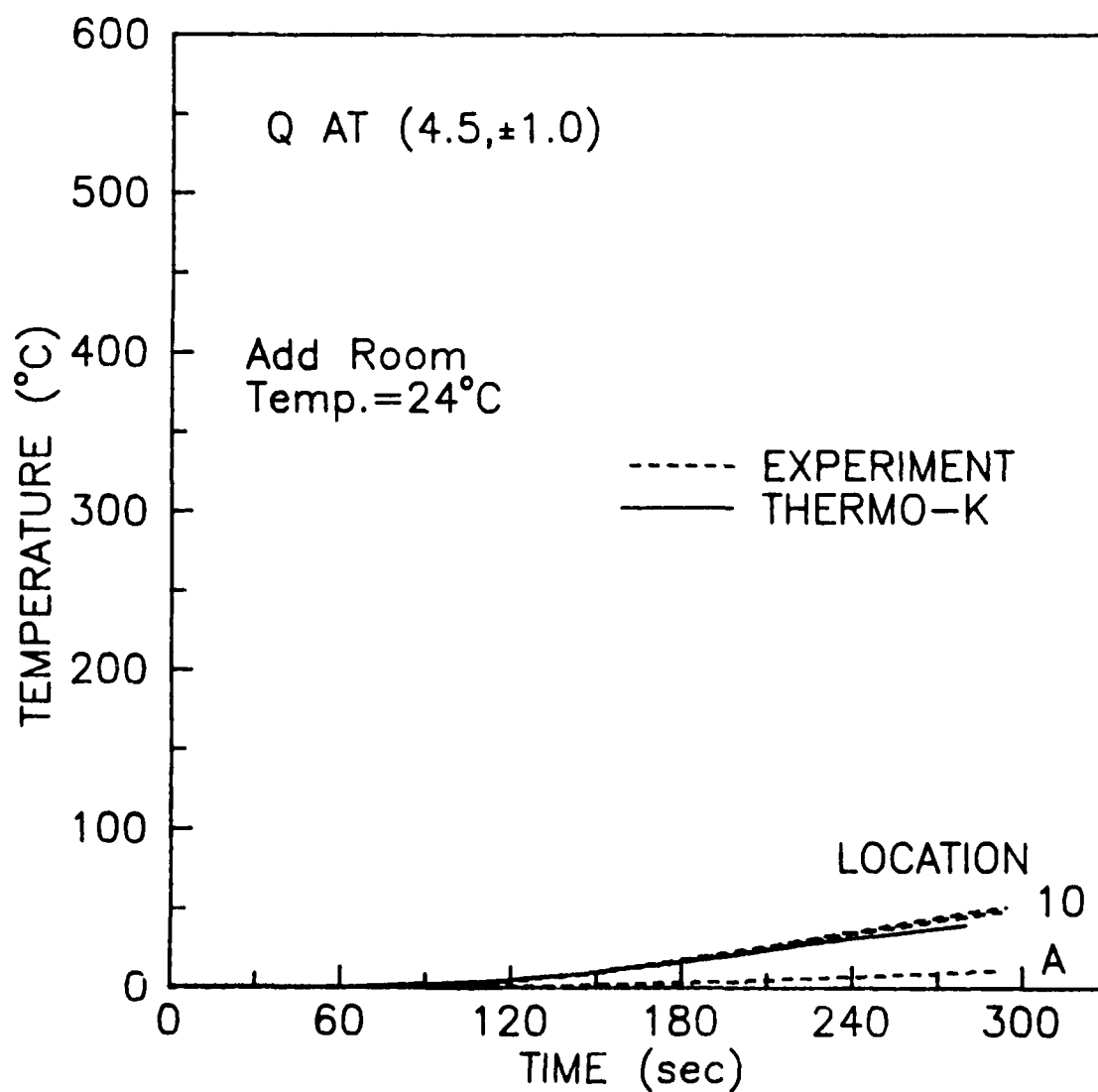


Figure 10-12. Results for Symmetrical Temperature Verification Tests at Locations 10 and A.

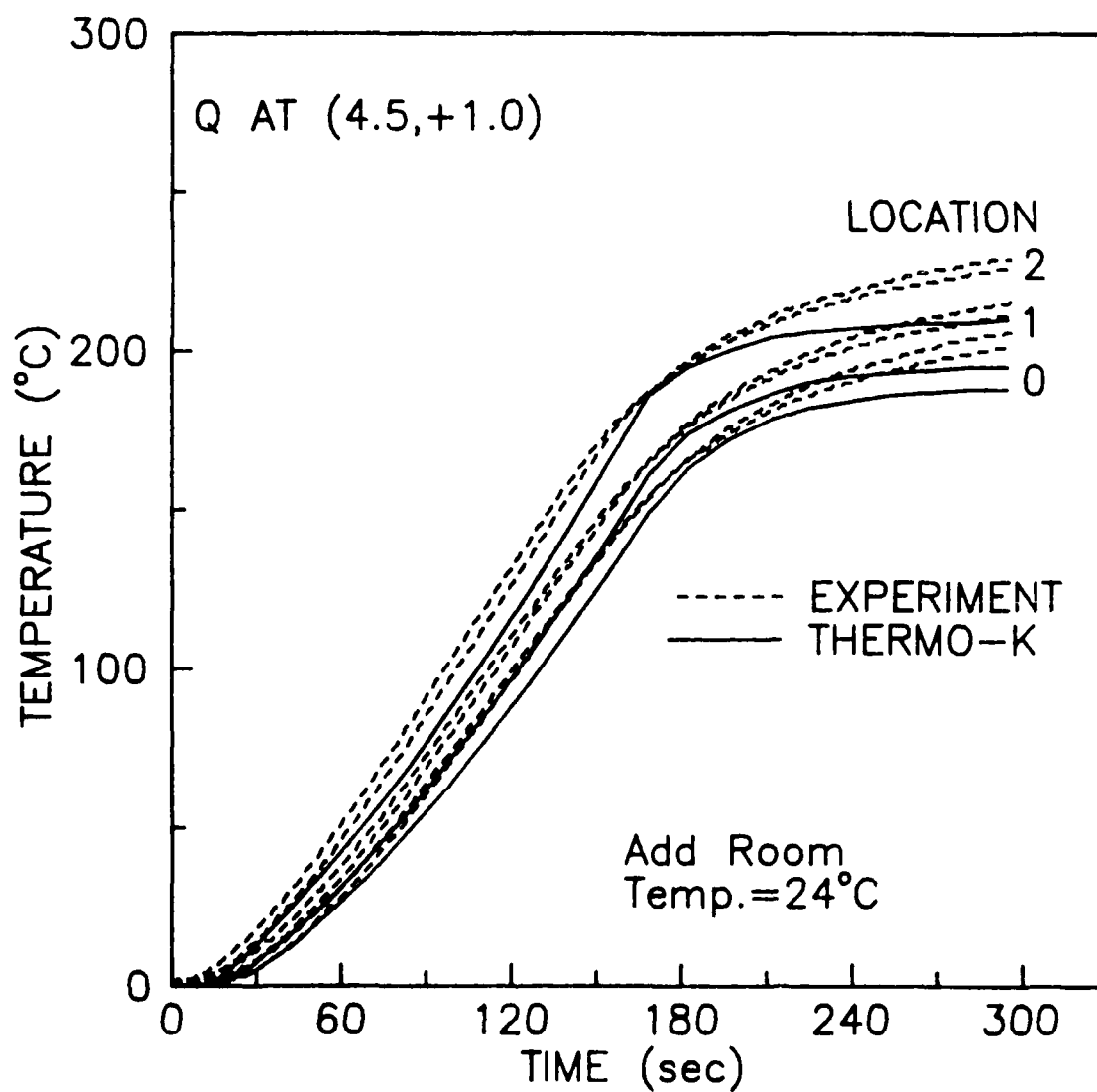


Figure 10-13. Results of Asymmetrical Temperature Verification Tests at Locations 0, 1 and 2

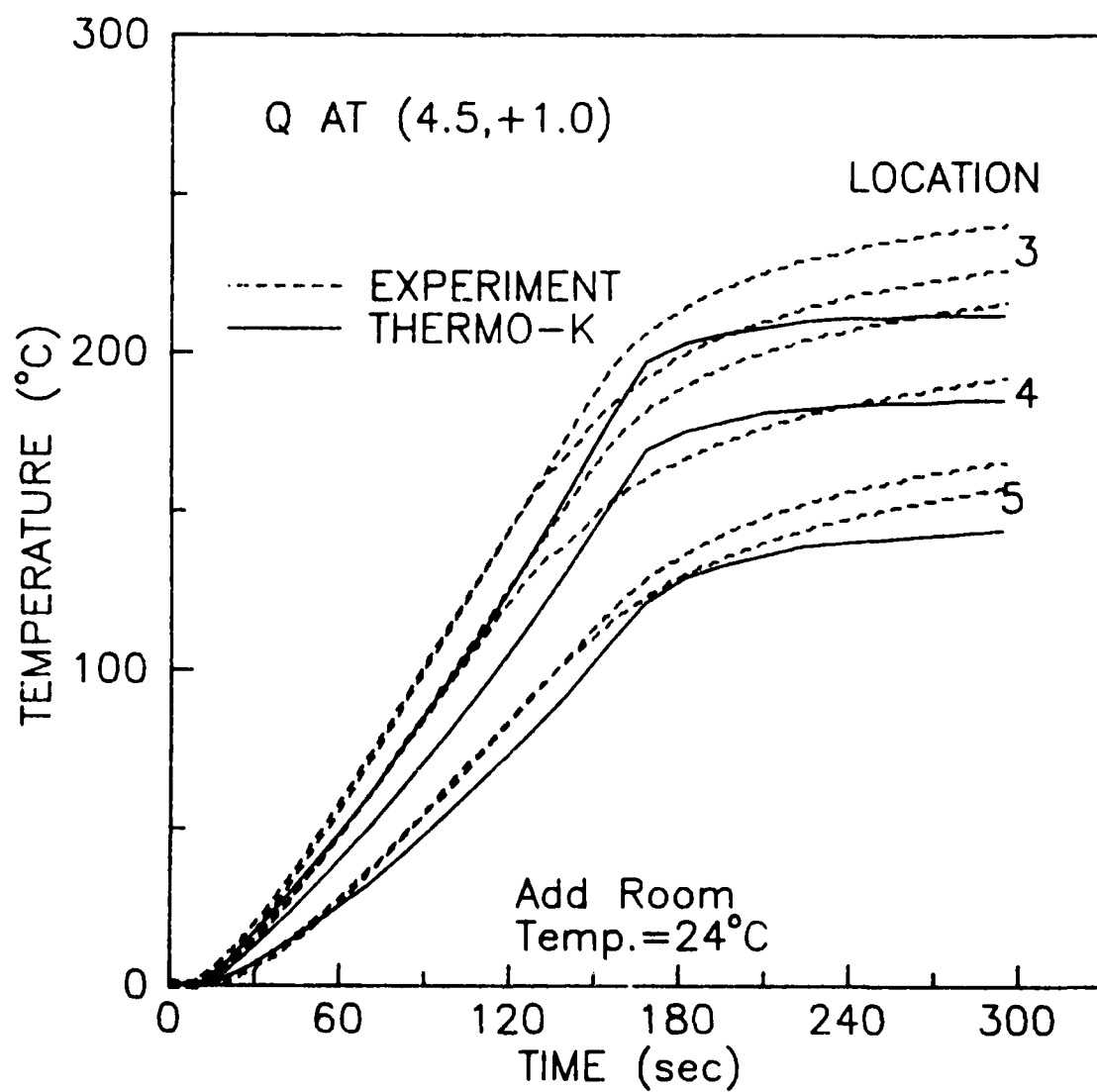


Figure 10-14. Results of Asymmetrical Temperature Verification Tests at Locations 3, 4 and 5

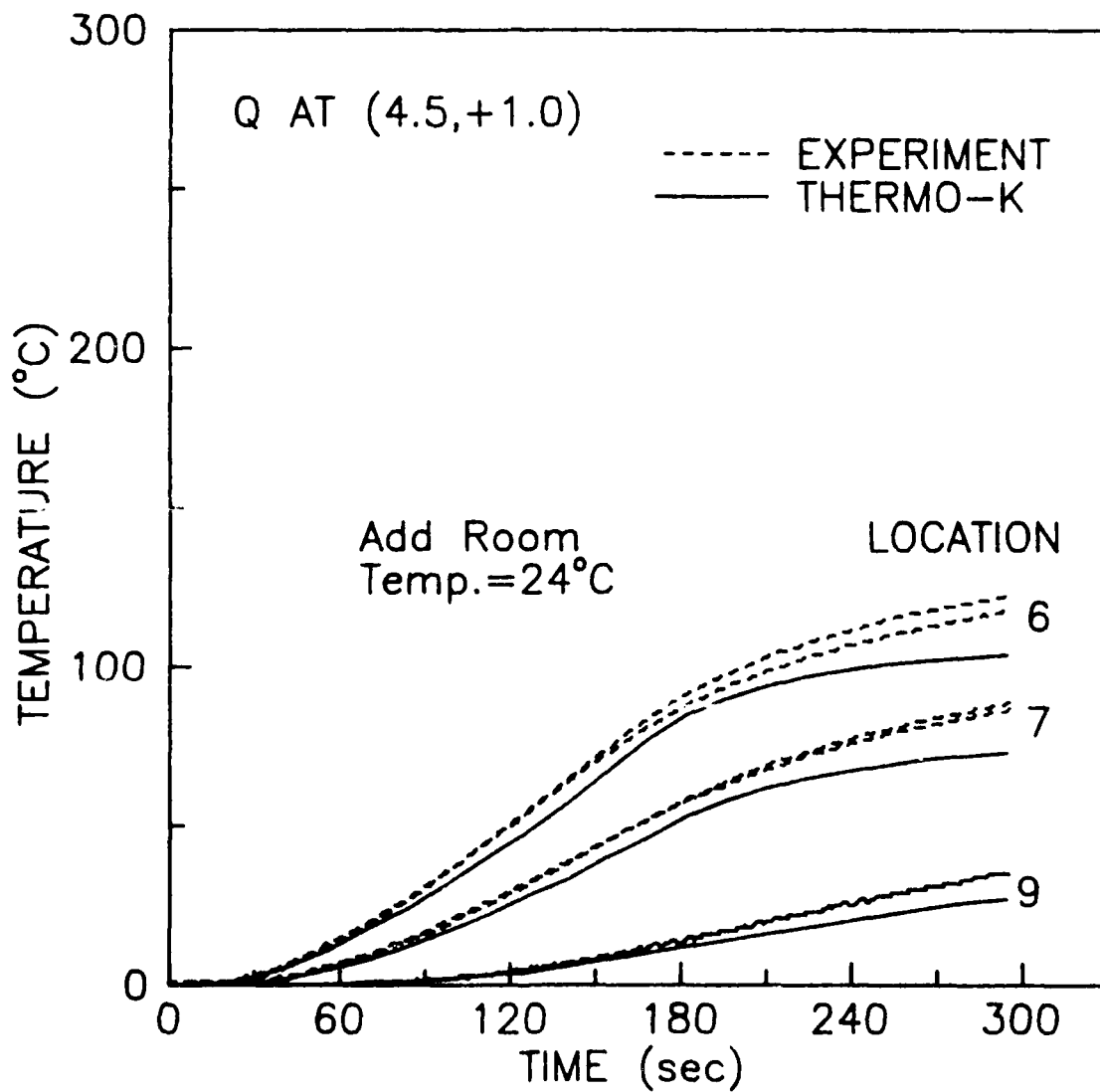


Figure 10-15. Results of Asymmetrical Temperature Verification Tests at Locations 6, 7 and 9

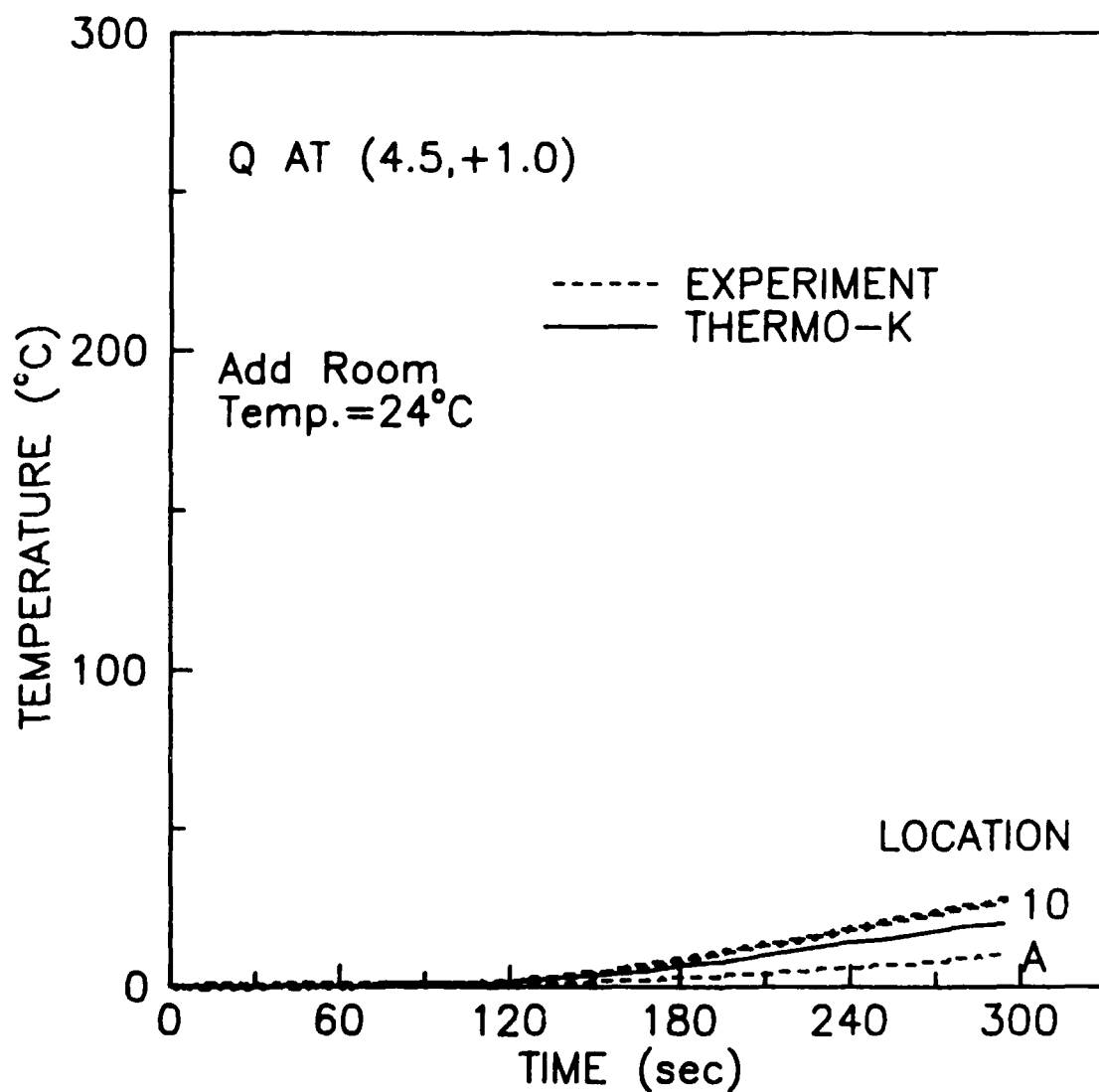
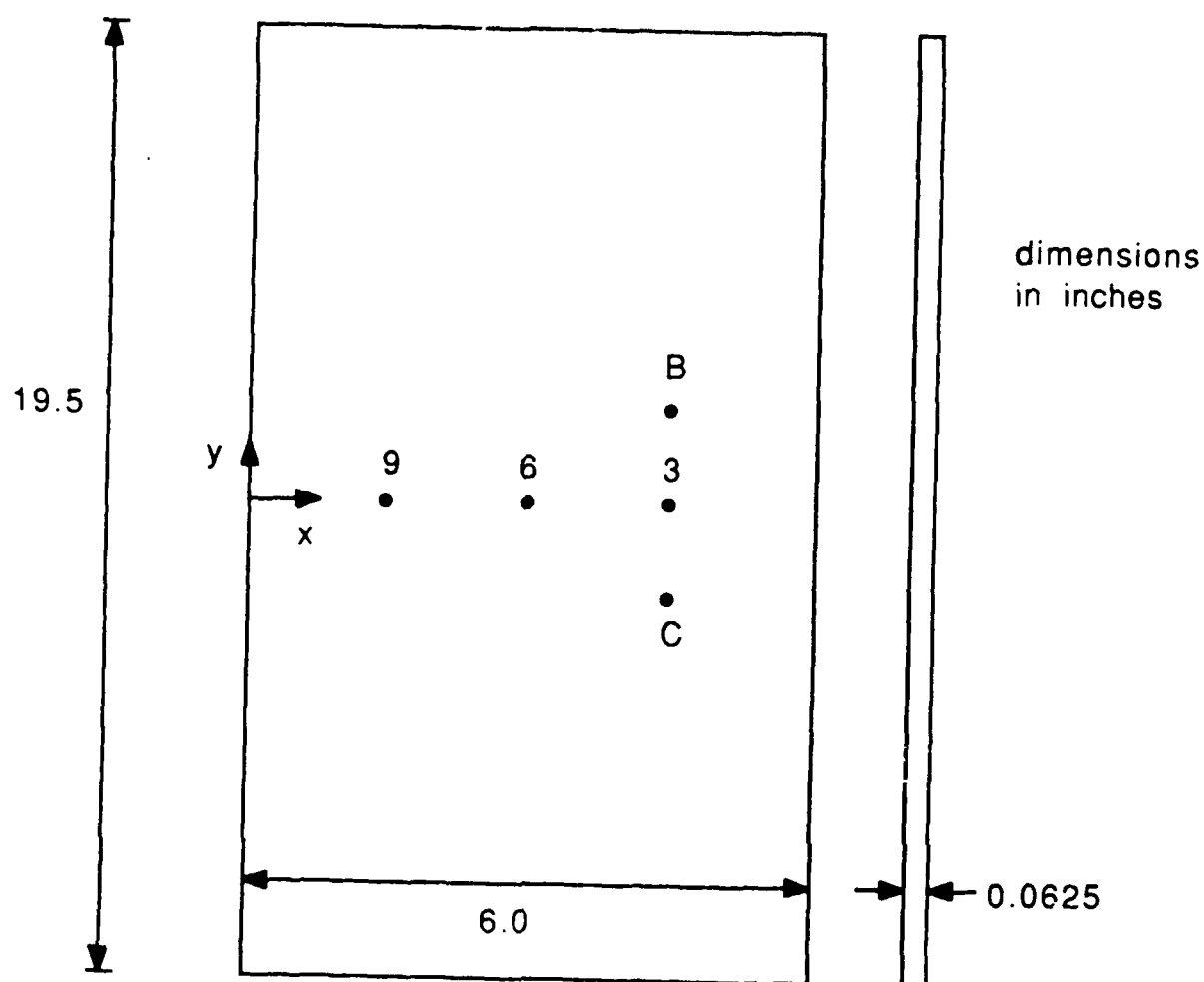


Figure 10-16. Results of Asymmetrical Temperature Verification Tests at Locations 10 and A



Location Number	(x,y) (in)	Remarks
B	(4.5,+1.0)	Thermal Load
C	(4.5,-1.0)	Thermal Load
3	(4.5, 0.0)	Strain Measurement
6	(3.0, 0.0)	Strain Measurement
9	(1.0, 0.0)	Strain Measurement

Figure 10-17. Test Setup for Strain Verification Tests

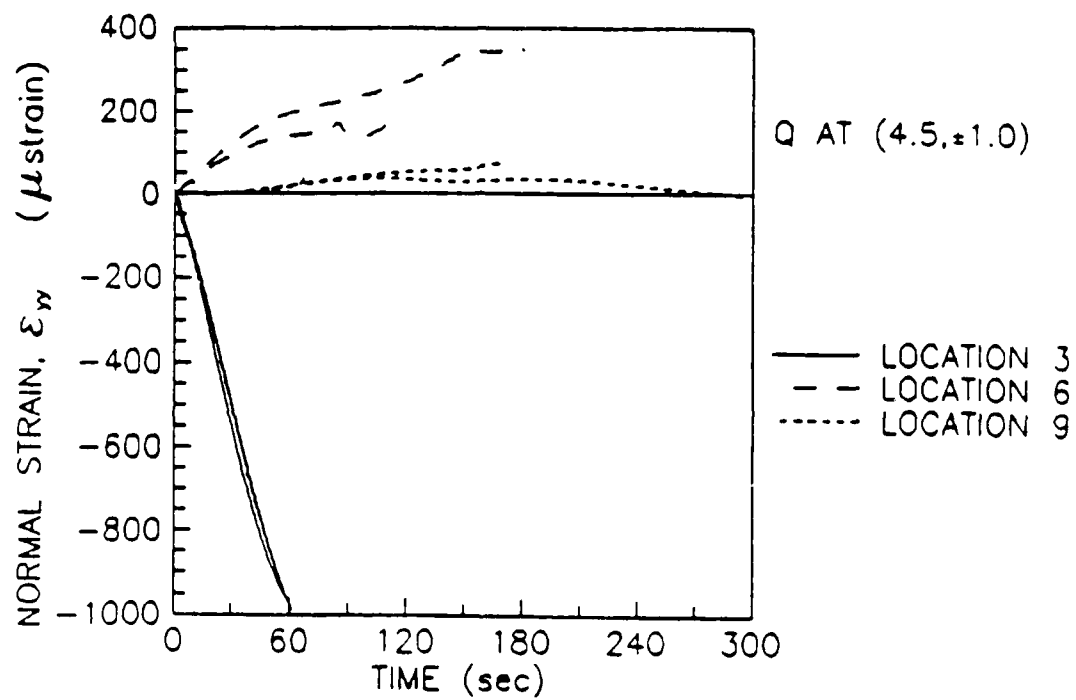


Figure 10-18. Results for Symmetrical Strain Verification
Tests - Strain

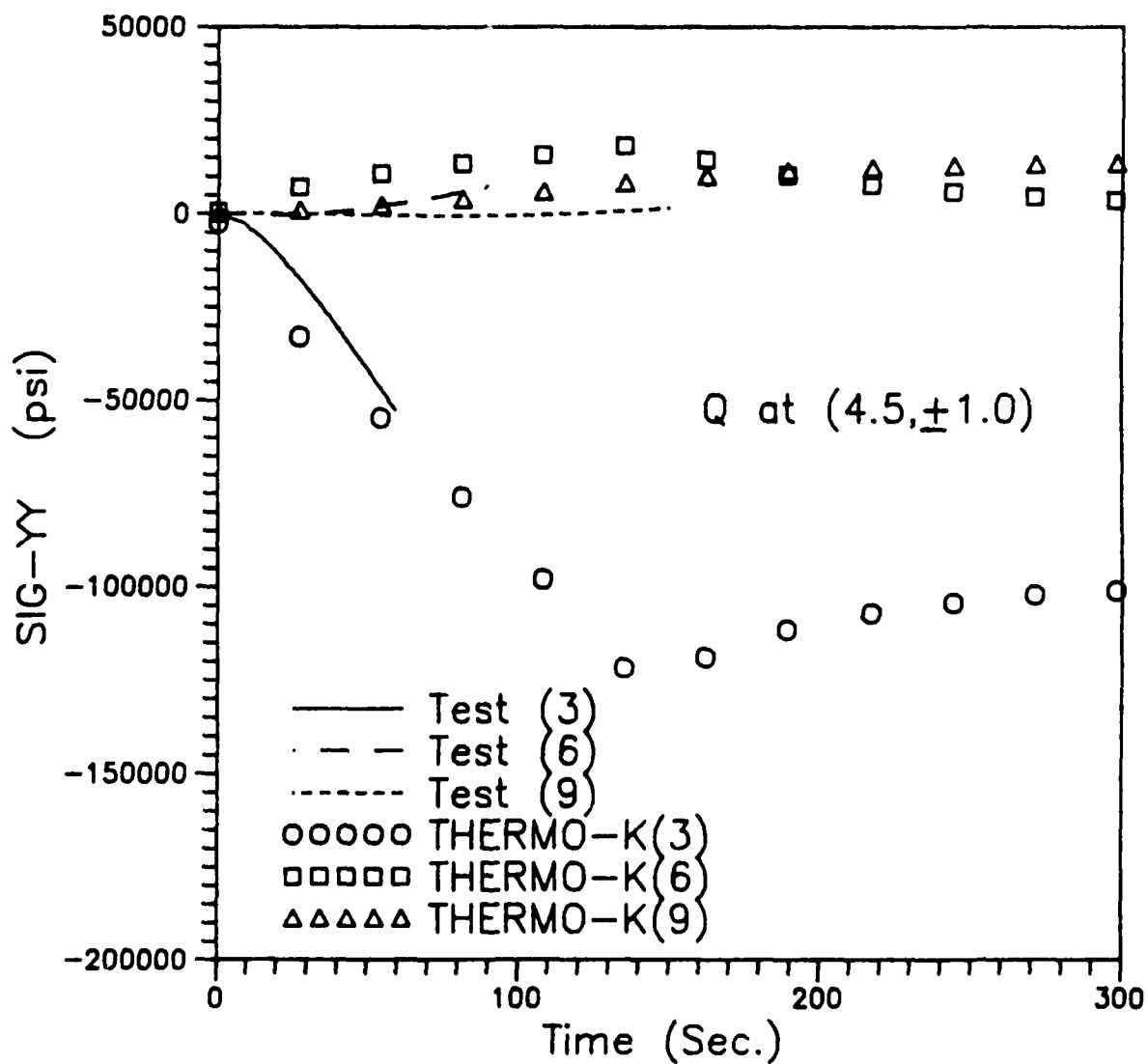


Figure 10-19. Results for Symmetrical Strain Verification Tests - Stress

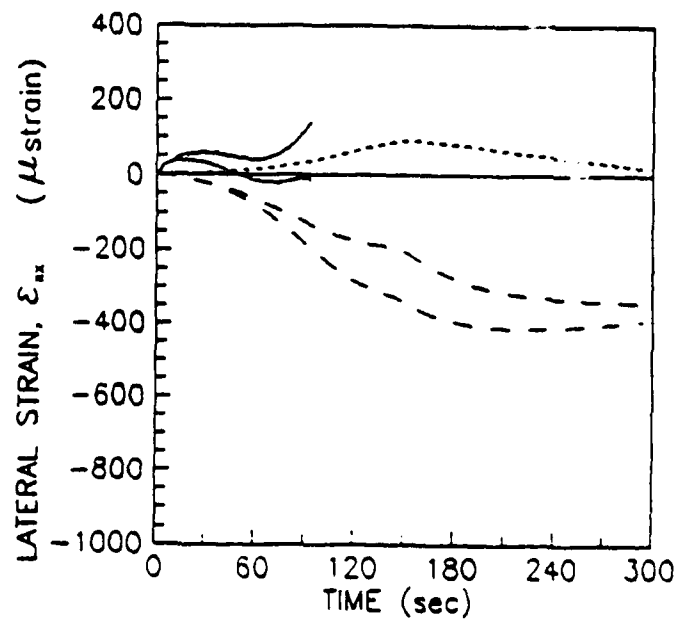
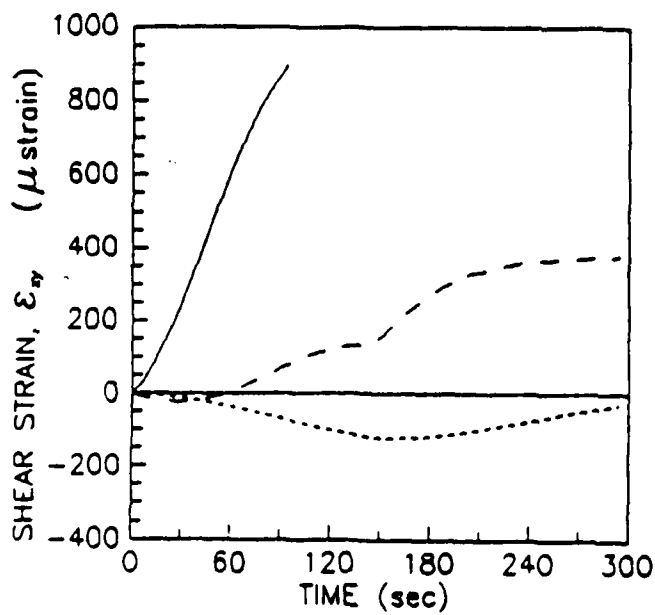
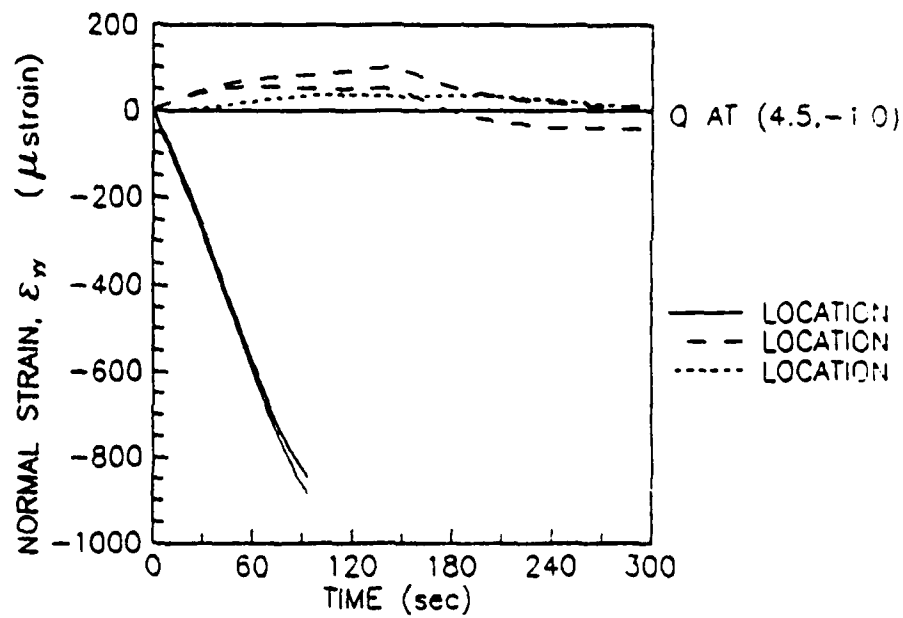


Figure 10-20. Results for Asymmetrical Strain Verification Tests - Strain

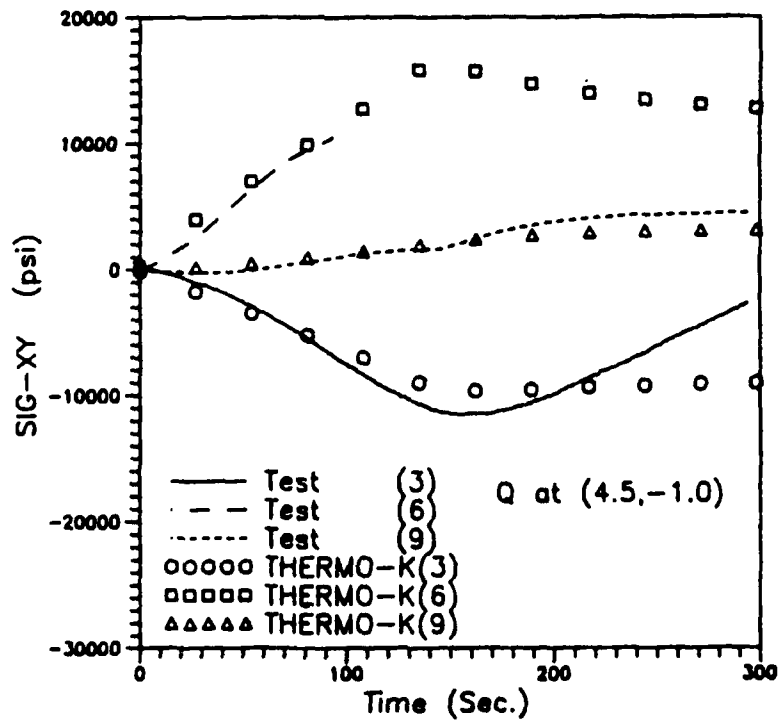
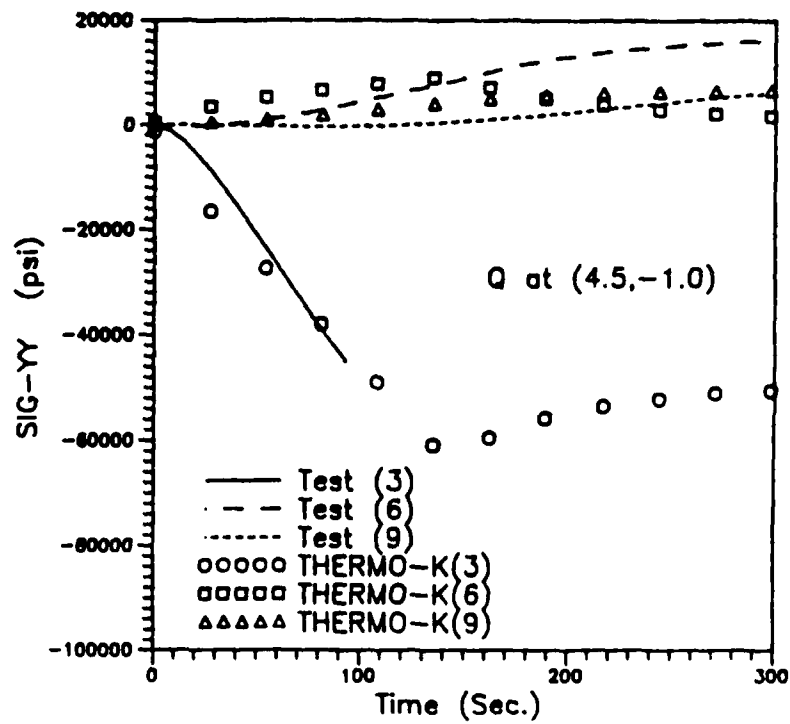
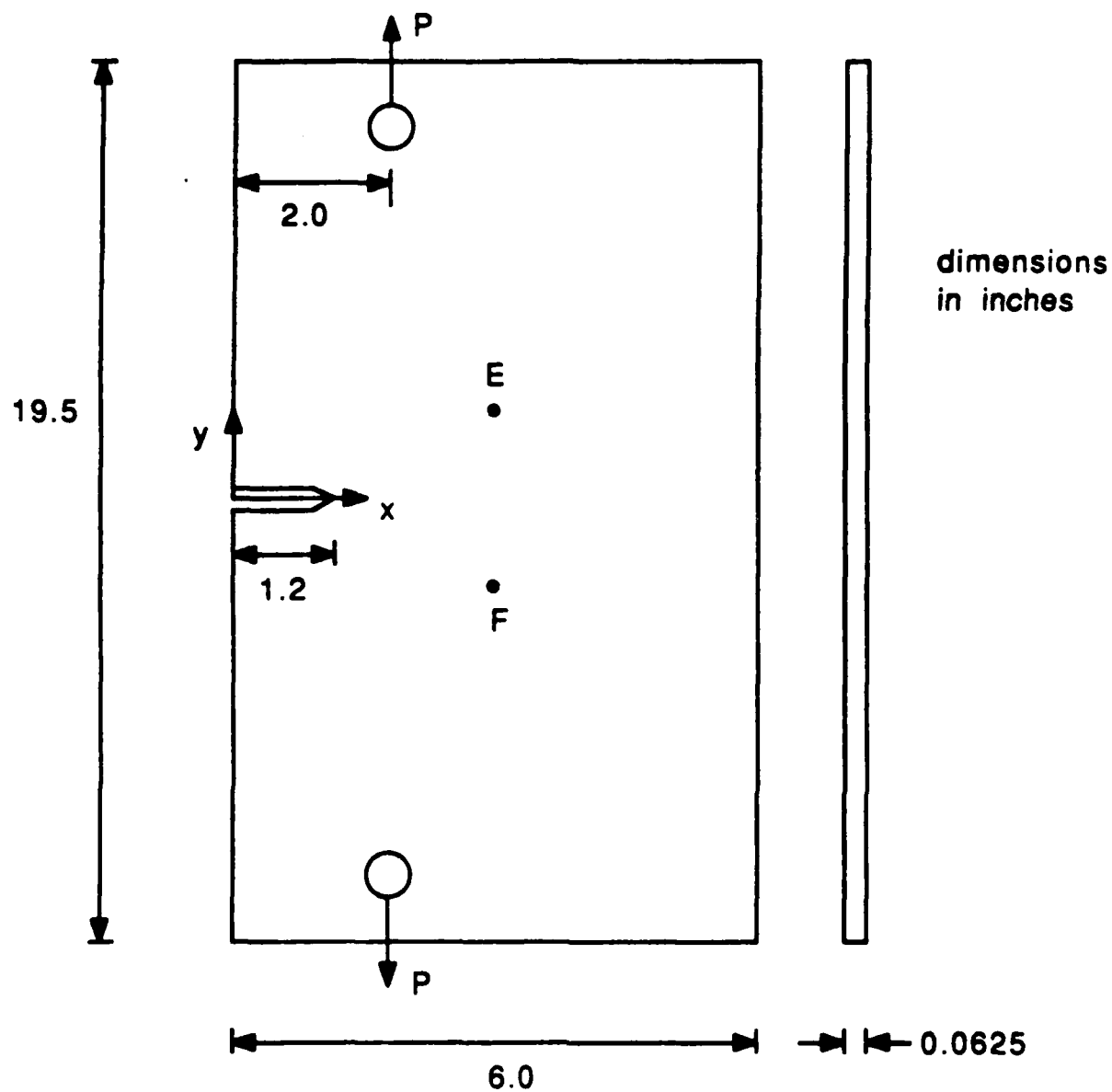


Figure 10-21. Results for Asymmetrical Strain Verification Tests - Stress



Location
Number

(x,y)
(in)

Remarks

E

(3.0,+1.0)

Thermal Load

F

(3.0,-1.0)

Thermal Load

Figure 10-22. Test Setup For Thermal-Mechanical Fracture Tests.

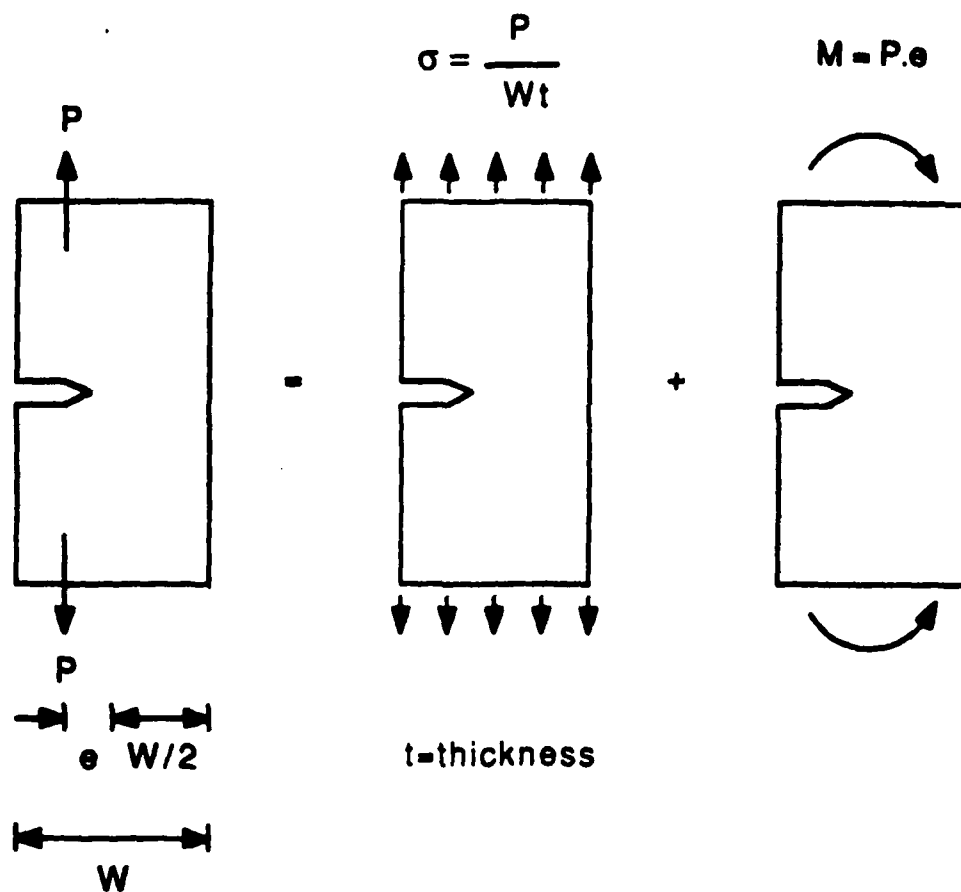


Figure 10-23. Principle of Superposition Used To Calculate The Stress Intensity Factor Due to Eccentric Pin Load.

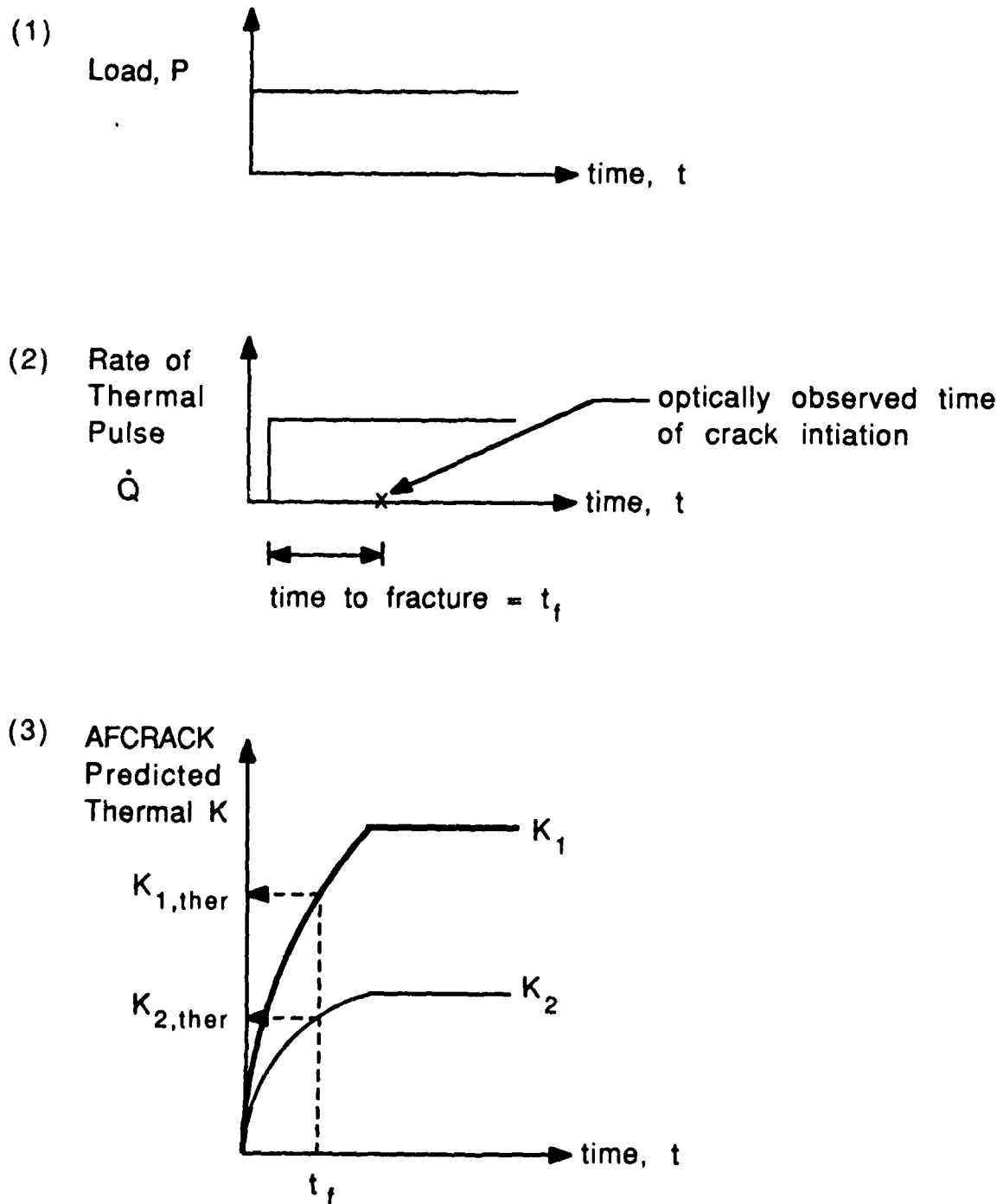


Figure 10-24. Procedure for Conducting Thermal-Mechanical Fracture Tests

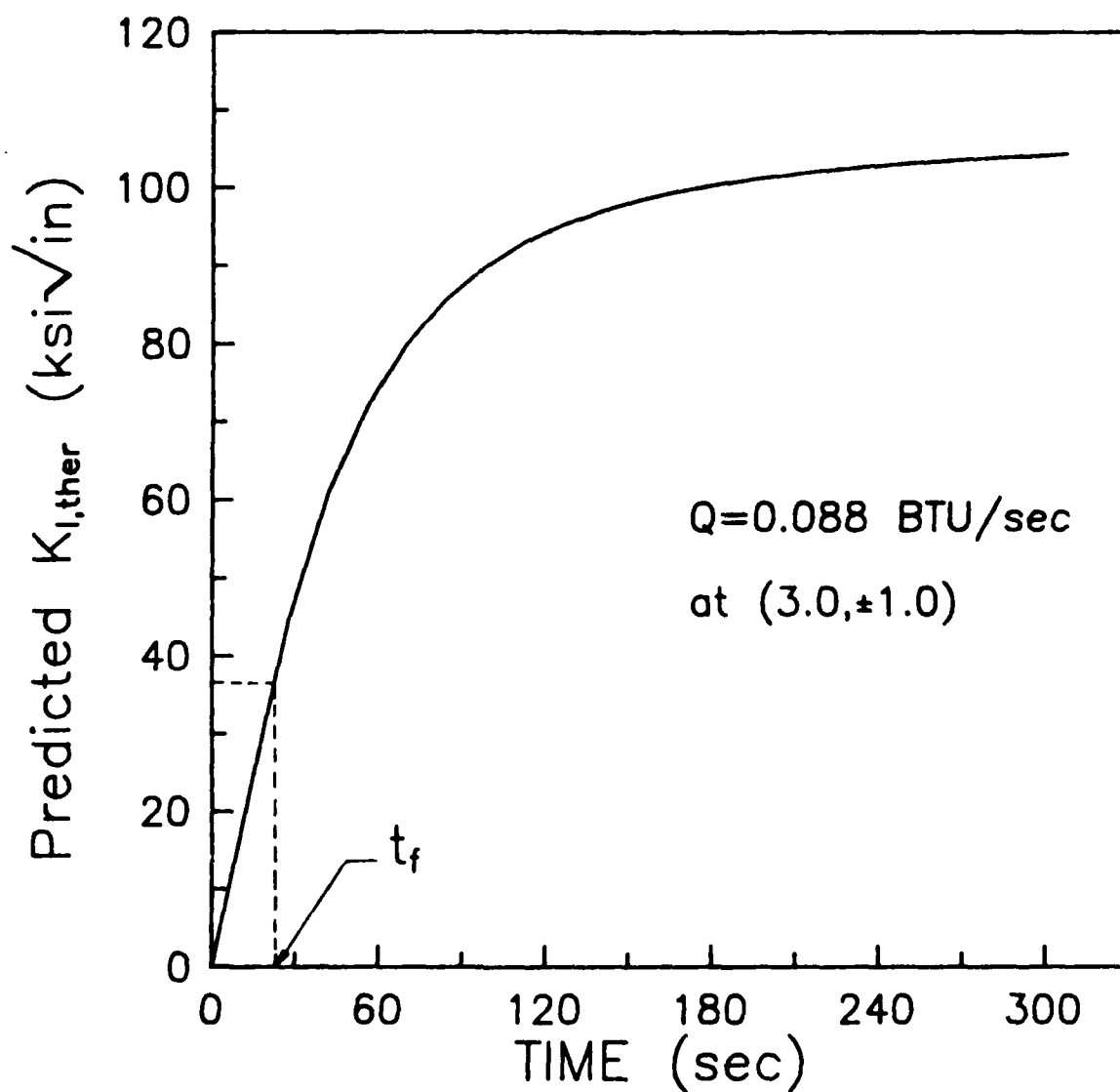


Figure 10-25. $K_{I,ther}$ Predicted Using THERMO-K for Mode I
Thermal-Mechanical Fracture Tests

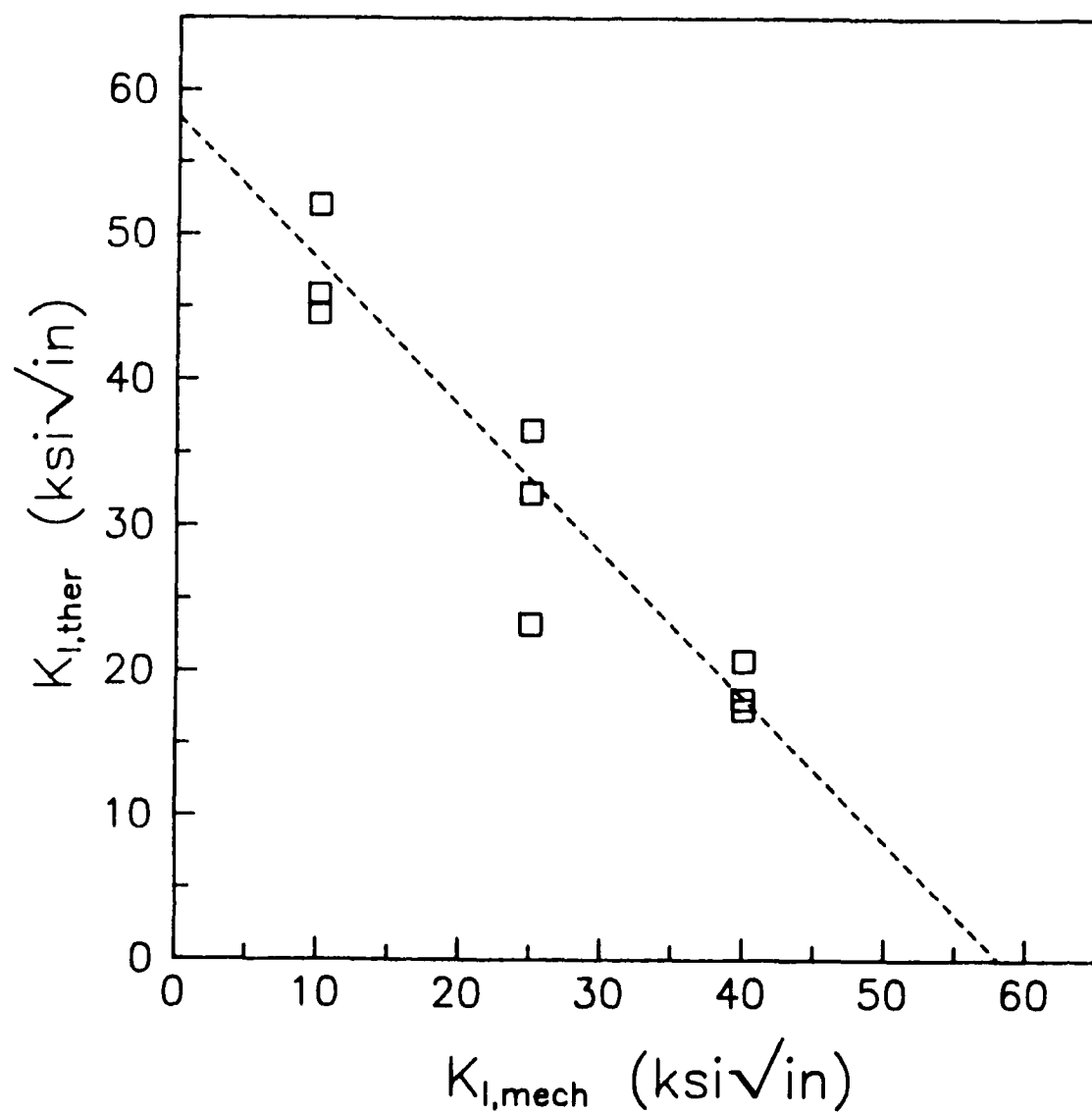


Figure 10-26. $K_{I,ther}$ Required to Fracture the Specimens as a Function of Applied $K_{I,mech}$

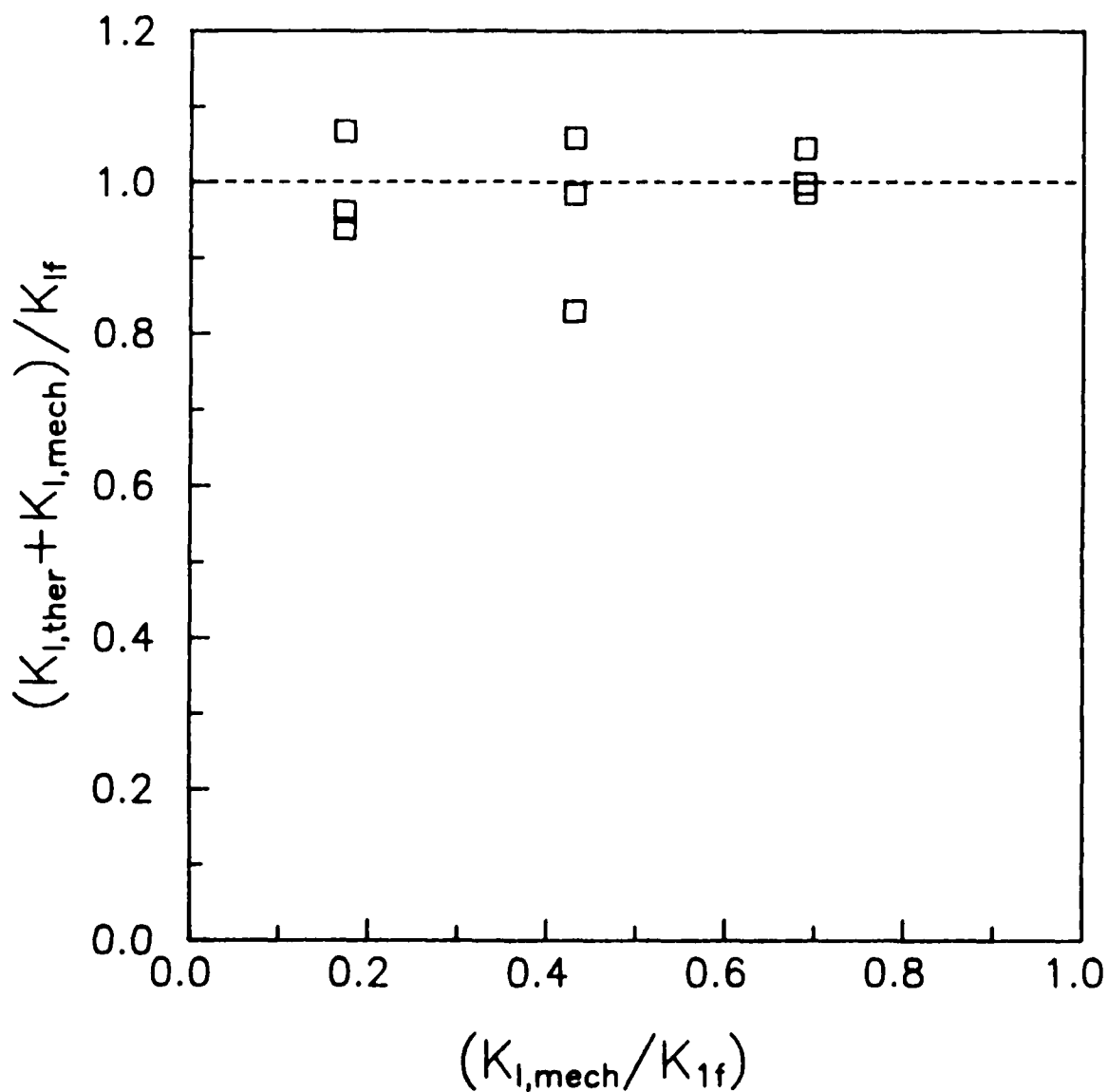


Figure 10-27. Plot Showing Constant $K_{l,total}$ ($=K_{l,ther} + K_{l,mech}$) for Different Levels of $K_{l,mech}$.

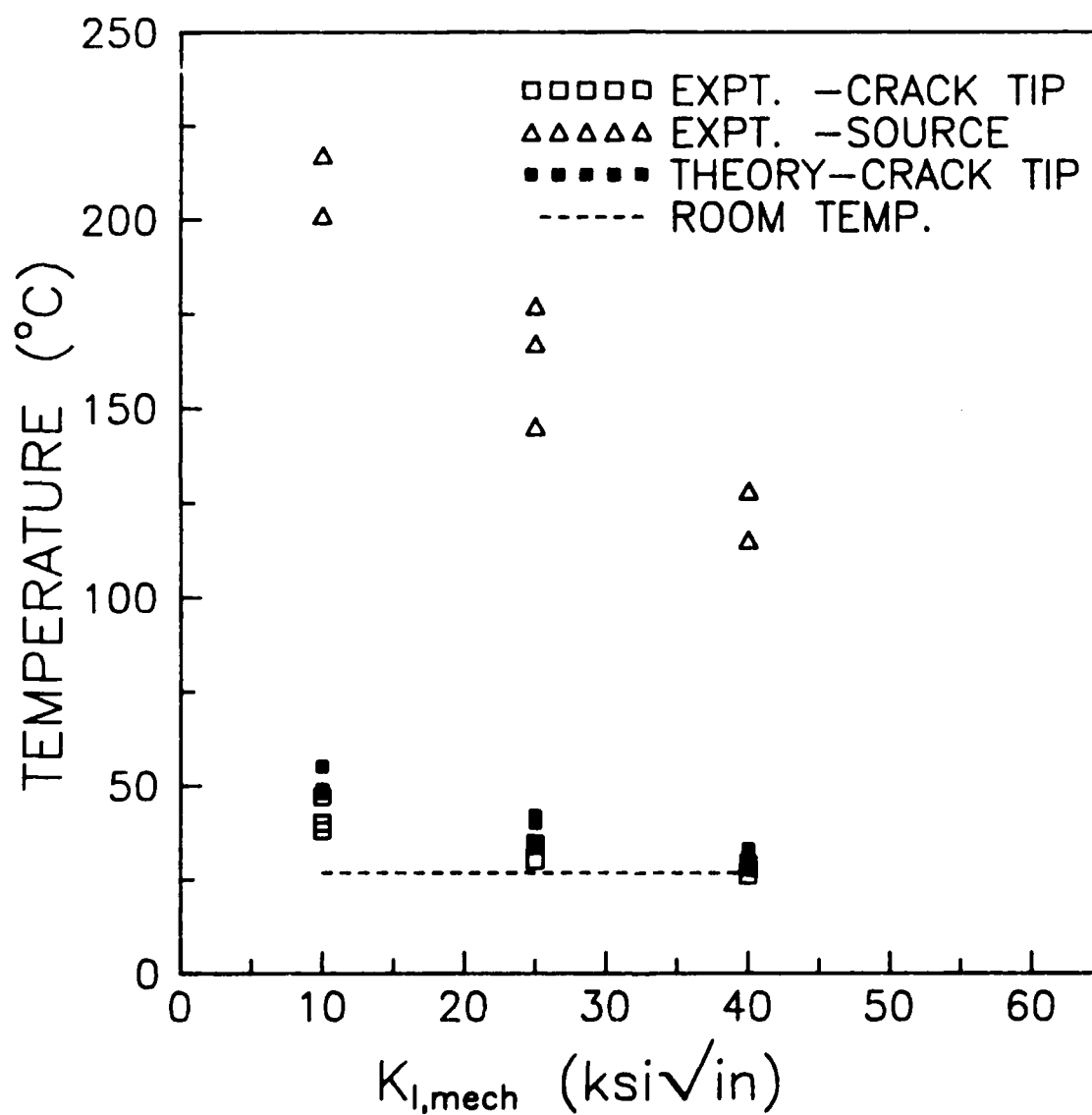


Figure 10-28. Plot of Temperatures Achieved at the Crack Tip and the Source for Various Levels of $K_{I,mech}$

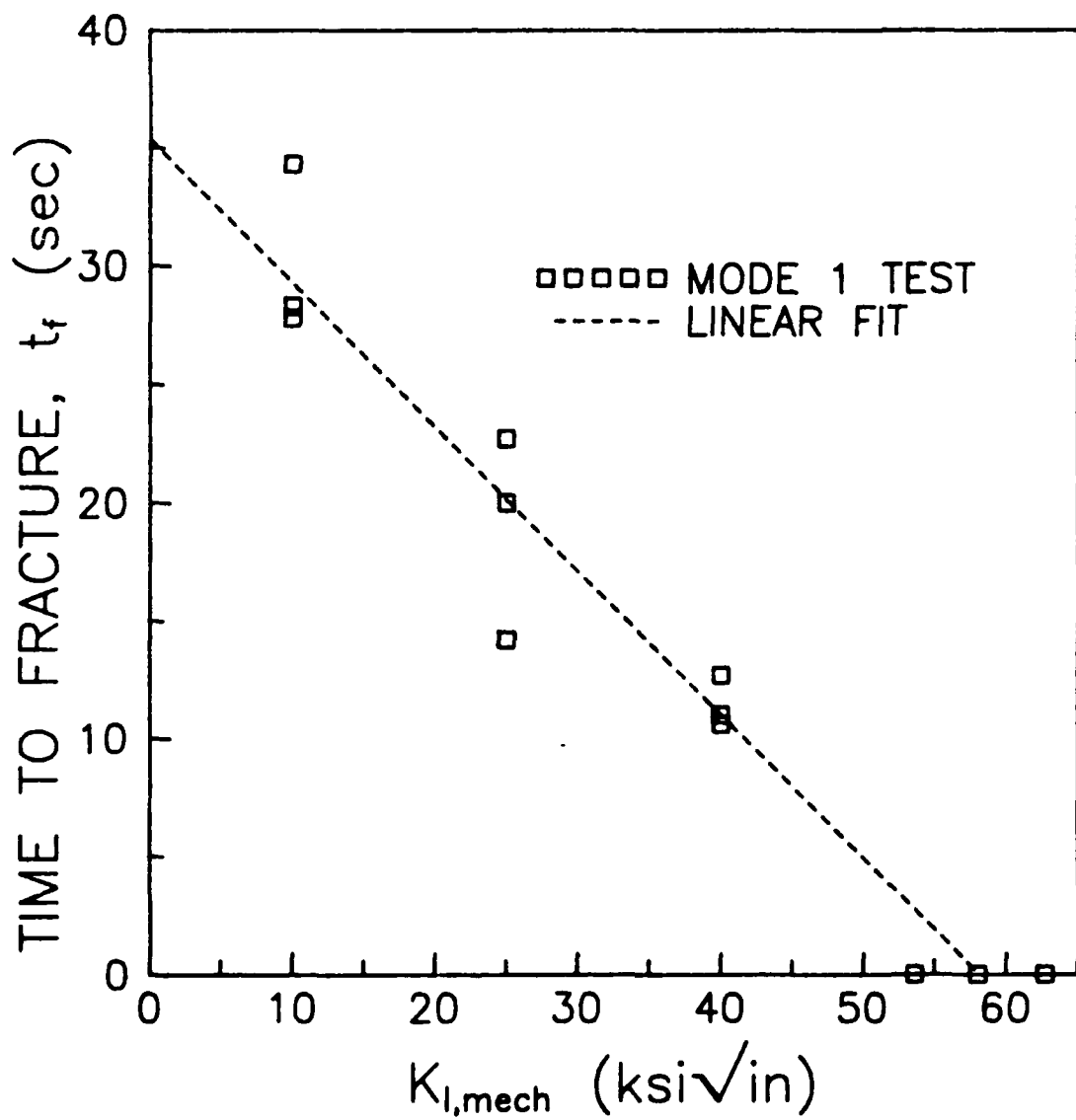


Figure 10-29. Time to Fracture the Specimen by Thermal Loading as a Function of Applied $K_{I,mech}$

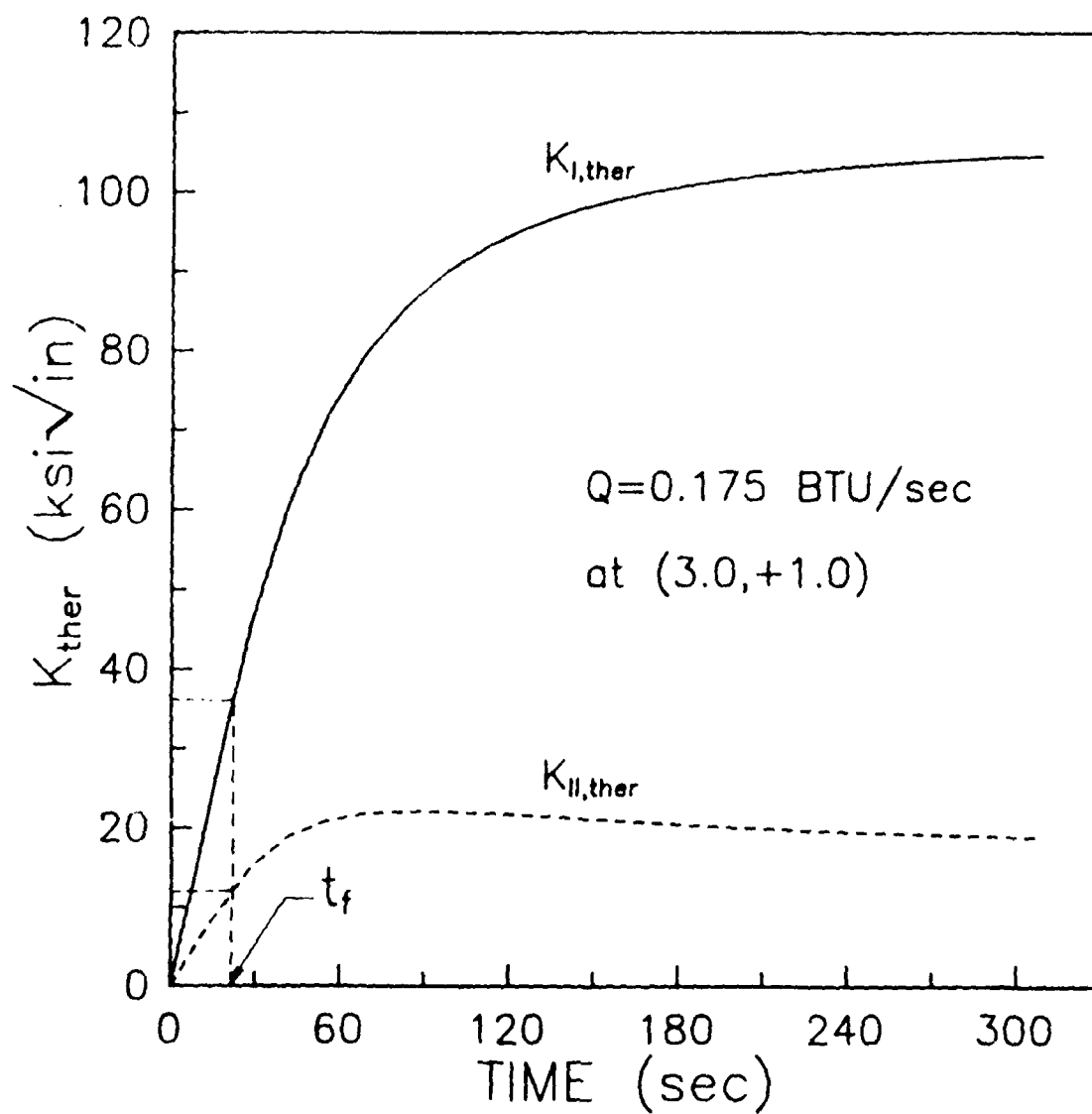


Figure 10-30. $K_{I,ther}$ and $K_{II,ther}$ Predicted Using THERMO-K for Mixed Mode Thermal-Mechanical Fracture Tests

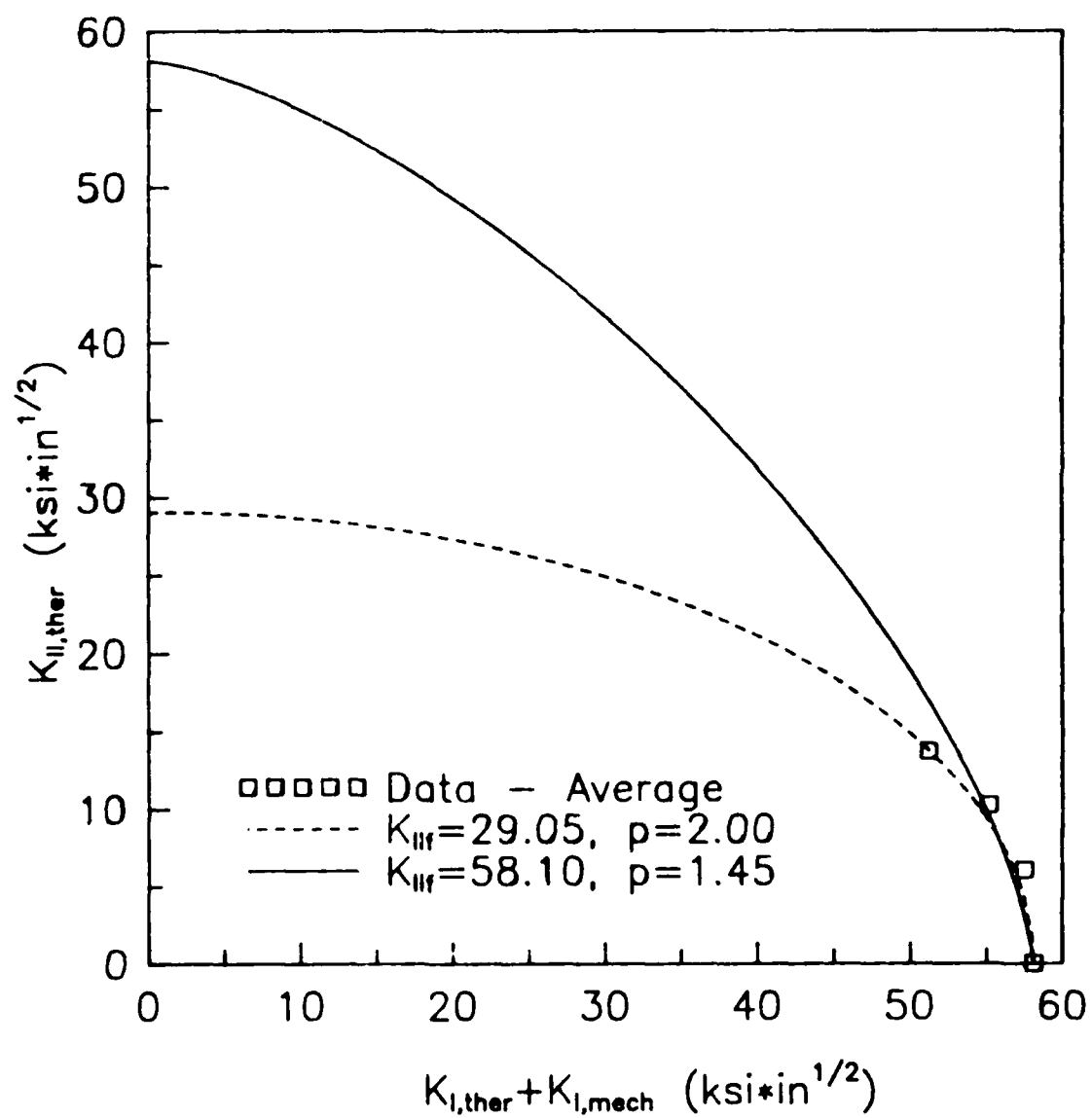


Figure 10-31. Comparison of Mixed Mode Thermal-Mechanical Fracture Data With Some K_1 - K_2 Fracture Envelope Curves

11.0 LINKING OF THERMO-K WITH LIFE PREDICTION CODE MODGRO

To study the effect of thermal stresses on fatigue crack growth, the University of Dayton conducted an analytical investigation involving combined thermal and cyclic mechanical loads. As a first approximation, the structure was assumed to be under steady state thermal conditions, i.e., the cyclic nature of thermal stresses was not considered. Also, only crack Model 4, an edge crack in an infinitely long plate strip, is considered in this section. The implementation procedure should be similar for other crack models. This approach was implemented in the life prediction code MODGRO (Harter, 1988). MODGRO and the accompanying preprocessor MODINP was supplied to the University of Dayton by the Flight Dynamics Laboratory at WPAFB, OH. A code to link THERMO-K and MODGRO effectively was developed for this purpose. Our theoretical approach is described in the next subsection.

11.1 Analytical Procedure

MODGRO uses the conventional cycle-by-cycle fatigue crack growth prediction algorithm. In MODGRO, the crack growth is described by the K_{\max} Walker formulation and the effects of overload are accounted using a Willenborg type retardation model.

The steady-state thermal conditions are assumed in the present analysis. As a result, the principle of superposition was adopted to account for the thermal stress intensity factor in the crack growth analysis. At the beginning of a cycle, the thermal stress-intensity factor (K_{ther}) corresponding to the crack length at the end of the previous cycle was determined using a linear interpolation scheme. Then during the cycle, this value of thermal stress intensity factor was superimposed on the externally applied maximum and minimum stress intensity factors

(K_{\max}^{ω} and K_{\min}^{ω} , respectively) to yield the combined (or total) stress-intensity factor values as:

$$K_{\max} = K_{\max}^{\omega} + K_{\text{ther}} \quad (11-1a)$$

$$K_{\min} = K_{\min}^{\omega} + K_{\text{ther}} \quad (11-1b)$$

The effects of overload were then obtained directly in terms of a resulting effective stress-intensity factor, where for a Willenborg-type model, one would obtain

$$K_{\max}^{\text{eff}} = K_{\max} - K_{\text{red}} \quad (11-2a)$$

$$K_{\min}^{\text{eff}} = K_{\min} - K_{\text{red}} \quad (11-2b)$$

and

$$R_{\text{eff}} = K_{\min}^{\text{eff}} / K_{\max}^{\text{eff}} \quad (11-3)$$

where

K_{\max}^{eff} and K_{\min}^{eff} = resulting maximum and minimum effective stress-intensity factors, respectively,

K_{red} = stress-intensity factor associated with load interaction, and

R_{eff} = effective stress ratio.

These effective stress-intensity factors were then directly used in the K_{\max} Walker crack growth description:

$$da/dN = f (K_{\max}^{\text{eff}}, R_{\text{eff}}) \quad (11-4)$$

for life calculations.

The approach described by Equation (10-1) was incorporated in the life prediction code MODGRO as discussed in the next section.

11.2 Code Implementation

For fatigue crack growth analysis, the thermal stress intensity factor versus crack length relationship is required. THERMO-K does not predict this relationship explicitly, but it yields the stress distribution in the uncracked structure at any given time. As discussed in Section 2, this stress distribution was converted into the corresponding K_{ther} versus crack length data using the influence function method. For this purpose, the University of Dayton developed an interactive code KVSAMG based on Equation (5-6).

The thermal stress distribution calculated by THERMO-K is available in the file PSTRESS.PRN. The interactive code KVSAMG uses this file and the geometry input file for THERMO-K to generate the thermal stress-intensity factor versus crack length data. KVSAMG should be located in the same directory as THERMO-K. Since Equations (5-6) and (5-8) to (5-11) are valid only up to crack length to width ratio (a/W) equal to 0.50, the code sets K_{ther} equal to 0.0 for crack lengths greater than $0.50*W$. The current version of KVSAMG is valid only for a single edge through crack geometry. KVSAMG allows the user to define the output filename, which is used to input the thermal stress intensity factor data into MODGRO.

The flowchart for linking THERMO-K with MODGRO is shown in Figure 11-1. The life prediction code MODGRO and the preprocessor MODINP were modified by the University of Dayton to include the effect of thermal stresses. The modified versions of MODGRO and MODINP are named MODGROT and MODINPT, respectively. The preprocessor MODINPT allows the user to include the K_{ther} versus crack length data (generated by KVSAMG) in the input file for MODGROT. In addition the user is allowed to multiply the crack

length and K_{ther} by constants to account for dimensional compatibility between MODGRO and THERMO-K. K_{ther} is added immediately after K_{max}^w and K_{min}^w are calculated. This corresponds to the beginning of the section, "Retardation in the Length Direction" in MODGROT. The input section of MODGROT was also modified for reading the file K_{ther} versus crack length data generated by KVSAMG. A linear interpolation scheme was included in MODGROT for determining K_{ther} corresponding to various crack lengths during the fatigue crack growth analysis.

11.3 Sample Analysis

A thermoelastic analysis was conducted on the long plate shown in Figure 11-2. This plate was subjected to two cases of localized spot heating; both cases utilized a constant heat input of 0.1 BTU/sec (=105.5 Watts). The first case corresponded to heat sources located at $(x,y) = (4.5, \pm 1.0)$ and for the second case the heat sources were located at $(x,y) = (3.0, \pm 1.0)$. The material chosen for the analysis was the spring steel having the thermophysical properties listed in Table 11-1. The analysis for crack growth effects was conducted in two stages.

The first stage involves the determination of the steady-state thermal stress-intensity factor for the two cases of thermal loading. The steady state THERMO-K predicted stress distributions are shown in Figure 11-3. It can be seen that the stress distribution depends significantly on the location of the heat sources. Using the code KVSAMG, the corresponding K_{ther} versus crack length relationship for a single cracked plate was calculated as shown in Figure 11-4. When the heat source is located in the center of the plate (i.e., $x=W/2$, first case), K_{ther} higher than K_{Ic} is generated. K_{ther} increases initially with increasing crack length and then decreases rapidly becoming negative as the crack approaches the compressive zone close to the heat source. For the second case, K_{ther} was negative for

small crack lengths. This is due to the compressive stresses occurring close to free edge as seen in Figure 11-3.

The second stage involved the crack growth analyses. The tabular data from the MODGRO library for 4340 steel was used to define the $da/dN-\Delta K$ relationship for the present material. The parameters used for fatigue crack analysis are reported in Table 11-1. The fatigue crack growth analysis was done for constant amplitude loading with σ_{max} varying from 15 to 40 ksi and σ_{min} equal to 0.0. The results of the analyses presented in Table 11.2. From this table, it can be seen that the steady state thermal stresses can significantly reduce the fatigue life (10 to 100 times). This effect is also sensitive to the location of the heat sources.

11.4 Summary

The fatigue life of a structure is significantly altered due to the presence of thermal stresses. The magnitude of the life change depends on the magnitude of the thermal pulses as well as the location of the thermal pulses, size of the initial flaw, geometry of the flawed structure, thermophysical properties of the material, and magnitude of the externally applied fatigue loads.

11.5 References

Harter, J.A., MODGRO - User's Manual, Version 1.1, AFWAL-TM-88-157-FIBE, Flight Dynamics Laboratory, Wright Patterson Air Force Base, OH, January, 1988.

Table 11-1

PARAMETERS USED FOR FATIGUE CRACK GROWTH ANALYSIS

Material: Steel 4340-180 KSI FORGING (IN-KSI)

Tabular da/dN-ΔK data:

da/dN	ΔK	Walker "m"
(in./cycle)	(ksi/√in)	
1.0E-09	4.837	0.335
2.0E-09	4.934	0.335
1.0E-08	5.038	0.337
2.0E-08	5.550	0.338
4.0E-08	6.300	0.338
6.0E-08	6.750	0.338
1.0E-07	7.676	0.410
2.0E-07	9.157	0.610
4.0E-07	11.200	0.612
6.0E-07	12.475	0.700
8.0E-07	13.760	0.750
1.0E-06	15.368	0.770
2.0E-06	20.525	0.754
4.0E-06	27.917	0.683
1.0E-05	40.405	0.664
2.0E-05	52.395	0.556
4.0E-05	64.036	0.539
1.0E-04	82.767	0.460
2.0E-04	94.958	0.450
4.0E-04	99.608	0.440
6.0E-04	101.845	0.439
8.0E-04	102.971	0.433
1.0E-03	103.919	0.424
4.0E-03	104.025	0.424
1.0E-02	104.143	0.423

R-LOW = -0.3 R-HIGH = 0.8

 $K_{Ic} = 65.0 \text{ ksi}/\sqrt{\text{in}}$ $\sigma_y = 150.0 \text{ ksi}$

Geometry Code : 2040 - Single Edge Through Crack

Width, W : 6.00 in. Thickness, t : 0.0625 in.
 Initial Crack, a_i : 0.88 in.

Table 11-2

RESULTS OF CRACK GROWTH ANALYSES WITH
AND WITHOUT THERMAL STRESSES

$$\sigma_{\min} = 0.0$$

σ_{\max} (ksi)	Final Crack Length (in)	Number of Cycles to Failure		
		Mech.* only	Mech.+Therm.1 [@]	Mech.+Therm.2 [#]
40	1.19	1469	1043	31
30	1.62	8170	6037	74
20	2.26	39605	28594	1997
15	2.69	94882	67516	7786

Note:

* Mech. -> Remote Mechanical Loading

@ Therm.1 -> Thermal Loading, Q at (4.5,1.0) and (4.5,-1.0)

Therm.2 -> Thermal Loading, Q at (3.0,1.0) and (3.0,-1.0)

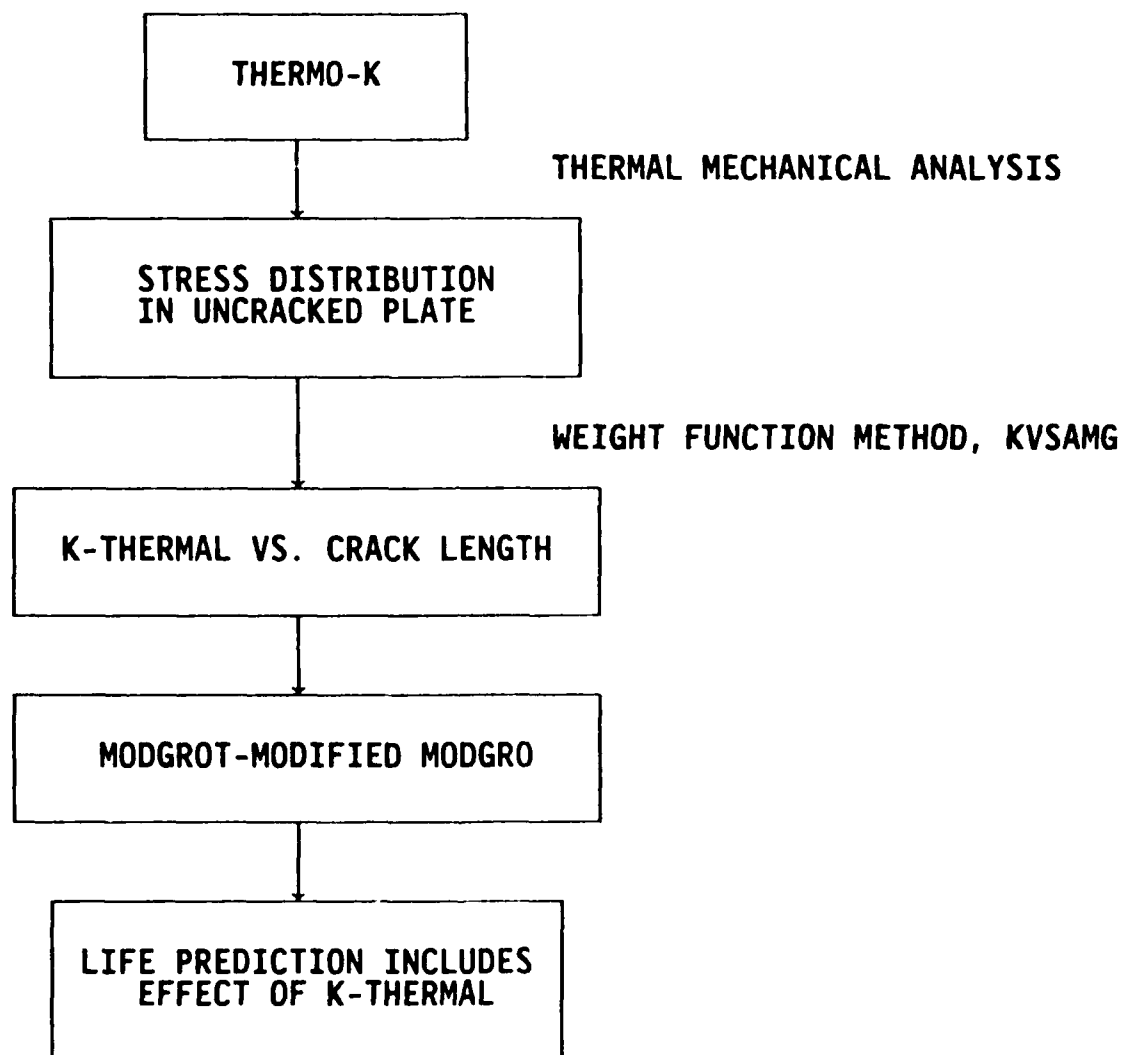
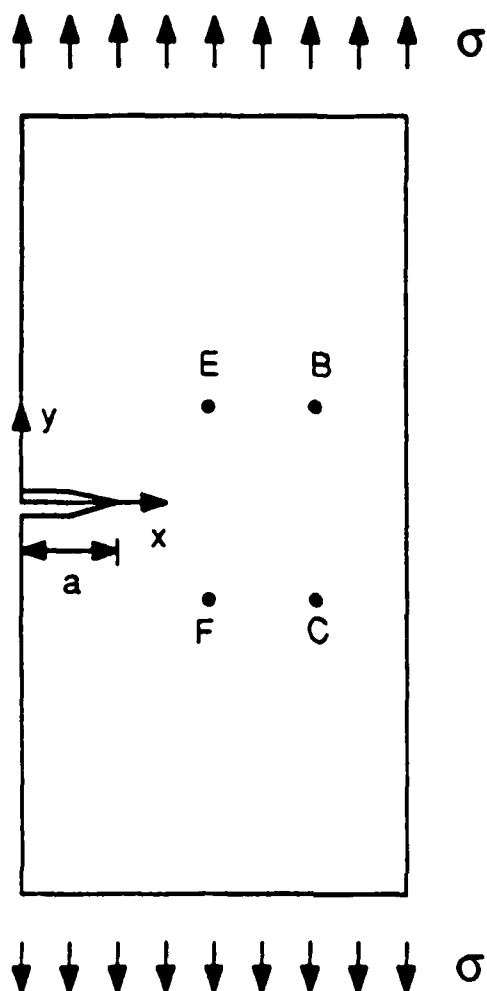


Figure 11-1. Flowchart for Linking THERMO-K and MODGRO



LOCATION OF HEAT SOURCES

Case No.	Location	
	No.	(x,y)
Therm. 1	B	(4.5,+1.0)
	C	(4.5,-1.0)
Therm. 2	E	(3.0,+1.0)
	F	(3.0,-1.0)

Figure 11-2. Mechanical and Thermal Loading Configurations
Used for Crack Growth Analysis

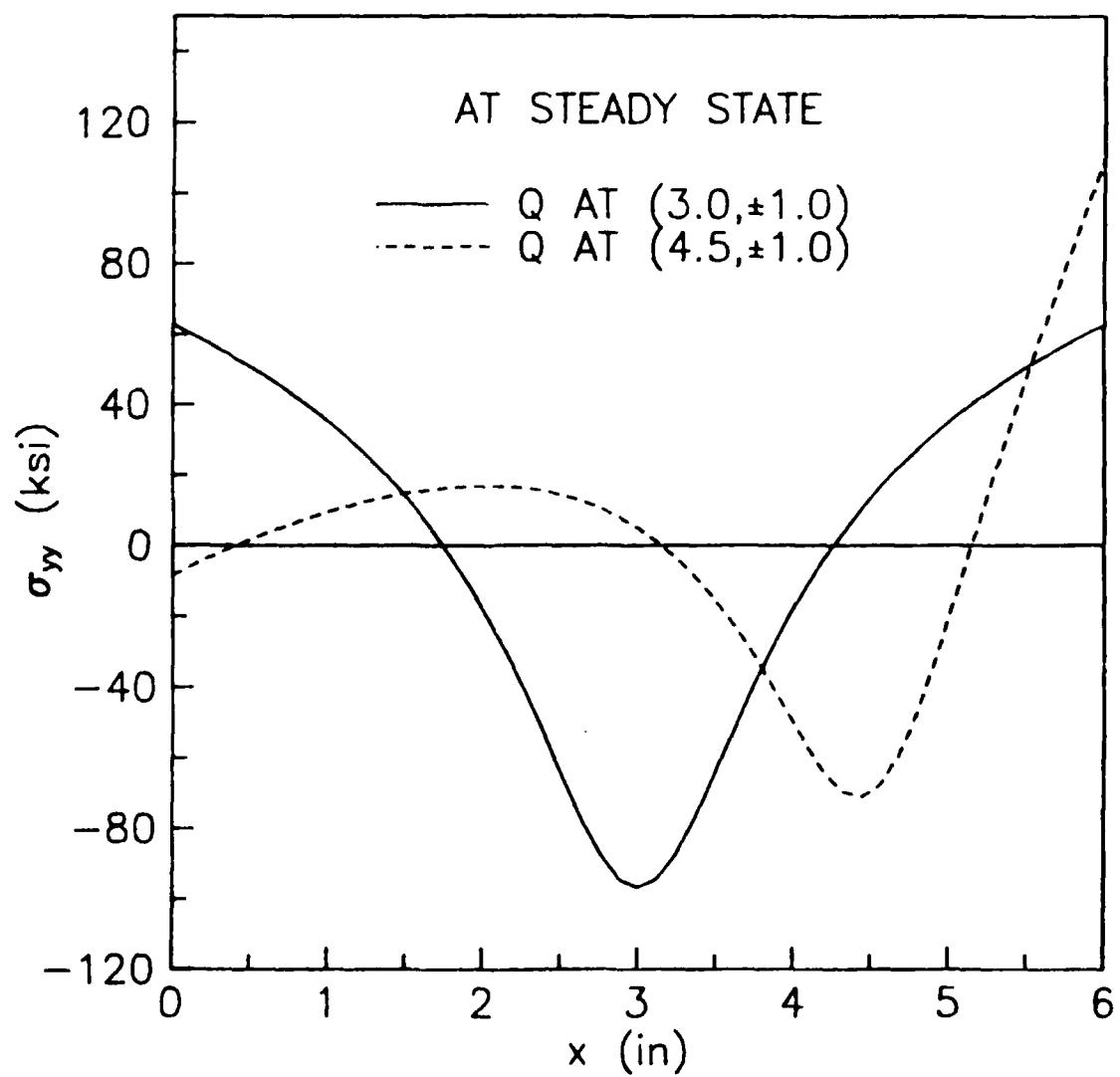


Figure 11-3. Stress Distribution in the Uncracked Plate at Steady State

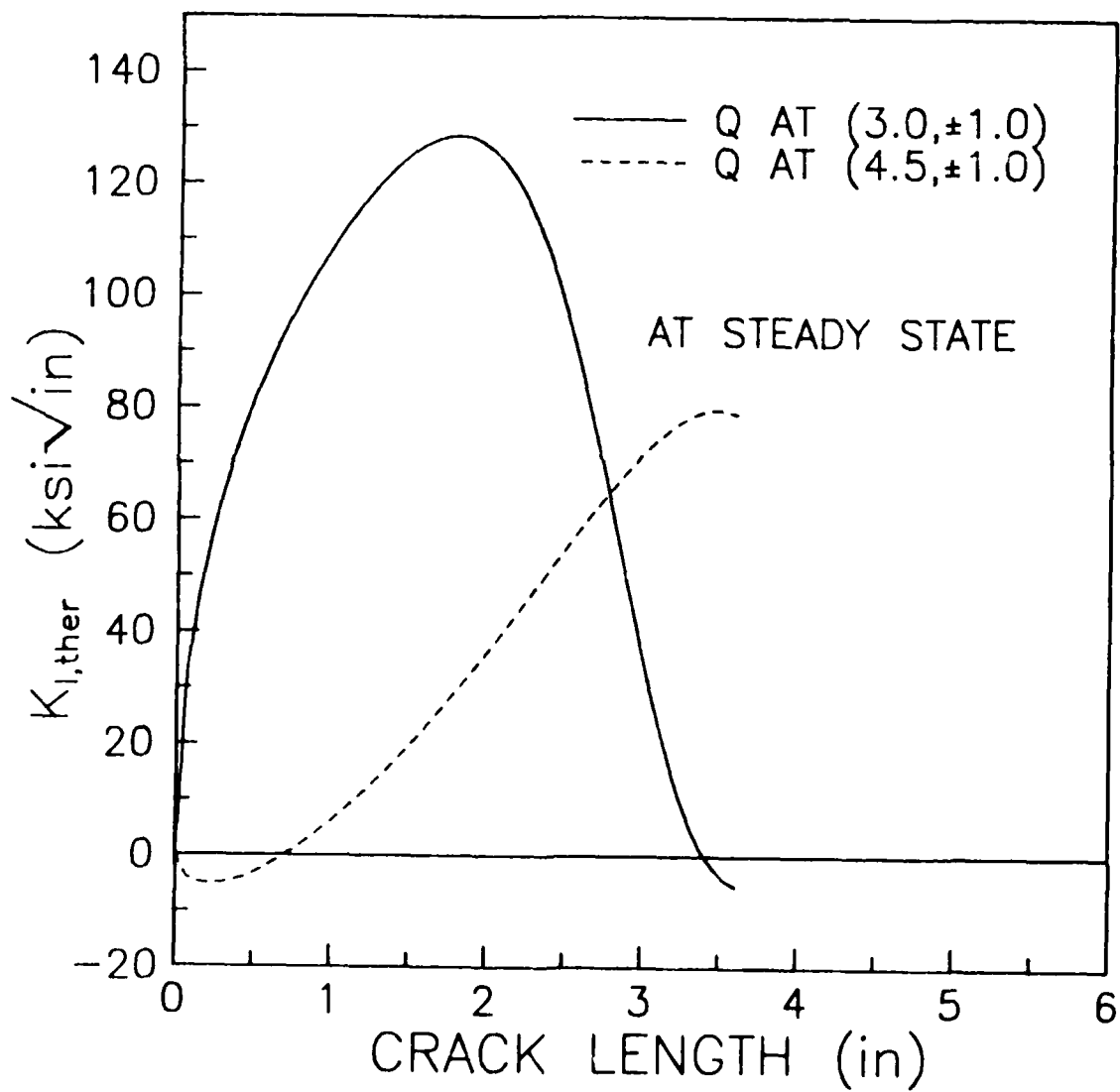


Figure 11-4. Steady State Thermal K_I Versus Crack Length Relationship for Two Different Locations of Heat Sources

APPENDIX A

EFFECTS OF CRACK SURFACE HEAT CONDUCTANCE
ON STRESS INTENSITY FACTORS

A1.0 ABSTRACT

Effects of crack surface heat conductance on stress intensity factors of Modes I, II, and III are investigated. The crack problem is first solved by assuming perfect (infinite) heat conductance at crack surfaces. Finite heat conductance at crack surfaces is then accounted for by imposing a set of distributed dipoles at the crack surfaces. Distribution function of the dipoles is the solution of a Fredholm integral Equation. It is shown that, for cracks in a homogeneous, isotropic, linear elastic solid, the degree of thermal conductivity at crack surfaces will affect the magnitude of Mode I and Mode II stress intensity factors but not Mode III stress intensity factor. It is also shown that, for a geometrically symmetric cracked solid, only Mode II stress intensity factor will be influenced by different crack surface heat conductance even if the thermal loading is not symmetric. More importantly, for a given material thermal conductivity (k) and crack surface heat convection coefficient (h), effects of crack surface heat conductance on stress intensity factors is found to depend upon crack size. This "size effect" implies that, for a given set of K and h , an extremely small crack can be treated as if the crack surfaces are insulated and a very long crack can be treated as if the crack surfaces are perfectly heat conductive. As an example, the problem of a finite crack in an infinite plate subjected to a constant temperature gradient at infinity is studied.

A2.0 INTRODUCTION

Stress intensity factors caused by thermal stresses have been of prime interest in aerospace, nuclear, and electronic industries. Conventionally, crack surfaces have been assumed to be insulated (e.g., Sih, 1962) when solving for thermal stress intensity factors. Such an assumption often leads to a question of how much the stress intensity factors will change when a more

realistic thermal conductivity is used for crack surfaces. This appendix outlines an analytical and numerical scheme for calculating thermal stress intensity factors for cracks with surface heat conductance ranging from zero (insulated) to infinity (perfectly conductive).

A3.0 FORMULATION

As illustrated in Figure A1, we consider a homogeneous, isotropic, linear elastic body V with a boundary surface S and a crack surface S_c . It is assumed that the crack surface S_c lies in a plane. It is also assumed that the quasi-static thermoelasticity theory is valid. Therefore, governing Equations and initial and boundary conditions for any point P in the elastic body are

$$\xi \nabla^2 T = T_{,t} \quad \xi = \frac{k}{\rho c} \quad (A-1)$$

$$\sigma_{ij,j} = 0 \quad (A-2)$$

$$\sigma_{ij} = 2G(\epsilon_{ij} + \frac{\nu}{1-2\nu} \epsilon_{mm} \delta_{ij} - \frac{\nu}{1-2\nu} \alpha T \delta_{ij}) \quad (A-3)$$

$$\epsilon_{ij} = (u_{i,j} + u_{j,i})/2 \quad (A-4)$$

$$T(P,0) = 0 \quad (A-5)$$

$$T(P,t) = T^0(P,t) \quad P \text{ on } S_T \quad (A-6)$$

$$\frac{\partial T}{\partial n}(P,t) = q^0(P,t) \quad P \text{ on } S_q \quad (A-7)$$

$$\frac{\partial T}{\partial n}(P,t) = \lambda [T(P^+,t) - T^-(P,t)] \quad P \text{ on } S_c \quad (A-8)$$

$$\lambda = \frac{h}{k} \quad (A-9)$$

$$\sigma_{ij} n_j = F_i^0 \quad P \text{ on } S_\sigma \quad (A-10)$$

$$u_i = u_i^0 \quad P \text{ on } S_u \quad (A-11)$$

$$\sigma_{ij} n_j = 0 \quad P \text{ on } S_c \quad (A-12)$$

In above Equations, k is thermal conductivity, ρ is mass density, c is specific heat, h is heat convection coefficient across the crack surface, P is a point within V , t is time, G is shear modulus, ν is Poisson's ratio, α is coefficient of thermal expansion, T^0 is prescribed temperature on S_T , q^0 is prescribed heat flux on S_q , $S = S_T + S_q$, P^+ and P^- stands for points at upper and lower crack surface respectively, λ is in the units of (1/length), F^0 is prescribed traction on S_σ , u_i^0 is prescribed displacement on S_u , and $S = S_\sigma + S_u$. In Equation (A-8), the crack surfaces are insulated when λ is zero and are perfectly heat conductive when λ is infinity. Since this is a linear problem, we can assume that

$$T(P,t) = T^{(1)}(P,t) + T^{(2)}(P,t) \quad (A-13)$$

$$\sigma_{ij}(P,t) = \sigma_{ij}^{(1)}(P,t) + \sigma_{ij}^{(2)}(P,t) \quad (A-14)$$

where functions with superscript (1) are solutions to the problem of $\lambda=\infty$ and functions with superscript (2) are complementary solutions which account for the proper crack surface thermal conductivity condition.

A4.0 SOLUTIONS TO PERFECTLY CONDUCTIVE CRACK SURFACES ($\lambda=\infty$)

$T^{(1)}$, $\sigma_{ij}^{(1)}$, and $u_i^{(1)}$ satisfy Equations (A-1) to (A-12) except Equation (A-8), which is replaced by

$$T^{(1)}(P^+, t) = T^{(1)}(P^-, t) \quad P \text{ on } S_c \quad (A-15)$$

In general, it is much easier to obtain temperature and stress intensity factor solutions to the problem of a perfectly heat conductive crack. Asymptotic stresses at the crack tip caused by thermal loading have been shown by Sih (1962) to have the same order of singularity $(-1/2)$ and distribution functions. Kassir and Sih (1966) have shown that asymptotic stress solutions at the crack border are

$$\sigma_{nn}^{(1)} = [K_I^{(1)} f_{nn}(\theta) + K_{II}^{(1)} g_{nn}(\theta)]/\sqrt{2\pi r} \quad (A-16)$$

$$\sigma_{zz}^{(1)} = [K_I^{(1)} f_{zz}(\theta) + K_{II}^{(1)} g_{zz}(\theta)]/\sqrt{2\pi r} \quad (A-17)$$

$$\sigma_{ss}^{(1)} = [K_I^{(1)} f_{ss}(\theta) + K_{II}^{(1)} g_{ss}(\theta)]/\sqrt{2\pi r} \quad (A-18)$$

$$\sigma_{nz}^{(1)} = [K_I^{(1)} f_{nz}(\theta) + K_{II}^{(1)} g_{nz}(\theta)]/\sqrt{2\pi r} \quad (A-19)$$

$$\sigma_{sz}^{(1)} = [K_{III}^{(1)} f_{sz}(\theta)]/\sqrt{2\pi r} \quad (A-20)$$

$$\sigma_{ns}^{(1)} = [K_{III}^{(1)} f_{ns}(\theta)]/\sqrt{2\pi r} \quad (A-21)$$

where, as depicted in Figure A-2, η , s , and z are normal, tangential, and vertical coordinates of a local coordinate system at the crack border, and r and θ are distance to the crack border and angle with η -axis, respectively, in the z - η plane. In Equations (A-16) to (A-21), $f_{ij}(\theta)$ and $g_{ij}(\theta)$ are defined as

$$f_{nn}(\theta) = [3 \cos(\theta/2) + \cos(5\theta/2)]/4 \quad (A-22)$$

$$f_{zz}(\theta) = [5 \cos(\theta/2) - \cos(5\theta/2)]/4 \quad (A-23)$$

$$f_{ss}(\theta) = 2\nu \cos(\theta/2) \quad (A-24)$$

$$f_{nz}(\theta) = [-\sin(\theta/2) + \sin(5\theta/2)]/4 \quad (A-25)$$

$$f_{sz}(\theta) = \cos(\theta/2) \quad , \quad f_{ns}(\theta) = -\sin(\theta/2) \quad (A-26)$$

$$g_{nn}(\theta) = [-7 \sin(\theta/2) + \sin(5\theta/2)]/4 \quad (A-27)$$

$$g_{zz}(\theta) = f_{nz}(\theta) \quad , \quad g_{ss}(\theta) = -2\nu \sin(\theta/2) \quad (A-28)$$

$$g_{nz}(\theta) = f_{nn}(\theta) \quad , \quad g_{sz}(\theta) = g_{ns}(\theta) = 0 \quad (A-29)$$

A5.0 PARTIALLY CONDUCTIVE CRACK SURFACES (FINITE λ)

In order to satisfy the actual crack surface thermal conductivity condition, Equation (A-8), a complementary solution, $T^{(2)}$, $u_i^{(2)}$, and $\sigma_{ij}^{(2)}$, must be added to the solution of perfect crack surface thermal conductivity given in Section A4.0. The complementary solution has to satisfy Equations (A-1) to (A-5) and the following boundary conditions:

$$\sigma_{ij}^{(2)} n_j = 0 \quad P \text{ on } S_\sigma \text{ and } S_c \quad (A-30)$$

$$u_i^{(2)}(P, t) = 0 \quad P \text{ on } S_u \quad (A-31)$$

$$T^{(2)}(P, t) = 0 \quad P \text{ on } S_T \quad (A-32)$$

$$\frac{\partial T^{(2)}}{\partial n}(P, t) = 0 \quad P \text{ on } S_q \quad (A-33)$$

$$\frac{\partial [T^{(1)} + T^{(2)}]}{\partial n}(P, t) = \lambda [T^{(2)}(P^+, t) - T^{(2)}(P^-, t)] \quad P \text{ on } S_c \quad (A-34)$$

From Equation (A-34), it is seen that, for a finite λ , temperature across the crack surfaces is not continuous, i.e., except at the crack tips, there is a temperature jump from one side of the crack to the other. Such a temperature jump across the crack surface resembles the temperature jump caused by distributed dipoles situated at a surface in the solid (Carslaw & Jaeger, 1959). Therefore, Equation (A-34) can be satisfied if we can find a set of dipoles properly distributed at the crack surfaces S_c . It has been shown by Carslaw and Jaeger (1959) that, with a set of distributed dipoles of strength $M(Q, t)$ at crack surface S_c , temperature distribution in V is

$$T^{(2)}(P, t) = \int_{S_c} \int_0^t T^G(P, Q, t-\tau) M(Q, \tau) d\tau dS(Q) \quad (A-35)$$

where $T^G(P, Q, t)$ is the temperature solution at point P due to an instantaneous dipole of unit strength applied at point Q at $t=0$. In other words, T^G has to satisfy Equations (A-1), (A-5), (A-32) and (A-33). With a method similar to that given by Carslaw and Jaeger (1959), it can be shown that $T^{(2)}$ given by Equation (A-35) will create a temperature jump of $M(P, t)/(\rho c \xi)$ at point P of the crack surface where ξ is defined in Equation (1). Therefore, Equation (A-34) becomes

$$\int_{S_c} \int_0^t M(Q, \tau) \frac{\partial T^G(P, Q, t-\tau)}{\partial n(Q)} d\tau dS(Q) + q(P, t) = \frac{\lambda}{\rho c \xi} M(P, t) \quad (A-36)$$

where

$$q(P,t) = \frac{\partial T^{(1)}(P,t)}{\partial n(P)} \quad (A-37)$$

is a known function from Section A4.0. Equation (A-36) is a standard Fredholm integral Equation. Thermal stresses due to $T^{(2)}$ can be written as

$$\sigma_{ij}^{(2)}(P,t) = \int_{S_c} \int_0^t \sigma_{ij}^G(P,Q,t-\tau) M(Q,\tau) d\tau dS(Q) \quad (A-38)$$

where $\sigma_{ij}^G(P,Q,t)$ is the stress distribution at point P due to an instantaneous dipole of unit strength applied at point Q at $t=0$.

Since a dipole is a degenerated case of a heat source and a heat sink of the same strength situated at two adjacent points. It can be shown that

$$\sigma_{ij}^G(P,Q,t) = \frac{\partial}{\partial z(Q)} \sigma_{ij}^U(P,Q,t) \quad Q \text{ on } S_c \quad (A-39)$$

where z is a local coordinate defined in Figure A-2 and $\sigma_{ij}^U(P,Q,t)$ is the stresses at point P due to an instantaneous heat source of unit strength applied at point Q at $t=0$. Asymptotically ($r \rightarrow 0$), σ_{ij}^U must have the same format as Equations (A-16) to (A-21), i.e.,

$$\sigma_{ij}^U(P,Q,t) = [C_{ij} f_{ij}(\theta) + D_{ij} g_{ij}(\theta)] / \sqrt{2\pi r(P)} \quad (A-40)$$

(no summation)

where $C_{ij} = C_{ij}(n(Q),s(Q),t)$ and $D_{ij} = D_{ij}(n(Q),s(Q),t)$ are scalar constants. Equations (A-39) and (A-40) lead to

$$\sigma_{ij}^G(P, Q, t) = \frac{1}{\sqrt{2\pi r(P)}} [E_{ij} f'_{ij}(\theta) + F_{ij} g'_{ij}(\theta)] \quad (A-41)$$

(no summation)

where $E_{ij} = C_{ij}(\eta(Q), s(Q), t)/r(Q)$, $F_{ij} = D_{ij}(\eta(Q), s(Q), t)/r(Q)$, and $r(Q) = [\eta(Q)^2 + s(Q)^2]^{0.5}$. By the definition of stress intensity factors and Equations (A-38) to (A-40) we have

$$\begin{aligned} K_I^{(2)} &= \sqrt{2\pi r(P)} [\sigma_z^{(2)}]_{\theta=0} \\ &= \int_{S_C} \int_0^t M(Q, \tau) F_{zz}(\eta(Q), s(Q), t-\tau) g'_{zz}(0) d\tau dS(Q) \\ &= \frac{1}{2} \int_{S_C} \int_0^t M(Q, \tau) F_{zz}(\eta(Q), s(Q), t-\tau) d\tau dS(Q) \end{aligned} \quad (A-42)$$

$$\begin{aligned} K_{II}^{(2)} &= \sqrt{2\pi r(P)} [\sigma_{nz}^{(2)}]_{\theta=0} \\ &= \int_{S_C} \int_0^t M(Q, \tau) E_{nz}(\eta(Q), s(Q), t-\tau) f'_{nz}(0) d\tau dS(Q) \\ &= \frac{1}{2} \int_{S_C} \int_0^t M(Q, \tau) E_{nz}(\eta(Q), s(Q), t-\tau) d\tau dS(Q) \end{aligned} \quad (A-43)$$

$$\begin{aligned} K_{III}^{(2)} &= \sqrt{2\pi r(P)} [\sigma_{sz}^{(2)}]_{\theta=0} \\ &= \int_{S_C} \int_0^t M(Q, \tau) E_{sz}(\eta(Q), s(Q), t-\tau) f'_{sz}(0) d\tau dS(Q) \\ &= 0 \end{aligned} \quad (A-44)$$

In Equations (A-42) to (A-44), it is found that, in general, K_I and K_{II} will be affected by the degree of thermal conductivity at crack surfaces while K_{III} is independent of crack surface thermal conductivity. In other words, different λ values in Equation (A-8) will generate different K_I and K_{II} solutions but will not change K_{III} solution.

A6.0 CRACKED SOLIDS WITH GEOMETRICAL SYMMETRY

For an elastic solid, of which the body V and all the boundary surfaces (S_σ , S_u , S_T , and S_q) are symmetric with respect to the plane containing the crack surface S_c , Equations (A-42-A.44) can be further simplified. Under this geometrical symmetry condition, D_{ij} in Equation (A-40) and thus F_{ij} in Equation (A-41) must equal to zero. Therefore, both $K_I^{(2)}$ and $K_{III}^{(2)}$ vanish in this case. Thus, for a geometrically symmetric cracked solid, its K_I and K_{III} solutions can be obtained by assuming that the crack surfaces are perfectly thermal conductive or insulated. Such a behavior can greatly simplify the computational effort when only K_I and K_{III} is of major concern, e.g. pressurized thermal shock of a reactor pressure vessel in nuclear industry. Examples to geometrically symmetric cracked solids are: center-cracked plates, single-edge cracked plates, a semi-elliptical surface crack in an plate of finite thickness, an elliptical crack in an infinite space, a circumferentially cracked pipe, and an axially cracked pipe. It should be noted that, in the class of symmetric cracked structures, even though the geometry and boundary surfaces are assumed to be symmetric with respect to the crack plane, mechanical and thermal loadings can still be non-symmetric, e.g., a finite crack in an infinite plate subjected to point heat sources at arbitrary locations (see Figure A-3).

A7.0 EXAMPLE PROBLEM

Let us consider a finite crack of length $2a$ in an infinite plate subjected to a steady-state temperature gradient of Ω at infinity. As shown in Figure A-3, the thickness of the plate is assumed to be D and the temperature gradient Ω is assumed to have an angle of β with the x -axis. The plate is assumed to be stress free at infinity.

For the case of $\lambda=0$, $T^{(1)}$ is a linear function of x and y . According to Boley and Weiner (1960), such a linear temperature field will not generate any stresses, i.e., $\sigma_{ij}^{(1)}=0$, $K_I^{(1)} = K_{II}^{(1)} = K_{III}^{(1)} = 0$. The next step is to solve the Fredholm Equation defined by Equation (A-36) for the dipole distribution function $M(x)$, $-a \leq x \leq a$. It is known (e.g., Carslaw and Jaeger, 1959) that for a dipole of unit strength applied at $(0,0)$ the steady state temperature solution is

$$T^G = \frac{Y}{2\pi k(x^2+y^2)} \quad (A-45)$$

Thus Equation (A-36) becomes

$$\Omega D \sin\beta + \int_{-a}^a \frac{M(\bar{x}) d\bar{x}}{2\pi k(x-\bar{x})^2} = \frac{\lambda M(x)}{\rho c \xi} \quad (A-46)$$

Temperature jumps across crack surface (see Section A5.0) due to this distributed dipoles are

$$T^{(2)}(x, 0^+) - T^{(2)}(x, 0^-) = M(x)/(kD) \quad (A-47)$$

where $M(x)$ is in the units of energy per time, e.g., Btu/Sec. It has been shown by Wilson and Yu (1977) that stress intensity factors due to thermal stresses can also be obtained by

integrating, over the crack surface, the product of an influence function $m(x)$ and the stresses for the uncracked body under the same temperature field. For a finite crack of length $2a$ in an infinite plate, the influence function for all three crack modes at right crack-tip ($x=a$) is (e.g., Tada, Paris, and Irwin, 1985, or Sih, 1973)

$$m(x) = \left[\frac{(a+x)}{\pi a(a-x)} \right]^{1/2} \quad (A-48)$$

Following the stress function method given by Boley and Weiner (1960) or Parkus (1968), it can be shown that thermal stresses at $y=0$ due to a dipole of unit strength applied at $(0,0)$ of an infinite plate (plane stress is implied) are

$$\sigma_{xy}^G(x,0) = \frac{Ga(1+\nu)}{2\pi kDx}, \quad \sigma_{yy}^G(x,0) = \sigma_{yz}^G(x,0) = 0 \quad (A-49)$$

By the definition of influence function and Equation (A-38), stress intensity factors can be written as

$$K_I^{(2)} = K_{III}^{(2)} = 0$$

$$\begin{aligned} K_{II}^{(2)} &= \frac{Ga(1+\nu)}{2\pi kD\sqrt{\pi a}} \int_{-a}^a \int_{-a}^a \frac{M(u)}{(x-u)} \left[\frac{(a+x)}{(a-x)} \right]^{1/2} du \, dx \\ &= \frac{Ga(1+\nu)}{2kD\sqrt{\pi a}} \int_{-a}^a M(x) \, dx \end{aligned} \quad (A-50)$$

Since

$$M_0 = 2kD\Omega\sqrt{(a+x)(a-x)}\sin\beta \quad (A-51)$$

is the solution of

$$\Omega D \sin\beta + \int_{-a}^a \frac{M_0(\bar{x}) d\bar{x}}{2\pi k(x-\bar{x})^2} = 0 \quad (A-52)$$

it is reasonable to express $M(x)$ as:

$$M(x) = \sqrt{(a+x)(a-x)} \sum_0^{\infty} d_j \left(\frac{x}{a}\right)^j \quad (A-53)$$

where d_j are coefficients to be determined. Both Equations (A-51) and (A-53) implicitly satisfy the crack tip temperature condition, $T(\pm a, 0^+) = T(\pm a, 0^-)$ or $M(\pm a) = 0$. Substituting Equation (A-53) into Equation (A-46) and going through an algebraic and complex function manipulation, we find that the coefficients d_j in Equation (A-53) can be determined by the following recurrence relations:

$$d_{2j-1} = e_{2j-1} = 0, \quad (j \geq 1)$$

$$d_0 = \frac{2kD\Omega \sin\beta}{1 + 2\lambda a}$$

$$d_{2j} = \frac{2\lambda a}{2j+1+2\lambda a} \sum_{m=1}^j (e_{2m} d_{2j-2m}), \quad (j \geq 1) \quad (A-54)$$

$$e_0 = 1, \quad e_2 = 1/2$$

$$e_{2m} = \frac{1}{2^m m!} \prod_{n=1}^m (2n-3), \quad (m \geq 2)$$

Physically, Equation (A-51) represents the dipole distribution for an insulated crack ($\lambda=0$) under a constant temperature gradient at infinity. Temperature jumps at the crack surface for the insulated crack can then be calculated by substituting Equation (A-51) into Equation (A-47) and is found to be

$$T(x, 0^+) - T(x, 0^-) = 2\Omega\sqrt{(a+x)(a-x)}\sin\beta \quad (A-55)$$

This temperature jump is identical to that given by Goodier and Florence (1959) ($m=1$ and $R=a/2$ in pages 26 and 27 of Goodier and Florence's report (1959)). Then, by Equation (A-50), the stress intensity factor due to $M_0(x)$ is

$$K_{II}^0 = \frac{1}{2} G\alpha(1+\nu)a\sqrt{\pi a} \Omega \sin\beta \quad (A-56)$$

K_{II}^0 in Equation (A-56) is the same as the solution to the same problem by Sih (1962) and Paris and Sih (1964).

For λ other than 0, $M(x)$, $T(x, 0)$, as well as K_{II} can be solved numerically through Equations (A-50), (A-53), and (A-54).

A8.0 NUMERICAL RESULTS AND DISCUSSION

In the numerical calculation, it is found that, with the first 50 terms included in Equation (A-53), K_{II} solution converges to within 0.5%. Resulting Mode II stress intensity factors for different λa values are plotted in Figure A-4 for λa up to 10. The stress intensity values shown in Figure A-4 have been normalized by the stress intensity factor solution for an insulated crack, K_{II}^0 in Equation (A-56). For λ value ranging from zero to infinity, the curve shown in Figure A-4 can be approximated, with error less than $0.02K_{II}^0$, by

$$(K_{II}/K_{II}^0) = 0.9827 - 2.247\phi + 2.6513\phi^2 - 1.405\phi^3 \quad (A-57)$$

where $\phi = \frac{2}{\pi} \tan^{-1}(\lambda a)$. For a given crack size a , as λ value increases the crack surface becomes more heat conductive and K_{II} value decreases toward zero monotonically. Temperature jumps

across the crack surface for $\lambda a=0$, $\lambda a=0.5$, and $\lambda a=2$ are illustrated in Figure A-5. As expected, in Figure A-5, temperature jumps decrease monotonically toward zero as the crack surface becomes more heat conductive. One important discovery out of Figures A-4 and A-5 is that, in addition to the independent variables G , α , ν , $a^{3/2}$, Ω , and β given in Equation (A-56), stress intensity factor K_{III} for a partially heat conductive crack has an additional independent variable of λa , which represents the degree of crack surface thermal conductivity. For a given set of K and h ($\lambda = \frac{h}{K} = \text{constant}$), the degree of influence on K_{III} by crack surface thermal conductivity depends upon the length of the crack. Therefore, for a given set of K and h , small cracks act more like being insulated and long cracks tend to behave like being perfectly conductive. In other words, effects of crack surface thermal conductivity on stress intensity factors are crack size dependent. This size effect could be a very important factor in designing a structural or electronic component for use in a transient temperature environment. For instance, if all the variables except crack size remain constant, the stress intensity factor is expected to reach a peak value and decay to zero as the crack length increases. Figure A-6 illustrates this size effect for the example problem. In Figure A-6, K_{III} values have been normalized by the constant, $0.5G\alpha(1+\nu)(\pi/\lambda^3)^{0.5}\Omega \sin\beta$.

To sum up this appendix, a few conclusions can be drawn:

- (1) For any crack geometries, K_{III} solution does not depend on crack surface thermal conductivity, only K_I and K_{II} do.
- (2) For cracks in a geometrically symmetric solid, neither K_I nor K_{III} depends upon crack surface thermal conductivity (λ), i.e., K_I and K_{III} for elastic solids of this class can be calculated by assuming the crack surface is perfectly conductive ($\lambda=\infty$) or insulated ($\lambda=0$).

- (3) The above conclusions are valid for both two and three dimensional cracks.
- (4) In general, conclusions (1-3) are not true for cracks in anisotropic materials or interfacial cracks in an isotropic solid because all the three fracture modes are coupled together in this case.
- (5) For cracks (including interfacial cracks) in a linear elastic, quasi-static solid (isotropic or anisotropic), the effects of crack surface thermal conductivity on stress intensity factors depend on the distribution of dipoles situated at the crack surfaces. Distribution function of the dipoles at the crack surfaces can be determined by a Fredholm integral equation.

A9.0 REFERENCES

Boley, B. A., and Weiner, J. H., 1960, Theory of Thermal Stresses, Wiley, New York, New York.

Carslaw, H. S. and Jaeger, J. G., 1959, Conduction of Heat in Solids, Oxford University Press, London, 1959.

Goodier, J. N., and Florence, A. L., 1959, "Thermal Stress Due to Disturbance of Uniform Heat Flow by Cavities and Inclusions," 1959, Technical Report No. 120, Division of Engineering Mechanics, Stanford University.

Kassir, M. K. and Sih, G. C., 1966, "Three-Dimensional Stress Distribution Around an Elliptical Crack Under Arbitrary Loadings," *Journal of Applied Mechanics*, Vol. 33, pp.601-611.

Parkus, H., 1968, Thermoelasticity, Blaisdell Publishing Co..

Paris, P. C., and Sih, G. C., 1964, "Stress Analysis of Cracks," in Fracture Toughness Testing and its Applications, ASTM STP-381, pp. 30-83.

Sih, G. C., 1962, "On the Singular Character of Thermal Stresses near a Crack Tip," *Journal of Applied Mechanics*, Vol. 29, pp.587-589.

Sih, G. C., 1973, Handbook of Stress Intensity Factors, Lehigh University, Bethlehem, PA.

Tada, H., Paris, P. C., and Irwin, G. R., 1985, The Stress Analysis of Cracks Handbook, Second Ed., Paris Productions Inc., St. Louis, MO.

Wilson, W. K., and Yu, I.-W., 1979, "The Use of the J-Integral in Thermal Stress Crack Problems," 1979, International Journal of Fracture, Vol. 15, pp. 377-387.

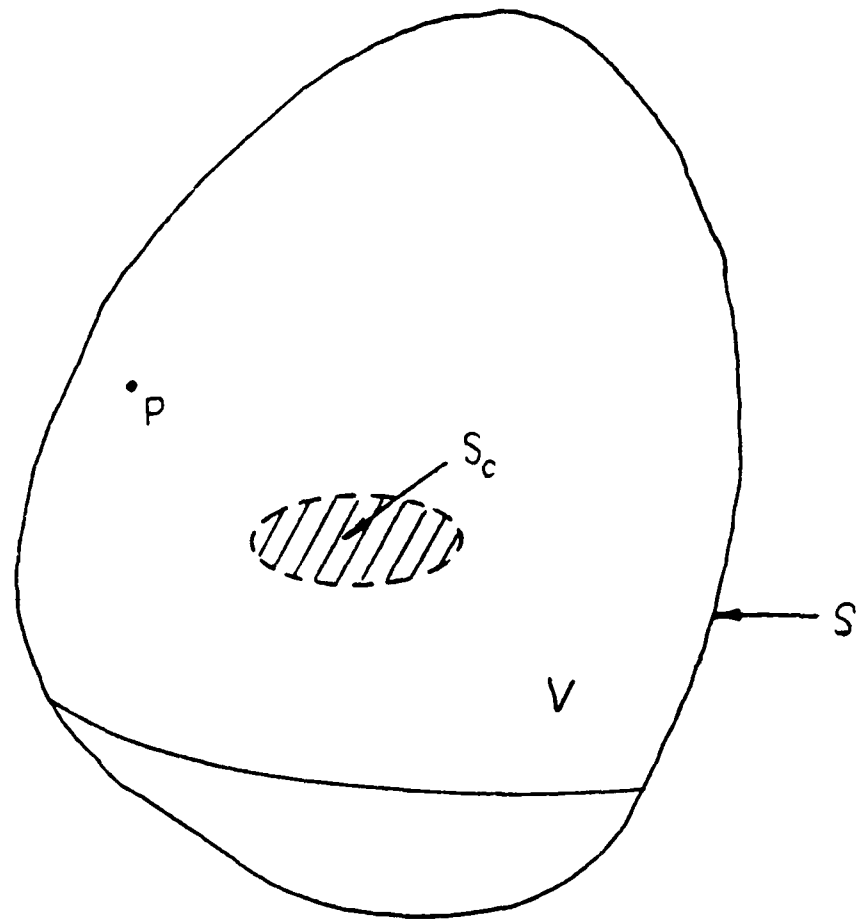


Figure A-1. A Crack in a Linear Elastic Solid

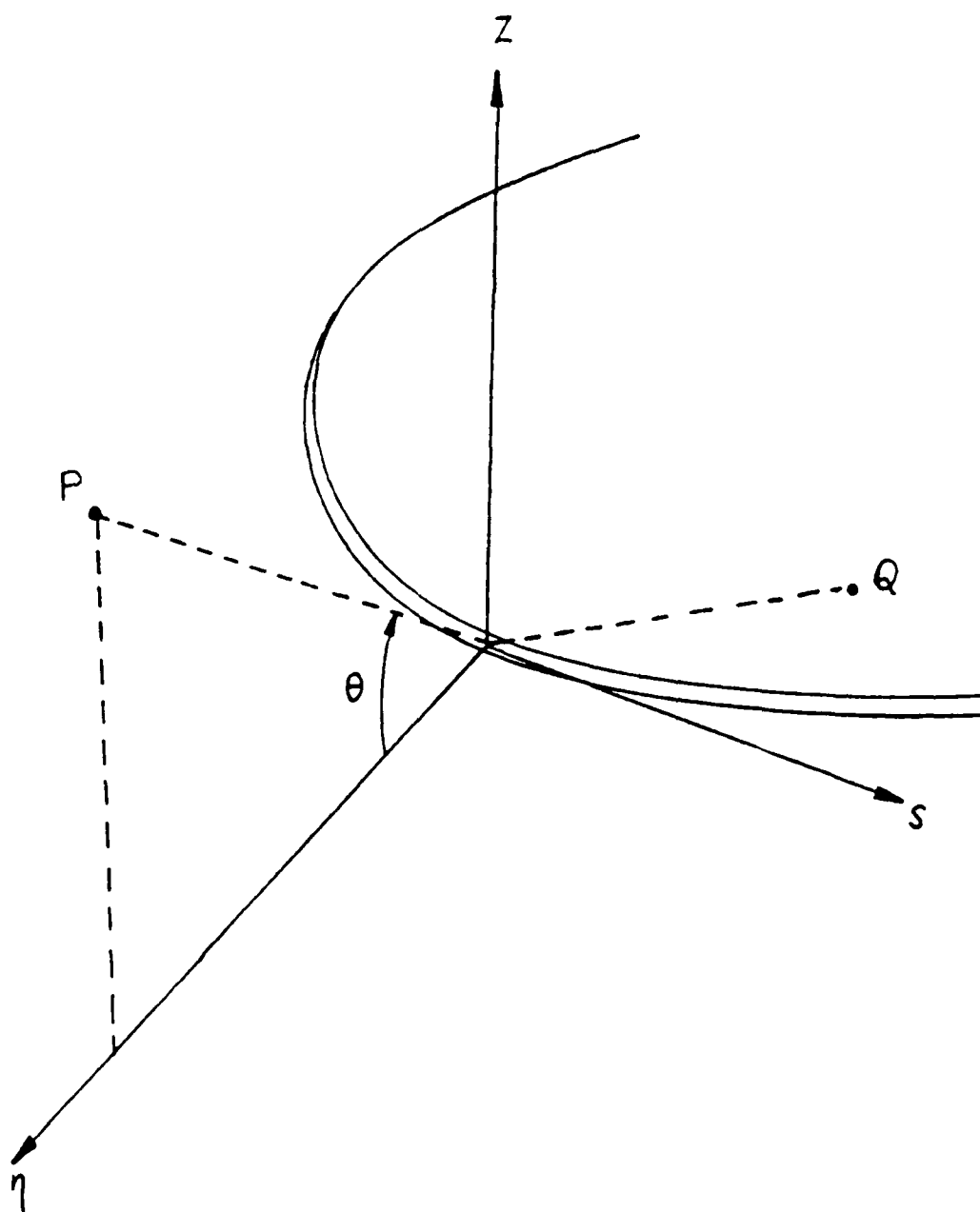


Figure A-2. Local Coordinate at Crack Border

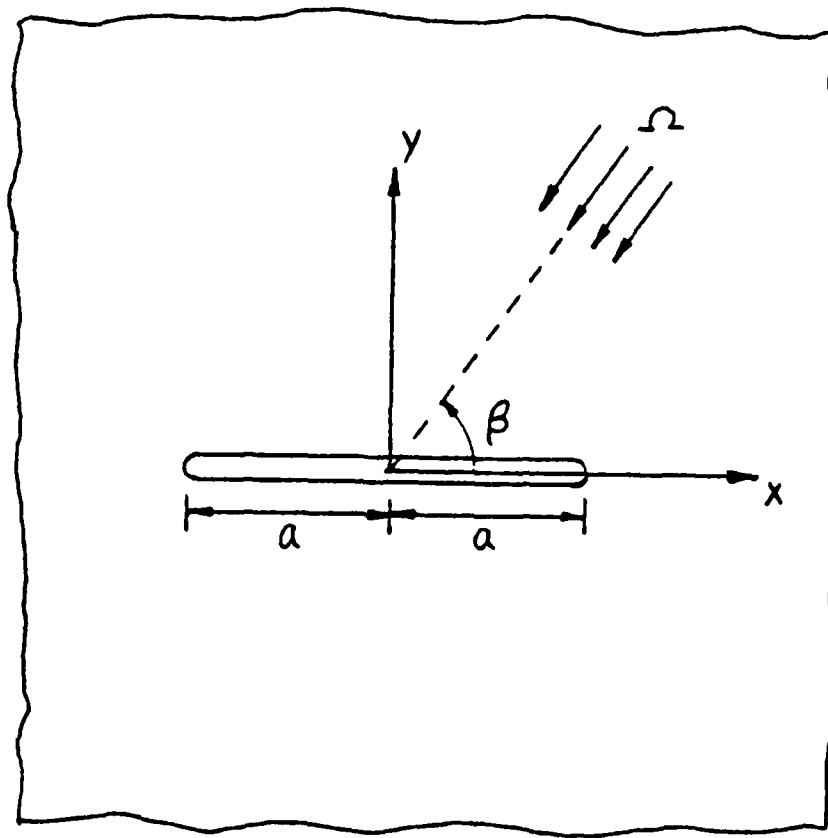


Figure A-3. A Finite Crack in an Infinite Plate

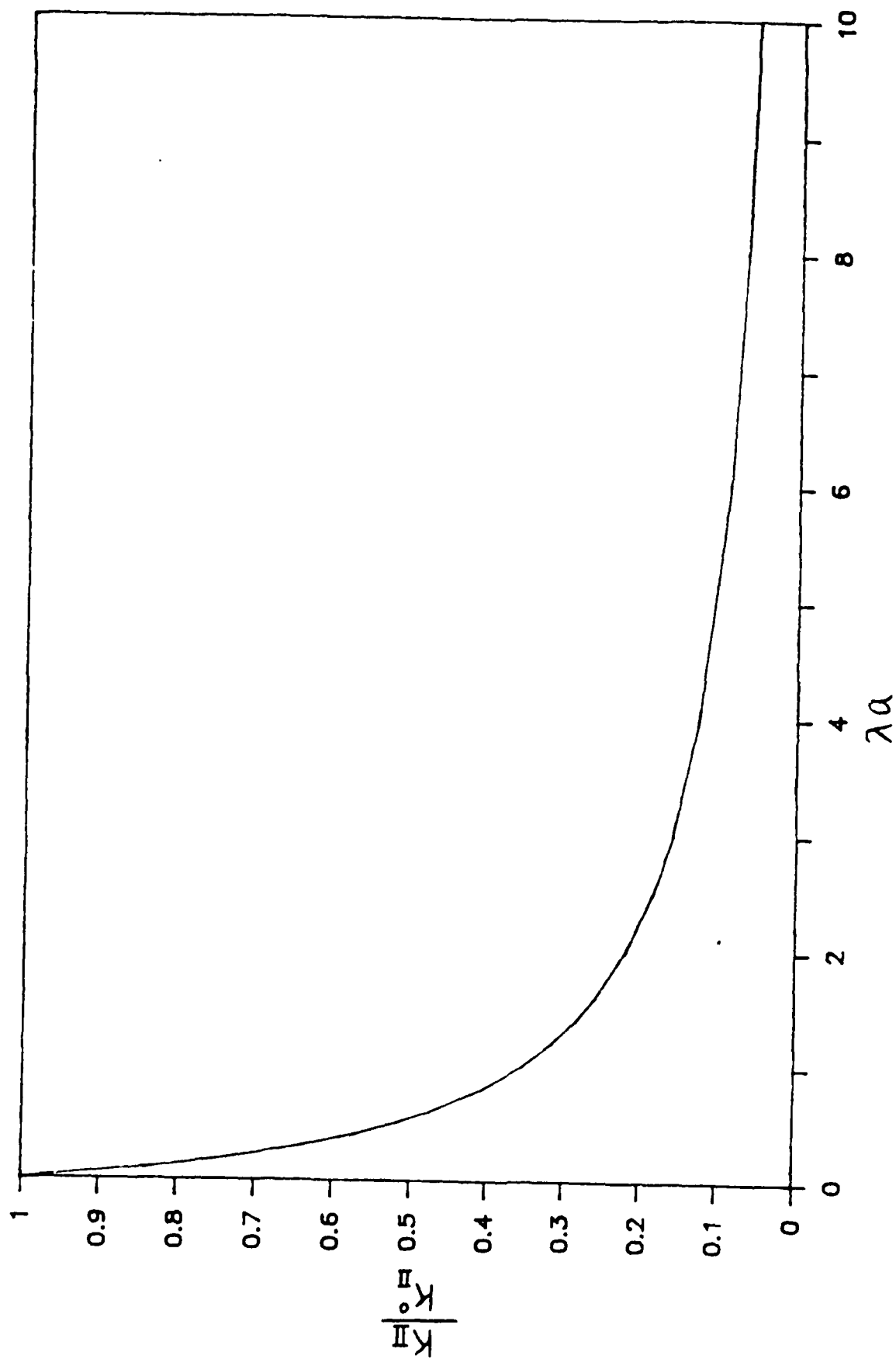


Figure A-4. Effects of Crack Surface Thermal Conductivity on K_{II}

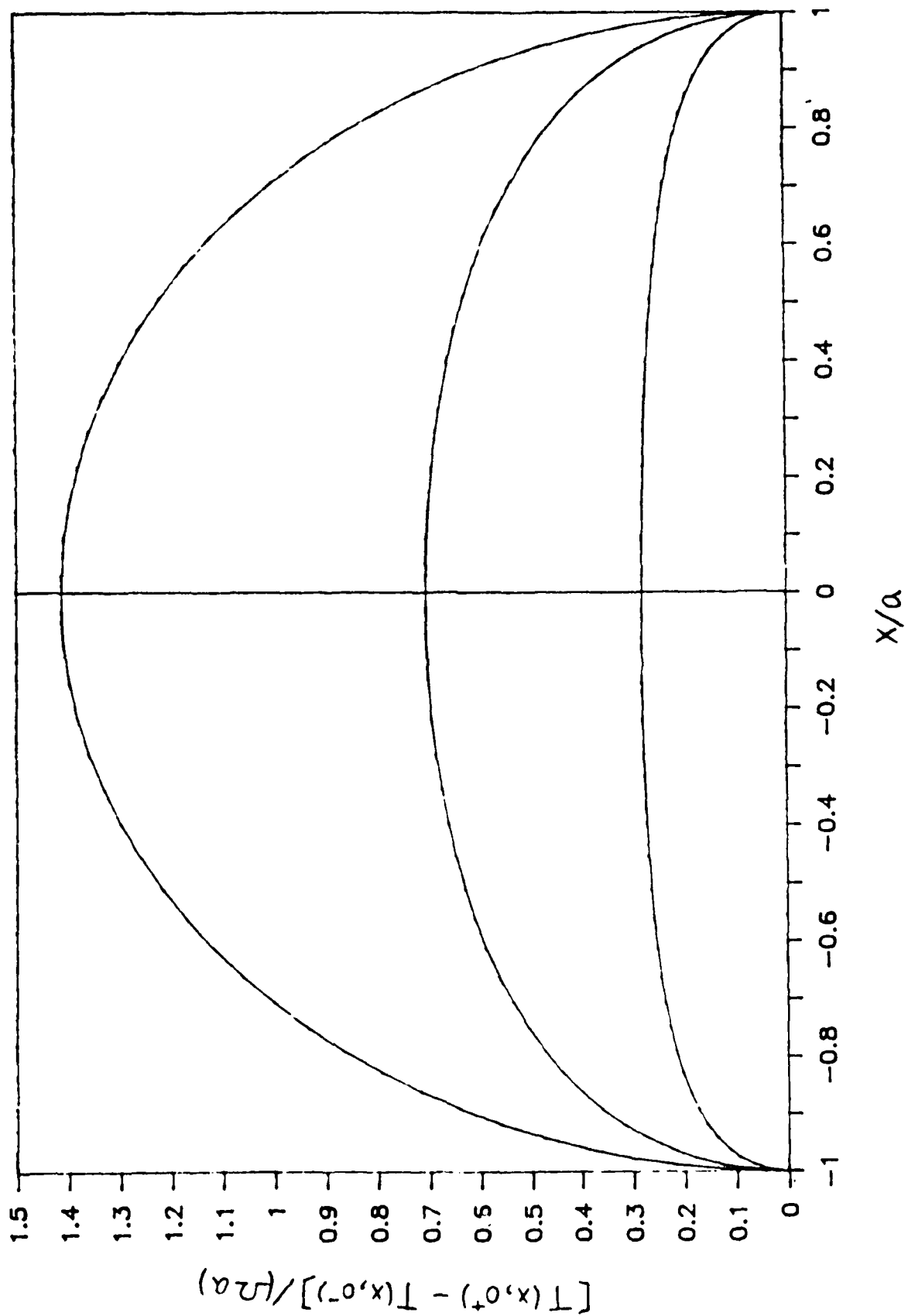


Figure A-5. Temperature Jumps at the Crack Surface

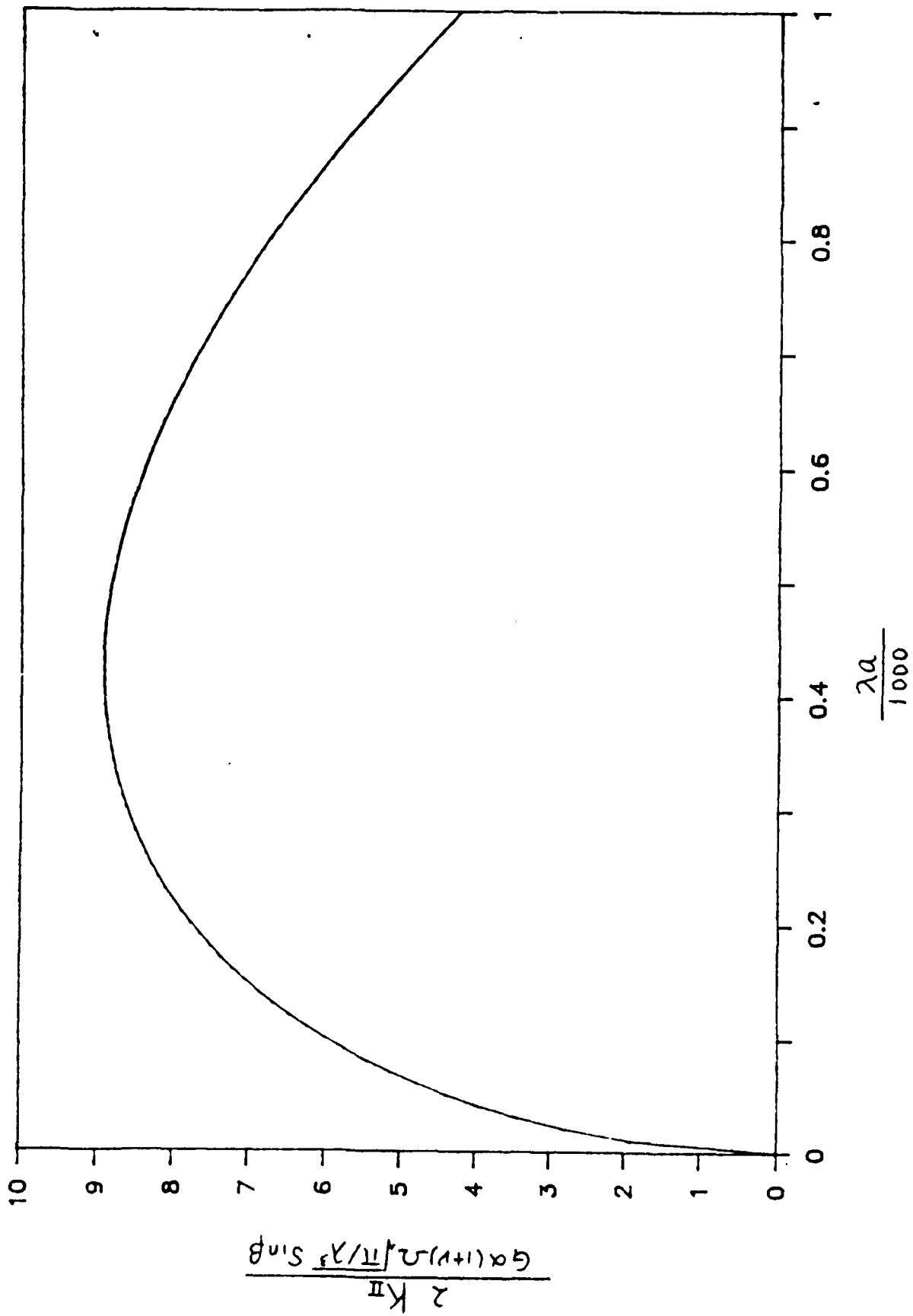


Figure A-6. Size Effects

Appendix B

NUMERICAL INTEGRATION SCHEME FOR INTEGRATING INFLUENCE FUNCTIONS FOR 2-D CRACK MODELS

B1.0 INTRODUCTION

For the five two-dimensional crack models, crack models 1 to 5, this appendix describes the numerical integration technique used in the computer program for integrating the product of stresses and influence functions for stress intensity factor calculation.

B2.0 INTEGRATION SCHEME FOR CRACK MODELS 2,3, AND 4

As shown in Figure B-1, for crack models 2, 3, and 4, stress intensity factors K_I and K_{II} can be evaluated by

$$\begin{aligned} K_I &= \int_0^a \sigma_{yy}(x) m_1(x) dx \\ &= \sum_{i=1}^{n/2} \left[\left(\frac{\pi}{n} \right) \sigma_{yy}(x_i) m_1(x_i) \sqrt{(a+x_i)(a-x_i)} \right] \end{aligned} \quad (B-1)$$

$$\begin{aligned} K_{II} &= \int_0^a \sigma_{xy}(x) m_2(x) dx \\ &= \sum_{i=1}^{n/2} \left[\left(\frac{\pi}{n} \right) \sigma_{xy}(x_i) m_2(x_i) \sqrt{(a+x_i)(a-x_i)} \right] \end{aligned} \quad (B-2)$$

where n is an even number, m_1 and m_2 are influence functions for Mode I and Mode II cracking, respectively, σ_{yy} and σ_{xy} are, respectively, normal and shear stresses acting on the crack region for an uncracked plate under the same temperature distribution and x_i are Chebyshev points defined as

$$x_i = a \cos\left[\left(\frac{2i-1}{2n}\right)\pi\right] \quad (B-3)$$

In the computer program, $n=100$ is used.

B3.0 INTEGRATION SCHEME FOR CRACK MODELS 1 AND 5

As shown in Figure B-2, for crack Models 1 and 5, stress intensity factors K_I and K_{II} can be evaluated by

$$\begin{aligned} K_I &= \int_{-a}^a \sigma_{yy}(x) m_1(x) dx \\ &= \sum_{i=1}^n \left[\left(\frac{\pi}{n}\right) \sigma_{yy}(x_i) m_1(x_i) \sqrt{(a+x_i)(a-x_i)} \right] \end{aligned} \quad (B-4)$$

$$\begin{aligned} K_{II} &= \int_{-a}^a \sigma_{xy}(x) m_2(x) dx \\ &= \sum_{i=1}^n \left[\left(\frac{\pi}{n}\right) \sigma_{xy}(x_i) m_2(x_i) \sqrt{(a+x_i)(a-x_i)} \right] \end{aligned} \quad (B-5)$$

where m_1 and m_2 are influence functions for Mode I and Mode II cracking, respectively, σ_{yy} and σ_{xy} are, respectively, normal and shear stresses acting on the crack region for an uncracked plate under the same temperature distribution and x_i are Chebyshev points defined as

$$x_i = a \cos\left[\left(\frac{2i-1}{2n}\right)\pi\right] \quad (B-6)$$

In the computer program, $n=100$ is used.

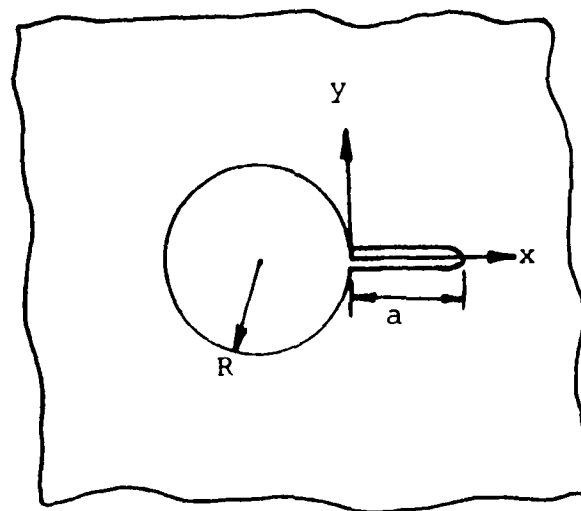
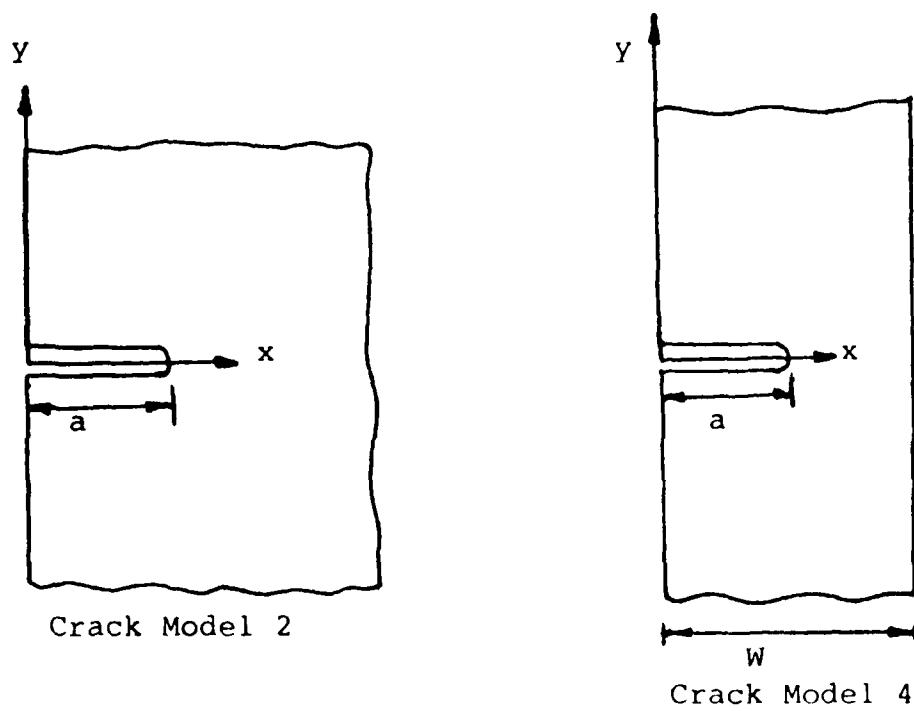
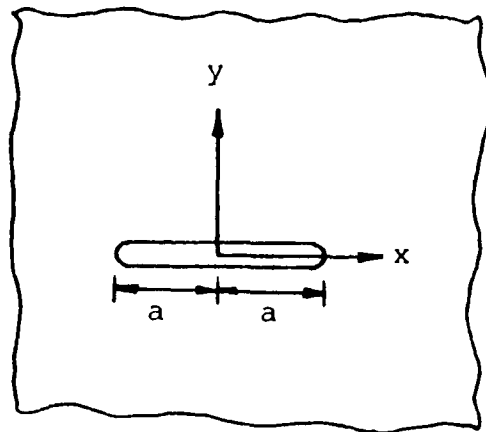
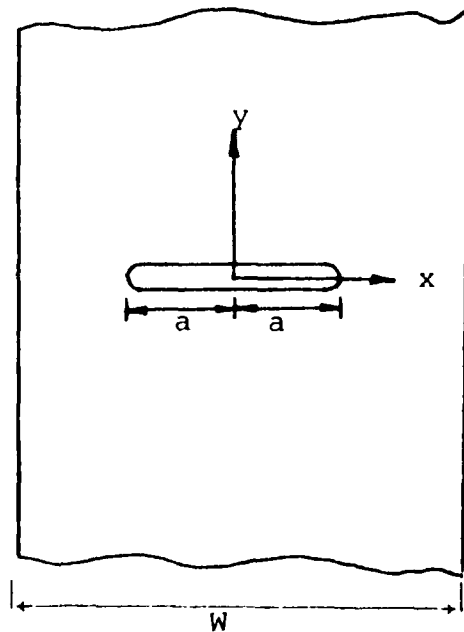


Figure B-1. Local Coordinates for Influence Function Integration for Crack Models 2, 3, and 4



Crack Model 1



Crack Model 5

Figure B-2. Local Coordinates for Influence Function Integration for Crack Models 1 and 5

Appendix C

EDGE SOLUTION FOR COMPLEMENTARY STRESS FUNCTION Ψ

C1.0 INTRODUCTION

This Appendix discusses the solution procedure for the stress function Ψ and its resulting edge effect functions.

C2.0 GOVERNING EQUATIONS AND SOLUTIONS

It has been discussed by Timoshenko and Goodier (1970) that the solution for the problem of an infinitely long plate strip subjected to edge loading as illustrated in Figure C-1 can be written as

$$\begin{aligned}\Psi(x,y) = & \frac{1}{\pi} \int_0^{\infty} (C_1 \cosh \beta \bar{x} + C_2 \sinh \beta \bar{x} + C_3 \bar{x} \cosh \beta \bar{x} + C_4 \bar{x} \sinh \beta \bar{x}) \cos \beta y \, d\beta \\ & + \frac{1}{\pi} \int_0^{\infty} (D_1 \cosh \beta \bar{x} + D_2 \sinh \beta \bar{x} + D_3 \bar{x} \cosh \beta \bar{x} + D_4 \bar{x} \sinh \beta \bar{x}) \sin \beta y \, d\beta\end{aligned}\tag{C-1}$$

where $\bar{x} = x - (W/2)$. In Equation (C-1), the eight constants C_1 , C_2 , ..., D_3 , and D_4 are determined by the stress boundary conditions at $x=0$ and $x=W$. In other words, stress function Ψ must satisfy the following boundary conditions

at $x=0$ ($\bar{x} = -W/2$),

$$2G \Psi_{,yy} = F_1(y)\tag{C-2}$$

$$2G \Psi_{,xy} = - F_2(y) \quad (C-3)$$

and at $x=W$ ($\bar{x}=W/2$),

$$2G \Psi_{,yy} = F_3(y) \quad (C-4)$$

$$2G \Psi_{,xy} = - F_4(y) \quad (C-5)$$

where, as shown in Figure C-1, $F_1(y)$, $F_2(y)$, $F_3(y)$, and $F_4(y)$ are prescribed stresses at the edges.

After solving the eight constants, C_1 , C_2 , ..., D_3 , and D_4 , stresses at $y=0$ resulting from stress function $\Psi(x,y)$ can be expressed in a double integration as follows

$$\begin{aligned} \hat{\sigma}_{yy} = & - \frac{2G}{\pi} \int_{-\infty}^{\infty} \int_0^{\infty} \{ [\beta^2 (R_1 \cosh \beta \bar{x} + R_2 \sinh \beta \bar{x} + R_3 \bar{x} \cosh \beta \bar{x} \\ & + R_4 \bar{x} \sinh \beta \bar{x}) F_1(y)] + [\beta^2 (-R_1 \cosh \beta \bar{x} + R_2 \sinh \beta \bar{x} \\ & + R_3 \bar{x} \cosh \beta \bar{x} - R_4 \bar{x} \sinh \beta \bar{x}) F_3(y)] \} \cos \beta y \, d\beta \, dy \\ & - \frac{2G}{\pi} \int_{-\infty}^{\infty} \int_0^{\infty} \{ [\beta^2 (V_1 \cosh \beta \bar{x} + V_2 \sinh \beta \bar{x} + V_3 \bar{x} \cosh \beta \bar{x} \\ & + V_4 \bar{x} \sinh \beta \bar{x})] [F_2(y) + F_4(y)] \} \sin \beta y \, d\beta \, dy \end{aligned} \quad (C-6)$$

$$\begin{aligned}
\hat{\sigma}_{xy} = & -\frac{2G}{\pi} \int_{-\infty}^{\infty} \int_0^{\infty} \{ [(V_1\beta \sinh\beta\bar{x} + V_2\beta \cosh \beta\bar{x} + V_3(\cosh\beta\bar{x} \\
& + \beta\bar{x} \sinh\beta\bar{x}) + V_4(\sinh\beta\bar{x} + \beta\bar{x} \cosh\beta\bar{x})] \\
& [F_3(y)+F_4(y)] \} \beta \sin\beta y \, d\beta \, dy \\
& -\frac{2G}{\pi} \int_{-\infty}^{\infty} \int_0^{\infty} \{ [(R_1\beta \sinh\beta\bar{x} + R_2\beta \cosh \beta\bar{x} \\
& + R_3(\cosh\beta\bar{x} + \beta\bar{x} \sinh\beta\bar{x}) + R_4(\sinh\beta\bar{x} + \beta\bar{x} \cosh\beta\bar{x})] F_1(y) \\
& + [-R_1\beta \sinh\beta\bar{x} + R_2\beta \cosh \beta\bar{x} + R_3(\cosh\beta\bar{x} + \beta\bar{x} \sinh\beta\bar{x}) \\
& -R_4(\sinh\beta\bar{x} + \beta\bar{x} \cosh\beta\bar{x})] F_3(y) \} \beta \sin\beta y \, d\beta \, dy \quad (C-7)
\end{aligned}$$

where

$$R_1 = \frac{1}{\beta^2} [\sinh(\frac{\beta B}{2}) + (\frac{\beta B}{2}) \cosh(\frac{\beta B}{2})] / (\beta B + \sinh\beta B) \quad (C-8)$$

$$R_2 = \frac{1}{\beta^2} [\cosh(\frac{\beta B}{2}) + (\frac{\beta B}{2}) \sinh(\frac{\beta B}{2})] / (\beta B - \sinh\beta B) \quad (C-9)$$

$$R_3 = -[\frac{1}{\beta} \cosh(\frac{\beta B}{2})] / (\beta B - \sinh\beta B) \quad (C-10)$$

$$R_4 = -[\frac{1}{\beta} \sinh(\frac{\beta B}{2})] / (\beta B + \sinh\beta B) \quad (C-11)$$

$$V_1 = - \left[\frac{B}{2\beta} \sinh\left(\frac{\beta B}{2}\right) \right] / (\beta B + \sinh \beta B) \quad (C-12)$$

$$V_2 = \left[\frac{B}{2\beta} \cosh\left(\frac{\beta B}{2}\right) \right] / (\beta B - \sinh \beta B) \quad (C-13)$$

$$V_3 = - \left[\frac{1}{\beta} \sinh\left(\frac{\beta B}{2}\right) \right] / (\beta B - \sinh \beta B) \quad (C-14)$$

$$V_4 = \left[\frac{1}{\beta} \cosh\left(\frac{\beta B}{2}\right) \right] / (\beta B + \sinh \beta B) \quad (C-15)$$

The integrations in Equations (C-6) and (C-7) can usually be evaluated numerically by the following formulae (Abramowitz and Stegun, 1965):

$$\int_0^{\infty} F(z) dz = \sum W_i F(z_i) \exp(z_i) \quad (C-16)$$

where

$$z_1 = 0.222846604179 \quad , \quad W_1 = 0.458964673950$$

$$z_2 = 1.188932101673 \quad , \quad W_2 = 0.417000830772$$

$$z_3 = 2.992736326059 \quad , \quad W_3 = 0.113373382074$$

$$z_4 = 5.775143569105 \quad , \quad W_4 = 0.103991974531 \times 10^{-1}$$

$$z_5 = 9.837467418383 \quad , \quad W_5 = 0.261017202815 \times 10^{-3}$$

$$z_6 = 15.982873980602 \quad , \quad W_6 = 0.898547906430 \times 10^{-6}$$

and

$$\int_{-\infty}^{\infty} F(z) dz = \sum W_i F(z_i) \exp(z_i^2) \quad (C-17)$$

$$z_{1,5} = \pm 2.0201828705, \quad W_{1,5} = 0.0199532421$$

$$z_{2,4} = \pm 0.9585724646, \quad W_{2,4} = 0.3936193232$$

$$z_3 = 0.0, \quad W_3 = 0.9453087205$$

As illustrated in Figure C-2, the edge loaded plate problem can be treated as the superposition of the solutions for two basic loading cases:

Basic Loading Case (1):

$$F_1(y) = -\frac{2P}{DW} \delta(y'), \quad F_2(y) = F_3(y) = F_4(y) = 0 \quad (C-18)$$

Basic Loading Case (2):

$$F_2(y) = -\frac{2S}{DW} \delta(y'), \quad F_1(y) = F_3(y) = F_4(y) = 0 \quad (C-19)$$

where, as shown in Figure C-2, P is a unit normal force applied at $(0, y')$ in positive x -direction, S is a unit shear force applied at $(0, y')$ in positive y -direction, $\delta(y')$ is a Delta function, and D and W are thickness and width of the plate strip respectively.

For basic loading case (1), we can calculate resulting stresses at cross section $y=0$, $\hat{\sigma}_{yy}(x)$ and $\hat{\sigma}_{xy}(x)$, by substituting Equation

(C-18) into Equations (C-6) to (C-15). These two stress components at cross section $y=0$ can then be normalized by $\frac{2P}{DW}$, i.e., define the dimensionless edge effect functions β_{yy} and β_{xy} as

$$\beta_{yy}(x/W, y'/W) = \hat{\sigma}_{yy}(x) / (\frac{2P}{DW}) \quad (C-20)$$

$$\beta_{xy}(x/W, y'/W) = \hat{\sigma}_{xy}(x) / (\frac{2P}{DW}) \quad (C-21)$$

By symmetry, it can be easily deduced that

$$\beta_{yy}(x/W, -y'/W) = \beta_{yy}(x/W, y'/W) \quad (C-22)$$

$$\beta_{xy}(x/W, -y'/W) = -\beta_{xy}(x/W, y'/W) \quad (C-23)$$

The edge effect functions β_{yy} , and β_{xy} for the basic loading case (1) are illustrated in Figures C-3 to C-8. It is seen from these figures that when the edge load is applied at a distance of more than one and one half times of the plate width away from crack plane, i.e., when $|y'| \geq 1.5W$, the edge functions become negligible.

Similarly, for basic loading case (2), another set of dimensionless edge effect functions, γ_{yy} and γ_{xy} , can be derived by substituting Equation (C-19) into Equations (C-6) to (C-15) and normalizing the resulting stresses by $(\frac{2S}{DW})$, i.e., define

$$\gamma_{yy}(x/W, y'/W) = \hat{\sigma}_{yy}(x) / (\frac{2S}{DW}) \quad (C-24)$$

$$\gamma_{xy}(x/W, y'/W) = \hat{\sigma}_{xy}(x) / (2S/DW) \quad (C-25)$$

where $\hat{\sigma}_{yy}$ and $\hat{\sigma}_{xy}$ are stresses at cross section $y=0$ resulting from basic problem (2). Again, by symmetry, it can be shown that

$$\gamma_{yy}(x/W, -y'/W) = -\gamma_{yy}(x/W, y'/W) \quad (C-26)$$

$$\gamma_{xy}(x/W, -y'/W) = \gamma_{xy}(x/W, y'/W) \quad (C-27)$$

Resulting edge effect functions γ_{yy} and γ_{xy} are plotted in Figures C-9 to C-16. Again, it is found that, when $|y'| \geq 1.5W$, the edge functions become negligible.

For any arbitrary loads applied along the two edges of the infinitely long plate strip, i.e., $F_1(y')$ and $F_2(y')$ in $(x=0, -\infty \leq y' \leq \infty)$ and $F_3(y')$ and $F_4(y')$ in $(x=W, -\infty \leq y' \leq \infty)$, the resulting normal and shear stresses at cross section $y=0$ can be calculated by integrating the solutions for the two basic loading cases:

$$\begin{aligned} \hat{\sigma}_{yy}(x, 0) = & \frac{2}{W} \int_{-\infty}^{\infty} \{ [-F_1(y) \beta_{yy}(\frac{x}{W}, \frac{y}{W})] + [F_2(y) \gamma_{yy}(\frac{x}{W}, \frac{y}{W})] + \\ & [-F_3(y) \beta_{yy}(1 - \frac{x}{W}, \frac{y}{W})] + [F_4(y) \gamma_{yy}(1 - \frac{x}{W}, \frac{y}{W})] \} dy \end{aligned} \quad (C-28)$$

$$\begin{aligned} \hat{\sigma}_{xy}(x, 0) = & \frac{2}{W} \int_{-\infty}^{\infty} \{ [F_1(y) \beta_{xy}(\frac{x}{W}, \frac{y}{W})] + [F_2(y) \gamma_{xy}(\frac{x}{W}, \frac{y}{W})] + \\ & [-F_3(y) \beta_{xy}(1 - \frac{x}{W}, \frac{y}{W})] + [F_4(y) \gamma_{xy}(1 - \frac{x}{W}, \frac{y}{W})] \} dy \end{aligned} \quad (C-29)$$

Since all the edge effect functions, β_{yy} , β_{xy} , γ_{yy} , and γ_{xy} , become negligible when $|y'| \geq 1.5W$, the lower and upper limits of the integrations in Equations (C-24) and (C-25) can be approximated by $-1.5 W$ and $1.5 W$, respectively.

C3.0 REFERENCES

Abramowitz, M., and Stegun, I, (1965), Handbook of Mathematical Functions, Dover, New York, New York.

Timoshenko, S. P., and Goodier, J. N., (1970), Theory of Elasticity, 3rd edition, McGraw Hill, New York, New York.

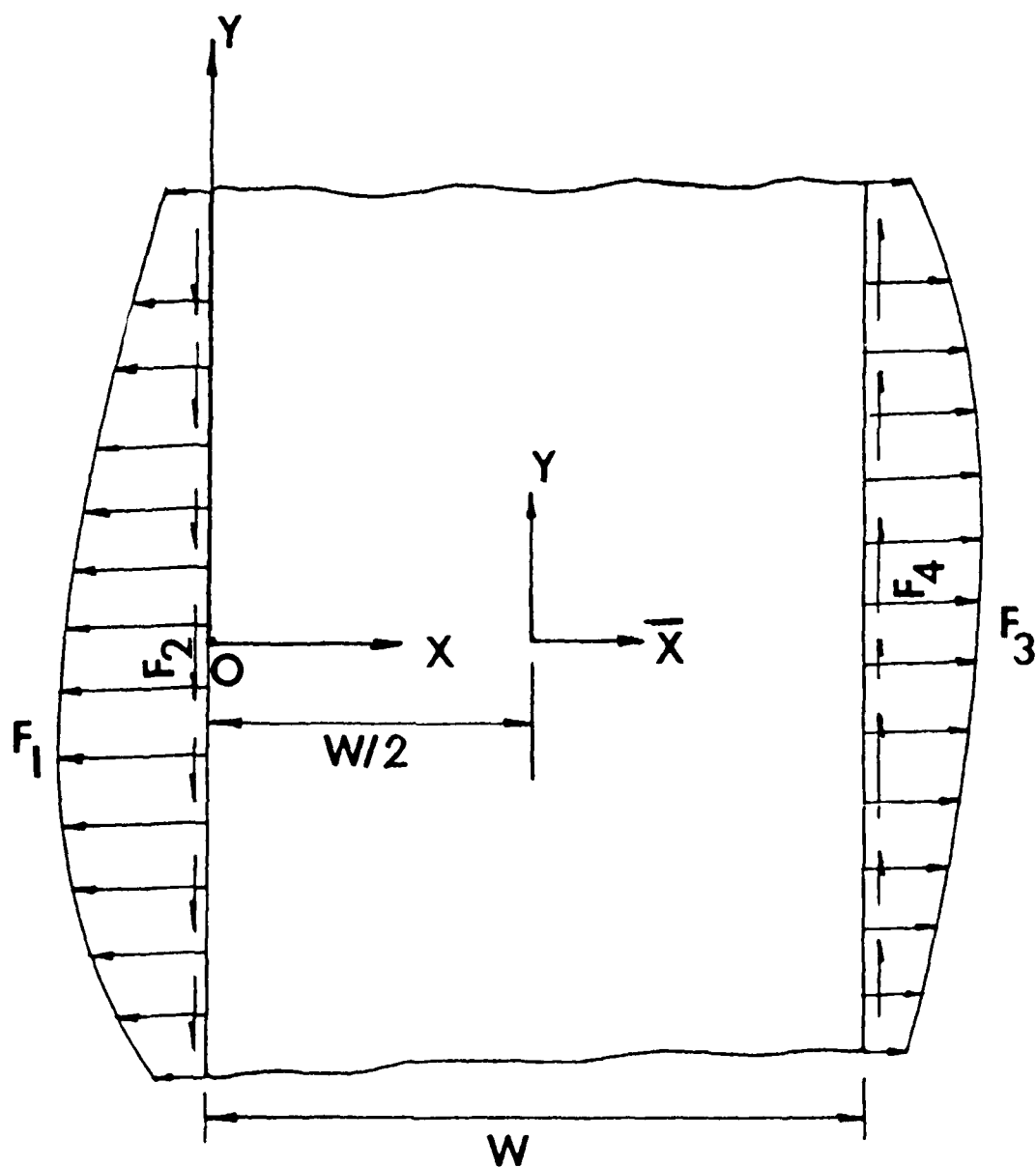


Figure C-1. A Plate Strip Subjected to Arbitrary Edge Loads

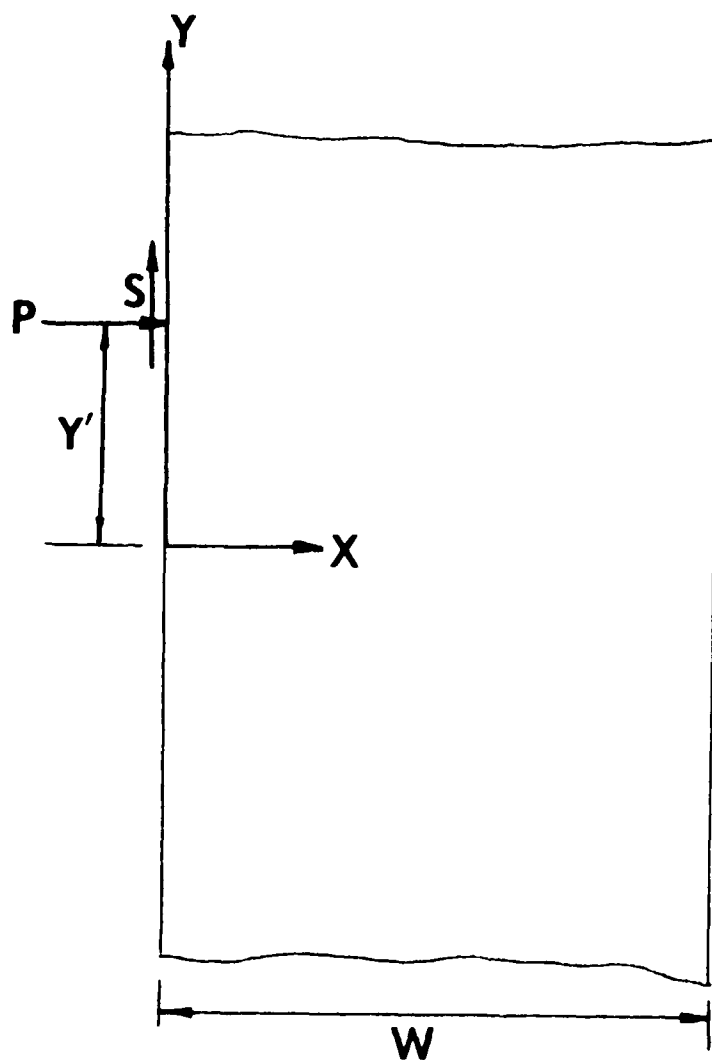


Figure C-2. Two Basic Loading Cases

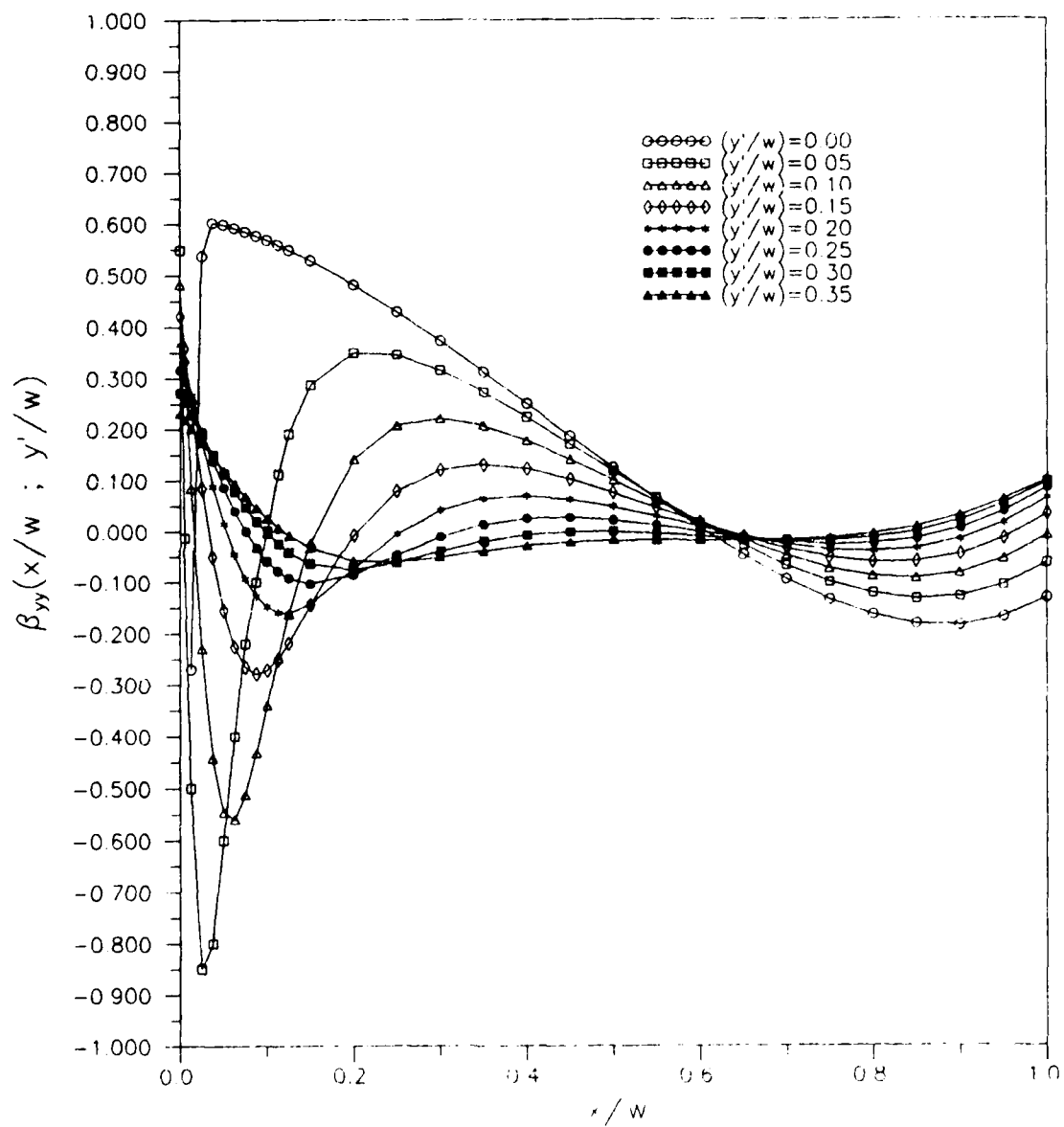


Figure C-3.

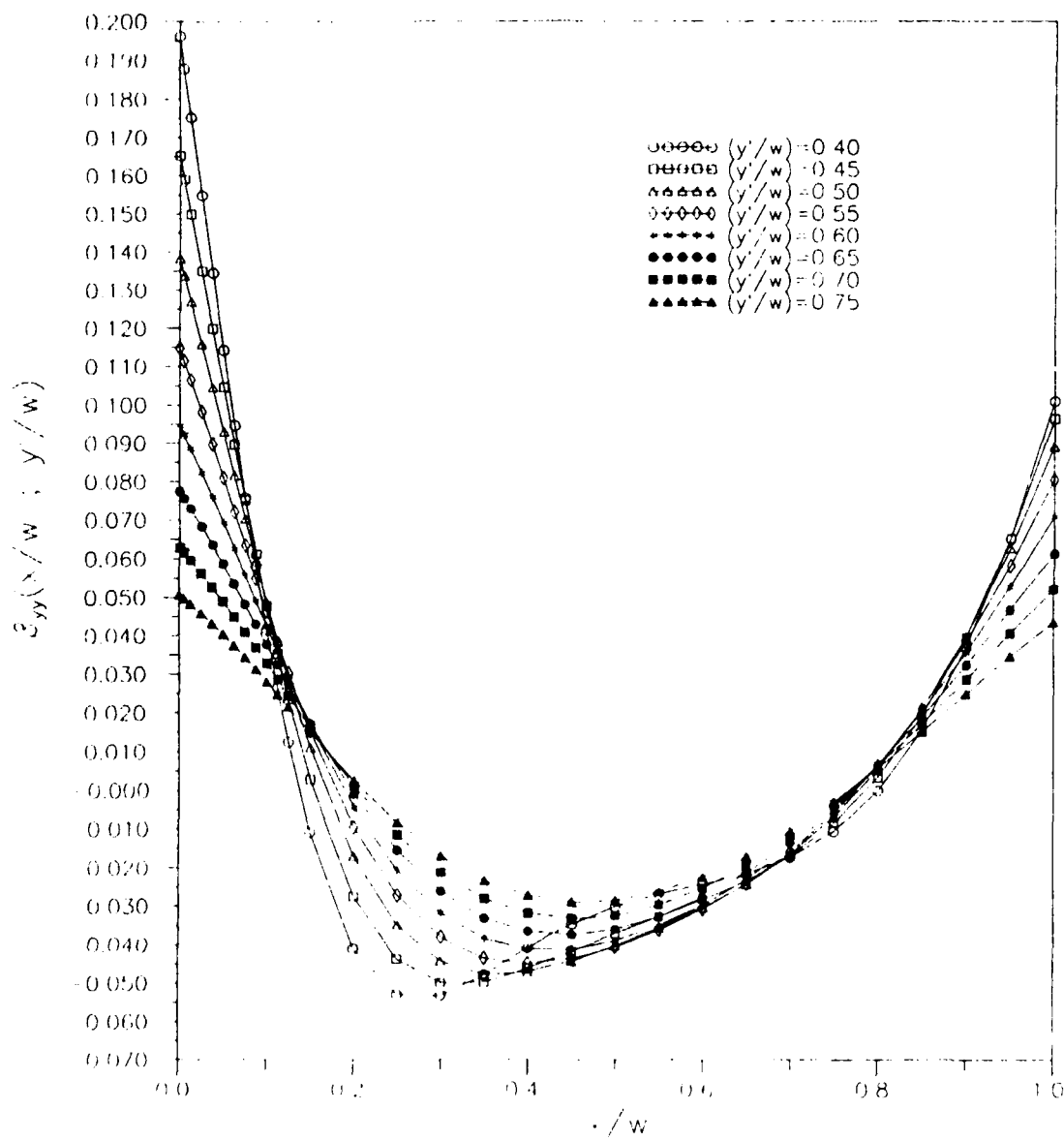


Figure C-4.

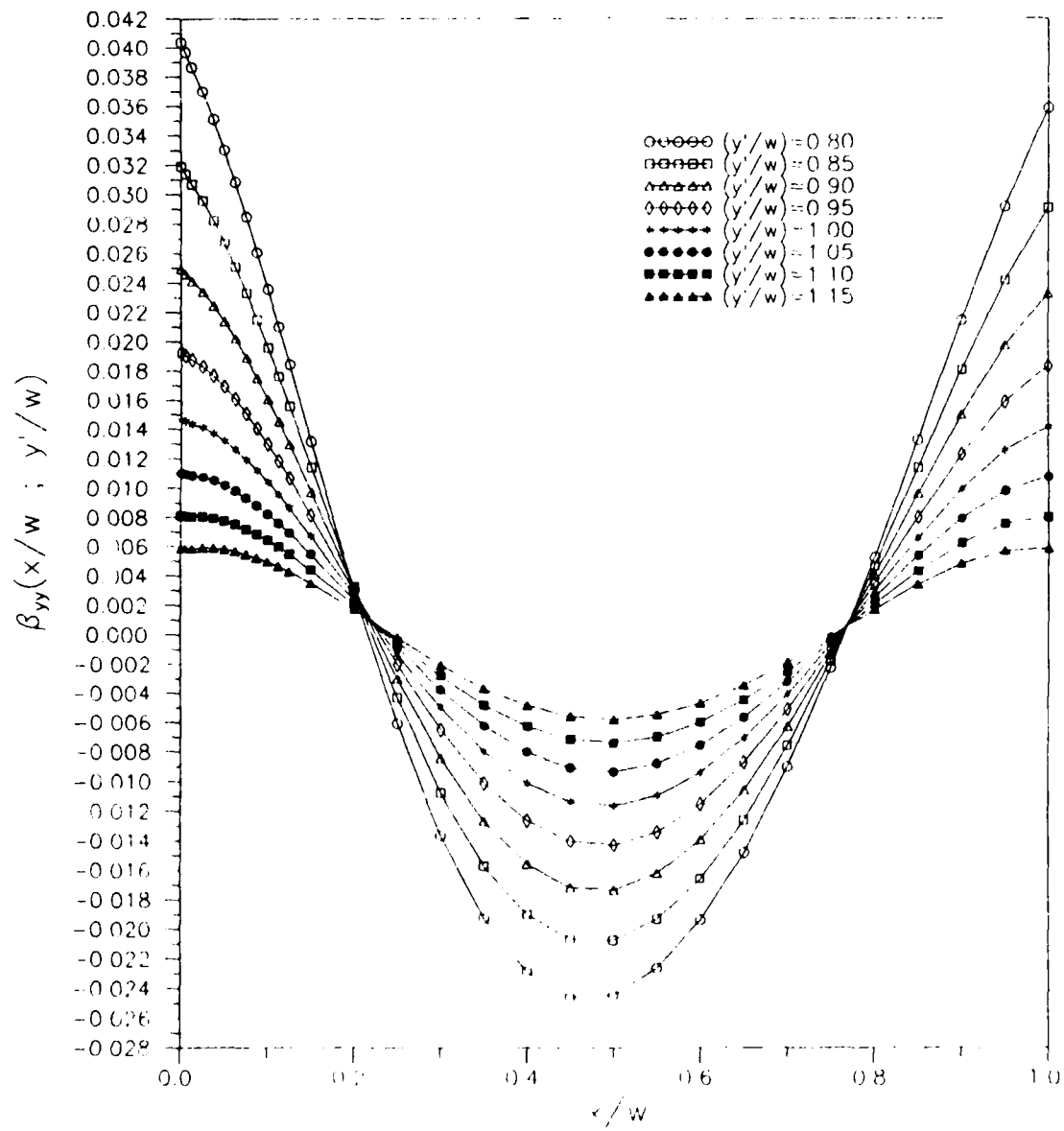


Figure C-5

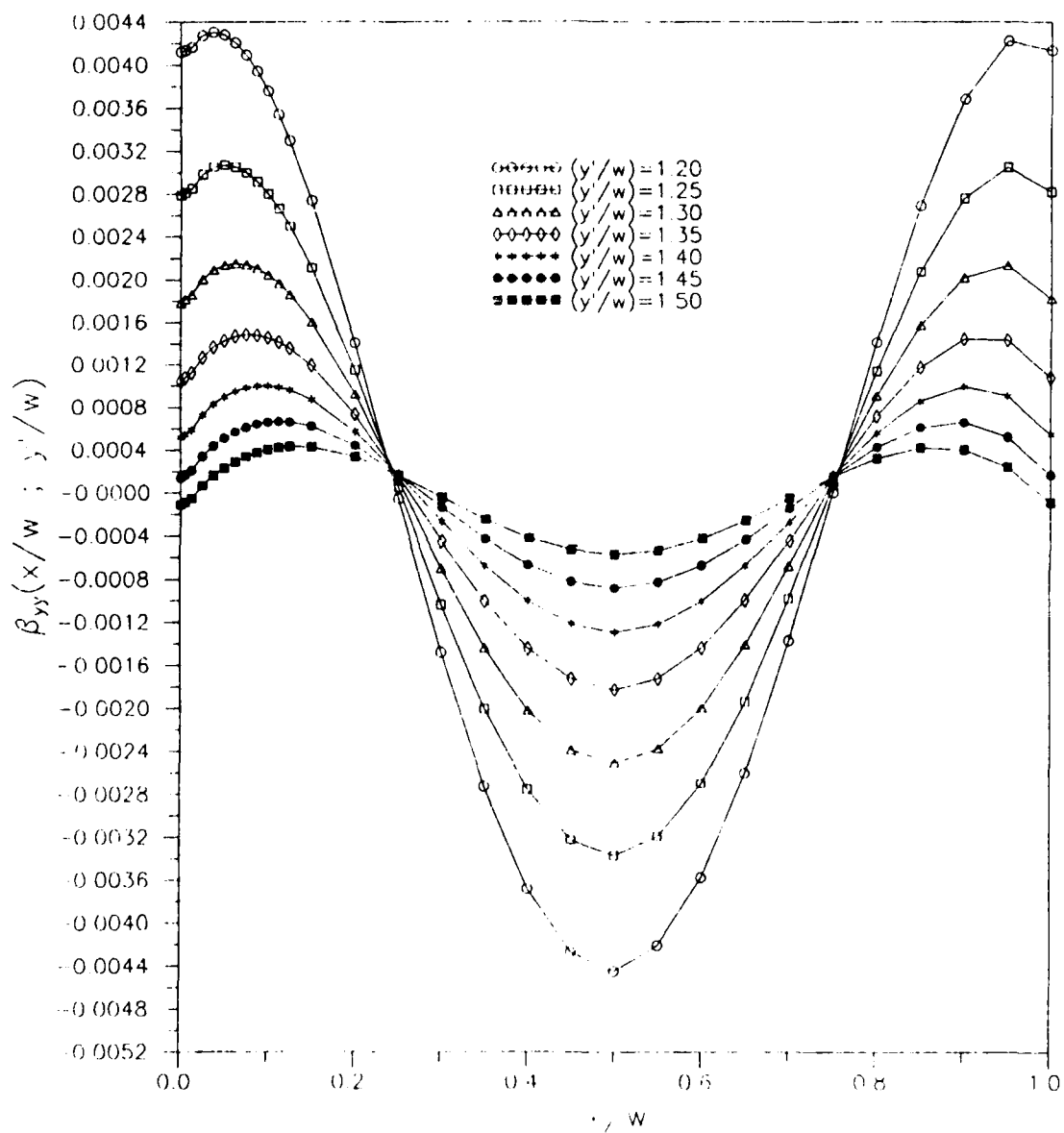


Figure C-6

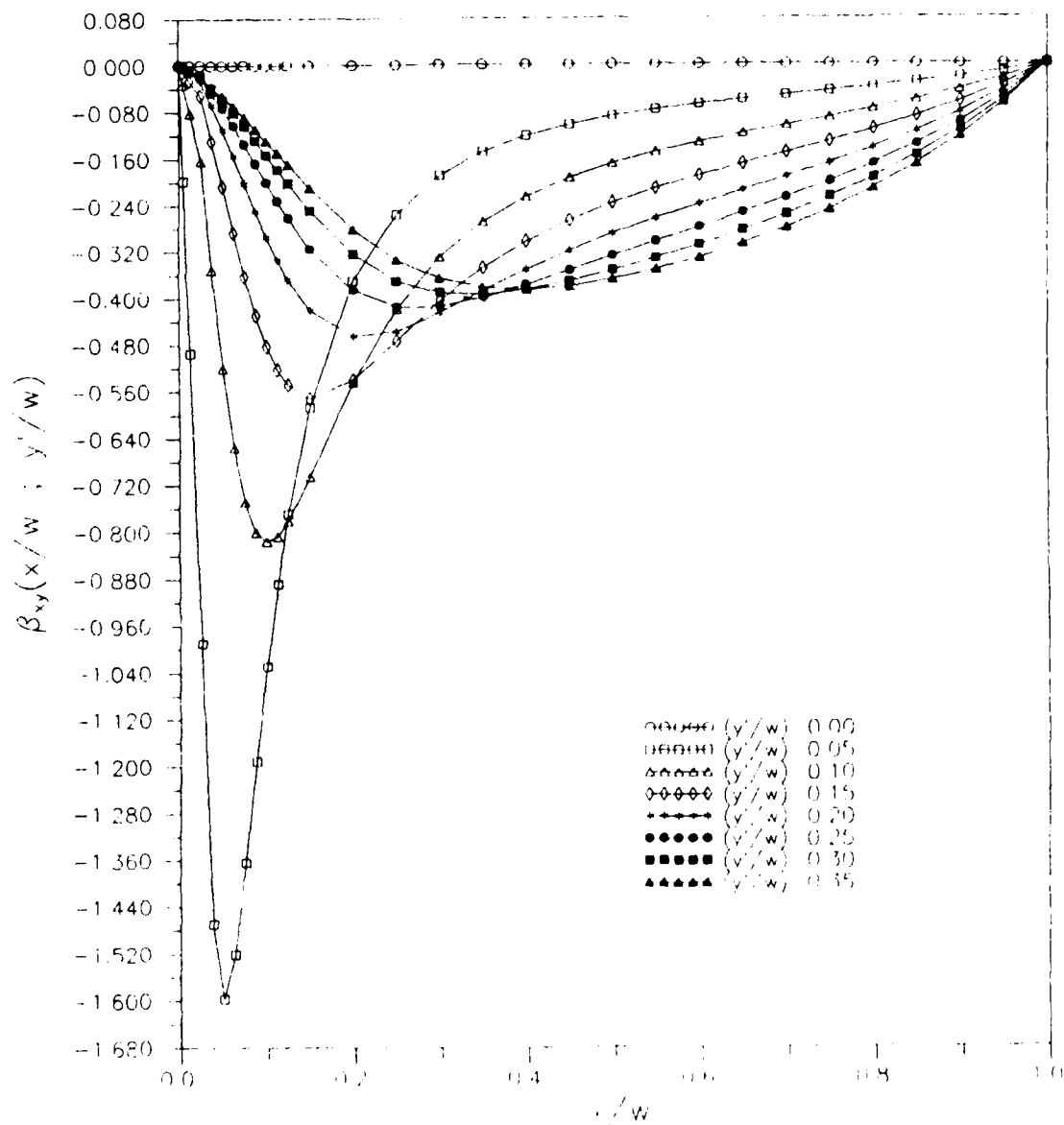


Figure C-7

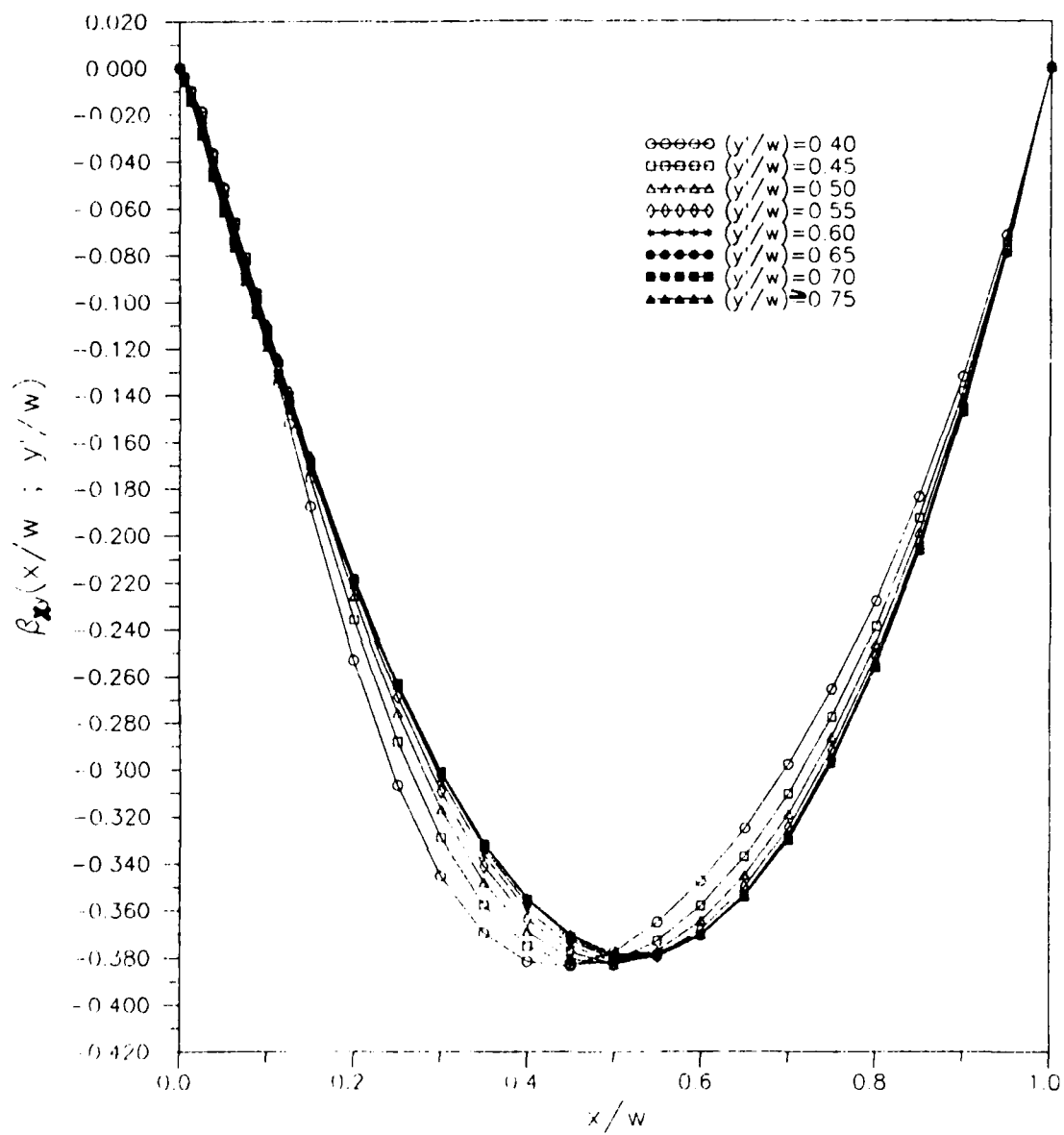


Figure C-8

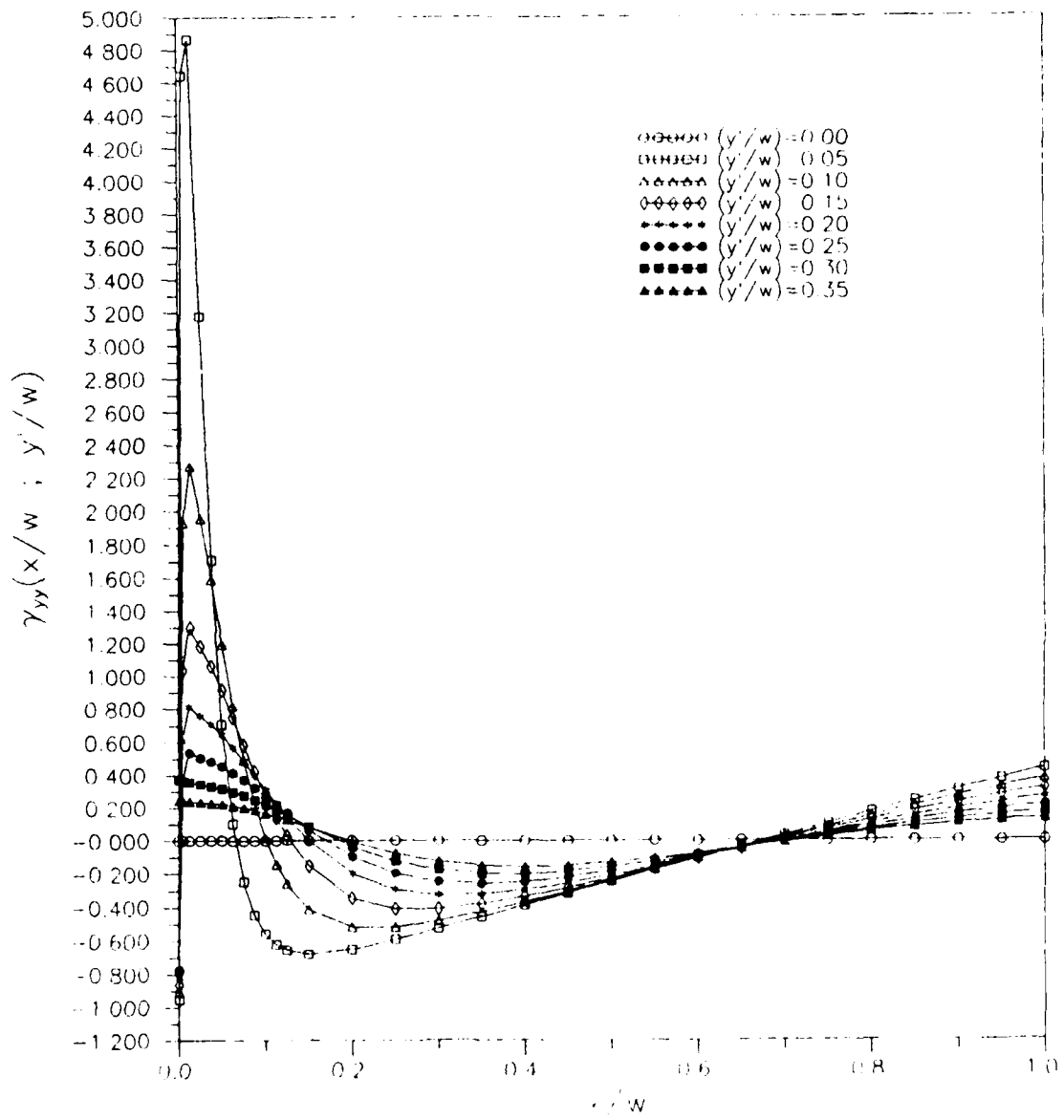


Figure C-9

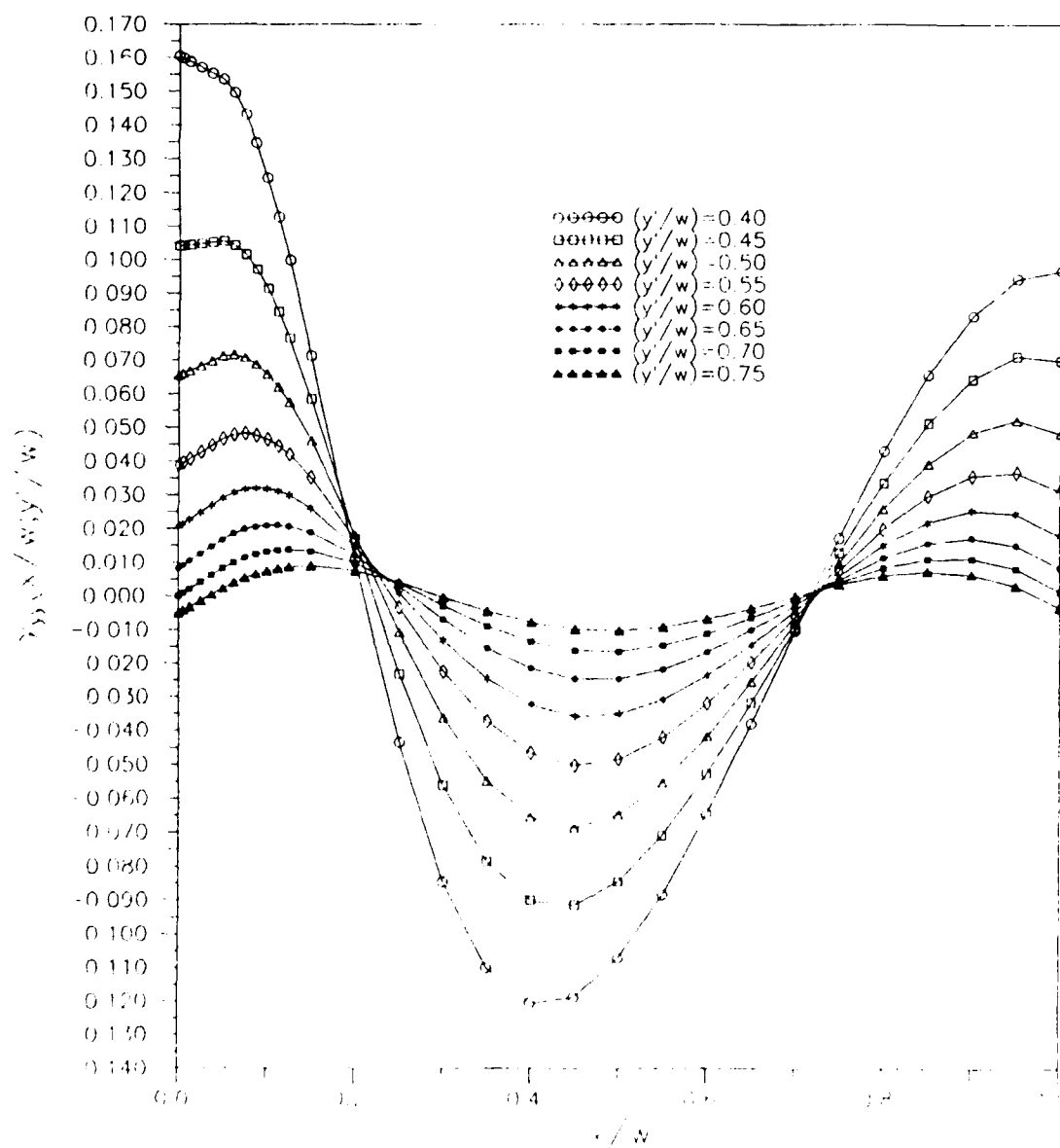


Figure C-10

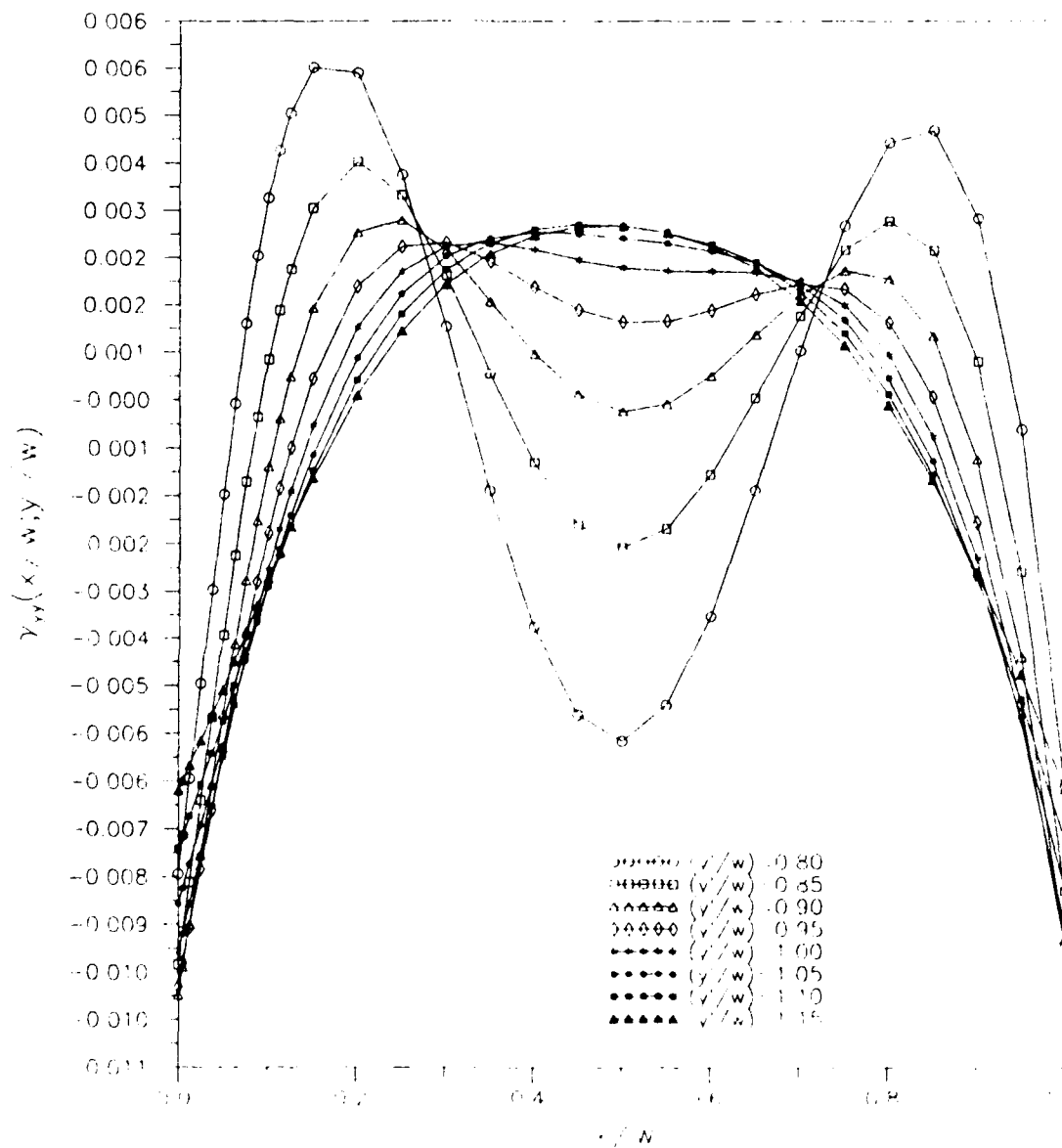


Figure C-11

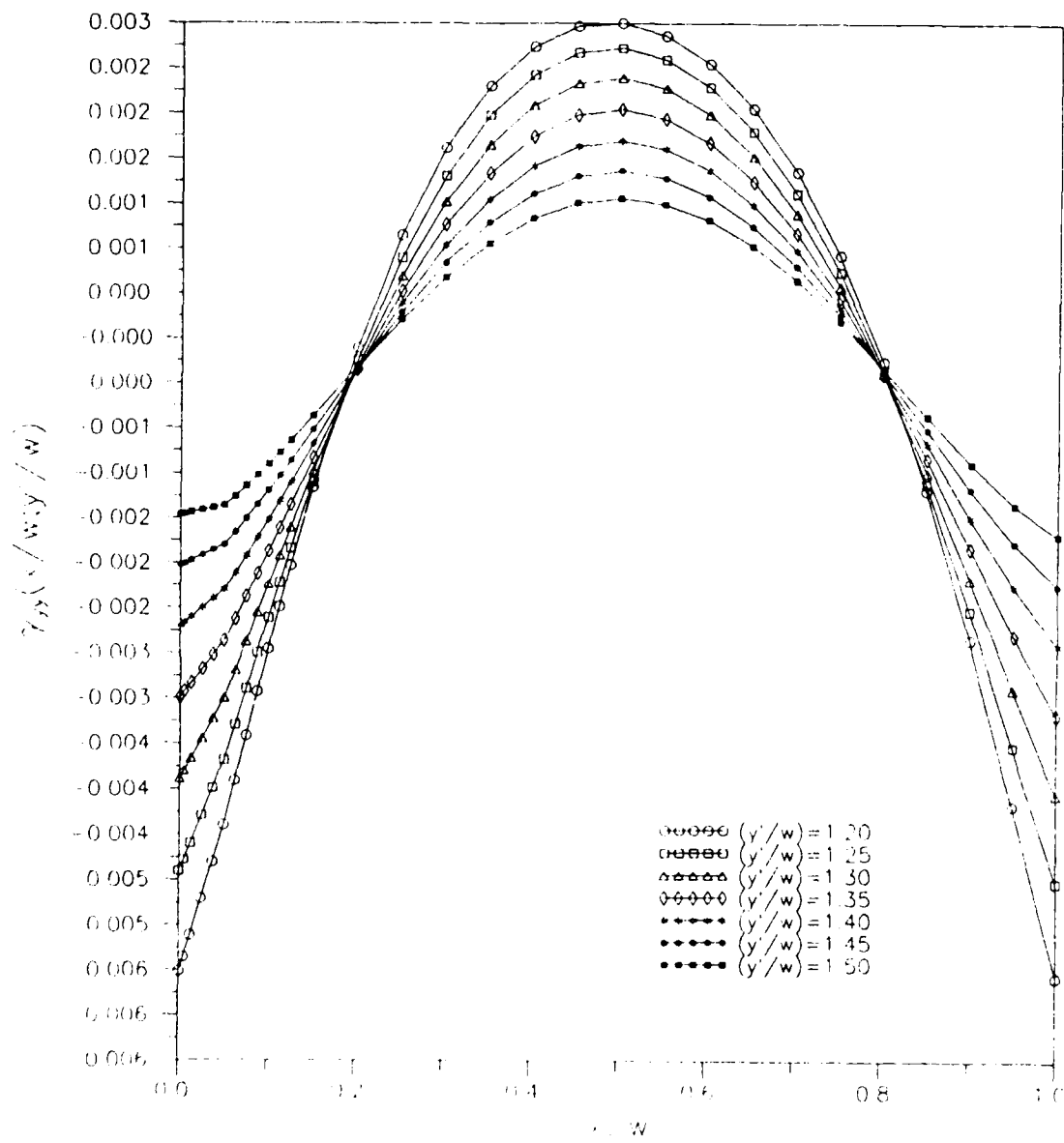


Figure C-12

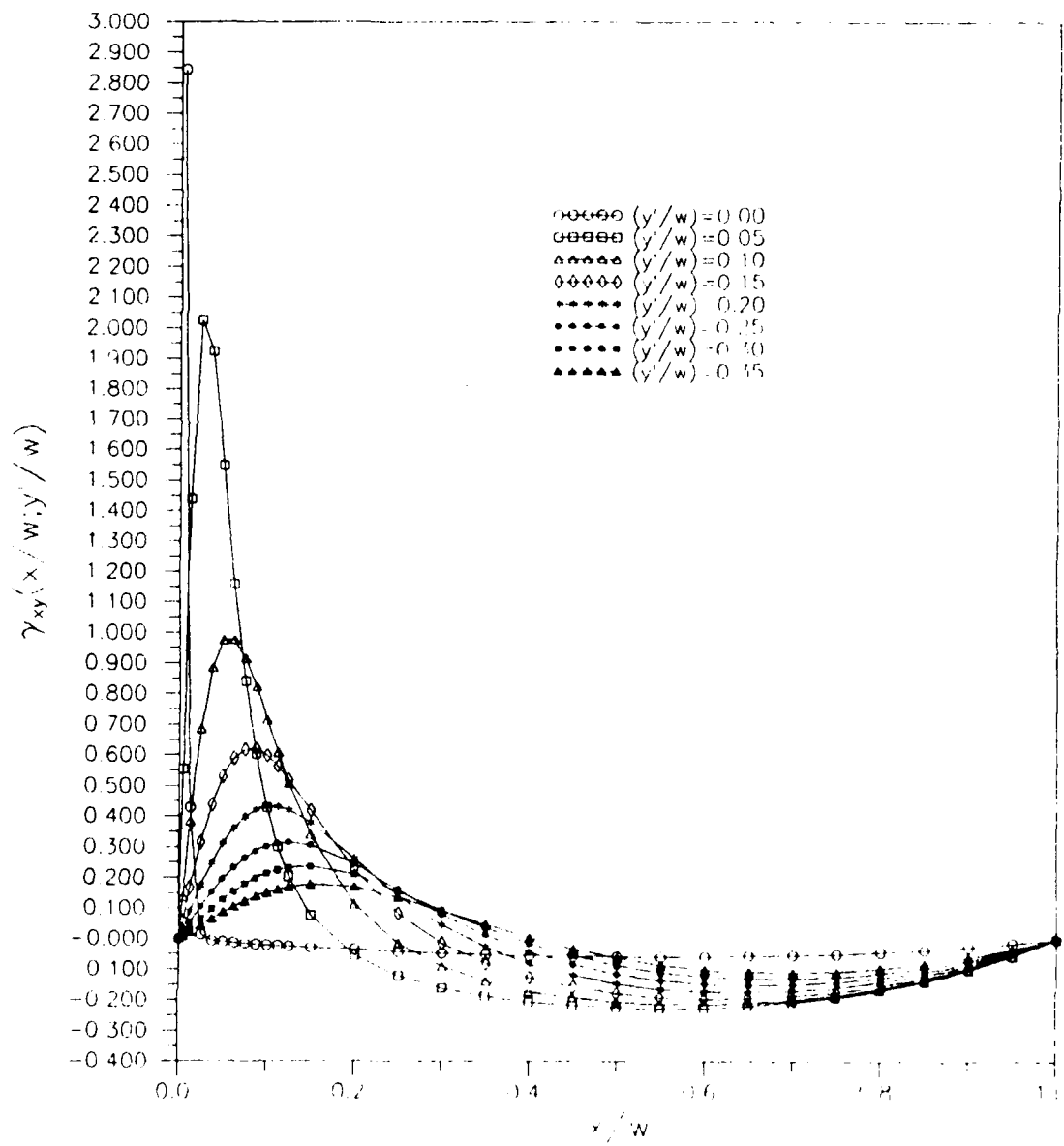


Figure C-13

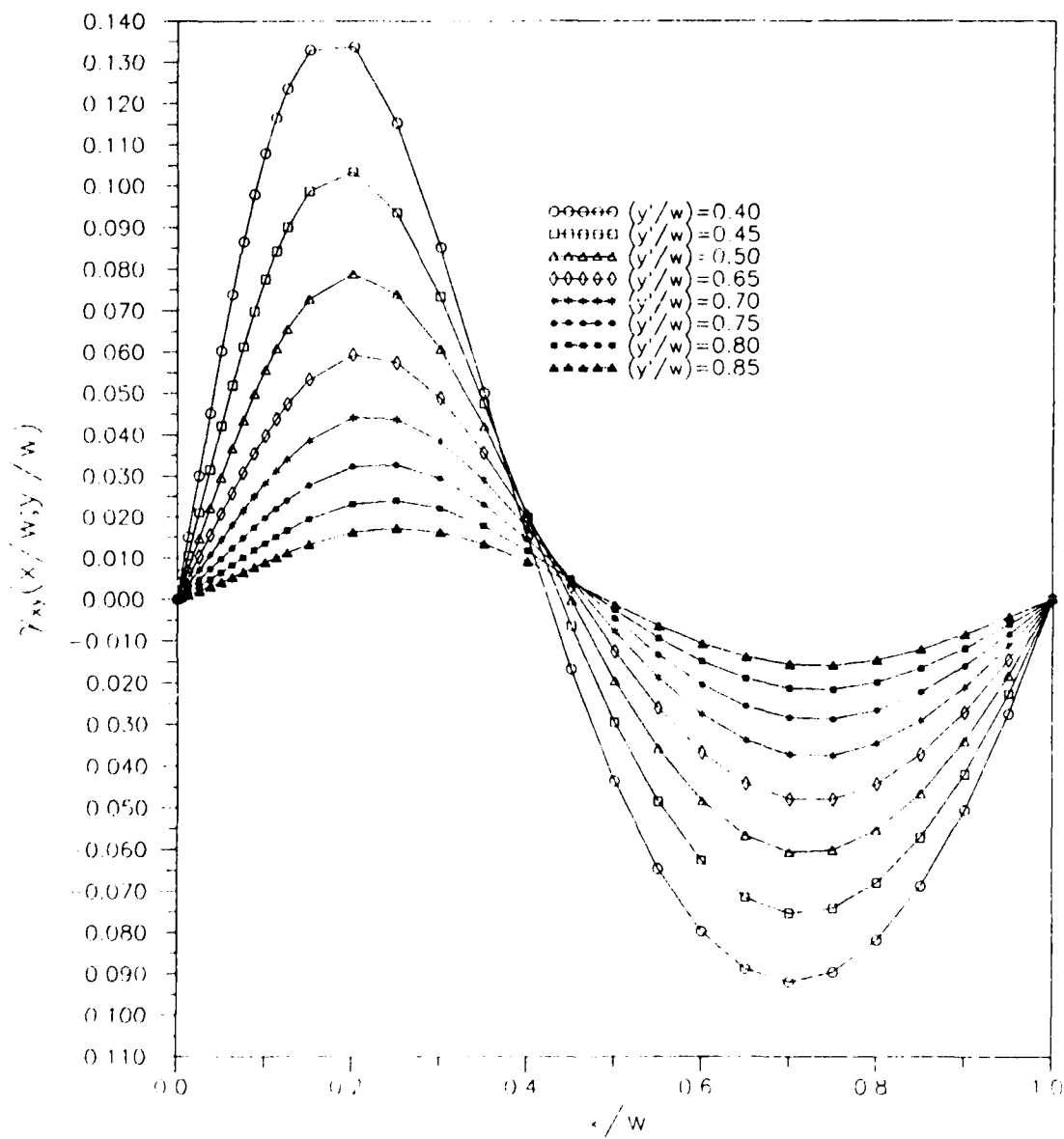


Figure C-14

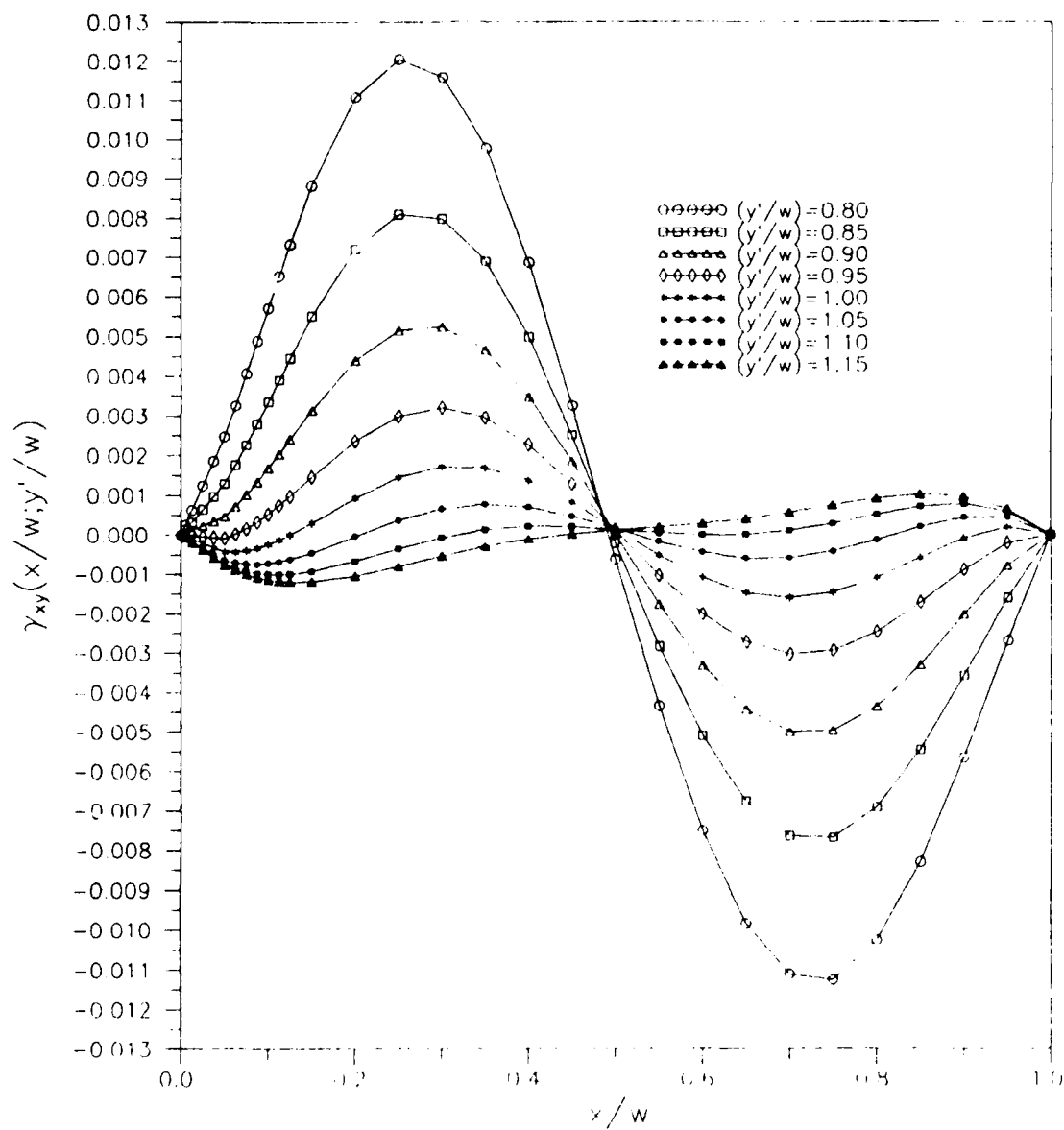


Figure C-15

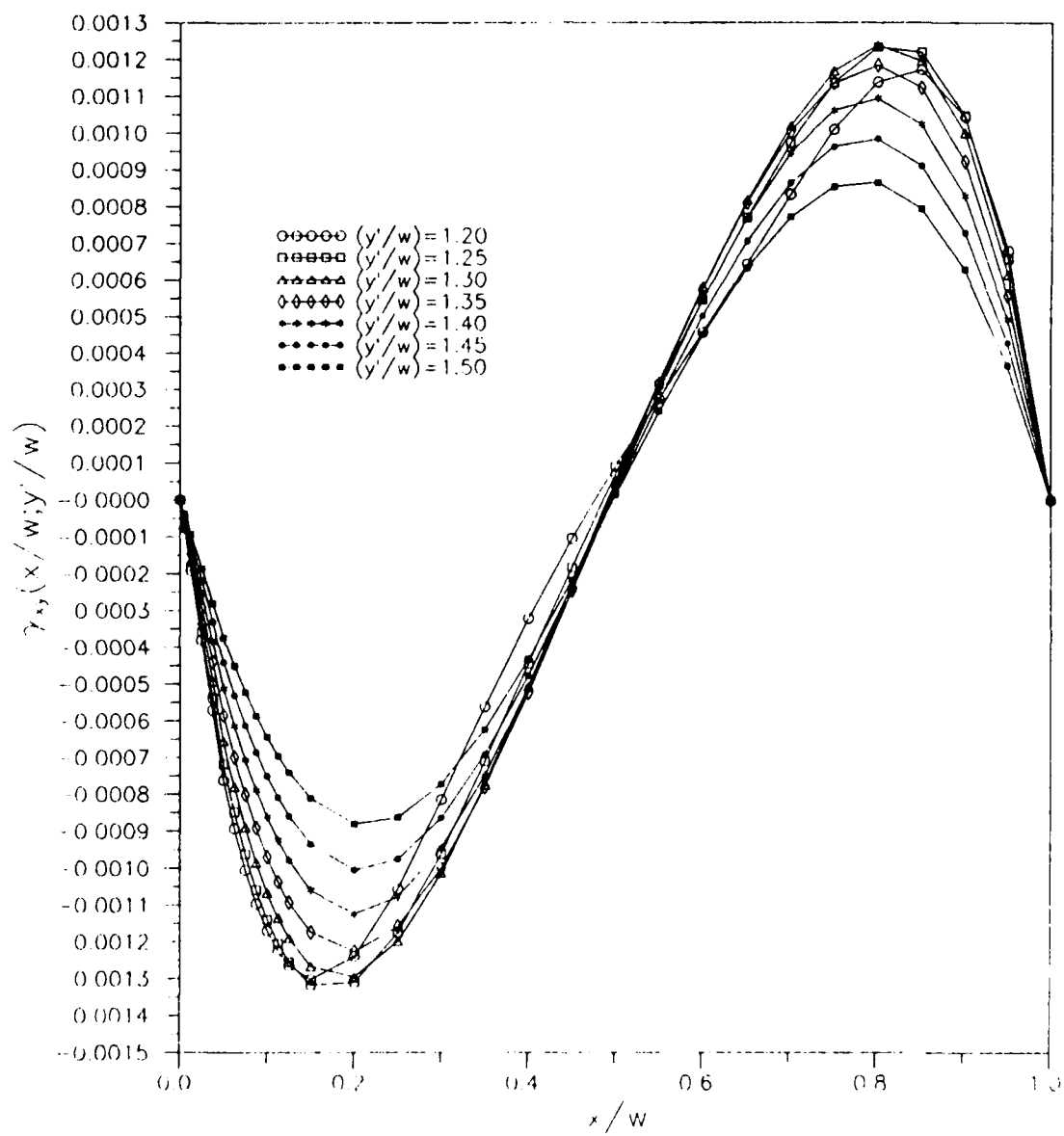


Figure C-16

Appendix D

INFLUENCE FUNCTIONS FOR SEMICIRCULAR CRACK
IN A SEMI-INFINITE SOLID

This appendix describes the numerical procedures for the influence functions used in the THERMO-K.

D1.0 CIRCULAR CRACK IN AN INFINITE SPACE

The theory on the influence functions for circular crack in an infinite space is presented in Section 7-3. The influence functions m_1 , m_{2r} , $m_{2\theta}$, m_{3r} and $m_{3\theta}$ are presented in Equations (7-13), (7-48), (7-49), (7-58) and (7-59).

The integrals in Equations (7-6) to (7-8) are double integral in the radial, r , and angular, θ , directions. To evaluate these double integrals, numerical integration procedures, Gaussian quadrature and Chebychev-Gauss Quadrature, are utilized. Equations (7-6) to (7-8) can be rewritten as

$$K_I(\theta) = \sum_{i=1}^{n/2} \sum_{j=1}^m \sigma_{zz}(r_i, \alpha_j) * M_1(r_i, \alpha_j, \theta) * r_i * \frac{\omega_j}{n} \quad (D-1)$$

$$K_{II}(\theta) = \sum_{i=1}^{n/2} \sum_{j=1}^m [\sigma_{zr}(r_i, \alpha_j) * M_2(r_i, \alpha_j, \theta) + \sigma_{z\theta}(r_i, \alpha_j) * M_3(r_i, \alpha_j, \theta)] * r_i * \frac{\omega_j}{2n} \quad (D-2)$$

$$K_{II}(\theta) = \sum_{i=1}^{n/2} \sum_{j=1}^m [\sigma_{zr}(r_i, a_j) * M_3(r_i, a_j, \theta) + \sigma_{z\theta}(r_i, a_j) * M_4(r_i, a_j, \theta)] * r_i * \frac{\omega_i}{2n} \quad (D-3)$$

where

$$M_1(r_i, a_j, \theta) = \frac{2\sqrt{\pi}}{\sqrt{a}} [1 + 2 \sum_{k=1}^K \left(\frac{r_i}{a}\right)^k \cos(ka_j) \cos(k\theta)] \quad (D-4)$$

$$M_2(r_i, a_j, \theta) = \frac{2\sqrt{\pi}}{\sqrt{a}(2-\nu)} \left\{ (2-\nu) * \left(\frac{r_i}{a}\right) + 2 \sum_{k=1}^K [1 + k\nu + (1-\nu-k\nu) * \left(\frac{r_i}{a}\right)^2] * \left(\frac{r_i}{a}\right)^{k-1} \cos(ka_j) \cos(k\theta) \right\} \quad (D-5)$$

$$M_3(r_i, a_j, \theta) = \frac{-4\sqrt{\pi}}{\sqrt{a}(2-\nu)} \left\{ \sum_{k=1}^K [1 - k\nu + (1+k\nu) * \left(\frac{r_i}{a}\right)^2] * \left(\frac{r_i}{a}\right)^{k-1} \sin(ka_j) \sin(k\theta) \right\} \quad (D-6)$$

$$M_4(r_i, a_j, \theta) = \frac{-4\sqrt{\pi}}{\sqrt{a}(2-\nu)} \left\{ \sum_{k=1}^K [1 - \nu(1+k)] * \left(\frac{r_i}{a}\right)^{k-1} \cos(ka_j) \sin(k\theta) \right\} \quad (D-7)$$

$$M_5(r_i, a_j, \theta) = \frac{4\sqrt{\pi}}{\sqrt{a}(2-\nu)} \left\{ \sum_{k=1}^K [1 - \nu(1+k) + (1+k\nu) * \left(\frac{r_i}{a}\right)^2] * \left(\frac{r_i}{a}\right)^{k-1} \sin(ka_j) \sin(k\theta) \right\} \quad (D-8)$$

$$r_i = a * \cos\left(\frac{2i-1}{2n}\pi\right) \quad (D-9)$$

$$\alpha_j = \frac{\pi}{2} (1 + \xi_j) \quad (D-10)$$

where ω_j is the weight functions of Gaussian integration and ξ_j is the Gaussian integration points.

D2.0 SEMICIRCULAR CRACK IN A SEMI-INFINITE SPACE

To obtain the stress distribution for a semicircular crack in an semi-infinite space, the first task is to solve Equation (7-34) numerically. First the equation is rewritten as follow:

$$I_{M,N}^n(\rho, \zeta) = \sum_{i=1}^{\infty} \int_{j_i}^{j_{i+1}} e^{-t|\zeta|} t^{n-1/2} J_M(\rho t) J_{N+1/2}(t) dt \quad (D-11)$$

If $\rho < 1$, j_i is the i th zero of $J_M(\rho t)$. If $\rho > 1$, j_i is the i th zero of $J_{N+1/2}(t)$. The zeros for the Bessel functions J_M and $J_{N+1/2}$ are determined, Olver (1960), using a 4-point Lagrangian interpolation formula as followed:

$$j_{n,s} = \frac{\beta_2 \beta_3 \beta_4 x_1}{(\beta_2 - \beta_1)(\beta_3 - \beta_1)(\beta_4 - \beta_1)} + \frac{\beta_1 \beta_3 \beta_4 x_2}{(\beta_1 - \beta_2)(\beta_3 - \beta_2)(\beta_4 - \beta_2)} \\ + \frac{\beta_1 \beta_2 \beta_4 x_3}{(\beta_1 - \beta_3)(\beta_2 - \beta_3)(\beta_4 - \beta_3)} + \frac{\beta_1 \beta_2 \beta_3 x_4}{(\beta_1 - \beta_4)(\beta_2 - \beta_4)(\beta_3 - \beta_4)} \quad (D-12)$$

where $j_{n,s}$ is the s th zero of Bessel function j of n th order and $\beta_i \equiv J_n(x_r)$ for $r = 1, 2, 3$, and 4 . To determine the zeros for Bessel function, the first zero is picked arbitrarily, then x_r is chosen at $\pm h$ and $\pm 2h$ of the arbitrarily zero where h is set as $\pi/10$. Then the zero $j_{n,s}$ is calculated using Equation (D-12). This value is back substituted into the Bessel function using the procedures described in Press, et. al. 1986, (pp 170-176). This

process is repeated until J_n is within a convergence criteria or equal to zero. When all the zeros are determined, then the Equation (D-11) is integrated by 3 points Gaussian Quadrature between successive zeros.

The next step is to set up the influence function $\Omega_i(x, z; \hat{r}, \hat{\theta})$, Equation (7-17) and the corresponding stress σ_{yy} , Equations (7-16), (7-51), and (7-62). First, the equations for σ_{yy} are rewritten, using Gaussian Quadrature, as:

$$\sigma_{yy}(x, 0, z) = \sum_{p=1}^{n/2} \sum_{q=1}^m \sum_{i=1}^3 \frac{\Omega_i(x, z; r_p, \alpha_q) \sigma_{zi}}{\pi^2 \sqrt{(a^2 - r_p^2)}} \frac{r_p}{2n} \omega_q \quad (D-13)$$

$$r_p = a \cos\left(\frac{2i-1}{2n}\pi\right) \quad (D-14)$$

$$\alpha_q = \frac{\pi}{2}(1 + \xi_j) \quad (D-15)$$

where n is the number of Chebychev points, m is the number of Gaussian points, ξ_j is the Gaussian integration points and ω_j is the weight function for Gaussian integration.

The σ_{yy} at $(x, 0, z)$ is due to the points loads at (r_p, α_q) and $(r_p, -\alpha_q)$ at the crack surface and Ω_i is due to σ_{zi} where $i = (z, \theta, r)$. Due to lengthy computation time, the crack surface is divided into six segments, a compromise between accuracy and computer time. The size of the six segments is 1° , 87° , 1° , 1° , 87° and 1° point from 0° to 180° along the crack front with 0° and 180° at the symmetry surface, $y = 0$. Smaller segments are chosen at 0° , 90° and 180° because the calculation of K_i , $i=I, II$ and III is chosen only for these three crack angles. Three Gaussian integration points and four Chebychev integration points are used for each segment. The influence function Ω_i is obtained

using Equation (7-17) for unit load case at all Gaussian and Chebychev integration points and saved as a data file for latter use.

The singularities of stress, σ_{yy} , at the symmetry surface, $y = 0$, near the crack tip is treated according to the formulation, Hartranft and Sih (1974). The symmetry surface is divided into six regions as shown in Figure D-1. The stress are computed at fewer points and the six point bivariate interpolation formula is used to get the values at the remaining points with the region. The number in parentheses in Figure D-1 is the number of values of x and the number of values of z . The stresses are calculated using Equation (D-13). The number in the brackets is the number of locations where stresses are obtained by six point bivariate interpolation formula. The six point bivariate interpolation is shown as follow:

$$\begin{aligned} f(x_0+ph, y_0+qk) = & \frac{q(q-1)}{2} f_{0,-1} + \frac{p(p-1)}{2} f_{-1,0} \\ & + (1 + pq - p^2 - q^2) f_{0,0} \\ & + \frac{p(p-2q+1)}{2} f_{1,0} \\ & + \frac{q(q-2p+1)}{2} f_{0,1} + pq f_{1,1} + O(h^3) \end{aligned} \quad (D-16)$$

where $h = x_{i+1} - x_i$ and $f_p = f(x_0 + ph)$, (p not necessarily integer).

For region I, it is closest to the crack tip. The stress σ_{yy} in this region is calculated as followed, Hartranft and Sih (1974),

$$\sigma_{yy}(x, 0, z) = \nu \sqrt{\pi} K \left[\frac{\cos\left(\frac{\phi_1}{2}\right)}{\sqrt{(2\rho_1)}} + \frac{\cos\left(\frac{\phi_2}{2}\right)}{\sqrt{(2\rho_2)}} \right] \quad (D-17)$$

where K is the average value of K_i at 0° and 180° and ρ and ϕ are defined as in Figure D-2.

D3.0 REFERENCES

Hilderbrand, F. B., "Introduction to Numerical Analysis," 2nd Edition, McGraw-Hill Book Company, 1974.

Press, W. H., Flannery, B. P., Teukolsky, S. A., and Vetterling, W. T., "Numerical Recipes, The Art of Scientific Computing," Cambridge University Press, 1986.

Olver, F. W., "Bessel Functions, Part III, Zeros and Associated Values," Royal Society Mathematical Tables, Vol. 7, University Press, Cambridge, 1960.

Abramowitz, M. and Stegun, I. A., "Handbook of Mathematical Functions With Formulas, Graphs, and Mathematical Tables," National Bureau of Standards, Applied Mathematics Series 55, November, 1970.

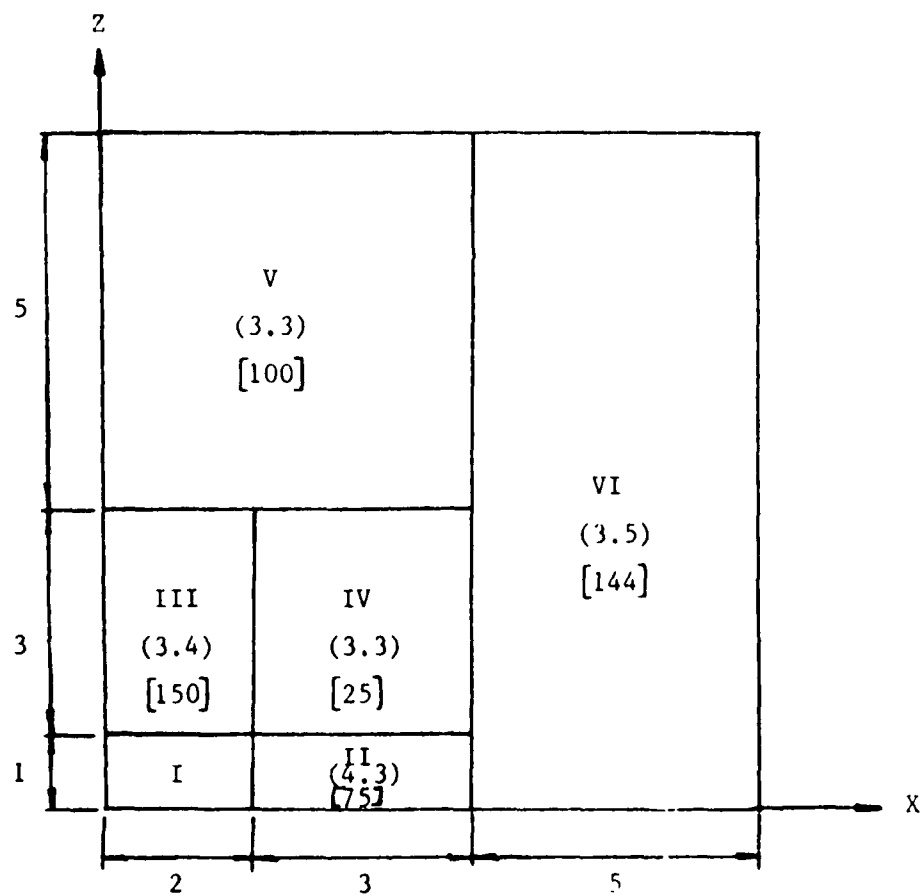


Figure D-1. Grid on Surface of Half-Space

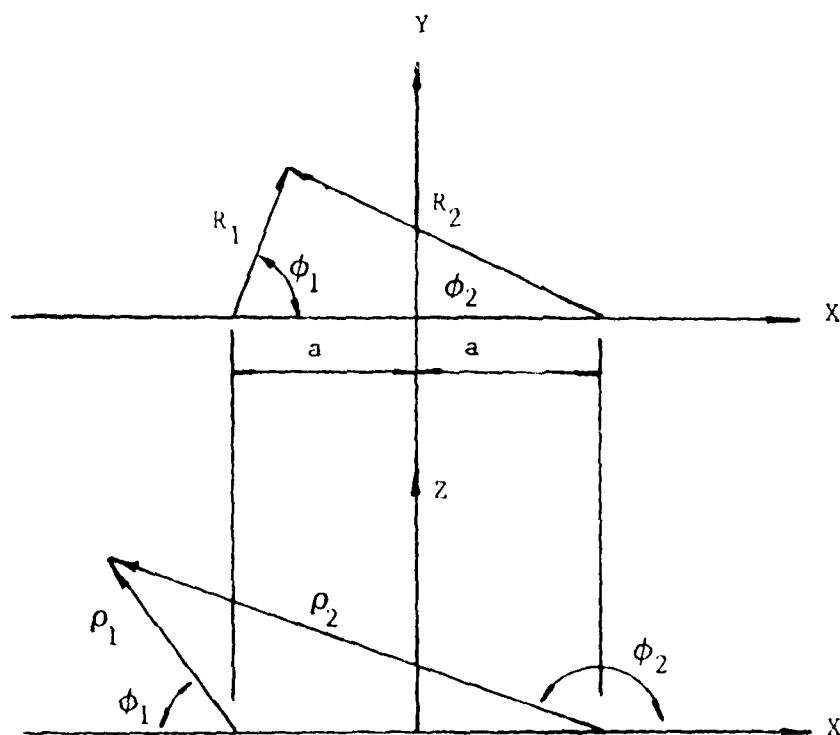


Figure D-2. Auxiliary Coordinate for Singular Solutions

Appendix E

Determination of the Coefficients for the
Approximated Mapping Function in Equation (4-8b)

E1.0 Expressions for A_n

This Appendix lists a recursive procedure for calculating the coefficients A_n 's in Equation (4-8b) for the approximated mapping function. Coefficients A_n 's are calculated by

$$A_1 = 1 + \epsilon \quad (E-1)$$

$$A_2 = (3 + 2\epsilon - \epsilon^2)/4 \quad (E-2)$$

$$A_n = \{C_n + 2\epsilon C_{n-1} + C_{n-2} - E_n + 2E_{n-1} - E_{n-2} + 4[1+(2-n)\epsilon] A_{n-1} + 2(2-n)A_{n-2}\}, \quad 3 \leq n \leq M \quad (E-3)$$

$$A_{M+1} = [(M+2)S_1 - S_2]/M \quad (E-4)$$

$$A_{M+2} = [-(M+1)S_1 + S_2]/(M+1) \quad (E-5)$$

where ϵ is defined in Equation (4-10), $(M+2)$ is the total number of terms included in Equation (4-8b), and

$$C_1 = C_2 = 0 \quad (E-6)$$

$$C_n = \sum_{k=2}^{n-1} (1-k)(1-n+k)A_k A_{n-k}, \quad n \geq 3 \quad (E-7)$$

$$E_1 = 0, \quad E_2 = A_1^2 = (1+\epsilon)^2 \quad (E-8)$$

$$E_3 = \sum_{k=1}^{n-1} A_k A_{n-k} \quad (E-9)$$

$$S_1 = 1 + \sum_{n=2}^M (1-n)A_n \quad (E-10)$$

$$S_2 = [2 + \sqrt{(1+\epsilon)/2} + \sqrt{2/(1+\epsilon)}] + \sum_{n=2}^M n(1-n)A_n \quad (E-11)$$

It should be noted that expressions for A_{M+1} and A_{M+2} in Equations (E-4) and (E-5) are derived from the conditions of

$$\omega'(1) = 0 \quad (E-12)$$

and

$$\omega''(1) = \frac{R}{1-\epsilon} [2 + \sqrt{(1+\epsilon)/2} + \sqrt{2/(1+\epsilon)}] \quad (E-13)$$

as recommended by Bowie (1973).

E2.0 References

Bowie, O. L., (1973), "Solution of Plane Crack Problem by Mapping Technique," in Method of Analysis and Solutions of Crack Problems, Vol. 1, ed. G. C. Sih, pp. 1-55, Noordhoff, Holland.